Investigation of the Mechanism of Radical Propagation in *E. coli* Ribonucleotide Reductase by Site-Specific Incorporation of Unnatural Amino Acids

by

Mohammad R. Seyedsayamdost

B.A./M.S. Biochemistry, B.S. Biology
Brandeis University, 2001

Submitted to the Department of Chemistry
in Partial Fulfillment of the Requirements for the Degree of

Doctor of Philosophy in Biological Chemistry

at the
MASSACHUSETTS INSTITUTE OF TECHNOLOGY
(February 2008)
October 2007

Signature of Author: _____
Department of Chemistry
October 25, 2007

Certified by: _____
JoAnne Stubbe
Novartis Professor of Chemistry and Professor of Biology
Thesis Supervisor

Accepted by: _____
Robert W. Field
Haslam and Dewey Professor of Chemistry
Chairman, Departmental Committee on Graduate Students

This Doctoral Thesis has been examined by a committee of the Department of Chemistry as follows:

Stuart Licht
Professor of Chemistry
Chair

JoAnne Stubbe
Novartis Professor of Chemistry and Professor of Biology
Thesis Supervisor

Daniel G. Nocera
W. M. Keck Professor of Energy and Professor of Chemistry

TO MY MOTHER

ACKNOWLEDGEMENTS

Well, after a long, exhilarating and revelatory journey, it's finally time to convey my appreciation to all the people that have contributed to this work and to my time at MIT. I would like to first express my sincere gratitude to my advisor and mentor, the one and only, JoAnne Stubbe, whose infinite dedication and enthusiasm for science are both unique and contagious. JoAnne's determination, passion and instinct for research, and her rigorous approach will always serve as the gold standard to me. I thank her for infusing me with her way, the right way, of doing science, sharing her deep insight on a daily basis, patiently tolerating my unusual work habits and making our partnership succeed. I also thank JoAnne for her advice in my postgraduate search and feel privileged to have had the opportunity to work with her.

I thank Dan Nocera for his PCET advice, helping us interpret our data, and his cool attitude to science. I am grateful to Stuart Licht for being an excellent Thesis Chair. Stuart was always available for a chat regarding anything from RNR to Britney Spears, and helped greatly with picking a postdoctoral lab. Many thanks also to Marina Bennati for years of exciting collaboration and to Peter Schultz for sharing his method of unnatural amino acid incorporation. I am also grateful to my Brandeis mentors, Liz Hedstrom, Melissa Moore and Dan Oprian who sparked my interest in Biochemistry.

Many Stubbe lab members have contributed to this work. Cyril was a great friend and mentor when I joined the lab and he guided me with his experience and keen perception about RNR. I am thankful to Streece who was a great friend and collaborator. I enjoyed our time together; we also had a memorable outing at the GRC in Ventura, 'everybody going craaazyyy'. I would also like to thank JR who was a great and loyal friend, who taught me a lot of inorganic chemistry and EPR, and always surprised me with his humor and taste in music, Bach and Eminem? Thanks also to Ally for giving the lab a home–like feel, volleyball and some enlightening late night chats about life and kids.

Debbie has been a great friend and I hope we can have many more coffee trips at HMS. Jamin was very kind and accommodating when I first joined the lab, Aaron and Jelena always made time to chat and help out and Jesse made the Scripps trip interesting. Chia brought a whole new culture of juice, cooking and snacking to the Stubbe lab – thanks for the graduation parties.

Dani was very supportive and a lot of fun, when are you gonna be back? Luke represented the Fashizzle lab in style. Kapil was a frequent late night labbie. Clement helped a lot with putting NH_2Y into $\alpha 2$ and provided for entertainment along with Jun. Q and Sumit brought some good old 3rd world fun to the lab. I also thank former and present Stubbe–ites Hiroshi, Naoko, Rachael, Joey, Michelle, Mimi, Jenny, Aimin, Ping, Daniel, Pinghua, Greg, Natalia, Ellen, Lenore, Lana and YT. In addition, many thanks to Jianming for teaching me the selection process in the Schultz lab as well as to Lubica, Eric and John for their support.

I would also like to thank people outside of lab. Pdiddy, scope & coffee at LaVerde's? I enjoyed lots of good times, and hopefully lots more to come, with Lil B, who helped crucially toward the end of Thesis writing. T, Will and Pdiddy, how about Caprice? RC, get back to Boston and let's hang out. Jess and BigAins have been great Drennan lab comrades, 'Jess, did we drop off Ains?' And then there's Luke, aka Bobbsey II. 'Walking into the wall?' and 'coffee in an hour' kept us going on the TR project. Many thanks also to Susan Brighton for spreading calmness and tranquility in a stress–packed environment.

And finally, and most importantly, I would like to express my deepest gratitude to my Mom and Dad, my Sisters, Elham and Nahid and my Brother, Hamid. For me, life started on the eve of war in Iran and the only reason I had the opportunity to partake in the MIT grad school voyage is because of my parents' many sacrifices and their dedication to a better education for their children. I dedicate this Thesis with all my love, gratitude and admiration to my mother, without whose unwavering devotion, this would not have been possible. My parents and my siblings have been and continue to be a constant source of unconditional support, love, wisdom, humor and confidence in my life for which I am eternally grateful and indebted.

I'm off to the next thing. Peace and thank you all.

Investigation of the Mechanism of Radical Propagation in *E. coli* Ribonucleotide Reductase by Site–Specific Incorporation of Unnatural Amino Acids

by

Mohammad R. Seyedsayamdost

Submitted to the Department of Chemistry in Partial Fulfillment of the Requirements for the Degree of Doctor of Philosophy in Biological Chemistry

Abstract

Inside the cell, ribonucleotide reductases (RNRs) are responsible for the conversion of nucleotides to 2'–deoxynucleotides, an essential step in DNA biosynthesis and repair. The *E. coli* RNR is the best studied RNR to date and consists of two protein subunits, α2 and β2. α2 is the site of nucleotide reduction and β2 contains a diiron tyrosyl radical (Y_{122}•) cofactor. Each turnover requires radical propagation from the Y_{122}• in β2 to the active site of α2 over 35 Å. The mechanism of this unprecedented, long–range radical propagation step is poorly understood. Based on structural studies, a pathway of aromatic residues has been proposed to participate in this process. Site–directed mutants of these residues have been uninformative. In an effort to understand radical propagation, we have employed expressed protein ligation and suppressor tRNA/aminoacyl–tRNA synthetase (RS) methodologies to site–specifically insert unnatural tyrosine analogues into β2 and α2, at residues believed to be involved. On the basis of results with the radical traps 3,4–dihydroxyphenylalanine (DOPA) and 3–aminotyrosine (NH_2Y), which we have incorporated into β2 and α2, respectively, and a series of fluorotyrosines (F_nYs, n=2, 3, 4), which we have established as probes for proton–coupled electron transfer reactions and incorporated into β2, we propose a mechanism for radical transfer in RNR. We show that binding of substrate and effector are essential for control and gating of radical propagation. We further demonstrate that three Ys, β2–Y_{356}, α2–Y_{731} and α2–Y_{730}, are redox–active and participate in hole propagation. The NH_2Y• observed with NH_2Y–α2s likely constitutes the first observation of a transiently oxidized intermediate during active radical propagation. In β2, Y_{356} participates in radical transfer by an orthogonal proton–coupled electron transfer mechanism, where long–range electron transfer is coupled to short–range, off–pathway proton transfer. Within α2, Y_{731} and Y_{730} participate by a hydrogen atom transfer mechanism where the proton and electron originate from and arrive at the same moiety. We also establish the positions of these three Ys in the α2/β2 complex and present direct evidence for the reversible nature of radical propagation.

TABLE OF CONTENTS

Dedication 5

Acknowledgements 7

Abstract 11

Table of Contents 13

List of Figures 23

List of Tables 30

List of Schemes 33

Abbreviations 35

Chapter 1 – Introduction to Ribonucleotide Reductases 39

General Introduction 40

The Class Ia RNR from *E. coli* 41

Protein Subunits of Class Ia *E. coli* RNR 42

Nucleotide Reduction Mechanism 45

Mechanism of C_{439}• Formation 47

Interaction between α2 and β2 48

The Radical Propagation Pathway 49

Evidence for Radical Transfer 52

Electron Transfer in Proteins 54

PCET and Oxidation of Amino Acids 59

Analysis of the PCET Pathway in RNR 64

Our Approach to Studying Radical Transfer 69

Chapter Preview 75

References 80

Chapter 2 – Site–Specific Insertion of 3,4–Dihydroxyphenylalanine into the β2 Subunit of *E. coli* Ribonucleotide Reductase 87

INTRODUCTION 88

MATERIALS AND METHODS 93
Materials 93
MALDI–TOF MS 94
Synthesis of DOPA–22mer peptide 94
Cleavage of peptide from solid–phase resin 95
Analytical and semi–preparative RP–HPLC 96
Removal of the t–buthio–protecting group 97
Growth and expression of β2–intein–CBD 97
Semisynthesis of DOPA–β2 98
MonoQ purification of ligation mixture 99
Electron spray ionization (ESI) MS analysis of DOPA–β2 99
Quantitation of radical content by UV–vis and EPR spectroscopies. 100
Quantitation of Fe content by the ferrozine assay 100
Growth, expression and purification of wt β2 101
Growth, expression and purification of α2 103
Growth, expression and purification of *E. coli* thioredoxin 105
Growth, expression and purification of *E. coli* thioredoxin reduductase 106
TR and TRR activity assays 107
Spectrophotometric RNR assay 107
Radioactive RNR assay 107
Binding of DOPA–β2 to α2. 108
Pre–reduction of α2 109
Monitoring reactions of DOPA–β2 by stopped–flow (SF) UV-vis spectroscopy 109
Reconstruction of the DOPA•–β2 UV–vis spectrum 110
Monitoring reactions of DOPA–β2 by EPR spectroscopy 110
Generation of DOPA• and catechol• 112
Generation of apo DOPA–β2 with lithium 8–hydroxyquinoline–6–sulfonate 112
Reconstitution of apo DOPA–β2 112
Preparation of high–field EPR and PELDOR samples 112
RESULTS 114

Synthesis of DOPA–22mer 114
Generation of semisynthetic DOPA–β2 115
Activty sssays of DOPA–β2 118
Trapping of a $DOPA_{356}$•–β2 120
Kinetics of DOPA• with various substrate/effecotor pairs 123
X–Band EPR characterization 126
180 GHz EPR spectroscopy and simulation of $DOPA_{356}$• 131
X–Band PELDOR measurements 134
DISCUSSION 138
DOPA as a probe for the radical initiation pathway 138
Semisynthesis and characterization of DOPA–β2 139
Trapping of $DOPA_{356}$• 141
Asymmetry in DOPA• formation 142
Environmental differences induced by NDP/(d)NTPs around DOPA• 144
REFERENCES 148

Chapter 3 – Reversible Radical Transfer and Asymmetric Complex Formation with the Y_{356}DOPA–β2 Heterodimer of *E. coli* Ribonucleotide Reductase 151
INTRODUCTION 152
METHODS 155
Semisynthesis of DOPA–ββ' 155
MonoQ purification of the ligation mixture 155
Analysis of the diiron Y_{122}• center of DOPA–ββ' 155
Interaction between DOPA–ββ' and α2 155
Activity assays of ββ' and DOPA–ββ' 156
Formation of DOPA•–ββ' monitored by SF UV–vis spectroscopy 156
Formation of DOPA•–ββ' monitored by EPR spectroscopy 156
Kinetic simulations 157
Rapid freeze–quench (RFQ) EPR spectroscopy 157
Preparation of high–field EPR and PELDOR samples 158
Sequential–mix SF UV–vis spectroscopy 158

Reduction of Y_{122}• by hydroxyurea monitored by UV–vis spectorsocpy 158
Increasing the radical content of DOPA–ββ' 159
RESULTS 161
Purification and general characterization of DOPA–ββ' 161
Interaction between DOPA–ββ' and α2 161
Formation of DOPA•–ββ' monitored by SF UV–vis spectroscopy 162
Formation of DOPA•–ββ' monitored by EPR spectroscopy 165
Kinetic simulations 167
SF UV–vis analysis of DOPA• formation with other substrate/effector pairs 168
RFQ EPR spectroscopy with ADP/dGTP 172
EPR analysis of DOPA• formation with other substrate/effector pairs 174
PELDOR spectroscopy to determine the distance between DOPA• and Y_{122}• in DOPA–ββ'/α2 177
The fate of DOPA•–ββ'/α2 179
Reaction of DOPA•–ββ'/α2 with hydroxyurea 179
The fate of DOPA•–ββ'/α2 studied by EPR spectroscopy 184
Enhancing the radical content of DOPA–ββ' 186
Oxidation of Y_{122} by DOPA• 186
DISCUSSION 191
An asymmetric model for α2/β2 interaction 191
Sources of asymmetry in the α2/β2 complex 192
Y_{122}• distribution and aggregation state 195
Initial asymmetric interaction in DOPA–β2/α2 and DOPA–ββ'/α2 197
Structural source of initial asymmetric interaction 199
Evidence for asymmetry from other experiments 200
Cooperativity in dCDP formation 202
Multiple conformations and fast interconversion 203
Testing the asymmetry model 204
Reverse radical migration in DOPA•–ββ'/α2 204
REFERENCES 207

Chapter 4 – Site–Specific Insertion of 3–Aminotyrosine into Subunit α2 of *E. coli* Ribonucleotide Reductase: Direct Evidence for Involvement of Y_{730} and Y_{731} in Radical Propagation 209

INTRODUCTION 210

MATERIALS AND METHODS 214

Materials 214

Qualitative assay for cellular uptake of NH_2Y by LC–MS 214

Directed evolution of NH_2Y–RS in *E. coli* 215

Expression of K_7NH_2Y–Z–domain 216

Cloning of pTrc–*nrdA* 218

Generation of pTrc–*nrdA*$_{730}$TAG and pTrc–*nrdA*$_{731}$TAG 218

Cloning of pAC–NH_2Y–RS 219

Attempts at expression of $Y_{730}NH_2Y$–α2 219

Successful expression of $Y_{730}NH_2Y$–α2 and $Y_{731}NH_2Y$–α2 220

Purification of $Y_{730}NH_2Y$–α2 and $Y_{731}NH_2Y$–α2 221

Reaction of NH_2Y–α2 with β2, CDP, and ATP monitored by EPR spectroscopy 222

Kinetics of NH_2Y•–α2 formation with β2, CDP and ATP by stopped–flow (SF) UV–vis spectroscopy 222

Spectrophotometric and radioactive activity assays for RNR 223

Reaction of NH_2Y–α2 with β2, N_3ADP and dGTP monitored by EPR spectroscopy 223

RESULTS 225

Toxicity and uptake of NH_2Y 225

Evolution of an NH_2Y–specific RS 225

Expression of K_7NH_2Y–Z–domain 226

Expression and purification of NH_2Y–α2s 227

Reaction of NH_2Y–α2s with wt β2, CDP and ATP monitored by EPR spectroscopy 229

Kinetics of NH_2Y•–α2 formation monitored by SF UV–vis spectroscopy 231

Kinetics of NH_2Y•–α2 decay monitored by EPR spectroscopy 237

Activities of NH_2Y–α2s 241

Kinetics of NH_2Y_{731}• decay in the presence of N_3UDP/ATP monitored by EPR spectroscopy 243

DISCUSSION 247

Generation of $Y_{730}NH_2Y$–α2 and $Y_{731}NH_2Y$–α2 247

Structural assignment of the new radical 247

Kinetics of NH_2Y•–α2 formation 248

Activity Assays of NH_2Y–α2s 249

Rate of decay of NH_2Y•–α2 249

Implications for mechanism of oxidation 251

REFERENCES 255

Chapter 5 – Detailed Kinetic and Spectroscopic Examination of NH_2Y• Formation with NH_2Y–α2s 261

INTRODUCTION 262

MATERIALS AND METHODS 266

Materials 266

Synthesis of 3–[^{15}N]–nitrotyrosine, [^{15}N]–NO_2Y 266

Synthesis of 3–[^{15}N]–aminotyrosine, [^{15}N]–NH_2Y 267

Growth, expression and purification of [^{15}N]–NH_2Y_{730}–α2 268

Activity assays 268

Reaction of $Y_{730}NH_2Y$–α2 with β2, NDP/(d)NTP monitored by EPR spectroscopy 268

Reaction of [^{15}N]–$Y_{730}NH_2Y$–α2 with β2 and NDP/(d)NTP monitored by EPR spectroscopy 268

Reaction of $Y_{730}NH_2Y$–α2 or [^{15}N]–$Y_{730}NH_2Y$–α2 with β2, NDP/(d)NTP in deuterated buffer monitored by EPR spectroscopy 268

Preparation of high–field EPR and PELDOR samples 269

Simulation of X–band EPR spectra 269

Computational studies 270

Reaction of $Y_{731}NH_2Y$–α2 with β2, NDP/(d)NTP monitored by EPR spectroscopy 270

Reaction of $Y_{730}NH_2Y$–α2 (or $Y_{731}NH_2Y$–α2) with His_6–$Y_{356}F$–β2 monitored by EPR spectroscopy 270

SF UV–vis spectroscopy of NH_2Y–α2/β2 with various NDP/(d)NTP pairs 270

Temperature–dependent SF UV–vis spectroscopy of $Y_{730}NH_2Y$–α2/β2 with CDP/ATP 271

RESULTS 272

Isotope labeling of NH_2Y to examine the new signal with NH_2Y–α2s by EPR spectroscopy 272

Preparation of [^{15}N]–NH_2Y 275

Preparation of [^{15}N]–NH_2Y–α2 277

Generation of [^{14}N]–NH_2Y_{730}• and [^{15}N]–NH_2Y_{730}• with various NDP/(d)NTP pairs 277

Analysis of NH_2Y_{730}• by 180 GHz EPR spectroscopy 281

Spectral simulations 282

Formation of NH_2Y_{731}• with other substrate/effector pairs 290

Distance measurements using PELDOR spectroscopy with NH_2Y–α2s 293

Reaction of NH_2Y–α2 with $Y_{356}F$–β2 296

SF UV–vis spectroscopy of NH_2Y–α2/β2 with various NDP/(d)NTP combinations 298

Temperature dependence in formation of NH_2Y_{730}• 305

DISCUSSION 309

Examination of the structure of NH_2Y_{730}• 309

Positions of NH_2Y_{730}• and NH_2Y_{731}• within the radical transfer pathway 314

Kinetics of NH_2Y• formation with various NDP/(d)NTP combinations 316

REFERENCES 319

Chapter 6 – Mono–, Di–, Tri–, and Tetra–Substituted Fluorotyrosines: New Probes for Enzymes that Use Tyrosyl Radicals in Catalysis 323

INTRODUCTION 324

MATERIALS AND METHODS 327

Materials 327

Synthesis of F_nYs 327

Synthesis of F_n–tyrosine methyl ester hydrochloride (F_nY–OMe·HCl) 328

Synthesis of N–acetyl–F_n–tyrosinamide (Ac–F_nY–NH_2) 329

4–Benzoyl–L–phenylalanyl–F_nY methyl ester trifluoroacetic acid (BPA–F_nY–OMe•CF_3COOH) 331

Physical measurements 332

pK_a determination of Ac–F_nY–NH_2 analogues using UV spectroscopy and ^{19}F NMR spectroscopy 333

Differential pulse voltammetry (DPV) 333
Generation of oxidized F_nYs and EPR measurements 334
Transient absorption (TA) spectroscopy 335
Computational methods 336
Global incorporation of 3–FY into β2 336
Extent of incorporation of 3–FY into β2 336
RESULTS AND DISCUSSION 338
pK_a determination of F_nYs by UV and ^{19}F NMR spectroscopy 338
pH Dependent oxidation of Ac–F_nY–NH_2s 343
Electronic structure calculations of Ac–F_nY–NH_2s 346
Spectroscopic characterization of F_nY•s 349
Incorporation of 3–FY into β2 355
CONCLUSION 358
REFERENCES 359

Chapter 7 – pH Rate Profiles of F_nY_{356}–β2s (n = 2, 3, 4) in *E. coli* Ribonucleotide Reductase: Further Evidence that Y_{356} is a Redox–Active Amino Acid Along the Radical Propagation Pathway and Elucidation of its Mechanism of Oxidation 363
INTRODUCTION 364
MATERIALS AND METHODS 369
Materials 369
Physical measurements 369
Synthesis of Fmoc–F_nYs 369
Peptide synthesis 370
Semisynthesis of β2 and F_nY_{356}–β2s 372
Purification of α2 and removal of contaminating β2 374
Determination of pH rate profiles of F_nY_{356}–β2s 374
RESULTS 375
Synthesis and characterization of F_nY_{356}/V_{353}G/S_{354}C–β2s 375
Problems encountered in the RNR activity assay 376
pH rate profiles for wt and F_nY_{356}–β2s 376
DISCUSSION 378
CONCLUSION 385

REFERENCES 387

Chapter 8 – Switching the Rate–Determining Step from a Conformational Change to Radical Propagation with 2,3,5–F_3Y–β2 of *E. coli* Ribonucleotide Reductase 391

INTRODUCTION 392

MATERIALS AND METHODS 397

Materials 397

Semisynthesis of F_nY–β2 and F_nY–ββ' 397

Growth, expression and purification of His_6–V_{353}G/S_{354}C–β2 397

Monitoring dCDP formation by RCQ studies 397

Data analysis of RCQ experiments 398

Generation of apo Y–β2, 2,3,5–F_3Y–β2 or 2,3,5–F_3Y–ββ' with lithium 8–hydroxy-quinoline–6–sulfonate 398

Reconstitution of apo F_nY–β2 399

Spectrophotometric and radioactive RNR Assay 399

Single wavelength and diode array SF UV–vis spectroscopy 399

RFQ–EPR spectroscopy 399

Kinetic simulations 400

pH rate profile for NH_2Y• formation in the reaction of 2,3,5–F_3Y–β2 with NH_2Y– α2s and CDP/ATP monitored by SF UV–vis spectroscopy 400

RESULTS 401

Rationale for pre–steady state experiments 401

Pre–steady state analysis of His_6–V_{353}G/S_{354}C–β2 by RCQ 402

Pre–steady state analysis of F_nY–β2s by RCQ 405

Increasing the radical content of semisynthetic F_nY–β2s 410

Diode array SF UV–vis spectroscopy with 2,3,5–F_3Y–ββ'/α2 412

SF UV–vis spectroscopy with 2,3,5–F_3Y–β2/α2 414

RFQ EPR spectroscopy with 2,3,5–F_3Y–β2 and 2,3,5–F_3Y–ββ' 414

Rationale for kinetic simulations of the α2/F_nY–β2 catalytic cycle 419

Kinetic simulations: forward or reverse radical propagation? 421

Kinetic simulations: reproducing the effect of pH on k_{cat} with 2,3,5–F_3Y–β2 429

SF UV–vis spectroscopy with 2,3,5–F_3Y–β2, NH_2Y–α2 and CDP/ATP as a readout for forward radical transfer 432

DISCUSSION 440

REFERENCES 445

List of Figures

Figure 1–1	Reaction catalyzed by RNR	40
Figure 1–2	Four classes of RNRs	41
Figure 1–3	Structural basis for allosteric regulation in the *T. maritima* class II RNR	43
Figure 1–4	The diiron Y_{122}• cofactor of *E. coli* RNR	44
Figure 1–5	Proposed mechanism for nucleotide reduction	46
Figure 1–6	Docking model for the interaction between α2 and β2	50
Figure 1–7	The proposed radical transfer pathway of *E. coli* RNR	51
Figure 1–8	Structures of mechanism–based inhibitors of RNR	53
Figure 1–9	PELDOR spectroscopy with N_3UDP and wt α2/β2	53
Figure 1–10	Parabolic driving force dependence for k_{ET}	56
Figure 1–11	Tunneling time table in Ru–modified proteins	58
Figure 1–12	PCET model systems	60
Figure 1–13	Square scheme for PCET	61
Figure 1–14	Two classes of PCET reactions	62
Figure 1–15	Peak potentials of Ac–Y–NH_2 and Ac–W–NH_2 as a function of pH.	64
Figure 1–16	Working model for cofactor assembly in *E. coli* β2	66
Figure 1–17	Superimposition of the active sites of RNRs from three different classes	68
Figure 1–18	Unnatural Y analogues incorporated into β2 or α2 in this Thesis.	70
Figure 1–19	Proposed mechanism of intein self–expulsion for the *S. cerevisiae* Vma intein	71
Figure 1–20	Semisynthesis of β2 via EPL	73
Figure 1–21	Chemical mechanism for long–range radical transfer in *E. coli* RNR	79
Figure 2–1	Low reduction potential Y analogues considered for insertion at position 356 of β2	89
Figure 2–2	The radical generation pathway with site–specific insertion of DOPA at residue 356	89
Figure 2–3	Reactions of catechol, catechol• and *o*–benzoquinone	91

Figure 2–4	Characterization of Fmoc–19mer peptide	115
Figure 2–5	Structures of Fmoc–DOPA(acetonide)–OH and Fmoc–Cys(t–Buthio)–OPfp	115
Figure 2–6	Characterization of purified DOPA–22mer	116
Figure 2–7	Generation of semisynthetic DOPA–β2	119
Figure 2–8	Characterization of the Y_{122}• in DOPA–β2	119
Figure 2–9	Binding of DOPA–β2 to α2	121
Figure 2–10	Kinetics of $DOPA_{356}$• formation and Y_{122}• disappearance	121
Figure 2–11	Control experiments for the SF UV–vis reactions of DOPA–β2	122
Figure 2–12	UV–vis spectrum of $DOPA_{356}$• using point–by–point spectral reconstruction	122
Figure 2–13	Trapping of $DOPA_{356}$• with different substrate effector pairs	124
Figure 2–14	Kinetics of $DOPA_{356}$• formation and Y_{122}• disappearance with ADP alone	124
Figure 2–15	EPR spectrum of $DOPA_{356}$•–β2/α2 in the presence of GDP/TTP	127
Figure 2–16	Microwave power dependence of Y_{122}• and $DOPA_{356}$•	128
Figure 2–17	X–band EPR spectra of DOPA• and catechol• generated by anaerobic photolysis at 77 K	129
Figure 2–18	EPR spectrum of $DOPA_{356}$•–β2/α2 in the presence of CDP/ATP	130
Figure 2–19	Comparison of $DOPA_{356}$•–β2/α2 as a function of substrate/effector pairs	130
Figure 2–20	180 GHz EPR spectrum of $DOPA_{356}$•	133
Figure 2–21	Simulation of 180 GHz EPR spectrum of $DOPA_{356}$•	133
Figure 2–22	Simulation of X–band $DOPA_{356}$• spectra	134
Figure 2–23	X–band PELDOR spectroscopy of Y_{122}•–$DOPA_{356}$• and $DOPA_{356}$•–$DOPA_{356}$•	137
Figure 2–24	PELDOR studies with the mechanism–based inhibitor N_3UDP	146
Figure 2–25	Delocalization of the unpaired spin on Y_{122}• over residues of the radical transfer pathway	146
Figure 2–26	PELDOR studies with DOPA–β2/α2	147

Figure 3–1	Diagrammatic view of the β2 subunits discussed in this chapter	154
Figure 3–2	Lack of Y_{122}• redistribution observed within ββ'	154
Figure 3–3	SDS PAGE Analysis of DOPA–ββ'	163
Figure 3–4	Characterization of the diiron Y_{122}• of DOPA–ββ'	163
Figure 3–5	Binding of DOPA–ββ' to α2	163
Figure 3–6	Kinetics of $DOPA_{356}$•–ββ' formation with α2, CDP and ATP	164
Figure 3–7	Point–by–point Reconstruction of the UV–vis Spectrum of $DOPA_{356}$•–ββ' by SF Spectroscopy	166
Figure 3–8	EPR spectrum of $DOPA_{356}$•–ββ'/α2 with CDP/ATP	166
Figure 3–9	$DOPA_{356}$• formation as a function of initial [DOPA–ββ'/α2]	167
Figure 3–10	Kinetic Simulation of $DOPA_{356}$• formation with DOPA–ββ'/α2	169
Figure 3–11	Kinetics of $DOPA_{356}$•–ββ'/α2 formation with UDP/ATP	169
Figure 3–12	Kinetics of $DOPA_{356}$•–ββ'/α2 formation with GDP/TTP	170
Figure 3–13	Kinetics of $DOPA_{356}$•–ββ'/α2 formation with ADP/dGTP	171
Figure 3–14	RFQ EPR Spectroscopy with DOPA–ββ'/α2 in the presence of ADP/dGTP	174
Figure 3–15	Comparison of $DOPA_{356}$•–ββ'/α2 as a function of substrate/effector pairs	175
Figure 3–16	Comparison of the EPR spectrum of $DOPA_{356}$• in DOPA–β2/α2 vs. DOPA–ββ'/α2 as a function of NDP/(d)NTP	177
Figure 3–17	X–band PELDOR spectroscopy of Y_{122}•–$DOPA_{356}$• with DOPA–ββ'/α2	178
Figure 3–18	Sequential–mix SF UV–vis spectroscopy monitoring reduction of $DOPA_{356}$• by HU	180
Figure 3–19	Kinetics of HU–mediated reduction of Y_{122}• with wt and $Y_{356}F$–β2	183
Figure 3–20	Decay Kinetics of $DOPA_{356}$•–ββ'/α2 with CDP/ATP	185
Figure 3–21	Summary of procedures used to generate DOPA–ββ' with a radical content 1.2 Y_{122}• per heterodimer	187
Figure 3–22	Purification of DOPA–ββ' with 1.2 Y_{122}• per heterodimer	189
Figure 3–23	Asymmetric model for RNR turnover	193
Figure 3–24	Sources of asymmetry in *E. coli* RNR	194
Figure 3–25	Diagram of the asymmetric α2/β2 complex structure from *S. typhimurium* determined by Uppsten et al at 4 Å resolution	194
Figure 3–26	Statistical distribution of Y_{122}• in DOPA–β2, DOPA–ββ' and wt β2	198
Figure 3–27	Current working hypothesis to explain yields of $DOPA_{356}$• with DOPA–ββ' and DOPA–β2	198

Figure 3–28	Pictorial presentation of PELDOR measurements with $DOPA_{356}$•–β2/α2 and $DOPA_{356}$•–ββ′/α2	206
Figure 4–1	The putative radical initiation pathway generated from the docking model of α2 and β2	213
Figure 4–2	MALDI–TOF MS and SDS PAGE analysis of K_7NH_2Y–Z–domain	228
Figure 4–3	Expression of $Y_{731}NH_2Y$–α2	230
Figure 4–4	Expression of $Y_{730}NH_2Y$–α2	230
Figure 4–5	SDS PAGE analysis of purified $Y_{730}NH_2Y$–α2	232
Figure 4–6	SDS PAGE analysis of purified $Y_{731}NH_2Y$–α2	232
Figure 4–7	Reaction of $Y_{730}NH_2Y$–α2/ATP with wt β2/CDP monitored by EPR spectroscopy	233
Figure 4–8	Microwave power dependence of Y_{122}• and NH_2Y_{730}• signal intensities	233
Figure 4–9	Reaction of $Y_{731}NH_2Y$–α2/ATP with wt β2/CDP monitored by EPR spectroscopy	234
Figure 4–10	Comparison between NH_2Y_{730}• from Fig. 4–7 and NH_2Y_{731}• from Fig. 4–9	234
Figure 4–11	Point–by–point reconstruction of the UV–vis spectrum of NH_2Y_{730}• and NH_2Y_{731}•	236
Figure 4–12	Kinetics of formation for NH_2Y_{730}• and NH_2Y_{731}•	237
Figure 4–13	Stability of NH_2Y_{730}• probed by EPR spectroscopy	239
Figure 4–14	Stability of NH_2Y_{731}• probed by EPR and UV–vis spectroscopy	240
Figure 4–15	N_3ADP assay for $Y_{730}NH_2Y$–α2	244
Figure 4–16	EPR spectral comparison of N•, Y_{122}• and NH_2Y_{730}•	244
Figure 4–17	N_3ADP Assay for $Y_{731}NH_2Y$–α2	245
Figure 4–18	Stability of NH_2Y_{731}• in the presence of N_3UDP/ATP probed by EPR spectroscopy	246
Figure 4–19	Working model for loss of spin during reaction of NH_2Y–α2s with CDP/ATP	253
Figure 4–20	Working model for loss of spin during reaction of NH_2Y–α2s with N_3ADP/dGTP	253
Figure 4–21	Mechanistic options for oxidation of C_{439} by NH_2Y_{730}•	254

Figure 5–1	The proposed radical initiation pathway within an αβ pair	263
Figure 5–2	Numbering scheme for *o*–aminophenol radicals data in Table 5–1	274
Figure 5–3	^{15}N–^{13}C J–couplings observed with [^{15}N]–NO_2Y and [^{15}N]–NH_2Y	275
Figure 5–4	Normalized EPR spectra of isotopically substituted NH_2Y_{730}•	280
Figure 5–5	EPR spectra of NH_2Y_{730}• at 180 GHz in the presence of CDP/ATP	281
Figure 5–6	Numbering scheme, g tensor axis orientation and conformations of NH_2Y•	282
Figure 5–7	Simulation of [^{15}N]–NH_2Y_{730}• EPR spectra in deuterated assay buffer	285
Figure 5–8	Simulation of NH_2Y_{730}• EPR spectra in protonated assay buffer	288
Figure 5–9	EPR spectra of NH_2Y_{731}• in the presence of various NDP/(d)NTPs	291
Figure 5–10	EPR spectra of NH_2Y_{731}• at 180 GHz	293
Figure 5–11	PELDOR spectroscopy with NH_2Y–α2s	295
Figure 5–12	Distances between Y_{122}• and other residues in the radical transfer pathway	296
Figure 5–13	Pathway dependence for NH_2Y• formation	298
Figure 5–14	Kinetics of NH_2Y_{730}• formation monitored by SF UV–vis spectroscopy	299
Figure 5–15	Kinetics of NH_2Y_{731}• formation monitored by SF UV–vis spectroscopy	301
Figure 5–16	Temperature–dependence of NH_2Y_{730}• formation	307
Figure 5–17	Structure of the NH_2Y_{730}•	313
Figure 6–1	UV spectra of phenol and phenolate forms of Ac–F_nY–NH_2Ys	339
Figure 6–2	UV spectra of Ac–2,3–F_2Y–NH_2 as a function of pH	340
Figure 6–3	Dependence of ^{19}F NMR chemical shifts on pH	341
Figure 6–4	Differential pulse voltammogram for Ac–F_nY^-–NH_2/Ac–F_nY•–NH_2s	344
Figure 6–5	Reduction potential vs. NHE as a function of pH for Ac–F_nY–NH_2 derivatives	345
Figure 6–6	DFT calculations for E_ps and pK_as of Ac–F_nY–NH_2Ys	348
Figure 6–7	Energy level diagram for frontier molecular orbitals of the phenolates of Ac–F_nY–NH_2s	349
Figure 6–8	Normalized EPR spectra of F_nY•s	352
Figure 6–9	TA spectroscopy with BPA–Y–OMe	353
Figure 6–10	UV–vis spectra of BPA–F_nY•–OMe derivatives	354
Figure 6–11	SDS PAGE analysis of 3–FY–β2	356
Figure 6–12	EPR spectrum and simulation of 3–FY_{122}•–β2	357

Figure 7–1	Putative PCET pathway of *E. coli* RNR based on the docking model	368
Figure 7–2	pH rate profiles of F_nY_{356}–β2s	377
Figure 7–3	Peak reduction potential of Ac–F_nY•–NH_2s as a function of pH	379
Figure 7–4	Redox potential regimes of RNR activity	380
Figure 7–5	Mechanism of Y_{356} oxidation during radical transfer	386
Figure 8–1	The proposed radical initiation pathway within an αβ pair	392
Figure 8–2	Kinetic model for the reaction of wt RNR	395
Figure 8–3	RCQ analysis of [^{14}C]–dCDP formation with His_6–$V_{353}G/S_{354}C$–β2 (1.1 Y_{122}•/dimer)	404
Figure 8–4	RCQ analysis of [^{14}C]–dCDP formation with Y–β2 (0.35 Y_{122}•/dimer) at pH 6.8	405
Figure 8–5	RCQ analysis of [^{14}C]–dCDP formation with 2,3,5–F_3Y–β2 (0.4 Y_{122}•/dimer)	407
Figure 8–6	RCQ analysis of [^{14}C]–dCDP formation with F_4Y–β2 (0.37 Y_{122}•/dimer)	408
Figure 8–7	Increasing the radical content of Y–β2 and 2,3,5–F_3Y–β2	411
Figure 8–8	SDS PAGE analysis of 2,3,5–F_3Y–β2 and 2,3,5–F_3Y–ββ' after chelation/reconstitution	412
Figure 8–9	Diode Array SF UV–vis spectroscopy of 2,3,5–F_3Y–ββ'/α2 (1.2 Y_{122}•/dimer) in the presence of CDP/ATP at pH 8.4	413
Figure 8–10	Single wavelength SF UV–vis spectroscopy of 2,3,5–F_3Y–β2/α2 (1.2 Y_{122}•/dimer) in the presence of CDP/ATP at pH 8.4	414
Figure 8–11	RFQ EPR spectroscopy of the reaction of 2,3,5–F_3Y–ββ' (1.2 Y_{122}•/dimer) and CDP with α2 and ATP	415
Figure 8–12	RFQ EPR spectroscopy of the reaction of 2,3,5–F_3Y–β2 (1.2 Y_{122}•/dimer) and CDP with α2 and ATP	416
Figure 8–13	RFQ EPR spectroscopy of the reaction of 2,3,5–F_3Y–β2 (1.2 Y_{122}•/dimer) and CDP with α2 and ATP	418
Figure 8–14	Kinetic model and result of simulation for the reaction of Y–β2	420
Figure 8–15	Kinetic model and result of simulation for the reaction of 2,3,5–F_3Y–β2 in which reverse radical transfer is rate–limiting	422
Figure 8–16	Kinetic model and result of simulation for the reaction of 2,3,5–F_3Y–β2 in which forward radical transfer is rate–limiting	424
Figure 8–17	Kinetic model and result of simulation for the reaction of 2,3,5–F_3Y–β2 in which forward radical transfer is rate–limiting with an altered Y_{122}• reformation rate constant	425

Figure 8–18 Kinetic model and result of simulations for the reaction of 2,3,5–F_3Y–β2 in which forward and reverse radical transfer are partially rate–limiting 428

Figure 8–19 Representative time courses for the reaction of NH_2Y–α2s with 2,3,5–F_3Y–β2 and CDP/ATP monitored by SF UV spectroscopy 434

Figure 8–20 SF UV spectroscopy of NH_2Y–α2s with 2,3,5–F_3Y–β2 and CDP/ATP as a function of pH 435

Figure 8–21 pH rate profile for NH_2Y• formation in the reaction of NH_2Y–α2 with 2,3,5–F_3Y–β2 439

List of Tables

Table 2–1	Relevant properties for the Y analogues DOPA, NH_2Y and MeS–Y	89
Table 2–2	Specific activities of wt β2, intein–wt β2 and DOPA–β2 in nmol/min mg	120
Table 2–3	Kinetics of $DOPA_{356}$•–β2/α2 formation with various substrate/effector combinations using SF UV–vis spectroscopy	125
Table 2–4	Comparison of X–band EPR parameters and stoichiometry of $DOPA_{356}$• formation with substrate only vs. substrate and effector	131
Table 2–5	Parameters used for simulation of $DOPA_{356}$• spectra in Figure 2–22	135
Table 3–1	Summary of kinetic parameters for $DOPA_{356}$•–ββ'/α2 formation as a function of substrate/effector pairs	172
Table 3–2	Comparison of X–band EPR parameters for $DOPA_{356}$•–β2/α2 and $DOPA_{356}$•–ββ'/α2 as a function of substrate/effector pairs	176
Table 3–3	Comparison of the extent of $DOPA_{356}$• formation with DOPA–β2/α2 and DOPA–ββ'/α2 as a function of substrate/effector pairs	176
Table 3–4	Summary of kinetic parameters in the reaction of $DOPA_{356}$•–ββ' with HU obtained using sequential SF UV–vis spectroscopy	182
Table 3–5	Determination of [DOPA•] and [Y_{122}•] in the reaction of DOPA–ββ'/GDP with α2/TTP on the minute time scale	188
Table 3–6	Determination of [DOPA•] and [Y_{122}•] in the reaction of DOPA–ββ'/CDP with α2 on the minute time scale	188
Table 3–7	Determination of [DOPA•] and [Y_{122}•] in the reaction of DOPA–ββ'/CDP with α2/ATP on the minute time scale	190
Table 3–8	Determination of [DOPA•] and [Y_{122}•] in the reaction of DOPA–β2/CDP with α2/ATP on the minute time scale	190
Table 4–1	Vectors used in this study	217
Table 4–2	Summary of kinetic data for formation of NH_2Y•–α2	238
Table 4–3	Monitoring the activity of NH_2Y–α2s by measuring deoxynucleotide and N• formation	241
Table 4–4	Analysis of the reaction of wt α2 or NH_2Y–α2s with β2 and N_3ADP/dGTP after 20 s	245

Table 5–1	Summary of EPR parameters (in MHz) previously reported for an *o*–aminophenol radical	274
Table 5–2	UV spectral properties of authentic ^{14}N–NH_2Y^a and synthetic ^{15}N–NH_2Y determined in H_2O at 25°C	276
Table 5–3	Yield of NH_2Y• and total spin after reacting $Y_{730}NH_2Y$–α2 with β2 and various NDP/(d)NTP pairs for 20 s	279
Table 5–4	Hyperfine coupling constants (in MHz) calculated for NH_2Y•. See Figures 5–6A and 5–6B for numbering scheme and conformation of NH_2Y•	283
Table 5–5	Hyperfine coupling constants (in MHz) calculated for NH_2Y• in an alternative conformation	283
Table 5–6	Parameters (in MHz) used for simulation of [^{14}N]–NH_2Y_{730}• and [^{15}N]–NH_2Y_{730}• EPR spectra in protonated or deuterated buffer	286
Table 5–7	Yield of NH_2Y• and total spin after reacting $Y_{731}NH_2Y$–α2 with β2 and various NDP/(d)NTP pairs for 20 s	292
Table 5–8	Summary of kinetic parameters for reaction of $Y_{730}NH_2Y$–α2 with β2 and various substrate/effector combinations at 25°C	300
Table 5–9	Summary of kinetic parameters for reaction of $Y_{731}NH_2Y$–α2 with β2 and various substrate/effector combinations at 25°C	302
Table 5–10	Summary of kinetic parameters for the reaction of $Y_{730}NH_2Y$–α2/β2 with CDP/ATP as a function of temperature	308
Table 5–11	Summary of thermodynamic parameters for NH_2Y• formation with $Y_{730}NH_2Y$– α2 in the presence of CDP/ATP	308
Table 6–1	A–tensors of nuclei with significant hyperfine interaction in 3–FY_{122}•–β2	342
Table 6–2	Physical data for tyrosine and fluorotyrosine derivatives	357
Table 7–1	Fluorotyrosine derivatives used to substitute Y_{356} of β2 and their physical properties	367
Table 7–2	Purification and yield of Fmoc–F_nY–COOH	371
Table 7–3	RP–HPLC and MALDI–TOF MS characterization of F_nY–22mers	372
Table 7–4	Physical and biochemical characterization of F_nY_{356}–β2s	373
Table 8–1	Summary of kinetic parameters from RCQ experiments monitoring [^{14}C]–dCDP formation	409

Table 8–2 Measured and simulated k_{cat} for 2,3,5–F_3Y–β2 as a function of pH using the kinetic model in Figure 8–17 430

Table 8–3 Measured and simulated k_{cat} for 2,3,5–F_3Y–β2 as a function of pH using the kinetic models in Figures 8–17 and 8–18 431

Table 8–4 Summary of the kinetic parameters for NH_2Y• formation in the reaction of $Y_{730}NH_2Y$–α2 or $Y_{731}NH_2Y$–α2 with 2,3,5–F_3Y_{356}–β2 in the presence of CDP/ATP 436

List of Schemes

Scheme 2–1	Involvement of DOPA• in melanin biogenesis	90
Scheme 4–1	One electron oxidation of NH_2Y	213
Scheme 5–1	Synthetic scheme used for preparation of ^{15}N–NH_2Y	275
Scheme 5–2	Different protonation states and pK_as of NH_2Y	276
Scheme 5–3	Rotation about the C_3–N bond in NH_2Y•	289
Scheme 6–1	Fluorotyrosine analogues prepared in this study	326

Abbreviations

ADP	Adenosine–5'–diphosphate
Amp	Ampicillin
ATP	Adenosine–5'–triphosphate
BPA	Benzophenone
CBD	Chitin binding domain
CAP	Calf–intestine alkaline phosphatase
CDP	Cytidine–5'–diphosphate
Ches	2–(Cyclohexylamino)ethanesulfonic acid
Cm	Chloramphenicol
CV	Column volume
dATP	2'–Deoxycytidine–5'–triphosphate
dC	2'–Deoxycytidine
dCDP	2'–Deoxycytidine–5'–diphosphate
DFT	Density functional theory
dGTP	2'–Deoxyguanosine–5'–triphosphate
DIPEA	N,N–Diisorpropylethylamine
DMF	N,N–Dimethylformamide
DOPA	3,4–Dihydroxyphenylalanine
DPV	Differential pulse voltammetry
DTT	Dithiothreitol
EDTA	Ethylenediaminetetraacetic acid
EPR	Electron paramagnetic resonance
ESI	Electrospray ionization
ET	Electron transfer
EtOAc	Ethyl acetate
Fmoc	9–Fluorenylmethoxycarbonyl
GDP	Guanosine–5'–diphosphate
GFP	Green fluorescent protein
GMML	Glycerol minimal media leucine

HAT	Hydrogen atom transfer
HATU	O–(7–Azabenzotriazol–1–yl)–N,N,N',N'–tetramethyluronium hexafluorophosphate
Hepes	4–(2–Hydroxyethyl)piperazine–1–ethanesulfonic acid
HOBt	1–Hydroxybenzotriazole
HU	Hydroxyurea
IPTG	Isopropyl–β–D–thiogalactopyranoside
Kan	Kanamycin
L–Ara	L–Arabinose
LB	Luria Bertani
MALTI–TOF	Matrix–assisted laser desorption/ionization time of flight
MeCN	Acetonitrile
MeOH	Methanol
Mes	2–(N–Morpholino)ethanesulfonic acid
Mesna	2–Mercaptoethanesulfonic acid
MeV	Methyl viologen
MS	Mass spectrometry
NADPH	β–Nicotinamide adenine dinucleotide phosphate (reduced form)
NMM	N–Methylmorpholine
NMR	Nuclear magnetic resonance
PCET	Proton–coupled electron transfer
PELDOR	Pulsed electron–electron double resonance
PLP	Pyridoxal–5'–phosphate
PMSF	Phenylmethanesulfonyl fluoride
RCQ	Rapid chemical quench
RFQ	Rapid freeze quench
RNAP	RNA polymerase
RP–HPLC	Reverse–phase high performance liquid chromatography
SDS PAGE	Sodium dodecylsulfate polyacrylamide gel electrophoresis
TA	Transient absorption
Taps	N–[Tris(hydroxylmethyl)methyl]–3–aminopropanesulfonic acid
Tet	Tetracycline

TFA	Trifluoroacetic acid
TIS	Triisopropylsilane
TLCK	Tosyl–L–lysyl chloromethane
TPCK	Tosyl–L–phenylalanyl chloromethane
TPL	Tyrosine phenol lyase
Tris	Tris(hydroxymethyl)aminomethane
TTP	Thymidine–5'–triphosphate
UDP	Uridine–5'–diphosphate
WSC	N–Ethyl–N'–(3–dimethylaminopropyl)carbodiimide

CHAPTER 1:

Introduction to Ribonucleotide Reductases

Adapted in part from: Seyedsayamdost, M. R.; Yee, C. S.; Stubbe, J. *Nat. Protoc.* **2007**, *2*, 1225.

General Introduction

In all organisms, ribonucleotide reductases (RNRs) play a central role in nucleic acid metabolism by catalyzing the conversion of nucleotides to 2'–deoxynucleotides (Figure 1–1), thereby providing all of the monomeric precursors required for DNA replication and repair.[1,2] To ensure that RNRs provide a balanced pool of deoxynucleotides, which is essential for the fidelity of DNA synthesis, they are tightly regulated at numerous levels inside the cell.[3,4] Because of this central role, RNRs have served as pharmaceutical targets and several RNR inhibitors are currently in clinical use or trial.[5-12]

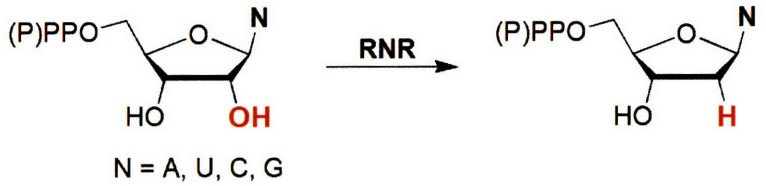

Figure 1–1. Reaction catalyzed by RNR.

RNRs have also served as a paradigm for a wide range of areas of interest in Chemistry and Biology.[1] They have been proposed to provide a major connection between the RNA and DNA worlds.[4,13-15] RNR is also the first enzyme, in which a tyrosyl free radical was discovered, and in which the chemistry of a protein–bound diiron center with O_2 was elucidated.[16-20] This chemistry involved formation of tryptophan cation radical, which to date is only one of three functionally relevant tryptophan cation radicals in Biology.[21-23] The nucleotide reduction mechanism was unprecedented at the time of its discovery and involved formation of the only known thiyl radical in Biology.[24] Finally research groups interested in the mechanism of oxidation of amino acids are concerned with RNRs to understand how the concomitant motion of electrons and protons are coordinated.[25] The work presented in this Thesis will focus on another hallmark of RNRs: long–range charge transfer using transient amino acid radical intermediates.

The reduction of nucleotides catalyzed by RNR employs complex radical chemistry, which requires generation of a thiyl radical (C•). Four classes of RNRs have been proposed

based on the mechanism attendant to C• generation (Figure 1–2).[1] Class I RNRs, the main focus of this Thesis, utilize a diiron tyrosyl radical (Y•) cofactor. Class II RNRs use a 5'–deoxyadenosyl radical derived from homolytic cleavage of the C–Co bond in adenosylcobalamin. Class III RNRs employ a glycyl radical (G•), the formation of which requires an activase 'radical SAM' enzyme, that harbors a [4Fe–4S] cluster and the cofactor S–adenosylmethionine. Finally, a recently identified class IV RNR uses a Mn^{IV}–Fe^{III} cofactor to generate C•.[26]

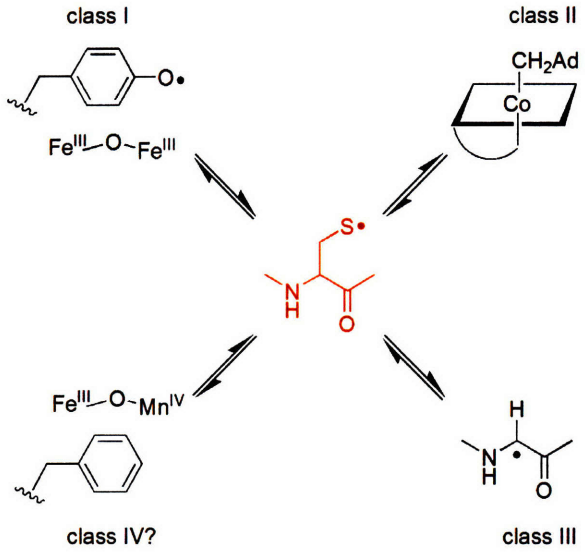

Figure 1–2. Four classes of RNRs. The classes are distinguished based on the metallocofactor used to generate a C• essesntial for catalysis. Class I RNRs use a diiron tyrosyl radical, class II RNRs use adenosylcobalamin, and class III RNRs employ a glycyl. Recently, a Mn^{IV}–Fe^{III} cluster has been proposed to generate a C• in *C. trachomatis*. This likely represents a fourth class of RNR.

The Class Ia RNR from *E. coli*

The focus of this Thesis will be the class Ia RNR from *E. coli*. This RNR is expressed by the *nrdA* and *nrdB* genes in *E. coli* and is different from the *nrdE* and *nrdF* genes, which comprise the class Ib RNR.[27-29] Class Ib differs from class Ia in several aspects. The class Ia RNR is present in all eukaryotes and some prokaryotes, whereas class Ib RNR is at present confined to bacteria. In *E. coli*, the class Ia RNR is essential, whereas class Ib RNR is not. Under normal growth conditions in *E. coli*, the class Ia RNR is predominantly expressed,

whereas expression of class Ib RNR is poor. The physiological role of this second RNR is not understood, although preliminary results indicate it to be involved under Fe limiting or oxidative stress conditions. At the molecular level, class Ib RNR differs from the class Ia in the geometry of its Y• cofactor, as delineated by spectroscopic and structural studies, the requirement for its disulfide reductant and its regulation of overall activity.[30]

Protein Subunits of Class Ia *E. coli* RNR

E. coli class Ia RNR consists of two protein subunits, α2 and β2.[31] α2, a dimer of 172 kDa, is the site of nucleotide reduction. It contains binding sites for the substrates CDP, GDP, UDP and ADP, and allosteric effectors ATP, dATP, TTP, and dGTP.[32,33] A remarkable feature of α2 is the numerous levels of allosteric regulation which have evolved to ensure that a single enzyme provides a balanced pool of four deoxynucleotides and is able to respond to the changing dNTP requirements of the cell. Binding of effectors to the allosteric site causes a conformational change that reaches the active site and thus governs which substrate is reduced. The structural basis for this regulation has been studied in the α2 subunit of *Salmonella typhimurium*,[34] a class Ib RNR, the class II RNR of *Thermotoga maritima*[35] (Figure 1–3) as well as the anaerobic class III *E. coli* RNR.[36,37] The model that has emerged from these studies is that allosteric effectors bind at a four–helix bundle in the dimer interface of α2.[4] Each monomer contributes residues to binding of the effector. Effector binding strongly influences the conformation of a loop at the dimer interface, loop 2 (Figure 1–3).[35] The changes in the structure of loop 2 are propagated to the active site, where binding of a specific substrate is preferred. In this fashion, effectors ATP and dATP stimulate reduction of CDP and UDP, TTP codes for GDP and dGTP for ADP. In *E. coli* RNR structural studies with various substrate/effector pairs have been unsuccessful due to the difficulty of obtaining diffractable crystals.

Class Ia enzymes also contain a second allosteric regulation site in α2, called the activity site, which controls the overall rate of nucleotide reduction. At the activity site ATP and low [dATP] stimulate rapid nucleotide reduction, whereas high [dATP] renders RNR inactive in nucleotide reduction.[32] This site allows the activity of RNR to be stimulated or inhibited based

on the ratio of [dATP] and [ATP] inside the cell. The activity site is known to reside in the N–terminal domain of α2 and contains a conserved KRDG motif, in which K and R interact with the phosphate groups of the nucleotide. Structures with ATP and the effector–free form of α2 have not revealed conformational differences; however, soaking experiments have suggested that the conformational change may not take place due to disruption or prevention of crystal lattice formation.[38] Thus, the structural basis of this mode of regulation is at present not well understood. It should be noted that the α2 subunits of class Ib RNRs lack an activity site.

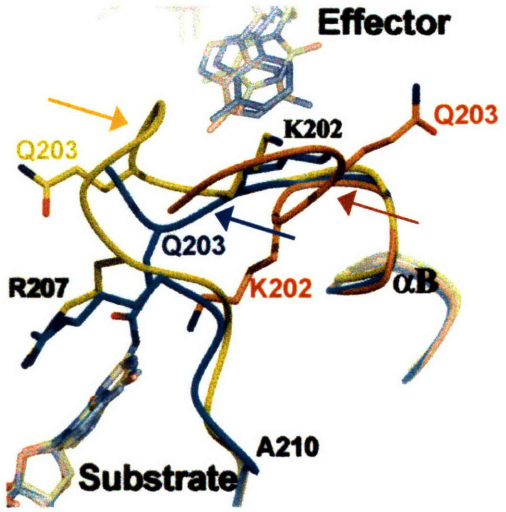

Figure 1–3. Structural basis for allosteric regulation in the *T. maritima* class II RNR.[35] Overlaid structures of *T. maritima* RNR with the conformation of loop 2 in the allosteric effector site shown as a function of CDP/dATP (blue), GDP/TTP (yellow) and ADP/dGTP (brown). The loop structure with UDP/dATP is very similar to that of CDP/dATP and is not shown. Arrows are pointing to loop 2 in each case

Studies with the mouse RNR have revealed a third allosteric regulation site, where high ATP concentrations have been postulated to cause hexamerization of α.[39,40] The location of this binding site and its mechanism of regulation remain to be established. Prokaryotic RNRs, such as the *E. coli* RNR, lack this third ATP binding site.

The second RNR subsunit, β2, is a homodimer of 87 kDa. It is the radical initiator subunit and contains the Y• cofactor. Seminal experiments in the 1970s demonstrated that the radical signal observed in β2 was associated with a Y•, which at the time, was the first Y• found

in an enzyme (Figure 1–4).[6] This was subsequently located to residue 122.[41,42] These experiments also established a correlation between the [Y_{122}•] and the level of activity suggesting a role for Y_{122}• in nucleotide reduction.[6] The UV–vis spectrum of the cofactor shows major features at 325, 365, 410 and 600 nm (Figure 1–4). The transition at 410 nm has been associated with the Y_{122}• with an ε of 3000–3700 $M^{-1}cm^{-1}$.[43-46] This is similar to properties of Y• in solution which also have a sharp peak at 410 nm and an ε of ~2800 $M^{-1}cm^{-1}$.[47] The other UV–vis transitions are related to the diferric center which is adjacent to the Y_{122}•. Mössbauer,[48,49] resonance Raman[50] and magnetic susceptibility[51] studies have shown that this center consists a μ–oxo–bridged high spin diferric ground state with an S=0 due to antiferromangetic interaction at –92 cm^{-1}. Structural studies have supported this assignment and shown that the Y_{122}• is within 5 Å of the diferric center.[52] Importantly, β2 purified by standard procedure contains a maximal amount of 1.2 Y_{122}• and 3–3.5 Fe per dimer. The distribution of the Y_{122}• and the Fe is a major unresolved issue and whether the substiochiometric ratios of Y_{122}• and Fe are artifacts of the purification procedure is not known. The in vivo levels of Y_{122}• and Fe are at present also unknown although they have been determined in yeast RNR.[53,54]

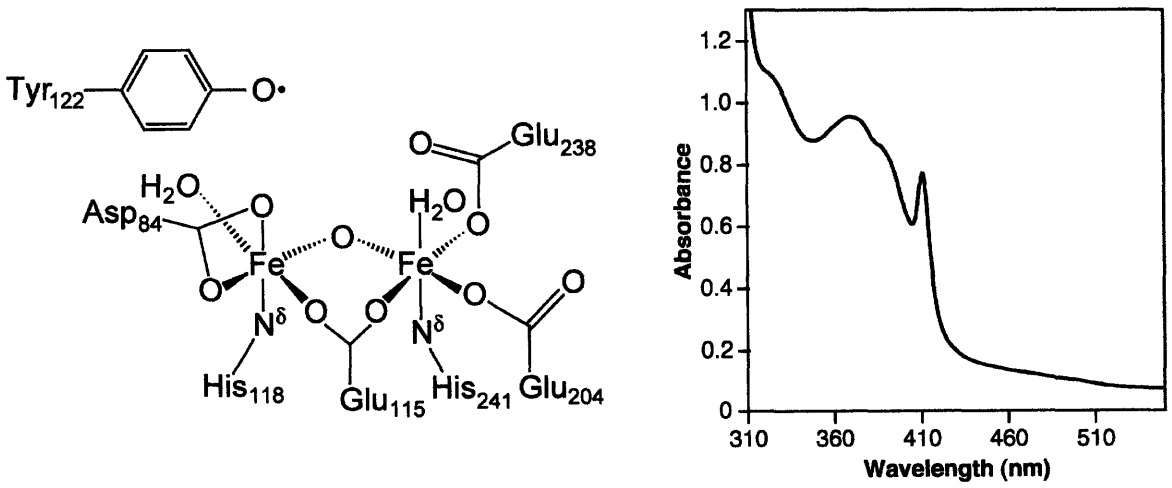

Figure 1–4. The diiron Y_{122}• cofactor of *E. coli* RNR. (Left) Structure of the cofactor from the cystal structure of Nordlund et al.[52] (Right) UV–vis spectrum of the cofactor. The sharp peak at 410 nm and a hump at 390 nm are due to the Y_{122}•. Transistions at 325 and 365 nm are due to the diiron center. The transition at 600 nm has a small ε and is not shown.

The structure of Y_{122}• has been explored by multiple isotopic substitutions and multi–frequency EPR and ENDOR methods.[55,56] Y_{122}• has been generated with ^{2}H, ^{13}C or ^{17}O isotopic substitutions using global replacement methods, and the anisotropic hyperfine tensors for the ring protons, the C_β–protons, the ring C–nuclei and the phenol oxygen have been elucidated. These have been used to provide a detailed picture of the spin density distribution. Consequently, the C_β–proton, the 3,5–ring protons and the phenol oxygen show the greatest hyperfine coupling constants indicative of significant spin density at the C_β, C_3/C_5 and the phenol oxygen, respecively. In addition, the conformation of the C_β–protons has been established from these investigations.

High field EPR studies have provided a sensitive measure for H–bonding at Y_{122}•. The g_x value has been found to correlate with the presence of hydrogen bonding to the phenol oxygen in Y•s of class I β2s.[30] A high g_x value (~2.0091) has been correlated with absence of an H–bond, as is the case in *E. coli* β2, whereas low g_x values (~2.0074) are indicative of an H–bond.[56-58] A physical explanation for the sensitivity of g_x to hydrogen bonding has been proposed.

The Y_{122}• is remarkably stable with a half life of ~4 days at 4°C.[48] In comparison, Y•s generated in solution react on the ms time scale.[59] Measurements of the reduction potential of Y_{122}• have revealed an estimated value of 1.0 ± 0.1 V.[60] This is similar to the potential of Y• measured in solution.[61-66] Thus, the stability of the Y_{122}• is not associated with a lowered reduction potential. Instead, studies with various reductants have indicated that its stability is related to the fact that the Y_{122}• is sequestered from solvent and resides in a pocket that is >11 Å from the surface of the protein.[52] Thus, steric, rather than electronic factors contribute mostly to the remarkable stability of Y_{122}•. Consistent with this idea, the Y• of mouse and human β2 are sterically more exposed to solvent and have a significantly shorter half life than that of *E. coli* β2.

Nucleotide Reduction Mechanism

Despite evolution of several mechanisms for C• formation, the mechanism of nucleotide reduction has been proposed to be common to all classes of RNRs.[67,68] This mechanism presented a mystery for some time, although a number of hypotheses mostly involving

phosphorylation of the 2'–hydroxyl group followed by elimination of the phosphate, had been presented.[69] Compelling evidence for a homolytic 3'–hydrogen abstraction mechanism was offered in the early 1980s when reactions with [3'–^{3}H]–NDPs demonstrated a significant wash out of ^{3}H into the solution. In addition, a tritium isotope effect on V/K in the range of 1.4–4.7 was observed under various conditions.[70,71] Thus, it was suggested that a radical was abstracting the 3'–hydrogen of the nucleotide. Proposal of the mechanism of ensuing steps in nucleotide reduction was based on model reactions on the dehydration of ethylene glycol.[68,72]

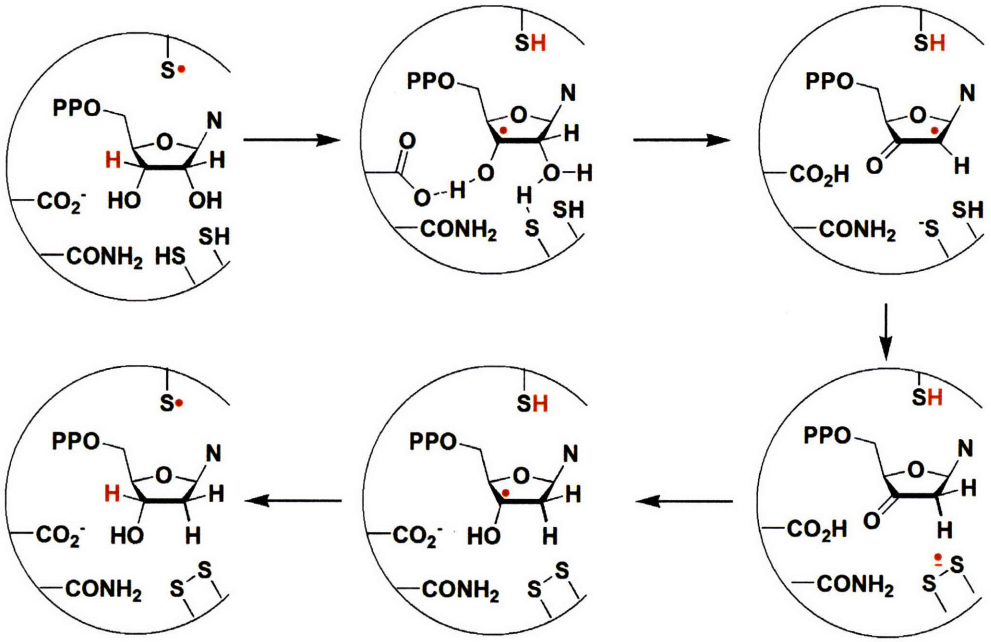

Figure 1–5. Proposed mechanism for nucleotide reduction. See text for a description of each step.

The current mechanism for nucleotide reduction is shown in Figure 1–5.[68] The C• abstracts a 3'–hydrogen atom from the substrate generating a 3'–nucleotide radical. This intermediate undergoes elimination of the 2'–hydroxyl group as water, which is proposed to be the irreversible step in the mechanism and is supported by numerous model studies. The 3'–keto–2'–deoxynucleotide radical then accepts a hydrogen atom from an active site Cys residue generating a disulfide radical anion, which has been observed spectroscopically,[73] and a

3'–keto–2'–deoxynucleotide, which is reduced by the disulfide radical anion to give a 2'–deoxy–3'–nucleotide radical. Abstraction of an H–atom from the active site Cys residue regenerates the C• and yields dNDP. The C• is then reduced by the cofactor; multiple turnover requires re–reduction of the active site disulfide and reformation of C•.

The evidence for this mechanism will not be reviewed here. It should however be mentioned that this mechanism has been supported by biochemical studies using site–directed mutagenesis of the active site residues, substrate analogues and mechanism–based inhibitors, as well as by theoretical, spectroscopic and structural studies of the different classes of RNRs.[68]

Mechanism of C_{439}• Formation

The mechanism of C• generation has been studied extensively in the class II RNR by Licht and Stubbe.[24,68,74] In this system, stopped flow (SF) UV–vis and rapid freeze quench (RFQ) EPR studies demonstrated formation of cob(II)alamin that was exchange–coupled to another radical species.[75,76] Isotopic substitution of Cys with C_β–[$^2H_2$]–Cys revealed a narrowing of the spectrum indicating that the spectrum consisted of a C• exchange–coupled to cob(II)alamin.[24] This was confirmed by rapid chemical quench (RCQ) experiments revealing formation of 5'–deoxyadenosine with similar kinetics as that of C•–cob(II)alamin. The C• has only been detected in the class II RNR, however, due to biochemical and structural similarity of all RNR active sites, it has been suggested to be involved in all RNRs. In the class II case, additional studies have revealed that C• formation is entropically driven,[77] that it is required for every turnover[78] and that its formation occurs in a concerted fashion, i.e. the 5'–deoxyadenosyl radical is not a distinct intermediate in the reaction pathway.[79]

In contrast the mechanism of C• formation in the class IV, class III and class I RNRs is ill–defined. In the class III case, a G• has been postulated to generate the essential C•.[36,80] This is consistent with structural studies which show that the G residue is within 5 Å of the C that needs to be oxidized. However, the gating step that initiates C• generation by the stable G• has not been examined. In the class I case, C• formation is much more complicated and is the topic of

this Thesis. To begin to address the mechanism of C• formation in the *E. coli* class I RNR, the interaction between α2 and β2 must first be considered.

Interaction between α2 and β2

The interaction between α2 and β2 has been explored by several groups. Initial studies using ultracentrifugation were carried out by Reichard and Thelander and showed that α2 and β2 form a 1:1 complex in the presence of ATP, TTP and dATP.[81,82] Biacore methods and inhibition studies lent further support for a 1:1 complex and revealed a K_d of ~0.2 μM in the presence of CDP/ATP.[83-85] While binding of various substrate/effector combinations to α2 has been examined,[86] a systematic investigation of the K_d between α2/β2 in the presence of different nucleotides has not been undertaken.

More recently, Climent and Sjöberg have used C–terminal β2 peptides and heterodimeric β2 to study the α2/β2 interaction.[83,84,87] These studies have found that a peptide consisting of the last 19–37 residues of the C–terminal tail of β2 is a good inhibitor of RNR activity with K_is in the range of 20–40 μM. Binding of heterodimeric β2, ββ', in which one β–monomer is full–length and the β'–monomer is missing the last 30 residues, occurrs with a K_d similar to that with the peptides. Accordingly, a two–step binding model has been proposed between α2 and β2. In the first step, the flexible C–terminal tail of β2 is proposed to be solely responsible for the interaction between α2 and β2 providing an explanation for the similar K_ds between the peptides and ββ'. In the second step, which only occurs with β2, binding of the second protomer was proposed to occur in a cooperative manner and was 17–fold tighter relative to binding of the first protomer. It has been proposed that this cooperativity is mediated by the remainder of β2, across the β2 dimer interface. Consistent with these ideas, only one 30mer peptide was found to bind each α2.

A structure of the active α2/β2 complex does not exist. However, from the individual structures of α2 and β2, Uhlin and Eklund have generated a docking model based on shape and charge complementarity.[88,89] This model is shown in Figure 1–6 and contains several important features. The C–terminal tail of β2 (residues 345–375) is not resolved in any structures solved to

date.[52] It is flexible and responsible for the majority of interaction between β2 and α2. The C–terminal tail of α2 (738–761) is also not resolved in the α2 structure. To obtain crystals of α2, a 21mer peptide identical to the C–terminal residues (355–375) of β2 needed to be co–incubated with α2. Of the peptide, only residues 360–375 are visible in the structure. The most important insight from the docking model has been that the Y_{122}• in β2 that initiates nucleotide reduction and the C_{439} residue in α2, which must be oxidized to a C•, are >35 Å removed. Thus, it was proposed that C• generation in class I RNRs requires long–range radical propagation.

The Radical Propagation Pathway

Based on the docking model and conserved residues, the radical transfer pathway in Figure 1–7 has been proposed. Interestingly, all residues in this pathway are universally conserved and play a major role in active site nucleotide reduction (C_{439}, E_{441}) or in assembly of the diiron Y_{122}• cofactor (W_{48}, D_{237}, H_{118}), except for three Tyr residues, Y_{356} in β2 and Y_{730}/Y_{731} in α2, the functions of which are undefined. These residues have been proposed to reversibly propagate the oxidizing equivalents across the subunit interface from β2 to α2. The proposition of long–range radical transfer in RNR is highly unusual. In no other systems are amino acids known to catalyze charge transport over a long distance. The only system known to perform a similar reaction is DNA photolyase, however, recent results have indicated that long–range radical transfer is not required for its function in vivo, although it is observed in vitro.[22,23] Charge transport in Biology usually involves metal centers; however, no metal cofactors are involved in radical propagation in RNR. Also, the vast majority of radical transfer pathways in Biology catalyze irreversible charge transport, whereas hole propagation in RNR is reversible.

To test the pathway, site–directed mutagenesis of each residue has been carried out. The Y_{122}F and W_{48}F mutants have been uninformative as they interfere with assembly of the Y_{122}• cofactor (see below).[90,91] Sjöberg and coworkers have previously generated the Y_{356}F–β2 mutant and have found it to be inactive.[83] The marginal activity measured was associated with endogenous wt RNR co–purifying with the mutant. In addition, in vivo complementation studies demonstrated that this residue was required for catalysis inside the cell.[92] The roles of Y_{730} and

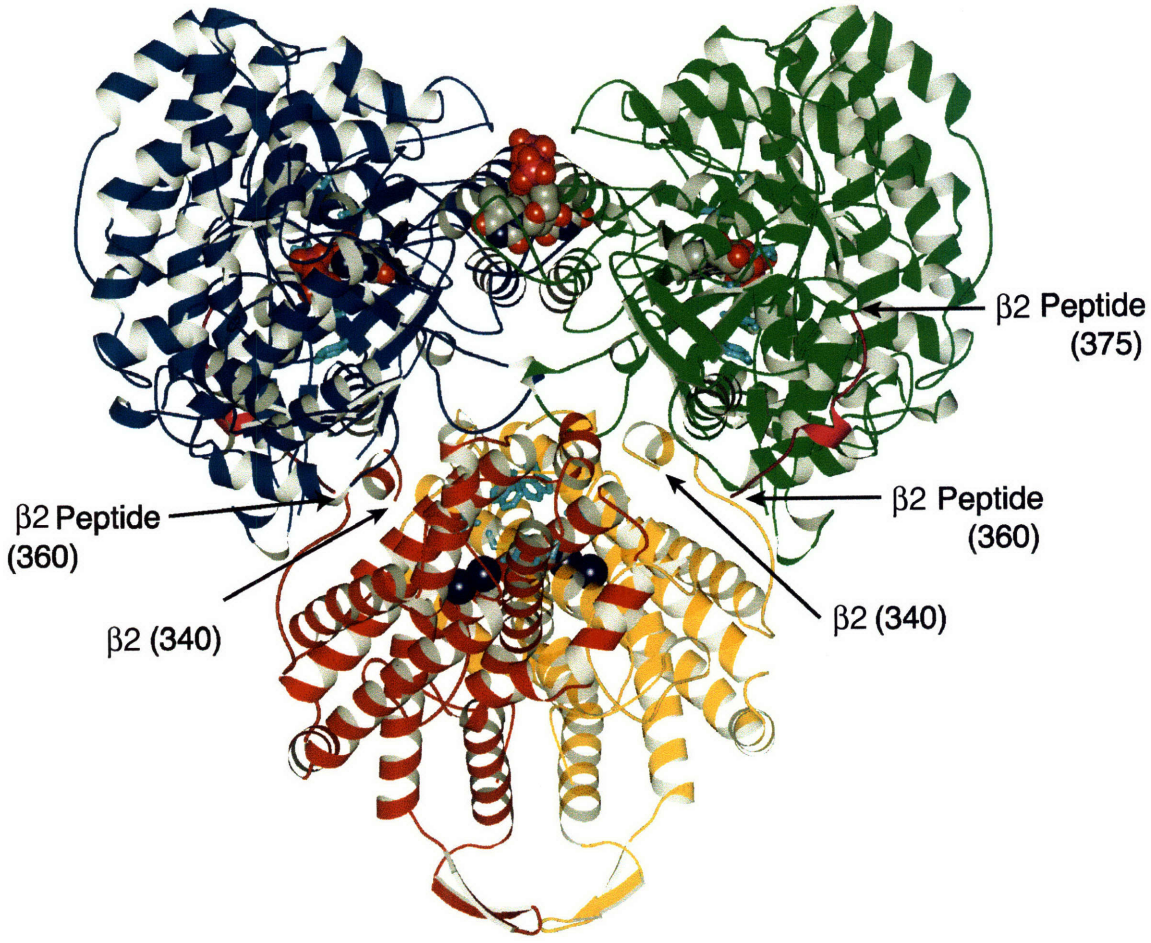

Figure 1–6. Docking model for the interaction between α2 and β2. This model was generated based on shape and charge complementarity between the two subunits. The monomers of α2 are shown in blue and green. Substrate GDP in the active site and effector TTP at the allosteric effector site are shown as spheres. Each monomer contains a 21mer peptide (shown in pink) consisting of the C–terminal residues of β2 (355–375). In this structure, only residues 360–375 are visible. Residues Y_{730} and Y_{731} are shown in cyan in α2. The monomeric units of β2 are shown in red and yellow. The Fe atoms of the diiron cluster are shown as dark blue spheres. Residues Y_{122}, W_{48} and D_{237} are shown in cyan. Residue 340 is the last residue that is observed in the structure. Residues 341–359 in β2 and residues 733–762 in α2 in absent from this model.

Y_{731} have also been interrogated by site–directed mutagenesis. Y_{730}F–α2 and Y_{731}F–α2 mutants have been generated and their structures have been solved by X–ray crystallography.[93] The results have shown that both mutants are inactive in vitro and in vivo, and that the mutations have little effect on the global structure of α2 and on binding to β2, all consistent with involvement of residues Y_{730} and Y_{731} in catalysis. Finally, studies with C_{439}S–α2 have

indicated the importance of this residue in nucleotide reduction, as expected based on the mechanism in Figure 1–5.[94] These studies have highlighted the importance of each residue in RNR function, however, due to their 'inactive' phenotype, mechanistic investigations, particularly the intermediacy of amino acid radicals, are precluded. Nevertheless, from these and other theoretical studies, a chemical mechanism for radical transport has been suggested.[93,95,96] This mechanism involves a series of hydrogen transfer steps between Y_{122} and C_{439} and involves formation of H_{118} and D_{237} radicals. There are several problems with this model. First, it is based on the absence of activity and on negative results. Direct positive evidence for the roles of the residues in Figure 1–7 has been missing. Second, the step between W_{48} and Y_{731}, according to the model, gaps a distance of 25 Å, which is the majority of the distance between Y_{122} and C_{439}. It is difficult to imagine how hydrogen atom transfer between W_{48} and Y_{731} can take place unless a large conformational change is involved. And finally, His and Asp radicals have never been observed in proteins and are likely to have high reduction potentials.

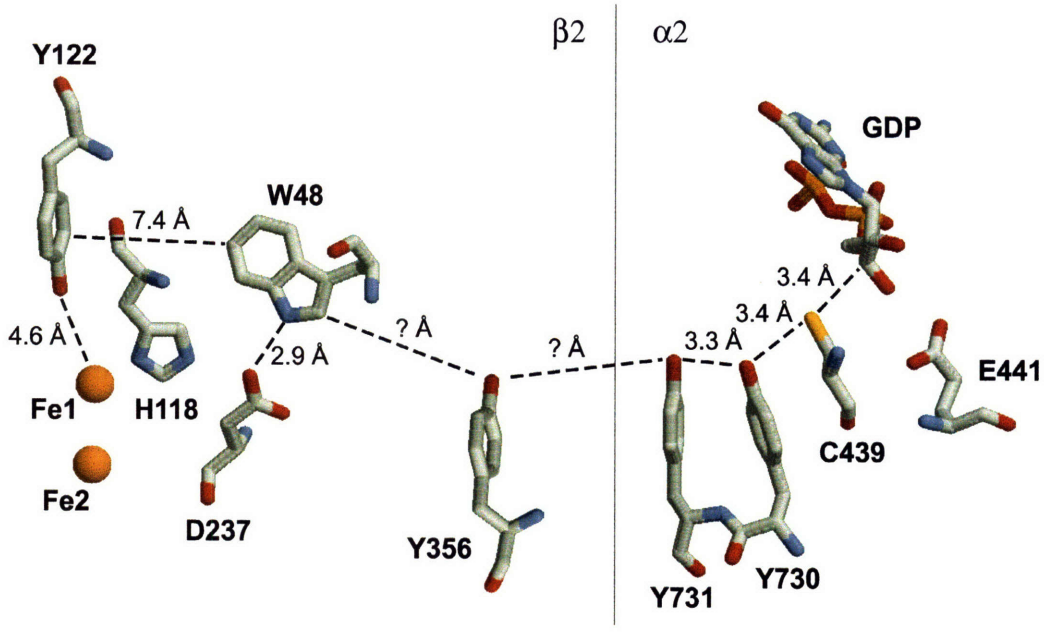

Figure 1–7. The proposed radical transfer pathway of *E. coli* RNR. Distances on the β2 side are from the high resolution structure of oxidized β2.[89] Distances on the α2 side are from the original structure.[88] Note that Y_{356} is not observed in any β2 structures and its position is unknown. The distance between W_{48}–Y_{731} is 25 Å.

Evidence for Radical Transfer

Despite much effort, an oxidized amino acid during radical transfer has not been observed by means of SF UV–vis or RFQ–EPR spectroscopies.[68] As will be described further below, a slow conformational change that precedes rapid radical transfer is responsible for the lack of build up of any observable intermediates.[97] However, two additional lines of evidence, aside from those alluded to above, strongly suggest that the radical is transferred from β2 into α2, and that the distance between Y_{122}• in β2 and C_{439} in α2 is relatively long.

Experiments with mechanism–based inhibitors of RNRs have provided compelling evidence for transfer of the oxidizing equivalents from β2 into α2 (Figure 1–8). Reaction of RNR with 2'–azido–2'–deoxyuridine–5'–diphosphate (N_3UDP) results in destruction of the Y_{122}• and formation of a new radical (N•) in the active site of α2.[98-101] Mutagenesis and isotopic replacement studies have shown that the inhibitor labels the active site of α2 via C_{225}.[102] In addition, with [3'–^{2}H]–N_3UDP an isotope effect on Y_{122}• is observed directly linking reduction of Y_{122}• to chemistry in the active site of α2.[100] Recent isotopic substitution and multifrequency EPR experiments along with computational studies have revealed the structure of the new radical in the active site of α2.[103]

Similar results are obtained with 2,2'–difluorodeoxycytidine–5'–diphosphate (F_2CDP): disappearance of Y_{122}• is accompanied by appearance of a new nucleotide–based radical. The mechanism of inhibition is complex and there are probably multiple pathways.[104] Nevertheless, F_2CDP provides a second example of nucleotide radical formation in the active site of α2 at the expense of Y_{122}• in β2.

A third well–studied mechanism–based inhibitor of RNRs has led to a similar conclusion as the inhibitors above.[105-107] Reaction of RNR with 2'–fluoromethylene–2'–deoxycytidine–5'–diphosphate (FMCDP), leads to loss of Y_{122}• and formation of a new active site radical. Thus, RNR inactivation is a result of rapid Y_{122}• loss in β2 and labeling of the active site in α2 subsequent to production of an active site radical. Isotopic substitution studies have established that the new radical is nucleotide–derived. In addition, the chemistry that leads to the putative

allylic radical with FMCDP is entirely consistent with C_{439}• formation. EPR power saturation studies, which reveal a $P_{1/2}$ of ~0.16 mW are in line with these conclusions, demonstrating a that the new radical is distant from the diiron center. In comparison the Y_{122}•, ~5 Å removed from the diferric cluster, has a $P_{1/2}$ value of 47 mW.

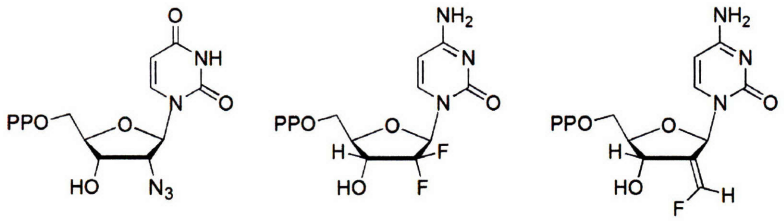

Figure 1–8. Structures of mechanism–based inhibitors of RNR.

Power saturation studies have been performed with FMCDP and with F_2CDP and these studies suggest that the distance between the active site and Y_{122}• is long.[104,107] This distance has recently been assessed directly using pulsed electron–electron double resonance (PELDOR) spectroscopy. This method has emerged as a molecular ruler for distance measurements between two unpaired spins separated by 15–80 Å.[108-110] In PELDOR the weak dipole–dipole coupling between two paramagnets is detected by application of a double frequency or, more recently, a 4–pulse sequence.[111] The strength of dipolar coupling is then related to the distance between the paramagnets. PELDOR spectroscopy has been used to measure the distance between the N•

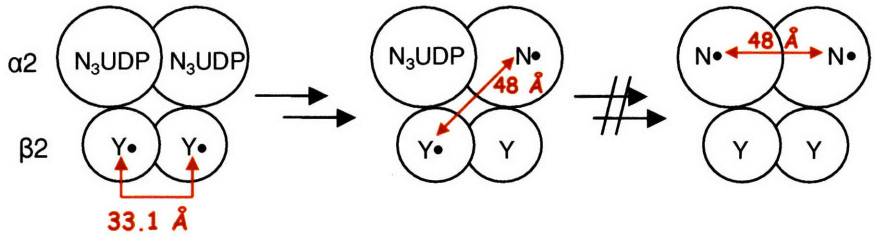

Figure 1–9. PELDOR spectroscopy with N_3UDP and wt α2/β2. PELDOR has been used to measure the distance between N• in one αβ pair and the remaining Y_{122}• in the other αβ pair. Note that due to half–sites reactivity in the first turnover, only one N• forms per α2/β2 complex. An N•–N• interaction is not observed. The distances measured by PELDOR between N•–Y_{122}• is consistent with the docking model which predicts a diagonal distance of 47–50 Å. A distance of 33.1 Å between Y_{122}•–Y_{122}• in resting β2 has been measured by PELDOR, which is consistent with the β2 structure.

generated with N_3UDP in the active site of α2 and the remaining Y_{122}• in β2 – the distance obtained by these studies is consistent with the docking model and establishes that a large conformational change that positions Y_{122}• in β2 into the vicinity of the α2 active site does not occur (Figure 1–9).[112] Accordingly, these results support the docking model and a pathway for long–range radical transfer.

Electron Transfer in Proteins

Radical transfer within the putative pathway in Figure 1–7 requires a series of oxidation/reduction steps. To understand this pathway in more detail, a brief description of electron transfer (ET) and proton–coupled ET (PCET) theory is necessary. ET in Chemistry and Biology is described by the Marcus–Levich relation (Eq. 1–1), where k_{ET} is the ET rate constant, h is Planck's constant, k_B is the Boltzmann constant, T is temperature, $\Delta G°$ is the reaction driving force, λ is the nuclear reorganization parameter and H_{AD} is electronic coupling between donor and acceptor in the transition state.[113] The equation contains a pre–exponential and an exponential factor related to electronic and nuclear reaction components, respectively.[114]

$$k_{ET} = \frac{2\pi^2}{h\sqrt{\pi\lambda k_B T}} H_{AD}^2 \exp\left\{-\frac{(\Delta G° + \lambda)^2}{4\lambda k_B T}\right\} \qquad (1–1)$$

Nuclear factors affecting k_{ET}. The nuclear factor depends on the driving force, $\Delta G°$, and the nuclear reorganization energy, λ. The driving force is defined as the reduction potential of the electron acceptor minus that of the electron donor. Ideally, this is measured in the system of interest. In cases where metal cofactors, such as Fe–S clusters or hemes, are involved, this is possible as the EPR, Mössbauer, UV–vis, fluorescence or IR properties are sensitive to the oxidation state of the metallocofactor. Therefore, $\Delta G°$ can be determined by applying an external potential and determining the change in the redox state of the cofactor.[115,116] Small molecule redox mediators are often necessary if the metal cofactor of interest is embedded within the protein.

In case of amino acid radicals, measurement of $\Delta G°$ is much more difficult as isolation of a single residue of interest is impossible given the numerous other residues that are redox active upon an externally applied potential. Thus, it is standard practice to use solution measurements to approximate reduction potentials of amino acids within proteins with the caveat that these may be perturbed. Tommos and Dutton have demonstrated the major effect that the protein medium can have on $\Delta G°$ by embedding a single W or Y residue within a synthetic three–helix bundle.[66] This study showed that the reduction potential of W was elevated by 0.35 V, relative to that determined for W in solution, whereas that of Y was elevated to an extent (>~0.45 V) that accurate measurements could not be made. Eq. 1–2, sometimes referred to as the Born equation, has been proposed to relate reduction potentials in media of varying dielectric constant.[117] In this equation, $\Delta\Delta G°$ is the increase of reduction potential in the group of interest with radius r, upon its introduction into a medium with dielectric ε. This equation shows that the change in reduction potential is inversely proportional to the medium dielectric. Thus, the lower the dielectric constant of the medium, the higher the reduction potential of the group of interest. However, this correlation depends on the charge distribution of the reactant and product and is thus reaction–specific.

$$\Delta\Delta G° = \frac{14.397}{\varepsilon \times r} \qquad (1–2)$$

$$\lambda = \lambda_i + \lambda_o \qquad (1–3)$$

λ is defined as the energy required to reorganize the nuclei from the equilibrium position of the reactants to that of the products. There are two contribution to λ, often referred to as inner and outer sphere λ (Eq. 1–3), abbreviated λ_i and λ_o, respectively. In polar solvents, the major component is λ_o, which arises from reorientation of solvent molecules upon conversion of the reactant to the product.[118] λ_o is diminished when the reaction is carried out in non–protic, apolar solvents. The second component of λ, λ_i, correlates with changes in bond length and bond angle of the donor and acceptor after ET. Classical descriptions of the λ_i are usually not sufficient to

describe ET reactions in model systems and quantum mechanical treatments have been developed. [114,119]

Another main aspect of the nuclear factor in Eq. 1–1 is the predicted free–energy dependence of k_{ET} (Figure 1–10).[25] At low driving forces, k_{ET} increases with $-\Delta G°$. The maximum rate constant is reached when $-\Delta G° = \lambda$. At this point, ET is said to be activationless. Further increase in the driving force results in a decrease of k_{ET}. This region, where $-\Delta G° > \lambda$, is called the inverted region. The prediction of the inverted effect by theory has by now been well–documented experimentally in various small molecule model systems[120-122] and in proteins.[123,124]

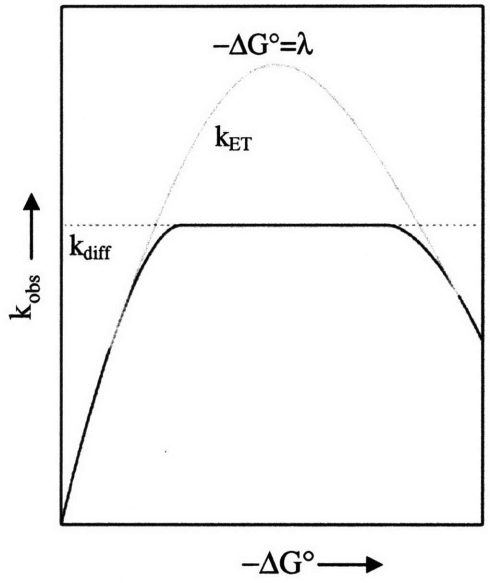

Figure 1–10. Parabolic driving force dependence for k_{ET}. k_{ET} (grey line) is shown as a function of driving force. k_{ET} increases as a function of $-\Delta G°$ until $-\Delta G° = \lambda$. Further increase in $-\Delta G°$ leads to the inverted region, where $\Delta G° > \lambda$ and a drop in k_{ET} is observed. Note that in bimolecular ET reactions, the diffusion limit, k_{diff} (dotted line), can mask k_{ET}. In this case, $k_{obs} = k_{diff}$ when $-\Delta G° \sim \lambda$.

Electronic factors affecting k_{ET}. The electronic factor in Eq. 1–1 is primarily a function of H_{AD}, the strength of coupling between the redox partners. ET within proteins is characterized by weak electronic coupling ($H_{AD} << k_BT$). H_{AD}^2 in Eq. 1–1 is the probability that the electron will transfer when the transition state is reached. In nonadiabatic ET reactions, the transition state must be reached many times before reaction can occur.

H_{AD} has been treated by homogenous barrier models. In this model, the electronic coupling results from direct overlap of the wave functions of the redox partners which are separated by a homogenous medium.[125] This model was first developed by Hopfield and independently by Levich,[126] and indicates that, similar to overlap of molecular wave function, the electronic coupling drops off exponentially with increasing distance between the redox partners. Eq. 1–4, describes H_{AD} as a function of distance: β is the distance decay constant, $H_{AD}°$ is the electronic coupling at contact, R is the distance between the redox partners and R_o is the distance at van der Waal contact. β is a measure of the height of the tunneling barrier and a value of 3.5–5 $Å^{-1}$ has been estimated for redox partners separated by vacuum. An intervening medium will reduce β. The extent of this reduction has been of interest to several research groups and is important for k_{ET} inside proteins.[127] Hopfield estimated a β value of 1.4 $Å^{-1}$ inside proteins; however, direct measurements have only been made in recent years (see below).

$$H_{AD} = H_{AD}° \exp^{-\beta(R-Ro)} \qquad (1–4)$$

To explain the effect of the intervening medium on H_{AD}, McConnell has developed a superexchange coupling model, in which structural units between redox partners mediate coupling and effectively stretch out the wave functions of the electron donor and acceptor to reduce β.[128] In this case H_{AD} is a function of the homologous structural units, or the 'bridge', that separates the redox partners. Beratan and coworkers have elaborated on this model and have suggested that the intervening medium between redox partners in proteins can be broken down into covalent bonds, hydrogen bonds and through–space jumps, each with its own β value.[129,130] In this case, the medium is not homogenous, as assumed by Hopfield, or homologous as described by McConnell, but inhomogenous with various β values, where electronic coupling is mediated to different extents by these various components. This model, known as the tunneling pathway model, has made a testable prediction that a β sheet is more effective at mediating electronic coupling between redox partners than α2 helices. The model has predicted a β value

of 1.0 $Å^{-1}$ and 1.26 $Å^{-1}$ for β sheets and α helices respectively. However, the strength of the hydrogen bonds can further change these β values. Treating hydrogen bonds as covalent bonds reduces the β value in α helices to 0.94 $Å^{-1}$.[114] Thus, the strength of hydrogen bonds appears to determine whether α helices are similar or vastly inferior to β sheets in mediating electronic coupling between two redox partners.

To measure β–values in proteins, Gray and coworkers have turned to small model proteins and determination of so called tunneling time tables (Figure 1–11).[114] A small protein, such as *P. aeruginosa* azurin, is appended with a Ru^{II} photooxidant at various distances from the natural Cu cofactor in this protein.[118] Using flash–quench methodologies and transient absorption spectroscopy, the activationless or coupling–limited ($-\Delta G°=\lambda$) k_{ET} is determined. Plotting the rate constant, or time constant for the reaction as a function of distance yields β.

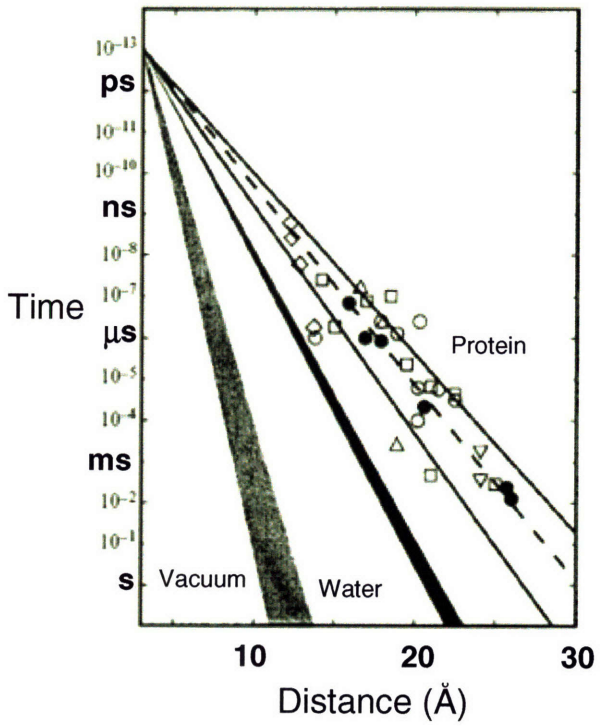

Figure 1–11. Tunneling time table in Ru–modified proteins.[118] Data for azuin (•), cytochrome C (○), myoglobin (Δ), cytochrome b_{562} (□) and hiPIP (◊) are shown and are consistent with a tunneling model and a β of 1.1 $Å^{-1}$. ET along a β strand and α helix with β values of 1.0 and 1.26 $Å^{-1}$, respectively is also shown. ET through water and vacuum are represented by the thin black and thick grey wedges, respectively.

These experiments have been performed with several model proteins and have demonstrated that β is a function of the composition of the intervening medium although a β of 1.2 ± 0.2 $Å^{-1}$ appears to hold for nearly all ET reactions in biology.[25] Importantly, description of the data obtained from these studies with several protein systems by the tunneling pathway model establishes that electrons tunnel inside proteins.

More recently, the importance of intervening aromatic residues that, in effect, reduce the β value and increase the coupling between donor and acceptor, has been recognized.[25,118] In these so called hops, an amino acid may bridge the distance between the electron donor and the final electron acceptor. This is clearly the case in RNR; however, the extent of rate enhancement of k_{ET} as a result of hopping is yet undefined. Gray and coworkers have begun generating hopping time tables, in which k_{ET} is determined as a function of one, two or three 'hops' between the donor and final acceptor. In this time table, k_{ET} is expected to be proportional to the number of hops between the redox partners. Initial studies indicate that k_{ET} is 10^3–fold faster when a distance of 18 Å between the donor and final acceptor is bridged by a single hop vs. direct tunneling through the intervening medium.[131] The insight gained from these studies will be of great importance to RNR, which appears to have separated Y_{122}• from C_{439}, a distance of ~38 Å by 4 'hops', one W and three Y residues.

PCET and Oxidation of Amino Acids

ET theory has been useful in dissecting many ET reactions that occur in photosynthetic and respiratory enzymes, which almost exclusively involve metal cofactors. In RNR, there is an additional complication in that amino acids, rather than metal cofactors participate in redox reactions. Thus far one–electron oxidation of amino acids has been limited to Cys, Gly, Tyr and Trp in enzymatic systems. Oxidation of these residues at neutral pH requires loss of an electron and a proton. The participation of proton in this reaction invokes proton–coupled ET (PCET) in oxidation of amino acid side chains.[132-134]

The need to account for the affect of the proton on electron movement (and vice versa) has required new theoretical and experimental models to understand PCET. Such model systems

were first designed and analyzed by Nocera and coworkers. The propensity of dicarboxylates to form cyclic dimers in non–protic solvents motivated synthesis of the compound in Figure 1–12.[135] In this case, a laser is used to excite the Ru^{II}–polypyridyl or Zn^{II}–porphyrin oxidant, which then reversibly transfers and electron to the organic acceptor. The rate constants for forward and reverse ET are then determined by transient absorption spectroscopy. A kinetic isotope effect of 1.6 and 1.7 on forward and reverse ET, respectively, when the carboxylates were deuterated, demonstrated that proton movement accompanied ET.[136] Charge redistribution within this system was negligible, thus, electronic coupling between donor and acceptor depended directly on the position of the proton at the interface, suggesting that the proton had an influence on electron flow. Asymmetric complexes shown in Figure 1–12 have also been generated.[137,138] In this case k_{ET} was found to depend on the organization of the interface: k_{ET} with D–[carboyxlate–ammidinium]–A was 40–fold slower than with D–[ammidinium–carboxylate]–A. It was concluded that the driving force and reorganization energy depended on the charge distribution of the electron and proton at the interface.

Model systems such as these have lead to development of theoretical formalisms for PCET, which express k_{PCET} as a function of ΔG, λ, H_{AD} and the initial and final states of the electron and proton, indicating that k_{PCET} is a function of the reaction pathway.[132,139] However,

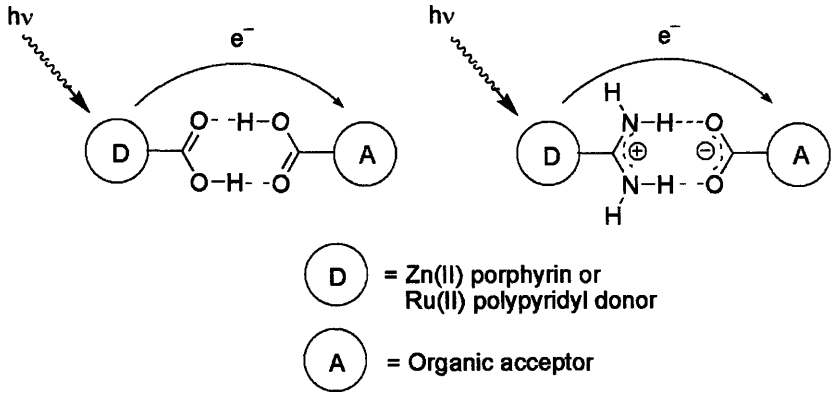

Figure 1–12. PCET model systems. (Left) A symmetric dicarboxylate hydrogen bonding interface. (Right) An asymmetric amidinium–carboxylate hydrogen bonding interface. In each case, the donor transfers an electron to the organic acceptor after photoexcitation. Transient absorption spectroscopy is used to measure forward and reverse ET.

an equation that is widely accepted, such as Eq. 1–1, has yet to be developed. Nevertheless, these studies underline the importance of the position of the proton during the transfer on k_{PCET}, which is pertinent to understanding the PCET pathway in RNR.

Thermodynamic and kinetic aspects of PCET. As indicated above, oxdiation of Tyr requires loss of a proton and electron and can occur by several mechanisms, which may be described by the square scheme in Figure 1–13.[132,133] In this scheme the pathways on the edges of the square correspond to step wise reactions. Accordingly, oxidation of Y may occur by proton transfer (PT) followed by ET, or in the reverse order, ET followed by PT. These pathways correspond to simple ET and PT reactions, not PCET. Alternatively, this reaction can occur in a concerted fashion, in which proton and electron move together, as shown in the diagonal path. This is the PCET pathway. There are many definitions of PCET. We define PCET any process in which proton movement affects the kinetics and thermodynamics of ET, and vice versa. Thus hydrogen atom transfer (HAT) is a subset of PCET.

The diagonal PCET pathway in the square scheme may further be broken down into two mechanisms. Here, we restrict the discussion to mechanisms that may be distinguished in protein systems. On the diagonal path, the proton and electron may be unidirectionally coupled as shown in Figure 1–14. In this case, the electron and proton originate from the same residue and arrive at the same group. This corresponds to HAT and the relevant property in this reaction is the bond dissociation energy (BDE). Alternatively, the electron and proton may be

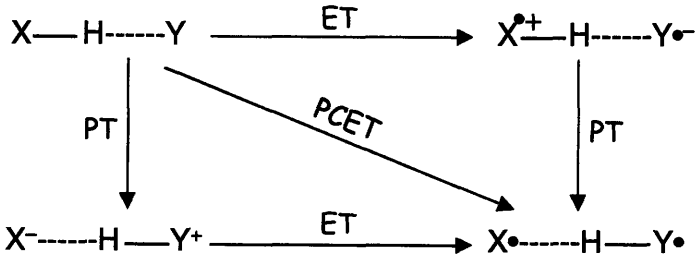

Figure 1–13. Square scheme for PCET. The edges of the square describe step wise PT/ET or ET/PT. The diagonal path corresponds to PCET. PCET is further divided into co–linear and orthogonal PCET (see Figure 1–14).

orthogonally coupled. In this case, the electron and proton originate from the same residue but have different destinations. The relevant properties in this case are $\Delta G°$ and pK_a.

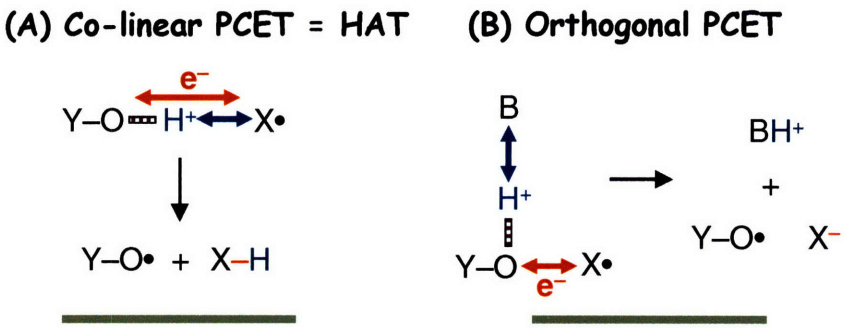

Figure 1–14. Two classes of PCET reactions. (A) Co–linear PCET or HAT involves direct coupling between proton and electron from the point of origin to the final destination. (B) In orthogonal PCET, the proton and electron originate from the same group but arrive at different moieties.

Thermodynamically, there is a bias toward the PCET pathway rather than the step wise ET/PT or PT/ET reactions.[134,140] Because the initial and final states in the square scheme are the same, all three pathways are isoenergetic. However, the diagonal path avoids charged intermediates, the formation of which is thermodynamically uphill inside proteins. Thus, ΔG° for PCET is always lower than that for the initial ET or PT along the paths on the edges of the square. On the other hand, avoiding charged intermediates comes at a cost as coordinating the movement of proton and electron has been proposed to result in a larger λ for PCET. Thus, the competition between a step wise process and PCET is determined by the extent of favorable energetics vs. larger reorganization energy. This has been demonstrated experimentally by Sjödin et al. with the Ru^{II}–polypyridyl–Y model systems.[141-143] In this case a covalent Ru^{II}–polypyridyl–Y model was prepared and used to study the mechanism of Y oxidation by transient absorption stectroscopy as function of pH, and temperature . The authors concluded that when the driving force for PCET, $\Delta G°_{PCET}$, was not great enough to account for its larger λ, step wise ET/PT was observed. Otherwise, the PCET reaction dominated.[143] However, the simplicity of this conclusion has been contested.[144,145]

As discussed above, a robust model that relates the rate constant for PCET to the variables of ET and PCET is currently been developed. Recently, Mayer and coworkers have approximated k_{PCET} using the Marcus cross relation in Eq. 1–5, where k_{XY} is the rate constant for the PCET reaction between groups X and Y, k_{XX} and k_{YY} are the self exchange reaction rate constant for X and Y, respectively, K_{XY} is the equilibrium constant for the reaction between X and Y, and f_{XY} is usually ~1.[146] This relation has been used with some success for a wide range of PCET reactions. Comparison of predicted k_{PCET} using Eq. 1–5, and knowledge of self exchange rate constants with experimentally determined k_{PCET}, shows a general agreement within an one–two orders of magnitude.

$$k_{XY} = \sqrt{k_{XX} k_{YY} K_{XY} f_{XY}} \qquad (1–5)$$

pH dependence in the driving force. The reduction potentials of Y and W have been measured in solution and protein maquettes. However, both of these potentials are highly pH–dependent, because, as noted above, oxidation of amino acids at neutral pH requires loss of electron and proton. The potential of N– and C–protected Y and W has been measured directly as a function of pH using differential pulse voltammetry.[66] This technique is often used for irreversible reactions and measures peak potentials that are within 30 mV to reduction potentials determined by cyclic voltammetry or pulse radiolysis. The results of these experiments are shown in Figure 1–15. They reveal two distinct regions, one which is pH dependent and one which is pH independent. The breaks in the curves occur at the pK_as of the reduced and oxidized forms. Below pH 3.7, W is oxidized by simple ET resulting in $WH^{\bullet+}$. Above pH 3.7, oxidation of W shows Nernstian behavior, a 59 mV drop per pH unit, until pH~p*K*a of the reduced form (pH~14). Similarly, oxidation of Tyr above pH 10.1 relates to the $Y^-/Y^\bullet$ couple. Below this pH, Tyr also displays Nernstian behavior until pH~p*K*a of the oxidized form (pH~ –2). DPV with Y and W shows that the proton has a major influence on the reduction potential, which is crucial for the mechanism and directionality of radical transfer as will become apparent below.

Analysis of the PCET Pathway in RNR

Having described ET and PCET in proteins, we return to the analysis of the radical transfer pathway of RNR. Our model for radical transfer has been hopping from [Y_{122}• ⇆ W_{48} ⇆ Y_{356}] within β2 to [Y_{731} ⇆ Y_{730} ⇆ C_{439} ⇆ nucleotide] within α2. The thermodynamics and kinetics of each of these steps, in models and in RNR, will be discussed below.

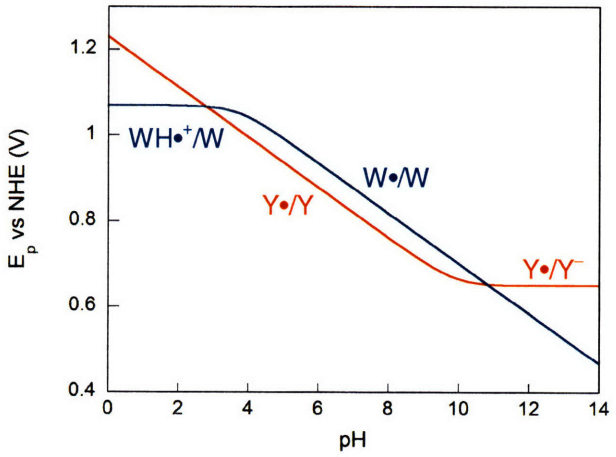

Figure 1–15. Peak potentials of Ac–Y–NH_2 and Ac–W–NH_2 as a function of pH.

Oxidation of W_{48} by Y_{122}•. According to our model, the first step in radical transfer involves oxidation of W_{48} by Y_{122}•. As discussed above, the thermodynamics of this reaction will depend on the protonation state of each residue. The reaction is highly unfavorable if the Y_{122}•/Y_{122}^- couple generates a $W_{48}H^{\bullet+}$ or W_{48}• as shown in Eqs. 1–6 & 1–7. If, however, Y_{122}• is protonated upon reduction, then the thermodynamics are more favorable, with $\Delta G°$ of 0.25 and 0.06 V, for $W_{48}H^{\bullet+}$ and W_{48}•, respectively, as shown in Eqs. 1–8 & 1–9. Thus, the positioning of the proton determines the thermodynamic and kinetics of this first step. In our model, Y_{122}• is protonated upon reduction. We have proposed that the water ligated to Fe1, the Fe^{III} ion closest to Y_{122}•, which is 4.1 Å removed, acts as the proton donor in forward radial transfer and as the proton acceptor in the reverse direction. However, we note that the Y_{122}• in *E. coli* β2 is not hydrogen bonded, though this is the case in other RNRs. Further, in our model the D_{237}–W_{48} dyad controls the gating of radical transfer (see below).

$$Y\bullet + W \longrightarrow Y^- + WH\bullet^+ \qquad \Delta G° = 0.42\ V \qquad (1–6)$$

$$Y\bullet + W \longrightarrow Y^- + W\bullet + H^+ \qquad \Delta G° = 0.23\ V \qquad (1–7)$$

$$Y\bullet + W + H^+ \longrightarrow Y + WH\bullet^+ \qquad \Delta G° = 0.25\ V \qquad (1–8)$$

$$Y\bullet + W \longrightarrow Y + W\bullet \qquad \Delta G° = 0.06\ V \qquad (1–9)$$

Evidence for reversible oxidation of W by Y• has come from dipeptide model systems. Studies with acylated W–Y (Ac–W–Y) have demonstrated chemical competence for oxidation of Y by W•, and vice versa.[147] It was found that W• oxidizes Y with a k_{obs} ~9×10^4 s^{-1} between pH 6–10. Above pH 10.9, Y• was found to oxidize W with a k_{obs} of 1.5×10^5 s^{-1}. As shown in Figure 1–15, this trend is predicted by the driving force dependence for each residue measured as a function of pH. Thus, the pH determines the directionality of this reaction. These model studies provide an answer for how RNR can prompt oxidation of W_{48} by Y_{122}• in forward radical transfer and catalyze oxidation of Y_{122} by W_{48}• in the reverse direction. Judicious positioning of the proton fine–tunes both forward and reverse reactions between Y_{122}• and W_{48}. For example, if the protein environment can enforce rapid protonation of Y_{122}• upon its reduction and deprotonation of $W_{48}H\bullet^+$, forward PCET could be favorable. deprotonates the $W_{48}H\bullet^+$, its reduction potential will be lower and forward PCET will be favorable. Conversely, if it can enforce $WH\bullet^+$ in the reverse direction, oxidation of Y_{122} will be most favorable.

Evidence for the oxidation of Y_{122} by $W_{48}H\bullet^+$ has come from examination of Y_{122}• cofactor assembly.[19,20,148] The model that has emerged for this reaction is shown in Figure 1–16.[16,25] Addition of Fe^{II} to apo β2, via intermediate P,[149] leads to intermediate X–$WH\bullet^+$ which can partition between two pathways. The outcome of the reaction is a function of [Fe^{II}] used to assemble the diiron cofactor. When excess Fe^{II} is used, intermediate X oxidizes Y_{122}. However, in the presence of limiting Fe^{II}, $WH\bullet^+$ directly oxidizes Y_{122}. Thus, this reaction provides direct evidence for communication between Y_{122}• and W_{48} in β2.

Gating of radical propagation. A major aspect of radical initiation is that it is gated, that is it relies on another step immediately prior to radical initiation. The Y_{122}• is directly

responsible for nucleotide reduction, therefore, its transfer into the active site of α2 and back must be exquisitely controlled. Reduction of the Y_{122}• results in an inactive enzyme. The mechanisms that have evolved to finely manage hole transfer are at present poorly understood. However, a clue regarding the control over radical transfer has come from pre–steady and steady state kinetics of RNR.[97] These studies have shown that radical propagation is preceded by a conformational change, which is rate–limiting in turnover at low [RNR] (~3 μM). In wt RNR, a k_{obs} of 4–16 s^{-1} has been measured for this conformational step. The failure to observe intermediates during radical transfer is directly related to the physical step that precedes rapid chemistry. A slow step followed by a series of rapid steps avoids build up of any transient intermediates. However, the detailed physical changes that occur to prompt hole propagation are not understood.

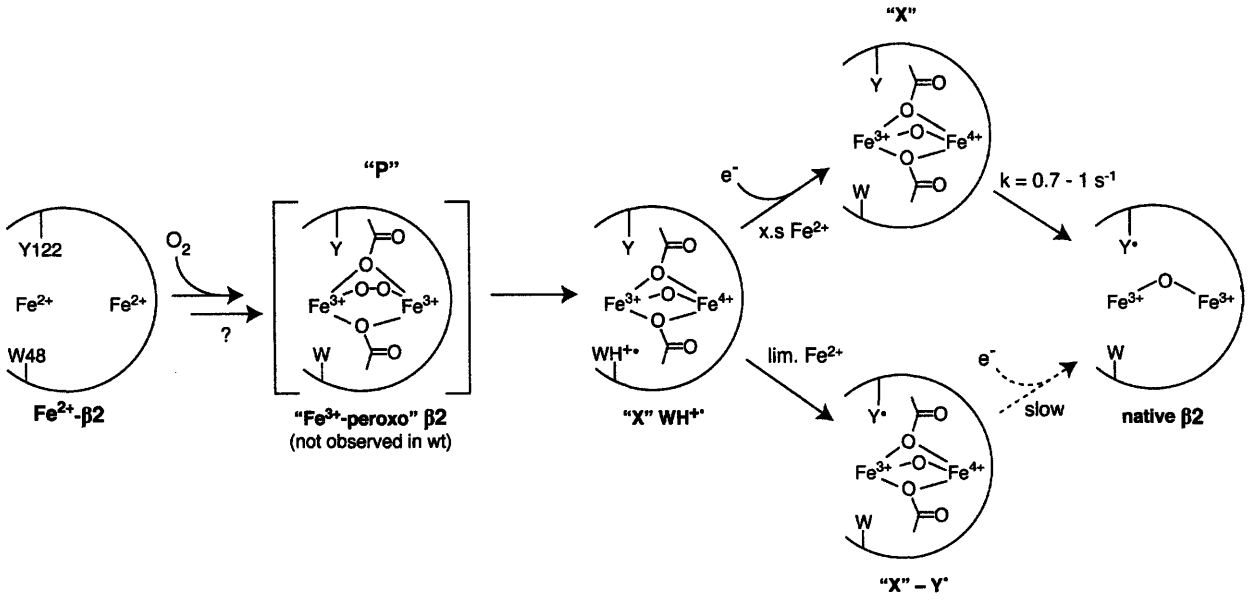

Figure 1–16. Working model for cofactor assembly in *E. coli* β2. Reaction of apo β2 with Fe^{II} and O_2 yields X–WH•$^+$ via a putative $(Fe^{III})_2$–peroxo species not observed in *E. coli* but seen in mouse β2.[147] Partitioning from X–WH•$^+$ depends on the [Fe^{II}]. In the presence of limiting Fe^{II}, WH•$^+$ oxidizes Y_{122}. X is subsequently reduces slowly by reductants in solution (ascorbate). In the presence of excess Fe^{II}, WH•$^+$ is reduced by Fe^{II}. X then oxidizes Y_{122} to generate Y_{122}•.

We have previously proposed that the D_{237}–W_{48} dyad could act as the gatekeeper for hole transfer. If D_{237} is distant from W_{48}, such that a hydrogen bond cannot form, then Y_{122}• must

oxidize W_{48} to a $W_{48}H^{\bullet+}$, which is uphill by 0.25–0.42 as shown in Eqs. 1–6 & 1–8. However, if a conformational change moves D_{237} close to W_{48}, so that the proton can be transferred to D_{237}, then $Y_{122}^{\bullet}$ is in effect generating a $W_{48}^{\bullet}$ and the energetics of this step are more favorable, 0.06–0.23 V, as shown in Eqs. 1–7 & 1–9. Thus, binding of substrate and effector could trigger a conformational change in α2 which is structurally conveyed to D_{237}, that lowers the reduction potential of W_{48} and allows hole transfer to commence. The experiments in the assembly of $Y_{122}^{\bullet}$ are consistent with this proposal as they suggest that the reduction potential of $W_{48}H^{\bullet+}$ is higher than that of $Y_{122}^{\bullet}$. Experiments performed in this Thesis will add to our knowledge regarding the changes that take place when substrate and/or effector bind to α2/β2.

Connectivity between W_{48} and Y_{356}. Next, we propose oxidation of Y_{356} by $W_{48}^{\bullet}$. The former is not visible in any β2 structures, thus its position is unknown. However, the same thermodynamic and kinetic considerations discussed above also hold for this reaction. At this juncture in the pathway, two mechanisms of Y_{356} oxidation may be envisioned: HAT or orthogonal PCET. In the former case, Y_{356} would need to be close to W_{48} and Y_{731} to participate in a hydrogen atom relay. This would require significant movement of Y_{356} to access W_{48} in β2 and Y_{731} in α2, as these residues are 25 Å apart in the docking model. In the latter case, conformational changes are not necessary as long range electron transfer would be coupled to short distance, off–pathway proton transfer. Experiments carried out in this chapter favor the latter model for Y_{356} oxidation.

The subunit interface: Y_{356}–Y_{731}–Y_{730}. The subunit interface is lined with three Y residues. Whether HAT or orthogonal PCET is the attendant mechanism of radical propagation, the three tyrosines that bridge the α2/β2 interface are likely to form an even energetic landscape. This design likely ensures that hole transfer occurs smoothly between α2/β2 in both directions, i.e. without a build up of any intermediates, and that the radical spends minimal time at the subunit interface where it is most exposed and therefore most susceptible to quenching. If Y_{356} is involved in orthogonal PCET, then it is likely that residue Y_{731} communicates with Y_{356} by the

same mechanism and with Y_{730} by HAT. Thus, Y_{731} could incorporate both PCET mechanisms (Figure 1–14) in each radical propagation event.

We have postulated that the mechanism of hole propagation within α2 occurs by HAT. This proposition is based on the vicinity of residues Y_{731}, Y_{730}, and C_{439} and on the superposition of the active site structures of three classes of RNRs shown in Figure 1–17.[25,150] In each case the oxidant that generates C• is adjacent to the Cys residue, and in each case, a HAT mechanism has been proposed. However, we note that recent computational studies have suggested that the distinction between HAT and PCET is sometimes difficult to make. Calculations on the phenoxyl radical/phenol self exchange reaction in the gas phase have indicated that it proceeds via a PCET mechanism in which the electron is transferred between π orbitals on the phenol and the proton is transferred between distinct orbitals of σ(O–H) symmetry.[151] Thus, this reaction is not derived from a genuine hydrogen atom. This distinction is exceedingly difficult to make experimentally in a protein. For the purpose of our studies, we may define HAT a process in

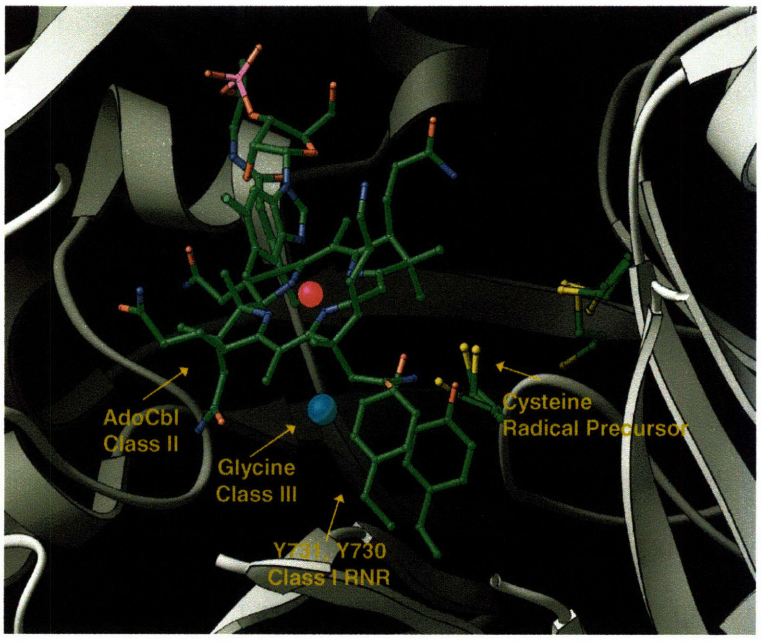

Figure 1–17. Superimposition of the active sites of RNRs from three different classes. This view of the active sites shows that the oxidants that generate C• in each class are superimposible in three–dimensional space.

which the proton and electron originate from the same moiety and have the same destination, regardless of the initial or final orbital. Experiments performed in this Thesis will suggest a mechanism for radical transfer between Y_{730} and C_{439}.

Connectivity between Y_{730}–C_{439}. The final step in radical transfer is generation of C_{439}• by Y_{731}•. Because this reaction is proposed to occur by HAT, the relevant properties to consider are BDEs. The BDE of aliphatic R–SH is 88–91 kcal/mol,[152,153] whereas that of phenol is 87 kcal/mol.[154] Therefore, oxidation of C_{439} by Y_{731} is uphill by 1–4 kcal/mol. This reaction is compensated for by steps in the nucleotide reduction process which are thermodynamically downhill, as has been discussed in detail by Licht and Stubbe.[68] Note that this reaction would be uphill by ~0.5 V or 11–12 kcal/mol, if orthogonal PCET was the operative mechanism. The kinetics of thiyl radical formation by a phenol radical have previously been studied by Land and coworkers.[59,155] They have used decay of a Y•–W in the presence of glutathione to estimate rate constants for glutathione radical formation. From these experiments they estimated a rate constant of 2×10^5 M^{-1} s^{-1}. Studies that more closely mimick the RNR radical transfer pathway, i.e. with C–Y dipeptides, were not carried out. Also, the experiments by Land and coworkers were performed at pH 8.1, where the Cys in glutathione was partially deprotonated. Thus, the mechanism in these model studies may be different from that proposed in RNR. Nevertheless, they show that oxidation of Cys by Y• is rapid and feasible under their experimental conditions.

Our Approach to Studying Radical Transfer

The studies above have indicated that the limited repertoire of natural amino acids accessible by site–directed mutagenesis does not allow a mechanistically informative perturbation of the radical initiation pathway in RNR. The site–directed mutants are inactive thus precluding mechanistic investigations. To learn more about this process the rate–limiting step must be changed from the conformational step to radical transfer. This requires subtle and direct perturbations at each residue in the pathway. In this Thesis we have taken a focused approach to site–specifically replace residues Y_{356}, Y_{730} and Y_{731} with unnatural amino acids that are structurally homologous to Y but have altered reduction potential and/or pK_as, properties that

are crucial for the mechanism of PCET. The unnatural amino acids that have been incorporated are shown in Figure 1–18. The Chapters described herein present mechanistic studies performed with β2 or α2 site–specifically substituted with one of the analogues in Figure 1–18. This has in turn required application of sophisticated methods for unnatural amino acid incorporation, which have only recently been developed. The two methods that are used in this Thesis are briefly discussed below.

Semisynthesis of β2 using EPL. We have used intein–mediated chemistry to replace Y_{356} in β2 with unnatural amino acids. An intein is a protein domain that catalyzes its own post–translational self–excision from a larger polypeptide in addition to splicing of the N–terminal and C–terminal domains (N–extein and C–extein) that flank the intein domain.[156,157] The first intein, Vma from *Saccharomyces cerevisiae,* was discovered in the early 1990s.[158] The potential usefulness of self splicing in protein engineering fueled detailed studies of the mechanism of action of this multi–step process. This understanding has led to the development of a number of re–engineered intein constructs that are now commercially available allowing

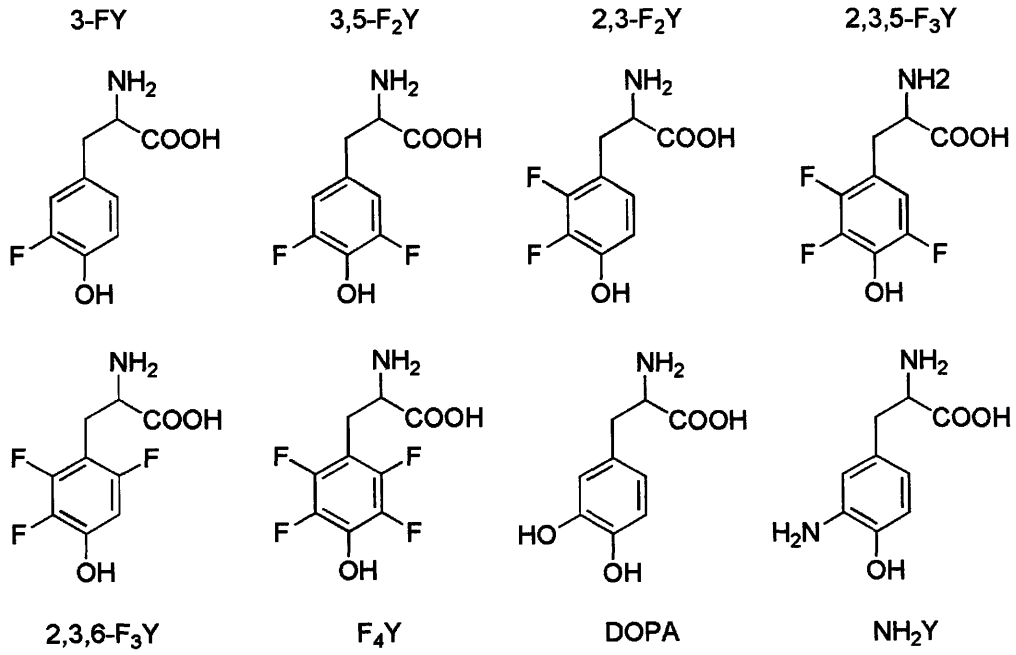

Figure 1–18. Unnatural Y analogues incorporated into β2 or α2 in this Thesis.

semisynthesis of proteins[159,160] and consequently site–specific incorporation of unnatural amino acids. In this Thesis, we have extensively used one of these techniques, expressed protein ligation (EPL), to construct β2 semisynthetically.

To demonstrate how EPL works, first the mechanism of intein self–expulsion must be outlined. The proposed mechanism for the *S. cerevisiae* Vma intein is shown in Figure 1–19.[161,162] Splicing is initiated by an N–S acyl shift that converts a peptide bond into a thioester at the N–extein junction site. Transthioesterification via the C–extein Cys residue results in a branched intermediate. This intermediate undergoes excision of the intein domain by attack of an Asn residue on the peptide bond at the C–extein junction site forming an intein succinimide and the spliced extein domain. Spontaneous S–N acyl rearrangement generates the ligated N and C–exteins connected via an amide bond.

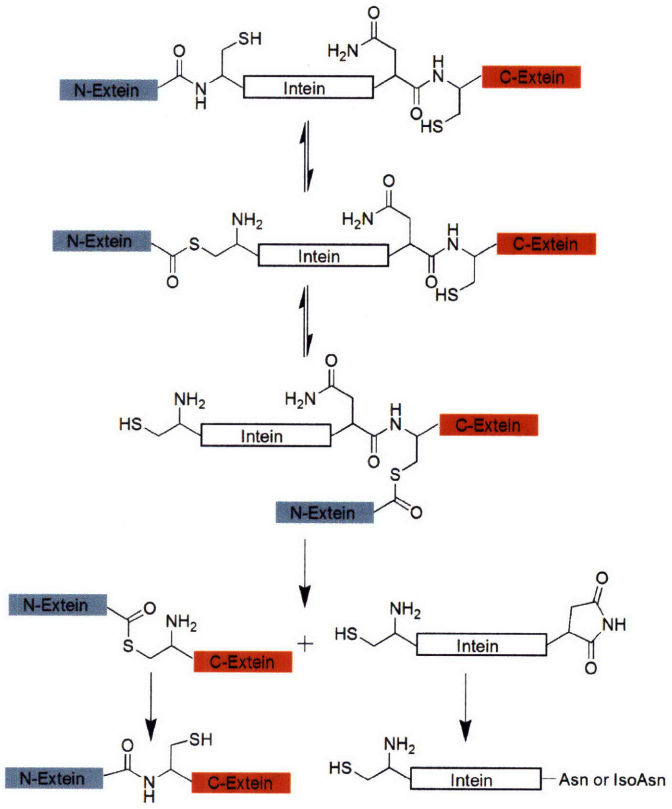

Figure 1–19. Proposed mechanism of intein self–expulsion for the *S. cerevisiae* Vma intein.

We have applied EPL to make the β2 subunit of *E. coli* RNR semi-synthetically.[163] β2 is a homodimer with each polypeptide containing 375 amino acids. The C–terminal 35 amino acids of *E. coli* β2 are disordered and this region houses Y_{356}, a residue proposed to be important in the mechanistically unusual radical propagation process described above. The general scheme that we have used for β2 semi-synthesis is shown in Figure 1–20. Residues 1–353, folded into a native state, are made via recombinant DNA technology and are ligated to residues 354–375, made by solid phase peptide synthesis (SPPS). The majority of β2 (residues 1–353) is fused to an intein–mutant, which lacks the C–extein Asn and Cys residues but contains a purification tag, the chitin binding domain (CBD). After recombinant expression, the engineered intein-fusion product catalyzes the first step of the self–cleavage reaction, but not the ensuing splicing steps. The thioester formed is then captured by a small molecule thiol, such as 2–mercaptoethanesulfonic acid (Mesna), via transthioesterification, resulting in cleavage of the target protein from the intein–CBD construct. The thioester–activated, truncated β2 is then ligated to the remainder of β2, a peptide containing residues 354–375 with the unnatural amino acid at residue 356 and a Cys at its N–terminus (residue 354). Transthioesterification of the N–terminal Cys residue of the peptide followed by a spontaneous S–N acyl shift yields full length β2. Wild type β2 contains a Ser at 354 and thus a second mutation, in addition to the unnatural amino acid, is introduced into β2 at residue 354.

Advantages and limitations of EPL. A number of methods are in the process of being developed for the incorporation of unnatural amino acids into proteins in a robust fashion. We have chosen EPL for the semi-synthesis of β2 for a number of reasons. First, 100 mg quantities of semi–synthetic β2, necessary for mechanistic biophysical experiments, are accessible. Second, purification with the CBD tag is robust. Third, residue Y_{356}, a member of the radical initiation chain and of great interest to us mechanistically (Figure 1), is at the disordered C–terminal tail of the protein, and therefore a good target for substitution by EPL. Finally, a number of inteins are now commercially available. As shown in Figure 4, we have used the thiol method to cleave the activated-truncated β2 from the intein–CBD construct, but temperature and pH–induced

cleavage may also be used to generate the desired species. Because of these advantages, the EPL method has been used by numerous investigators and excellent reviews on its applications are available.[164,165]

EPL also has a number of limitations. First, site–specific incorporation of probes can only occur close to the N– or C–termini of the protein because peptides longer than 40–50 residues are difficult to synthesize and purify. Second, the site of ligation must be accessible to solvent in the native protein. If the site of ligation is buried, then the ligation reaction needs to be carried out under denaturing conditions, and methods to refold the protein are required. Third, the thioester–truncated protein undergoes hydrolysis in competition with ligation to the peptide. The rate of ligation, a bimolecular reaction, is elevated by increasing concentrations. However, the ligation is still slow and consequently hydrolysis almost always accompanies the desired reaction. Methods are thus required to separate the truncated protein from the full–length, ligated protein. This problem is aggravated if the protein of interest is multimeric, as in the case of β2.

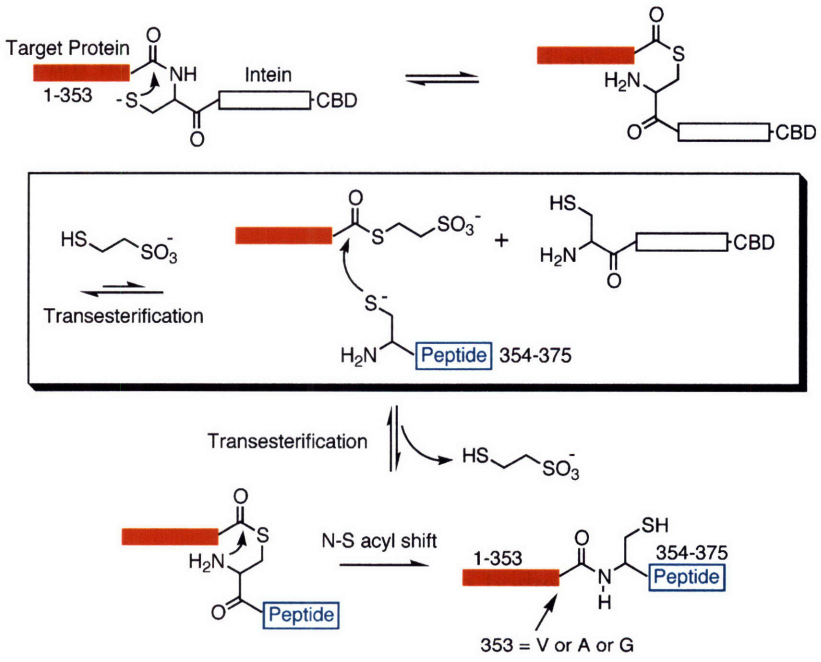

Figure 1–20. Semisynthesis of β2 via EPL. Residues 1–353 are expressed recombinantly as an intein–CBD chimera. After the initial N–S acyl shift, the small molecule thiol, Mesna, is used to cleave the truncated β2 from the intein–CBD domain. The resulting Mesna–activated β2 is ligated to a β2–22mer which is prepared by SPPS and contains residues 354–375 with an unnatural amino acid at residue 356. Note that the $V_{353}G$ mutation was necessary to increase cleavage and ligation yields.

Suppressor tRNA/aminoacyl–tRNA synthase method. Schultz and coworkers have recently developed a robust in vivo method for site–specific incorporation of unnatural amino acid.[166-170] In this method, an aminoacyl–tRNA synthetase (RS) that is specific for the unnatural amino acid of interest, is selected from a library of synthetases using a variety of screens. This RS has a cognate tRNA that contains the amber stop codon and is optimized for interacting with the library of RSs. Importantly the tRNA/RS pair is orthogonal to those in the host, that is, the amber suppressor tRNA cannot cross–react with any in vivo RSs, and the evolved RS cannot charge any in vivo tRNAs with a natural or unnatural amino acids. In addition, the in vivo RSs are not able to charge their cognate tRNAs with the unnatural amino acid. Finally, the unnatural amino acid must be taken up by the cells and must not be toxic. If these criteria are met, and the gene of interest is expressed inside the host with the amber stop codon at the residue where the unnatural amino acid is to be incorporated along with the tRNA/RS pair specific for that unnatural amino acid, then expression of the protein of interest results with high fidelity and specificity. So far, this method has been applied to *E. coli*, yeast and mammalian expression hosts. In *E. coli* the *Methanococcus jannaschii* tRNA/RS pair has been manipulated to fit the criteria above. In yeast and mammalian cells, the *E. coli* tRNA/RS pair has been used. These pairs have allowed insertion of ~30 unnatrual Y analogues into target proteins with high fidelity and specificity. In this Thesis, we have evolved a RS that is specific for NH_2Y (Figure 1–18) and used the suppressor tRNA/RS method to site–specifically incorporate NH_2Y into residues 730 or 731 in α2.

The advantage of this method is that the unnatural amino acid may be incorporated anywhere in the protein, not just at the C– or N–termini, as is the case with standard intein ligation methods. In addition, this method can be used to study target proteins in vivo with a site–specific unnatural probe. On the other hand, unnatural amino acid that are not taken up by or are toxic to the cell cannot be used in this method. In addition, each unnatural amino acid requires evolution of a new tRNA synthetase.

Chapter Preview

At the outset of this work, many aspects regarding radical propagation in RNR were unknown. Most importantly, there was no direct evidence that this pathway was functional in hole transport over a long distance. Intermediacy of amino acid radicals had not been demonstrated and the roles of Y_{356}, Y_{730} and Y_{731} were experimentally undefined. It seemed highly unusual that Nature would choose a seemingly bizarre long–range radical transfer pathway to perform the essential cellular task of nucleotide reduction. In addition, the mechanism of oxidation at each residue, if long–range radical transfer occurred, was undetermined. Models had been proposed by several groups; however, no mechanistic studies had been undertaken, mostly due to the inactive phenotype of the site–directed pathway mutants. Finally, the method of regulation of radical transport and the role of substrate and effector in this process were unknown. No models had been contemplated regarding the timing of radical transfer, i.e. whether it occurred simultaneously or consecutively within both pathways in the $\alpha 2/\beta 2$ complex.

In this Thesis, we have focused on intein ligation and suppressor tRNA/synthetase methodologies to site–specifically replace residues Y_{356}, Y_{730} and Y_{731} with unnatural amino acids. In **Chapter 2**, we describe incorporation of 3,4–dihydroxyphenylalanine (DOPA) into residue Y_{356} of the $\beta 2$ subunit. Our studies demonstrate formation of a DOPA radical (DOPA•), which we have characterized using UV–vis and EPR spectroscopies. The requirement of DOPA• formation on the presence of substrate and/or effector implicates pathway dependence. We find that DOPA• formation is kinetically competent, however, only half of the total Y_{122}• participates in DOPA• formation, the rest remains unreacted invoking half–sites reactivity in the $\alpha 2/\beta 2$ complex. We also show that the substrate/effector pair bound in $\alpha 2$ determine the kinetics of DOPA• formation and its conformation at the $\alpha 2/\beta 2$ interface. Finally, in collaboration with Prof. Marina Bennati, we have used PELDOR spectroscopy to measure the distance between the DOPA• in one $\alpha\beta$ pair with the unreacted Y_{122}• in another $\alpha\beta$ pair. This provides the first

structural constraint for residue 356, which is invisible in all structures of β2 solved to date, and is consistent with radical initiation only within one of two αβ pairs in the complex.

In **Chapter 3**, we examine heterodimeric DOPA–β2, DOPA–ββ', in which the β–monomer is full–length and contains DOPA at residue 356, but the β–monomer is truncated at residue 353. Inspection of this variant also reveals kinetically competent DOPA• formation only in the presence of substrate and effector. We present characterization of the DOPA• by UV–vis and EPR spectroscopies and find that the local environment of DOPA• in DOPA–ββ' is very similar to that in DOPA–β2. DOPA–ββ' maintains the essential conformational changes for triggering radical migration and formation of a DOPA• in a kinetically competent fashion suggesting that the second C–terminal tail of β2 is not required for propagation in the first αβ pair. An asymmetric interaction is proposed between β2 and α2 to explain the yields of DOPA• in DOPA–β2 compared to those in DOPA–ββ'. In addition, evidence is obtained for reverse radical transfer from DOPA• to Y_{122}• with DOPA–ββ'/α2. This marks the first direct observation of reverse hole migration and provides evidence for the reversible nature of the radical transfer pathway.

In **Chapter 4** we demonstrate evolution of a suppressor tRNA/synthetase pair that is specific for the unnatural amino acid NH_2Y, which is 190 mV easier to oxidize than Y. Using this technology we generate $Y_{730}NH_2Y$–α2 and $Y_{731}NH_2Y$–α2 with high fidelity in yields comparable to wt α2. Using these constructs, we test the involvement of Y_{730}/Y_{731} in long–range radical migration. The results demonstrate kinetically competent radical transfer from Y_{122}• across the subunit interface and trapping of NH_2Y_{730}• or NH_2Y_{731}• in α2. This event is triggered by binding of substrate and effector. Steady state activity assays in conjunction with reactions with the suicide inhibitor N_3ADP indicate that $Y_{730}NH_2Y$–α2 and $Y_{731}NH_2Y$–α2 are competent in nucleotide reduction. These results are consistent with a HAT mechanism for oxidation of C_{439} by NH_2Y_{730}•. This likely represents the first observation of an radical intermediate during active hole transfer and nucleotide reduction.

In **Chapter 5** we further investigate the structure of the putative NH_2Y• using ^{15}N and ^{2}H isotopic substitution, 9 GHz and 180 GHz EPR spectroscopies, EPR spectral simulations and DFT calculations. Our results unambiguously demonstrate that the new signal is associated with the NH_2Y probe, provide insight into the conformation of NH_2Y_{730}• within α2, and yield spin densities for the major nuclei interacting with the unpaired spin. This is the first detailed characterization of an NH_2Y• within an enzyme. The position of the NH_2Y• within the α2/β2 complex is examined using PELDOR spectroscopy. The results give distances between the newly formed NH_2Y•, at residue 730 or 731, in one αβ pair and the remaining Y_{122}• in the other αβ pair, which are consistent with the distances predicted by the docking model. In addition, studies with $Y_{356}F$–β2 show that formation of NH_2Y_{730}• and NH_2Y_{731}• is pathway–dependent. Alternative pathways circumventing Y_{356} do not exist. Finally, X–band EPR and SF UV–vis spectroscopic methods with various substrate/effector combinations reveal that the substrate provides the main binding determinants for radical initiation and that the effector redistributes a larger population of α2/β2 into a conformation competent in turnover.

In **Chapter 6,** we report the synthesis and physical characterization of F_nYs (n=1, 2, 3, 4) and their N– and C–protected derivatives, Ac–F_nY–NH_2s. We also develop the methodologies for determining $\Delta G°_{ET}$ and $\Delta G°_{PT}$ for the half of the PCET reaction involving fluorotyrosine oxidation by measuring the reduction potentials for the radical and the pK_a of the phenolic protons for Ac–F_nY–NH_2s. The results show that the reduction potential and pK_a of a residue can be varied by 0.32 V and >4 pK_a units, respectively, upon insertion of F_nY. Thus, F_nYs effectively decouple proton and electron and provide a valuable probe for analysis of PCET reactions involving oxidation of Ys. Furthermore, we report the spectroscopic properties of the F_nY•s using EPR and transient absorption UV/Vis spectroscopies.

In **Chapter 7,** we present the semisynthesis of F_nY–β2s (n=2, 3, 4) in which Y_{356} is replaced with F_nYs (Figure 1–18). These β2 analogues allow us to study the role of Y_{356} in the radical propagation process. The results suggest that an increase in the peak reduction potential of the F_nY analogue relative to Y by 80 mV results in a change in the rate-limiting step from a

conformational step to the radical propagation process. These studies support the proposal that the protonation state of the phenol of this residue is not important in conformational gating, that the proton can be lost from this pathway without affecting the overall enzymatic activity, and that Y_{356} is a redox–active amino acid on the radical propagation pathway. We propose that during radical propagation with wt β2, the phenolic proton is transferred off–pathway, probably to E_{350}, which is highly conserved in class I RNRs. Additionally, the rigorous assessment of the enzymatic activity of F_nY_{356}–β2s establish that the energetics of radical hopping through Y_{356} is finely tuned in wt class I RNR and can only operate within a ~130 mV window for the Y•/Y redox couple.

In **Chapter 8,** we show that no intermediates are observed by SF UV–vis or EPR spectroscopies in the reaction of 2,3,5–F_3Y–β2 with wt α2, CDP and ATP at high pH, where radical transfer is proposed to be rate–limiting. Kinetic simulations show that forward or forward and reverse radical transfer may be slow in turnover without generating a build–up of intermediates. RCQ experiments are in line with this model, in that no burst of dCDP is observed, which is predicted by the simulations. Most convincingly, in experiments with NH_2Y–α2s and 2,3,5–F_3Y–β2, the pre–steady state pH rate profile for NH_2Y• formation is similar to the steady state pH rate profile of 2,3,5–F_3Y–β2 for dCDP production. This holds for $Y_{730}NH_2$Y–α2 and $Y_{731}NH_2$Y–α2. These results support our interpretation of the data in Chapter 7, where we suggested a switch in the rate–limiting step in radical transfer owing to an increase in the reduction potential of residue 356. Substitution of F_nYs into the radical transfer pathway provides the required energy barrier to slow hole migration. However, the slow conformational change that precedes radical transfer and rapid reformation of Y_{122}• avoid build–up of any intermediates.

Based on these results, we propose the following mechanism for radical transport in *E. coli* RNR: A conformational change, triggered by binding of substrate and effector, prompts radical initiation, which in the first turnover occurs in only one of two pathways within an α2/β2 complex. The radical hops through residues Y_{356}, Y_{731} and Y_{731}, which propagate it across the

subunit interface. There appear to be no alternative pathways for radical transport into α2. In β2, Y_{356} transfers the oxidizing equivalents by an orthogonal PCET mechanism, where long–range ET is coupled to short–range, off–pathway PT. At residues Y_{730}/Y_{731} in α2, HAT is the operative mechanism of hole transport (Figure 1–21).[133] Thus residue Y_{731} communicates with Y_{356} and Y_{730} via orthogonal PCET and HAT, respectively. After dCDP formation, the pathway catalyzes reformation of Y_{122}• using a similar mechanism as in the forward direction.

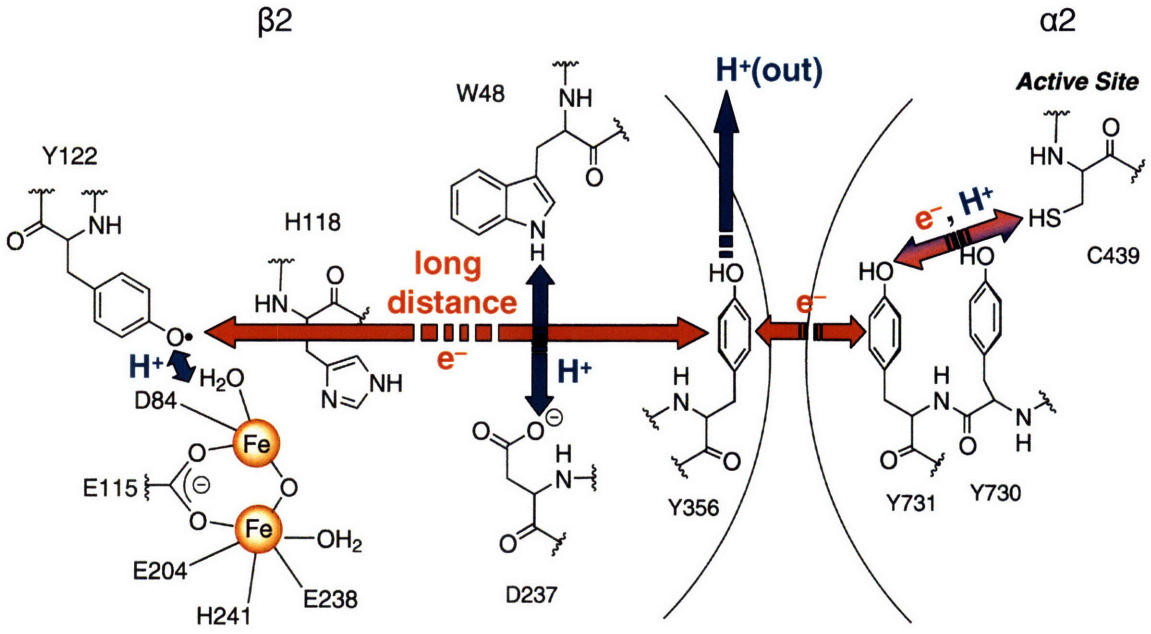

Figure 1–21. Chemical mechanism for long–range radical transfer in *E. coli* RNR. Residues Y_{356}, Y_{730} and Y_{731} paticipate in radical propagation. In β2, reversible long–range ET (red arrows) is coupled to short–distance PT (blue arrows). Accordingly, the proton at Y_{356} is transferred off–pathway to a base. In α2, radical transport occurs by reversible HAT.

REFERENCES

(1) Stubbe, J.; van der Donk, W. A. *Chem. Rev.* **1998**, *98*, 705.

(2) Jordan, A.; Reichard, P. *Annu. Rev. Biochem.* **1998**, *67*, 71.

(3) Gon, S.; Beckwith, J. *Antioxid. Redox Signal* **2006**, *8*, 773.

(4) Nordlund, P.; Reichard, P. *Annu. Rev. Biochem.* **2006**, *75*, 681.

(5) Rosenkranz, H. S.; Garro, A. J.; Levy, J. A.; Carr, H. S. *Biochim. Biophys. Acta* **1966**, *114*, 501.

(6) Ehrenberg, A.; Reichard, P. *J. Biol. Chem.* **1972**, *247*, 3485.

(7) Abratt, R. P. *Anti-Cancer Drugs* **1995**, *6*, 63.

(8) Heinemann, V.; Xu, Y. Z.; Chubb, S.; Sen, A.; Hertel, L. W.; Grindey, G. B.; Plunkett, W. *Mol. Pharmacol.* **1990**, *38*, 567.

(9) Heinemann, V.; Xu, Y.-Z.; Chubb, S.; Sen, A.; Hertel, L. W.; Grindey, G. B.; Plunkett, W. *Cancer Res.* **1992**, *52*, 533.

(10) Nocentini, G. *Crit. Rev. Oncol. Hematol.* **1996**, *22*, 89.

(11) Wnuk, S. F. R., M. J. *Antriviral Res.* **2006**, *71*, 122.

(12) Cerqueira, N. M. P., S.; Fernandes, P. A.; Ramos, M.J. *Curr. Med. Chem.* **2005**, *12*, 1283.

(13) Stubbe, J.; Ge, J.; Yee, C. S. *Trends Biochem. Sci.* **2001**, *26*, 93.

(14) Stubbe, J. *Curr. Opin. Struct. Biol.* **2000**, *10*, 731.

(15) Stubbe, J. *Proc. Natl. Acad. Sci. U. S. A.* **1998**, *95*, 2723.

(16) Stubbe, J. *Chem. Commun.* **2003**, 2511.

(17) Bollinger Jr., J. M.; Edmondson, D. E.; Huyuh, B. H.; Filley, J.; Norton, J. R.; Stubbe, J. *Science* **1991**, *253*, 292.

(18) Bollinger Jr., J. M.; Stubbe, J. *J. Am. Chem. Soc.* **1991**, *113*, 6289.

(19) Bollinger Jr., J. M.; Tong, W. H.; Ravi, N.; Huynh, B. H.; Edmondson, D. E.; Stubbe, J. *J. Am. Chem. Soc.* **1994**, *116*, 8024.

(20) Bollinger, J. M., Jr.; Tong, W.-H.; Ravi, N.; Huynh, B.-H.; Edmonson, D. E.; Stubbe, J. *J. Am. Chem. Soc.* **1994**, *116*, 8015.

(21) Hoffman, B. M. *Acc. Chem. Res.* **2003**, *36*, 522.

(22) Aubert, C., Vos, M. H.; Mathis, P.; Eker, A. P.; Brettel, K. *Nature* **2000**, *405*, 586.

(23) Kavakli, I. H., Sancar, A. *Biochemistry* **2004**, *43*, 15103.

(24) Licht, S.; Gerfen, G. G.; Stubbe, J. *Science* **1996**, *271*, 477.

(25) Stubbe, J.; Nocera, D. G.; Yee, C. S.; Chang, M. C. Y. *Chem. Rev.* **2003**, *103*, 2167.

(26) Jiang, W.; Yun, D.; Saleh, L.; Barr, E. W.; Xing, G.; Hoffart, L. M.; Maslak, M. A.;

Krebs, C.; Bollinger, J. M., Jr. *Science* **2007**, *316*, 1188.

(27) Jordan, A., Gibert, I.; Barbe, J. *J. Bacteriol.* **1994**, *176*, 3420.

(28) Jordan A, P. E., Atta M, Krook M, Gibert I, Barbe J, Reichard P. *Proc. Natl. Acad. Sci. U.S.A.* **1994**, *91*, 12892.

(29) Hartig, E., Hartmann, A.; Schatzle, M.; Albertini, A. M.; Jahn, D. *Appl. Environ. Microbiol.* **2006**, *72*, 5260.

(30) Pesavento, R. P.; van der Donk, W. A. *Adv. Prot. Chem.* **2001**, *58*, 317.

(31) Brown, N. C.; Canellakis, Z. N.; Lundin, B.; Reichard, P.; Thelander, L. *Eur. J. Biochem.* *1969*, *9*, 561.

(32) Brown, N. C.; Reichard, P. *J. Mol. Biol.* **1969**, *46*, 39.

(33) von Dobeln, U., Reichard, P. *J. Biol. Chem.* **1976**, *253*, 3616.

(34) Uppsten, M.; Färnegårdh, M.; Jordan, A.; Eliasson, R.; Eklund, H.; Uhlin, U. *J. Mol. Biol.* **2003**, *330*, 87.

(35) Larsson, K.-M.; Jordan, A.; Eliasson, R.; Reichard, P.; Logan, D. T.; Nordlund, P. *Nature Struct. Mol. Biol.* **2004**, *11*, 1142.

(36) Logan, D. T.; Andersson, J.; Sjöberg, B.-M.; Nordlund, P. *Science* **1999**, *283*, 1499.

(37) Larsson, K. M.; Andersson, J.; Sjöberg, B.-M.; Nordlund, P.; Logan, D. T. *Structure* **2001**, *9*, 739.

(38) Eriksson, M.; Uhlin, U.; Ramaswamy; Ekberg, M.; Regnström, K.; Sjöberg, B.-M.; Eklund, H. *Structure* **1997**, *5*, 1077.

(39) Kashlan, O. B.; Scott, C. P.; Lear, J. D.; Cooperman, B. S. *Biochemistry* **2002**, *41*, 462.

(40) Scott, C. P.; Kashlan, O. B.; Lear, J. D.; Cooperman, B. S. *Biochemistry* **2001**, *40*, 1651.

(41) Sjöberg, B. M.; Reichard, P.; Gräslund, A.; Ehrenberg, A. *J. Biol. Chem.* **1978**, *253*, 6863.

(42) Sjöberg, B. M.; Reichard, P. *J. Biol. Chem.* **1997**, *252*, 536.

(43) Gräslund, A.; Sahlin, M. *Annu. Rev. Biophys. Biomol. Struct.* **1996**, *25*, 259.

(44) Gräslund, A.; Sahlin, M.; Sjöberg, B.-M. *Environ. Health Perspect.* **1985**, *64*, 139.

(45) Nyholm, S.; Thelander, L.; Gräslund, A. *Biochemistry* **1993**, *32*, 11569.

(46) Bollinger Jr., J. M.; Tong, W. H.; Ravi, N.; Huynh, B. H.; Edmondson, D. E.; Stubbe, J. *Methods Enzymol.* **1995**, *258*, 278.

(47) Feitelson, J.; Hayon, E. *J. Phys. Chem.* **1973**, *77*, 10.

(48) Atkin, C. L.; Thelander, L.; Reichard, P. *J. Biol. Chem.* **1973**, *248*, 7464.

(49) Lynch, J. B.; Juarez-Garcia, C.; Munck, E.; Que, L. J. *J. Biol. Chem.* **1989**, *264*, 8091.

(50) Sjöberg, B. M.; Loehr, T. M.; Sanders-Loehr, H. *Biochemistry* **1982**, *21*, 96.

(51) Sahlin, M.; Petersson, L.; Gräslund, A.; Ehrenberg, A.; Sjöberg, B. M.; Thelander, L. *Biochemistry* **1987**, *26*, 5541.

(52) Nordlund, P.; Sjöberg, B.-M.; Eklund, H. *Nature* **1990**, *345*, 593.

(53) Wu, C. H.; Jiang, W.; Krebs, C.; Stubbe, J. *Biochemistry* **2007**, *46*, 11577.

(54) Ortigosa, A. D.; Hristova, D.; Perlstein, D. L.; Zhang, Z.; Huang, M.; Stubbe, J. *Biochemistry* **2006**, *45*, 12282.

(55) Hoganson, C. W.; Sahlin, M.; Sjöberg, B.-M.; Babcock, G. T. *J. Am. Chem. Soc.* **1996**, 118, 4672.

(56) Bender, C. J.; Sahlin, M.; Babcock, G. T.; Barry, B. A.; Chandrashekar, T. K.; Salowe, S. P.; Stubbe, J.; Lindstrom, B.; Petersson, L.; Ehrenberg, A.; Sjöberg, B.-M. *J. Am. Chem. Soc.* **1989**, *111*, 8076.

(57) Gerfen, G. J.; Bellew, B. F.; S., U.; Bollinger, J. M., Jr.; Stubbe, J.; Griffin, R. G.; Singel, D. J. *J. Am. Chem. Soc.* **1993**, *115*, 6420.

(58) Un, S.; Atta, M.; Fontecave, M.; Rutherford, A. W. *J. Am. Chem. Soc.* **1995**, *117*, 10713.

(59) Prütz, W. A.; Butler, J.; Land, E. J. *Int. J. Radiat. Biol.* **1983**, *44*, 183.

(60) Silva, K. E.; Elgren, J. L.; Que, L. J.; Stankovich, M. T. *Biochemistry* **1995**, *34*, 14093.

(61) Harriman, A. *J. Phys. Chem.* **1987**, *91*, 6102.

(62) DeFelippis, M. R.; Murthy, C. P.; Broitman, F.; Weinraub, D.; Faraggi, M.; Klapper, M. H. *J. Phys. Chem.* **1991**, *95*, 3416.

(63) DeFelippis, M. R.; Murthy, C. P.; Faraggi, M.; Klapper, M. H. *Biochemistry* **1989**, *28*, 4847.

(64) Jovanovic, S. V.; Harriman, A.; Simic, M. G. *J. Phys. Chem.* **1986**, *90*, 1935.

(65) Lind, J.; Shen, X.; Eriksen, T. E.; Merenyi, G. *J. Am. Chem. Soc.* **1990**, *112*, 479.

(66) Tommos, C.; Skalicky, J. J.; Pilloud, D. L.; Wand, A. J.; Dutton, P. L. *Biochemistry* **1999**, *38*, 9495.

(67) Eklund, H.; Uhlin, U.; Färnegårdh, M.; Logan, D. T.; Nordlund, P. *Prog. Biophys. Mol. Biol.* **2001**, *77*, 177.

(68) Licht, S.; Stubbe, J. In *Comprehensive Natural Products Chemistry*; Barton, S. D., Nakanishi, K., Meth-Cohn, O., Poulter, C. D., Eds.; Elsevier Science: New York, 1999; p. 163.

(69) Thelander, L.; Reichard, P. *Annu. Rev. Biochem.* **1979**, *48*, 133.

(70) Stubbe, J.; Ackles, D. *J. Biol. Chem.* **1980**, *255*, 8027.

(71) Stubbe, J.; Ator, M.; Krenitsky, T. *J. Biol. Chem.* **1983**, *258*, 1625.

(72) Lenz, R.; Giese, B. *J. Am. Chem. Soc.* **1997**, *119*, 2784.

(73) Lawrence, C. C.; Bennati, M.; Obias, H. V.; Bar, G.; Griffin, R. G.; Stubbe, J. *Proc. Natl. Acad. Sci. U.S.A.* **1999**, *96*, 8979.

(74) Lawrence, C. C.; Stubbe, J. *Curr. Opin. Chem. Biol.* **1998**, *2*, 650.

(75) Orme-Johnson, W. H.; Beinert, H.; Blakley, R. L. *J. Biol. Chem.* **1974**, *249*, 2338.

(76) Tamao, Y.; Blakley, R. L. *Biochemistry* **1973**, *12*, 24.

(77) Licht, S. S.; Lawrence, C. C.; Stubbe, J. *Biochemistry* **1999**, *38*, 1234.

(78) Licht, S. S.; Lawrence, C. C.; Stubbe, J. *J. Am. Chem. Soc.* **1999**, *121*, 7463.

(79) Licht, S. S.; Booker, S.; Stubbe, J. *Biochemistry* **1999**, *38*, 1221.

(80) Andersson, J.; Westman, M.; Hofer, A.; Sjöberg, B.-M. *J. Biol. Chem.* **2000**, *275*, 19443.

(81) Brown, N. C.; Reichard, P. *J. Mol. Biol.* **1969**, *46*, 25.

(82) Thelander, L. *J. Biol. Chem.* **1973**, *248*, 4591.

(83) Climent, I.; Sjöberg, B. M.; Huang, C. Y. *Biochemistry* **1992**, *26*, 4801.

(84) Climent, I.; Sjöberg, B.-M. *Biochemistry* **1991**, *30*, 5164.

(85) Kasrayan, A.; Birgander, P. L.; Pappalardo, L.; Regnström, K.; Westman, M.; Slaby, A.; *Gordon*, E.; Sjöberg, B.-M. *J. Biol. Chem.* **2004**, *279*, 31050.

(86) Ormo, M.; Sjöberg, B. M. *Anal. Biochem.* **1990**, *189*, 138.

(87) Sjöberg, B. M.; Karlsson, M.; Jornvall, H. *J. Biol. Chem.* **1987**, *262*, 9736.

(88) Uhlin, U.; Eklund, H. *Nature* **1994**, *370*, 533.

(89) Hogböm, M.; Galander, M.; Andersson, M.; Kolberg, M.; Hofbauer, W.; Lassmann, G.; *Nordlund*, P.; Lendzian, F. *Proc. Natl. Acad. Sci. U. S. A.* **2003**, *100*, 3209.

(90) Tong, W.; Burdi, D.; Riggs-Gelasco, P.; Chen, S.; Edmondson, D.; Huynh, B. H.; Stubbe, J.; Han, S.; Arvai, A.; Tainer, J. *Biochemistry* **1998**, *37*, 5840.

(91) Bollinger, J. M., Jr.; Krebs, C. *J. Inorg. Biochem.* **2006**, *100*, 586.

(92) Ekberg, M.; Birgander, P.; Sjöberg, B.-M. *J. Bacteriol.* **2003**, *185*, 1167.

(93) Ekberg, M.; Sahlin, M.; Eriksson, M.; Sjöberg, B.-M. *J. Biol. Chem.* **1996**, *271*, 20655.

(94) Mao, S. S.; Yu, G. X.; Chalfoun, D.; Stubbe, J. *Biochemistry* **1992**, *31*, 9752.

(95) Ekberg, M. P., S.; Sandin, E.; Thunnissen, M.; Nordlund, P.; Sahlin, M.; Sjöberg, B. M. *J.* Biol. *Chem.* **1998**, *273*, 21003.

(96) Siegbahn, P. E. M.; Eriksson, L.; Pavlov, F. H. M. *J. Phys. Chem. B* **1998**, *102*, 10622.

(97) Ge, J.; Yu, G.; Ator, M. A.; Stubbe, J. *Biochemistry* **2003**, *42*, 10071.

(98) Thelander, L.; Larsson, B.; Hobbs, J.; Eckstein, F. *J. Biol. Chem.* **1976**, *251*, 1398.

(99) Sjöberg, B.-M.; Gräslund, A.; Eckstein, F. *J. Biol. Chem.* **1983**, *258*, 8060.

(100) Salowe, S. P.; Ator, M. A.; Stubbe, J. *Biochemistry* **1987**, *26*, 3408.

(101) Salowe, S.; Bollinger Jr., J. M.; Ator, M.; Stubbe, J. *Biochemistry* **1993**, *32*, 12749.

(102) van der Donk, W. A.; Stubbe, J.; Gerfen, G. G.; Bellew, B. F.; Griffin, R. G. *J. Am. Chem.* Soc. **1995**, *117*, 8909.

(103) Fritscher, J.; Artin, E.; Wnuk, S.; Bar, G.; Robblee, J. H.; Kacprzak, S.; Kaupp, M.; Griffin, R. G.; Bennati, M.; Stubbe, J. *J. Am. Chem. Soc.* **2005**, *127*, 7729.

(104) van der Donk, W. A.; Yu, G.; Pérez, L.; Sanchez, R. J.; Stubbe, J. *Biochemistry* **1998**, *37*, 6419.

(105) van der Donk, W. A.; Yu, G.; Silva, D. J.; Stubbe, J. *Biochemistry* **1996**, *35*, 8381.

(106) van der Donk, W. A.; Gerfen, G. G.; Stubbe, J. *J. Am. Chem. Soc.* **1998**, *120*, 4252.

(107) Gerfen, G. G.; van der Donk, W. A.; Yu, G.; McCarthy, J. R.; Jarvi, E. T.; Matthews, D. P.; Farrar, C.; Griffin, R. G.; Stubbe, J. *J. Am. Chem. Soc.* **1998**, *120*, 3823.

(108) Milov, A. D.; Maryasov, A. G.; Tsvetkov, Y. D. *Appl. Magn. Reson.* **1998**, *15*, 107.

(109) Schiemann, O.; Prisner, T. F. *Q. Rev. Biophys.* **2007**, *40*, 1.

(110) Bennati, M.; Weber, A.; Antonic, J.; Perlstein, D. L.; Robblee, J.; Stubbe, J. *J. Am. Chem. Soc.* **2003**, *125*, 14988.

(111) Jeschke, G.; Bender, A.; Paulsen, H.; Zimmermann, H.; Godt, A. *J. Magn. Reson.* **2004**, *169*, 1.

(112) Bennati, M.; Robblee, J. H.; Mugnaini, V.; Stubbe, J.; Freed, J. H.; Borbat, P. *J. Am.* Chem. *Soc.* **2005**, *127*, 15014.

(113) Marcus, R. A.; Sutin, N. *Biochim. Biophys. Acta* **1985**, *811*, 265.

(114) Gray, H. B.; Winkler, J. R. *Annu. Rev. Biochem.* **1996**, *65*, 537.

(115) Dutton, P. L. *Methods Enymol.* **1978**, *54*, 411.

(116) Prince, R. C.; Lloyd-William, P.; Bruce, J. M.; Dutton, P. L. *Methods Enymol.* **1986**, *125*, 109.

(117) Rich, P. R.; Meunier, B.; Mitchell, R.; Moody, A. J. *Biochim. Biophys. Acta* **1996**, *1275*, 91.

(118) Gray, H. B.; Winkler, J. R. *Q. Rev. Biophys.* **2003**, *36*, 341.

(119) Brunschwig, B. S.; Sutin, N. *Comments Inorg. Chem.* **1987**, *6*, 209.

(120) Closs, G. L.; Miller, J. R. *Science* **1988**, *240*, 440.

(121) Wasielewski, M. R.; MNimczyk, M. P.; Swec, W. A.; Pewitt, E. B. *J. Am. Chem. Soc.* **1985**, *107*, 1080.

(122) Fox, L. S.; Kozik, M.; Winkler, J. R.; Gray, H. B. *Science* **1990**, *247*, 1069.

(123) McLendon, G.; Miller, J. R. *J. Am. Chem. Soc.* **1985**, *107*, 7811.

(124) McLendon, G.; Hake, R. *Chem. Rev.* **1992**, *92*, 481.

(125) Hopfiled, J. J. *Proc. Natl. Acad. Sci. U. S. A.* **1974**, *71*, 3640.

(126) Levich, V. G. *Adv. Electrochem. Electrochem. Eng.* **1966**, *4*, 249.

(127) Onuchic, J. N.; Beratan, D. N.; Winkler, J. R.; Gray, H. B. *Annu. Rev. Biophys. Biomol. Struct.* **1992**, *21*, 349.

(128) Hopfield, J. J. *Proc. Natl. Acad. Sci. U. S. A.* **1974**, *71*, 3640.

(129) Beratan, D. N.; Onuchic, J. N.; Hopfield, J. J. *J. Chem. Phys.* **1987**, *86*, 4488.

(130) Beratan, D. N.; Betts, J. N.; Onuchic, J. N. *Science* **1991**, *252*, 1285.

(131) Gray, H. B. *Gordon Research Conference "Protein Cofactors, Radicals & Quinones", Ventura, CA 2006.*

(132) Cukier, R. I.; Nocera, D. G. *Annu. Rev. Phys. Chem.* **1998**, *49*, 337.

(133) Reece, S. Y.; Hodgkiss, J. M.; Stubbe, J.; G., N. D. *Philos. Trans. R. Soc. Lond. B Biol. Sci.* **2006**, *361*.

(134) Mayer, J. M.; Rhile, I. J. *Biochim. Biophys. Acta* **2004**, *1655*, 51.

(135) Turro, C.; Chang, C. K.; Leroi, G. E.; Cukier, R. I.; Nocera, D. G. *J. Am. Chem. Soc.* **1992**, *114*, 4013.

(136) Zhao, X. G.; Cukier, R. I. *J. Phys. Chem.* **1995**, *99*, 945.

(137) Roberts, J. A.; Kirby, J. P.; Nocera, D. G. *J. Am. Chem. Soc.* **1995**, *117*, 8051.

(138) Kirby, J. P.; Roberts, J. A.; Nocera, D. G. *J. Am. Chem. Soc.* **1997**, *119*, 9230.

(139) Chang, C. J.; Chang, M. C. Y.; Damrauer, N. H.; Nocera, D. G. *Biochim. Biophys. Acta* **2004**, *1655*, 13.

(140) Mayer, J. M. *Annu. Rev. Phys. Chem.* **2004**, *55*, 363.

(141) Magnuson, A.; Berglund, H.; Korall, P.; Hammarstrom, L.; Akermark, B.; Styring, S.; Sun, L. *J. Am. Chem. Soc.* **1997**, *117*, 10720.

(142) Sjodin, M.; Styring, S.; Akermark, B.; Sun, L.; Hammarstrom, L. *J. Am. Chem. Soc.* **2000**, *122*, 3932.

(143) Sjodin, M.; Styring, S.; Wolpher, H.; Xu, Y.; Sun, L.; Hammarstrom, L. *J. Am. Chem. Soc.* **2005**, *127*, 3855.

(144) Ishikita, H.; Soudackov, A. V.; Hammes-Schiffer, S. *J. Am. Chem. Soc.* **2007**, *129*, *11146.*

(145) Hammes-Schiffer, S.; Iordanova, N. *Biochim. Biophys. Acta* **2004**, *1655*, 29.

(146) Roth, J. P.; Yoder, J. C.; Won, T.-J.; Mayer, J. M. *Science* **2001**, *294*, 2524.

(147) Reece, S. Y.; Nocera, D. G.; Stubbe, J. *Biochim. Biophys. Acta* **2005**, *1706*, 232.

(148) Ravi, N.; Bollinger Jr., J. M.; Huynh, B. H.; Edmondson, D. E.; Stubbe, J. *J. Am. Chem. Soc.* **1994**, *116*, 8007.

(149) Yun, D.; Garcia-Serres, R.; Chicalese, B. M.; H., A. Y.; Huynh, B. H.; Bollinger, J. M., Jr. *Biochemistry* **2007**, *46*, 1925.

(150) Sintchak, M. D.; Arjara, G.; Kellogg, B. A.; Stubbe, J.; Drennan, C. L. *Nat. Struct. Biol.* **2002**, *9*, 293.

(151) Mayer, J.; Hrovat, D.; Thomas, J.; Borden, W. *J. Am. Chem. Soc.* **2002**, *124*, 11124.

(152) McMillen, D. F.; Golden, D. M. *Ann. Rev. Phys. Chem.* **1982**, *33*, 493.

(153) Benson, S. W. *Chem. Rev.* **1978**, *78*, 23.

(154) Mulder, P.; Korth, H.-G.; Prett, D. A.; DiLabio, G. A.; Valgimigli, L.; Pedulli, G. F.; Ingold, K. U. *J. Phys. Chem. A* **2005**, *109*, 2647.

(155) Prütz, W. A.; Butler, J.; Land, E. J.; Swallow, A. J. *Int. J. Radiat. Biol.* **1898**, *55*, 539.

(156) Paulus, H. *Annu. Rev. Biochem.* **2000**, *69*, 447.

(157) Cooper, A. A.; Stevens, T. H. *Trends Biochem. Sci.* **1995**, *20*, 351.

(158) Kane, P. M. et al. *Science* **1990**, *250*, 651.

(159) Muralidharan, V.; Muir, T. W. *Nat. Methods* **2006**, *3*, 429.

(160) Perler, F. B. *IUBMB Life* **2005**, *57*, 469.

(161) Chong, S. et al. *J. Biol. Chem.* **1996**, *271*, 22159.

(162) Perler, F. B.; Xu, M. Q.; Paulus, H. *Curr. Opin. Chem. Biol.* **1997**, *1*, 292.

(163) Yee, C. S.; Seyedsayamdost, M. R.; Chang, M. C. Y.; Nocera, D. G.; Stubbe, J. *Biochemistry* **2003**, *42*, 14541.

(164) Muir, T. W. *Annu. Rev. Biochem.* **2003**, *72*, 249.

(165) Hofman, R. M.; Muir, T. W. *Curr. Opin. Biotechnol.* **2002**, *13*, 297.

(166) Wang, L.; Brock, A.; Herberich, B.; Schultz, P. G. *Science* **2001**, *292*, 498.

(167) Wang, L.; Schultz, P. G. *Angew. Chem. Int. Ed. Engl.* **2004**, *44*, 34.

(168) Xie, J.; Schultz, P. G. *Methods* **2005**, *36*, 227.

(169) Wang, L.; Xie, J.; Schultz, P. G. *Annu. Rev. Biophys. Biomol. Struct.* **2006**, *35*, 225.

(170) Xie, J.; Schultz, P. G. *Nat. Rev. Mol. Cell Biol.* **2006**, *7*, 775.

CHAPTER 2:

Site–Specific Insertion of 3,4–Dihydroxyphenylalanine into the β2 Subunit of *E. coli* Ribonucleotide Reductase

Adapted in part from: Seyedsayamdost, M. R.; Stubbe, J. *J. Am. Chem. Soc.* **2006**, *118*, 2522.

INTRODUCTION

In this chapter, we considered the incorporation of a thermodynamic trap, a tyrosine analogue with a low reduction potential, into the radical initiation pathway. In choosing this unnatural amino acid analogue, several criteria were important. First, the analogue should sterically resemble tyrosine. Residue 356 is on the disordered C–terminal tail of β2 and not visible in any structures. Therefore, its role in binding to α2 is not clearly defined.[1] To avoid changing the interaction with α2 as a result of the probe, steric homology to tyrosine is essential. Second, the analogue should have known phenolic pK_a and one electron reduction potential appropriate for analysis of PCET. Third, the UV–vis and EPR properties of the one electron oxidized state of the analogue should be known. And finally, the analogue should be synthetically readily accessible and stable to the highly basic and acidic conditions used in solid–phase peptide synthesis. We considered the three unnatural amino acids shown in Figure 2–1: 3–thiomethyltyrosine (MeS–Y),[2] 3–aminotyrosine (NH_2Y)[3,4,5] and 3,4–dihydroxyphenyl–alanine (DOPA).[6,7,8] The known properties of these are listed in Table 2–1. While all three analogues would serve as efficient radical traps, based on the electrochemical data in Table 2–1, the UV–vis and EPR properties for the NH_2Y radical and the MeS–Y radicals are unknown. In addition, incorporation of NH_2Y and MeS–Y proved synthetically difficult and these analogues were no longer pursued (M. Seyedsayamdost, J. Stubbe, unpublished results). Therefore, only DOPA fulfilled all four criteria and this chapter describes the insights gained about the radical propagation event by generating and examining DOPA–β2 (Figure 2–2).

The interest in DOPA and DOPA•s stems from its involvement in melanogenesis, the process that converts DOPA into melanin pigments, which protect the skin from solar UV radiation (Scheme 2–1).[9,10,11] Extensive work on natural and synthetic melanin and its generation, has lead to a detailed understanding regarding the chemical reactivity of DOPA, DOPA•s and DOPA–quinones. These properties are shown in Figure 2–3 and are important to consider for the topic for this chapter. Note that catechol has been used as a model for reactions of DOPA.

Figure 2–1. Low reduction potential Y analogues considered for insertion at position 356 of β2. Some properties of these unnatural amino acids are summarized in Table 2–1.

Table 2–1. Relevant properties for the Y analogues DOPA, NH_2Y and MeS–Y.

Property	DOPA	NH_2Y	MeS–Y
pK_a	8.8[a], 9.8[b]	4.9[c], 10.1[b]	9.9[b]
$E^{\circ\prime}$ (V vs NHE)[d]	0.57	0.64	0.6
λ_{max} (nm)	305[e]	–	–
ε ($M^{-1}cm^{-1}$)	12,000[e]	–	–

[a] pK_a of the 3–hydroxyl substituent. [b] Phenol pK_a. [c] pK_a of the 3–amino substituent. Data for DOPA are from Refs. 6-8, for NH_2Y from Refs. 3-5 and for MeS-Y from Ref. 2. [d] Data are from Ref. 6 for DOPA, Ref. 5 for NH_2Y and Ref. 2 for MeS–Y. [e] From Ref. 8.

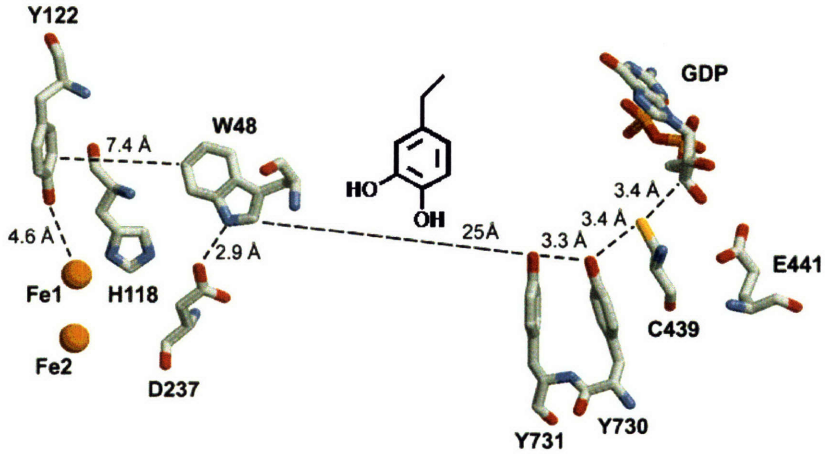

Figure 2–2. The radical generation pathway with site–specific insertion of DOPA at residue 356. See Chapter 1 for a detailed discussion of the pathway.

Accordingly, catechol is stable at neutral pH; however, it may react with hydroxyl radicals (OH•) to give an OH–adduct, which after elimination of water yields a catechol• (Figure 2–3A).[12,13] Superoxide ($O_2^{\bullet -}$) may also oxidize catechol to generate a catechol• (Figure 2–3B). The catechol•, in turn, can react with oxidants, such as HO_2• (Figure 2–3C) and O_2^- (Figure 2–3D) at rate constants of ~10^9 $M^{-1}s^{-1}$, to yield an *o*–benzoquinone. Reaction of some *o*–semiquinones with O_2 has also been described, though a catechol• was not tested (Figure 2–3E). Catechol•s may also dismutate to generate catechol and *o*–benzoquinone (Figure 2–3F). *o*–Benzouinones, generated via dismutation or oxidation of a catechol•, are susceptible to Michael addition nucleophiles in solution (Figure 2–3G).[12]

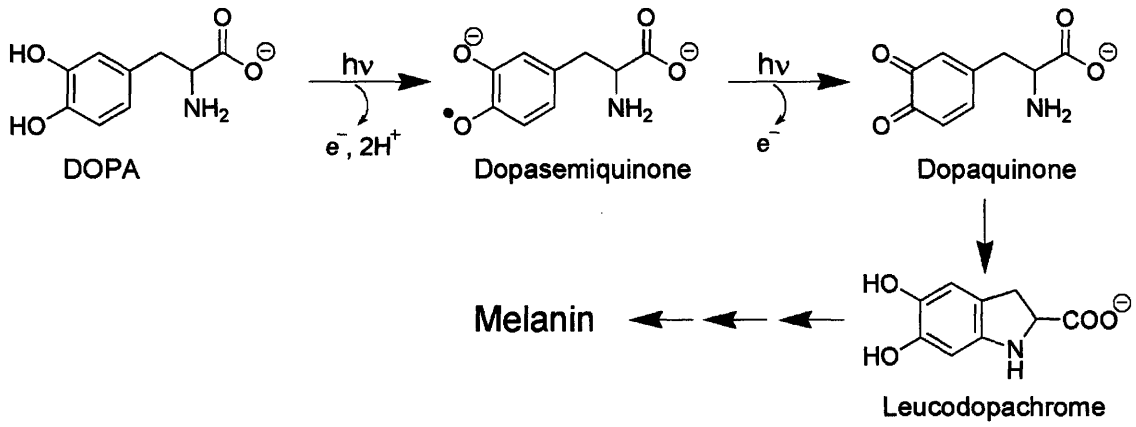

Scheme 2–1. Involvement of DOPA• in melanin biogenesis. UV light generates a DOPA• (dopasemiquinone), which upon further oxidation yields dopaquinone. Michael addition by the amine group results in leucodopachrome, which gives rise to melanin in a multi–step process.

The DOPA• is 260 mV, or 6 kcal/mol, more stable than a tyrosyl radical (Y•).[6] At the outset, the main question was whether a 260 mV thermodynamic trap would suffice to generate a stable radical in the radical transfer pathway at the α2/β2 interface. The structure at the α2/β2 interface has not been determined at resiude 356. Further, the factors that modulate the oxidation potentials of amino acids inside proteins are to date ill–defined. Therefore, a potential of 830 mV and 570 mV, which have been determined in solution for Y[14] and DOPA,[6] respectively, may not hold in the protein milieu. Previous studies with NO_2Y–β2, where the analogue 3–nitroY was inserted at residue 356, indicated that the pK_a at this residue was not perturbed and that a

~200 mV or a 4.6 kcal/mol barrier was sufficient to shut down nucleotide reduction.[15] Thus, we expected that DOPA–β2 would form rapidly but would be unable to oxidize residue 731 resulting in a block during radical transfer into α2. In addition, Marcus–Levich theory dictates that the ET rate constant between $DOPA_{356}$• and Y_{731} would be ~800–fold slower than that between Y_{356}• and Y_{731}, based on potentials at pH 7 (assuming that both residues are on the pathway and $\lambda = 1.2$ eV).[16]

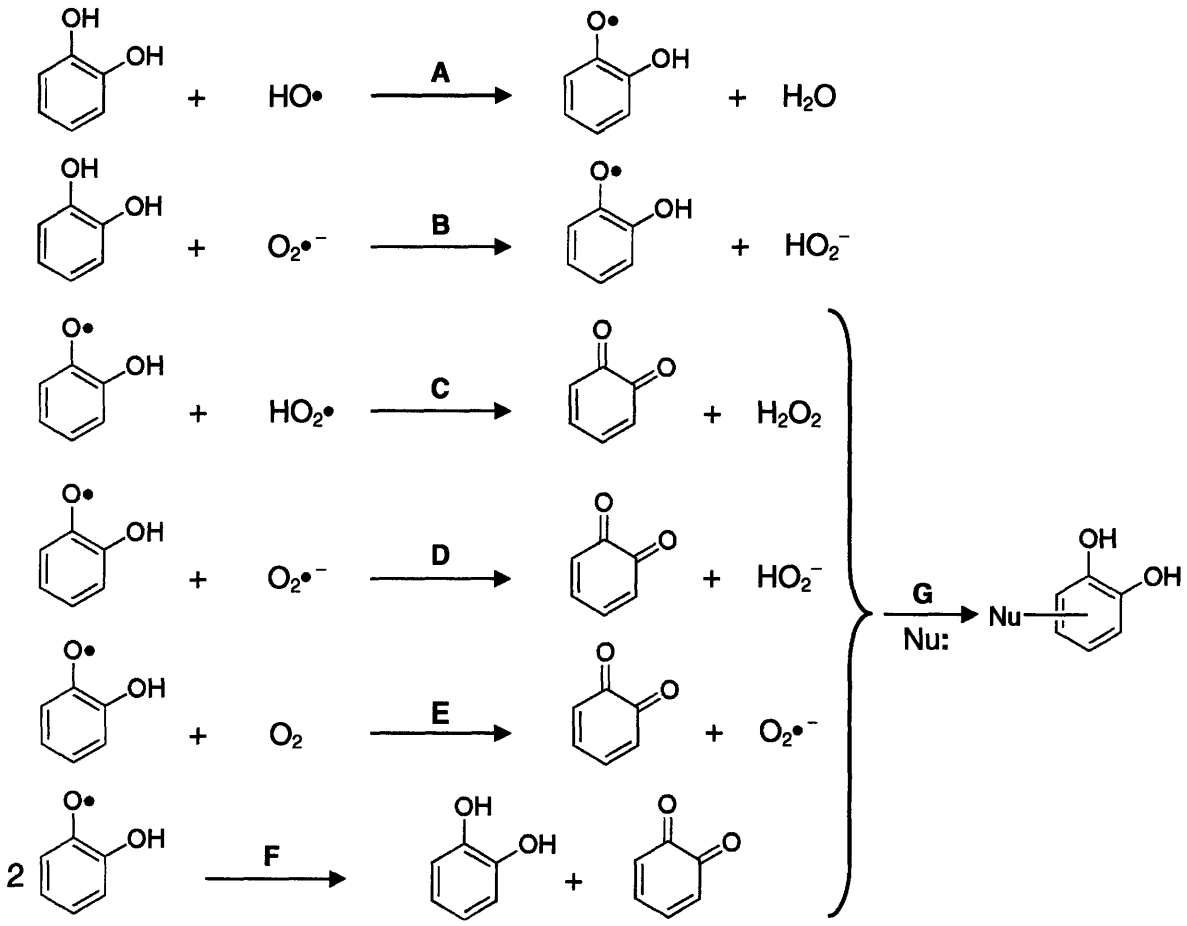

Figure 2–3. Reactions of catechol, catechol• and *o*–benzoquinone. Reliable rate constants have not been reported in each case, although the reactions have been reported by several groups. (A, B) Oxidation of catechol to catechol• by hydroxyl radical (HO•) and superoxide radical ($O_2•^-$), respectively. This occurs with rate constants of 10^6 M^{-1} s^{-1} and 10^9 M^{-1} s^{-1}, respectively. (C, D, E) Reaction of catechol• with perhydroxy radical (HO_2•, protonated superoxide with pK_a ~4.9), superoxide and dioxygen, respectively. Rate constant of 10^9 M^{-1} s^{-1} have been estimated for the reactions in (C) and (D). Note that the primary reaction of the catechol• is via $O_2•^-$ (D). Reaction with O_2 (E) has been reported for some *o*–semiquinones, although the catechol• was not tested. (F) Dismutation of two catechol•s to yield catechol and *o*–benzoquinone. (G) The *o*–benzoquinone produced in C–F may react with nucleophiles by Michael addition, covalently modifying catechol.

Contributing to the stability of a DOPA• in DOPA–β2 would be its lack of propensity to dismutate with another DOPA• or to oxidize to the quinone form, as HO• and $O_2^{\bullet -}$ are not present. On the other hand, DOPA would be stable because redox reactions with nearby residues, such as C_{354}, would be energetically unfavorable as all natural amino acids have redox potentials greater than 570 mV. Therefore, we hoped that insertion of DOPA at residue 356 would generate a stable DOPA• that could be detected by UV–vis and EPR spectroscopic methods. This would serve as a probe for involvement of residue 356 in radical initiation.

Experiments described in this chapter present the first trapping of a redox–active amino acid and thereby direct evidence for involvement of a residue in the proposed long–range radical propagation pathway. Formation of $DOPA_{356}$• is kinetically competent and is gated primarily by substrate binding, indicative of pathway dependence. The results show that DOPA is a conformational probe, revealing physical changes that would not be detectable by other available methods, as well as a reporter of the environment at the α2/β2 interface. Finally, the results with DOPA–β2 implicate subtle asymmetry in the α2/β2 interaction, which is inconsistent with the α2/β2 docking model.

MATERIALS AND METHODS

Materials. Fmoc–DOPA(acetonide)–OH, Fmoc–Leu–OH, Fmoc–Gln(Trt)–OH, Fmoc–Phe–OH, Fmoc–Asn(Trt)–OH, Fmoc–Ser(OtBu)–OH, Fmoc–Asp(OtBu)–OH, Fmoc-Thr(OtBu)–OH, Fmoc–Val–OH, Fmoc–Glu(OtBu)–OH, Fmoc–Ile–OH, Fmoc–Gly–OH, Fmoc–Asp(OtBu)–Ser($\psi^{Me,Me}$pro)–OH, Fmoc–Cys(^{t}Buthio)–OPfp and 1–hydroxybenzotriazole hydrate (HOBt) were obtained from Novabiochem. Fmoc–L–Leu–PEG–PS (0.2 mmol/g) and O–(7–Azabenzotriazole–1–yl)–N,N,N',N'–tetramethyluronium hexafluorophosphate (HATU) were obtained from Applied BioSystems. N,N–dimethyl formamide (DMF), diisopropyl ethylamine (DIPEA), piperidine, trifluoroacetic acid (TFA), triisopropyl silane (TIS), 2–mercaptoethane sulfonic acid (Mesna), ampicillin (Amp), chloramphenicol (Cm), Triton X–100, Sephadex G–25, Sephadex G–75, Fast Flow DEAE Sepharose, 2',5'–ADP affinity resin, phenylmethanesulfonyl fluoride (PMSF), glycerol, Bradford Reagent, sodium ascorbate, iron ammonium sulfate hexahydrate ($Fe^{II}(NH_4)_2(SO_4)_2$), ethylenediamine tetraacetic acid (EDTA), perchloric acid (~70 %) α–cyano–4–hydroxycinnamic acid and MALDI–TOF standards for mass spectrometer calibration: angiotensin (1044.54 Da), P14R synthetic peptide (1531.85 Da), ACTH fragment (2463.20) and oxidized B chain insulin (3492.65 Da) were all obtained from Sigma–Aldrich. Methanol (MeOH), ethyl acetate (EtOAc), acetic acid (AcOH), acetonitrile (MeCN), dichloromethane (CH_2Cl_2), diethyl ether, magnesium sulfate ($MgSO_4$), sodium chloride (NaCl), ammonium bicarbonate (NH_4HCO_3) and potassium phosphate (KPi) were obtained from Mallinckrodt. Disposable fritted Econo–Pac columns for manual peptide synthesis and Dowex AG–1×8 resin were from Biorad. BL21(DE3) codon+ cells were from Stratagene. Luria–Bertani Medium (LB) was from Becton Dickinson. Isopropyl–β–D–thiogalacto–pyranoside (IPTG) and DL–dithiothreitol (DTT) were from Promega. Chitin beads were from NEB. Tris(hydroxymethyl)aminomethane (Tris base) and bovine pancreas DNase I were from Roche. 4–(2–hydroxyethyl)piperazine–1–ethanesulfonic acid (Hepes) was obtained from EMD Bioscience. [U–^{14}C]–Cytidine diphosphate (^{14}CDP, 40–60 mCi/mmol) was obtained from

Moravek. Polypropylene falcon tubes (15 or 50 mL) were from BD Bioscience. Dialysis tubing (1000 Da cut–off) for anaerobic peptide dialysis was obtained from SpectraPor. Centriprep protein concentration device (YM–30) and Amicon ultrafiltration device (YM–30) were obtained from Millipore.

MALDI–TOF MS. MALDI–TOF spectra were acquired on a Bruker OmniFlex MALDI–TOF Mass Spectrometer equipped with Reflectron accessory at the Department of Chemistry Instrumentation Facility. Spectra were obtained under negative mode using α–cyano–4–hydroxycinnamic acid as the matrix. The matrix was prepared by suspending 10 mg of CHA into a 1 mL solution of 50 % MeCN and 0.1 % TFA – 1 μL of the peptide (0.5 – 3 mM) solution was then co–spotted with 1 μL of the matrix solution onto the MALDI–TOF target and allowed to dry for 0.5–1 h prior to analysis. The MALDI TOF Mass Spectrometer was calibrated with a mixture of angiotensin II (1044.5423 Da), P14R synthetic peptide (1531.8582 Da), ACTH fragment (2463.1989 Da) and insulin, oxidized B chain (3492.6513 Da) under negative ionization mode.

Synthesis of DOPA–22mer peptide. The first 19 residues of the DOPA–22mer peptide (H_2N–CS-DOPA$_{20}$-L$_{19}$VGQID$_{14}$S$_{13}$EVDTDDLSNFQL$_1$–COOH) were prepared on a Pioneer Peptide Synthesizer (Applied Biosystems) as previously described.[15] Residues 13 (Ser) and 14 (Asp) were added as a pseudoproline dipeptide to avoid peptide aggregation. Automated deblocking of the 9–fluorenyl methoxycarbonyl (Fmoc) protecting group was carried out in DMF containing 20 % (v/v) piperidine and 0.1 M HOBt for 10 min with a pre–set instrument flow rate. The coupling reactions utilized 4 equiv of Fmoc–protected amino acid, 3.6 equiv of HATU, 8 equiv of DIPEA relative to the amount of peptide at final concentrations of 0.5 M, 0.45 M and 1 M, respectively, and proceeded for 1 h. After synthesis of the 19mer, a small amount of peptide was cleaved from the resin and its purity and identity established by reverse–phase HPLC (RP–HPLC) and MALDI–TOF MS (see below for detailed description of these methods). The resin–bound peptide 19mer was stable at –80°C for at least one year.

The remaining three residues, $DOPA_{20}$, Ser_{21} and Cys_{22} were added manually at room temperature. Manual peptide synthesis was performed in a disposable, fritted Econo–pac column on a vortexer fitted with an adapter suitable for holding a 50 mL falcon tube, which in turn holds the Econo–pac column. Removal of the Fmoc protecting group was performed by shaking the resin–bound peptide twice for 10–12 min each or three times for 7–8 min each in DMF containing 20 % (v/v) piperidine and 0.1 M HOBt. Fifteen mL of deblocking solution was used per g of resin. After each deblocking step, the resin-bound peptide was washed 4–5 times with DMF by adding 7–8 mL of DMF per g of resin, vortexing for ~1 min and draining the DMF from the column by removing the top and bottom caps of the column. After the last wash, N_2 gas was passed through the column to completely remove residual DMF.

Manual coupling reactions were carried out by shaking the resin–bound peptide for 1 h with at least 6 equiv of N–Fmoc–protected amino acid, 5.4 equiv of HATU and 12 equiv of DIPEA in DMF at final concentrations of 0.5 M, 0.45 M and 1 M, respectively. The coupling mixture was prepared by first dissolving the Fmoc–protected amino acid in the required volume of DMF, followed by HATU and DIPEA. The reaction vessel was vortexed for ~10–15 sec to completely dissolve the components before adding it to the resin-bound peptide in the Econo–pac column. After each coupling reaction, the resin–bound peptide was washed 2–3 times with DMF as described above.

The N–terminal Cys residue was coupled as a pentafluorophenol–activated (OPfp) and t–Buthio–protected derivative. Coupling of this residue was carried out by vortexing the resin–bound peptide with 6 equiv of Fmoc–Cys(t–Buthio)–OPfp and 6 equiv of HOBt at final concentrations of 0.5 M each for 1.5 h. The resin–bound pepide was then washed 2–3 times with DMF and 2–3 times with CH_2Cl_2 as described above. Finally, the Econo–pac column was capped at the top and connected to a vacuum line at the bottom for 5–10 min to completely dry the resin.

Cleavage of peptide from solid–phase resin. The resin–bound peptide was vortexed with a solution consisting of 95 % (v/v) TFA, 2.5 % (v/v) TIS and 2.5 (v/v) % water for 4 h.

Typically, 25 mL of cleavage solution was used per g of resin. After 4 h, the TFA solution was drained into a 50 mL falcon tube. The resin was washed 2–3 times with a small volume of TFA. The TFA washes were combined with the original cleavage solution containing the peptide. The peptide was then concentrated by blowing $N_2(g)$ over the solution until precipitation occurred. At this point, 8–10 volumes of chilled diethyl ether were added and the mixture incubated at 4°C for ~45 min. The peptide was collected by centrifugation (~5,000 × g, 10–15 min, 4°C) and the ether supernatant discarded. The precipitate was washed once with cold diethyl ether by adding the same volume as before to the precipitate, incubating for ~5 min at 4°C and discarding the ether after centrifugation. Residual ether was removed by sitting the falcon tube uncapped in a fume hood at room temperature overnight. The peptide was stored at –80°C, where it was stable for at least one year.

Analytical and semi–preparative RP–HPLC. RP–HPLC was performed on a Waters HPLC system with a 2487 dual absorption detector and 515 HPLC pumps running on Millenium Software. The peptide was dissolved in a solution of 0.1 M NH_4HCO_3, pH 6.8 to a concentration of 0.5–2 mM. Addition of solid NH_4HCO_3 aided in peptide dissolution. Analytical scale analysis was carried out with a Jupiter Phenomenex C_{18} 5 μm (150 × 4.6 mm) column. Typically 20–100 nmol peptide were loaded (0.2 mL or 0.5 mL injection loop) to assess purity and identity, monitoring absorbance at 215 and 280 nm (λ_{max} of DOPA is at 280 nm with ε = 2760 M^{-1} cm^{-1}).[17] The peptide was eluted with a linear gradient from 10 to 75 % MeCN vs. 0.1 M NH_4HCO_3, pH 6.8 over 45 min at 1 mL/min. The major peak was collected by hand, lyophilized, redissolved in a small volume (10–100 μL) to yield a concentration of 0.3 to 2 mM and analyzed by MALDI–TOF MS as described above.

Semi–preparative scale purifications were carried out with a Waters XTerra MS C_{18} 5 μm (19 × 100 mm) column at a flow rate of 7 mL/min. Up to 2 μmol peptide were loaded (5 mL injection loop) in each run. The peptide was eluted with a linear gradient from 10 % to 20 % MeCN over 5 min, followed by a linear gradient of 20 % to 35 % MeCN vs. 0.1 M NH_4HCO_3, pH 6.8 over 23 min. The desired product was collected by hand in a 50 mL polypropylene

falcon tube, frozen and lyophilized to dryness. The purified t–Buthio–protected DOPA–22mer peptide was obtained in 70 % yield and was stable at –80°C for at least two years.

Removal of the t–buthio–protecting group. The purified, Cys–blocked peptide was dissolved in 0.1 M NH_4HCO_3, pH 6.8 to a concentration of 0.5–2 mM and transferred to a pear–shaped flask. The mixture was supplemented with 0.1 volumes of a solution of 250 mM Tris, pH 7.3 and deoxygenated on a Schlenk line by alternating cycles of evacuation followed by re–addition of argon gas. A total of 6–8 cycles were performed. In each cycle the flask is degassed by pulling a vacuum for ~2–5 min and then flushed with argon with stirring for ~5 min. Then, solid DTT was added to a 15–fold molar excess over peptide. During this addition, the peptide solution is briefly exposed to atmosphere, therefore, the degassing procedure was repeated and the mixture stirred at room temperature for 4 h. At this point, the reaction mixture was transferred to a dialysis bag and dialyzed anaerobically (see below) against 5 mM KPi, pH 6.0 (1 L, 2–3 changes of 4 h each). After dialysis, the solution was transferred to a falcon tube, frozen and lyophilized to dryness. The dry, purified and fully deprotected peptide was stable at –80°C for a year. Anaerobic dialysis was performed in an Erlenmeyer flask or a lyophilization flask at room temperature. Low oxygen concentration during dialysis was maintained by bubbling the KPi buffer with argon gas for 15 min prior to immersion of the dialysis bag and continuously thereafter.

Growth and expression of β2–intein–CBD. The vector pβ2–intein–CBD[15] was transformed into BL21(DE3) codon+ (RIL) cells using instructions by the manufacturer. Growths were carried out on a 10–25 L scale in a 10 L fermentor at 37°C, 500 rpm and, if necessary, in additional 6 L flasks (each containing 1.5 L media) in a shaker/incubator at 37°C, 200 rpm with Amp (100 μg/mL) and Cm (50 μg/mL). A 5 mL LB/Amp/Cm starter culture (in a 12 mL bacterial culture tube) was inoculated with a single colony and grown to saturation (~12 h). Then, 0.5 mL of the saturated culture was diluted into a 100 mL LB/Amp/Cm solution (in a 500 mL Erlenmeyer flask), which was grown to saturation overnight (~12 h). Finally, the saturated culture was diluted 200–fold into a 12–25 L large culture consisting of a fermentor

flask and several 6 L Erlenmeyer flasks. When $OD_{600\,nm}$ reached 0.7–0.8 (~4 h after inoculation of the large culture), the temperature setting was lowered to 23 °C. After 15 min, IPTG was added to a final concentration of 0.5 mM and the expression continued for 5–6 h at 23°C. At that point, cells were harvested by centrifugation (10,000 × g, 15 min, 4°C), frozen in liquid N_2 and stored at –80°C. A yield of 4–5 g per L culture was typical. The ligation was performed within several days of expression of β2–intein–CBD.

Semisynthesis of DOPA–β2. Each g of wet cell paste was resuspended in 5 mL of lysis buffer (30 mM Hepes, 500 mM NaCl, 0.1 % Triton X–100, pH 7.6) supplemented with 1 mM PMSF and 25 U DNase I. The cells were lysed with a single pass through a French Pressure Cell operating at 14,000 psi. Then, 5 mg of each sodium ascorbate and $Fe^{II}(NH_4)_2(SO_4)_2$ per g of wet cell paste were dissolved in ~10 mL of lysis buffer and added dropwise over 10 min at 4°C with stirring. The mixture was stirred for an additional 15 min at 4°C and the cell debris was removed by centrifugation (15,000 × g, 35 min, 4°C). The supernatant was loaded onto a chitin column that had been equilibrated in lysis buffer at a flow rate of ~2 mL/min; five mL of chitin resin were used per g of wet cell paste. For 200 mL of resin, a column with dimensions of 5 × 10 cm was used. The resin was washed with 30–40 column volumes (CV) of lysis buffer containing 0.2 mM PMSF, then with 2 CV of cleavage buffer (50 mM Hepes, 500 mM NaCl, pH 7.6). Next, the column was loaded with 1.5 CV of cleavage buffer containing 100 mM Mesna. The reaction was allowed to proceed for ~24 h. At that point, Mesna–activated, truncated β2 was eluted in cleavage buffer. Elution was continued until no more protein was detected by the Bradford Reagent assay. Mesna–activated β2 was concentrated to 20–25 mg/mL using an Amicon concentration device with a YM–30 membrane. Excess Mesna was removed from the Mesna–activated β2 using a Sephadex G–25 (~200 mL, 2.5 × 40 cm) column equilibrated in cleavage buffer, now with a pH of 7.3. This desalting step results in dilution of Mesna–activated β2, therefore, it was concentrated again to 20–25 mg/mL using an Amicon concentrator as before. The concentrated Mesna–activated β2 was then transferred to a 50 mL pear–shaped flask and deoxygenated on a Schlenk with a total of ~10 vacuum–argon fill cycles. Each cycle

consisted of evacuating the flask for 5–10 sec followed by argon fill for 1 min. During the argon fill the flask was gently swirled. After the 5th cycle, argon gas was blown over the solution on the Schlenk line for ~15–30 min. Then, an additional 5 cycles of vacuum–argon fill were performed. At that point, the deoxygenated Mesna–activated β2 sample was taken into the glove box along with the purified and deprotected DOPA–22mer peptide. The ligation reaction contained 16 μmol DOPA–22mer and 8 mL of 25 mg/mL (2.3 μmol) Mesna–activated, truncated β2. It was supplemented with 0.1 volumes of 1.5 M Hepes, 0.4 mM EDTA, pH 7.3. The reaction proceeded at 4°C in the anaerobic chamber for ~36 h. It was gently swirled 4–5 times during the incubation period. After 36 h, it was taken out of the anaerobic chamber, aliquoted, quick–frozen in liquid N_2 and stored at –80°C.

MonoQ purification of ligation mixture. Preparative–scale purification of the ligation mixture was carried out on a MonoQ HR 16/10 Anion Exchange Column (10 μm, 2 × 10.5 cm, 33 mL – Amersham Bioscience) on a Sprint Biocad FPLC System (Applied Biosystems). Column operation was carried out at a flow rate of 3 mL/min monitoring the absorbance at 280 nm. The column was equilibrated in 50 mM Tris, 5 % glycerol, 1 mM DTT, pH 7.3 (Buffer Q). Loading was carried out with a 2 mL injection loop, typically 12–15 mg of the ligation reaction were loaded per run. After loading, the column was washed for 2 min with Buffer Q. The protein was then eluted with a linear gradient from 0 to 200 mM NaCl in Buffer Q over 3 min, followed by a linear gradient from 200 to 440 mM NaCl in Buffer Q over 37 min. Full–length β2 typically elutes at 360–380 mM NaCl in Buffer Q. The desired products (heterodimeric and homodimeric DOPA–β2) were collected on a fraction collector or by hand, concentrated to 70–350 μM, flash–frozen in liquid N_2 and stored at –80°C. The concentration of DOPA–β2 was determined using $\varepsilon_{280\,nm} = 131\ mM^{-1}cm^{-1}$. A column recovery of 80 % was typical.

Electron spray ionization (ESI) MS analysis of DOPA–β2. Purified DOPA–β2 constructs were characterized by ESI–MS at M. I. T. Biopolymers Laboratory on a PE Sciex API365 Triple Quad Mass Spectrometer from Applied Biosystems. Twenty μL of DOPA–β2 (~60 μM) was exchanged into water using Micro Bio–Spin–30 columns. The samples were

diluted to a final concentration of ~5 μM with 50% MeCN, 50% water, and 0.2% acetic acid immediately before analysis. Approximately 1–5 pmol of the diluted sample was loaded via direct infusion at 5 μL/min, and data were collected under positive ionization mode.

Quantitation of radical content by UV–vis and EPR spectroscopies. Radical content is reported per β2 throughout the text. UV–vis spectra were collected on an Agilent 8453 Diode Array Spectrophotometer or a Varian Cary 3 UV–vis Spectrophotometer. The dropline method was used to quantitate the amount of Y_{122}• using the following equation (Eq. 2–1):[18]

$$[Y_{122}\bullet] = \frac{Abs_{411\ nm} - \left\{\frac{Abs_{406\ nm} + Abs_{416\ nm}}{2}\right\}}{1783\ M^{-1}cm^{-1}} \times \text{Dilution Factor} \qquad (2\text{–}1)$$

EPR spectra were recorded at the Department of Chemistry Instrumentation Facility at 77 K on a Bruker ESP–300 X-band (9.4 GHz) spectrometer equipped with an Oxford liquid helium cryostat and an Oxford ITC 503 temperature controller or alternatively with a quartz finger dewar filled with liquid N_2. EPR parameters were as follows: Power = 50 μW, modulation amplitude = 1.5 G, modulation frequency = 100 kHz, time constant = 5.12 ms and scan time = 41.9 s. The microwave frequency was 9.38 GHz with the liquid helium cryostat and 9.34 GHz with the quartz finger dewar. The normalized double integral (DI/N) intensity was obtained on Bruker WinEPR software, which, by default, corrects for sweep time, gain and sweep width. The DI/N was further corrected for the number of scans, power and modulation amplitude using Eq. 2–2 to yield DI/N_c. The [Y_{122}•] was then computed by comparison to a known concentration of Cu^{II} standard, the double integral of which was also corrected using Eq. 2–2 and 2–3.[19] Note that subscripts 'SAM' and 'STD' refer to unknown sample and Cu^{II} standard spectra, respectively.

Quantitation of Fe content by the ferrozine assay. The previously reported Ferrozine assay was scaled down with minor modifications:[20] A solution of DOPA–β2 (100 μL, 20 μM)

was mixed with 0.1 volumes of a 50 % trichloroacetic acid solution and inverted several times. After centrifugation (14,000 × g, 12 min, rt), the supernatant was removed, diluted to 440

$$DI/N_c = \frac{DI/N}{\#\ Scans \times \sqrt{[Power\ (mW)]} \times Modulation\ Amp\ (G)} \qquad (2\text{–}2)$$

$$\frac{(DI/N_c)_{STD}}{(g_{ave})_{STD} \times [\,]_{STD}} = \frac{(DI/N_c)_{SAM}}{(g_{ave})_{SAM} \times [\,]_{SAM}} \qquad (2\text{–}3)$$

μL with doubly–deionized water and supplemented with 20 μL of each 75 mM sodium ascorbate, 10 mM ferrozine and a saturated solution of NH_4OAc. The absorbance of the $(Ferrozine)_3$–Fe complex was recorded at 562 nm (ε = 27.9 $mM^{-1}cm^{-1}$) and subtracted from the $Abs_{562\ nm}$ of a blank solution which contained water in place of protein.

Alternatively, DOPA–β2 (30 μL, 80 μM) was mixed with 70 μM of 2 M HCl in an eppendorf tube, inverted several times and boiled in a sand bath (95°C) for 5 min. Precipitated protein was pelleted by centrifugation (14,000 × g, 12 min, rt), the supernatant transferred to an eppendorf tube and the pellet combined with 100 μL of 2 M HCl and boiled again for 15 min as before. After centrifugation (14,000 × g, 12 min, rt), the two supernatants were combined and supplemented with 200 μL of 10 mM ferrozine solution, 40 μL of 75 mM sodium ascorbate and 200 μL of a saturated NH_4OAc solution. The absorbance of the protein sample and the blank sample were recorded at 562 nm as described above.

Growth, expression and purification of wt β2. Wild type β2 was expressed in BL21(DE3) *E. coli* cells from vector pTB2, which contains the β2 gene under control of a T7 promoter and terminator and an Amp^R marker. Vector pTB2 was transformed into BL21(DE3) competent cells using manufacturer's instructions. Flask growth and expression of β2 were carried out on a ~4–8 L scale in a shaker/incubator at 37°C and 200 rpm with Amp (100 μg/mL). A single colony was inoculated into a 5 mL LB/Amp starter culture (in a 12 mL bacterial culture tube) and grown to saturation (~12 h). The saturated culture was then diluted 200–fold into a

100 mL LB/Amp solution (in a 500 mL Erlenmeyer flask) and grown to saturation overnight (~12 h). The saturated culture was then diluted 200–fold into a large LB/Amp meidum in Erlenmeyer flasks. When the $OD_{600\ nm}$ reached ~0.6 (3–4 h), IPTG was added to a final concentration of 0.5 mM and expression continued at 37°C for 4–5 h. The cells were harvested by centrifugation (10,000 × g, 15 min, 4°C), flash–frozen in liquid N_2 and stored at –80°C. Typically a yield of 4 g wet cell paste per L culture growth was obtained.

β2 was usually isolated from ~20 g of wet cell paste. All purification steps were carried out at 4°C. Each g of wet cell paste was resuspended in 50 mM Tris, 5 % glycerol, 0.5 mM PMSF (β2 Buffer). After homogenization, cells were lysed by a single passage through a French Pressure Cell operating at 14,000 psi. Sodium ascorbate and $Fe(NH_4)_2SO_4$ (5 mg each per g cell paste) were dissolved in ~10 mL β2 Buffer and added dropwise to the crude extract over 10 min. The lysate was stirred for an additional 15 min and the cell debris removed by centrifugation (15,000 × g, 35 min, 4°C). DNA was precipitated by dropwise addition of 0.2 volumes of 6 % streptomycin sulfate in β2 Buffer to the crude extract over ~15 min. Stirring was continued for an additional 15 min. Precipitated DNA was removed by centrifugation (15,000 × g, 40 min, 4°C). The supernatant was transferred to a beaker and the protein precipitated by addition of 39 g of solid $(NH_4)_2SO_4$ per 100 mL supernatant over 20 min (66 % saturation). The mixture was stirred for an additional 35–45 min. The $(NH_4)_2SO_4$ precipitate was then isolated by centrifugation (15,000 × g, 45 min, 4°C). Next, the precipitated protein was redissolved in a minimal volume of β2 Buffer and desalted on a Sephadex G–25 column (2.5 × 45 cm, 220 mL) equilibrated in β2 Buffer. The visible brown protein band eluting from the column was collected by hand and loaded directly onto a DEAE Fast Flow Anion Exchange column (5 × 15 cm, 300 mL), which had been equilibrated in β2 Buffer. The column was washed with 2 CV of Buffer A, followed by 1.5 CV of β2 Buffer containing 110 mM NaCl. β2 was then eluted with a linear gradient (500 × 500 mL) from 100 to 500 mM NaCl in β2 Buffer A. β2 containing fractions, as determined by Y_{122}• absorption at 411 nm, were pooled, diluted with an equal volume of β2 Buffer and loaded onto a Q–Sepharose column (5 × 10 cm, 200 mL) which had been equilibrated

in β2 Buffer. The column was washed with 1.5 CV of β2 Buffer containing 200 mM NaCl. β2 was then eluted with a linear gradient (500 × 500 mL) from 200 to 700 mM NaCl in β2 Buffer. Fractions containing β2 were pooled, diluted with an equal volume of β2 Buffer (without PMSF), concentrated to ~25 mg/mL, aliquoted, flash–frozen in liquid N_2 and stored at –80°C. Typically, 30 mg of pure β2 were obtained per g of wet cell paste with a specific activity of ~7000 nmol/min mg, as measured by the spectrophotophetric RNR assay, and a radical content of 1.2 per β2 dimer (see above). The concentration of wt β2 was determined using $\varepsilon_{280\ nm}$ = 131 $mM^{-1}cm^{-1}$.

Growth, expression and purification of α2. Protein α2 was expressed in BL21(DE3) *E. coli* cells from plasmid pMJ1–α2, which contains the α2 gene under control of a T7 promoter and terminator and an Amp^R marker.[21] Vector pMJ1–α2 was transformed into BL21(DE3) competent cells using instructions by the manufacturer. Large–scale growth and expression of α2 were carried out on a 15–20 L scale in a 10 L fermentor at 37°C, 500 rpm and additionally in 6 L Erlenmeyer flasks (each containing 1.5 L media) in a shaker/incubator at 37°C, 200 rpm with Amp (100 μg/mL). A single colony was inoculated into a 5 mL LB/Amp starter culture (in a 12 mL bacterial growth tube) and grown to saturation (~12 h). The saturated culture was then diluted 200–fold into a 100 mL LB/Amp culture (in a 500 mL Erlenmeyer flask) and grown to saturation overnight (~12 h). This saturated culture was then diluted 200–fold into a large LB/Amp culture in the fermentor and Erlenmeyer flasks. When the $OD_{600\ nm}$ reached ~0.8 (3–4 h), IPTG was added to a final concentration of 0.5 mM and expression continued at 37°C for 5–6 h. The cells were harvested by centrifugation (10,000 × g, 15 min, 4°C), flash–frozen in liquid N_2 and stored at –80°C. Typically a yield of 4 g wet cell paste per L culture growth was obtained for wt α2.

α2 was usually isolated from 80 g of wet cell paste. All purification steps were carried out at 4°C. Each g of wet cell paste was resuspended in 50 mM Tris, 1 mM EDTA, 5 % glycerol, 5 mM DTT, 1 mM PMSF (α2 Buffer). After homogenization, cells were lysed by a single passage through a French Pressure Cell operating at 14,000 psi followed by removal of cell

debris by centrifugation (15,000 × g, 35 min, 4°C). DNA was precipitated by dropwise addition of 0.2 volumes of 6 % streptomycin sulfate in α2 Buffer to the crude extract over ~15 min. Stirring was continued for an additional 15 min. Precipitated DNA was removed by centrifugation (15,000 × g, 40 min, 4°C). The supernatant was transferred to a beaker and the protein precipitated by addition of 39 g of solid $(NH_4)_2SO_4$ per 100 mL supernatant (66 % saturation) over 20 min. The mixture was stirred for an additional 35–45 min. The $(NH_4)_2SO_4$ precipitate was then isolated by centrifugation (15,000 × g, 45 min, 4°C) and stored at 4°C overnight. Next, the precipitated protein was dissolved in a minimal volume of α2 Buffer and desalted on a Sephadex G–25 column (5 × 50 cm, 1 L) equilibrated in α2 Buffer. The visible brown protein band eluting from the column was collected by hand and loaded directly onto a DEAE Fast Flow Anion Exchange column (7 × 12 cm, 500 mL), which had been equilibrated in α2 Buffer. The column was washed with 4 CV α2 Buffer or until protein no longer eluted as judged by the Bradford Reagent Assay. α2 was then eluted with a linear gradient (800 × 800 mL) from 0 to 400 mM NaCl in α2 Buffer. Twenty mL fractions were collected and those containing α2, as determined by the spectrometric assay (see below), were pooled and loaded directly onto a dATP column (4 × 8 cm, 100 mL), which had been equilibrated in α2 Buffer (now containing 0.5 mM PMSF) at a flow rate of 2–3 mL/min. The column was washed with α2 Buffer (plus 0.5 mM PMSF) overnight at a flow rate of ~1 mL/min until protein no longer eluted as judged by the Bradford assay. α2 was then eluted with 50 mM Tris, 15 mM $MgSO_4$, 1 mM EDTA, 10 mM ATP, 10 mM DTT, pH 7.6 (Elution Buffer) until no more protein was detected by the Bradford assay. At that point, α2 was concentrated to 60–80 mL and desalted on a Sephadex G–25 column (5 × 50 cm, 1 L), which had been equilibrated in Elution Buffer without ATP. α2–containing fractions were pooled, concentrated to ~40 μM, divided into 1 mL aliquots, flash–frozen and stored at –80°C. Typically, 5 mg of pure α2 were obtained per g of wet cell paste with a specific activity of 2000–2800 nmol/min mg by the spectrophotophetric RNR assay. The concentration of α2 was determined using $\varepsilon_{280\,nm} = 189\ mM^{-1}cm^{-1}$.

Growth, expression and purification of *E. coli* thioredoxin. Thioredoxin (TR) was expressed from plasmid pTRX under control of the T7 promoter and terminator and an Amp^R marker in BL21(DE3) *E. coli* cells.[22] Growth and expression were carried out with 70 μg/mL Amp in an incubator/shaker at 37°C and 200 rpm. pTRX was transformed into BL21(DE3) cells following instructions by the manufacturer. A 5 mL culture of LB/Amp was inoculated with a single colony and grown overnight (~13 h). A 100 mL culture was then inoculated with 1 mL of the saturated small culture and grown to saturation (4–5 h), which was diluted 1000–fold into a large LB/Amp culture. When $OD_{600\ nm}$ reached 0.8 (~6 h), IPTG was added to a final concentration of 1 mM and expression continued for 3 h. At that point, cells were harvested by centrifugation (10,000 × g, 15 min, 4°C), quick–frozen in liquid N_2 and stored at –80°C. Typically a yield of 2.5 g wet cell paste per L culture was obtained.

TR was isolated from ~20 g of wet cell paste. All purification steps were performed at 4°C. Each g of wet cell paste was resuspended in 7 mL of 50 mM Tris, 3 mM EDTA, pH 7.4 (TR Buffer A) containing 0.5 mM TPCK and 1 mM TLCK. After homogenization, cells were lysed in an ice–water bath by sonication using 20 × 15 sec pulses with 1.5 min intervals between each pulse. Cell debris was removed by centrifugation (14,000 × g, 30 min, 4°C). The DNA was precipitated by dropwise addition of 0.2 volumes of 4.8 % streptomycin sulfate in TR Buffer A to the crude extract over 15 min with stirring. The mixture was stirred for an additional 15 min and precipitated DNA removed by centrifugation (14,000 × g, 30 min, 4°C). The supernatant was then diluted 3–fold into 50 mM KPi, 3 mM EDTA, pH 7.3 (TR Buffer B) and loaded onto a DE–52 anion exchange column (4 × 13 cm, 150 mL) which had been equilibrated in TR Buffer B. The column was washed with 3 CV of TR Buffer B and TR was eluted with a linear gradient (1.2 × 1.2 L) from 50 mM to 200 mM KPi (with 3 mM EDTA, pH 7.3). Fractions (20 mL) containing TR, as judged by the TR acitivty assay (see below), were pooled and concentrated on an Amicon concentrator with a YM–3 membrane to ~5 mL (~600 μM) and loaded onto a Sephadex G–75 column (1.5 × 80 cm, 140 mL) which had been equilibrated in TR Buffer B at 1 mL/min. TR was eluted isocratically in TR Buffer B. Fractions containing TR, as

judged by activity assays, were pooled, concentrated to ~ 1 mM, aliquoted, flash–frozen in liquid N_2 and stored at –80°C. The yield was ~2 mg TR per g of wet cell paste with a specific activity of 13 μmol/min•mg.[23] The concentration of TR was determined using $\varepsilon_{280\,nm} = 13.7\ mM^{-1}cm^{-1}$.

Growth, expression and purification of *E. coli* thioredoxin reduductase. *E. coli* thioredoxin reductase (TRR) was isolated from strain pMR14–K91, in which vector pMR14 contains the *E. coli* thioredoxin reductase b gene under control of a lpp promoter and terminator and an Amp^R marker.[24] Growth and expression of TRR were carried out in the presence of 100 μg/mL Amp in an incubator/shaker at 37°C and 200 rpm. A glycerol stock of pMR14–K91 was streaked out onto LB/Amp Agar plates and incubated overnight. A single colony was used to inoculate a 5 mL LB/Amp starter culture which was grown overnight (~16 h). The saturated culture was diluted 5000–fold into a 500 mL LB/Amp solution, which was grown to saturation overnight (~16 h). Each of 8 flasks containing 1.5 L LB/Amp were inoculated with 25 mL of the overnight culture. The large culture was grown to saturation (9 h), at which point the cells were harvested by centrifugation (2000 × g, 30 min, 4°C), flash–frozen and stored at –80°C. Five g of wet cell paste were obtained per L culture.

TRR was isolated from ~60 g of wet cell paste. All purification steps were performed at 4°C. Each g of cell paste was resuspended in 4 mL of 50 mM Tris, 1 mM βME, pH 8.0 (TRR Buffer A), homogenized and lysed with two passages through a French Pressure Cell operating at 14,000 psi. Cell debris was pelleted by centrifugation (13,000 × g, 45 min, 4°C). The crude extract was supplemented with a final concentration of 1.2 % (w/v) streptomycin sulfate over 20 min, the mixture stirred for additional 20 min and precipitated DNA removed by centrifugation (10,000 × g, 25 min, 4 °C). The supernatant was loaded onto a DE–52 column (5 × 15 cm, 300 mL) which had been equilibrated in 0.1 M KPi, 1 mM EDTA, pH 7.0. Bound TRR was eluted with a linear gradient (2 × 2 L) from 0.1 M to 0.25 M KPi (with 1 mM EDTA, pH 7.0). Fractions containing TRR, as judged by activity, were pooled and loaded directly onto a 2',5'–ADP Agarose column (2 × 8 cm, 25 mL), which had been equilibrated in 50 mM KPi, 3 mM EDTA, pH 7.6 (TRR Buffer B). The column was washed with 4 CV of TRR Buffer B

containing 0.2 M NaCl. TRR was then eluted with 3 CV of TRR Buffer B containing 1 mM NADPH. Fractions containing TRR, as judged by activity, were pooled, concentrated to ~40 μM, aliquoted, flash–frozen and stored at –80°C. A typical yield of ~1 mg pure TRR per g wet cell paste with a specific activity of 1400 nmol/min mg was obtained. The concentration of TRR was determined with the Lowry Assay using BSA as standard.

TR and TRR activity assays. *E. coli* TR and TRR were assayed using DTNB as a substrate. Stocks of DTNB were prepared fresh in EtOH. The assay contained in a final volume of 300 or 400 μL: 100 mM Tris, pH 8.0, 25 mM EDTA, 0.1 mM NADPH, 0.15 mM DTNB, 25 μM TR and 0.1 μM TRR. The initial reaction rate was determined by monitoring the absorption change at 412 nm, where the product thiolate has ε = 13.6 $mM^{-1}cm^{-1}$, on a Varian Cary 3 UV–vis Spectrophotometer. When TR was assayed, it was added to the mixture last and the observed rate corrected for TR–independent reduction of DTNB; the same procedure was carried out for TRR assays.

Spectrophotometric RNR assay. The assay contained in a volume of 300 μL: 3 μM α2, 3 μM DOPA–β2, 1 mM CDP, 3 mM ATP, 30 μM TR, 0.5 μM TRR, 0.2 mM NADPH in assay buffer. The reaction was initiated with addition of DOPA–β2 and the absorbance monitored at 340 nm (ε = 6.22 $mM^{-1}cm^{-1}$) on a Varian Cary 3 UV-vis Spectrophotometer. The temperature was maintained at 25°C with a Lauda RC6 circulating water bath. The observed absorbance change at 340 nm was corrected for the background change prior to addition of DOPA–β2. Each activity reported is the average of three independent measurements.

When wt α2 was assayed, wt β2 was in 5–fold molar excess. Likewise, assays of wt β2 contained 5–fold molar excess of wt α2. The subunit that was assayed was present at a final concentration of 0.1–1 μM.

Radioactive RNR assay. The assay contained in a volume of 230 μL: 3 μM α2, 3 μM β2, 1 mM [2–^{14}C]–CDP (8150 cpm/nmol), 3 mM ATP, 30 μM TR, 0.5 μM TRR and 1 mM NADPH in assay buffer. For each reaction nucleotides, TR, TRR and α2 were incubated at 25°C for 1.5–2 min. The reaction was then initiated by addition of DOPA–β2 and NADPH. At

defined timepoints, 40 μL were withdrawn and quenched in 25 μL 2 % (v/v) perchloric acid. At the end of the timepoint, the reactions were neutralized with 20 μL 0.5 M KOH. The quenched and neutralized timepoint samples were incubated at −20°C overnight to ensure complete precipitation of potassium perchlorate. The samples were then thawed on ice and spun down for 3 min in a tabletop centrifuge. Each supernatant was transferred to a 1.5-mL screw–top microfuge tube, to which was added 14 units of calf–intestine alkaline phosphatase, 120 nmol of carrier deoxycytidine (dC), and final concentrations of 75 mM Tris, 0.15 mM EDTA (pH 8.5). The samples were incubated at 37°C for 2 h and the amount dC in each sample was quantitated using the method of Steeper and Steuart.[25]

Binding of DOPA–β2 to α2. The affinity of DOPA–β2 for α2 was assessed by using it as a competitive inhibitor of nucleotide reduction.[26] First, the Y_{122}• of DOPA-β2 was reduced by incubating it (~80 μM) with 30 mM hydroxyurea at room temperature for 30 min, followed by desalting on a Sephadex G–25 column (1.5 x 25 cm, 45 mL) equilibrated in assay buffer (50 mM Hepes, 15 mM $MgSO_4$, 1 mM EDTA, pH 7.6). The met form of DOPA–β2 was then used as an inhibitor of nucleotide reduction without further modification. The assay mixture consisted of final concentrations of 0.15 μM α2 (2300 nmol/min mg), 0.3 μM wt β2 (7200 nmol/min mg), 50 μM thioredoxin, 1 μM thioredoxin reductase, 1 mM CDP, 1.6 mM ATP, 0.2 mM NADPH and varying concentrations of competitive inhibitor, met–DOPA–β2. Nucleotide reduction activity at each concentration of the inhibitor was determined by monitoring the absorption at 340 nm. The data was then fit to Eq. 2–4,

$$[\text{met–DOPA–}\beta2]_{\text{bound}} = \frac{[\text{met–DOPA–}\beta2]_{\text{max}} \times [\text{met–DOPA–}\beta2]_{\text{free}}}{K_d + [\text{met–DOPA–}\beta2]_{\text{free}}} \qquad (2\text{–}4)$$

where $[\text{met–DOPA–}\beta2]_{\text{bound}}$ is the concentration of the α2/met–DOPA–β2 complex, $[\text{met–DOPA–}\beta2]_{\text{max}}$ is the concentration of the α2/met–DOPA–β2 complex at maximal $[\text{met–DOPA–}\beta2]_{\text{free}}$, which equals 0.09 μM in the assay conditions used above, and K_d is the dissociation constant for interaction of met–DOPA–β2 and α2. $[\text{met–DOPA–}\beta2]_{\text{bound}}$ and [met-

DOPA–β2]$_{free}$ were computed as previously described.[27] Briefly, it is assumed thar the relative activity is a scaling factor indicative of the amount of wt α2/β2 complex present. At the concentration of α2 and β2 used in these assays, with [met–DOPA–β2]$_{total}$ = 0, [α2/β2] = 0.09 μM (using a K_d of 0.15 μM as previously reported for wt α2/β2). Inhibition of activity is assumed to be due to α2/met–DOPA–β2 complex formation, the concentration of which is calculated using Eq. 2–5. Accordingly, [met–DOPA–β2]$_{free}$ is computed using Eq. 2–6.

$$[\text{met–DOPA–}\beta2]_{bound} = 0.09 - \text{relative activity} \times [\alpha2/\beta2]_{at\ [\text{met-DOPA-}\beta2]=x} \quad (2\text{–}5)$$

$$[\text{met–DOPA–}\beta2]_{free} = [\text{met–DOPA–}\beta2]_{total} - [\text{met–DOPA–}\beta2]_{bound} \quad (2\text{–}6)$$

Pre–reduction of α2. Pre–reduced α2 was generated by incubation of ~40 mg α2 (~40 μM) with 35 mM DTT at room temperature for 40 min. Then, HU and additional DTT were added to final concentrations of 15 mM, each, and the incubation continued for 15 min. α2 was desalted on a Sephadex G–25 column (1.5 × 28, 50 mL) column, which had been equilibrated in assay buffer (50 mM Hepes, 15 mM $MgSO_4$, 1 mM EDTA, pH 7.6). Fractions containing α2, as judged by the Bradford Reagent Assay, were pooled, concentrated to ~80 μM, aliquoted, flash–frozen and stored at –80°C.[28]

Monitoring reactions of DOPA–β2 by stopped–flow (SF) UV-vis spectroscopy. SF kinetics was performed on an Applied Photophysics DX. 17MV instrument using PMT detection at 410 nm (λ_{max} of Y_{122}• with ε = 3700 $M^{-1}cm^{-1}$)[18] and 305 nm (reported λ_{max} of DOPA• with ε = 12,000 $M^{-1}cm^{-1}$).[8] Because the λ_{max} of DOPA•–β2 is shifted to 315 nm (see Results), the ε used at 305 nm was calculated using Eq. 2–7.

$$\varepsilon_{305\ nm} = \frac{\varepsilon_{315\ nm}}{(12{,}000\ M^{-1}cm^{-1})} \times \frac{Abs_{305\ nm}}{Abs_{315\ nm}} \quad (2\text{–}7)$$

The temperature was maintained at 25°C with a Lauda RE106 circulating water bath. All experiments were performed in assay buffer (50 mM Hepes, 15 mM $MgSO_4$, 1 mM EDTA, pH

7.6). Pre–reduced α2 and effector in one syringe were mixed with DOPA–β2 and substrate from another syringe in equal volumes to yield final concentrations of 23–30 μM α2, 1 mM substrate, 23–30 μM DOPA–β2 and 200 μM effector, respectively. Effector ATP was used at a final concentration of 3 mM, dNTP effectors were used at a final concentration of 200 μM. Exerpiemnts were carried out with following substrate/effector combinations: CDP/ATP, CDP/TTP, GDP/TTP, UDP/ATP, ADP/dGTP, CDP alone, GDP alone, UDP alone, ADP alone, TTP alone, ATP alone and dGTP alone. In all cases α2 and DOPA–β2 were shot against each other, where the substrate (if present) was in the same syringe as DOPA–β2 and the effector (if present) was in the same syringe as α2 to avoid consumption of pre–reduced α2 due to background levels of wt β2 in the α2 preparations. Data was collected in split time–base mode, where the first 500–1000 points were collected in the first 500–1000 ms and the remaining 500–3000 time points were collected over additional 0.5–12 s. Time courses shown are the average of at least 6 individual traces. Each trace consumed ~70 μL of sample from each syringe. Prior to the experiment, the lines were washed extensively with water, followed by buffer, and the instrument blanked from 290 nm to 600 nm in assay buffer. Curve fitting was performed with OriginPro or KaleidaGraph Software.

Reconstruction of the DOPA•–β2 UV–vis spectrum. For point–by–point analysis of the DOPA•–β2 UV–vis spectrum, α2 and TTP in one syringe were mixed in a 1:1 ratio with DOPA–β2 and GDP from another syringe to yield final concentrations of 17 μM, 1 mM, 17 μM and 200 μM. The kinetics were monitored between 300 and 380 nm in 5 nm intervals. At each λ, 3–4 traces were averaged and the resulting averaged amplitude was corrected for the absorption change associated with Y_{122}• (using the published ε between 300 and 380 nm) and plotted against λ.[29,30]

Monitoring reactions of DOPA–β2 by EPR spectroscopy. The reaction was carried out in an Eppendorf tube and contained in a volume of 250 μL: 20–30 μM pre-reduced α2 and DOPA–β2, 1 mM CDP and 3 mM ATP in assay buffer. Pre–reduced α2 and effector were mixed with DOPA–β2 and substrate. At a defined time point, the contents of the tube were

transferred to an EPR tube. The reaction was hand–quenched in liquid N_2 and the EPR spectrum recorded as described above.

Experiments were also carried out with the substrate effector combinations of UDP/ATP, GDP/TTP, ADP/dGTP, CDP/dATP (with various dATP concentrations), CDP alone, GDP alone and TTP alone. Substrate was always at a final concentration of 1 mM. ATP was always at 3 mM, whereas TTP and dGTP were at 200 μM. The concentration of dATP was 5 μM or 1 mM. The final concentrations of nucleotides are listed in figure legends. In all cases, α2 and effector (if present) were mixed with DOPA–β2 and substrate (if present).

Spin quantitation was performed using Cu^{II} standard as described above. Deconvolution of the signals observed in these experiments was performed using an Excel program written by Dr. John Robblee. This program converts the magnetic field values (G) to g values using Eq. 2–8, where h is Planck's constant, ν is the resonance wavelength, β is the Bohr magneton and B_0 is the applied magnetic field. This program further allows variation in the amount of Y_{122}• subtracted, which is judged visually by comparing the overlap of the standard Y_{122}• spectrum with the observed spectrum in the low field region, where there is no overlap with the DOPA• signal. The ratio of these signals was assessed by comparing the double integral intensity of each trace as described above. Spectral subtractions were performed using the Y_{122}• spectrum of DOPA–β2 as reference.

$$g = h\nu / \beta B_0 \qquad (2\text{–}8)$$

Simulation of DOPA•–β2 EPR spectra with different substrate/effector pairs were carried out using SimFonia software (Bruker). For all simulations, a Lorentzian/Gaussian ratio of 0.3 was used. For DOPA•–β2 spectra in the presence of GDP/TTP and ADP/dGTP, g values measured by Prof. Marina Bennati at 180 GHz were used. In addition hyperfine couplings from two I=1/2 nuclei were varied to yield the best fit to experimental data. For simulation of DOPA•–β2 with CDP/ATP and UDP/ATP, g values were varied along with hyperfine interactions from two nuclei with I=1/2.

Generation of DOPA• and catechol•. DOPA amino acid (Sigma, catalog # D9628) and catechol (Sigma, catalog # C9510) were dissolved in water to a concentration of 10 mM and the pH of the solution adjusted to 7. Each sample was transferred to an EPR tube and the contents sparged with $Ar_{(g)}$ for 10–15 min. The tube was then capped under Ar pressure and immediately frozen by immersing into liquid N_2. Each tube was irradiated with a 1000 W xenon lamp at 77 K in a liquid N_2 finger dewar for 45 s.[31,32] The EPR spectrum was then recorded, as described above, immediately after irradiation.

Generation of apo DOPA–β2 with lithium 8–hydroxyquinoline–6–sulfonate. Apo DOPA–β2 was generated using the previously published method of Atkin et al. with minor modifications.[33] Briefly, a solution of 1.5 mL of DOPA–β2 (~10 mg, 77 μM) was dialyzed against 400 mL of chelator solution consisiting of 1 M imidazole, 30 mM NH_2OH, 50 mM 8–hydroxyquinoline–6–sulfonate (pH 7.0) in a 3 mL–Slide–a–lyzer cassette for 3 h. The chelator was then removed by dialysis against Hepes buffer (50 mM Hepes, 5 % glycerol, pH 7.6) for 3 h and further by desalting on a Sephadex G-25 column (1.5 × 23, 40 mL), which had been equilibrated in Hepes buffer.

Reconstitution of apo DOPA–β2. The apo protein was concentrated to 60–80 μM using a YM–30 centriprep device, transferred to a 25 mL pear–shaped flask, degassed on a Schlenk line as described above and brought into the anaerobic chamber, where it was reconstituted: A 5–fold molar excess of $Fe(NH_4)_2(SO_4)_2$ (as measured by the ferrozine assay) was added to the mixture, which was incubated at 4°C in the anaerobic chamber for 5–10 min. Then, the mixture was taken out of the anaerobic chamber mixed with O_2–saturated Hepes buffer (3.5–fold excess O_2), which was generated by sparging Hepes buffer with $O_{2(g)}$ for 10–15 min at 4°C. Finally, 15 min after addition of O_2, sodium ascorbate was added to a final concentration of 10 mM and the protein was desalted on a Sephadex G–25 column (1.5 × 23, 40 mL), which had been equilibrated in assay buffer, to remove excess iron.

Preparation of high–field EPR and PELDOR samples. Pre–reduced α2 and DOPA–β2 were combined in equimolar ratio and concentrated at 4°C in a minicon concentration

device (YM–30 membrane) to a final complex concentration of 200–300 μM ($\varepsilon_{280\ nm\ (\alpha2+DOPA-\beta2)}$ = 320 $mM^{-1}cm^{-1}$). The concentrated sample was divided into 100 μL aliquots and placed in 1.5 mL Eppendorf tubes, flash–frozen in liquid N_2 and shipped on dry ice along with substrate/effector and glycerol–containing buffer solutions to Prof. Marina Bennati at the University of Frankfurt (Germany). High–field EPR and PELDOR samples were prepared by Prof. Marina Bennati by thawing each aliquot on ice and adding 5 μL of a substrate/effector mix to yield final concentrations of 2.5 mM substrate (CDP, UDP, ADP or GDP), 6 mM effector ATP or 0.3 mM effector dNTP (dGTP or TTP). The reaction was allowed to proceed for 30 sec, at which point 15 μL of glycerol buffer (100 mM Hepes, 30 mM $MgSO_4$, 2 mM EDTA, 50 % glycerol, pH 7.6) was added to yield a final glycerol concentration of ~6 %. The reaction was quenched after a total reaction time of 60–90 sec by hand–freezing in liquid N_2. High–field (180 GHz) EPR and X–band PELDOR spectra were recorded and analyzed by Prof. Marina Bennati.

RESULTS

Synthesis of DOPA–22mer. Synthesis of the 22mer peptide containing DOPA was performed in two steps (Figure 2–1). In the first step, the first 19 residues (H_2N–$L_{19}VGQID_{14}S_{13}EVDTDDLSNFQL_1$–COOH) were made on an automated peptide synthesizer, where residues S_{13} and D_{14} were incorporated as a pseudo–proline dipeptide, as previously described.[15] After completion of the Fmoc–19mer synthesis, a small amount of peptide was cleaved from the resin and its purity and molecular weight assessed by RP–HPLC and MALDI–TOF MS, respectively. A typical Fmoc–19mer MALDI–TOF mass spectrum and RP–HPLC elution profile are presented in Figure 2–4. The HPLC elution profile shows peptide migration with a R_t of 24 min with >90 % purity. The mass spectrum performed under negative mode shows major peaks at 2351.3 and 2367.1, corresponding to $[M–2H+Na]^-$ (exp 2353) and $[M–2H+K]^-$ (exp 2367), respectively. The minor peaks with m/z of 2388.9 and 2403.9 are related to the $[M–3H+Na+K]^-$ (exp 2389) and the $[M–3H+2K]^-$ (exp 2405) species.

In the second step of DOPA–22mer synthesis, the remaining three residues, $DOPA_{20}$, S_{21} and C_{22}, were attached manually. The catechol functionality of DOPA contained the acid–labile acetonide protecing group (Figure 2–5). The thiol moiety of C contained a thiol–labile, but acid and base stable, t–Buthio protecting group. In addition, C was coupled in its pre–activated pentafluorophenol form (Figure 2–5), obviating the need for a base in the coupling reaction. Purification of DOPA–22mer was carried out at pH 7.0 to minimize base–catalyzed oxidation of DOPA. Figure 2–6 presents the characterization of pure DOPA–22mer peptide. A representative HPLC elution profile, monitored at 215 and 280 nm, is shown in Figures 2–6A and 2–6B. The profiles demonstrate that DOPA–22mer migrates with a R_t of 18.5 min and is >95 % pure. The presence of the intact DOPA residue was confirmed by UV spectroscopy (Figure 2–6C) and MALDI–TOF MS in the t–Buthio–protected (Figure 2–6D) and deprotected (Figure 2–6E) forms. The UV spectrum of pure DOPA–22mer consists of a relatively narrow absorption feature with a λ_{max} at 280 nm and ε of ~2500 $M^{-1}cm^{-1}$ using the mass of lyophilized

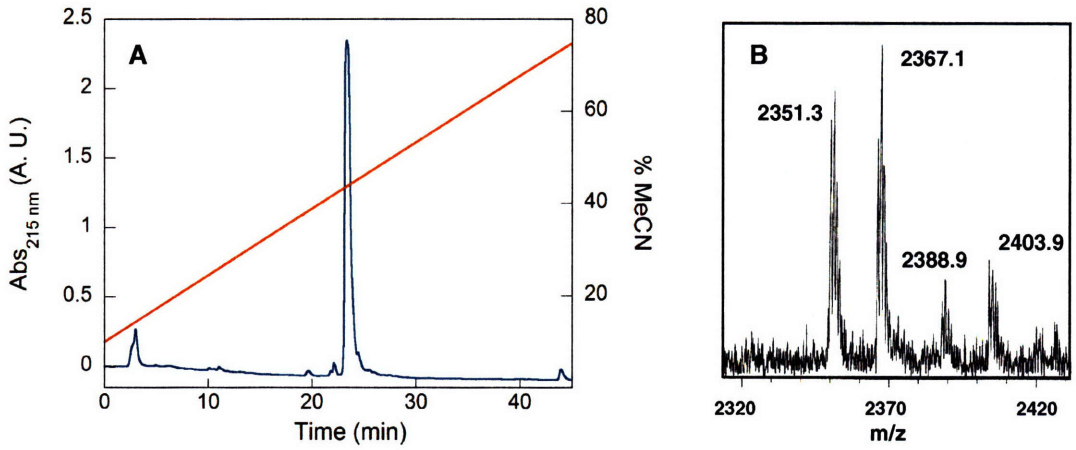

Figure 2–4. Characterization of Fmoc–19mer peptide. (A) Analytical RP–HPLC profile on a Phenomenex Jupiter column (see Methods). (B) MALDI–TOF mass spectrum of Fmoc–19mer under negative ionization mode. The peaks correspond to $[M–2H+Na]^-$ (exp 2351), $[M–2H+Na]^-$ (exp 2367), $[M–3H+Na+K]^-$ (exp 2389) and $[M–3H+2K]^-$ (exp 2405).

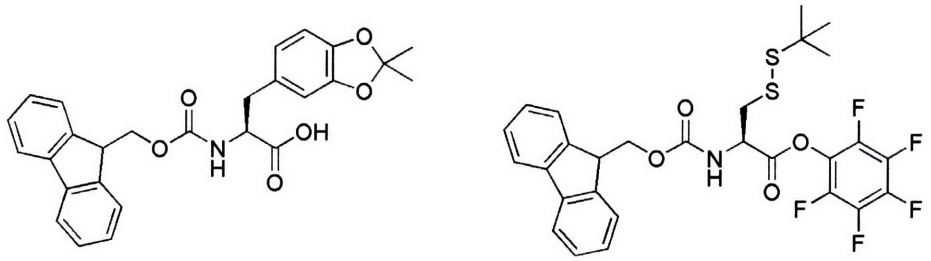

Figure 2–5. Structures of Fmoc–DOPA(acetonide)–OH (left) and Fmoc–Cys(t–Buthio)–OPfp (right).

DOPA–22mer to calculate peptide concentration. These numbers are similar to those previously determined for free DOPA amino acid (280 nm and 2760 $M^{-1}cm^{-1}$, repectively). In addition, MALDI–TOF MS in the negative ionization mode for the t–Buthio–protected variant consists of two peaks at m/z 2585.1 and 2602.1, corresponding to the $[M–2H+Na]^-$ (exp 2586) and $[M–2H+K]^-$ (exp 2602) forms, respectively. The spectrum in Figure 2–6E was taken prior to ligation of DOPA–22mer to truncated, Mesna–activated β2 and contains one major peak with m/z 2513.3, which corresponds to the $[M–2H+K]^-$ (exp 2514) form of the peptide. The MALDI–TOF data shows that the DOPA probe is in tact after the synthetic procedures. As described in the introduction, side reactions of DOPA would lead to addition of water or other nucleophiles to the phenol ring, which would be detected in the mass

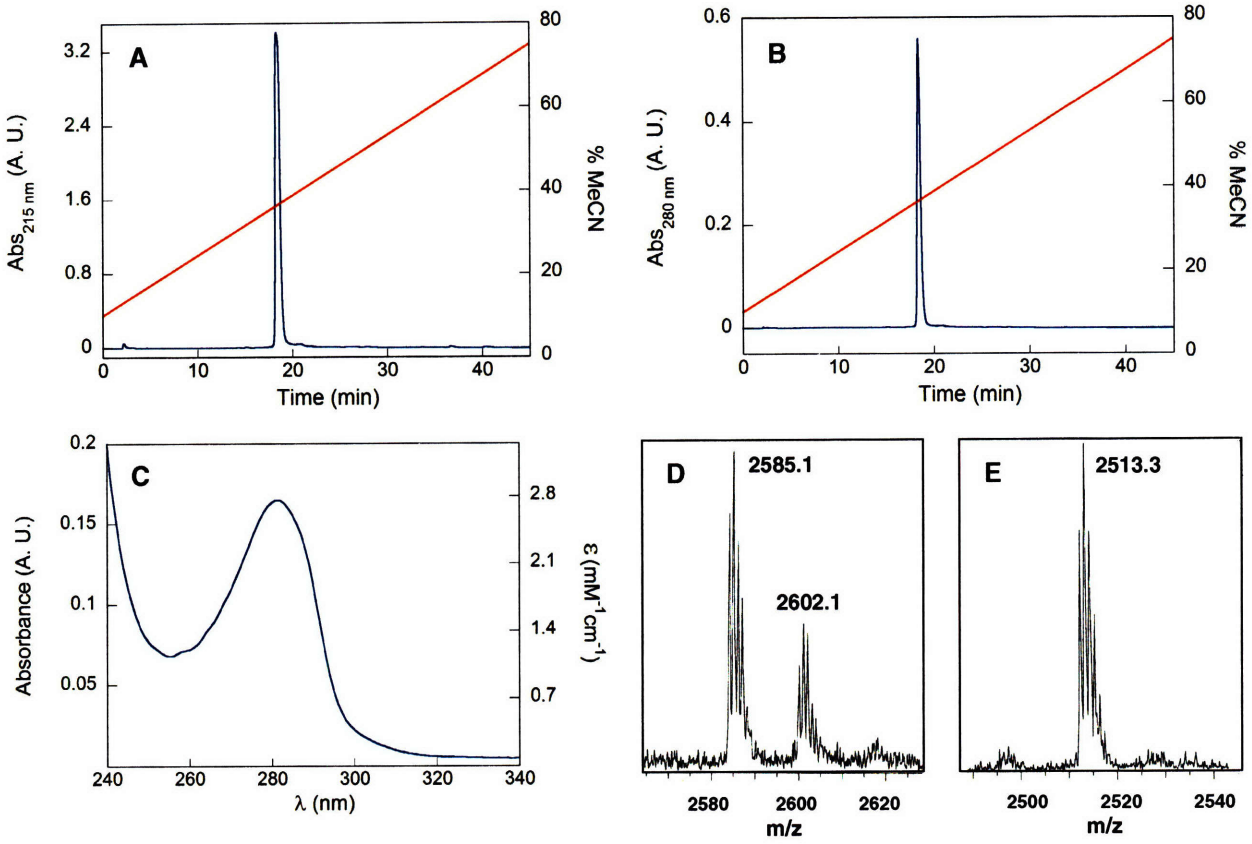

Figure 2–6. Characterization of purified DOPA–22mer. RP–HPLC elution profile of DOPA–22mer at 215 nm (A) and 280 nm (B) with R_t of 18.5 min. (C) The UV spectrum of DOPA–22mer contains a single absorption feature with a λ_{max} of 280 nm. (D) MALDI–TOF MS of t–Buthio–protected DOPA–22mer. The peaks correspond to the Na^+ salt (exp 2586) and K^+ salt (exp 2602) of the peptide. (E) MALDI–TOF MS of free DOPA–22mer immediately before ligation to truncated β2. The single peak is associated with the K^+ salt of the peptide (exp 2514).

spectrum. Together, the data in Figure 2–6 illustrate that DOPA–22mer was synthesized with >95 % purity and that purification and deprotection procedures at neutral pH successfully avoided side reactions that DOPA may undergo if the precautions above had not been made.

Generation of semisynthetic DOPA–β2. Truncated, Mesna–activated β2 was prepared as previously described. The yield of Mesna–activated β2 is dependent on the Mesna concentration used to cleave truncated β2 from the β2–intein–CBD construct. With 60 mM Mesna, ~3 mg of truncated β2 per g of cell paste was obtained. Semisynthetic β2 obtained in this fashion, encompasses a greater radical content (0.45 Y_{122}•/β2) due to the propensity of thiol–containing compounds to reduce the essential Y_{122}•. At 100 mM Mesna, the yield of

truncated β2 was increased to ~5 mg/g cell paste with a radical content of 0.3 Y_{122}•/β2. In the present semisynthesis, a high Mesna concentration was used (100 mM) for the cleavage reaction to obtain the large quantities of DOPA–β2 necessary for biophysical experiments.

After cleavage of truncated β2 from the chitin resin, the protein was exchanged into neutral pH buffer and ligated to DOPA–22mer peptide under anaerobic conditions. An SDS gel of the products of the ligation reaction is shown in Figure 2–7A, which reveals that the ligation yield was ~50 %. Presumably, the lower yield, relative to prior ligations, is due to the lower pH of the reaction, chosen to safeguard the DOPA probe.

Incomplete ligation results in three products, truncated β2, heterodimeric DOPA–β2 and full–length homodimeric DOPA–β2. These products can be separated on a MonoQ anion exchange column due to the presence of six negative charges in the 22mer peptide. Reducing conditions are employed during MonoQ chromatography to ensure that the cysteine resiudes, used for the intein ligation reaction, do not form inter or intramolecular disulfide linkages. A typical elution profile is shown in Figure 2–7B. The first peak, eluting at ~300 mM NaCl, contains truncated β2 homodimer; the second contains the DOPA–β2 heterodimer, where one of the monomers is truncated. Finally, the last peak, eluting at ~380 mM NaCl is the desired full–length DOPA–β2 homodimer. The purity of heterodimeric and homodimeric DOPA–β2 was assessed on an SDS gel and demonstrates that each construct was prepared to >95 % purity (Figure 2–7C).

DOPA–β2 was then subjected to ESI–MS and analyzed for its Fe and radical content. Low resolution ESI–MS under positive detection mode reveals two peaks at m/z $[M+H]^+$ 43771 and 43949 (data not shown). The former represents DOPA–β2 (exp 43776); the latter is an +176 Da adduct which has been observed in all β2 preparation that have been analyzed by ESI–MS.[15] The origin of this species is unknown. The UV–vis spectrum of DOPA–β2 shows that the Fe center is intact, consistent with an Fe content of 3.2 per DOPA–β2 as determined by the ferrozine assay (data not shown). In addition, dropline quantitation of the UV–vis spectrum shows that low amounts of Y_{122}•, 0.28 per DOPA–β2, are present (Figure 2–8A). This result is

similar to spin quantitation obtained by EPR methods, which yield 0.3 Y_{122}•/DOPA–β2. Importantly, however, the EPR spectral features of Y_{122}•–DOPA–β2 are similar to those reported for wt β2 (Figure 2–8B). In addition, the stability of the Y_{122}•–DOPA–β2 is similar to that of wt β2. No loss of Y_{122}• occurs upon storage of DOPA–β2 at –80°C or after freeze–thaw cylces. Together, the data above establish that DOPA–β2 has been prepared in >95 % purity and that its diferric Y_{122}• center is intact, albeit at low Y_{122}• concentrations. The EPR spectrum of this radical reveals it is unperturbed by substitution of DOPA at residue 356.

Activty sssays of DOPA–β2. First the effect of DOPA insertion on the α2/DOPA–β2 interaction was considered. Climent et al. have shown that the C–terminal tail of β2 accounts for most of the binding interaction between β2 and α2. However, assays with Y_{356}F–β2 indicated its interaction with α2 was similar to that between wt β2 and α2, demonstrating that the α2/β2 interaction is tolerant to minimal structural changes at this position. Consequently, we expected that replacement of residue 356 with DOPA would not significantly perturb the interaction with α2. To test this hypothesis, we employed the assay used by Climent et al.[26] In this assay, the met form (reduced Y_{122} form) of the β2 variant of interest is used as a competitive inhibitor of nucleotide reduction. First, the met form of DOPA–β2 was generated via hydroxyurea treatment followed by desalting on a Sephadex G–25 column. The UV–vis spectrum of DOPA–β2 after incubation with hydroxyurea is shown in Figure 2–9A. The inset is a blow–up of the features associated with the di–iron Y_{122} center. A comparison of Figure 2–8B with Figure 2–9A reveals that hydroxyurea completely reduces the Y_{122}• leaving the Fe center intact. This form of DOPA–β2 was then added at increasing concentrations to the assay mixture containing wt α2 and β2, and the activity subsequently examined. From this analysis, a K_d of 0.34 ± 0.05 μM was determined. Thus, the K_d between DOPA–β2/α2 is 1.5–fold higher than that reported for by Climent et al. for the interaction between wt β2 and α2. Accordingly, insertion of DOPA at residue 356 has a minimal effect on subunit interaction.

Next, we investigated whether DOPA–β2 was competent in turnover. We suspected that $DOPA_{356}$ could be readily oxidized during radical propagation catalyzed by RNR. However, a

DOPA radical (DOPA•) would be unlikely to oxidize Y_{731} in α2, thus preventing nucleotide reduction. Consistent with this model, the spectrophotometric and radioactive assays with DOPA–β2 failed to reveal any turnover (Table 2–2). We therefore estimate that the specific activity of DOPA–β2 is $<1/10^4$ that of wt β2 generated by the intein method.

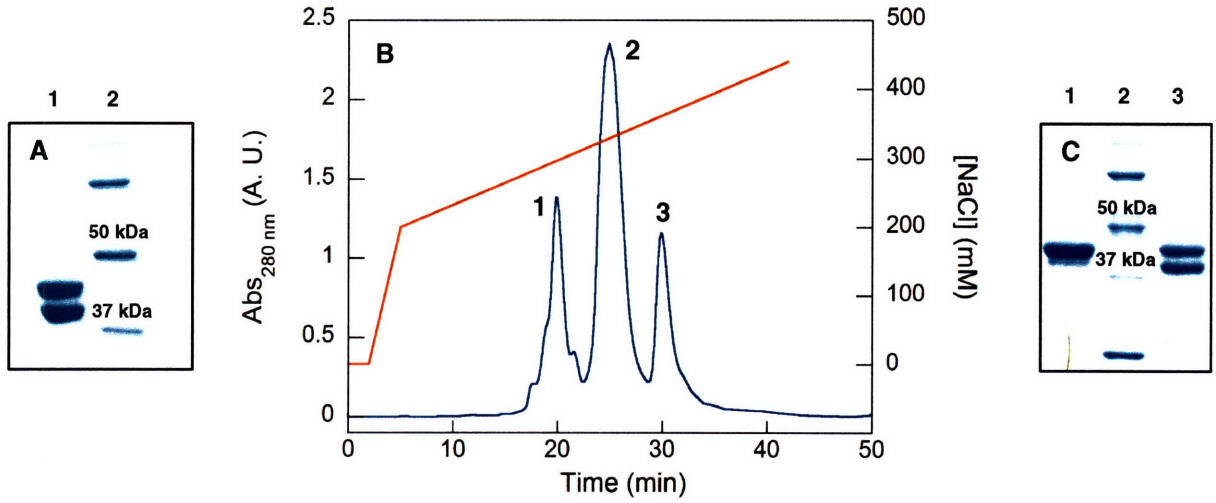

Figure 2–7. Generation of semisynthetic DOPA–β2. (A) SDS gel of after ligation of DOPA–22mer peptide to truncated, Mesna–activated β2. Lane 1, ligation mixture; lane 2, MW marker. (B) Mono Q elution profile of the DOPA–β2 ligation mixture. The peaks correspond to truncated homodimeric β2 (1), truncated/full–length heterodimer (2) and full–length DOPA–β2 homodimer (3). (C) SDS gel after MonoQ chromatography. Lane 1, pure DOPA–β2 homodimer; lane 2, MW marker; lane 3; pure DOPA–β2 heterodimer.

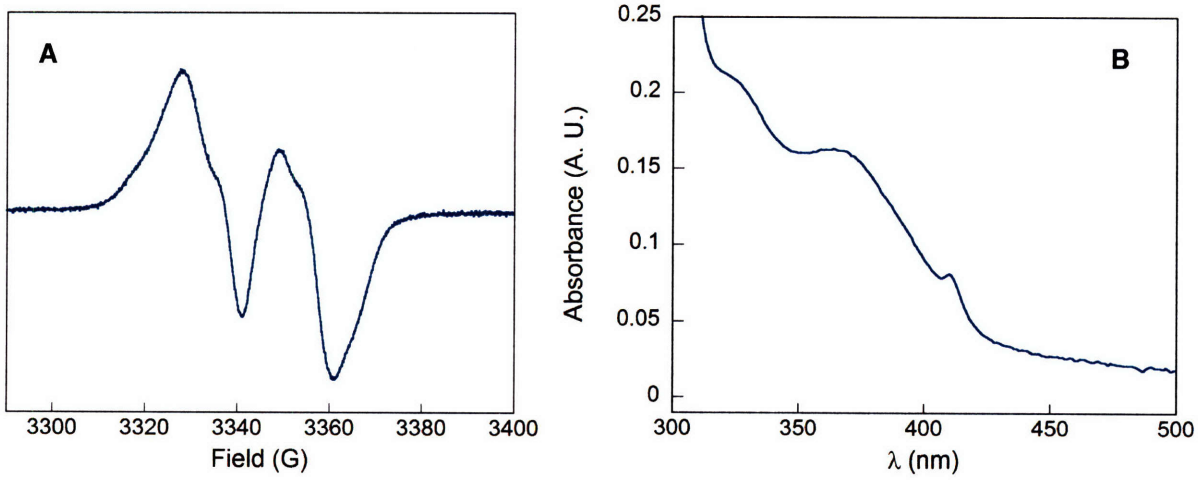

Figure 2–8. Characterization of the Y_{122}• in DOPA–β2. (A) EPR spectrum of pure DOPA–β2. (B) UV–vis spectrum showing the diiron Y_{122}• features of DOPA–β2.

Table 2–2. Specific activities of wt β2, intein–wt β2 and DOPA–β2 in nmol/min mg.

Assay	wt β2[a]	Intein–wt β2[b]	DOPA–β2
Spectrometric	7600 ± 250	490 ± 15	< 12[c]
Radioactive	4800 ± 100	450 ± 18	< 0.5[c]

[a] wt β2 contained 1.2 Y_{122}•/dimer. [b] Intein–wt β2 contained 0.3 Y_{122}•/dimer. [c] Lower limit of detection by these assays.

Trapping of a $DOPA_{356}$•–β2. After the extensive characterization of semisynthetic DOPA–β2 presented above, we sought direct evidence for the involvement of residue 356 in β2 during radical migration. First, stopped flow (SF) UV–vis experiments were carried out. In a typical experiment, DOPA–β2 and GDP in one syringe were rapidly mixed with pre–reduced α2 and effector TTP in a second syringe. The reaction was monitored at 305 nm, the reported λ_{max} of DOPA• (ε = 12,000 $M^{-1}cm^{-1}$), and at 410 nm, the λ_{max} of Y_{122}• (ε = 3700 $M^{-1}cm^{-1}$).[8,18] As shown in Figure 2–10, the Y_{122}• (red) disappears, while a feature absorbing at 305 nm (blue), grows in with similar kinetics. Analysis of the kinetic traces reveals a fast phase followed by a slow phase, where each phase can be fit to a single exponential. The rate constants obtained from the fits are 27 and 1.7 s^{-1} at 305 nm and 36 and 1.6 s^{-1} at 410 nm. The slower of the two rate constants is similar to the rate constant determined for the conformational step that gates radical initiation. Initial analysis shows that the reaction appears to be complete by 2 s and remains unchanged for 30 s. At the endpoint, only 57 and 51 % of the total initial Y_{122}• appears to be trapped as determined at 305 nm and 410 nm, respectively.

Several controls were carried out to ensure that formation of the proposed DOPA• is associated with the pathway for radical propagation. In one control, DOPA–β2 was examined alone (data not shown). In the second control, DOPA–β2 and α2 were rapidly mixed in the absence of substrate and effector and in the third control, met DOPA–β2 and substrate in one syringe was mixed with pre–reduced α2 and effector from another syringe (Figure 2–11). No spectral changes were observed in any of these cases.

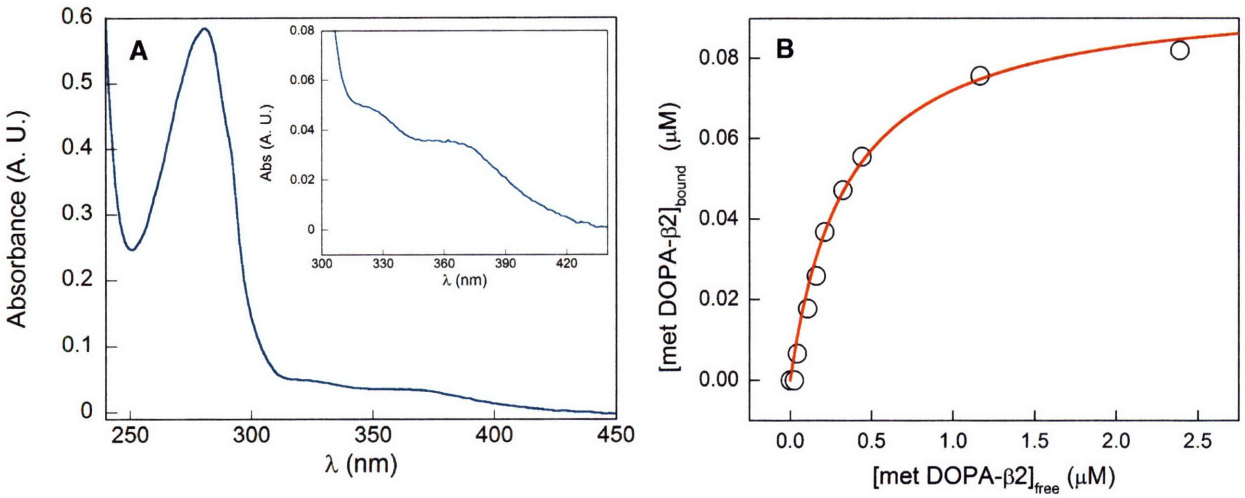

Figure 2–9. Binding of DOPA–β2 to α2. (A) UV–vis spectrum of met DOPA–β2. The inset shows a blow–up of the features related to the diferric Y_{122} center. (B) Complex formation between met DOPA–β2 and α2 as a function of free [met DOPA–β2] (see Methods). The red line represents a fit to the data (Eq. 2–4) yielding a K_d of 0.34 ± 0.05 μM for the interaction between met DOPA–β2 and α2.

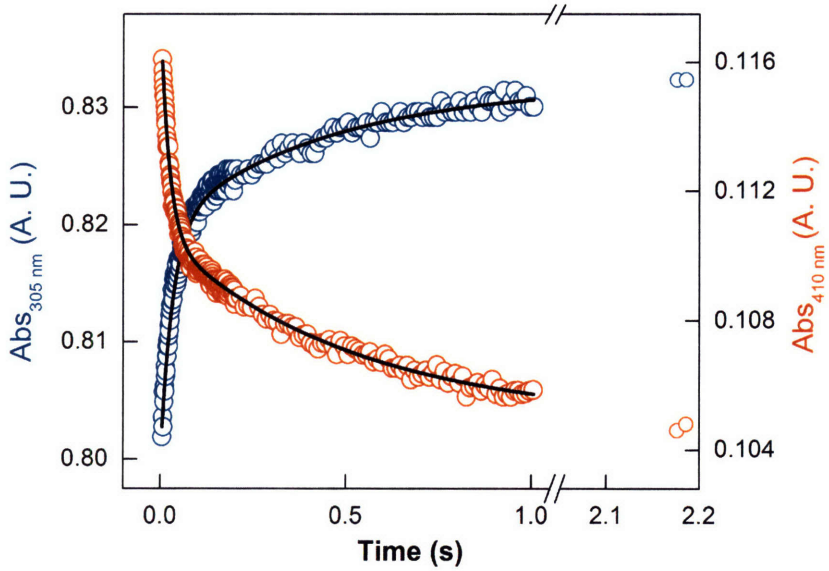

Figure 2–10. Kinetics of $DOPA_{356}$• formation and Y_{122}• disappearance. DOPA–β2 (45 μM) and GDP (2 mM) in one syringe were mixed in a 1:1 ratio with pre–reduced α2 (45 μM) and TTP (200 μM) from another syringe monitoring DOPA• formation (blue, 305 nm) and Y_{122}• loss (red, 410 nm). A total of 7 traces were averaged at each λ. Black lines describe biexponential fits to the data.

To confirm the identity of the new radical, analysis of the UV–vis spectrum between 300 and 375 nm at 5 nm intervals was performed with DOPA–β2/α2 and the GDP/TTP pair. The absorbance change after 2 s, corrected for the changes associated with Y_{122}•, was then plotted against λ revealing the spectrum in Figure 2–12. This spectrum shows a new species containing

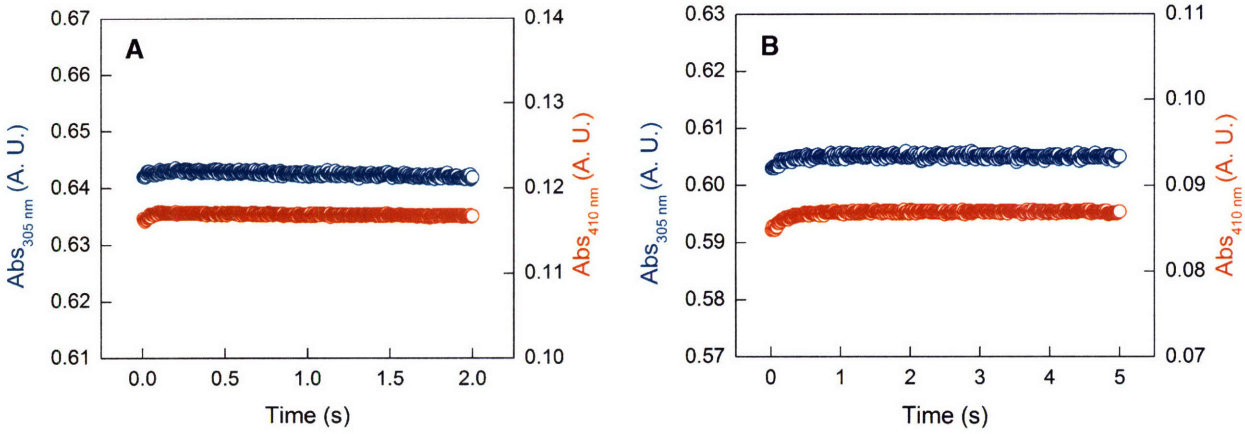

Figure 2–11. Control experiments for SF UV–vis reactions of DOPA–β2. (A) One syringe contained pre–reduced α2 (40 μM) and ATP (6 mM) and was mixed in a 1:1 ratio with met DOPA–β2 (40 μM) and CDP (2 mM) from another syringe. (B) Pre–reduced α2 (40 μM) was mixed in a 1:1 ratio with DOPA–β2 (40 μM) from another syringe.

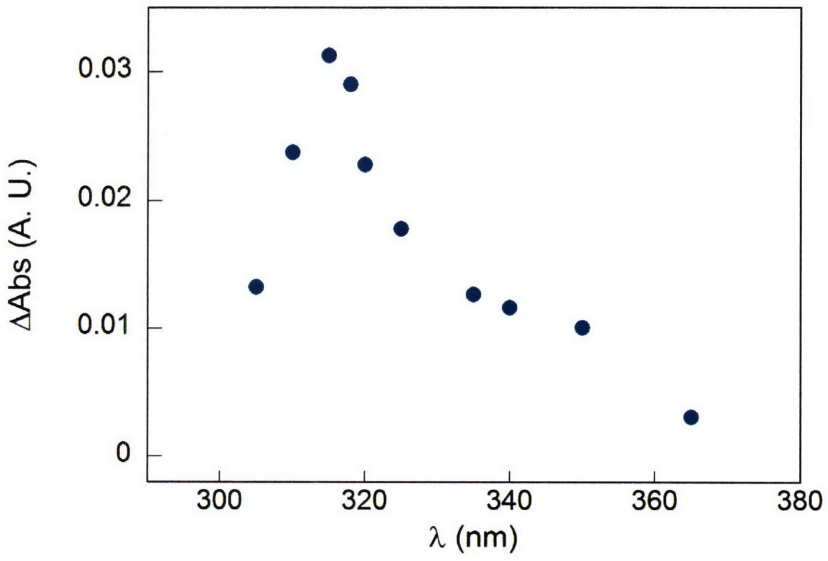

Figure 2–12. UV–vis spectrum of $DOPA_{356}$• using point–by–point spectral reconstruction. DOPA–β2 (40 μM) and GDP (2 mM) were mixed in a 1:1 ratio with pre–reduced α2 (40 μM) and TTP (200 μM). The absorbance was monitored in 5–10 nm intervals between 300 and 375 nm. At each λ, 3–4 traces were averaged and the absorbance change plotted against λ after correction for absorbance by Y_{122}• in this region.

a λ_{max} at 315 nm and a shoulder at ~350 nm. It is identical to the spectrum previously reported for a DOPA•, as determined by pulse radiolysis, except that it is red–shifted by 10 nm, suggesting an effect of the protein environment at the α2/DOPA–β2 interface.[8]

Kinetics of DOPA• with various substrate/effecotor pairs. To examine the generality of the observations above, additional reactions were carried out with CDP/TTP, CDP/ATP, UDP/ATP and ADP/dGTP (Figure 2–13). The kinetic parameters obtained from these reactions are listed in Table 2–3. In all cases, triphasic kinetics was observed. As with the GDP/TTP reaction, the rate constants determined at 410 and 305 nm were similar. Three main observations are common to the five reactions with various substrate/effector pairs. First, a slow kinetic phase that resembles the rate constant expected for the conformational trigger that gates radical migration is observed in all reactions. This result indicates that DOPA–β2 is a conformational probe, which allows direct observation of the physical step prior to radical initiation. Second, in all cases, additional kinetic phases with faster rate constants than that expected for the rate–limiting conformational change are observed. These additional phases highlight that DOPA is a conformational probe reporting on different conformational states of the α2/DOPA–β2 complex that do not interconvert. And finally, in all cases 45–54 % of the total initial Y_{122}• is trapped as a DOPA•. The stoichiometry from these experiments will be discussed below in light of an asymmetric interaction between α2 and β2.

Additional SF UV–vis experiments were carried out to examine the effect of substrate (GDP, CDP, UDP, ADP) and effector (TTP, ATP, dGTP) individually. With CDP, GDP and UDP, the kinetics are similar to those observed in the presence of the respective allosteric effectors (Table 2–3). That is, in the presence of only CDP, GDP or UDP, the reaction extent and rate constants are similar to those with CDP/ATP, GDP/TTP or UDP/ATP, respectively. In the case of ADP, however, the absence of its allosteric effector, dGTP, results in a drastic drop in the extent and rate of DOPA• formation (Figure 2–14). Only 18 % of total initial Y_{122}• is trapped as a DOPA•, which occurs in single kinetic phase with a k_{obs} of 0.12 s^{-1}. Intriguingly, the changes at 305 nm and 410 nm in the first 150 ms of the time course are not correlated. At

315 nm, an increase with a rate constant of 15 s^{-1} is observed. At 410 nm, instead of a loss of absorption, a rise with a rate constant of 33 s^{-1} occurs. After this initial phase, the growth at 315 nm is kinetically linked to disappearance at 410 nm indicating formation of DOPA• concomitant with disappearance of Y_{122}•. The unusual kinetics with ADP alone cannot be explained at this point.

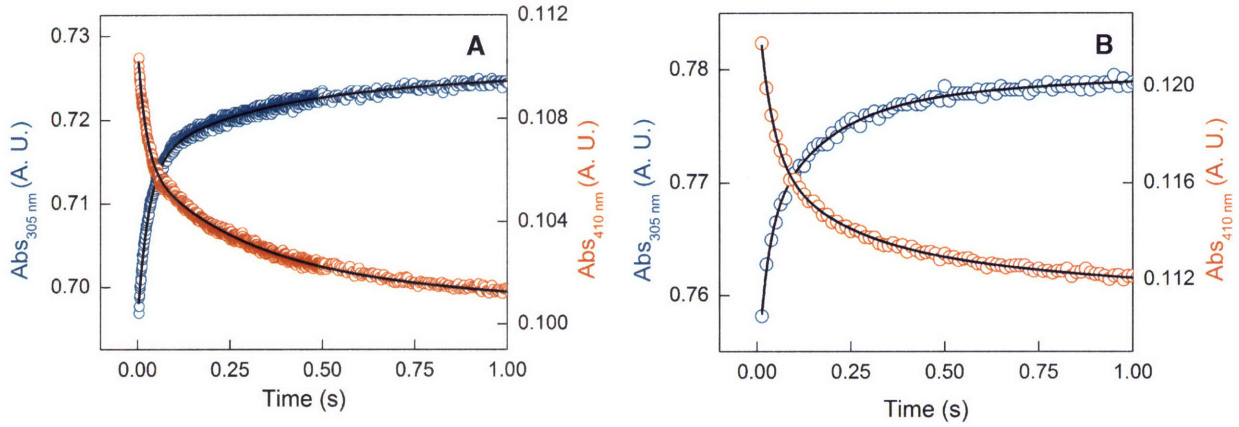

Figure 2–13. Trapping of $DOPA_{356}$• with different substrate/effector pairs. (A) DOPA–β2 (45 μM) and CDP (2 mM) were rapidly mixed in a 1:1 ratio with pre–reduced α2 (45 μM) and TTP (200 μM). (B) DOPA–β2 (58 μM) and CDP (2 mM) were rapidly mixed in a 1:1 ratio with pre–reduced α2 (58 μM) and ATP (6 mM).

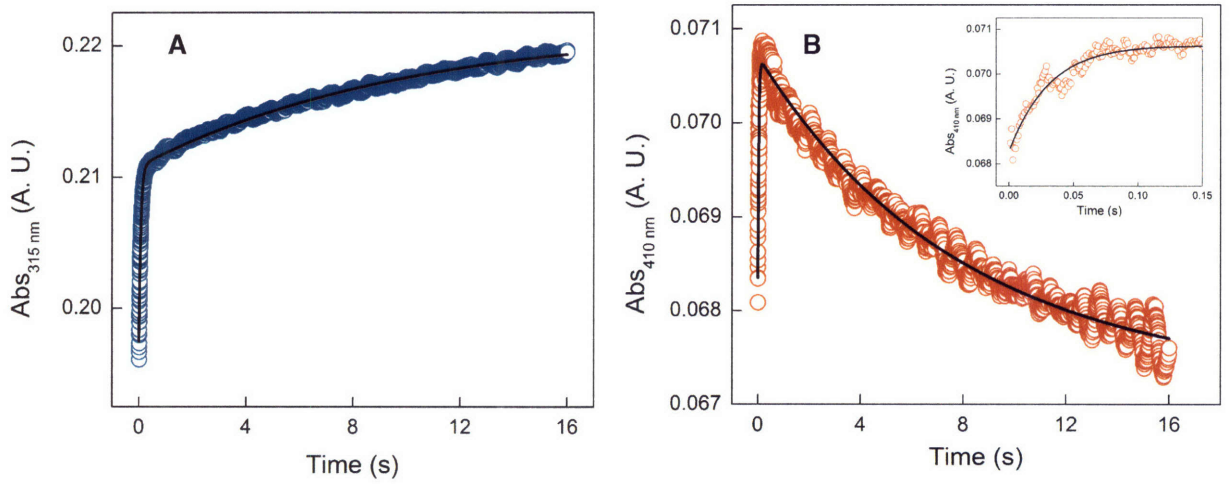

Figure 2–14. Kinetics of $DOPA_{356}$• formation and Y_{122}• disappearance with ADP alone. DOPA–β2 (28 μM) and ADP (2 mM) in one syringe were mixed in a 1:1 ratio with pre–reduced α2 (28 μM) monitoring DOPA• formation (A) and Y_{122}• disappearance (red). A total of 6 traces were averaged at each λ. The inset (bottom) shows a magnified view of the first 150 ms of the time course at 410 nm.

DOPA• formation with effector alone is inefficient and slow, except in the presence dGTP. With ATP alone and TTP alone a single, slow kinetic phase and reduced reaction extents are observed (Table 2–3). With dGTP, however, 38 % of total initial Y_{122}• forms a DOPA• in

Table 2–3. Kinetics of $DOPA_{356}$•–β2/α2 formation with various substrate/effector combinations using SF UV–vis spectroscopy.

Substrate/ Effector	RNR Subunits	1st Phase[a] k_{obs} (s^{-1}), Amp (%)[b]	2nd Phase[a] k_{obs} (s^{-1}), Amp (%)[b]	3rd Phase[a] k_{obs} (s^{-1}), Amp (%)[b]
GDP/TTP	α2/ DOPA–β2	32 ± 5, 31 ± 2	1.7 ± 0.1, 23 ± 1	–[c]
GDP	α2/ DOPA–β2	13 ± 3, 26 ± 2	0.8 ± 0.1, 13 ± 1	–
TTP	α2/ DOPA–β2	0.4 ± 0.01, 14 ± 1	–	–
CDP/ATP	α2/ DOPA–β2	38 ± 1, 21 ± 1	6.8 ± 0.1, 17 ± 1	0.7 ± 0.1, 9 ± 2
CDP/TTP	α2/ DOPA–β2	43 ± 3, 22 ± 2	4.2 ± 0.6, 14 ± 1	0.7 ± 0.1, 10 ± 0.4
CDP	α2/ DOPA–β2	28 ± 0.3, 9 ± 2	6.8 ± 0.6, 21 ± 0.3	0.5 ± 0.1, 11 ± 2
ATP	α2/ DOPA–β2	0.06 ± 0.01, 29 ± 3	–	–
UDP/ATP	α2/ DOPA–β2	16 ± 0.3, 20 ± 2	5.0 ± 0.5, 16 ± 3	0.6 ± 0.1, 9 ± 1
UDP	α2/ DOPA–β2	16.4 ± 0.5, 18 ± 2	4.3 ± 0.3, 22 ± 3	0.5 ± 0.1, 9 ± 1
ADP/dGTP	α2/ DOPA–β2	46 ± 14, 26 ± 8	3.8 ± 1.5, 15 ± 1	0.8 ± 0.3, 10 ± 2
ADP	α2/ DOPA–β2	0.12 ± 0.02, 18 ± 1	–	–
dGTP	α2/ DOPA–β2	1.1 ± 0.3, 10 ± 1	0.24 ± 0.02, 28 ± 1	–
–	α2/ DOPA–β2	–	–	–
CDP/ATP	α2/met DOPA–β2	–	–	–

[a] The rate constants reported are the average of those measured at 410 nm for Y_{122}• loss and 305 or 315 nm for $DOPA_{356}$• formation. In case of DOPA• formation at 305 nm, an ε of 8500 $M^{-1}cm^{-1}$ was used (see Methods). [b] Amp, amplitude; the amount of Y_{122}• trapped as a DOPA• in each kinetic phase is indicated as a % of total initial Y_{122}•.[c] No changes observed.

biphasic fashion with k_{obs} of 1.1 and 0.24 s^{-1}. As in the ADP alone case, the kinetics at 315 nm and 410 nm are decoupled in the first 150 ms of the time course (data not shown). A rise in absorbance occurs at 315 nm and at 410 nm with k_{obs} of 17 s^{-1} and 22 s^{-1}, respectively. After this phase, the changes at 315 nm are linked to those at 410 nm. The kinetics of DOPA•–β2/α2 with ADP alone and dGTP alone require further studies.

Together, the kinetic experiments show that formation of DOPA• with GDP/TTP, CDP/TTP, CDP/ATP, UDP/ATP and ADP/dGTP is kinetically competent and is linked to the disappearance of Y_{122}•. Further, DOPA• formation does not occur in DOPA–β2 alone or in the DOPA–β2/α2 complex without nucleotides and therefore requires substrate and/or effector. The substrate, not the effector, appears to be the major determinant for gating of radical initiation, though ADP is an exception to this trend. Further, studies with effector alone indicate that ATP and TTP are inefficient in DOPA• formation. The cases of ADP alone and dGTP alone require further examination, as an unusual decoupling of spectral changes at 315 nm and 410 nm are observed. These observations may be indicative of formation of another intermediate species that absorbs in this spectral region.

X–Band EPR characterization. To provide further evidence for formation of the $DOPA_{356}$•, an experiment under similar conditions to those described above was carried out. DOPA–β2 and GDP were mixed with α2 and TTP. After 5 s, the sample was hand–frozen in liquid N_2 and subsequently examined by 9.4 GHz EPR spectroscopy. The observed spectrum is shown in Figure 2–15. Consistent with the SF UV–vis experiments, the spectrum is a composite consisting of unreacted Y_{122}• and a newly formed radical. Subtraction of 0.53 equiv of Y_{122}• gives rise to an isotropic spectrum that with a g value of 2.0045 and a line width of 14 G. These parameters and the spectrum are highly suggestive of a DOPA•, which has previously been reported (see below).[10] Importantly, in the absence of substrate/effector, no DOPA• was observed confirming the results from SF UV–vis experiments (Figure 2–15, inset).

Power saturation studies are in agreement with the assignment of the new species as a DOPA•. The power dependence of the spectral amplitude of the new radical is shown in Figure

2–16 along with that of the Y_{122}•. This analysis reveals a marked difference in the power saturation profile of Y_{122}• adjacent to the diiron center, and that of the putative $DOPA_{356}$•. The data was fit to Eq. 2–8, where K is a proportionality constant, b is the homogeneity parameter and $P_{1/2}$ is the microwave power at half saturation of the integrated EPR signal.[34]

$$\text{Signal Amplitude} = \frac{K \times (\sqrt{P})}{[1+(P/P_{1/2})]^{0.5\times b}} \qquad (2\text{–}8)$$

This analysis yields a $P_{1/2}$ of 28 ± 4 mW for the Y_{122}•, in decent agreement with previous measurements of 47 ± 12.[35,36] For the new signal, a $P_{1/2}$ of 0.8 ± 0.15 mW was obtained indicating that this species is distant from the diferric cluster.

The EPR spectrum of a free DOPA amino acid radical in water at a variety of pH values has been reported by several groups as a featureless, nearly isotropic spectrum.[10,37,38,39] To compare the spectrum of our new intermediate with that of an unblocked DOPA• in solution, an

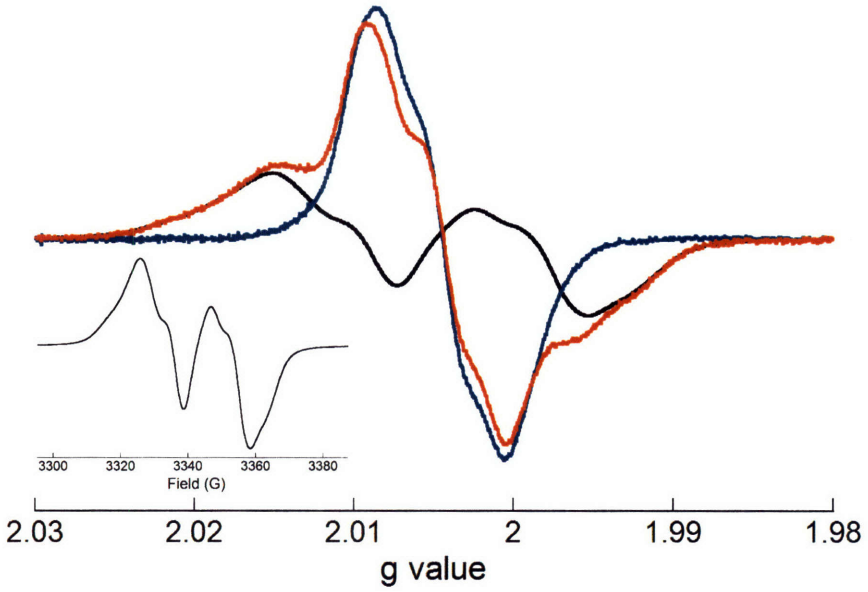

Figure 2–15. EPR spectrum of $DOPA_{356}$•–β2/α2 in the presence of GDP/TTP. DOPA–β2 and GDP were mixed with pre–reduced α2 and TTP. After 5 s, the reaction was quenched by hand–freezing in liquid N_2. The observed spectrum (red) consists of 53 % Y_{122}• (black) and 47 % $DOPA_{356}$• (blue). Inset: DOPA–β2 was reacted with pre–reduced α2 in the absence of substrate and effector. The reaction was quenched by freezing in liquid N_2 after 5 s.

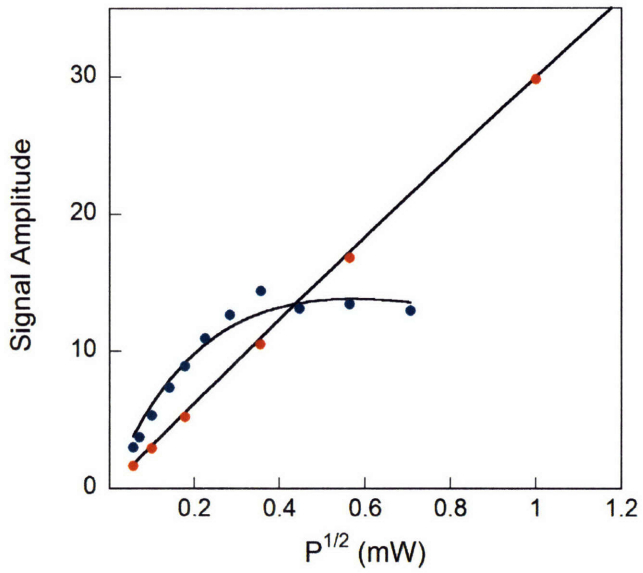

Figure 2–16. Microwave power dependence of Y_{122}• and $DOPA_{356}$•. The EPR spectrum of the Y_{122}• and $DOPA_{356}$• were recorded as a function of microwave power and the integrated intensity of each signal plotted against the square root of power. Black lines represent fits to the data using Eq. 2–8 and yield $P_{1/2}$ of 28 ± 4 mW and 0.8 ± 0.15 mW for Y_{122}• (red) and $DOPA_{356}$• (blue), respectively.

anaerobic solution of DOPA amino acid was irradiated with a 1000 W xenon lamp at 77 K. The EPR spectrum recorded immediately after irradiation is shown in Figure 2–17 and consists of a g_{av} of 2.0045 and is similar to previous reports.[40] The catechol radical was generated in similar fashion (Figure 2–17B). Its EPR spectrum consists of a g_{av} of 2.0048 and is also consistent with previous findings. Comparison of the data in Figures 2–16 and 2–17 shows that each radical consists of a similar g_{ave} value and is an isotropic singlet supporting the assignment of the new feature as a $DOPA_{356}$•. Nevertheless, the protein–bound $DOPA_{356}$• has features that are distinct from the unblocked DOPA• in solution.

For direct comparison with SF UV–vis experiments, we examined the generality of DOPA• formation with various substrate/effector combinations by EPR spectroscopy. The EPR spectrum of $DOPA_{356}$•–β2/α2 in the presence of CDP/ATP is shown in Figure 2–18A. Comparison of this spectrum with that in the presence of GDP/TTP reveals small, but distinct changes in the line shape and line width. This may be more clearly discerned when the spectra

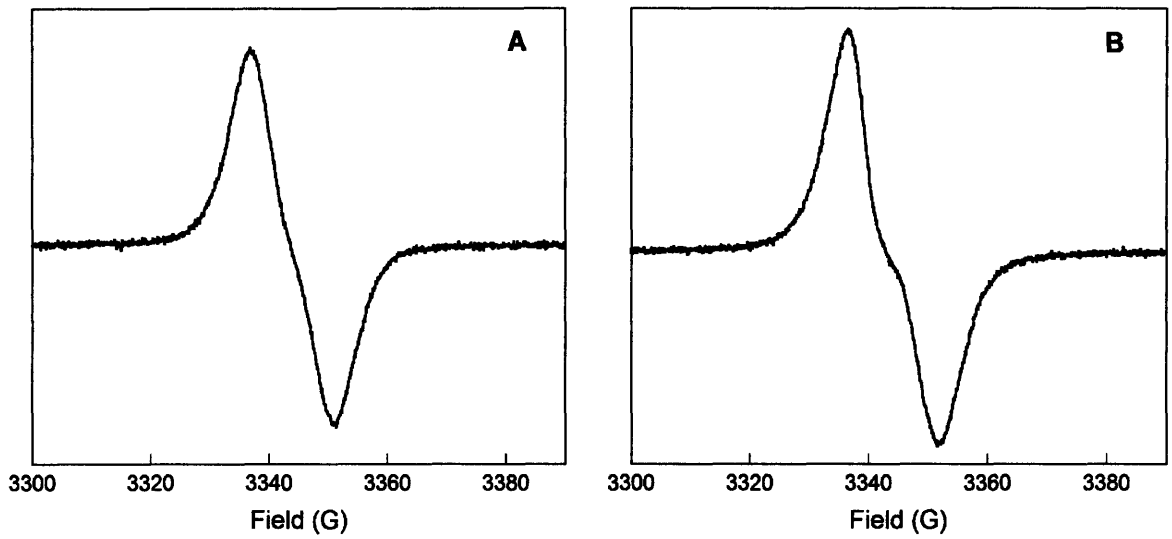

Figure 2–17. X–band EPR spectra of DOPA• (A) and catechol• (B) generated by anaerobic photolysis at 77 K. The g values and line widths were 2.0045 and 14 G for DOPA• and 2.0048 with line widths of ~15 G for the catechol•.

are overlaid (Figure 2–18B). Additional experiments have been carried out with UDP/ATP, ADP/dGTP and CDP/dATP. These results are shown in Figure 2–19. Subtle differences in the DOPA• line shapes and line widths may be discerned as a function of substrate/effector pairs. The parameters of each of these spectra are summarized in Table 2–4. Interestingly with a high dATP concentration (1 mM), which has been shown to completely inhibit dNDP formation, no DOPA• was detected.

EPR experiments were also carried out in the presence of substrates only. The spectral parameters from these experiments are summarized in Table 2–4. Interestingly, EPR spectra with substrate alone resemble those recorded with substrate and effector (data not shown). Therefore, the environment generated around $DOPA_{356}$• appears to be predominantly controlled by substrate binding. In addition, CDP, UDP and GDP alone suffice to generate similar amounts of DOPA• as those observed with substrate and effector. In contrast, with ADP alone, 2.5–fold less DOPA• is generated. These results are consistent with the SF UV–vis experiments presented in Table 2–3. Note that the extents of DOPA• formation are more accurately measured by SF UV–vis than by EPR methods, as freezing artifacts may occur in the latter case. The

interference from these artifacts may be dependent on the substrate and/or effector present in the α2 subunit.

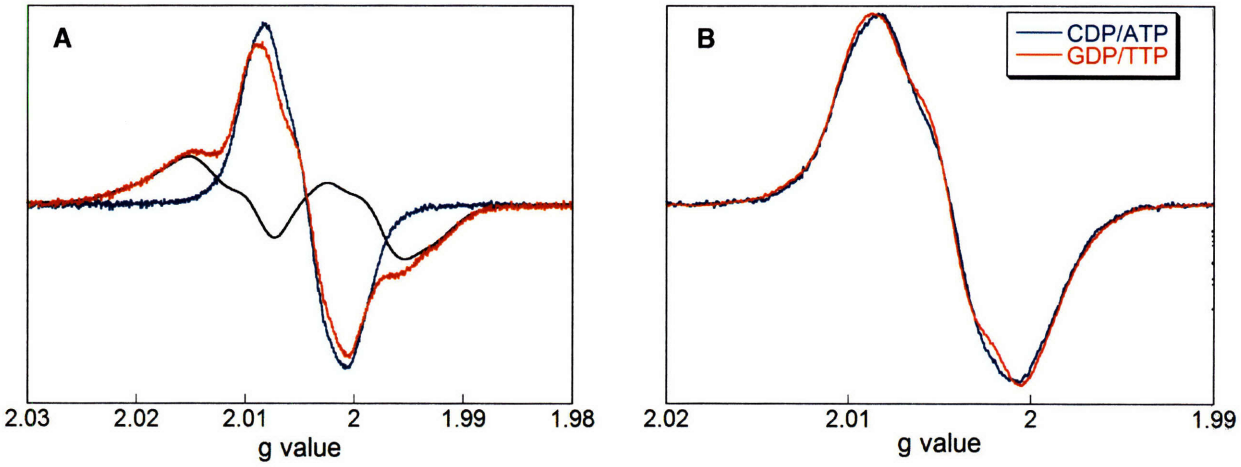

Figure 2–18. EPR spectrum of $DOPA_{356}$•–β2/α2 in the presence of CDP/ATP. (A) DOPA–β2 and CDP were mixed with pre–reduced α2 and ATP. After 5 s, the reaction was quenched by hand–freezing in liquid N_2. The observed spectrum (red) consists of 52 % Y_{122}• (black) and 48 % $DOPA_{356}$• (blue). (B) Comparison of the spectrum of $DOPA_{356}$•–β2/α2 with GDP/TTP (from Fig. 2–15) to that with the CDP/ATP pair.

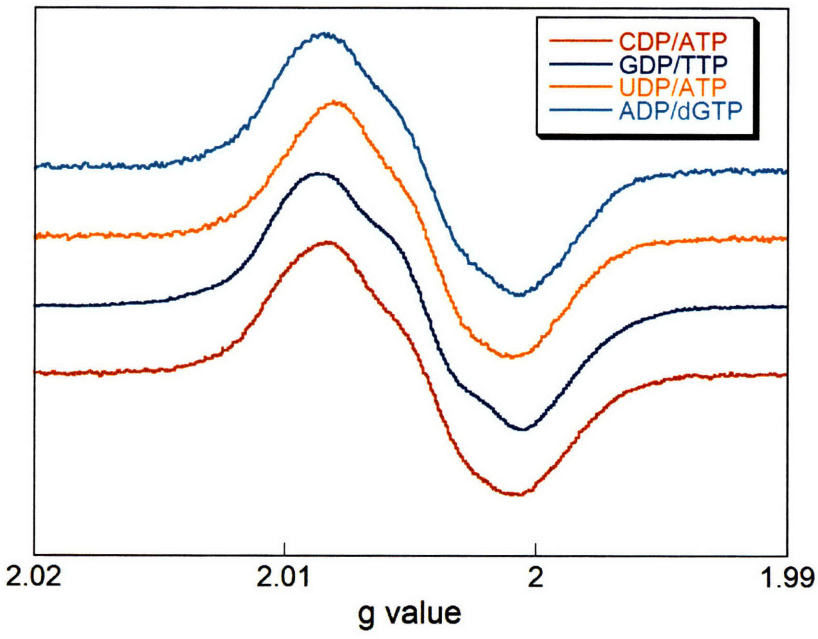

Figure 2–19. Comparison of $DOPA_{356}$•–β2/α2 as a function of substrate/effector pairs.

Additional information regarding the structure of the new radical may be obtained by high–field EPR spectroscopy. This method has previously been used to delineate the structure and reactivity of Y•s and semiquinones in various systems.[41] For example, high field EPR has been employed to identify hydrogen bonded Y•s in the small subunit of mouse and HSV1 RNRs as well as the Y_Z• and Y_D• of photosystem II.[41] To gain additional insight into the properties of the new $DOPA_{356}$• and to facilitate simulation of the spectra in Figure 2–19, high field EPR spectra of $DOPA_{356}$• were recorded.

Table 2–4. Comparison of X–band EPR parameters and stoichiometry of $DOPA_{356}$• formation with substrate alone vs. substrate and effector.

Substrate/ Effector	g value	Spectral width (G)	% Y_{122}• trapped as DOPA• by EPR	% Y_{122}• trapped as DOPA• by SF
GDP/TTP	2.0045	14	47	54
GDP	2.0045	14	48	39
CDP/ATP	2.0044	13	49	47
CDP	2.0044	13	48	41
UDP/ATP	2.0044	12	48	45
UDP	2.0044	12	47	49
ADP/dGTP	2.0045	13	40	51
ADP	2.0045	13	16	18

180 GHz EPR spectroscopy and simulation of $DOPA_{356}$•. High–field EPR samples require spin concentrations of ~70–100 μM. Initially our efforts focused on increasing the radical content of DOPA–β2 using the method of Atkin et al.[33] Apo DOPA–β2 was successfully generated using the 8–hydroxyquinoline–5–sulfonate chelation procedure, as judged by SDS PAGE and UV–vis analysis (data not shown). However, in vitro reconstitution of apo DOPA–β2 with Fe^{II} and sodium ascorbate led to destruction of the DOPA probe indicating that $DOPA_{356}$ may participate in diferric Y_{122}• assembly. The only other method to increase the [DOPA•] for high field EPR experiments is to use high concentrations of the α2/DOPA–β2

complex. Previous studies have revealed that α2 has low solubility which decreases in the presence of nucleotides. Therefore, our approach was to concentrate α2/DOPA–β2 to levels necessary for high field EPR measurements (~250 μM) and then initiate DOPA• formation by addition of nucleotides.

Accordingly, samples of DOPA• were prepared by first concentrating DOPA–β2 (0.3 Y_{122}•/dimer) and α2 in the absence of nucleotides to ~230–280 μM. The concentrated DOPA–β2/α2 complex was then mixed with nucleotides, frozen in liquid N_2 after 1–1.5 min and its 180 GHz EPR spectrum recorded (Figure 2–20). The observed spectrum at 10 K (blue trace) is a composite of the Y_{122}• and DOPA• signals. Due to differences in relaxation properties between the DOPA• and the Y_{122}• (Figure 2–16), which is adjacent to the diiron center, only the DOPA• is observed at 70 K (red trace). This analysis reveals g anisotropy in the DOPA• signal, not apparent at X–band frequencies. Subtraction of 0.43 equiv of $DOPA_{356}$• from the observed spectrum at 10 K yields the previously reported high–field spectrum of Y_{122}• (black trace). Simulation of the 180 GHz spectrum of DOPA•, shown in Figure 2–21, yields a g matrix of [2.00560, 2.00560, 2.00227].

The X–band EPR spectrum of chemically generated DOPA• has previously been studied by Sealy and colleagues.[37] They showed that a ring proton and a β–methylene proton exhibited hyperfine interactions of 3.58 G and 5.23 G, respectively. Using the g values obtained by high field EPR and the hyperfine couplings, determined by Sealy and coworkers as benchmarks, we attempted to simulate the X–band $DOPA_{356}$• spectra with different substrate/effector pairs. The spectra in Figure 2–19 were simulated by varying the hyperfine constants of *only* two I=1/2 nuclei.

The simulation of $DOPA_{356}$• in the presence of the four different substrate/effector pairs are presented in Figure 2–22; the hyperfine coupling constants and principal g values are summarized in Table 2–5. The 180 GHz EPR spectrum of $DOPA_{356}$• shows that it contains prolate axial symmetry about the unpaired electron. The g values obtained from the simulation of the high–field spectrum (Figure 2–21) were close to those used in the simulation of X–band

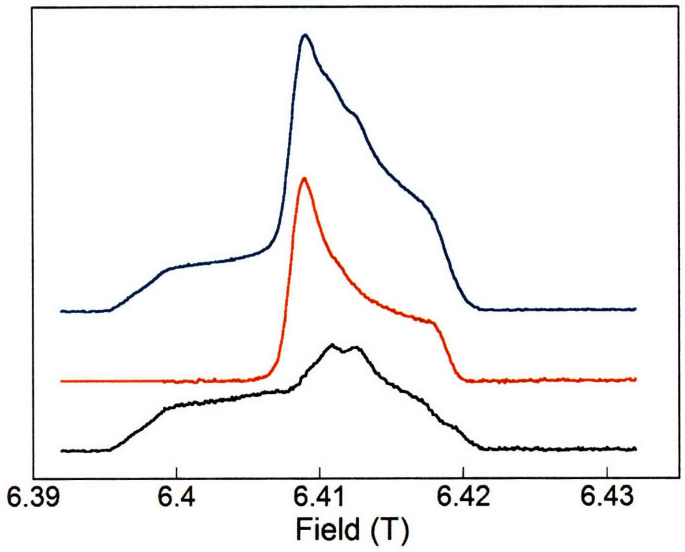

Figure 2–20. 180 GHz EPR spectrum of $DOPA_{356}$•. The reaction contained 240 μM DOPA–β2/α2 complex, 2.5 mM GDP and 0.25 mM TTP in assay buffer with 6 % glycerol. The blue spectrum was recorded at 10 K and is a composite of Y_{122}• and DOPA• profiles. The red trace is the DOPA• spectrum observed at 70 K. Subtraction of 0.43 equiv of DOPA• from the blue trace obtained at 10 K, yields the Y_{122}• signal (black trace).

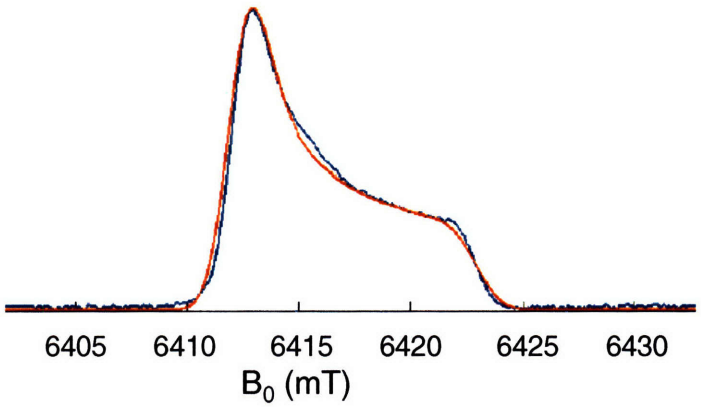

Figure 2–21. Simulation of 180 GHz EPR spectrum of $DOPA_{356}$•. The simulated spectrum (red trace) with a g values of [2.00560, 2.00560, 2.00227] is overlaid on top of the observed DOPA• at 70 K (blue trace).

spectra for purine substrates. For pyrimidine substrates, however, only oblate axial symmetry resulted in good simulations of the X–band EPR spectra. Further, the g values were significantly different from those measured with GDP/TTP at 180 GHz (Table 2–5). Therefore, in the absence of a 180 GHz spectrum and its correlating g values for each substrate/effector pair, the

X–band simulations indicate, at a qualitative and quantitative level, that the environment and/or conformation of the $DOPA_{356}$• is dependent on the nucleotides bound in the active site of α2. This constitutes a long–distance communication between the active site at α2 and the α2/ DOPA–β2 interface.

X–Band PELDOR measurements. Recent results with the mechanism–based inhibitor 2'–azido–2'–deoxyuridine–5'–diphosphate (N_3UDP), which upon reaction with α2/β2 gives rise to a stable N–centered radical (N•), have implicated asymmetry in the active RNR complex.[42]

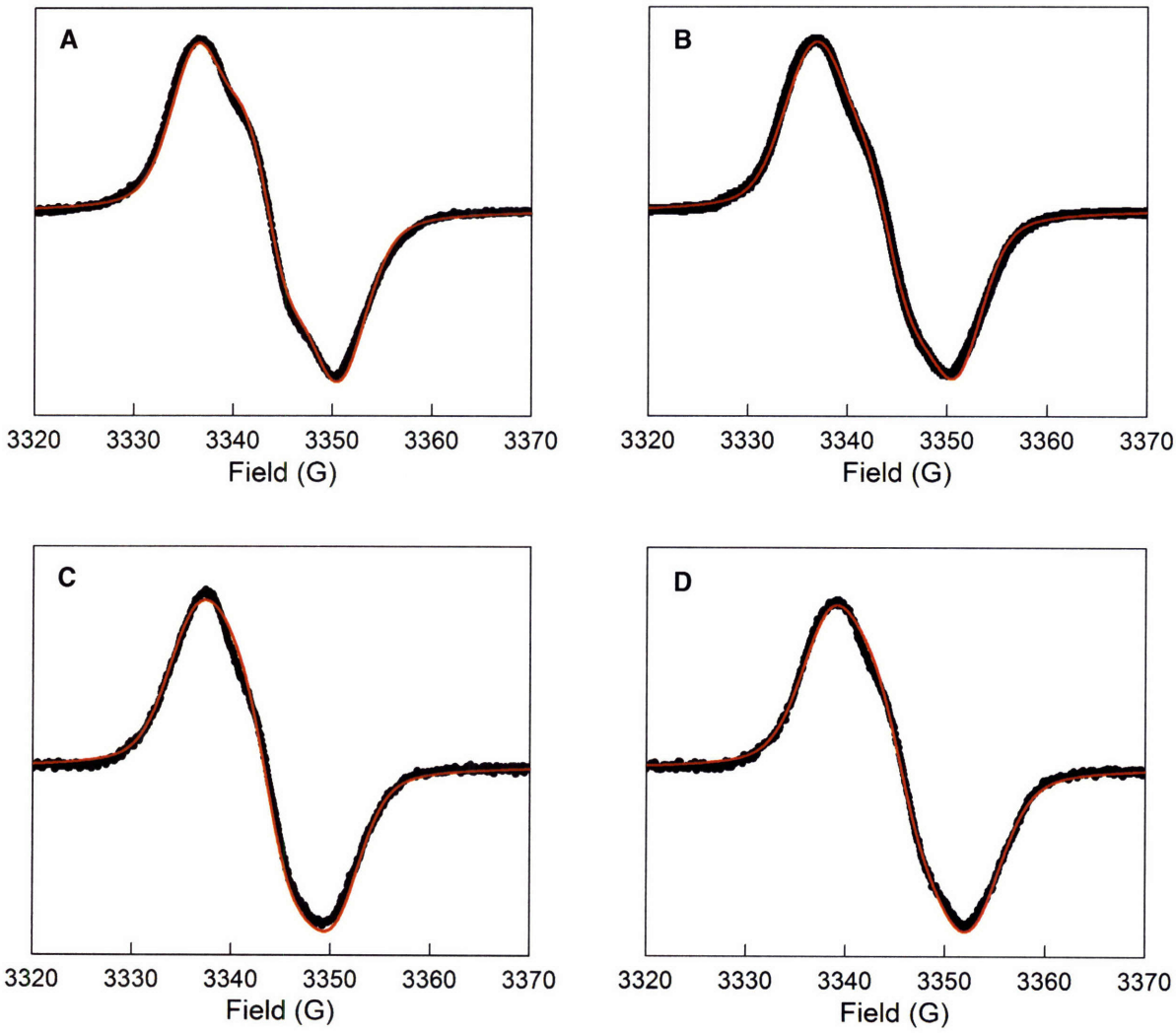

Figure 2–22. Simulation of X–band $DOPA_{356}$• spectra. The experimental spectra (black) are from Figure 2–19 for GDP/TTP (A), CDP/ATP (B), UDP/ATP (C) and ADP/dGTP (D). The simulation is overlaid on top of each spectrum (red trace). The parameters used for these simulations are summarized in Table 2–5.

The results with DOPA–β2 are also consistent with an asymmetric interaction between α2 and DOPA–β2. Explanation of the observation of asymmetry in $DOPA_{356}$• formation requires an understanding of the distribution of Y_{122}• in DOPA–β2, and in β2 in general, which is an unresolved issue for all class I RNRs. If a significant proportion of the DOPA–β2 population contains 2 Y_{122}•/dimer, then after trapping of $DOPA_{356}$•, the weak dipolar interaction between Y_{122}• from one protomer with $DOPA_{356}$• from the other protomer may be detected by PELDOR spectroscopy. In addition, the DOPA•–DOPA• interaction may also be detected, if it forms in a large enough population in solution. Moreover, residue 356 lies within the disordered C–terminal tail of β2 and is not visible in any structures of β2 that have been solved to date. Therefore, no structural information is available in this region and PELDOR measurements would provide the first distance and structural constraints regarding residue 356 at the C–terminal tail of β2.

Table 2–5. Parameters used for simulation of $DOPA_{356}$• spectra in Figure 2–22.

Substrate/ Effector	**g matrix [g_x g_y g_z]**	**$^1A_{iso}$ (G)**	**$^2A_{iso}$ (G)**
GDP/TTP	2.0052 2.0052 2.0032	4.1	6.25
CDP/ATP	2.0065 2.0037 2.0037	4.0	6.25
UDP/ATP	2.0065 2.0037 2.0037	4.1	5.50
ADP/dGTP	2.0052 2.0052 2.0032	4.0	6.00

To begin addressing some of these issues, PELDOR experiments were carried out with DOPA–β2/α2 and different substrate/effector pairs. DOPA–β2 and α2 were first concentrated to ~280 μM. Then, DOPA• formation was initiated by addition of nucleotides. The sample was supplemented with glycerol, frozen after 1 min and PELDOR measurements performed at 6 K and 70 K for detection of dipolar coupling between Y•–DOPA• and DOPA•–DOPA•,

respectively. PELDOR data acquisition and all data analysis including extraction of distance information were performed by Marina Bennati.[43] The results are shown in Figure 2–23. In PELDOR, two microwave frequencies must be applied to the sample. In the current case, one of the MW pulses is at a frequency resonant with the Y_{122}•, while the other is resonant with the DOPA•. The position of these 'pump' and 'detect' frequencies is shown in Figure 2–23A on top of the X–band absorption spectrum of the DOPA• with the GDP/TTP pair (black arrows). When the DOPA•–DOPA• magnetic dipolar interaction was examined, frequencies indicated by the blue arrows in Figure 2–23A were used. Note that the latter is carried out at 70 K, where the Y_{122}• signal is not observed owing to its faster relaxation time resulting from its vicinity to the diiron center.

At 6 K, excitation of Y_{122}• by the MW frequency causes a change in the dipolar field of the DOPA• resulting in modulation of its spin–echo signal. This dipolar oscillation contains the desired distance information and is shown for the GDP/TTP and CDP/ATP pairs in Figure 2–23B. This experiment has been carried out with all 4 substrate/effector pairs (data for UDP/ATP and ADP/dGTP not shown). Analysis of the traces in Figure 2–23B and those for the UDP/ATP and ADP/dGTP pairs shows that the distance between Y_{122}• and $DOPA_{356}$• is 30.6 ± 0.5 Å for all four substrate/effector pairs. Importantly, when X–band PELDOR was performed at 70 K, no oscillation was observed indicating that DOPA•–DOPA• pairs, if present, are below the lower limit of detection by this method. This result shows that each complex generates only a single DOPA•, eventhough a sufficient population of DOPA–β2s harbor 2 Y_{122}• per dimer. Therefore, only one radical initiation event appears to occur in the complex. These results are consistent with the SF UV–vis and EPR experiments described above, which show that only ~50 % of the original Y_{122}• generates a $DOPA_{356}$•.

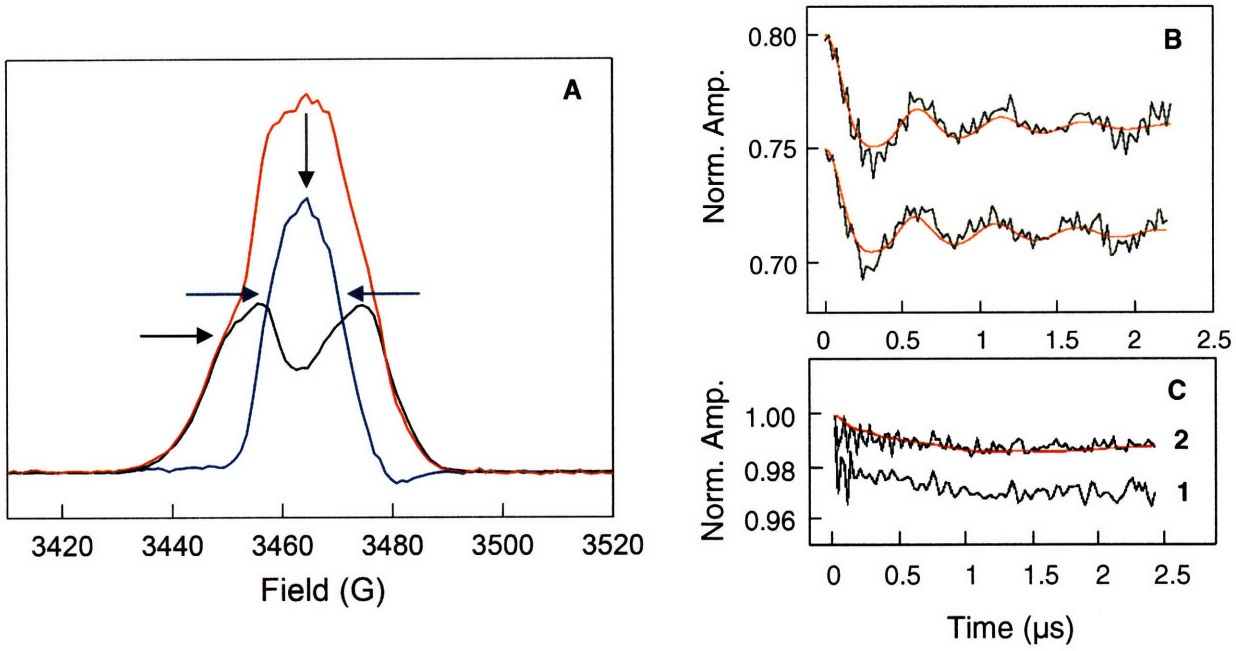

Figure 2–23. X–band PELDOR spectroscopy between Y_{122}•–$DOPA_{356}$• and $DOPA_{356}$•–$DOPA_{356}$•. (A) EPR absorption spectrum of DOPA•–β2/α2 with GDP/TTP. The observed spectrum (red trace) is a composite of 0.43 equiv of $DOPA_{356}$• (blue trace) and 0.57 equiv of unreacted Y_{122}• (black trace). Pump and detect microwave frequencies (υ) used for PELDOR spectra are indicated by arrows. Note that the detection υ is at a higher field value than the perturbation or 'pump' υ. Black arrows show the positions of the frequencies used for Y_{122}•–$DOPA_{356}$• PELDOR. Blue arrows show frequencies used for $DOPA_{356}$•–$DOPA_{356}$•. (B) Dipolar osciallation observed for Y_{122}•–$DOPA_{356}$• PELDOR with GDP/TTP (top trace) and CDP/ATP (bottom trace). This analysis has been performed with all four substrate/effector pairs. In all cases the distance extracted from fitting the data (red line) is 30.6 ± 0.5 Å. (C) No dipolar oscillation is observed in $DOPA_{356}$•–$DOPA_{356}$• PELDOR. Spectrum '1' is the average of 480 scans, spectrum '2' is the average of 1200 scans. The red line is a simple exponential decay rather than an oscillatory function.

DISCUSSION

DOPA as a probe for the radical initiation pathway. A major unresolved issue in the class I RNRs involves the pathway and mechanism of radical propagation, the event that transfers the oxidizing equivalent from Y_{122}• in β2 to the active site in α2. The working hypothesis in the field was put forth by Uhlin and Eklund based on in silico docking of the individual crystal structures of α2 and β2 taking into account their shape and charge complementarities.[44] This model imposed a distance of >35 Å between the Y_{122}• and C_{439} in α2, which carries major implications for the mechanism of radical transfer. However, the model does not exclude a major conformational change that would place Y_{122}• near the active site in α2.

Initially, a large conformational change was dismissed based on the rigid, predominantly α–helical structure of β2.[45] More recently, results from PELDOR spectroscopy and a mechanism–based inhibitor, N_3UDP, have provided experimental evidence which eliminates this mechanistic option. Using PELDOR, a distance of 48 Å was measured between the N–centered radical (N•) and the remaining Y_{122}• in the second protomer of β2, consistent with the docking model, which predicts a distance of 47–50 Å (Figure 2–24).[42] Accordingly, a pathway or pathways must exist that transport the radical across the subunit interface.

Uhlin and Eklund, based on their docking model, proposed the pathway shown in Figure 2–2. The most intriguing residues in this pathway are Y_{356} in β2 and Y_{730}/Y_{731} in α2 because they are the only universally conserved residues, that are not involved in Y_{122}• assembly or active site chemistry. It has been proposed that they serve to shuttle the radical across the subunit interface between Y_{122} and C_{439} in both directions. Residue Y_{356} plays an especially important role in this putative pathway as it gaps the largest distance (25 Å) and lies on the disordered C–terminal tail of β2 rendering it invisible in any β2 structures solved to date. Its involvement in radical initiation has previously been interrogated by site–directed mutagensis. It was shown that Y_{356}F–β2 is completely inactive and that the mutation did not inversely affect interaction with α2.[26] Importantly, complementation studies demonstrated that it was essential

for RNR function in vivo. Together, these studies show that Y_{356} plays an important in catalysis.[46]

In this Chapter, an alternative approach was used to examine the function of Y_{356} in radical propagation. Intein–mediated semisynthesis of the β2 subunit, recently developed by our lab, was used to site–specfically replace residue 356 with the unnatural amino acid DOPA.[15] Due to its participation in melanogenesis, the chemical properties of DOPA have been examined in detail. These studies show that the DOPA• has a reduction potential 260 mV lower that that of Y•.[6] Thus, the DOPA• is more stable by 25 kJ/mol (6 kcal/mol). Further, the UV–vis and EPR absorption profiles of a DOPA• have been reported.[8,37] The reaction kinetics of catechol, the side chain of DOPA, with bimolecular redox–active compounds has also been examined and compared to that of phenol. Steenken and Neta have demonstrated that a phenol radical oxidizes ascorbate >2000–fold faster than a catechol• thereby providing direct evidence for the weak oxidizing ability of the catechol•.[47] The reaction of phenol and catechol• has also been studied using hydroquinone, which is chemically and thermodynamically very similar to catechol, as an analogue. These studies show that a phenoxyl radical irreversibly oxidizes hydroquinone with diffusion limited kinetics, 2×10^9 $M^{-1}s^{-1}$. By inference, a catechol• cannot oxidize phenol in a bimolecular reaction. Together, thermodynamic and kinetic experiments with catechol and DOPA emphasize their ease of oxidation with moderate oxidants, the stability of their one electron oxidized product, and show that reaction of a phenol radical with an analogue of catechol leads to irreversible oxidation of the latter.

Semisynthesis and characterization of DOPA–β2. Building on these model chemical reactions, we reasoned that site–specific insertion of DOPA at residue 356 would lead to reactions similar to those studied by Steenken and Neta. Accordingly, Y_{122}• would generate a DOPA•, which would be unable to oxidize Y_{730} in the α2 subunit. Thus, radical transfer would be halted at $DOPA_{356}$• allowing for its detection by various methods, if residue 356 is in fact on the radical migration pathway.

Precautions were made to avoid side reactions of the DOPA probe during semisynthesis of DOPA–β2. MALDI–TOF MS of the peptide immediately before ligation showed that DOPA was intact (Figure 2–6). Based on the chemical reactivity of DOPA (Figure 2–3), three main side reactions could have occurred after oxidation of DOPA: first, intramolecular Michael addition with the N–terminal Cys; second, intermolecular Michael addition with the N–terminal Cys residue of another peptide; finally, Michael addition by a hydroxyide anion.[12] The first reaction would yield a modified peptide with a similar mass as unreacted DOPA–22mer. However, this derivative of DOPA–22mer would not be competent in the ligation reaction. The second and third side reactions would have resulted in peptide dimers and hydroxylated DOPA, respectively, which were not detected in the MALDI–TOF spectrum. Thus, based on reactions that DOPA has been shown to undergo, our results establish that DOPA–22mer was intact before its ligation to the remainder of truncated β2.

DOPA–β2 was subsequently purified to homogeneity at neutral pH. Analysis of its diiron Y_{122}• center by Fe quantitation, UV–vis and EPR spectroscopic methods shows that the diferric center is intact and that the Y_{122}• content is low similar to previous semisynthetic β2s (Figure 2–8). Importantly, however, the EPR spectrum of the Y_{122}• of DOPA–β2 and the DOPA–β2/α2 complex is identical to that of recombinant wt β2. This is consistent with previous results, which have failed to reveal changes in the properties of the Y_{122}• upon binding to α2 using EPR[36] and resonance Raman spectroscopies.[48] Therefore, insertion of DOPA and the additional $V_{353}G/C_{354}S$ mutations do not affect the EPR properties of the Y_{122}• center.

Binding assays show that these mutations also do not affect the interaction with α2 (Figure 2–9). A K_d of 0.34 ± 0.05 μM is similar to 0.2 μM previously determined for the wt α2/β2 interaction.[26] Activity assays failed to reveal formation of dNDPs (Table 2–2). The aforementioned controls demonstrate that the absence of activity is not due to changes in the Y_{122}• or the interaction with the α2 subunits. It is therefore a direct result of interference by the DOPA probe with the radical transfer event.

Trapping of $DOPA_{356}$•. Many investigators have sought direct evidence for involvement of the Y_{122}• in catalysis. However, pre–steady state experiments with wt and numerous α2/β2 variants by SF UV–vis, SF EPR or RFQ EPR spectroscopies, have never revealed loss of Y_{122}•.[1,49] Therefore, the best evidence for participation of Y_{122}• in catalysis comes from correlation of activity with [Y_{122}•][50] and from formation of active site nucleotide radicals with mechanism–based inhibitors at the expense of the Y_{122}•.[51] The inability to observe changes in [Y_{122}•] has been a major argument for the kinetic model of *E. coli* RNR, recently proposed by our lab. The analysis of DOPA–β2 above indicated that examination of its pre-steady state reactions would be interesting. Indeed, SF UV–vis experiments, for the first time, show disappearance of Y_{122}• concomitant with appearance of a species absorbing at 305 nm.

Compelling evidence has been presented that the feature absorbing at 305 nm is a $DOPA_{356}$•. First, its formation requires Y_{122}•, as reactions with met DOPA–β2 failed to reveal changes at 305 or 410 nm (Figure 2–11A). Second, point by point reconstruction of its UV–vis spectrum reveals an absorption profile very similar to that previously reported for a DOPA• (Figure 2–12). The 10 nm red shift of its λ_{max} is an affect of the protein environment on the electronic absorption properties of the DOPA• at the α2/DOPA–β2 interface. Third, EPR analysis under similar conditions followed by subtraction of the Y_{122}• yields a spectrum very similar to that previously reported for a DOPA• (Figures 2–15 and 2–18).[10,37,38] And finally, the power saturation profile of the EPR signal of the DOPA• shows that it is distant from the diferric center. A $P_{1/2}$ of 28 mW was determined for the Y_{122}•, which is >30–fold greater than the $P_{1/2}$ of 0.8 mW for the DOPA• (Figure 2–16). Interestingly, nucleotide radicals, which form with RNR mechanism–based inhibitors, have a $P_{1/2}$ of 0.16 mW, 5–fold lower than the $P_{1/2}$ value of the $DOPA_{356}$•.[35] Thus, the DOPA• may still preserve a weak magnetic interaction with the diiron center. Together, the evidence above shows that with DOPA–β2, a DOPA• forms at the expense of the Y_{122}•. This represents direct evidence that residue 356 is redox active during radical propagation.

Several controls were performed to ensure that DOPA• formation is associated with the pathway for hole migration (Figure 2–11). First, control experiments with met DOPA–β2 by SF UV–vis show that DOPA• formation requires the presence of Y_{122}•. Second, no DOPA• is observed with DOPA–β2 alone or with DOPA–β2/α2 in the absence of nucleotides, even though solution measurements reveal it to be 25 kJ/mol more stable than a Y•. This conclusion is also reached with EPR experiments, in which only the Y_{122}• is observed with DOPA–β2 alone or with DOPA–β2/α2 in the absence of nucleotides. And finally, DOPA• formation is kinectially competent (see below). The requirements for substrate/effector and Y_{122}• in DOPA• formation implicate pathway dependence. Nevertheless, insertion of DOPA at another residue, which is not involved in radical propagation, would represent a more direct control for pathway dependence and has yet to be performed.

Asymmetry in DOPA• formation. Kinetic analyses of the SF traces show that DOPA• formation occurs in a kinetically competent fashion. Reactions performed with five substrate/effector pairs (GDP/TTP, CDP/ATP, CDP/ TTP, UDP/ATP, ADP/dGTP) show that trapping of a DOPA• with kinetic competence and multiple kinetic phases is a general feature (Table 2–3). Comparison of these reactions reveals three additional common features.

First, in all cases a slow rate constant is observed, which is characteristic for the rate determining conformational change that has been proposed to precede radical propagation. Note that this rate constant is 3–4 fold lower for intein wt β2, which carries the $V_{353}G/S_{354}C$ mutations, than for wt β2.[15] Thus, DOPA–β2 is a reporter on conformational changes and allows direct observation of this conformational step.

Second, additional fast kinetic phases are observed, which have not been seen before. These are reporting on further conformational equilibria, which eliminate a kinetic barrier and/or affect the thermodynamics of the pathway so as to allow radical migration to commence. At the same time, these fast kinetic phases may be related to a phenomenon previously observed with the class II RNR from *L. leichmanii*. In this case, fast breaking and reforming of the C–Co bond in the cofactor adenosylcobalamin (AdoCbl) was detected (by loss of ^3H from labeled AdoCbl to

solution); however, no cob(II)alamin was observed in SF UV–vis experiments.[52] Therefore, the C–Co bond was rapidly breaking and reforming. In analogy, the fast physical changes may relate to conformations, in which the unpaired electron is delocalized over other residues in the pathway. In the wt complex, this conformation would lead to rapid reformation of Y_{122}•, but in the case of DOPA–β2, it leads to irreversible generation of $DOPA_{356}$• (Figure 2–25). It should be noted that the idea that the unpaired electron of Y_{122}• may delocalize over other residues in the pathway has been proposed and tested before.[53] However, steady state experiments failed to reveal equilibration of the unpaired spin, presumably to due fast reverse radical migration to Y_{122}.

Finally, in all SF experiments with various substrate/effector pairs, only 45–54 % of total initial Y_{122}• was trapped as $DOPA_{356}$• (Table 2–4). Results from EPR experiments are in line with this quantitation showing that 40–49 % of initial Y_{122}• gives rise to a DOPA•. The quantitation from these experiments appears to be indicative of asymmetry in the α2/β2 complex as only half of the available Y_{122}• participates in the reaction. The source of asymmetry is unclear at this point. It could originate from β2 or α2, or alternatively upon α2/β2 complex formation.

PELDOR studies with DOPA–β2/α2 agree with quantitations above as they failed to detect any DOPA•–DOPA• interaction; the only PELDOR interaction observed originated from pairs of Y_{122}•–$DOPA_{356}$• (Figure 2–26). Together, these results indicate that radical propagation and DOPA• formation occurs only once per α2/DOPA–β2 complex. Therefore, regardless of the distribution of available Y_{122}•, which is a major unresolved aspect of class I RNRs, there appears to be an inherent asymmetry that allows radical migration along only one of the two symmetrically related radical transfer pathways.

This complex asymmetry seems at odds with results from steady state and pre-steady state experiments, which suggest that both active sites of the α2 subunit are active.[28] However, both models are reconciled when considering that the radical may cross from one subunit to the next, as previously proposed, or, alternatively, that the second radical initiation event does not require a slow physical step but occurs upon a signal from the first hole migration/active–site

chemistry event. The former is feasible with 1 or 2 Y_{122}•s / β2, whereas the latter would require 2 Y_{122}•s / β2. The issue of asymmetry is examined further in Chapter 3 using heterodimeric DOPA–β2, where one of the monomers lacks the last 22 residues and therefore cannot interact with α2.

Environmental differences induced by NDP/(d)NTPs around DOPA•. There are also differences in the kinetics of DOPA• formation with various substrate/effector pairs. The amplitudes and rate constants are influenced by the nucleotide pair bound in the α2 subunit. The effects of different substrate/effector pairs on DOPA• formation are also seen in the distinct local environments generated around the DOPA• (Figure 2–19 and Table 2–4). Two pieces of information allow us to relate the changes in EPR parameters to variation in the dihedral angle between the C_β–H bond and the π system of the aromatic ring, which is perpendicular to the plane of the ring. First, the reaction of DOPA–β2/α2 with GDP/TTP was analyzed by EPR spectroscopy at 180 GHz yielding the principal g tensors for $DOPA_{356}$• (Figures 2–20 and 2–21). These were used in X–band simulations with GDP/TTP and ADP/dGTP (Figure 2–22). With the CDP/ATP and UDP/ATP pairs, however, the anisotropic g values were varied in the spectral simulations because those determined with GDP/TTP did not give satisfactory fits (Table 2–5). Better simulations may result with CDP/ATP and UDP/ATP if the principal g factors are experimentally determined. Second, Felix and Sealy have demonstrated that the DOPA• contains two major hyperfine couplings >1 G, which they assigned to one of the ring protons (3–H) and one of the C_β protons.[37] This demonstrates that the EPR spectra may be simulated using hyperfine coupling to two I=1/2 nuclei. Thus, the difference in the X–band EPR spectra with various NDP/(d)NTPs may be simulated as arising from a slight change in the dihedral angle of one of the two β–protons.

Using the McConnell relation (Eq. 2–9)[54,55], where B is an empirical constant with a value of ~57 G, ρ is the electron spin density at the adjacent ring carbon (C_1), and θ is the dihedral angle between the C_β–H bond and the π molecular orbital at C_1, and assuming a Bρ value of 9.64 G, as previously used by Felix and Sealy,[37] the differences in the β–proton

hyperfine coupling constants result in dihedral angles of 55° (GDP and CDP), 57° (ADP) and 60° (UDP). These θ angles are similar to that determined for DOPA• in solution (60°); however, they are somewhat speculative as the Bρ value used by Felix and Sealy was determined on the 4–methylcatechol radical.

EPR analysis of various class I RNRs has previously demonstrated that the main differences are hydrogen bonding patterns and β–proton dihedral angles. However, hyperfine coupling constants from hydrogen bonds would be within the line width of the spectra in Figure 2–19 and require ENDOR spectroscopy for its detection. Therefore, our working model is that long range communication between the active site in α2 and the subunit interface affects the local environment of residue 356 leading to minor changes in the dihedral angle, θ. These experiments also showcase the sensitivity of EPR to small environmental perturbations.

$$A_{iso} = B\rho \times \cos^2 \theta \qquad (2\text{–}9)$$

Experiments with substrate alone and effector alone have begun to address the function of each nucleotide in the gating of radical propagation. EPR experiments indicate that substrate alone is competent in generating a local environment around $DOPA_{356}$•, which is very similar to that generated by substrate and effector (Table 2–4). Consistently, SF UV–vis experiments show that this holds for the stoichiometry and kinetics of DOPA• formation in all cases except with ADP/dGTP, where the effector is required for efficient trapping of a DOPA•.

ADP alone displays unusual kinetics in that the spectral changes at 315 nm are not linked to those at 410 nm in the first 150 ms of the time course. Additional experiments are required to delineate what these spectral changes are associated with. In contrast, dGTP alone leads to efficient and rapid trapping of a DOPA•. This is in agreement with experiments from the *L. leichmannii* class II RNR, where effector dGTP is sufficient for fast and efficient formation of cob(II)alamin. With TTP and ATP alone, lower amounts of DOPA• form with slow mono–exponential kinetics. Therefore, in general, substrate appears to provide the main binding

determinants that trigger hole propagation. The experiments above show that DOPA–β2 offers an environmentally and conformationally senstitive probe, which indicates whether the complex is in an active or an inactive state. It may be used to reinvestigate the issue of allosteric regulation, which, in case of the *E. coli* RNR, has not been revisited since the initial model was proposed by Reichard and coworkers almost 40 years ago.

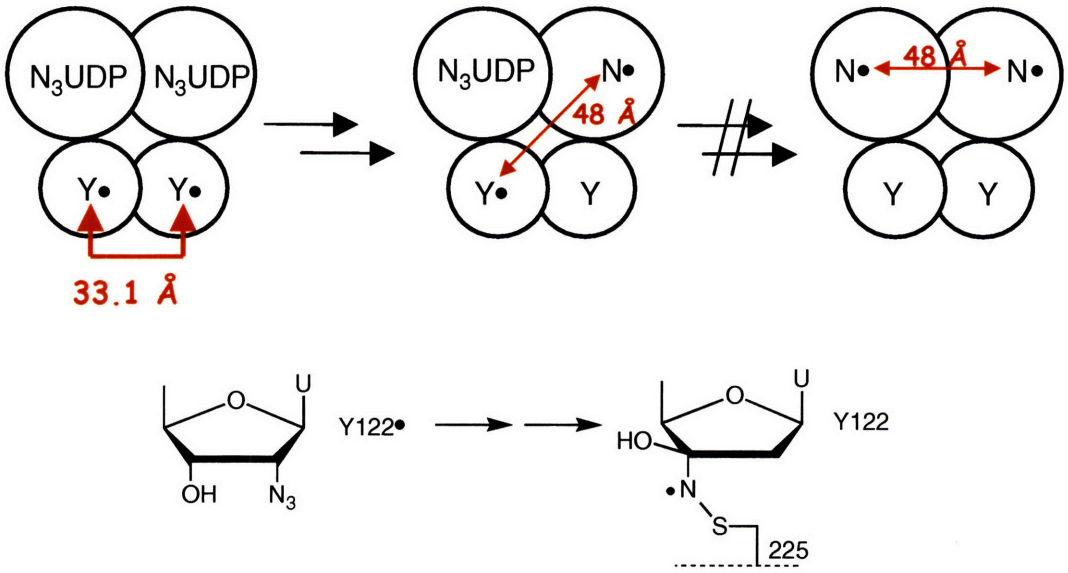

Figure 2–24. PELDOR studies with the mechanism–based inhibitor N_3UDP. (Top) PELDOR has been used to measure the distance between the two Y_{122}•s and between an N•, generated with N_3UDP and the remaining Y•. These experiments yield distances of 33 Å and 48 Å, respectively, and are consistent with the docking model. Temperature and field–dependent experiments show that the N•–N• pair is not formed. (Bottom) The structure of N_3UDP and the N• are shown. The diphosphate moiety has been omitted for clarity.

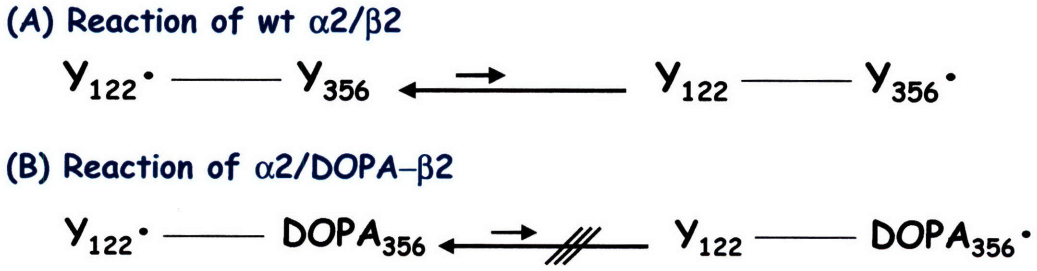

Figure 2–25. Delocalization of the unpaired spin on Y_{122}• over residues of the radical transfer pathway. (A) The equilibration is not observed in wt α2/β2 due to fast reverse radical transfer to Y_{122}•, where the radical is stable. (B) With DOPA–β2, this equilibration is observed because it leads to irreversible formation of $DOPA_{356}$•.

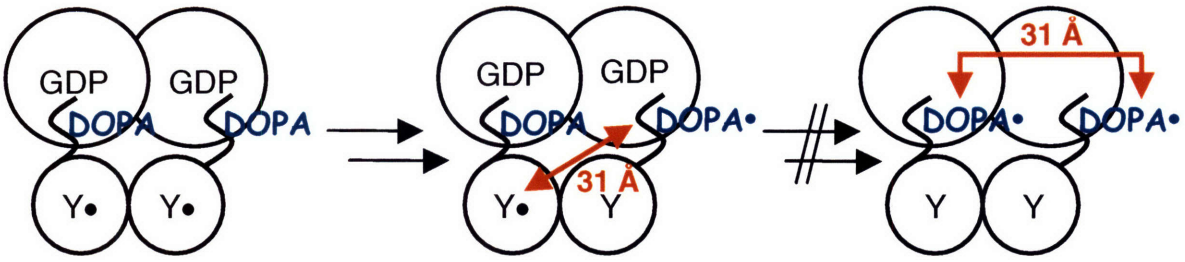

Figure 2–26. PELDOR studies with DOPA–β2/α2. PELDOR experiments with all four NDP/(d)NTP pairs show dipolar coupling between Y_{122}•–$DOPA_{356}$•, which are separated by 30.6 ± 0.5 Å. Importantly, no dipolar coupling is detected between $DOPA_{356}$•–$DOPA_{356}$• indicating that radical migration occurs only across one of two radical transfer pathways under pre–steady state conditions in the DOPA–β2/ α2 complex.

REFERENCES

(1) Stubbe, J.; Nocera, D. G.; Yee, C. S.; Chang, M. C. Y. *Chem. Rev.* **2003**, *103*, 2167.

(2) Yee, C. S. *Ph. D. Thesis.* Massachusetts Institute of Technology, **2004**.

(3) Cowgill, R. W. *Photochem. Photobiol.* **1971**, *13*, 183.

(4) Sokolovsky, M.; Riordan, J. F.; Vallee, B. L. *Biochem. Biophys. Res. Commun.* **1967**, *27*, 20.

(5) DeFelippis, M. R.; Murthy, C. P.; Broitman, F.; Weinraub, D.; Faraggi, M.; Klapper, M. H. *J. Phys. Chem.* **1991**, *95*, 3416.

(6) Jovanovic, S. J.; Steenken, S.; Tosic, M.; Marjanovic, B.; Simic, B. G. *J. Am. Chem. Soc.* **1994**, *116*, 4846.

(7) Martin, B. R. *J. Phys. Chem.* **1971**, *75*, 2657.

(8) Craw, M.; Chedekel, M. R.; Truscott, T. G.; Land, E. J. *Photochem. Photobiol.* **1984**, *39*, 155.

(9) Blois, M. S.; Zahlan, A. B.; Maling, J. E. *Biophys. J.* **1964**, *4*, 471.

(10) Sealy, R. C.; Hyde, J. S.; Felix, C C. *Science* **1982**, *217*, 545.

(11) Thompson, A.; Land, E. J.; Chedekel, M. R.; Subbarao, K. V.; Truscott, T. G. *Biochim. Biophys. Acta* **1985**, *843*, 49.

(12) Bors, W.; Saran, M.; Michel, C.; Lengfelder, E.; Fuchs, C.; Spöttl, R. *Int. J. Radiat. Biol.* **1975**, *28*, 353.

(13) Bielski, B. H. J.; Gebicki, J. M. **1970**, Advances in Radiation Chemistry, edited by M. Burton and Magee, J. L. (New York: Wiley Intersciences), p. 177.

(14) Tommos, C.; Skalicky, J. J; Pilloud, D. L.; Wand, J.; Dutton, P. L. *Biochemistry* **1999**, *38*, 9495.

(15) Yee, C. S.; Seyedsayamdost, M. R.; Chang, M. C. Y.; Nocera, D. G.; Stubbe, J. *Biochemistry* **2003**, *42*, 14541.

(16) Marcus, R. A.; Sutin, N. *Biochim. Biophys. Acta* **1985**, *811*, 265.

(17) Kalyanaraman, B.; Felix, C. C.; Sealy, R. C. *Photochem. Photobiol.* **1982**, 36, 5.

(18) Bollinger, Jr. J. M.; Tong, W. H.; Ravi, N.; Hyunh, B. H.; Edmondson, D. E.; Stubbe, J. *Methods Enzymol.* **1995**, *258*, 278.

(19) Palmer, G. *Methods Enzymol.* **1967**, *10*, 595.

(20) Fish, W. W. *Methods Enzymol.* **1988**, *158*, 357.

(21) Salowe, S. P.; Stubbe, J. *J. Bacteriol.* **1986**, *165*, 363.

(22) Chivers, P. T.; Prehoda, K. E.; Volkman, B. F.; Kim, B.-M.; Markley, J. L.; Raines, R. T. *Biochemistry* **1997**, *36*, 14985.

(23) Lunn, C. A.; Kathju, S.; Wallace, B. J.; Kushner, S. R.; Pigiet, V. *J. Biol. Chem.* **1984**, *259*, 10469.

(24) Russel, M.; Model, P. *J. Bacteriol.* **1985**, *163*, 238.

(25) Steeper, J. R.; Steuart, C. D. *Anal. Biochem.* **1970**, *34*, 123.

(26) Climent, I.; Sjöberg, B.-M. ; Huang, C. Y. *Biochemistry* **1992**, *31*, 4801.

(27) Chang, M. C. Y. *Ph. D. Thesis.* Massachusetts Institute of Technology, **2004**.

(28) Ge, J.; Ator, M. A.; Stubbe, J. *Biochemistry* **2003**, *42*, 10071.

(29) Gräslund, A.; Sahlin, M.; Sjöberg, B.-M. *Environ. Health Perspect.* **1985**, *64*, 139.

(30) Nyholm, S.; Thalander, L.; Gräslund, A. *Biochemistry* **1993**, *32*, 11569.

(31) Hulsebosch, R. J.; van den Brink, J. S.; Nieuwenhuis, S. A. M.; Gast, P.; Raap, J.; Lugtenburg, J.; Hoff, A. J. *J. Am. Chem. Soc.* **1997**, *119*, 8586.

(32) Seyedsayamdost, M. R.; Reece, S. Y.; Nocera, D. G.; Stubbe, J. *J. Am. Chem. Soc.* **2006**, *128*, 1569.

(33) Atkin, C. L.; Thelander, L.; Reichard, P.; Lang, G. *J. Biol. Chem.* **1973**, *248*, 7464.

(34) Chen-Barrett, Y.; Harrison, P. M.; Treffry, A.; Quail, M. A.; Arosio, P.; Santambrogio, P.; Chasteen, N. D. *Biochemistry* **1995**, *24*, 7847.

(35) Gerfen, G. J.; van der Donk, W. A.; Yu, G.; McCarthy, J. R.; Jarvi, E. T.; Matthews, D. P.; Farrar, C.; Griffin, R. G.; Stubbe, J. *J. Am. Chem. Soc.* **1998**, *120*, 3823.

(36) Sahlin, M.; Petersson, L.; Gräslund, A.; Ehrenberg, A.; Sjöberg, B.-M.; Thelander, L. *Biochemistry* **1987**, *26*, 5541.

(37) Felix, C. C.; Sealy, R. C. *J. Am. Chem. Soc.* **1981**, *103*, 2831.

(38) Grady, F. J.; Borg, D. C. *J. Am. Chem. Soc.* **1968**, *90*, 2949.

(39) Chen, C. L.; Chen, W.; Zweier, J. L.; Augusto, O.; Radi, R.; Mason, R. P. *J. Biol. Chem.* **2004**, *279*, 18054.

(40) Neta, P.; Fessenden, R. W. *J. Phys. Chem.* **1974**, *78*, 523.

(41) Pesavento, R. P.; van der Donk, W. A. *Adv. Prot. Chem.* **2001**, *58*, 317.

(42) Bennati, M.; Robblee, J. H.; Mugnaini, V.; Stubbe, J.; Freed, J. H.; Borbat, P. *J. Am. Chem. Soc.* **2005**, *127*, 15014.

(43) Bennati, M.; Weber, A.; Antonic, J.; Perlstein, D. L.; Robblee, J.; Stubbe, J. *J. Am. Chem. Soc.* **2005**, *125*, 14988.

(44) Uhlin, U.; Eklund, H. *Nature* **1994**, *370*, 533.

(45) Nordlund, P.; Sjöberg, B.-M.; Eklund, H. *Nature* **1990**, *345*, 593.

(46) Ekberg, M.; Birgander, P.; Sjöberg, B.-M. *J. Bacteriol.* **2003**, *185*, 1167.

(47) Steenken, S.; Neta, P. *J. Phys. Chem.* **1979**, *83*, 1134.

(48) Backes, G.; Sahlin, M.; Sjöberg, B.-M.; Loehr, T. M.; Sanders-Loehr, J. *Biochemistry* **1989**, *28*, 1923.

(49) Licht, S.; Stubbe, J. In *Comprehensive Natural Products Chemistry*; Barton, S. D.; Nakanishi, K.; Meth-Cohn, O.; Poulter, C. D.; Eds.; Elsevier Science: New York, 1999; p. 163.

(50) Ehrenberg, A.; Reichard, P. *J. Biol. Chem.* **1972**, *247*, 3485.

(51) Stubbe, J.; van der Donk, W. A. *Chem. Rev.* **1998**, *98*, 705.

(52) Chen, D.; Abend, A.; Stubbe, J.; Frey, P. A. *Biochemistry* **2003**, *42*, 4578.

(53) Ekberg, M.; Sahlin, M.; Eriksson, M.; Sjoberg, B.-M. *J. Biol. Chem.* **1996**, *271*, 20655.

(54) McConnell, H. M. *J. Chem. Phys.* **1956**, *24*, 764.

(55) Heller, C.; McConnell, H. M. *J. Chem. Phys.* **1960**, *32*, 1535.

CHAPTER 3:

Reversible Radical Transfer and Asymmetric Complex Formation with the Y_{356}DOPA–β2 Heterodimer of *E. coli* Ribonucleotide Reductase

Adapted in part from: Seyedsayamdost, M. R.; Stubbe, J. *J. Am. Chem. Soc.* **2007**, *129*, 2226.

INTRODUCTION

In the previous Chapter, DOPA–β2 was semisynthesized and used to uncover several aspects regarding the mechanism of radical initiation. Most notably, the results showed that formation of DOPA• occurs only once per α2/DOPA–β2 complex implicating an asymmetric interaction between the two homodimeric subunits. This is inconsistent with to the docking model, which depicts a symmetric interaction in the α2/β2 complex.[1,2] While there is ample structural evidence for symmetry in each subunit,[3,4,5] biochemical evidence for asymmetry has been just as abundant, specifically from examination of mechanism–based inhibitors reacting with RNR.[6,7,8,9,10] However, a model to explain the phenomena indicative of an asymmetric interaction, which have appeared over several decades, has been missing.

The interaction between α2 and β2 has been studied before by Climent and Sjöberg, who used a heterodimeric form of β2, ββ', in which the β–monomer was full length and the β'–monomer was proteolyzed and contained residues 1–345 (Figure 3–1).[11] They proposed a two step binding in the interaction between α2 and β2. In the first step, the flexible C–terminal tail of β2 was solely responsible for the interaction between α2 and β2. Accordingly, binding between ββ' and α2 occurred with a K_d similar to that between a peptide identical to the last 30 residues of β2 and α2.[12] In β2, binding of the second protomer was proposed to be cooperative, 17–fold tighter relative to binding of the first protomer. Climent and Sjöberg proposed that this cooperativity was mediated by the remainder of β2, that is, it was communicated across the β2 dimer interface. Consistent with these ideas, only one 30mer peptide was bound per α2.

In a separate study, Sjöberg et al. used the same ββ' construct and showed that it was inactive.[13] Inconsistent with this observation, ββ' was inhibited by N_3CDP/ATP – this apparent contradiction remained unexplained. Interestingly, however, in the reaction of ββ' with N_3CDP/ATP, ~50 % of total initial Y_{122}• was lost, whereas with β2, all initial Y_{122}• was consumed. The kinetics of Y_{122}• loss was similar with β2 and ββ'. Using global incorporation of deuterated Tyr, β,β–D_2–Tyr, into the full–length protomer of ββ', and protonated Tyr in the

truncated protomer, Sjöberg et al. also showed that the Y_{122}• does not redistribute within the β' and β monomers in the ββ'/α2 complex in the presence of N_3CDP/ATP (Figure 3–2, top), and that the subunit lacking the C–terminal 30 residues was incompetent in triggering radical migration. In addition, when ββ' was isolated after reacting with α2 and N_3CDP/ATP, and was mixed with CDP/ATP in the presence of α2, no dCDP and no loss of Y• were observed. This experiment showed that redistribution of Y_{122}• also does not occur in the presence of CDP/ATP (Figure 3–2, bottom).

The lack of observation of Y_{122}• redistribution carries several caveats: First, migration of the Y_{122}• to the second protomer may require the C–terminal tail, specifically Y_{356};[14] second, the C–terminal tail may be involved in transmitting the signal for radical transfer across the dimer interface.

The foregoing studies demonstrate that ββ' is useful in examining the binding between α2 and β2. It would also be useful in studying the early events of radical migration, if it were active. Our semisynthesis of β2 leads to three protein products: β'2, which consists of two truncated protomers, ββ', in which the β–monomer is full length and the β'–monomer contains residues 1–353, and β2, a full length homodimer (Figure 3–1).[15] Thus, our ββ' contains 8 more residues on the β'–monomer than that previously examined.

In this Chapter, the issue of asymmetry, implicated by the results with DOPA–β2, is reinvestigated using heterodimeric DOPA–ββ'. This construct is a by–product of the ligation reaction during semisynthesis of DOPA–β2. The results show that DOPA–ββ' maintains the essential conformational changes for triggering radical migration and formation of a DOPA• in a kinetically competent fashion. An asymmetric interaction is proposed between β2 and α2 to explain the yields of DOPA• in DOPA–β2 compared to those in DOPA–ββ'. In addition, evidence is obtained for reverse radical transfer from DOPA• to Y_{122} within DOPA–ββ'/α2. This is the first direct observation of reverse hole migration and provides further evidence for the reversitble nature of the radical transfer pathway.

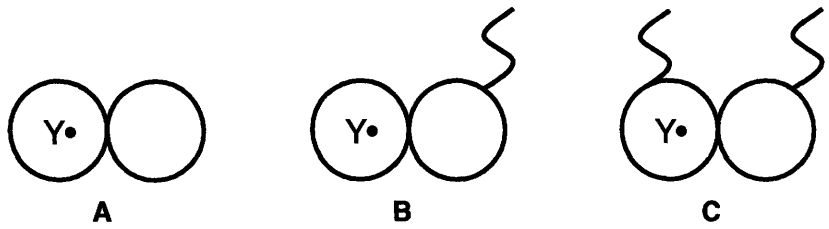

Figure 3–1. Diagrammatic view of the β2 subunits discussed in this chapter. Shown are (A) truncated homodimer, β'2, (B) full length–truncated heterodimer, ββ', and (C) full length homodimer, β2. Note that the truncated protomer used in this chapter contains residues 1–353. The truncated protomer previously used by Sjöberg et al. contains residues 1–345.[13]

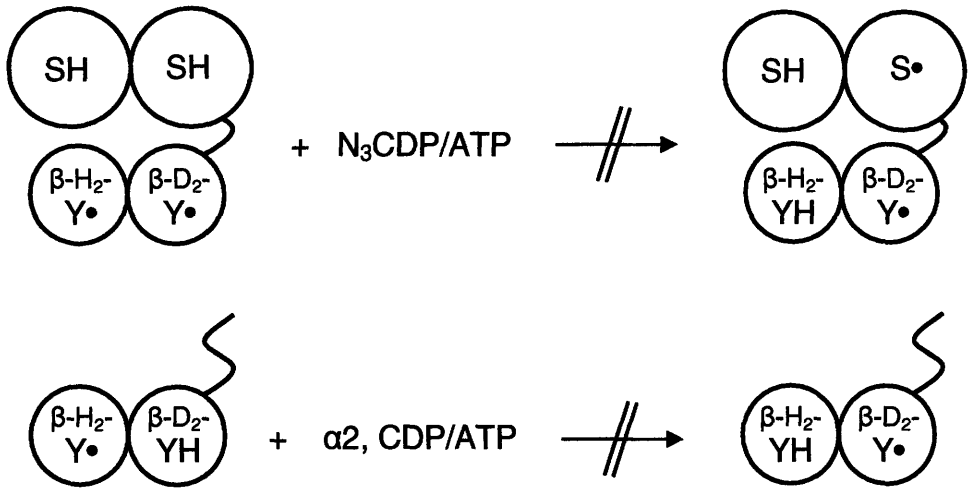

Figure 3–2. Lack of Y_{122}• redistribution observed within ββ'. Selective growth of the full length protomer with deuterated Tyr and the trunctated protomer with protonated Tyr followed by the chelation/reconstitution procedure yields the ββ' used in these studies. The experiments show that the Y_{122}• does not redistribute within ββ' in the presence of α2 and N_3CDP/ATP. Instead, disappearance of only β–D_2–Y• is observed (top). After this reaction, ββ', now containing β–H_2–Y• and β–D_2–YH in the truncated and full length protomers, respectively, was isolated and reacted with α2 and CDP/ATP (bottom). Radical migration and dCDP formation were not observed in this reaction.

METHODS

Semisynthesis of DOPA–ββ'. Solid phase peptide synthesis of Y–22mer and DOPA–22mer, cleavage from the solid phase resin, peptide purification, removal of the t–buthio protecting group, growth and expression of β2–intein–CBD and ligation to DOPA–22mer were carried out as detailed in Chapter 2.

MonoQ purification of the ligation mixture. Preparative–scale purification of the ligation mixture was carried out on a MonoQ HR 16/10 Anion Exchange Column (10 μm, 2 × 10.5 cm, 33 mL – Amersham Bioscience) on a Sprint Biocad FPLC System (Applied Biosystems) as described in detail in Chapter 2. The heterodimers ββ' and DOPA–ββ' typically elute at ~320 mM NaCl. The desired products (ββ' or DOPA–ββ') were collected using a fraction collector or by hand, concentrated to 70–350 μM, flash–frozen in liquid N_2 and stored at –80°C. The concentration of ββ' and DOPA–ββ' were determined using $\varepsilon_{280\,nm} = 131\ mM^{-1}cm^{-1}$. A column recovery of 80 % was typical. Usually, 2–2.5 mg of pure ββ' and DOPA–ββ' were obtained per g of wet cell paste.

Analysis of the diiron Y_{122}• center of DOPA–ββ'. Fe content determination was carried out by the ferrozine assay described in Chapter 2. Radical content is reported per DOPA–ββ'. The [Y_{122}•] was determined using UV–vis and EPR spectroscopic methods as described in detail in Chapter 2 using Eqs. 2–1, 2–2 and 2–3.

Interaction between DOPA–ββ' and α2. Binding affinity of DOPA–ββ' for α2 was analyzed using the assumptions described in Chapter 2. Briefly, the Y_{122}• of DOPA–ββ' was reduced by incubating it (~80 μM) with 30 mM hydroxyurea at room temperature for 30 min, followed by desalting on a Sephadex G–25 column (45 mL, 1.5 x 25 cm) equilibrated in assay buffer (50 mM Hepes, 15 mM $MgSO_4$, 1 mM EDTA, pH 7.6). This procedure generates the met form of DOPA-ββ', which was then used as an inhibitor of nucleotide reduction without further modification. The assay mixture consisted of final concentrations of 0.15 μM α2 (2300 nmol/min mg), 0.3 μM wt β2 (7200 nmol/min mg), 50 μM thioredoxin, 1 μM thioredoxin

reductase, 1 mM CDP, 1.6 mM ATP, 0.2 mM NADPH and varying concentrations of competitive inhibitor, met DOPA–ββ'. Nucleotide reduction activity at each concentration of the inhibitor was determined by monitoring the change in $\Delta A_{340\,nm}$. The K_d was then determined as described in Chapter 2 using Eqs. 2–4, 2–5 and 2–6.

Activity assays of ββ' and DOPA–ββ'. Spectrometric and radioactive RNR assays were carried out as described in Chapter 2. The specific activity of [2–^{14}C]–CDP was 8150 cpm/nmol.

Formation of DOPA•–ββ' monitored by SF UV–vis spectroscopy. Pre–reduction of α2 was carried out as described in Chapter 2. SF kinetics was performed on an Applied Photophysics DX. 17MV instrument using PMT detection at 410 nm (λ_{max} of Y_{122}• with ε = 3700 $M^{-1}cm^{-1}$) and at 315 nm (λ_{max} of DOPA•–ββ' with ε = 12,000 $M^{-1}cm^{-1}$)[16] or 305 nm (ε = 8,500 $M^{-1}cm^{-1}$ – see Eq. 2–7). The temperature was maintained at 25°C with a Lauda RE106 circulating water bath. All experiments were performed in assay buffer (50 mM Hepes, 15 mM $MgSO_4$, 1 mM EDTA, pH 7.6). Pre–reduced α2 and effector in one syringe were mixed with DOPA–ββ' and substrate from another syringe in equal volumes to yield final concentrations of 24–30 μM α2, 1 mM substrate, 24–30 μM DOPA–ββ' and 200 μM effector, respectively. Effector ATP was used at a final concentration of 3 mM, dNTP effectors were used at a final concentration of 200 μM. Experiments were carried out with CDP/ATP, GDP/TTP, UDP/ATP and ADP/dGTP. Data acquisition and curve fitting was performed as in Chapter 2. Reconstruction of the UV–vis spectrum of DOPA•–ββ'/α2 was carried out with CDP/ATP and GDP/TTP. Data acquisition and analysis, including subtraction of the absorbance associated with Y_{122}•, was outlined in Chapter 2.

Formation of DOPA•–ββ' monitored by EPR spectroscopy. The reaction was carried out in an Eppendorf tube and contained in a volume of 250 μL: 25–30 μM pre–reduced α2 and DOPA–ββ', 1 mM CDP and 3 mM ATP in assay buffer. Pre–reduced α2 and effector were mixed with DOPA–β2 and substrate. At a defined time point, the contents of the eppendorf tube were transferred to an EPR tube. The reaction was hand–quenched in liquid N_2 and the EPR spectrum recorded as described in Chapter 2. Experiments were also carried out with GDP/TTP,

UDP/ATP, ADP/dGTP, CDP alone and GDP alone. Substrate was always at a final concentration of 1 mM, whereas ATP, TTP and dGTP were at 3 mM, 200 μM and 200 μM, respectively. Spin quantitation and deconvolution of the observed signals by spectral subtraction were carried out as detailed in Chapter 2.

Kinetic simultaions. Kinetc simulations were carried out using KinSim, available free of charge from the web (http://www.biochem.wustl.edu/cflab/message.html). In all simulations, a rapid equilibrium for binding between α2 and β2 was assumed.

Rapid freeze–quench (RFQ) EPR spectroscopy. RFQ EPR samples were prepared using an Update Instruments 1019 Syringe Ram Unit, a Model 715 Syringe Ram Controller and a quenching bath, which consisted of a large outer stainless steel pot that contained a smaller ~7 L liquid isopentane bath. The temperature of the liquid isopentane bath was controlled with a Fluke 52 Dual Input Thermometer, equipped with an Anritsu Cu Thermocouple probe for the isopentane bath and the funnel. The volume of reaction loops were determined by filling each with water and determining the weight on a microbalance. Stainless steel packers were purchased from McMaster–Carr and were cut to a length of 40 cm and deburred at the MIT machine shop. A spray nozel with a diameter of 0.33 mm was used in all experiments. The dead–time of the set–up was determined to be 16 ± 2 ms with two independent measurements of the Myoglobin/NaN_3 test reaction. A packing factor of 0.60 ± 0.05 was reproducibly obtained as tested with wt β2 samples. Routinely, a ram push velocity of 1.25 or 1.6 cm/s was used and the displacement was adjusted to expel 300 μL sample after the reaction.

Operation of the apparatus was similar to the procedure previously described.[17,18] Briefly, the temperature of the isopentane bath was lowered to −135 to −140°C with liquid N_2 in the outer bath. One syringe contained 70 μM DOPA–ββ' and 3.5 mM ADP in assay buffer and was mixed with 70 μM pre–reduced α2 and 0.5 mM dGTP in assay buffer from a second syringe. When the temperature of the EPR tube–funnel assembly had equilibrated to the bath temperature, the contents of each syringe were mixed rapidly in a mixing chamber and aged for a pre–determined time period by traversing the contents through a reaction loop. The sample was

sprayed into the EPR tube–funnel assembly which was held at a distance of ≤1 cm from the spray nozzle. After the sample was squirted into the funnel, the assembly was immediately returned to the bath and the crystals allowed to settle for 15–30 s. The sample was then packed into the EPR tube using the stainless steel packers described above. After packing, excess isopentane was removed with a Pasteur pipette and the EPR tube stored in liquid N_2 until the EPR spectrum was recorded. Acquisition of EPR spectra was carried as detailed in Chapter 2.

Preparation of high–field EPR and PELDOR samples. Pre–reduced α2 and DOPA–β2 were combined in equimolar ratio and concentrated at 4°C in a minicon concentration device (YM–30 membrane) to a final complex concentration of 250–320 μM ($\varepsilon_{280\ nm\ (\alpha2+DOPA-\beta\beta')}$ = 320 $mM^{-1}cm^{-1}$). The concentrated sample was divided into 100 μL aliquots and placed in 1.5 mL Eppendorf tubes, flash–frozen in liquid N_2 and shipped on dry ice along with substrate/effector and glycerol–containing buffer solutions to Prof. Marina Bennati at the University of Frankfurt (Germany). High–field EPR and PELDOR sample preparations were performed by Prof. Marina Bennati as described in detail in Chapter 2. High–field (180 GHz) EPR and X–band PELDOR spectra were recorded and analyzed by Prof. Marina Bennati.

Sequential–mix SF UV–vis spectroscopy. General procedures for performing SF UV–vis spectroscopy experiments were described in Chapter 2. In sequential mix SF experiments, one syringe contained 55 μM pre–reduced α2 and 150 μM TTP and was mixed in a 1:1 ratio with 55 μM DOPA–ββ' and 2 mM GDP. After an aging time of 5 s, the contents were combined with hydroxyurea in assay buffer from a third syringe to yield final concentrations 19 μM Hetero–DOPA–β2/α2, 0.45 mM GDP, 61 μM TTP and 1.5 or 75 mM hydroxyurea. Absorbance at 315 nm was monitored, where the DOPA• has an ε of 12,000 $M^{-1}\,cm^{-1}$.

Reduction of Y_{122}• by hydroxyurea monitored by UV–vis spectorsocpy. UV–vis spectra were acquired on a Cary 3 Spectrophotometer equipped with a circulating water bath. The reaction was carried out at 25 °C and contained in a final volume of 300 μL: 10 μM wt β2 or Y_{356}F–β2 in assay buffer (50 mM Hepes, 15 mM $MgSO_4$, 1 mM EDTA, pH 7.6) and 10 mM HU. After addition of HU, UV–vis spectra were acquired at defined time points. The [Y_{122}•] was

computed using the dropline procedure described in Chapter 2 and plotted against reaction time. The decay rate constant was obtained by fitting the data to a mono–exponential decay function using OriginPro software.

Increasing the radical content of DOPA–ββ'. The procedure was carried out on 24 g of wet cell paste, which was grown and expressed as described in Chapter 2. Cell lysis, CBD column purification and removal of excess Mesna after elution from the CBD column were also performed as described in Chapter 2. After removal of excess Mesna, the Mesna–activated, truncated β2 was concentrated to 25 mg/mL in a centriprep protein concentration device with a YM–30 membrane. The sample (6.5 mL, 25 mg/mL) was deoxygenated as described in Chapter 2, and transferred into the anaerobic chamber. Solid sodium dithionite ($Na_2S_2O_4$) and methyl viologen (MeV) were also brought into the anaerobic chamber, where a stock solution of each was prepared in water to concentrations of 60 mM and 25 mM, respectively.[19] Mesna–activated, truncated β2 was then supplemented with final concentrations of 7 mM $Na_2S_2O_4$ and 30 μM MeV. The solution was sky–blue as a result the reduced MeV chromophore. The mixture was incubated for 1 h at 4°C in the anaerobic chamber. Then, the Fe^{II} chelator ferrozine was added to a final concentration of 12 mM. Upon ferrozine addition, the sample turned deep purple. The mixture was incubated in the anaerobic chamber for 15 min at room temperature. Then, it was taken out of the anaerobic chamber and the $(ferrozine)_3Fe$ complex removed by Sephadex G–25 chromatography (2.5 × 40 cm, 200 mL) in cleavage buffer (50 mM Hepes, 500 mM NaCl, pH 7.6). The apo Mesna–activated, truncated β2 sample was concentrated to ~13 mg/mL, degassed as outlined in Chapter 2 and transferred into the glove box. Reconstitution was carried out as previously described with 5–fold excess Fe^{II} and 3.5–fold excess O_2 (see Chapter 2). After reconstitution, excess Fe was removed by adding 8 mM sodium ascorbate to the sample, incubation for 10 min at 4°C, followed by desalting on a Sephadex G–25 column (2.5 × 40 cm, 200 mL) in cleavage buffer. The Mesna–activated β2 was then concentrated to ~25 mg/mL using a YM–30 centriprep device, deoxygenated as before and transferred into the glove box, where ligation to DOPA–22mer peptide was carried out. The ligation reaction contained 3.5 mL

of 27 mg/mL holo, Mesna–activated, truncated β2 (1.1 μmol, 1.5 rad/dimer) and 1.6 mM DOPA–22mer peptide (6 μmol) supplemented with 400 μL of ligation buffer (1.5 M Hepes, 0.4 mM EDTA, pH 7.3). The mixture was incubated at 4°C in the anaerobic chamber for 40 h. It was then taken out of the chamber, aliquoted, flash–frozen in liquid N_2 and stored at –80°C. Subsequently MonoQ purification was carried out as described in Chapter 2 to separate the truncated homodimer from the DOPA–ββ' fraction.

RESULTS

Purification and general characterization of DOPA–ββ'. The results from the previous chapter suggest that the α2/β2 interaction is asymmetric, which makes specific predictions that may be tested with DOPA–ββ'. Semisynthesis of the β2 subunit results in formation of a heterodimer as well as the full length and truncated homodimers. We examined the activity of our intein wt heterodimer construct, ββ', in which the β'–monomer lacks the last 22 residues, and measured a specific activity ~25 ± 1 % that of the corresponding intein wt homodimer, β2. Therefore, the additional residues present in our heterodimer construct, but absent from the construct studied by Climent et al, appear to confer nucleotide reduction activity in the presence of α2, substrate and effector. We therefore decided to investigate the steady state and pre–steady state reactions of DOPA–ββ' with α2, substrate and effector.

Due to incomplete ligation in the semisynthesis of DOPA–β2, the yield of DOPA–ββ' is in fact greater than that of DOPA–β2 (Chapter 2, Figure 2–7). The DOPA–ββ' fraction was purified from full length DOPA–β2 and truncated β2 using Mono Q anion exchange chromatography. SDS PAGE analysis of this product, shown in Figure 3–3, demonstrates that it is >95 % pure and that it consists of a 1:1 ratio of truncated and full length β protomers.

Characterization of the diferric Y_{122}• center in DOPA–ββ' is presented in Figure 3–4. The UV–vis absorption profile indicates that the diiron center is intact, consistent with an Fe content determination of 3.4/DOPA–ββ'. However, as with DOPA–β2 and other intein β2 constructs, a low radical content of 0.33–0.37 Y_{122}•/DOPA–ββ' was obtained. The EPR spectrum of this Y_{122}•, shown in Figure 3–4, is identical to that of wt β2 generated by recombinant methods. Therefore, truncation of the β'–monomer and insertion of DOPA at residue 356 in the full length protomer in addition to the $V_{353}G/S_{354}C$ mutations do not perturb the EPR properties of the Y_{122}• cofactor.

Interaction between DOPA–ββ' and α2. Design of experiments with DOPA–ββ' requires knowledge of its interaction with the α2 subunit. The dissociation constant, K_d, for the

interaction between DOPA–ββ' and α2 was determined using the method first reported by Climent et al (Figure 3–5).[11] In this method, the Y_{122}• of DOPA–ββ' is reduced by reaction with hydroxyurea, and the resulting met DOPA–ββ' is used as a competitive inhibitor of nucleotide reduction, which is measured by the spectrophotometric assay using wt α2 and β2, as outlined in Chapter 2 (Figure 2–9). Using this method, a K_d of 11 ± 2 μM was determined for the interaction between DOPA–ββ' and α2, indicating that removal of the C–terminal 22 residues in one protomer of the DOPA–β2 dimer, reduces its affinity for α2 by a factor of ~32 (K_d of DOPA–β2/α2 was 0.34 ± 0.05 μM). This K_d is similar to the K_d of 13 μM measured by Climent et al. for the interaction of their ββ' (where β' contains residues 1–345) with α2.[11]

Formation of DOPA•–ββ' monitored by SF UV–vis spectroscopy. Activity assays of DOPA–ββ' reveal no dCDP formation, similar to results with DOPA–β2, using the spectrometric and radioactive assays. Therefore, the specific activity of DOPA–ββ' was $<1/10^4$ that of wt β2. To examine the ability of DOPA–ββ' to generate a DOPA•, SF UV–vis experiments were carried out in which DOPA–ββ' and CDP in one syringe was rapidly mixed with α2 and ATP from a second syringe. The reaction was monitored at 305 nm (λ_{max} of a DOPA•, ε = 12000 $M^{-1}cm^{-1}$),[16] and at 410 nm (λ_{max} for Y_{122}•, ε = 3700 $M^{-1}cm^{-1}$).[20] As shown in Figure 3–6, the Y_{122}• (red) disappears and the DOPA• (blue) grows in with similar kinetics. The data can be fit to a single exponential with a k_{obs} of 1 ± 0.2 s^{-1}, which is similar to the rate constant for the slow conformational change that gates radical propagation. Further, 24 ± 1 % of the total initial Y_{122}• is trapped as a $DOPA_{356}$•. In contrast, in the absence of CDP and ATP no decay of Y_{122}• and no formation of a $DOPA_{356}$• was observed indicating that in the DOPA–ββ'/α2 complex, CDP/ATP are involved in the conformational event that triggers radical transfer (Figure 3–6B).

A number of differences were found between the results with DOPA–ββ' and those with DOPA–β2. First, DOPA• formation with DOPA–β2 was multi–phasic with k_{obs}s of 38, 6.8 and 0.7 s^{-1}, in contrast to a single exponential at 1 ± 0.2 s^{-1} for DOPA–ββ'.[21] Second, in DOPA–ββ', the yield of DOPA• by SF UV–vis spectroscopy is 24 ± 1 % of total Y_{122}•, whereas with the homodimer, 47 % of total Y_{122}• formed a DOPA•. The difference in kinetics between the two

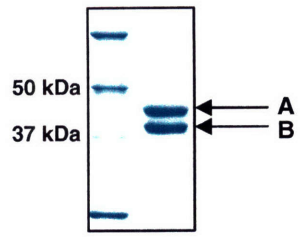

Figure 3–3. SDS PAGE Analysis of DOPA–ββ'. The left lane contains a molecular weight marker; the right lane contains 5 μg of DOPA–ββ'. (A) Full length β–protomer containing residues 1–375 with DOPA at 356. (B) Truncated β'–protomer containing residues 1–353.

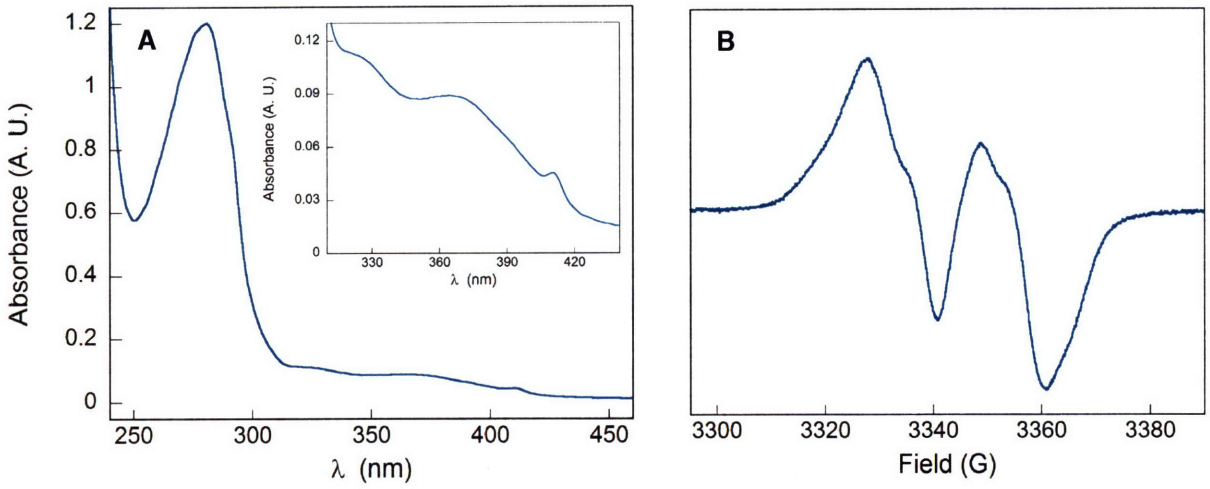

Figure 3–4. Characterization of the diiron Y_{122}• of DOPA–ββ'. (A) UV–vis spectrum of DOPA–ββ'. The inset is a magnified view of the features associated with the cofactor. (B) EPR spectrum of DOPA–ββ'. The radical and Fe contents were 0.33 and 3.4 per DOPA–ββ', respectively.

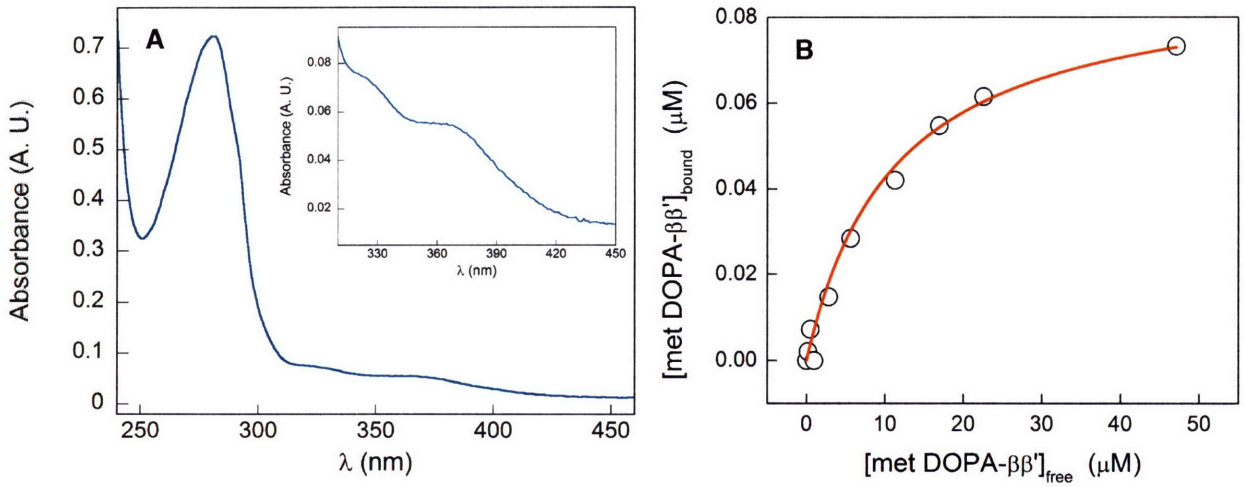

Figure 3–5. Binding of DOPA–ββ' to α2. (A) UV–vis spectrum of met DOPA–ββ' after treatment with hydroxyurea. The inset shows a close–up of the spectral region related to the diferric cluster. (B) Measurement of the affinity of DOPA–ββ' to α2 by using its met form as an inhibitor of nucleotide reductase activity. The red line is a fit according to Eq. 2–4 and yields a K_d of 11 ± 2 μM.

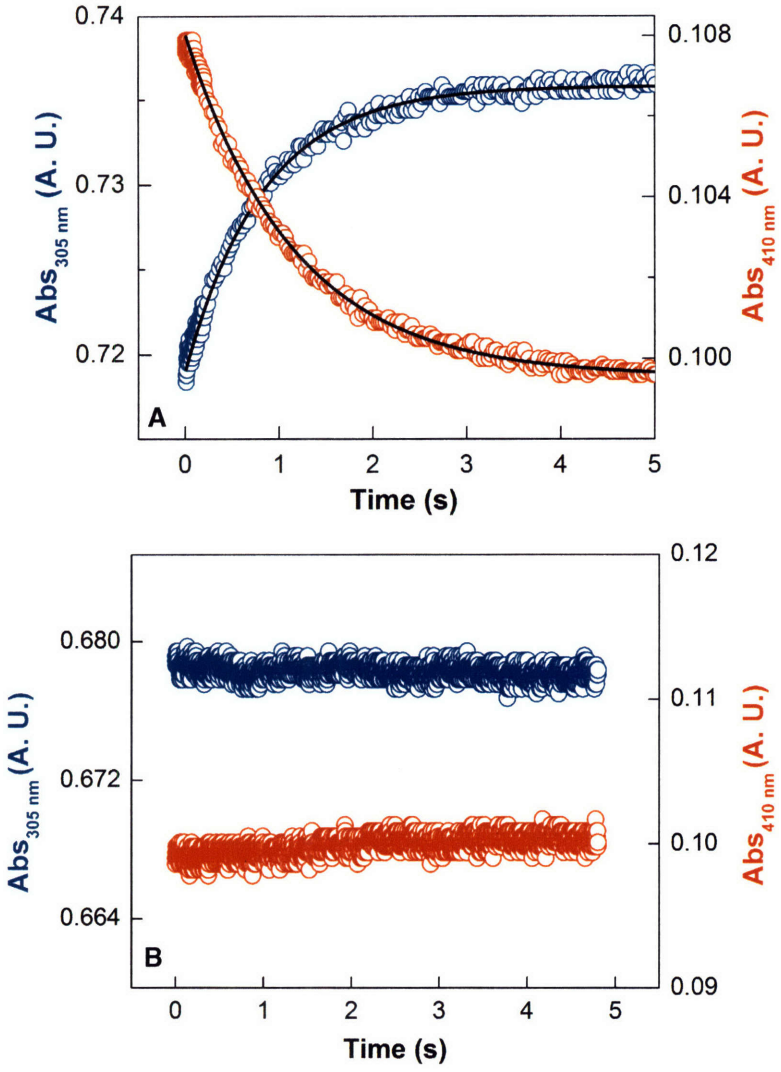

Figure 3–6. Kinetics of $DOPA_{356}$•–ββ' formation with α2, CDP and ATP. (A) DOPA–ββ' (55 μM) and CDP (2 mM) from one syringe were mixed in a 1:1 ratio with pre–reduced α2 (55 μM) and ATP (6 mM) from another syringe. Black lines indicate mono–exponential fits to each trace. Each time course is the average of 7 individual traces. (B) Averaged time course after mixing DOPA–ββ' (50 μM) with pre–reduced α2 (50 μM) in the absence of substrate/effector. The radical content in these experiments was 0.33 per DOPA–ββ'.

constructs suggests that deletion of the C–terminal tail in the β'–monomer reduces conformational flexibility in the α2/DOPA–ββ' complex, but can preserve the essential conformational change gating radical transfer. The difference in the extent of DOPA• formation is consistent with an asymmetric interaction between α2 and β2 and is discussed further below.

To ensure that the species absorbing at 305 nm is in fact a DOPA•, point–by–point analysis of the spectrum at the 5 s time point was carried out by SF spectroscopy. The result of this reconstructed spectrum is shown in Figure 3–7 in the presence of CDP/ATP. The absorption profile is very similar to that of DOPA•–β2 with a λ_{max} at 315 nm and a shoulder at 350 nm.[21] Therefore, the subunit interface generated by the DOPA–ββ'/α2 complex appears to be similar to that generated by the DOPA–β2/α2 complex.

Formation of DOPA•–ββ' monitored by EPR spectroscopy. DOPA•–ββ' was also characterized by EPR spectroscopy. Pre–reduced α2 and ATP were mixed with DOPA–ββ' and CDP. The reaction was freeze–quenched by hand in liquid N_2 after 5 s and its EPR spectrum recorded. As shown in Figure 3–8, the observed spectrum is a composite of Y_{122}• and $DOPA_{356}$•. Subtraction of the Y_{122}• component, which constitutes 74 % of the total signal, yields the blue spectrum in Figure 3–8, which is identical to the DOPA•–β2 spectrum, with a g value of 2.0044 and a line width of 13 G. Consistent with the SF UV–vis experiments, 26 % of the total initial Y_{122}• was trapped as a DOPA•. In the absence of CDP/ATP, only Y_{122}• was observed again underlining the involvement of substrate and effector in the essential conformational change required for radical propagation (Figure 3–8B).

To ensure that the lower yield of DOPA• with DOPA–ββ', relative to that with DOPA–β2, is not a function of the lower affinity of the α2/DOPA–ββ' complex, varying concentrations of α2/DOPA–ββ' were reacted with CDP/ATP, and the amount of DOPA• assessed by EPR. The amount of initial DOPA–ββ'/α2 complex formed was varied between 18–60 % based on the K_d of 11 μM. If DOPA• formation is in fact determined by the amount of initial DOPA–ββ'/α2 complex, then 4–15 % of initial Y_{122}• should be trapped in these experiments. If, however, the extent of DOPA• formation is a function of the asymmetric nature of the DOPA–ββ'/α2 complex, then similar amounts of DOPA• should be generated in these experiments, regardless of the concentration of initial α2/DOPA–ββ' complex. Analysis of this set of experiments shows that 25–30 % of initial Y_{122}• was trapped as a DOPA• indicating a similar yield independent of the concentration of the initial DOPA–ββ'/α2 complex (Figure 3–9). These results suggest that

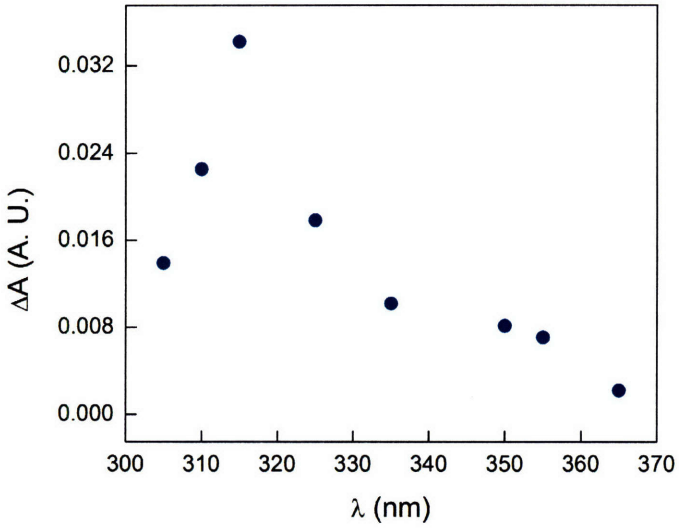

Figure 3–7. Point–by–point Reconstruction of the UV–vis Spectrum of $DOPA_{356}$•–ββ' by SF Spectroscopy. DOPA–ββ' (60 μM) and CDP (2 mM) in one syringe were mixed in a 1:1 ratio with pre–reduced α2 (60 μM) and ATP (6 mM) from another syringe. A total of 3–4 traces were averaged at each wavelength. The absorbance change due to the Y_{122}• in this region has been subtracted. The radical content was 0.37 per DOPA–ββ' in this experiment.

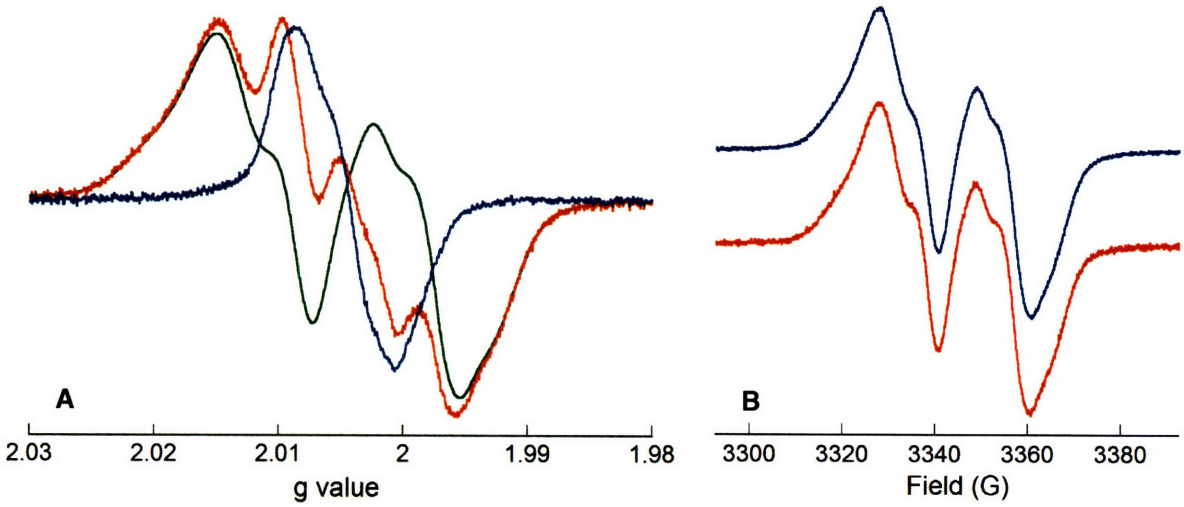

Figure 3–8. EPR spectrum of $DOPA_{356}$•–ββ'/α2 with CDP/ATP. (A) DOPA–ββ' and CDP were mixed with pre–reduced α2 and ATP to yield final concentrations of 25 μM, 1 mM, 25 μM and 3 mM, respectively. The red trace is the observed spectrum after 5 s of reaction time and contains contributions from Y_{122}• and DOPA•. The spectrum was deconvoluted by subtracting the Y_{122}• component (green, 74 % of total spin) yielding the DOPA• spectrum (blue, 26 % of total spin) with a g value of 2.0044 and a spectral width of 13 G. (B) EPR spectrum of DOPA–ββ' alone (blue) and after reaction of DOPA–ββ' with α2 (red) at final concentrations of 15 μM each. The radical content was 0.37 per DOPA–ββ' in these experiments.

equilibration of the DOPA–ββ'/α2 complex is rapid relative to the conformational change, which limits the rate of DOPA• formation. Thus, binding of α2 to DOPA–ββ' is pulled to the right due to irreversible DOPA• formation in the timescale of this experiment.

Kinetic simulations. To test this model, kinetic simulations using KinSim were carried out. The outcome of these kinetic simulations is shown in Figure 3–10. The simulations capture the trend of the experimental data, when rapid equilibration between α2 and DOPA–ββ' was modeled. Under these conditions, regardless of the starting concentration of α2 and DOPA–ββ', the extent of DOPA• formation was similar and its rate constant was approximated by that for the rate–limiting physical step that triggers radical migration. The simulations presented here are in excellent agreement with the experimental data. At DOPA–ββ' and α2 concentrations of 8 μM each, where 33 % of total DOPA–ββ'/α2 is initially complexed, the simulations yield a k_{obs} of 0.9 s^{-1} for DOPA• formation. The experimental data under these conditions show DOPA•

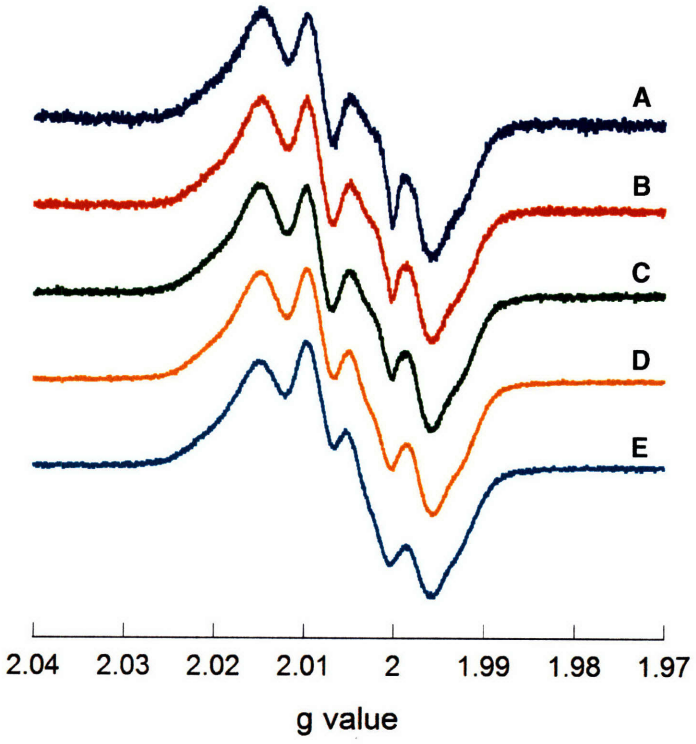

Figure 3–9. $DOPA_{356}$• formation as a function of initial [DOPA–ββ'/α2]. EPR spectra of DOPA• in the presence of CDP/ATP at DOPA–ββ'/α2 complex concentrations of 3 μM (A), 5 μM (B), 10 μM (C), 25 μM (D) and 40 μM (E); the yield of DOPA• was 25 %, 27 %, 26 %, 28 % and 30 %, respectively.

formation with a rate constants of 1.3 ± 0.2 s^{-1} (data not shown). Similarly, at DOPA–ββ' and α2 concentrations of 25 μM, where 52 % of total DOPA–ββ'/α2 is initially complexed, the simulations yield a k_{obs} of 0.9 s^{-1} for DOPA• formation. The experimental data under these conditions give a rate constant of 1.0 ± 0.2 s^{-1} (Figure 3–6). The data along with their simulation highlight the importance of the rate–determining conformational change that controls the kinetics of DOPA• formation as well as the importance of rapid and reversible binding between α2 and DOPA–ββ', which ensures that the extent of DOPA• formation is not limited by the weak affinity between these subunits.

SF UV–vis analysis of DOPA• formation with other substrate/effector pairs. DOPA has proven to be a conformational probe that allows an examination of the physical changes that occur upon binding of substrate and/or effector. To characterize these conformational changes with heterodimeric β2, we analyzed the reaction of DOPA–ββ' with α2 as a function of substrate/effector pairs using SF UV–vis and EPR spectroscopies. These experiments also test the generality of the observation of asymmetry in the α2/β2 complex.

The kinetics of DOPA• formation with various substrate/effector pairs is presented in Figures 3–11 through 3–13 and Table 3–1. In case of CDP/ATP, DOPA• formation occurred with mono–exponential kinetics and a k_{obs} of 1.0 ± 0.2 s^{-1}, which is indicative of the slow physical step prior to radical transfer (Figure 3–6). With the UDP/ATP pair (Figure 3–11), the results mirror those with CDP/ATP: mono–exponential formation of DOPA• with a k_{obs} of 1.1 ± 0.1 s^{-1}. Furthermore, with CDP/ATP and UDP/ATP, 24 ± 1 % and 28 ± 2 % of the initial Y_{122}• was trapped as a DOPA•, respectively. With GDP/TTP (Figure 3–12), 33 % of the initial Y_{122}• is trapped as a DOPA• in a biphasic fashion, with rate constants of 6.1 s^{-1} (25 %) and 1.0 s^{-1} (8 %). In contrast with the results from CDP/ATP and UDP/ATP, an additional conformational change is detected. The ADP/dGTP pair displays the most unusual kinetics of DOPA• generation among the four pairs tested (Figure 3–13). While with the other three substrate/effector pairs, decay of the Y_{122}• is directly correlated with formation of DOPA•, with ADP/dGTP, there is no connection between these two events in the first 250 ms of the kinetic

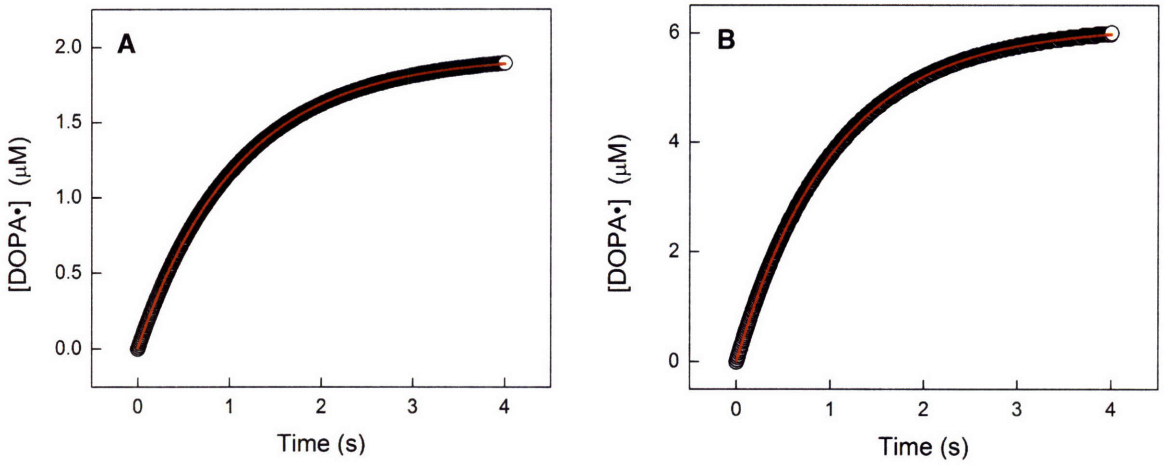

Figure 3–10. Kinetic Simulation of $DOPA_{356}$• formation with DOPA–ββ'/α2. Simulations were carried out with initial DOPA–ββ'/α2 concentrations of 8 μM (A) and 25 μM (B), where 33 % and 52 % of total DOPA–ββ'/α2 has formed a complex, respectively. The simulation was performed using the scheme above. A K_d of 11 μM, fast equilibration, as well as a k_2 of 1 s^{-1} were used to model the kinetics of DOPA• formation. The simulations yield rate constants of 0.9 s^{-1} (A) and 1 s^{-1} (B) for DOPA• formation which agree well with experimentally determined rate constants of 1.3 s^{-1} and 1 s^{-1}, respectively.

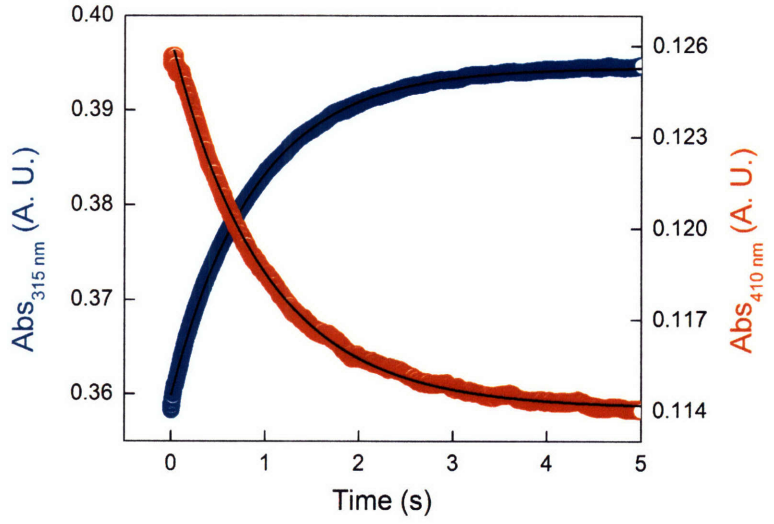

Figure 3–11. Kinetics of $DOPA_{356}$•–ββ'/α2 formation with UDP/ATP. DOPA–ββ' (55 μM) and UDP (2.5 mM) in one syringe were mixed in a 1:1 ratio with pre–reduced α2 (55 μM) and ATP (6 mM) from another syringe. Black lines represent mono–exponential fits to the data with a k_{obs} 1.1 s^{-1}. A total of 6 traces were averaged at each wavelength.

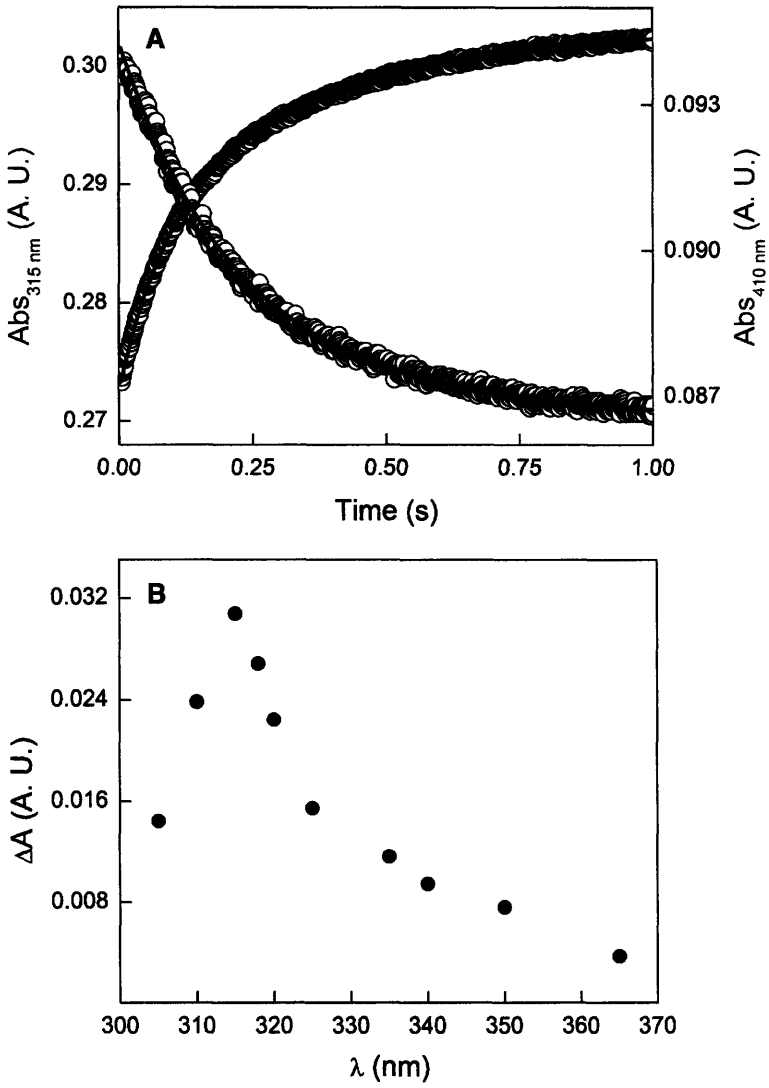

Figure 3–12. Kinetics of $DOPA_{356}$•–ββ'/α2 formation with GDP/TTP. (A) DOPA–ββ' (40 μM) and GDP (2 mM) in one syringe were mixed in a 1:1 ratio with pre–reduced α2 (40 μM) and TTP (0.2 mM) from another syringe. Black lines are bi–exponential fits to the data with k_{obs}s of 6.1 and 1.0 s^{-1}. A total of 6 traces were averaged at each wavelength. (B) Point–by–point reconstruction of the DOPA• UV–vis spectrum with GDP/TTP. Reaction conditions were identical to those in (A). At least 3 traces were averaged at each wavelength. The absorbance change associated with Y_{122}• in this spectral region has been subtracted. The radical content was 0.37 per DOPA–ββ' in these experiments.

trace. DOPA• formation occurs in four distinct phases with rate constants of 146 s^{-1} (12 % of total $\Delta A_{315\ nm}$), 16 s^{-1} (30 %), 2.2 s^{-1} (27 %) and 0.13 s^{-1} (32 %). At 410 nm, instead of decay of the Y_{122}•, there is an initial biphasic burst with rate constants of 230 s^{-1} (13 % of total $\Delta A_{410\ nm}$) and 17 s^{-1} (34 %) followed by a slow decay of 0.12 s^{-1} (53 %).

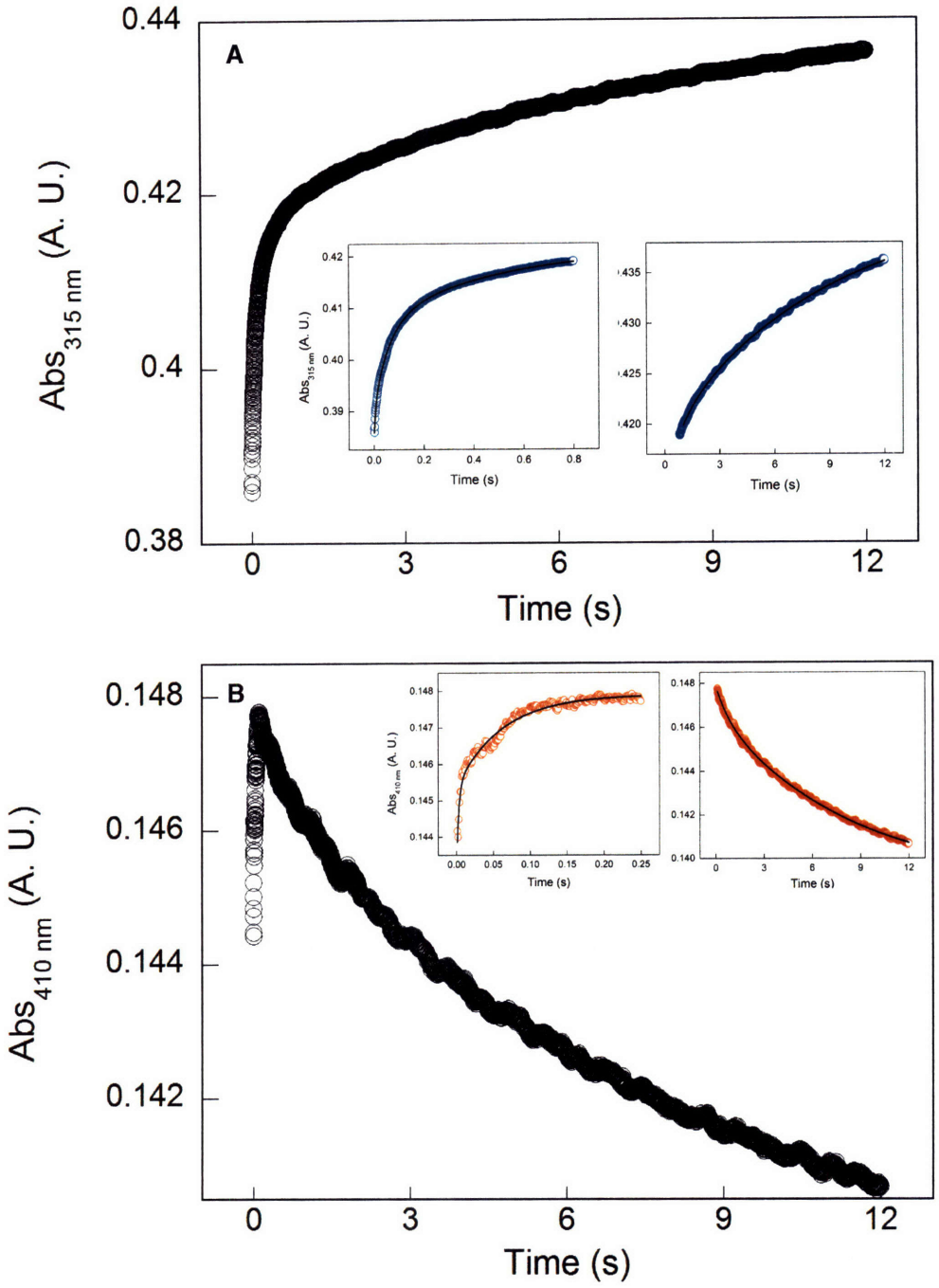

Figure 3–13. Kinetics of $DOPA_{356}$•–ββ'/α2 formation with ADP/dGTP. DOPA–ββ' (55 μM) and ADP (2.5 mM) in one syringe were mixed in a 1:1 ratio with pre–reduced α2 (55 μM) and dGTP (0.4 mM) from another syringe. (A) Observed time course monitoring formation of DOPA•. Insets show kinetic fits to the data for the fast burst phase and the slow phase of DOPA• formation. (B) Observed time course monitoring [Y_{122}•]. Insets show kinetic fits to the data for the fast growth phase and the slow decay phase. A total of 8 traces were averaged at each wavelength.

The data at 410 nm show disappearance of 20 % of initial Y_{122}• with a k_{obs} of 0.12 s^{-1}. This disappearance is kinetically linked to DOPA• formation which shows trapping of 14 % of initial Y_{122}• with a k_{obs} of 0.13 s^{-1}. The fast kinetic phases for DOPA• formation, however, are not linked to simultaneous fast disappearance of Y_{122}•. Therefore, Y_{122}• does not oxidize $DOPA_{356}$ in this fast kinetic segment, and a different moiety must be oxidizing DOPA to a DOPA•. In an effort to identify this oxidizing agent,RFQ EPR experiments were carried out.

Table 3–1. Summary of kinetic parameters for $DOPA_{356}$•–ββ'/α2 formation as a function of substrate/effector pairs.

Substrate/ Effector	1st Phase[a] k_{obs} (s^{-1}), Amp (%)[b]	2nd Phase[a] k_{obs} (s^{-1}), Amp (%)[b]
None	–[c]	–
CDP/ATP	1 ± 0.2, 24 ± 1	–
GDP/TTP	6.1 ± 1.2, 25 ± 1	1.0 ± 0.3, 8 ± 1
UDP/ATP	1.1 ± 0.1, 28 ± 2	–
ADP/dGTP	0.13 ± 0.01, 17 ± 3[d]	–

[a] The rate constants reported are the average of those measured at 410 nm for Y_{122}• loss and at 305 or 315 nm for DOPA• formation. [b] Amp = amplitude; the amount of Y_{122}• trapped in each kinetic phase is indicated as a % of total initial Y_{122}•. [c] No changes observed. [d] Note that the unusual kinetics with ADP/dGTP may be related to high [ADP] used in this experiment.

RFQ EPR spectroscopy with ADP/dGTP. The kinetics with ADP/dGTP suggest that DOPA• formation takes place prior to decay of Y_{122}•. Similar results have been obtained before with the mechanism–based inhibitor 2'–azido–2'–deoxyUDP (N_3UDP), which, upon reaction with α2/β2 gives rise to a stable N–centered radical (N•). Salowe et al. observed that inactivation of RNR occurred prior to loss of Y_{122}•.[9] In this case, a tight non–covalent complex was postulated to drive inhibition of RNR activity, followed by slow loss of Y_{122}•. This proposal has recently been confirmed using size exclusion chromatographic methods, which show tight complex formation in the presence of N_3UDP/ATP.[22] In addition, Ekberg et al. observed a

2–fold faster rate of N• formation than Y_{122}• loss during inhibition of $D_{237}E$–β2/α2 activity with N_3CDP using flow EPR methods.[23] This result is similar to the kinetics observed with DOPA–ββ'/α2 and ADP/dGTP in that an oxidant other than Y_{122}• appears to be giving rise to the new radical (N• or DOPA•).

To investigate what this new oxidant may be, RFQ–EPR experiments were carried out with DOPA–ββ'/α2 and the ADP/dGTP pair. The experiment was carried out under identical conditions as in Figure 3–13. The reaction was quenched at 111 ms, 214 ms and 324 ms, where the SF UV–vis experiments indicated formation of DOPA• independent of Y_{122}• loss (Figure 3–13B, inset), and the EPR spectrum subsequently recorded. The results are shown in Figure 3–14. Between 0 and 323 ms, only the Y_{122}• is observed. No new signal is seen with wider sweep widths (1000 G to 5000 G) or at lower temperatures (15 K, data not shown). Spin quantitation indicates that no Y_{122}• has been lost or gained at these short time points suggesting that the increase at 410 nm is not associated with Y_{122}•, but with another species. In addition, at the end of the experiment, the contents of the two syringes were mixed, transferred to an EPR tube and hand–quenched after 20 s. In this case an EPR composite spectrum consisting of DOPA• and Y_{122}• signals was observed, similar to those in Figure 3–8A, indicating that the sample was competent in DOPA• formation on the second time scale.

The data from the SF UV–vis and RFQ–EPR experiments appear to be at odds, since kinetics obtained from the former shows that at the 324 ms time point, DOPA• should have formed. The RFQ–EPR studies, however, reveal no DOPA•. This apparent inconsistency may be reconciled by considering that the fast spectral changes may not be related to changes in the concentration of DOPA• or Y_{122}•, i.e. the absorbance changes are not related to redox reactions. Similar observations have previously been made with NO_2Y–β2 (Yee and Stubbe, unpublished results). It is unclear what these absorption changes correspond to and additional experiments are required to determine their relevance to radical initiation.

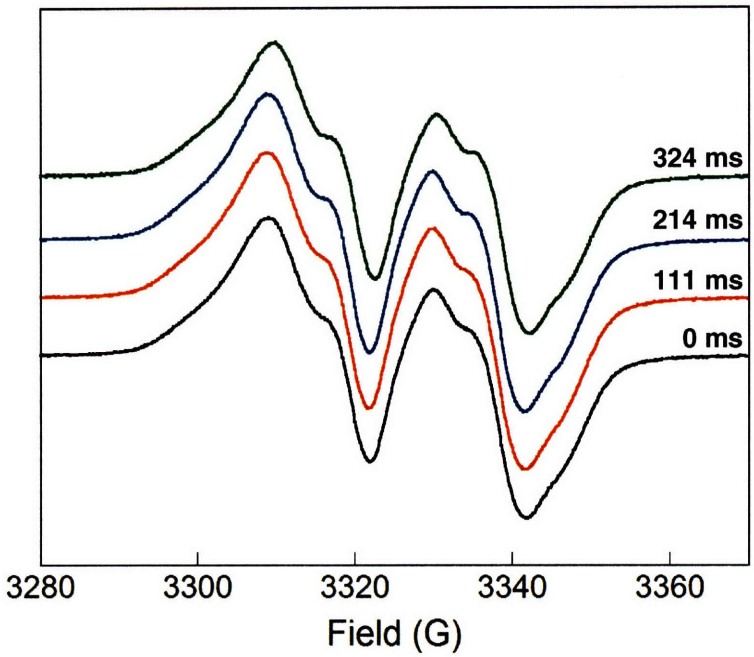

Figure 3–14. RFQ EPR Spectroscopy with DOPA–ββ'/α2 in the presence of ADP/dGTP. DOPA–ββ' and ADP were rapidly mixed with pre–reduced α2 and dGTP to give final concentrations of 35 μM DOPA–ββ'/α2, 1.75 mM ADP and 0.25 mM dGTP. The reaction was quenched at the times indicated and the EPR spectrum subsequently recorded at 77 K. Acquisition with wider sweep width and lower T (15 K) revealed no additional features. The dead–time of the instrument (16 ms) has been accounted for in the quench times above.

EPR analysis of DOPA• formation with other substrate/effector pairs. The SF UV–vis data above show differences in the kinetics of DOPA• formation as a function of the substrate/effector pair bound in the active site of α2. To examine whether the conformation of the DOPA• in the α2/DOPA–ββ' depends on the nucleotides in α2, as in the case of DOPA–β2, reactions with other substrate/effectors were monitored by EPR spectroscopy. The resulting spectra at 9.4 GHz (X–band) are shown in Figure 3–15. As with DOPA–β2, small differences in the line width and g value may be discerned as a function of the regulatory state of α2. These parameters are summarized in Table 3–2 and are markedly similar to those determined with DOPA–β2/α2 with the same substrate/effector pairs. Comparison of these spectra with those obtained with DOPA–β2/α2, shows that the substrate/effector pairs generate, by the criteria of EPR spectroscopy, a DOPA• in an environment similar to that in DOPA–β2, despite the absence

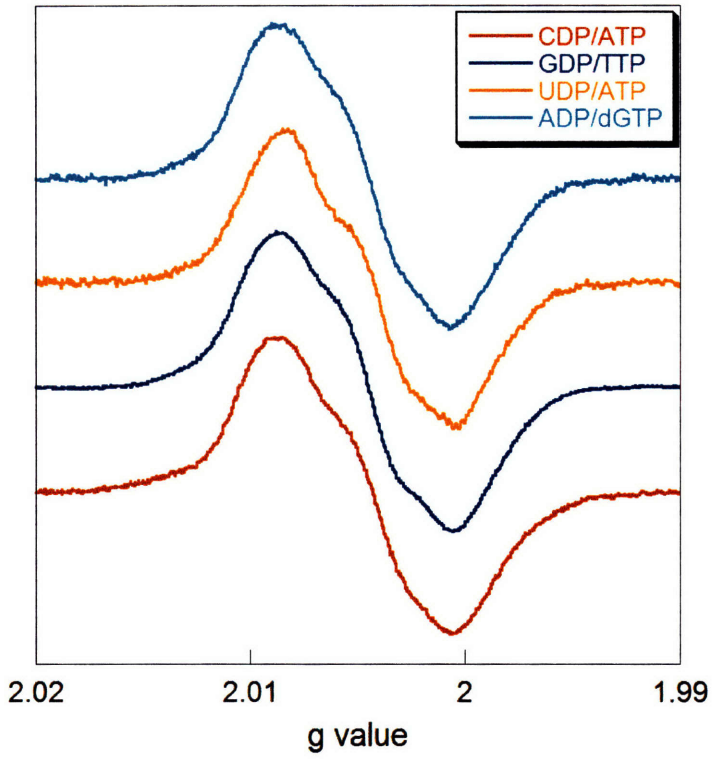

Figure 3–15. Comparison of $DOPA_{356}$•–ββ'/α2 as a function of substrate/effector pairs. Spectra have been normalized for number scans.

of a second C–terminal tail known to be responsible for subunit interactions (Figure 3–16, Table 3–2). This indicates that truncation in the β'–protomer does not abolish communication between the α2 subunit and the β–protomer of DOPA–ββ'. Thus, the C–terminal 22 residues missing from the β'–protomer are not involved in radical migration or allosteric communication within the α/β pair, an observation that has important implications for the nature of the α2/β2 complex.

Further support for an asymmetric α2/β2 complex is obtained by comparing the extents of DOPA• formation with DOPA–β2 and DOPA–ββ'. These data are summarized in Table 3–3 for various substrate/effector pairs and show that with the former, 48 ± 4 % of total initial Y_{122}• is trapped as a DOPA•, whereas with the latter 27 ± 5 % of initial Y_{122}• forms a DOPA•. Therefore, DOPA–β2 forms more DOPA• by a factor of 1.8 ± 0.2. A model to explain these results will be presented below.

Table 3–2. Comparison of X–band EPR parameters for $DOPA_{356}$•–β2/α2 and $DOPA_{356}$•–ββ'/α2 as a function of substrate/effector pairs.

Substrate/ Effector	DOPA–β2/α2 g value	DOPA–β2/α2 Line width (G)	DOPA–ββ'/α2 g value	DOPA–ββ'/α2 Line width (G)
GDP/TTP	2.0045	14	2.0045	14
CDP/ATP	2.0044	13	2.0044	13
UDP/ATP	2.0044	12	2.0044	13
ADP/dGTP	2.0045	13	2.0045	13

Table 3–3. Comparison of the extent of $DOPA_{356}$• formation with DOPA–β2/α2 and DOPA–ββ'/α2 as a function of substrate/effector pairs.

NDP/(d)NTP	DOPA–β2/α2[a]	DOPA–ββ'/α2[a]
SF UV–vis		
CDP/ATP	47	24
GDP/TTP	54	33
UDP/ATP	45	28
ADP/dGTP	51	20
EPR		
CDP/ATP	49	28
GDP/TTP	47	35
UDP/ATP	48	25
ADP/dGTP	40	26

[a] The amount of Y_{122}• trapped in SF UV–vis and EPR experiments is indicated as % of total initial Y_{122}•.

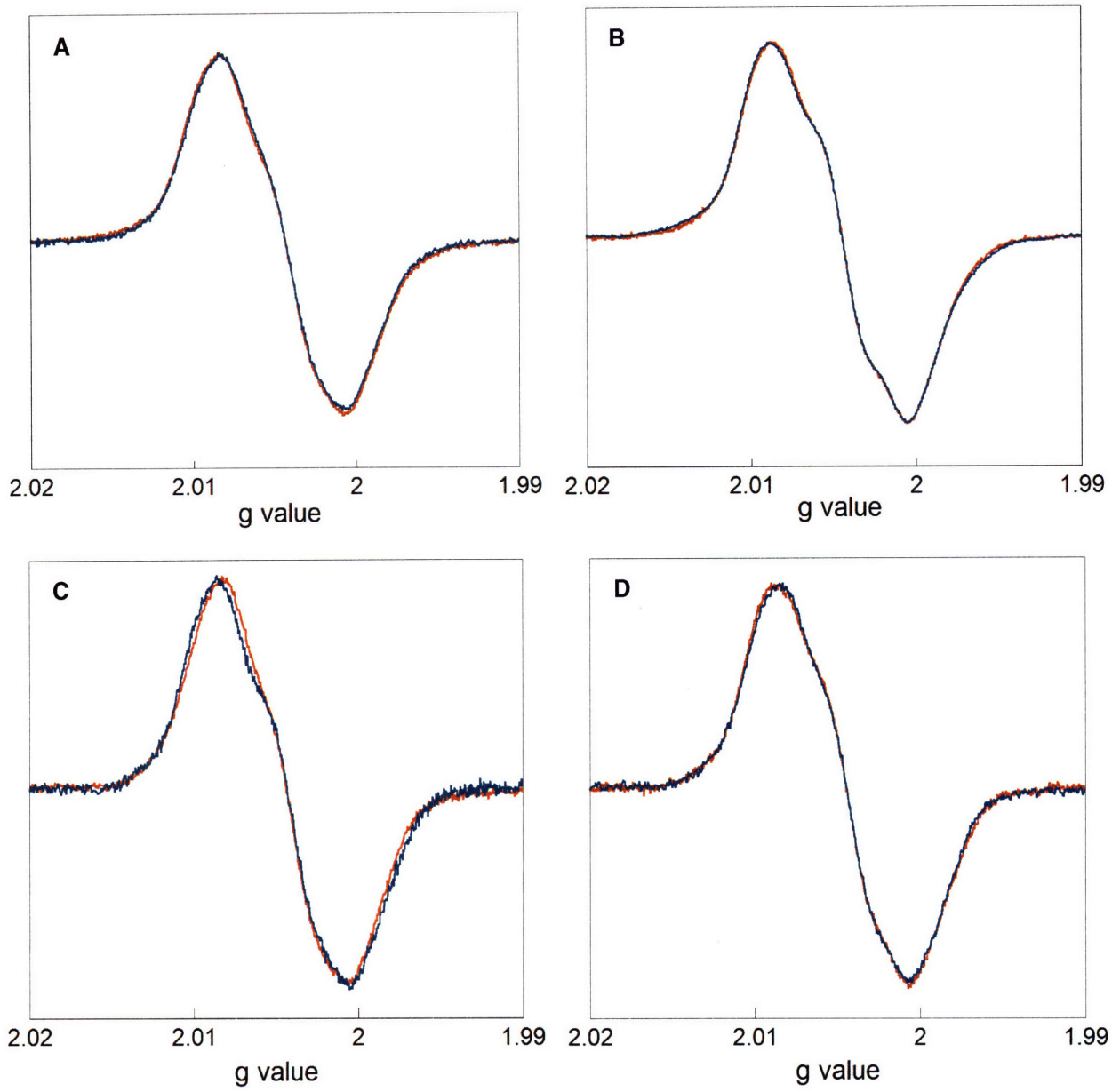

Figure 3–16. Comparison of the EPR spectrum of $DOPA_{356}$• in DOPA–β2/α2 vs. DOPA–ββ'/α2 as a function of NDP/(d)NTP. DOPA•–β2/α2 (red traces) overlaid on top of DOPA•–ββ'/α2 (blue traces) in the presence of CDP/ATP (A), GDP/TTP (B), UDP/ATP (C) and ADP/dGTP (D).

PELDOR spectroscopy to determine the distance between DOPA• and Y_{122}• in DOPA–ββ'/α2. PELDOR studies with DOPA–β2 demonstrated that hole migration takes place along only one of the two symmetrically related radical transfer pathways in the α2/β2 complex. Trapping of a DOPA• during this process allowed the first distance constraints to be made for

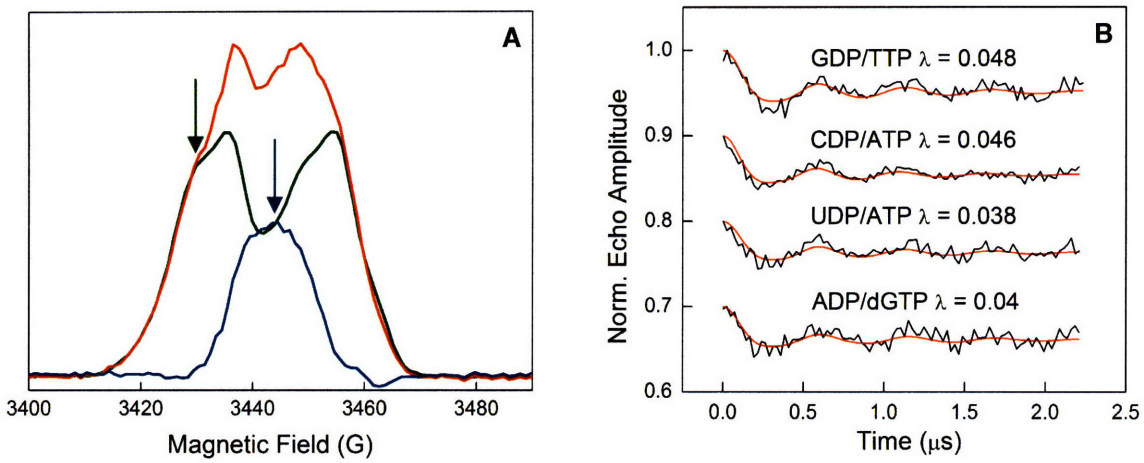

Figure 3–17. X–band PELDOR spectroscopy of Y_{122}•–$DOPA_{356}$• with DOPA–ββ'/α2. (A) EPR absorption spectrum of DOPA•–ββ'/α2 with GDP/TTP. The observed spectrum (red trace) is a composite of 0.26 equiv of $DOPA_{356}$• (blue trace) and 0.73 equiv of unreacted Y_{122}• (green trace). Pump and detect microwave frequencies used for PELDOR spectra are indicated by arrows. Note that the detection υ (blue arrow) is at a higher field than the perturbation or 'pump' υ (green arrow). (B) Dipolar oscillation observed for Y_{122}•–$DOPA_{356}$• with various NDP/(d)NTP pairs. In all cases the distance extracted from fitting the data (red line) is 30.6 ± 0.5 Å. The modulation amplitude, is a function of the number of Y_{122}•–DOPA• detected in the sample.

residue Y_{356}, which is part of the conformationally flexible C–terminal tail and hence invisible in all β2 structures solved to date. The distance measured between Y_{122}• and the DOPA• diagonally across the dimer interface was 30.6 ± 0.5 Å. Similar experiments were performed with DOPA–ββ' with all substrate/effector pairs and are presented in Figure 3–17. As with DOPA–β2, PELDOR measurements and data analysis with DOPA–ββ' were performed by Prof. Marina Bennati.[24,25] DOPA–ββ'/α2 were mixed with various substrate/effector pairs at room temperature to yield a final complex concentration of 0.28 mM. The sample was transferred to an EPR tube and hand–quenched in liquid N_2 after 45–60 s of reaction time. The X–band EPR absorption spectrum for the CDP/ATP pair recorded at 6 K is shown in Figure 3–17A along with 'pump' and 'detect' frequencies used to excite the Y_{122}• and detect the echo modulations from the DOPA•–ββ'. The echo modulation as a function of substrate/effector pairs is shown in Figure 3–17B along with the modulation amplitude, λ, which is dependent on the number of Y_{122}•–DOPA• pairs in the sample. Simulation of this data indicates that, similar to DOPA–β2,

the distance between Y_{122}•–DOPA• is 30.6 ± 0.5 Å, irrespective of the substrate/effector pair bound in the α2 subunit. Therefore, truncation of the C–terminal 22 residues in the β'–protomer does not affect the distance between DOPA• on the β–protomer and the Y_{122}• in the β'–monomer of DOPA–ββ'. The implications of this result will be discussed in the light of an asymmetric α2/β2 model below.

The fate of DOPA•–ββ'/α2. Having characterized the kinetics and stoichiometry of DOPA• formation as well as elucidated subtle structural features of the DOPA• at the subunit interface, its fate was examined next. Two aspects of the trapped DOPA•–ββ' were investigated: First, its accessibility to small molecules in solution, and, second, its stability within the DOPA–ββ'/α2 complex. It was hoped that these studies would begin to delineate factors that stabilize a radical within the RNR complex as well as the reactions involved in its reduction.

Reaction of DOPA•–ββ'/α2 with hydroxyurea. We first examined the accessibility and reactivity of $DOPA_{356}$• with hydroxyurea (HU). The mechanism of HU–mediated inhibition of RNR activity is not understood.[26,27] In solution, a 2nd order k_{obs} of 1.9×10^6 M^{-1} s^{-1} has been determined for reduction of a pulse–generated Y• by HU.[28] With RNRs, reaction with HU yields different products based on the origin of β2. While HU reduces the Y_{122}• in *E. coli* β2,[27] in mouse β2, it can reduce the Y• as well as the diferric center yielding 2 Fe^{II} per iron center; the ferrous irons subsequently dissociate from the protein leaving behind apo–β2.[29] The difference in products is likely related to the distinct reduction potentials of the $Fe^{III}Fe^{III}$–$Fe^{II}Fe^{III}$ couples in *E. coli* and mouse β2, which have been estimated at –0.2 V and +10–115 mV, respectively.[19,30]

An important set of experiments has been carried out by Sjöberg and coworkers with *E. coli* β2: When HU was reacted with β2 alone, a 2nd order k_{obs} of 0.5 M^{-1} s^{-1} was determined.[31] However, in the presence of α2, substrate and effector, i.e. in the regulatory state, HU–mediated reduction was 8–fold faster. It is unclear whether this is due to an altered reactivity of the diiron Y_{122}• center, as indicated by results from Stankovich et al.,[32] or whether HU can directly interact with transient amino acid radicals during hole migration between α2 and β2. Studies by Gräslund and Thelander on mouse β2 led them to favor the former model.[33] Determination of

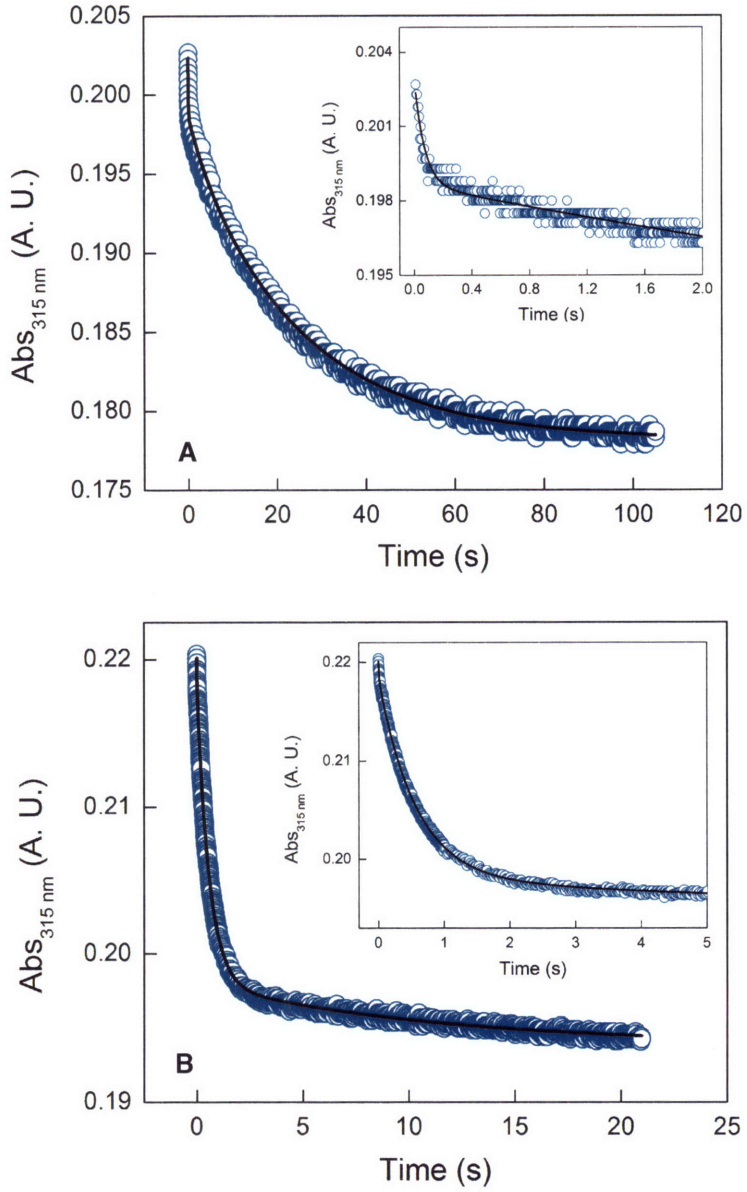

Figure 3–18. Sequential–mix SF UV–vis spectroscopy monitoring reduction of $DOPA_{356}$• by HU. DOPA–ββ' and GDP in one syringe were rapidly mixed with pre–reduced α2 and TTP from another syringe and the mixture aged for 5 s in an aging loop. The mixture was then combined with HU at final concentrations of (A) 1.5 mM or (B) 75 mM. Insets in each plot show a magnified view of the initial rapid absorbance changes. Tri–phasic decay of the DOPA• is observed in both cases; the rate constants and amplitudes are summarized in Table 3–8.

HU–mediated reduction of the Y• with various pathway mutants yielded similar rate constants. Thus, they suggested that reduction by HU did not require an intact radical transfer pathway. However, their conclusion may not apply to *E. coli* β2 as the properties of its diferric Y_{122}• are

different from those in mouse β2. In addition, these experiments were carried out in the absence of α2, substrate and effector.

DOPA–β2 offers an ideal probe for examining the interaction of HU with the radical transfer pathway at residue 356. To investigate whether HU can reduce $DOPA_{356}$•, sequential mix SF UV–vis experiments were carried out. In these experiments, DOPA–ββ' and GDP were mixed with pre–reduced α2 and TTP and the mixture aged for 5 s, where DOPA•–ββ' formation was complete but no decay had occurred, in an aging loop. After this period, the mixture was rapidly mixed with HU to yield final concentrations of 1.5 mM or 75 mM. The results of these experiments are presented in Figure 3–18. When DOPA•–ββ'/α2 in complex with GDP/TTP is combined with assay buffer containing no HU, no decay of DOPA• is observed (data not shown). With 1.5 mM HU (Figure 3–18A), rapid decay of 95 % of the initially formed DOPA• is observed, while with 75 mM HU (Figure 3–18B) the DOPA• is completely reduced. Rapid disappearance of DOPA• in the presence of HU strongly suggests that it can directly access and react with residue 356 in the radical transfer pathway.

The kinetics of HU–mediated DOPA• reduction relative to those with Y_{356}• could be informative. The caveat is that DOPA• is harder to reduce than Y_{356}• (assuming the reduction potential is not perturbed in the pathway) and that the [DOPA•] is at least ~20–fold higher than [Y_{356}•] during radical transfer. With 1.5 and 75 mM HU, the kinetic data can be fit to three exponentials. The kinetic parameters are summarized in Table 3–4. With 1.5 mM HU, 77 % of the total change occurs with an apparent 2nd order k_{obs} of 14 M^{-1} s^{-1}. Similary, with 75 mM HU, 78 % of the total reaction occurs with a k_{obs} of 12 M^{-1} s^{-1}. Therefore, reduction of DOPA• appears to be dominated by this kinetic phase (with k_{obs} of ~12–14 $M^{-1}s^{-1}$), which is not saturated at 75 mM HU, as these rate constants are similar. At 1.5 mM HU, 15 % of the total change occurs with a fast rate constant of 4940 $M^{-1}s^{-1}$; the remaining 7 % disappear with a k_{obs} of 84 $M^{-1}s^{-1}$ (Table 3–4). With 75 mM HU, the remaining kinetic phases differ from those at 1.5 mM. In this case, 16 % of the total change occurs with a 2nd order rate constant of 0.6 $M^{-1}s^{-1}$,

similar to that reported by Sjöberg for the reduction of Y_{122}•.[31] The remaining 7 % disappear at 550 $M^{-1}s^{-1}$ (Table 3–4).

The data above suggest that HU can interact with the radical transfer pathway. The fast rate constant at both HU concentration, may represent direct reaction with DOPA•, whereas the slow rate constants, and certainly the 0.6 $M^{-1}s^{-1}$ observed before, may be conformationally gated. Accounting for the difference in reduction potentials between Y• and DOPA•, which by solution measurements is 260 mV, the 2nd order rate constants for reaction with Y_{356}• would be 1.2×10^8 and 2×10^6 $M^{-1}s^{-1}$ with 1.5 and 75 mM, respectively. The latter is in the range of rate constant observed for reaction of HU with pulse–generated Y• in solution. This may be interpreted as indicating that reaction of HU with Y_{356} during radical transfer is feasible.

Table 3–4. Summary of kinetic parameters in the reaction of $DOPA_{356}$•–ββ' with HU obtained using sequential SF UV–vis spectroscopy.

[Hydroxyurea] (mM)	1st Phase[a] k_{obs} (M^{-1} s^{-1}), Amp (%)[b]	2nd Phase[a] k_{obs} (M^{-1} s^{-1}), Amp (%)[b]	3rd Phase[a] k_{obs} (M^{-1} s^{-1}), Amp (%)[b]
0	–[c]	–	–
1.5	4940 ± 300, 15 ± 1	84 ± 8, 7 ± 1	14 ± 1, 78 ± 1
75	550 ± 47, 7.0 ± 0.3	12 ± 1, 77 ± 1	0.63 ± 0.01, 16 ± 1

[a] 2nd order rate constants are reported. [b]Amp = amplitude; the amount of $DOPA_{356}$• reduced in each kinetic phase is indicated as a % of total initial $DOPA_{356}$•. [c] No changes observed.

The disparate kinetics of DOPA• loss in the presence of different concentrations of hydroxyurea has interesting implications for the interaction between HU and residue 356. With DOPA–ββ'/α2 and GDP/TTP, 2 distinct, non–interconverting conformations result in DOPA• formation. In the current experiment, tri–phasic reduction kinetics is observed indicting three distinct conformations. The fact that one of these conformations is similar between the reactions with 1.5 mM and 75 mM HU, whereas the other two are different, may indicate that HU itself is

affecting the conformational flexibility in DOPA–ββ'. This needs to be examined using a similar reaction with DOPA–ββ' and DOPA–β2 at multiple [HU].

To assess whether an intact radical transfer pathway is required for reaction of HU with Y_{122}•, wt β2 and Y_{356}F–β2 were reacted with HU and the reduction rate constant determined by UV–vis spectroscopy using the dropline method. The results are shown in Figure 3–19 and yield 2nd order rate constants or 0.41 ± 0.02 $M^{-1}s^{-1}$ and 0.47 ± 0.02 $M^{-1}s^{-1}$ for Y_{356}F– and wt β2, respectively. Thus, an intact pathway is not required, that is, HU does not reduce Y_{122}• by injecting reducing equivalents through the pathway used for radical propagation during turnover.

In conclusion, the working model that emerges from the experiments and analyses above is that HU can react with $DOPA_{356}$• and Y_{356}• during radical transfer, though the rate constant strongly depends on the [Y_{356}•] during this process. The reaction of HU with Y_{122}• does not require Y_{356}. The 8–fold increase that is observed in the regulatory state of RNR is likely due to an altered accessibility and/or reactivity of Y_{122}•. Nevertheless, the pathway radical at residue 356 is more exposed than Y_{122}•, as demonstrated by the faster reduction kinetics with $DOPA_{356}$•, despite its lower reduction potential. During turnover with wt RNR, reaction of HU with Y_{356}• is

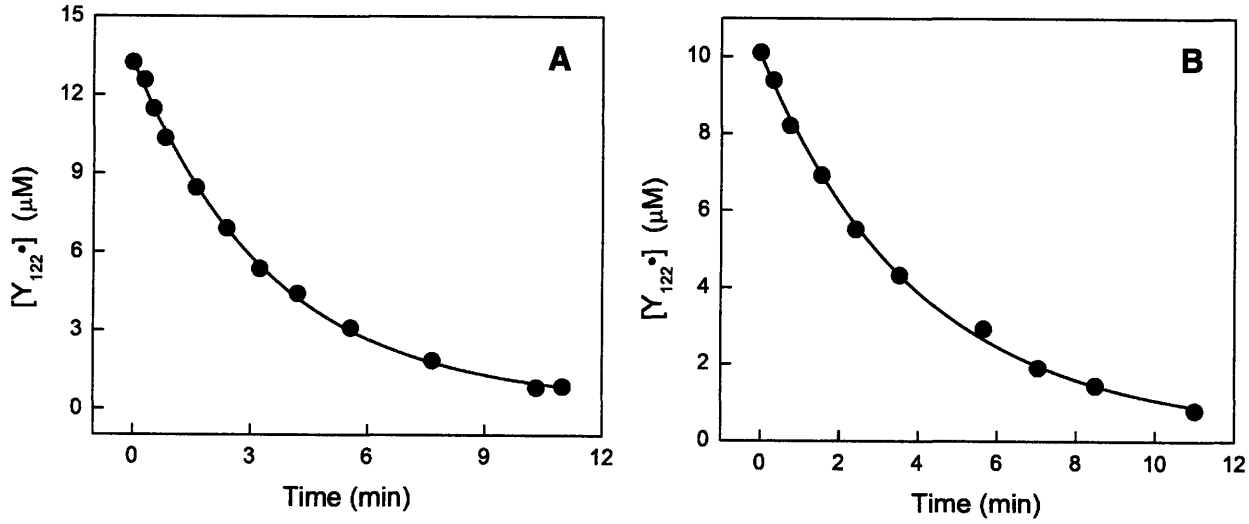

Figure 3–19. Kinetics of HU–mediated reduction of Y_{122}• with wt and Y_{356}F–β2. The reaction contained 10 μM of (A) wt β2 (1.3 Y_{122}•/dimer) or (B) Y_{356}F–β2 (1.0 Y_{122}•/dimer) and 1 mM HU in assay buffer at 25°C. Black lines represent mono–exponential fits to the data and yield 2nd order k_{obs}s of 0.47 ± 0.02 M^{-1} s^{-1} (A) and 0.41 ± 0.02 M^{-1} s^{-1} (B).

avoided by ensuring that a build–up does not occur. Additional experiments, specifically, studies in the regulatory state with $Y_{356}F$–β2, or with α2 pathway mutants are necessary to further refine this model.

The fate of DOPA•–ββ'/α2 studied by EPR spectroscopy. The studies above demonstrate that HU does interact with DOPA• suggesting that it is sufficiently exposed for small molecules to gain access. To study the properties of $DOPA_{356}$• further, its stability within the complex with α2 was examined as a function of substrate/effector pairs. DOPA–ββ' and CDP were mixed with pre–reduced α2 and ATP. At defined time points, an aliquot was removed from the reaction mixture, transferred to an EPR tube and freeze–quenched by hand in liquid N_2. Subsequently, the total spin and its distribution between Y_{122}• and DOPA• were determined by EPR methods. Time–dependent EPR spectra of DOPA•–ββ'/α2 generated by incubation with CDP/ATP are shown in Figure 3–20. The DOPA• decays with a time constant, τ, of ~7 min and a half–life, $\tau_{1/2}$, of 4.8 min. At the 1 min time point, 24 % of the total radical is present as DOPA• and 76 % as Y_{122}•. By 8 min, ~6 % DOPA• remains but the amount of Y_{122}• unexpectedly increased by >10 %. This result was reproduced in a second similar experiment, where an increase of ~12 % in [Y_{122}•] was observed. The experiment was repeated to determine whether an increase in [Y_{122}•] would occur with GDP/TTP. The result is summarized in Table 3–5 and shows that the DOPA• is more stable in the presence of GDP/TTP. An endpoint was not reached in this experiment, that is loss of DOPA• may not be complete at the last time point recorded. It is estimated that in the presence of α2 and GDP/TTP, the DOPA• decays with $\tau \geq 8.5$ min and $\tau_{1/2} \geq 6$ min. Importantly, the total spin lost in this experiment can all be accounted for by loss of DOPA•. Therefore, in contrast to the CDP/ATP case, no increase in [Y_{122}•] is observed. Finally, a similar experiment was performed with CDP alone revealing DOPA• decay kinetics with τ of 4.8 min and $\tau_{1/2}$ of 3.4 min (Table 3–6). As with GDP/TTP, no increase in [Y_{122}•] was observed.

The data show that with the CDP/ATP pair, an increase in [Y_{122}•] takes place at the expense of DOPA•. The loss of DOPA• and increase in Y_{122}• occur with similar kinetics

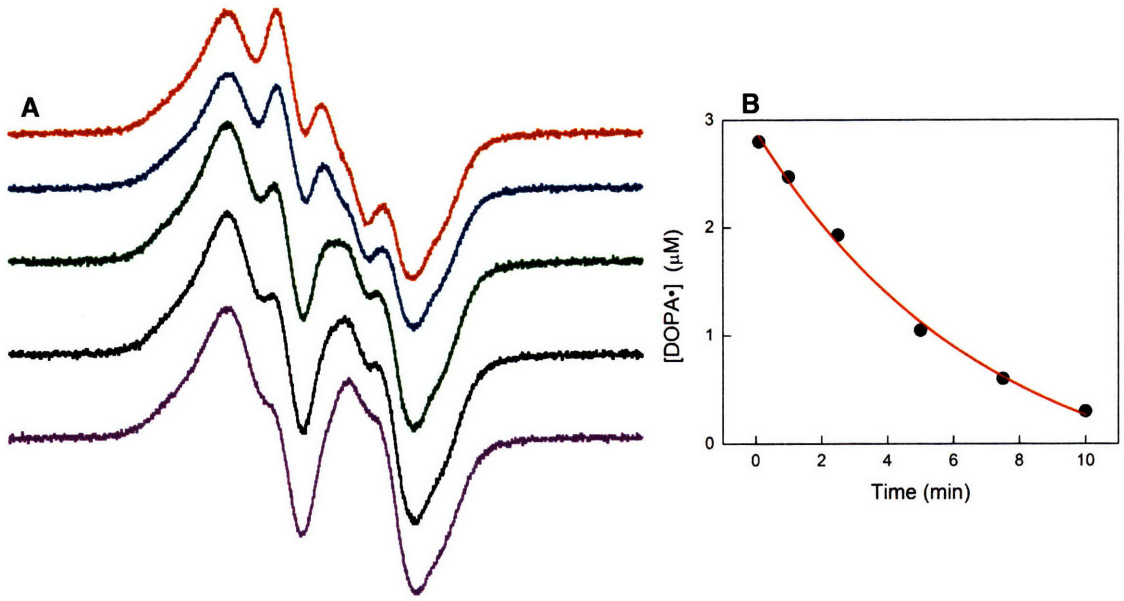

C

Time (min)	[Spin] (μM)	% Y_{122}•	% DOPA•	[Y_{122}•] (μM)	[DOPA•] (μM)
0	11	100		11	
0.08	10.8	73	27	7.8	2.9
1	10.3	76	24	7.8	2.5
2.5	10.4	82	18	8.5	1.9
5	9.5	89	11	8.5	1.0
8	9.2	95	5	8.7	0.5

Figure 3–20. Decay Kinetics of $DOPA_{356}$•–ββ'/α2 with CDP/ATP. (A) DOPA–ββ' and CDP were mixed with pre–reduced α2 and ATP. At defined time points, an aliquot was removed, transferred to an EPR tube and frozen in liquid N_2. The quench times are 0 min (purple), 1 min (red), 2.5 min (blue), 5 min (green), 8 min (black). The 0.08 min spectrum is similar to that in Figure 3–8A and has been omitted. (B) DOPA• decay kinetics can be fit to a mono–exponential function with a $\tau_{1/2}$ of 4.8 min. (C) The total spin and its distribution between Y_{122}• and DOPA• were determined by EPR quantitation methods and are summarized in this table.

suggesting that a fraction of the DOPA• is able to re–oxidize Y_{122}. However, because of the low Y_{122}• content of DOPA–ββ', which is typical for all semisynthetic β2s made thus far, the increase in [Y_{122}•] observed, is close to the lower limit of detection that can be quantitated (~0.5–1 μM). To increase the sensitivity of this experiment and obtain compelling evidence for

re–oxidation of Y_{122} by DOPA•, a new method is required to enhance the radical content of semisynthetic β2s.

Enhancing the radical content of DOPA–ββ'. A number of different protocols were attempted to increase the radical content of DOPA–ββ'. The method of Atkin et al. was attempted using the procedure described in Chapter 2.[34] However, as with DOPA–β2, the chelation/reconstitution procedure leads to destruction of the DOPA probe. Therefore, increasing the radical content of DOPA–ββ' requires reconstitution of the Y_{122}• on Mesna–activated β2, prior to ligation to DOPA–22mer peptide. The procedure developed to generate high radical content DOPA–ββ' is shown in Figure 3–21. In this method, Mesna–activated β2, generated by intein chemistry, is subjected to reductive chelation followed by treatment with the ferroine chelator, ferrozine, to yield apo, Mesna–activated β2. This protein is then reconstituted by the usual procedure generating Mesna–activated β2 with a high Y_{122}• content, which is then ligated to DOPA–22mer peptide at 4°C for 40 h. Incomplete ligation results in homodimeric, truncated and full–length β2, and heterodimeric β2s, which are separated by Mono Q anion exchange chromatography. The elution profile is shown in Figure 3–22A.

The UV–vis spectrum of DOPA–ββ' generated in this fashion is shown in Figure 3–22B. Dropline quantitation yields 1.2 Y_{122}• per DOPA–ββ'. Using this method, 0.6–0.8 mg of pure DOPA–ββ' were isolated per g of wet cell paste. Note that the yields for DOPA–β2 containing a radical content 1.2 Y_{122}•/dimer are much lower due hydrolysis of the Mesna–thioester which occurs throughout the procedure above.

Oxidation of Y_{122} by DOPA•. The experiments to examine the fate of the DOPA• were repeated with DOPA–ββ' containing 1.2 Y_{122}• per dimer. The results are shown in Table 3–7 for the CDP/ATP pair. At 0.5 min, 27 % of the total radical is present as DOPA•, and 73 % as Y_{122}•. By 10 min, <3 % DOPA• remains, but the amount of Y_{122}• has increased by >14 % relative to the 0.5 min signal. These results clearly indicate re–formation of Y_{122}• at the expense of the DOPA•. Importantly, the increase in [Y_{122}•] by >2.4 μM, is well above the lower limit of detection of 0.5–1 μM by EPR methods. The experiment was replicated five times to determine

the error associated with this measurement. From these studies, 36 ± 4 % of the initially formed DOPA• is capable of reoxidizing Y_{122}. The remaining 64 % is quenched by alternative mechanisms.

To examine the generality of this observation, additional experiments were performed with UDP/ATP (data not shown) and with DOPA–β2 with CDP/ATP (Table 3–8) and CDP alone (data not shown). While in all experiments DOPA• is observed, no increase in [Y_{122}•] occurred on quenching of DOPA•. Thus, the conformation of α2/DOPA–ββ' in the presence of CDP/ATP is unique relative to all other combinations of protein, substrate and effector tested.

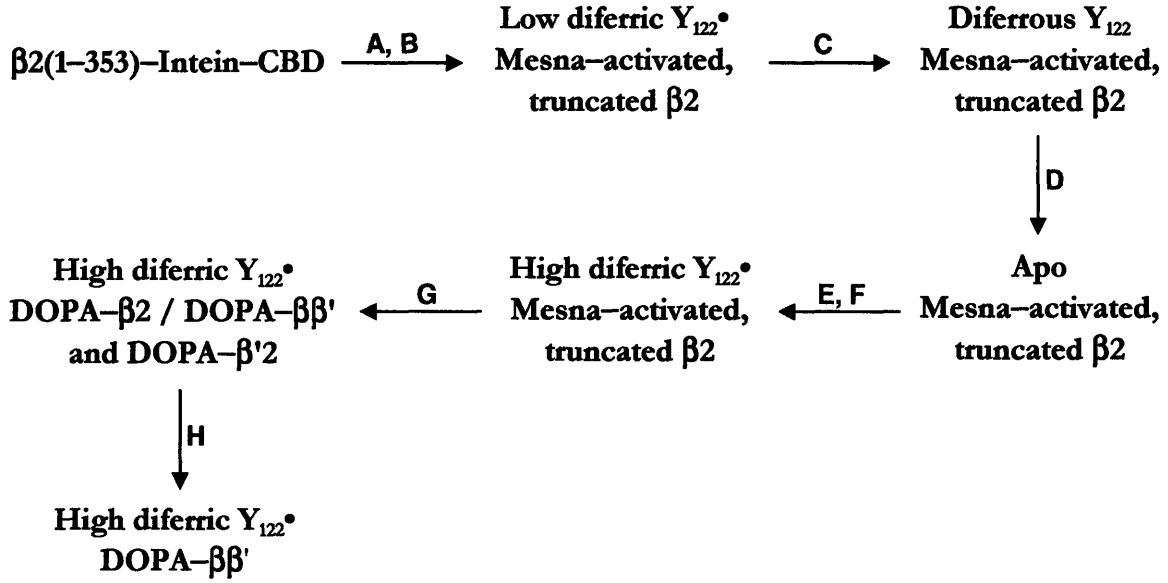

Figure 3–21. Summary of procedures used to generate DOPA–ββ' with a radical content 1.2 Y_{122}• per heterodimer. (A) Expression of β2–intein–CBD and purification by chitin chromatography yields truncated β2 with low Y_{122}• content. (B) Transthioesterification with Mesna followed by desalting on a Sephadex G–25 column. (C) Anaerobic reduction of the diiron Y_{122}• center with $Na_2S_2O_4$ and methyl viologen. (D) Removal of diferrous iron with ferrozine followed by Sephadex G–25 chromatography to generate apo, Mesna–activated truncated β2. (E) Reconstitution of the diferric Y_{122}• cofactor with anaerobic addition of Fe^{II} followed by addition of O_2 yields Mesna–activated, truncated β2 with a high Y_{122}• content. (F) Removal of adventitiously–bound ferric iron by incubation with sodium ascorbate, followed by desalting on a Sephadex G–25 column. (G) Anaerobic ligation to DOPA–22mer peptide. (H) Removal of excess peptide and MonoQ chromatography (see Figure 3–22A) gives DOPA–ββ' with a Y_{122}• content similar to wt β2 prepared by recombinant expression.

Table 3–5. Determination of [DOPA•] and [Y_{122}•] in the reaction of DOPA–ββ'/GDP with α2/TTP on the minute time scale.

Time (min)[a]	[Spin] (μM)[b]	% Y_{122}•[c]	% DOPA•[c]	[Y_{122}•] (μM)	[DOPA•] (μM)
1	10.1	65	35	6.6	3.5
3	9.4	71	29	6.7	2.7
4.5	9.5	71	29	6.7	2.8
6.5	8.6	77	23	6.7	2.0
9	8.3	82	19	6.8	1.6

[a]Reaction time. [b]EPR spin quantitation was performed using Cu^{II} as standard. [c]Spectral point-by-point subtractions were performed using Y_{122}•-DOPA-ββ' as reference. The % of Y_{122}• and DOPA• out of total spin at each time point is shown.

Table 3–6. Determination of [DOPA•] and [Y_{122}•] in the reaction of DOPA–ββ'/CDP with α2 on the minute time scale.

Time (min)[a]	[Spin] (μM)[b]	% Y_{122}•[c]	% DOPA•[c]	[Y_{122}•] (μM)	[DOPA•] (μM)
0	9.1	100		9.1	
1	9.3	73	27	6.8	2.5
2.5	8.6	78	22	6.7	2.0
4	7.8	87	13	6.8	1.0
5.5	7.5	89	11	6.7	0.8
7	7.1	96	4	6.8	0.3
9.5	6.9	100		6.9	0

[a]Reaction time. [b]EPR spin quantitation was performed using Cu^{II} as standard. [c]Spectral point-by-point subtractions were performed using Y_{122}•–DOPA-ββ' as reference. The % of Y_{122}• and DOPA• out of total spin at each time point is shown.

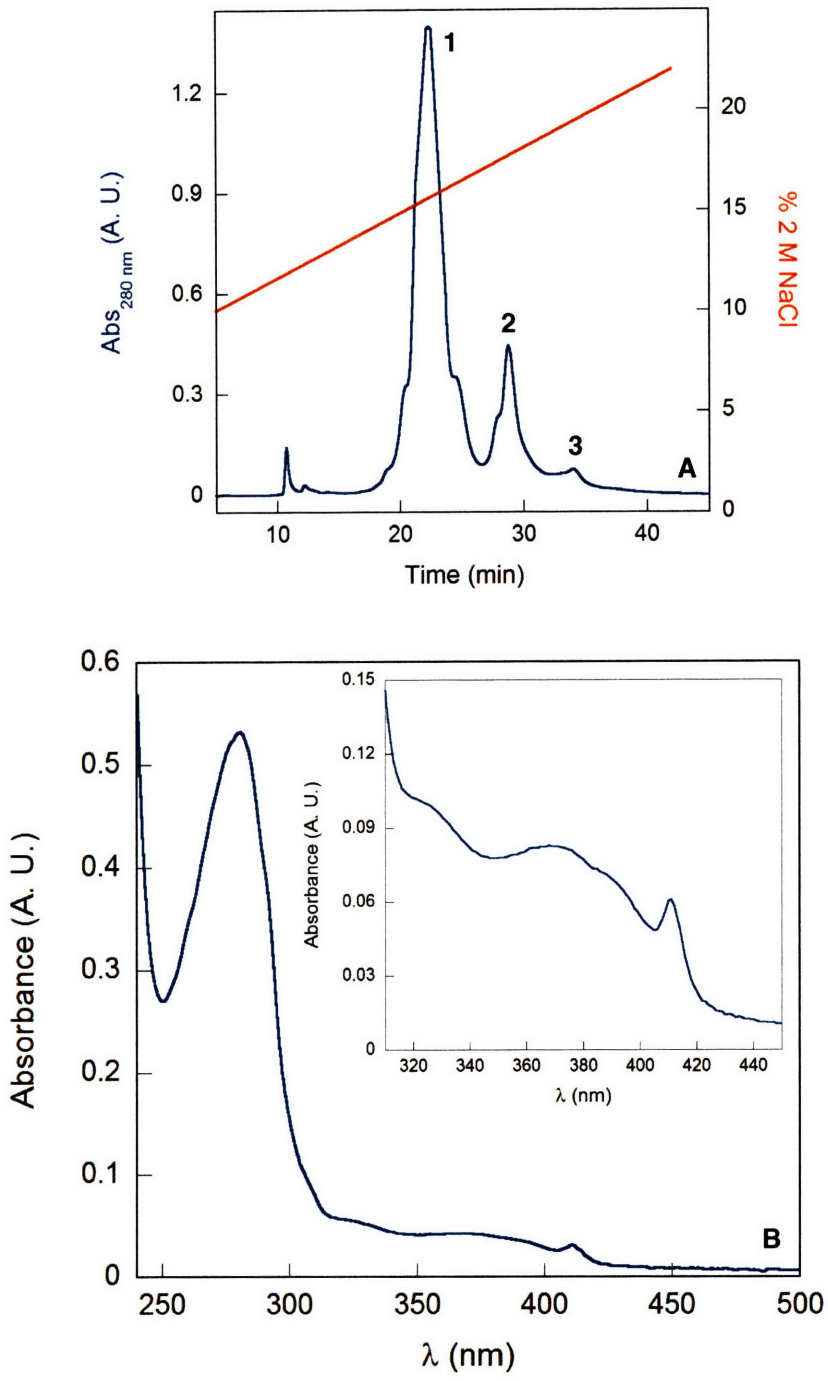

Figure 3–22. Purification of DOPA–ββ' with 1.2 Y_{122}• per heterodimer. (A) MonoQ elution profile of the ligation mixture of DOPA–22mer peptide with high radical content, Mesna–activated β2. The lengthy procedure required for chelation and reconstitution of the diferric Y_{122}• results in major hydrolysis of the Mesna–activated thioester complex and thus low ligation yields: (1) β'2, (2) DOPA-ββ' and (3) DOPA–β2. (B) UV–vis spectrum of DOPA–ββ' with 1.2 Y_{122}• / heterodimer. The inset is a magnified view of the spectral region related to the diferric Y_{122}• center.

Table 3–7. Determination of [DOPA•] and [Y_{122}•] in the reaction of DOPA–ββ'/CDP with α2/ATP on the minute time scale. In this experiment DOPA–ββ' contained 1.2 Y_{122}•/dimer.

Time (min)[a]	[Spin] (μM)[b]	% Y_{122}•[c]	% DOPA•[c]	[Y_{122}•] (μM)	[DOPA•] (μM)
0	22.3	100		22.3	
0.08	22.0	72	28	15.8	6.2
0.5	21.8	73	27	15.9	5.9
2	19.8	83	17	16.4	3.4
5	19.6	87	12	17.1	2.3
10	18.8	> 97	< 3	> 18.2	< 0.5

[a]Reaction time. [b]EPR spin quantitation was performed using Cu^{II} as standard. [c]Spectral point-by-point subtractions were performed using Y_{122}•-DOPA-ββ' as reference. The % of Y_{122}• and DOPA• out of total spin at each time point is shown.

Table 3–8. Determination of [DOPA•] and [Y_{122}•] in the reaction of DOPA–β2/CDP with α2/ATP on the minute time scale.

Time (min)[a]	[Spin] (μM)[b]	% Y_{122}•[c]	% DOPA•[c]	[Y_{122}•] (μM)	[DOPA•] (μM)
0	7.8	100		7.8	
5 sec	7.7	52	48	4	3.7
2.5	7.4	55	45	4.1	3.5
10	4.8	86	15	4.1	0.7

[a]Reaction time. [b]EPR spin quantitation was performed using Cu^{II} as standard. [c]Spectral point-by-point subtractions were performed using Y_{122}•-DOPA-ββ' as reference. The % of Y_{122}• and DOPA• out of total spin at each time point is shown.

DISCUSSION

The results presented in this chapter have important implications for the initial events that occur in nucleotide reduction. A model is presented below, which attempts to incorporate these along with previous results with mechanims–based inhibitors, and structural and mechanistic studies.

An asymmetric model for α2/β2 interaction. The model proposed based on current RNR knowledge is shown in Figure 3–23. First, the features of the model will be described, then the evidence for each step will be elaborated and evaluated using available data below.

In the first step of the model (K_d, Figure 3–23), there is an initial asymmetric interaction between α2 and β2, such that two complexes are formed: one in which the Y_{122}• is in the active αβ pair (E_{active}), and one in which there is no Y_{122}• in the active αβ pair ($E_{inactive}$). After complex formation, radical initiation results in C_{439}• formation (k_c) in E_{active}. This thiyl radical initiates nucleotide reduction to yield dCDP (k_n). A step involved in this chemistry, perhaps disulfide formation, results in hole propagation from C_{439}• in one active site into the adjacent C_{439} (k_x). This second radical transfer step does not require a slow conformational change, but occurs rapidly. In addition, an event involved in this chemistry, perhaps release of dCDP, results in interconversion of complex $E_{inactive}$ into an active complex (k_{int}). This interconversion is fast relative to the conformational change that precedes radical transfer. Conversion of CDP into product in the second α active site results in a disulfide. Upon reverse radical propagation (k_r), the subunits dissociate and α2 must be re–reduced before another catalytic cycle can take place.

This model has three main features: First, the initial interaction in the α2/β2 complex is asymmetric (see below for a definition) leading to hole propagation along only one of two radical transfer pathways, which in the structural model of Uhlin and Eklund are related by C_2–symmetry.[1] Second, dCDP production is cooperative, that is, after formation of the first dCDP, a signal allows rapid generation of the second dCDP and a slow conformational trigger, which was required for the first radical transfer event, is not necessary.[14] And finally, different

conformational states of α2/β2 are in equilibrium and rapidly interconverting under turnover conditions, but not with mutants that do not form deoxynucleotides (see below).[21]

Evidence for the model will be presented below and it will be evaluated using data obtained from studies of different steps in the nucleotide reduction process. These studies include benzophenone–maleimide–labeled β2, mechanism–based inhibitors, such as 2'–azido–2'–deoxyUDP (N_3UDP), 2',2'–difluoro–CDP (F_2CDP) and 2'–fluoromethylene-CDP (FM–CDP), semisynthetic β2 variants, and pre–steady state experiments monitoring dCDP formation with wt RNR in the first turnover. Each of these approaches interferes with different steps of the radical initiation event and provides snapshots at different stages of this process. Y_{356}C–Bpa–β2 (Bpa_{356}–β2) is incompetent in turnover and allows investigation of the initial binding mode to α2. DOPA–β2 and DOPA–ββ' pass the initial binding step but block formation of a thiyl radical in α2 by trapping an intermediate on the pathway. With suicide inhibitors binding of α2 to β2 and radical generation are not perturbed, however, intermediates in the nucleotide reduction process partition in unexpected ways and deoxynucleotides are not formed. Finally, in pre–steady state experiments, binding, radical initiation and active site chemistry are not perturbed. However, turnover may be rapidly quenched before onset of the steady state.

Sources of asymmetry in the α2/β2 complex. A main feature of the model is that the initial interaction between α2 and β2 is asymmetric. There are several sources of asymmetry in RNR and before discussing the model in Figure 3–23, it is important to define what is meant by 'asymmetry' in the current context. Here, asymmetry is defined as a complex, in which the interaction between one αβ pair is different from that between the other αβ pair. That is, the two αβ pairs within the complex are not related by C_2–symmetry, unlike the picture described by the docking model. Asymmetry may also be provided by the distribution of Y_{122}• or by the missing C–terminal tail in β2 (Figure 3–24). However, in the discussion that follows, it is not referring to these types of asymmetry, but to the lack of symmetry between the two αβ pairs in the α2/β2 complex. Recently, Uppsten et al. were able to crystallize the α2/β2 complex of *S. typhimurium* with an unusual oligomeric state and solve the structure to 4 Å resolution.[35] The structure that

has emerged is a good presentation of our definition of asymmetry. It shows that the interaction between one αβ pair in the complex is different from that of the other αβ pair. In this structure, one αβ pair appears to be ready to engage in radical transfer, it is structurally similar to the model of Uhlin and Eklund. The other αβ pair, however, is not interacting at all. Consequently, the distance between the Y• and C• in one αβ pair is 44 Å, in the other, however, it is >60 Å (Figure 3–25).

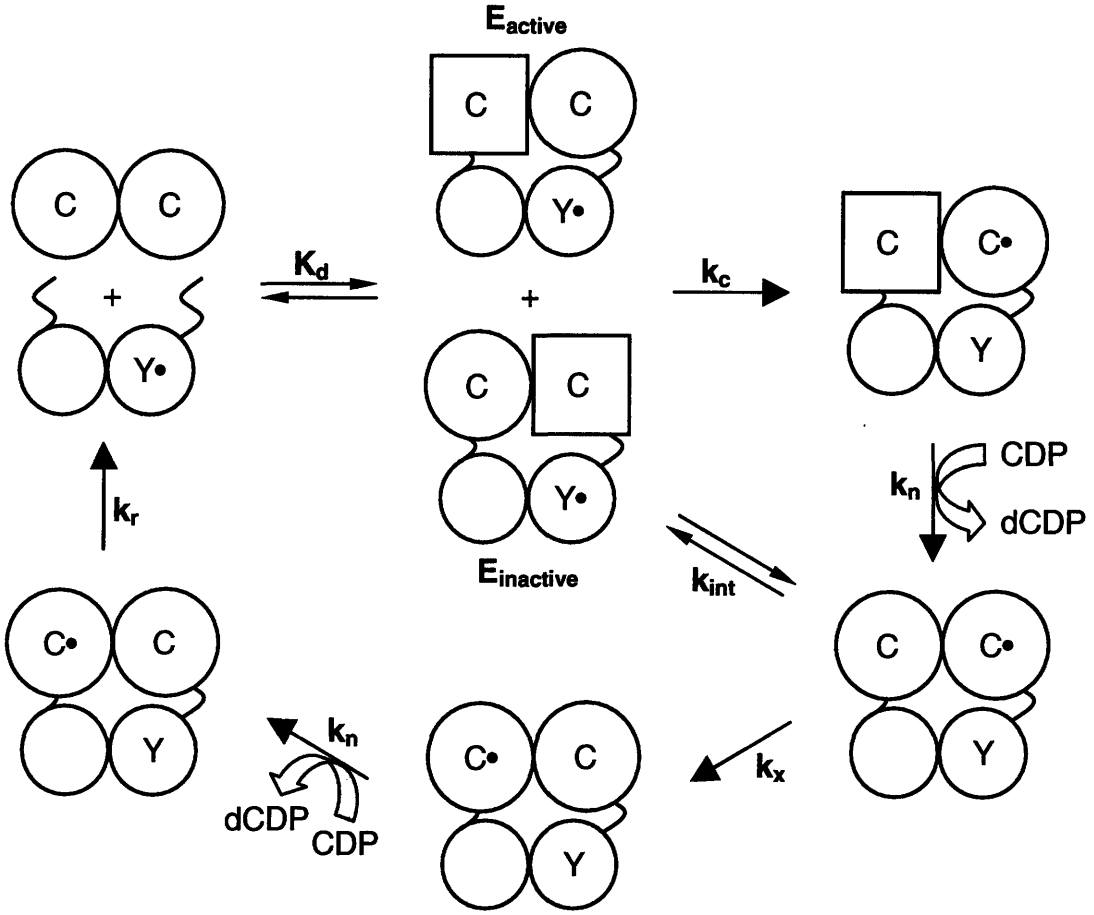

Figure 3–23. Asymmetric model for RNR turnover. The asymmetry shown here is generated upon complex formation (K_d) in the α2 subunit. The square monomeric units are inactive, as a result of an asymmetric interaction, the circle monomeric units are active. Therefore, after complex formation, only half of total Y_{122}• participates in radical migration (k_c). Subsequent to formation of the first dCDP (k_n), a signal acitavates the second subunit, allowing for thiyl radical generation (k_x) and another turnover of CDP. The inactive complex from the initial interaction also equilibrates into an active form. The complex can catalyze a maximum of two nucleotide reduction events before the active site cystines must be re–reduced (k_r), which is, at least, partially rate limiting in the steady state.

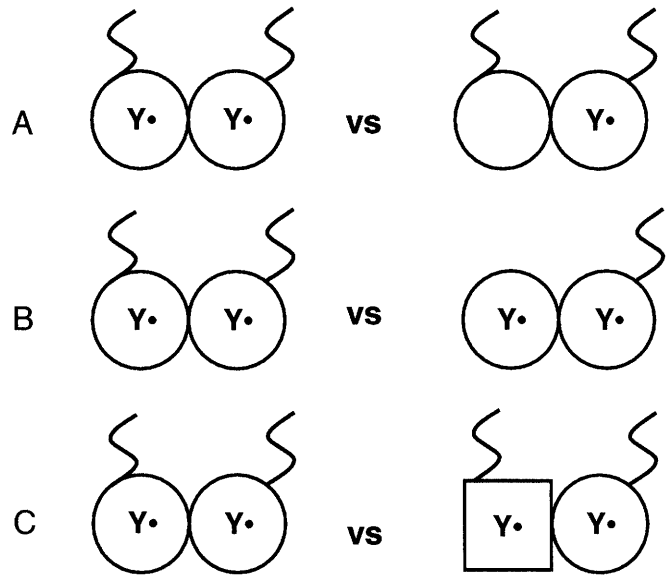

Figure 3–24. Sources of asymmetry in *E. coli* RNR. Asymmetry may be generated by distribution of the Y_{122}• cofactor (A), by removal of the C–terminal tail (B), or by an asymmetric interaction that renders one of the monomeric units inactive (C). Note that in our model, (C) occurs upon α2/β2 complex formation as shown in Figure 3–23.

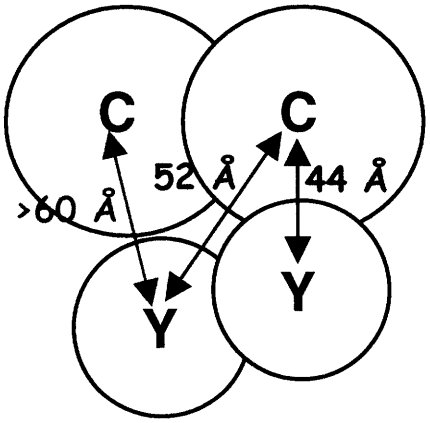

Figure 3–25. Diagram of the asymmetric α2/β2 complex structure from *S. typhimurium* determined by Uppsten et al at 4 Å resolution. The distances shown were determined in Pymol (pdb code 2BQ1) from the phenolic oxygen atom of Y_{105} (*E. coli* equiv of Y_{122}) to the sulfur atom of C_{388} (*E.coli* equiv C_{439}).

Y_{122}• distribution and aggregation state. Before discussing and evaluating the features of the model, two important issues need to be addressed. The distribution of Y_{122}•s and the aggregation state of the α2/β2 complex as a function of concentration and nucleotides are two major unresolved issues in all class I RNRs. For the discussion below, we will assume a 1:1 complex of α2/β2, regardless of the initial subunit concentrations, and a random distribution of Y_{122}•s within β2. These are further elaborated below in this section.

Three different scenarios regarding the Y_{122}• distribution are possible. Sjöberg and colleagues have previously assumed a "one or none" Y_{122}•/β2 scenario, that is each β2 contains either one Y_{122}•/dimer or none.[13] The maximal Y_{122}• content is 1/β2. This distribution was assumed because their wt β2 preparation routinely yielded one Y_{122}•/dimer. Mutants that had a lower radical content were thought to contain a certain population that carried zero Y_{122}•s/dimer. While this simplifies analysis of biochemical experiments, it does not explain the normal stoichiometry of ~1.2 Y_{122}•/β2 obtained as expression and purification methods have been optimized over the years. It also is inconsistent with recent PELDOR results, which detect the weak dipolar coupling between two Y_{122}•s in β2.[24] Quantitative PELDOR analysis, would be the ideal method for measuring the distribution of Y_{122}•s; however, such methods have yet to be established.

An alternative scenario for Y_{122}• distribution would be an 'all or none case', i.e. each β2 contains either 2 Y_{122}•s/β2 or none. The relative proportion of each of these populations would then determine the ensemble average Y_{122}• content. Biochemically, such a distribution may come about if there exists stringent cooperativity between the two Y_{122}• sites in β2, that is each time one β is loaded with Y_{122}•, cofactor assembly in its adjacent momomer is much more likely than in another β2. This model is in accord with recent reconstitution experiments with YfaE, an important enzyme in the assembly and maintenance of the diiron Y_{122}• cofactor in vivo, which yield ~2 Y_{122}•s/β2.[36,37] This scenario also explains the observation of PELDOR signals between the two Y_{122}•s even at low β2 concentrations. However, there is also evidence that may argue against such a distribution. First, studies by Pierce et al. using Mn^{II} as a probe indicate negative

cooperativity between two monomers of β2; that is, after cofactor assembly in one monomer, assembly in the adjacent monomer is less likely than in another β2.[38] Pierce et al. also argue that the substoichiometric Fe content is a result of this negative cooperativity. However, the relevance of these studies to our β2s, which in most cases are assembled in vivo, is unclear. Further, the 'all or none' scenario may be inconsistent with pre–steady state experiments, which have revealed 1.5 ± 0.3 dCDP per Y_{122}• in a single kinetic phase (see below). However, the scatter in the pre–steady state kinetic data does not allow this scenario to be eliminated.[14]

As noted above, this discussion will assume that the Y_{122}• is statistically distributed among β2, that is, in each β2 preparation, there are populations that contain 0, 1 or 2 Y_{122}•s/dimer. The relative proportions of these are statistically determined. The observation of a PELDOR signal requires a certain population with 2 Y_{122}•s per β2. The observation of 1.5 ± 0.3 dCDP per Y_{122}• requires a certain population of 1 Y_{122}• per β2. Therefore, a random distribution of Y_{122}•s is a compromise between the two extreme scenarios discussed above and reconciles results from PELDOR studies, the stoichiometry of 1.2 Y_{122}•/β2 as well as results by Ge et al.[14]

The consequences of a statistical distribution of Y_{122}• are shown in Figure 3–26 for DOPA–β2, DOPA–ββ' and wt β2. Using a radical content of 0.3 for DOPA–β2, each monomer has (0.3/2) a 15 % chance of containing a Y_{122}•. Therefore, 2.25 % (0.15^2) of total protein will have two Y_{122}• per DOPA–β2, 25.5 % ($2 \times 0.15 \times 0.85$) will have 1 Y_{122}• per DOPA–β2 and the remaining 72.25 % (0.85^2) will contain no Y_{122}•. This indicates there are (25.5/2.25) ~11 times more DOPA–β2 with 1 Y_{122}• per dimer than with 2 Y_{122}•s per dimer, i.e. the vast majority of radical containing protein has 1 Y_{122}• per DOPA–β2. Therefore, the contribution form the 2.25 % may be ignored. The same analysis may be applied to DOPA–ββ', demonstrating that 3.4 %, 30.2 % and 66.4 % of total protein contains 2, 1 and 0 Y_{122}•s per DOPA–ββ', respectively. Figure 3–26 also shows the distribution of Y_{122}• in wt β2.

A second problem is that the quarternary structure of the active complex as a function of concentration and bound nucleotides is not understood. *E. coli* α2 alone can be a monomer or a dimer. When the active site Cys residues are oxidized, it is primarily monomeric.[39] *E. coli* β2 is

always dimeric, when its diiron Y_{122}• cofactor is assembled. In the apo form, it is also dimeric, however, the monomers can exchange. At low concentrations, the α2/β2 complex consists of a 1:1 dimer of each subunit. Experiments previously performed in our lab indicate that the rate determining step in turnover shifts from a conformational change at low complex concentrations, to the re–reduction step, at high concentrations, perhaps indicative of changes in the quarternary structure of α2/β2 as a function of concentration.[14] To simplify the discussion below, a 1:1 complex between α2 and β2 is assumed under all experimental conditions.

Initial asymmetric interaction in DOPA–β2/α2 and DOPA–ββ'/α2. The first step of the model consists of an initial asymmetric interaction. A strong case can be made for this step with DOPA–β2 and DOPA–ββ'. Part of this evidence was presented in Chapter 2, where only 48 ± 4 % of initial Y_{122}• generated a $DOPA_{356}$•; the other ~52 % of the Y_{122}• remained unreacted (Table 3–3). This proposal was assessed by PELDOR experiments, where an interaction was observed only between Y_{122}•–DOPA•, but not between DOPA•–DOPA• pairs. The quarternary structure is not known at concentrations of 0.25–0.3 mM, which was used for PELDOR experiments; but, as noted above we will assume a 1:1 complex. In addition, a lower limit of detection in PELDOR experiments has yet to be established. Nevertheless, our interpretation of the lack of detectable interaction between DOPA•–DOPA• in the PELDOR studies is that in the first turnover, radical initiation occurs along only one of two possible pathways (Figures 2–23 & 2–26), that is radical migration is not synonymous or synchronous across both pathways.

Several observations, presented in this Chapter, further support an initial asymmetric interaction: SF UV–vis and EPR experiments demonstrate that only 27 ± 5 % of total initial Y_{122}• is trapped as DOPA• (Table 3–3). Compared with DOPA–β2, this corresponds to an approximately 2–fold (1.8 ± 0.2) lower yield in DOPA• formation. One element of asymmetry is provided by the subunit interaction, leading to ~50 % of DOPA• formation with DOPA–β2. With DOPA–ββ' additional asymmetry is provided by removal of the last 22 residues in the β'–monomer. Therefore, the observed stoichiometry of DOPA• formation is rationalized as shown in Figure 3–27 and is consistent with initial asymmetry in the complex.

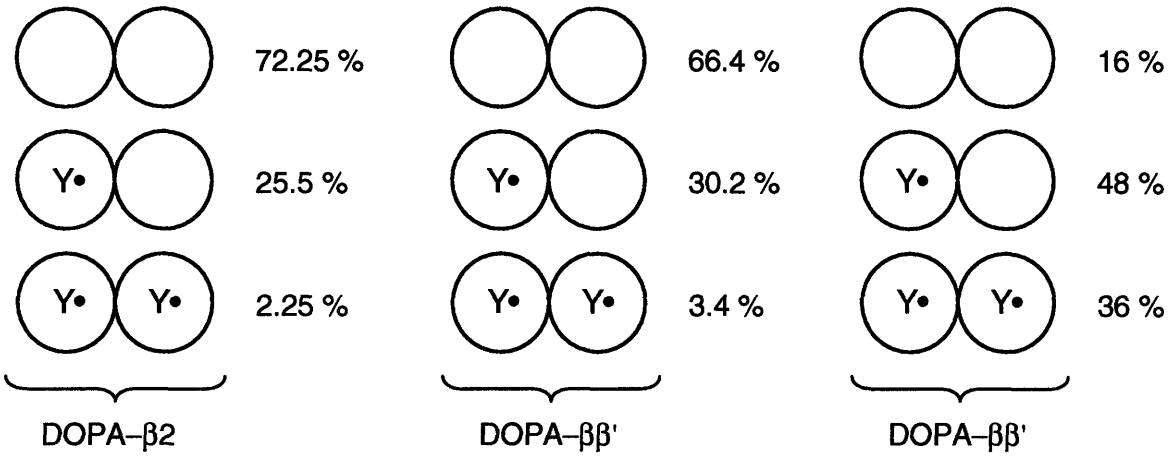

Figure 3–26. Statistical distribution of Y_{122}• in DOPA–β2, DOPA–ββ' and wt β2. The radical contents were 0.3, 0.37 and 1.2 per DOPA–β2, DOPA–ββ' and wt β2 respectively. The % of total protein containing 0, 1 or 2 Y_{122}•s per dimer is indicated.

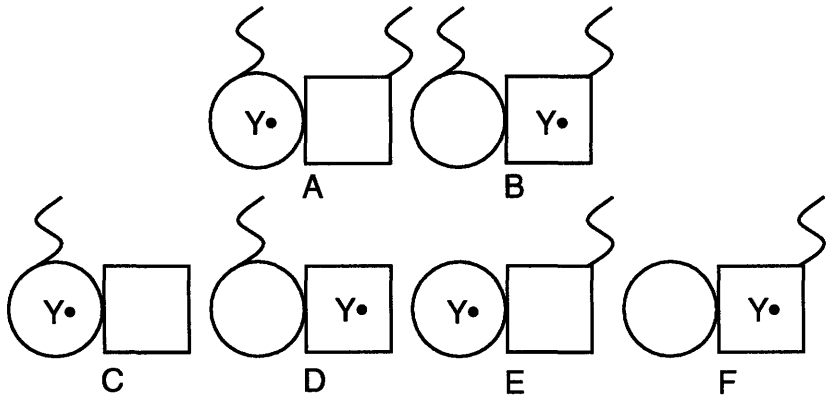

Figure 3–27. Current working hypothesis to explain yields of $DOPA_{356}$• with DOPA–ββ' and DOPA–β2. DOPA amino acid has been omitted from the diagram for clarity. In this model, α2 has been omitted for clarity and the asymmetry is shown in the β subunits. Here, only one of the monomers in the DOPA–β2 dimer is active (circle), whereas the other is inactive (square) as a result of an asymmetric interaction. Thus, conformer (A) of full-length DOPA–β2 traps a DOPA•, while conformer (B) remains inactive, resulting in 50 % DOPA• formation. In DOPA–ββ', only (C) leads to generation of a DOPA•, whereas (D), (E) and (F) are inactive due to absence of the C–terminal tail or of the essential Y_{122}•; hence 25 % of total Y_{122}• is trapped.

In addition, X–band EPR and SF UV–vis analysis presented in this chapter show that the DOPA•–ββ' resides in a local environment which is very similar to that of DOPA•–β2 (Figures 3–7 & 3–16). Moreover, DOPA–ββ' preserves the essential conformational changes which allow for kinetically competent DOPA• formation in a local environment which maintains communication with the α2 subunit. It was shown in Chapter 2, that binding of different substrate/effector pairs influences the conformation of DOPA•–β2. The experiments here show that substrate/effector pairs in the DOPA–ββ'/α2 complex have a similar effect on DOPA•–ββ' as evidenced by the EPR spectrum of DOPA•–ββ', which is very similar to that of DOPA•–β2 regardless of the substrate/effector pair bound in α2. Accordingly, allosteric changes caused by binding of substrate and effector are transmitted to the subunit interface by contacts between an αβ pair in the complex, rather than diagonally across the subunit interface.

PELDOR measurements in the presence of all four substrate/effector pairs yield a distance of 30.6 ± 0.5 Å, very similar to the distance measured in DOPA–β2 (Figure 3–28). This suggests that the β'–monomer in DOPA•–ββ' maintains a structure similar to the second β–monomer in DOPA•–β2. Thus, despite the presence of the C–terminal tail in DOPA–β2, the position of the second β–monomer appears to be similar to the β'–monomer, which cannot interact with α2. This suggests that radical transfer along on αβ pair commences as soon as β2 binds α2 and before interaction in the other αβ pair is established. In addition, deletion of the C–terminal tail in DOPA–ββ' does not affect the stability of the DOPA• as the half–life for DOPA•–ββ' is 6.5 min and 5 min in the presence of GDP/TTP and CDP/ATP, respectively, similar to that determined for DOPA•–β2.

In summary, the observations in the previous and in this chapter regarding the stoichiometry of DOPA• formation, environment of the DOPA• in DOPA–β2 and DOPA–ββ', the stability of the DOPA• and PELDOR studies are all consistent with an initial asymmetric interaction with α2.

Structural source of initial asymmetric interaction. What might be the cause of this initial asymmetry in α2/β2 complex formation? Structural studies with holo and apo β2 suggest

that it contains C_2–symmetry along the dimer interface.[3,40] In these structures, the C–terminal tail is never resolved due to thermal instability, suggesting that it is disordered, rather than a source of asymmetry. Structural studies with α2 also suggest that it contains C_2–symmetry along the dimer interface.[1,4] Binding studies with substrate, product and allosteric effector by show that it contains ~2 binding sites per dimer, suggesting that both monomers are capable of binding substrate and effector.[41,42,43] These binding studies are normally carried out with α2 alone. An interesting experiment was performed by Ehrenberg. They used [5–F]–dCDP to examine binding to α2 by NMR methods.[10] They found that α2 contained 2 binding sites for this product analogue; however, the number of sites was halved, to 0.9 ± 0.1, when β2 was added. A similar result was obtained with dCDP. Bases on these results, we propose that the asymmetry arises upon complex formation between α2 and β2, similar to the two–step binding model suggested by Sjöberg et al, which was described in the Introduction. However, the nature of this asymmetry remains unresolved.

Evidence for asymmetry from other experiments. An initial asymmetric interaction has been tested with Bpa_{356}–β2 experiments. The caveat in these studies is that there are several different conformations, that are in equilibrium, that the interaction between α2 and Bpa_{356}–β2 is not stable, that crosslinking is inefficient and that separation of the different species is difficult by anion exchange chromatogrphay. However, in these experiments, SDS PAGE reveals a major band that corresponds to an α–β crosslinked product. The α2–β2 crosslinked product is below the lower limit of detection (~0.1 μg) by this method. Careful fractionation of the reaction has yielded a product which contains one αβ crosslink and is further accompanied by one equivalent of non–crosslinked α and β. These observations may be interpreted as an initial asymmetric interaction resulting in one crosslinking event per α2/β2 complex.

Results with the mechanism–based inhibitors N_3UDP may be used to test the model in Figure 3–23. An important caveat with N_3UDP is that mechanistic models for this reaction do not involve active site disulfide formation.[9,44,45] Therefore, with N_3UDP, radical propagation and active site chemistry within only one αβ pair should be observed. PELDOR studies with N_3UDP

failed to reveal N•–N• dipolar coupling, though as noted above, a lower limit of detection has not been established.[25] Nevertheless, the Y_{122}•–N• interaction is dominant in these studies. With N_3UDP, inactivation is due to loss of Y_{122}• and α2 activity, where 50 % of the initial Y_{122}• is lost rapidly resulting in N• formation. The N• then decomposes slowly releasing 3–ketodeoxy–nucleotide along with slow loss of the remaining 50 % Y_{122}•. With [5'–^{3}H]–N_3UDP, 0.9–1.1 sugar labels per α2, as well as loss of 0.9 uracil and 0.9 N_2 per α2 is observed.[9] It is possible that the slow decay of N• is associated with active site disulfide formation, thus enabling the remaining Y_{122}• to participate in C_{439}• formation. However, more mechanistic experiments regarding the slow chemistry of N• loss are required to assess this hypothesis. While the slow loss of ~50 % Y_{122}• is not understood, studies with N_3UDP are indicative of half–sites reactivity as only one active site of α2 appears to be involved. In our model this results from an asymmetric interaction.

Similar studies have been carried out with F_2CDP and [1'–^{3}H]–F_2CDP. In this case 1.0 sugar labels per α2 is observed concomitant with loss of 1.0 cytosine per α2. These observations are consistent with asymmetry demonstrating that only 1 active site in α2 is active in the initial turnover.[8] Presumably, the signal that activates the second active site has not occurred in the chemistry with F_2CDP, though this has yet to be determined. In this case 100 % of α2 activity is lost in multi–phasic fashion and the kinetics of this loss is not understood. Further assessment of the reactions that ensue with F_2CDP requires the detailed mechanism of inactivation, which to date has not been elucidated.

Observations with FM–CDP may be more difficult to reconcile. In this case, with 1 and 2 equivalent of inhibitor per α2, 65 % and 80 % loss of Y_{122}•, and 20 % and 100 % loss of α2 activity is observed in multi–phasic fashion, respectively.[7] With [5'–^{3}H]–FM–CDP and [6–^{14}C]–FM–CDP, 1.2–1.4 and 1.0 labels per α2 is observed, respectively. In addition, 1.4 and 0.5 equivalents of fluoride and cytosine are lost, respectively. FM–CDP inhibition has been proposed to involve partitioning between multiple pathways. Some of these involve active site disulfide radical formation, whereas others do not. Given that multiple pathways are involved,

however, and that the partitioning ratio between these pathways is unknown, it is difficult to assess our model using results with this inhibitor.

Cooperativity in dCDP formation. The second main feature of the model is cooperative formation of dCDP. Here, with cooperative, we mean that the second equivalent of dCDP per α2 does not require a slow conformational change. Evidence for cooperativity in dCDP formation comes mainly from pre–steady state analysis of the wt α2/β2 reaction and the requirement for an initially asymmetrical interaction. Ge et al. demonstrated that 1.8 ± 0.4 (1.4–2.2) dCDPs are produced per α2 in a single kinetic phase. Because a similar result was obtained with $C_{754}/C_{759}S$–α2, both active sites in α2 must be operative.[14] The evidence discussed above shows that both radical transfer pathways do not propagate at the same time. Therefore, for 1.8 equiv. of dCDP to be produced in the same kinetic phase, the additional hole migration event, required for the second dCDP in the first turnover, must occur without a rate–determining conformational change. Moreover, the observation of 1.5 dCDP per Y_{122}• requires transport of the radical to both α2 active sites, even in populations of β2 that contain only 1 Y_{122}•/dimer. As discussed before by Ge et al., this may occur at W_{48}, which are 17 Å apart in the docking model. Alternatively, this may occur at Y_{356}, the position of which has not been defined.

Following from the arguments above, there must be a signal that transports the oxidizing equivalent into the second active site of α2 (for β2 with 1 Y_{122}•) or initiates radical transfer within the second pathway (for β2 with 2 Y_{122}•). Several candidate events may be considered: release of product from the first radical migration/active site chemistry event, reverse hole migration and reformation of Y_{122}•, or disulfide bond formation in the active site between C_{225} and C_{462}. Interestingly, comparison of oxidized and reduced structures of α2 shows that C_{462} moves 7 Å upon oxidation, which leads to other changes in β sheet interactions at C_{462}, as well as to movements in neighboring strands.[4] Therefore, we favor disulfide formation in the active site of α2 as the signal that promotes radical transfer diagonally across the interface of the two αβ pairs. However, the lack of data and difficulty in studying this physical switch prevents a more thorough assessment of the other two options.

Multiple conformations and fast interconversion. The third main feature of the model is the interconversion of conformational states during turnover (k_{int}). Initial studies by Brown, Reichard and Thelander demonstrated multiple aggregation states of α2 and α2/β2 in the presence of various nucleotides and as a function of active site Cys oxidation state.[46,39] The SF UV–vis data presented in Chapter 2 have highlighted the propensity of RNR to exist in various conformational states. Furthermore, EPR data of DOPA•–β2 and DOPA•ββ' have shown that nucleotides have a discernible effect on the structure and local environment of the α2/β2 interface. Conformational flexibility is a hallmark of RNRs, as they must coordinate the allosteric regulation by several (d)NTPs to reduction of four NDPs. Multiple non–interconverting conformations have been observed with DOPA–β2, DOPA–ββ' (in the presence of GDP/TTP) and even with the mechanism–based inhibitors, where partitioning of reaction intermediates may be linked to conformations of the complex. However, the requirement for 1.8 dCDPs per α2 suggests that in the first turnover, and subsequently under multiple turnover conditions, these various conformational states converge to produce dCDP in a cooperative manner *in the wt reaction.* Therefore, after an initial asymmetric interaction, where half of the complex population does not participate in radical initiation, these 'inactive' complexes must rapidly interconvert into conformations which are competent in turnover (k_{int}, Figure 3–23). This interconversion is a direct consequence of the asymmetrical interaction and observation of 1.8 dCDP per α2. In fact, the latter can only occur if all populations that contain 2 Y_{122}•/β2 produce 2 dCDP molecules (2 × 0.36 – see Fig. 3–26) and all populations containing 1 Y_{122}•/β2 also produce 2 dCDP molecules per α2 (2 × 0.48 – see Fig. 3–26) leading to (0.72 + 0.96 =) 1.7 dCDP per α2.

Direct observation of a fast interconversion, relative to the rate–determining physical step that gates hole propagation, was made with DOPA–ββ' (Figures 3–9 & 3–10). A weak interaction between DOPA–ββ' and α2 dictates that the majority of DOPA–ββ' is initially not complexed. However, SF UV–vis and EPR experiments demonstrate that all possible DOPA•, as described in Figure 3–27, is trapped in a single kinetic phase. Therefore, association of

DOPA–ββ' with α2 and active complex formation must be much faster than the rate–limiting conformational change. Kinetic simulations, where fast equilibration of free DOPA–ββ' and α2 was assumed, were consistent with this model (Figure 3–10).

Testing the asymmetry model. In summary, a model has been proposed that attempts to reconcile observations from decades of research using various approaches. Evidence with DOPA–β2, DOPA–ββ', pre–steady state experiments and studies with mechanism–based inhibitors are consistent with this model. Additional experiments are required to test and refine the model in Figure 3–23. Fluorescence binding studies with ββ' may further test cooperative binding and asymmetric interaction. In these studies, we would expect the K_d of heterodimeric β2 to be similar to that of a peptide containing the last 30 residues of β2. Single turnover experiments with heterodimeric β2, i.e. Y_{356}F/wt ββ', would be informative in testing k_x and k_{int} in Figure 3–23, as would pre–steady state analysis of ββ', where the β'–monomer is truncated. In the former case, the results would show whether radical transfer diagonally across the αβ pairs occurs at Y_{356}; in the latter case, we would expect to see ½ of dCDP per α2 in one kinetic phase relative to the wt reaction. In addition, studies with β2, where one monomer contains protonated Y and the other contains deuterated Y may allow direct observation of radical transfer diagonally across the αβ pair interface after a single turnover (k_x, Figure 3–24).

Reverse radical migration in DOPA•–ββ'/α2. In this chapter, we also presented further characterization of the DOPA•. Specifically, the fate of the DOPA• was monitored upon incubation at 25°C or upon rapid mixing with HU. Results in the former experiment demonstrate, for the first time, that 36 % of the DOPA• engages in reverse hole propagation highlighting the reversible nature of the radical initiation pathway. Experiments with HU show that it can directly interfere with the radical propagation event, as previously proposed by Karlsson et al.

Initial experiments monitoring the fate of DOPA• showed an unexpected increase in the [Y_{122}•] in the presence of CDP/ATP. However, due to the low radical content of DOPA–ββ' (0.37), the increase was close to the lower limit of quantitation by EPR methods. Efforts to

increase the population of the α2/DOPA•–ββ' complex participating in reverse radical transfer failed. Therefore, a new protocol was necessary which would allow us to increase the Y_{122}• content of DOPA–ββ' in order to obtain better evidence for reverse hole migration. This has been difficult because the standard protocol reported by Atkin et al. leads to destruction of the DOPA probe.[34]

We devised a method based on reductive chelation of the diiron center, which was previously developed by Perez et al. In this procedure, the Y_{122}• is reduced with hydroxylamine and the diiron center is reduced and removed using $Na_2S_2O_4$/methyl viologen and the ferrous chelator ferrozine, respectively. Reconstitution of Y_{122}• on trunctated Mesna–activated β2, before DOPA–22mer ligation, ensures that DOPA does not interfere with the redox reactions involved in Y_{122}• assembly.

With DOPA–ββ', containing 1.2 Y_{122}•, clear evidence for reverse hole migration was obtained. The generality of this observation was tested by performing reactions with CDP alone, GDP/TTP, GDP alone or UDP/ATP. With all NDP/(d)NTP pairs, a DOPA• was observed with distinct half–lives, indicative of nucleotide–mediated structural changes at the subunit interface. However, reverse hole migration was not observed. Our interpretation of these results is that 36 ± 4 % of the complex with CDP/ATP exists in a specific conformation which results in reverse radical transfer. Steenken and Neta, as discussed in Chapter 2, demonstrated that a benzosemiquinone, and by inference an *o*–semiquinone, cannot oxidize phenol in a bimolecular reaction.[47] Thus, the results with CDP/ATP may suggest that in the conformation that undergoes reverse hole migration, the reduction potential of Y_{122}• and/or $DOPA_{356}$• are perturbed. While a rate constant for reverse radical transfer was not determined, the data indicates that this process is slow. Temperature–dependent studies may reveal whether this is due to the unfavorable thermodynamics of the reaction, i.e. an ET/PCET–limited reaction, or gated by conformational changes.[2,48]

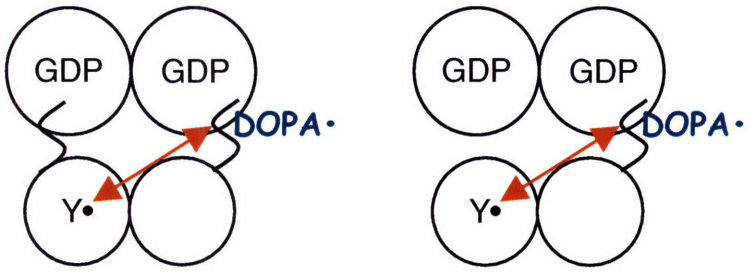

Figure 3–28. Pictorial presentation of PELDOR measurements with $DOPA_{356}$•–β2/α2 (left) and $DOPA_{356}$•–ββ'/α2 (right). In both cases, a distance of 30.6 ± 0.5 Å was determined regardless of the substrate/effector pair bound.

REFERENCES

(1) Uhlin, U.; Eklund, H. *Nature* **1994**, *370*, 523.

(2) Stubbe, J.; Nocera, D. G.; Yee, C. S.; Chang, M. C. Y. *Chem. Rev.* **2003**, *103*, 2167.

(3) Nordlund, P.; Sjöberg, B.-M.; Eklund, H. *Nature* **1990**, *345*, 593.

(4) Eriksson, M.; Uhlin, U.; Ramaswamy, S.; Ekberg, M.; Regnstrom, K.; Sjoberg, B.-M.; Eklund, H. *Structrue* **1997**, *5*, 1077.

(5) Hogbom, M.; Galander, M.; Andersson, M.; Kolberg, M.; Hofbauer, W.; Lassmann, G.; Nordlund, P.; Lendzian, F. *Proc. Natl. Acad. Sci. U.S.A.* **2003**, *100*, 3209.

(6) Stubbe, J.; van der Donk, W. A. *Chem. Rev.* **1998**, *98*, 705.

(7) van der Donk, W. A.; Yu, G.; Silva, D. J.; Stubbe, J.; McCarthy, J. R.; Jarvi, E. T.; Matthews, D. P.; Resvick, R. J.; Wagner, E. *Biochemisty* **1996**, *35*, 8381.

(8) van der Donk, W. A.; Yu, G.; Perez, L.; Sanchez, R. J. ; Stubbe, J. ; Samano, V. ; Robins, M. J. *Biochemistry* **1998**, *37*, 6419.

(9) Salowe, S. P.; Ator, M. A.; Stubbe, J. *Biochemistry* **1987**, *26*, 3408.

(10) Roy, B.; Decout, J. L.; Beguin, C.; Fontecave, M.; Allard, P.; Kuprin, S.; Ehrenberg, A. *Biochim. Biophys. Acta* **1995**, *1247*, 284.

(11) Climent, I.; Sjöberg, B.-M.; Huang, C. Y. *Biochemistry* **1992**, *31*, 4801.

(12) Climent, I.; Sjöberg, B.-M.; Huang, C. Y. *Biochemistry* **1991**, *30*, 5164.

(13) Sjöberg, B.-M.; Karlsson, M.; Jornvall, H. *J. Biol. Chem.* **1987**, *262*, 9736.

(14) Ge, J.; Yu, G.; Ator, M. A.; Stubbe, J. *Biochemistry* **2003**, *42*, 10071.

(15) Yee, C. S.; Seyedsayamdost, M. R.; Chang, M. C. Y.; Nocera, D. G.; Stubbe, J. *Biochemistry* **2003**, *42*, 14541.

(16) Craw, M.; Chedekel, M. R.; Truscott, T. G.; Land, E. J. *Photochem. Photobiol.* **1984**, *39*, 155.

(17) Ballou, D. P. *Methods Enzymol.* **1978**, *54*, 85.

(18) Ballou, D. P.; Palmer, G. *Anal. Chem.* **1974**, *46*, 1248.

(19) Sahlin, M.; Gräslund, A.; Petersson, L.; Ehrenberg, A.; Sjöberg, B.-M. *Biochemistry* **1989**, *28*, 2618.

(20) Bollinger, Jr. J. M.; Tong, W. H.; Ravi, N.; Huynh, B. H.; Edmondson, D. E.; Stubbe, J. *Methods Enzymol.* **1995**, *258*, 278.

(21) Seyedsayamdost, M. R.; Stubbe, J. *J. Am. Chem. Soc.* **2006**, *128*, 2522.

(22) Wang, J.; Lohman, G. J.; Stubbe, J. *Proc. Natl. Acad. Soc. U.S.A.* **2007**, *104*, 14324.

(23) Ekberg, M.; Potsch, S.; Sandin, E.; Thunnissen, M.; Nordlund, P.; Sahlin, M.; Sjöberg, B.-M. *J. Biol. Chem.* **1998**, *273*, 21003.

(24) Bennati, M.; Weber, A.; Antonic, J.; Perlstein, D. L.; Robblee, J.; Stubbe, J. *J. Am. Chem. Soc.* **2003**, *125*, 14988.

(25) Bennati, M..; Robblee, J. H.; Mugnaini, V.; Stubbe, J.; Freed, J. H.; Borbat, P. *J. Am. Chem. Soc.* **2005**, *127*, 15014.

(26) Rosenkranz, H. S.; Garro, A. J.; Levy, J. A.; Carr, H. S. *Biochim. Biophys. Acta* **1966**, *114*, 501.

(27) Ehrenberg, A.; Reichard, P. *J. Biol. Chem.* **1972**, *247*, 3485.

(28) Elford, H. L.; van't Riet, B. *In Inhibitors of Ribonucleotide Diphosphate Reductase Activity* **1989**. Corey, J. G. and Corey A. H., eds (Pergamon Press, Inc., New York) p. 189.

(29) Nyholm, S.; Thelander, L.; Gräslund, A. *Biochemistry* **1993**, *32*, 11569.

(30) Gerez, C.; Fontecave, M. *Biochemistry* **1992**, *31*, 780.

(31) Karlsson, M.; Sahlin, M.; Sjöberg, B.-M. *J. Biol. Chem.* **1992**, *267*, 12622.

(32) Zlateva, T.; Auaroni, L.; Que, L.; Stankovich, M. T. *J. Biol. Chem.* **2004**, *279*, 18742.

(33) Davydov, A.; Öhrström, M.; Liu, A.; Thelander, L.; Gräslund, A. *Inorganica Chim. Acta* **2002**, *331*, 65.

(34) Atkin, C. L.; Thelander, L.; Reichard, P.; Lang, G. *J. Biol. Chem.* **1973**, *248*, 7464.

(35) Uppsten, M.; Farnegardh, M.; Domkin, V.; Uhlin, U. *J. Mol. Biol.* **2006**, *359*, 365.

(36) Wu, C.-H.; Jiang, W.; Krebs, C.; Stubbe, J. *Biochemistry* **2007**, *46*, 11577.

(37) Ortigosa, A. D.; Hristova, D.; Perlstein, D. L.; Zhang, Z.; Huang, M.; Stubbe, J. *Biochemistry* **2006**, *45*, 12294.

(38) Pierce, B. S.; Elgren, T. E.; Hendrich, M. P. *J. Am. Chem. Soc.* **2003**, *125*, 8748.

(39) Thelander, L.; Reichard, P. *Annu. Rev. Biochem.* **1979**, *48*, 133.

(40) Logan, D. T.; deMare, F.; Persson, B. O.; Slaby, A.; Sjoberg, B.-M.; Nordlund, P. *Biochemistry* **1998**, *37*, 10798.

(41) Brown, N. C.; Reichard, P. *J. Mol. Biol.* **1969**, *46*, 39.

(42) von Dobeln, U.; Reichard, P. *J. Biol. Chem.* **1976**, *251*, 3616.

(43) Ormö, M.; Sjöberg, B.-M. *Anal. Biochem.* **1990**, *189*, 138.

(44) Salowe, S.; Bollinger, Jr. J. M.; Ator, M.; Stubbe, J.; McCraken, J.; Peisach, J.; Samano, M. C.; Robins, M. J. *Biochemistry* **1993**, *32*, 12749.

(45) Fritscher, J.; Artin, E.; Wnuk, S.; Bar, G.; Robblee, J. H.; Kacprzak, S.; Kaupp, M.; Griffin, R. G.; Bennati, M.; Stubbe, J. *J. Am. Chem.* Soc. **2005**, *127*, 7729.

(46) Brown, N. C.; Reichard, P. *J. Mol. Biol.* **1969**, *46*, 25.

(47) Steenken, S.; Neta, P. *J. Phys. Chem.* **1979**, *83*, 1134.

(48) Davidson, V. L. *Acc. Chem. Res.* **2000**, *35*, 119.

CHAPTER 4:

Site–Specific Insertion of 3–Aminotyrosine into Subunit α2 of *E. coli* Ribonucleotide Reductase: Direct Evidence for Involvement of Y_{730} and Y_{731} in Radical Propagation

INTRODUCTION

In all organisms, ribonucleotide reductases (RNRs) catalyze the conversion of nucleotides to 2'–deoxynucleotides, providing the precursors required for DNA biosynthesis and repair.[1-3] The mechanism of nucleotide reduction is conserved in all RNRs and requires formation of a transient active site thiyl radical (C_{439}•).[4,5] However, the mechanism of active site thiyl radical generation, the radical initiation event, is not conserved and provides the basis for distinction between four classes of RNRs.[6-9] A major unresolved mechanistic issue is that of thiyl radical formation in class I RNRs, and presumably in the recently identified class IV RNR. In this Chapter, we report site–specific incorporation of 3–aminotyrosine (NH_2Y) into one of the subunits of *E. coli* RNR and present the insights provided by these mutants into the mechanism of radical initiation.

The *E. coli* class I RNR consists of two homodimeric subunits, α2 and β2, which form an active 1:1 complex during turnover.[10-12] α2 is the business end of the complex. It contains the active site where thiyl radical–mediated nucleotide reduction occurs, as well as multiple allosteric effector binding sites which modulate substrate specificity and turnover rate.[13] β2 houses the stable diferric tyrosyl radical (Y_{122}•)[14-16] cofactor which is required for formation of the transient C_{439}• in the active site of α2.[4-6] The structure of α2[6,17] and β2[18,19] have been solved and a structure containing both subunits has also been reported.[20] A structure of the active α2/β2 complex, however, has remained elusive. From the individual structures of α2 and β2, Uhlin and Eklund have generated a docking model of the α2/β2 complex based on shape and charge complementarities and conserved residues.[6] This model suggests that the Y_{122}• in β2 is located >35 Å away from C_{439} in α2 (Figure 4–1).[21-23] Hole propagation over this long distance requires the involvement of transient amino acid radical intermediates.[24-26] The residues proposed to participate in this pathway are universally conserved in all class I RNRs.

Evidence in support of the long distance between Y_{122}• and C_{439} has recently been obtained from pulsed electron–electron double resonance spectroscopic measurements[27] with a

mechanism based inhibitor.[28-32] The distance obtained from this study is consistent with the docking model and establishes that a large conformational change, that positions Y_{122}• in β2 adjacent to C_{439} in α2, does not occur.[32]

To examine the validity of the proposed pathway, site–directed mutagenesis[33,34] and complementation studies[35] have been carried out. These studies demonstrate that each residue in Figure 4–1 plays an important role in RNR function. However, the absence of activity in these mutants precludes mechanistic investigations.[33,34]

At present, evidence for the involvement of only one of the proposed pathway residues, Y_{356}, is substantial. Demonstration of the involvement of this residue is particularly important as it resides within a disordered region of β2 and hence its distance to W_{48} in β2 and to Y_{731} in α2 is long and not known (Figure 4–1). We have recently been able incorporate unnatural amino acids at residue 356 using expressed protein ligation methods, to generate mechanistically informative mutants.[36,37] In one variant, Y_{356} was replaced with the radical trap 3,4–dihydroxyphenylalanine (DOPA).[38] Studies with $DOPA_{356}$–β2 and α2 in the presence of substrate and/or effector showed formation of a DOPA radical (DOPA•) in a kinetically competent fashion directly demonstrating that residue 356 is redox–active (Chapter 2).[38] We have also employed a DOPA heterodimer, DOPA–ββ′ (where the β′–monomer lacks the C–terminal 22 residues), to show reverse hole migration from residue 356 to Y_{122} (Chapter 3).[39] The most compelling evidence, however, for the redox–active role of Y_{356} has come from a series of F_nY_{356}–β2s (n=2, 3, or 4).[40-43] These F_nY_{356}–β2 derivatives have allowed systematic modulation of the reduction potential and pK_a of this residue, key to unraveling the role of proton–coupled electron transfer within the pathway (see Chapter 6).[21,40] Activity assays of F_nY_{356}–β2s showed that radical initiation, and thus nucleotide reduction, is turned on or off based on the reduction potential difference between the F_nY and Y.[43] In addition, modulation of the pK_a in F_nY–β2s, allowed us to show that there was no obligate coupling between the electron and proton at this residue during radical transport (see Chapter 7).[43] Studies using semi–synthetic β2s have thus defined the function and mechanism of residue 356 in radical propagation.

In contrast, the roles of α2 residues Y_{730} and Y_{731} in radical propagation are still ill–defined. Mutagenesis studies have demonstrated their importance in RNR function.[34,44,45] However, as with residue Y_{356} in β2, the inactivity of these mutants ($Y_{730}F$–α2 and $Y_{731}F$–α2) precluded mechanistic interrogation of the role of Y_{730} and Y_{731} in radical propagation. Furthermore, incorporation of unnatural amino acids into α2 is not feasible by expressed protein ligation given the location of these residues. We have thus sought an alternative method to site–specifically incorporate unnatural amino acids.

We now report evolution of an NH_2Y–specific *Methanococcus jannaschii* aminoacyl–tRNA synthetase (NH_2Y–RS) and its use in vivo with the appropriate *M. jannaschii* amber suppressor tRNA, to incorporate NH_2Y at residues Y_{730} and Y_{731} of the α2 subunit.[46-50] NH_2Y was chosen as a probe because its reduction potential (0.64 V at pH 7.0, Scheme 4–1)[51] is 0.19 V lower than that of Y, indicating that it might act as a radical trap, similar to DOPA, and directly report on participation of residues Y_{730} and Y_{731} in hole migration (Figure 4–1). Furthermore NH_2Y is more stable to oxidation than DOPA, making it a more practical target.[51,52] Using this methodology, 100 mg quantities of each NH_2Y–α2 has been generated. Incubation of $Y_{730}NH_2Y$–α2 (or $Y_{731}NH_2Y$–α2) with β2, substrate and allosteric effector, results in formation of an NH_2Y radical (NH_2Y•) in a kinetically competent fashion as demonstrated by stopped–flow (SF) UV–vis and EPR spectroscopy. Unexpectedly, the NH_2Y–α2s retain the ability to make deoxynucleotides, suggesting that the NH_2Y• observed, occurs during radical propagation in a complex that is competent in nucleotide reduction. These results suggest that direct hydrogen atom transfer is the operative mechanism for hole migration within α2.

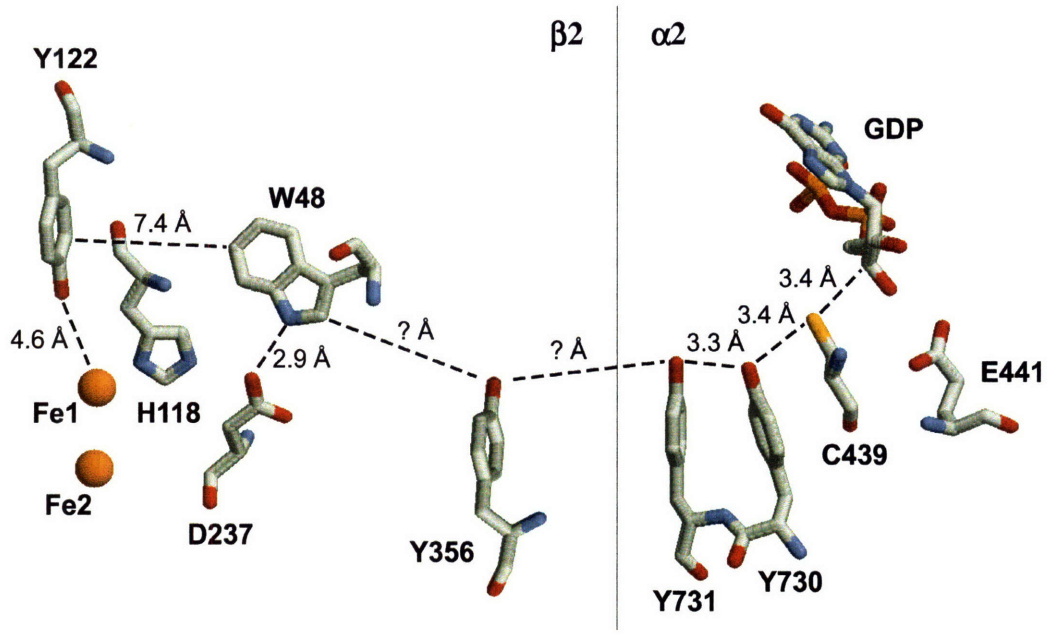

Figure 4–1. The putative radical initiation pathway generated from the docking model of α2 and β2.[6] Y_{356} is not visible in any structures because it lies on the disordered C–terminal tail of β2. Therefore, the distances from Y_{356} to β2–W_{48} and to α2–Y_{731} are not known. Distances on the α2 side are from the structure determined by Uhlin and Eklund,[6] those on the β2 side are from the high–resolution structure of oxidized β2.[19]

Scheme 4–1. One electron oxidation of NH_2Y.[51]

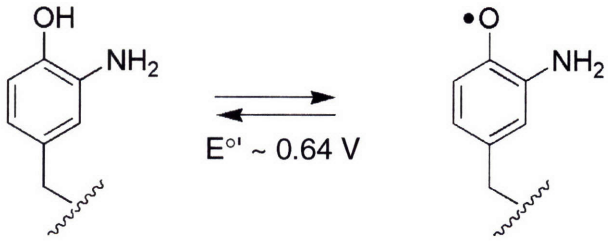

MATERIALS AND METHODS

Materials. Luria Bertani (LB) medium, BactoAgar, 2YT medium, and small and large diameter (100 and 150 mm) Petri dish plates were obtained from Becton–Dickinson. NH_2Y, M9 salts, tetracycline (Tet), kanamycin (Kan), ampicillin (Amp), L–arabinose (L–Ara), chloramphenicol (Cm), L–leucine (Leu), D–biotin, thiamine HCl, ATP, cytidine–5'–diphosphate (CDP), NADPH, ethylenediamine tetraacetic acid (EDTA), glycerol, Bradford Reagent, Sephadex G–25, phenylmethanesulfonyl fluoride (PMSF), streptomycin sulfate, hydroxyurea, 2'–deoxycytidine and 2'–deoxyguanidine–5'–triphosphate (dGTP) were purchased from Sigma–Aldrich. Isopropyl–β–D–thiogalactopyranoside (IPTG), DL–dithiothreitol (DTT) and T4 DNA ligase were from Promega. DH10B competent cells and oligonucleotides were from Invitrogen. Site–directed mutagenesis was carried out with the Quickchange Kit from Stratagene. Calf–intestine alkaline phosphatase (CAP, 20 U/μL) was from Roche. KpnI and XboI restriction enzymes were from NEB. The pTrc vector was a generous gift of Prof. Sinskey (Department of Biology, M. I. T.). The purification of *E. coli* thioredoxin[53] (TR, 40 units/mg), *E. coli* thioredoxin reductase[54] (TRR, 1400 units/mg), and wt β2[55] (6200–7200 nmol/min•mg, 1–1.2 radicals per dimer) have been described. The concentrations of α2, $Y_{730}NH_2Y$–α2 and $Y_{731}NH_2Y$–α2 were determined using $\varepsilon_{280\,nm} = 189\ mM^{-1}cm^{-1}$. Glycerol minimal media leucine (GMML) contains final concentrations of 1 % (v/v) glycerol, 1× M9 salts, 0.05 % (w/v) NaCl, 1 mM $MgSO_4$, 0.1 mM $CaCl_2$ and 0.3 mM L–leucine. RNR assay buffer consists of 50 mM Hepes, 15 mM $MgSO_4$, 1 mM EDTA, pH 7.6.

Qualitative assay for cellular uptake of NH_2Y by LC–MS. The uptake assay was performed as previously described with minor modifications.[48] DH10B *E. coli* cells were grown to saturation at 37°C in GMML in the presence of 1 mM NH_2Y and 0.1 mM DTT and subsequently harvested and lysed as outlined previously. Chromatography of the crude extract was performed on a Zorbax SB–C18 (5 μm, 4.6 × 150 mm) column with a linear gradient from 5 % to 25 % MeCN in 0.1 % TFA solution over 8 min at 0.5 mL/min. Under these conditions,

NH_2Y elutes at ~13 % MeCN. For HPLC–ESI–MS analysis, NH_2Y standard solutions were prepared in water.

Directed evolution of NH_2Y–RS in *E. coli*. Positive and negative selection cycles were carried out as detailed previously.[48] Briefly, plasmid pBK–JYRS encodes a library of *M. jannaschii* TyrRS variants, which are randomized at 6 residues within 6.5 Å of the Tyr binding cleft, under the control of the *E. coli GlnRS* promoter and contains a Kan^R marker.[46] Plasmid pREP/YC–J17 was used for positive selections;[56] it encodes a chloramphenicol acetyl transferase (CAT) gene with a nonessential amber mutation, $Asp_{112}TAG$, and a T7 RNA polymerase (T7 RNAP) gene with two nonessential amber mutations, Met_1TAG and $Gln_{107}TAG$. It also contains a gene for the cognate mutant $tRNA_{CUA}$ ($mutRNA_{CUA}$) that is charged by the library of TyrRSs, a GFPuv gene, the expression of which is driven by T7 RNAP and a Tet^R marker. Plasmid pLWJ17B3 was used for negative selections;[57,58] it encodes a toxic barnase gene with three nonessential amber mutations, Gln_2TAG, $Asp_{44}TAG$ and $Gly_{65}TAG$, under the control of an *Ara* promoter. It also contains the $mutRNA_{CUA}$ gene and an Amp^R marker (Table 4–1).

In each positive selection round, the pBK–JYRS plasmid library, containing the library of mutant TyrRSs, was transformed into *E. coli* DH10B competent cells containing plasmid pREP/YC–J17 by electroporation.[48] The cells were recovered in SOC medium and grown at 37 °C for 1 h. They were then washed twice with GMML and plated onto 6–8 GMML agar plates (150 mm) containing 12 μg/mL Tet, 25 μg/mL Kan, 60 μg/mL chloramphenicol (Cm), 1 mM NH_2Y and 100 μM DTT. DTT was included in all solutions or plates that contained NH_2Y in order to maintain a reducing environment. Plates were incubated at 37 °C for 72 h. Surviving cells were scraped from the plates and pooled into GMML liquid medium. The cells were then subjected to plasmid isolation using the Qiagen Miniprep Kit. The pBK–JYRS library (~3 kb) was separated from pREP/YC–J17 (~10 kb) by agarose gel electrophoresis and extracted from the gel with the Qiagen Gel Extraction Kit. Plasmid DNA was quantitated using $OD_{260\,nm}$.

To perform a negative selection, plasmid DNA isolated from the positive selection was transformed by electroporation into *E. coli* DH10B competent cells containing pLWJ17B3.[48] The

cells were recovered in SOC medium, shaken at 37 °C for 1 h and plated onto LB agar plates containing 100 μg/mL Amp, 50 μg/mL Kan and 0.2 % L–Ara. The plates were incubated at 37 °C for 10–12 h. Surviving cells were recovered and plasmid isolation was performed as described above.

After a total of 6 rounds (3 positive and 3 negative selections), the 4th positive selection was performed by spreading cells onto two sets of plates. One set contained NH_2Y/DTT as described for the positive rounds, the other contained only DTT. The two sets of plates were examined for differences in green fluorescence stemming from GFPuv, the expression of which is driven by T7 RNAP on the positive selection plasmid (Table 4–1). A total of 48 single colonies were selected from the plates which contained NH_2Y/DTT and inoculated into 100 μL GMML in a 96 well plate. One μL from each resulting cell suspension was plated onto two sets of GMML agar plates containing 0, 20, 40, 60, 80 and 110 μg/mL Cm and 0.1 mM DTT in the presence and absence of 1 mM NH_2Y. Plates were incubated at 37 °C for 72–120 h. Candidate clones are able to survive on plates with NH_2Y/DTT and high concentrations of Cm (~100 μg/mL) and emit green fluorescence under UV light, but die on plates without NH_2Y at low concentration of Cm (20 μg/mL). Candidate clones were inoculated into 5 mL 2YT medium containing 24 μg/mL Tet and 50 μg/mL Kan and grown to saturation. Plasmid DNA was then isolated as described above and analyzed by DNA sequencing. The plasmid containing the NH_2Y–RS gene, which was selected by the procedures above, is pBK–NH_2Y–RS.

Expression of K_7NH_2Y–Z–domain. The efficiency of NH_2Y incorporation using pBK–NH_2Y–RS was tested using the C–terminally His–tagged Z–domain of protein A (Z–domain), as previously described.[48] pLEIZ,[57,59] which encodes the Z–domain with an amber stop codon at residue 7 and mutRNA_{CUA}, and pBK–NH_2Y–RS were cotransformed into BL21(DE3) competent cells. All growths were carried out in the presence of Kan (50 μg/mL) and Cm (35 μg/mL) at 37°C. A single colony was inoculated into a 5 mL 2YT medium and grown to saturation (~13 h). One mL of this saturated culture was diluted into 25 mL 2YT medium and grown to saturation overnight (~11 h). Ten mL of this culture were then diluted

into each of 2 × 250 mL GMML medium. When the $OD_{600\ nm}$ reached 0.65 (9 h), one of the cultures was supplemented with NH_2Y and DTT (final concentrations of 1 mM and 0.1 mM, respectively); the other culture was supplemented only with DTT (0.1 mM). Fifteen min after addition of NH_2Y/DTT (or DTT), IPTG was added to each culture to a final concentration of 1 mM. After 5 h, cells were harvested by centrifugation. Z–domain grown in the presence and absence of NH_2Y was then purified by Ni^{2+} affinity chromatography, as previously described, and subjected to SDS PAGE and MALDI–TOF MS analysis.[48] For MALDI–TOF MS analysis, the Z–domain was exchanged into water by dialysis and mass spectra were subsequently obtained under positive ionization mode at the Scripps Center for Mass Spectrometry.

Table 4–1. Vectors used in this study.

Plasmid	Description	Reference
pBK–JYRS	*M. jannaschii* TyrRS library, Kan^R	46
pREP/YC–J17	Positive selection plasmid: CAT ($Asp_{112}TAG$), T7 RNAP (Met_1TAG, $Gln_{107}TAG$), $mutRNA_{CUA}$, GFPuv, Tet^R	56
pLWJ17B3	Negative selection plasmid: barnase (Gln_2TAG, $Asp_{44}TAG$, $Gly_{65}TAG$), $mutRNA_{CUA}$, Amp^R	57, 58
pBK–NH_2Y–RS	NH_2Y–RS, Kan^R	This study
pLEIZ	Z–Domain, Cm^R	57, 59
pTrc–*nrdA*	*nrdA* expression vector: *nrdA* ($Tyr_{730}TAG$ or $Tyr_{731}TAG$) with trc promoter, Amp^R	This study
pAC–NH_2Y–RS	NH_2Y–RS, 6 × $mutRNA_{CUA}$, Tet^R	This study
pMJ1–*nrdA*	*nrdA* expression vector: *nrdA* with T7 promoter, Amp^R	This study
pBAD–*nrdA*	*nrdA* expression vector: *nrdA* with L–Ara promoter, $mutRNA_{CUA}$, Tet^R	This study

Cloning of pTrc–*nrdA*. To generate vector pTrc–*nrdA*, the *nrdA* gene was amplified with primers 1 (5'–AT AAT TGG TAC CCA AAA ACA GGT ACG ACA TAC ATG AAT C–3') and 2 (5'–GCT GCA GGT CGA CTC TAG AGG ATC CCC CCT TCT TAT C–3') using Pfu Turbo polymerase. The primers contain KpnI and XboI cut sites at the 5' and 3' ends of the gene (underlined), respectively. The fragment was purified using the PCR Purification Kit from Qiagen. The isolated DNA was then incubated with KpnI and XboI, the resulting products separated on an agarose gel, and extracted with the Qiagen Gel Extraction Kit. The gene fragment was ligated into pTrc, which had been cut with the same restriction enzymes. Incubation of the insert–vector in a ratio of 3:1 and ligation with T4 DNA ligase at 16°C for 30 min resulted in pTrc–*nrdA*. Generation of pTrc–*nrdA* was performed by Clement Chan.

Expression of wt α2 from vector pTrc–*nrdA* was performed in BL21(DE3) cells as previously described for expression from plasmid pMJ1–*nrdA* and yielded 3 g of wet cell paste per L culture.[55,60] Purification of α2 (see below) yielded 10 mg of α2 per g of wet cell paste with >95 % purity and a specific activity of 2500 nmol/min•mg as measured by the spectrophotometric RNR assay (see below). Expression of wt α2 from pTrc–*nrdA* was performed by Clement Chan.

Generation of pTrc–*nrdA*$_{730}$TAG and pTrc–*nrdA*$_{731}$TAG. The TAG codon was inserted into position 730 or 731 of the *nrdA* gene in vector pMJ1–*nrdA* using the Stratagene Quickchange Kit. Primers 3 (5'–G GTC AAA ACA CTG TAG TAT CAG AAC ACC CG–3') and 4 (5'–CG GGT GTT CTG ATA CTA CAG TGT TTT GAC C– 3') were used for incorporation of TAG into position 730 of α2. Primers 5 (5'–G GTC AAA ACA CTG TAT TAG CAG AAC ACC CG–3') and 6 (5'–CG GGT GTT CTG CTA ATA CAG TGT TTT GAC C–3') were used for incorporation of TAG into position 731 of α2. The mutations were confirmed by sequencing the entire gene at the MIT Biopolymers Laboratory. The *nrdA*$_{730}$TAG and *nrdA*$_{731}$TAG genes were then amplified with primers 1 and 2 and ligated into vector pTrc as described above for wt *nrdA*.

Cloning of pAC–NH_2Y–RS. The pAC vector is analogous to vector pSup, which has been described, except that it contains the Tet^R selection marker rather than the Cm^R marker.[61] In addition, pAC–NH_2Y–RS contains the NH_2Y–RS gene under control of *glnS'* promoter and *rrnB* terminator and six copies of the $mutRNA_{CUA}$ gene under control of a *proK* promoter and terminator. To generate pAC–NH_2Y–RS, the NH_2Y–RS gene was subcloned into the pAC vector from pBK–NH_2Y–RS using the PstI and NdeI restriction sites, which are 3' and 5' of the NH_2Y–RS gene, respectively. Cloning of pAC–NH_2Y–RS was carried out by Youngha Ryu and Roshan Perrera in the Schultz Lab.

Attempts at expression of $Y_{730}NH_2Y$–α2. In an effort to maximize production of α2 containing NH_2Y, without generation of NH_2Y•, growth conditions were examined at different temperatures, under aerobic and anaerobic conditions and with hydroxyurea in the media to reduce the Y_{122}• in wt β2.

In each case, a single colony of DH10B or BL21(DE3) *E. coli* cells was used to inoculate a 5 mL 2YT small culture. After saturation, this culture was diluted 100–fold into 2 × 100 mL GMML media. When $OD_{600\,nm}$ was ~0.6–0.8, and after the variations detailed below, one flask was supplemented with NH_2Y and DTT to final concentrations of 1 mM and 0.1 mM. The other growth served as the control. After 15 min, expression of NH_2Y–α2 was induced by addition of IPTG to both 100 mL cultures (or 0.2 % (w/v) L–arabinose with expression system (1) – see below). Small aliquots were removed from each flask after a defined time period (5–12 h) and expression of α2 assessed by SDS PAGE analysis in the presence and absence of NH_2Y/DTT.

When the effect of temperature on expression of $Y_{730}NH_2Y$–α2 was tested, growth conditions for the small culture were identical to those above. When $OD_{600\,nm}$ was ~0.6–0.8, the temperature setting was changed to 25 or 30°C. After 15 min, NH_2Y and DTT were added and the growth was continued as described above.

When the effect of Y_{122}•–β2 on expression of $Y_{730}NH_2Y$–α2 was tested, growth conditions for the small culture were identical to those described above. When $OD_{600\,nm}$ was 0.6–0.8, hydroxyurea was added to a final concentration of 65 mM. After 15 min, NH_2Y and

DTT were added to final concentrations of 1 mM and 0.1 mM, respectively. After an additional 15 min, induction was carried out as above. Each hour after induction, the culture was supplemented with an additional 15 mM hydroxyurea.

When the effect of O_2 on expression of $Y_{730}NH_2Y$–α2 was tested, growth conditions for the small culture were identical to those described above. When the small culture was saturated, it was diluted 100–fold into a 250 mL 2YT medium containing the appropriate antibiotics in a 1 L Erlenmeyer flask. At saturation, the culture was diluted 50–fold into 5–7 L GMML medium in a fermenter flask with appropriate antibiotics. When $OD_{600\ nm}$ was 0.6–0.8, the air was replaced with $N_{2(g)}$. After 15 min, NH_2Y and DTT were added to final concentrations of 1 mM and 0.1 mM, respectively, and the growth continued as described above.

Several expression systems were tested: (1) the pBK–NH_2Y–RS/pBAD–α2, in which pBK–NH_2Y–RS carries the NH_2Y–RS gene under control of the constitutive *E. coli* Gln–RS promoter and terminator and a Kan^R marker, and vector pBAD–α2 carries the α2 gene with the appropriate amber codon under control of an L–Ara–inducible promoter and a *rrnB* terminator as well as the $mutRNA_{CUA}$ gene under control of a *lpp* promoter and *rrnC* terminator and a Tet^R marker; (2) The pBK–NH_2Y–RS/pMJ1–*nrdA* vector combination, in which vector pMJ1–*nrdA* carries the *nrdA* gene with the amber codon under control of T7 promoter and terminator and a Amp^R marker. (3) The pAC–NH_2Y–RS/pMJ1–*nrdA* system, where pAC–NH_2Y–RS carries the NH_2Y–RS gene under control of *glnS'* promoter and *rrnB* terminator, six copies of the $mutRNA_{CUA}$ gene under control of a *proK* promoter and terminator and a Tet^R marker (Table 4–1).

Successful expression of $Y_{730}NH_2Y$–α2 and $Y_{731}NH_2Y$–α2. Successful expression of $Y_{730}NH_2Y$-α2 was achieved with the pTrc–$nrdA_{730}$TAG/pAC–NH_2Y–RS expression system, where vector pTrc–$nrdA_{730}$TAG contains the *nrdA* gene with an amber codon at position 730 under control of the *trp/lac* (trc) promoter and *rrnB* terminator and an Amp^R marker. *E. coli* DH10B cells were transformed with vectors pTrc–$nrdA_{730}$TAG and pAC–NH_2Y–RS, and grown at 37°C on LB/Agar plates containing Amp (100 μg/mL) and Tet (25 μg/mL) for two days. All

liquid culture growths contained Amp (100 μg/mL) and Tet (25 μg/mL) and were carried out in a shaker/incubator at 37°C and 200 rpm. A single colony from the plate was inoculated into 5 mL of 2YT medium and grown to saturation (~2 days). The 5 mL saturated culture was then diluted into 180 mL of 2YT medium and grown to saturation (~1 day). Twenty five mL of this culture were then inoculated into each of 6 × 6 L Erlenmeyer flasks, each containing 1 L of GMML medium supplemented with D–biotin (1 μg/mL), thiamine (1 μg/mL) and a 1× heavy metal stock solution. A 1000× heavy metal stock solution contains the following per L as described:[62] 500 mg $MoNa_2O_4 \cdot 2H_2O$, 250 mg $CoCl_2$, 175 mg $CuSO_4 \cdot 5H_2O$, 1 g $MnSO_4 \cdot H_2O$, 8.75 g $MgSO_4 \cdot 7H_2O$, 1.25 g $ZnSO_4 \cdot 7H_2O$, 1.25 g $FeCl_2 \cdot 4H_2O$, 2.5 g $CaCl_2 \cdot 2H_2O$, 1 g H_3BO_3 and 1 M HCl. When $OD_{600\,nm}$ reached 0.6 (12–18 h), NH_2Y and DTT were added to final concentrations of 1 mM and 0.1 mM, respectively. After 15 min, IPTG was added to a final concentration of 1 mM and the growth continued for 4.5 h, at which point the cells were harvested by centrifugation, frozen in liquid N_2 and stored at –80°C. Typically, 1.5 g of wet cell paste were obtained per L culture. Expression of $Y_{731}NH_2Y$–α2 was carried out in identical fashion using vectors pTrc–*nrdA*$_{731}$TAG and pAC–NH_2Y–RS. Expression of $Y_{730}NH_2Y$–α2 and $Y_{731}NH_2Y$–α2 was performed by Clement Chan.

Purification of $Y_{730}NH_2Y$–α2 and $Y_{731}NH_2Y$–α2. NH_2Y–α2s were typically purified from 10 g of wet cell paste. All purification steps were performed at 4°C. Each g of wet cell paste was resuspended in 5 mL of α2 Buffer (50 mM Tris, 1 mM EDTA, pH 7.6) supplemented with 1 mM PMSF and 5 mM DTT. The cells were lysed by passage through a French Pressure cell operating at 14,000 psi. After removal of cell debris by centrifugation (15,000 × g, 35 min, 4°C), DNA was precipitated by dropwise addition of 0.2 volumes of α2 Buffer containing 8 % (w/v) streptomycin sulfate. The mixture was stirred for an additional 15 min and the precipitated DNA was removed by centrifugation (15,000 × g, 35 min, 4°C). Then, 3.9 g of solid $(NH_4)_2SO_4$ was added per 10 mL of supernatant over 15 min (66 % saturation). The solution was stirred for an additional 30 min and the precipitated protein isolated by centrifugation (15,000 × g, 45 min, 4°C). The pellet was re–dissolved in a minimal volume of α2 Buffer and desalted using a

Sephadex G–25 column (1.5 × 25 cm, 45 mL). The desalted protein was loaded at a flow rate of 0.5 mL/min directly onto a dATP column (1.5 × 4 cm, 6 mL), which had been equilibrated in α2 Buffer. The column was washed with 10 column volumes of α2 Buffer. NH_2Y–α2 was then eluted in 3–4 column volumes of α2 Buffer containing 10 mM ATP, 15 mM $MgSO_4$ and 10 mM DTT. ATP was subsequently removed by Sephadex G–25 chromatography. The protein was flash–frozen in small aliquots in liquid N_2 and stored at –80°C. Typically 4–6 mg of pure NH_2Y–α2 were obtained per g of wet cell paste.

Reaction of NH_2Y–α2 with β2, CDP, and ATP monitored by EPR spectroscopy. Pre–reduced wt–α2 or NH_2Y–α2s were generated by incubating each variant (40 μM) with 35 mM DTT at room temperature for 40 min. Hydroxyurea and additional DTT were added to final concentrations of 15 mM, and the incubation continued at room temperature for an additional 20 min. Each protein was then desalted on a Sephadex G–25 column (1.5 × 25 cm, 45 mL), which had been equilibrated in assay buffer (see Materials).

Pre–reduced NH_2Y–α2 and ATP were mixed with wt β2 and CDP in assay buffer to give final concentrations 20–24 μM, 3 mM, 20–24 μM and 1 mM, respectively. The reaction was hand–quenched in liquid N_2 from 10 s to 12 min. EPR spectra were recorded at 77 K in the Department of Chemistry Instrumentation Facility on a Bruker ESP–300 X–band spectrometer equipped with a quartz finger dewar filled with liquid N_2. EPR parameters were as follows: microwave frequency = 9.34 GHz, power = 30 μW, modulation amplitude = 1.5 G, modulation frequency = 100 kHz, time constant = 5.12 ms, scan time = 41.9 s. Analysis of the resulting spectra was carried out using WinEPR (Bruker) and an in–house written program in Excel. These programs facilitate fractional subtraction of the unreacted Y_{122}• signal from the recorded spectrum, yielding the spectrum of NH_2Y•–α2. The ratio Y_{122}• and NH_2Y• signals was assessed by comparing the double integral intensity of each trace. EPR spin quantitation was carried out using Cu^{II} as standard.[63]

Kinetics of NH_2Y•–α2 formation with β2, CDP and ATP by stopped–flow (SF) UV–vis spectroscopy. SF kinetics was performed on an Applied Photophysics DX. 17MV

instrument equipped with the Pro–Data upgrade using PMT detection at λs indicated in figure legends. The temperature was maintained at 25°C with a Lauda RE106 circulating water bath. Pre–reduced $Y_{730}NH_2Y$–α2 (or $Y_{731}NH_2Y$–α2) and ATP in one syringe were mixed in a 1:1 ratio with wt β2 and CDP from a second syringe to yield final concentrations of 8–10 μM, 3 mM, 8–10 μM and 1 mM, respectively, in assay buffer. Data was collected in split time–base mode. Time courses shown are the average of at least 6 individual traces. For point–by–point reconstruction of the $Y_{730}NH_2Y$•–α2 and $Y_{731}NH_2Y$•–α2 absorption profiles, 2–4 traces were averaged between 305 and 365 nm in 5 nm intervals. The absorption change was corrected for the absorption of Y_{122}• in this region, based on the published ε at these λs,[64-66] and then plotted against λ. Calculation of the ε for $Y_{730}NH_2Y$•–α2 (10500 $M^{-1}cm^{-1}$) and $Y_{731}NH_2Y$•–α2 (11000 $M^{-1}cm^{-1}$) were performed using the ε of Y_{122}• ($\varepsilon_{410\ nm}$ = 3700 $M^{-1}cm^{-1}$)[66] and assuming that consumption of each mole of Y_{122}• leads to formation of one mole of NH_2Y• in α2. Curve fitting was performed with OriginPro or KaleidaGraph Software.

Spectrophotometric and radioactive activity assays for RNR. The spectrophotometric and radioactive RNR assays were performed as described before.[36,43] The concentration of NH_2Y–α2 was 0.2, 1 or 3 μM; β2 was present at a 5–fold molar excess. [5–^{3}H]–CDP (1190 cpm/nmol) was used in the radioactive assay. Radioactive assays were performed by Clement Chan.

Reaction of NH_2Y–α2 with β2, N_3ADP and dGTP monitored by EPR spectroscopy. 2'–Azido–2'–deoxyadenosine–5'–diphosphate (N_3ADP) was previously prepared by Scott Salowe.[60] Pre–reduced $Y_{730}NH_2Y$–α2 ($Y_{731}NH_2Y$–α2 or wt α2) and dGTP were mixed with wt β2 and N_3ADP in assay buffer to yield final concentrations of 20 μM, 1 mM, 20 μM and 250 μM, respectively. The reaction was hand–quenched in liquid N_2 after 20 s. EPR data acquisition and spin quantitation with Cu^{II} were performed as described above. The resulting spectra were analyzed using WinEPR (Bruker) and an in–house written Excel program. Deconvolution of the three signals observed in these experiments was performed by first subtracting the N• signal which has been reported and was reproduced here with the wt α2/β2 reaction. Then, unreacted

Y_{122}• was subtracted from this spectrum, yielding the NH_2Y•–α2 spectrum. The ratio of the three signals was assessed by comparing the double integral intensity of each trace.

RESULTS

Toxicity and uptake of NH_2Y. Evolution of an NH_2Y–specific aminoacyl–tRNA synthetase (RS) requires that NH_2Y is taken up by *E. coli*, that it is not toxic, and that it is not incorporated into proteins by any endogenous RSs. All three requirements were met by NH_2Y. When DH10B *E. coli* cells were grown in liquid GMML medium in the presence of NH_2Y (1 mM) or NH_2Y and DTT (1 mM and 0.1 mM, respectively), NH_2Y was observed in all cell extracts as judged by HPLC and ESI–MS (data not shown).[48] Toxicity of NH_2Y was assessed by growing DH10B *E. coli* cells in liquid GMML medium and on Agar plates in the presence of NH_2Y or NH_2Y/DTT. Growth rates were not significantly affected by the presence of NH_2Y. The presence of DTT however, caused cells to grow at a rate 25–35 % more slowly than those in the presence of only NH_2Y or absence of NH_2Y/DTT (data not shown).

Evolution of an NH_2Y–specific RS. The Schultz lab has developed a robust in vivo method for incorporation of unnatural amino acids into any target protein.[46-50] In this method, the RS is selected from a library of *M. jannaschii* TyrRS mutants. A cognate amber suppressor *M. jannaschii* tRNA, $mutRNA_{CUA}$, does not require modification as the region of interaction between $mutRNA_{CUA}$ and the RSs in the library is not varied.[67] Iterative rounds of positive and negative selections are carried out on the RS library which has been randomized at six residues in and around the Y binding cleft: Tyr32, Leu65, Phe108, Gln109, Asp158 and Leu162. The positive selection is based on suppression of an amber stop codon at a permissive site in the CAT gene in the presence of NH_2Y/DTT and the cognate tRNA (Table 4–1).[46] Surviving clones carry RSs that are functional with the host cell translation machinery and incorporate NH_2Y or other amino acids in response to the amber stop codon. The negative selection is based on lack of suppression of three amber codons in the toxic barnase gene in the absence of NH_2Y (Table 4–1).[68] Surviving clones carry RSs that do not incorporate any natural amino acids in response to the amber stop codon.

After seven selection cycles, 48 colonies were examined for their ability to suppress the amber stop codon. Single colonies containing pBK–NH_2Y–RS and pREP/YC–J17 were picked from the last positive selection (7^{th} round) and plated on GMML agar containing variable concentrations of Cm (0–110 μg/mL) in the presence or absence of NH_2Y. Ability to grow with NH_2Y/DTT indicates that the amber codon in the CAT gene is suppressed by incorporation of NH_2Y. Further, the amber codons in the T7 RNAP gene are suppressed in a similar fashion and drive expression of GFPuv, resulting in emission of green fluorescence, when the cells are irradiated with UV light. The desired colonies are those that grow in high concentrations of Cm (~100 μg/mL) and NH_2Y/DTT and emit green fluorescence upon irradiation, but die at low Cm concentrations (~20 μg/mL) in the absence of NH_2Y. Of the 48 colonies tested, 2 met these criteria and were pursued further.

DNA sequencing of the plasmids from these colonies revealed identical RSs with the following residues at the randomized positions: Gln32, Glu65, Gly108, Leu109, Ser158 and Tyr162. Interestingly, residue 32, a Tyr in wt *M. jannaschii* TyrRS and positioned within 2 Å of the C–atom ortho to the hydroxyl group of bound Tyr ligand, is a Gln in the selected RS.[69,70] The crystal structure of wt *M. jannaschii* TyrRS suggests that the Gln allows accommodation of the *o*-NH_2 group and perhaps provides favorable hydrogen bonding interactions. The RS identified from these clones was used for all subsequent experiments.

Expression of K_7NH_2Y–Z–domain. To test the efficiency and fidelity of NH_2Y incorporation with the selected RS, the C–terminally His–tagged Z–domain protein (Z–domain), with an amber stop codon at the permissive Lys7 residue, served as a model.[57, 71] Expression in the presence of NH_2Y/DTT in GMML medium, yielded 5 mg of Z–domain per L culture after purification. SDS PAGE analysis (Figure 4–2, inset) demonstrated that in the absence of NH_2Y, the amount of Z–domain protein expressed was below the level of detection. The purified protein was subjected to MALDI–TOF MS analysis. Previous studies have shown that the Z–domain is post–translationally modified by removal of the N–terminal Met followed by acetylation of the resulting N–terminal amino acid.[57] Accordingly, MALDI–TOF MS analysis of

Z–domain expressed in the presence of NH_2Y/DTT revealed four peaks with MW = 7812, 7854, 7943 and 7985 Da (Figure 4–2). These features correspond to K_7NH_2Y–Z–domain minus the first Met (MW_{exp}= 7813 Da), its acetylated form (MW_{exp}= 7855 Da), full length K_7NH_2Y–Z–domain (MW_{exp}= 7944 Da) and its acetylated form (MW_{exp}= 7986 Da), respectively. Importantly, no K_7Y–Z–domain was detected (MW_{exp}= 7929 Da for the full length form). Together, the studies with the Z–domain demonstrate that the evolved RS is specific for NH_2Y and is efficient at its incorporation into this target protein.

Expression and purification of NH_2Y–α2s. Having evolved an NH_2Y–specific RS and confirmed the efficiency and fidelity of NH_2Y insertion, we next sought an overexpression system for α2 that is compatible with the plasmid/host requirements for NH_2Y incorporation. Several different growth conditions and expression systems were investigated in an effort to maximize α2 production and NH_2Y insertion at residue 730. Growth under anaerobic conditions or in the presence of hydroxyurea was investigated to minimize the reaction of wt β2 with NH_2Y–α2, which could lead to premature trapping of an NH_2Y• and destruction of the probe. In the former case, the anaerobic class III RNR is operative in *E. coli* and therefore wt class I β2 is not expressed.[1,72] In the latter case, presence of hydroxyurea leads to reduction of the essential Y_{122}• in class I β2 so that it cannot react with NH_2Y–α2.[73,74] Temperature manipulation was also investigated to minimize formation of inclusion bodies.

Three different expression systems were investigated (see Methods for details): (1) pBK–NH_2Y–RS/pBAD–*nrdA*, (2) pBK–NH_2Y–RS/pMJ1–*nrdA* and (3) pAC–NH_2Y–RS/ pMJ1–*nrdA* (see Table 4–1). With system (1), expression of full–length α2 at levels 1.5–fold above endogenous α2 were observed. With system (2), only truncated α2 was observed and with system (3) overproduction of truncated α2 was accompanied by expression of full–length α2 that was similar to endogenous levels of α2 (data not shown). The failed or low levels of expression may be due to limiting $mutRNA_{CUA}$ inside the cell and/or the low levels of expression of α2 from the pBAD–*nrdA* and the pMJ1–*nrdA*.

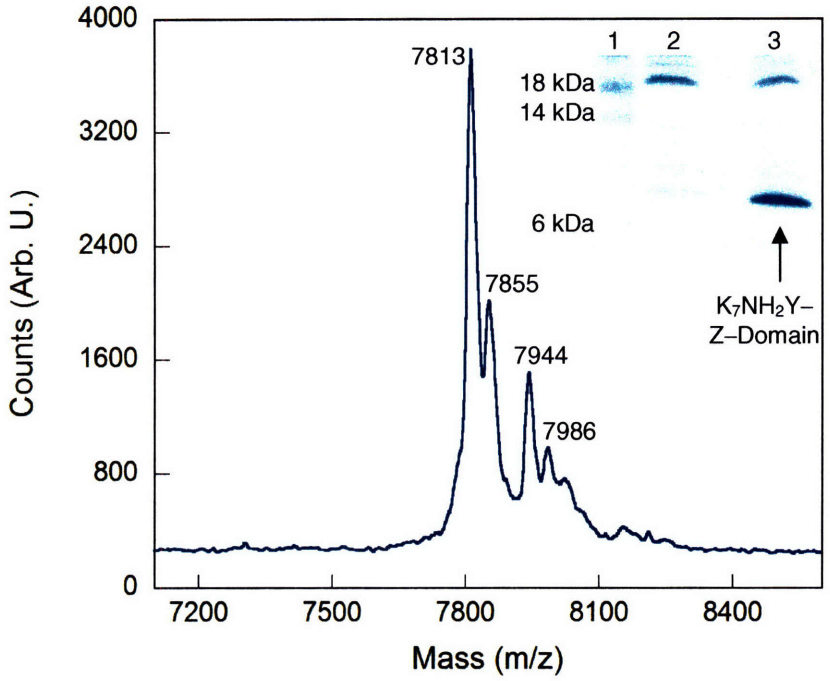

Figure 4–2. MALDI–TOF MS and SDS PAGE analysis of K_7NH_2Y–Z–domain. MALDI–TOF MS of purified K_7NH_2Y–Z–domain obtained under positive ionization mode. The m/z $[M+H]^+$ are indicated for the main peaks in the spectrum. They correspond to N–terminally cleaved Met form of K_7NH_2Y-Z–Domain (exp. 7814) and its acetylated form (exp 7856), full–length K_7NH_2Y–His–Z–Domain (exp. 7945) and its acetylated form (exp 7987). *Inset:* SDS gel of purified Z–domain after expression in the absence (lane 2) or presence (lane 3) of NH_2Y. The arrow designates the K_7NH_2Y–Z–domain band. Protein ladder and corresponding MW are shown in lane 1.

The recent report of successful expression and incorporation of unnatural amino acids into *E. coli* nitroreductase using pTrc,[75] prompted us to investigate the pAC–NH_2Y–RS/ pTrc–*nrdA* expression system. The pTrc–*nrdA* vector carries the α2 gene under control of the *trp/lac* (*trc*) promoter with the amber stop codon at the desired residue.[76] Importantly, pAC–NH_2Y carries six copies of $mutRNA_{CUA}$ increasing the concentration of the cognate tRNA inside the cell.[61]

Expression of wt α2 from pTrc–*nrdA* was examined first. Overproduction and subsequent purification, gave 10 mg of pure α2 per g of wet cell paste. This expression level is 2–4× greater than the expression of α2 from pMJ1, which has been routinely used in our lab to

express α2 and α2 mutants (data not shown). In addition, the specific activity of α2 was similar to that produced from pMJ1–*nrdA* (2500 nmol/min•mg).

Expression of $Y_{731}NH_2Y$–α2 in DH10B cells doubly transformed with pAC–NH_2Y–RS and pTrc–*nrdA* is shown in Figure 4–3. In the presence of the IPTG inducer and NH_2Y/DTT, the amber stop codon is suppressed and NH_2Y–α2 is overexpressed. In the absence of NH_2Y, overproduction of only truncated α2 is observed. Finally, in the absence of inducer IPTG and NH_2Y, no overexpression of α2 occurs. A similar profile is obtained for the expression of $Y_{730}NH_2Y$–α2 (Figure 4–4). Purification of NH_2Y–α2 using dATP affinity chromatography gives 4–6 mg of the target protein per L culture in >90 % homogeneity (Figures 4–5 & 4–6).[55,60] The mutant proteins behaved similarly to wt α2 during the purification procedure.

Reaction of NH_2Y–α2s with wt β2, CDP and ATP monitored by EPR spectroscopy. The availability of NH_2Y–α2s has allowed us to assess the participation of Y_{730} and Y_{731} in radical propagation across the β2–α2 interface. The experimental design is based on the radical trapping method previously established with DOPA–β2.[38,39] In this method, a stable radical is trapped with an unnatural Y analog that is more easily oxidized than Y. If the trapping requires the presence of β2, substrate, and allosteric effector, then it provides direct evidence for redox activity of that residue during radical propagation. Lack of radical formation may indicate that the residue is not redox–active or that the oxidized product is unstable. We proposed that the ease of oxidation of NH_2Y (E° is 190 mV lower than Y at pH 7) would lead to generation of an NH_2Y• allowing its detection by UV–vis and EPR methods.[51] Unfortunately, spectroscopic characterization of NH_2Y• has not been previously reported.

Based on our studies DOPA–β2,[38] we anticipated that the NH_2Y• might be stabilized to some extent by the protein environment. With DOPA–β2, maximal amounts of DOPA• were generated by 5 s, which was stable for 2.5 min.[38,39] Thus, $Y_{730}NH_2Y$–α2 (or $Y_{731}NH_2Y$–α2) was mixed with wt β2, substrate (CDP) and effector (ATP), incubated at 25°C for variable periods of time (10 s to 12 min) and quenched manually in liquid N_2. EPR spectra of these reactions revealed a new signal that was present in maximal amounts at the 10 s time point (Figure 4–7).

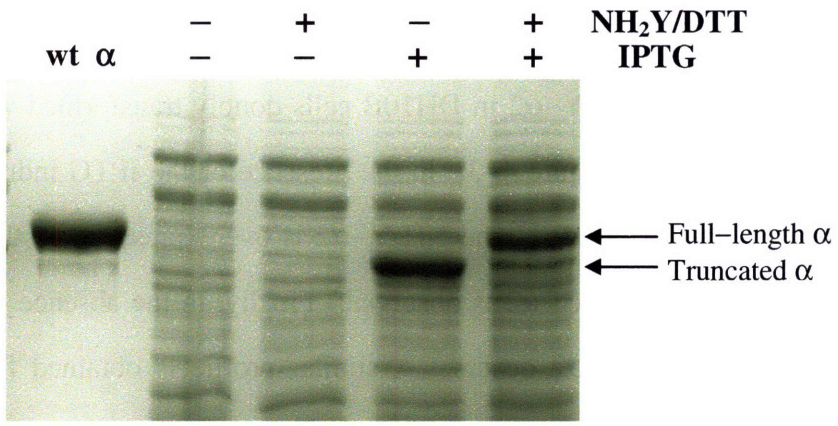

Figure 4–3. Expression of $Y_{731}NH_2Y$–α2. Cells were grown in the presence or absence of IPTG and NH_2Y/DTT as indicated and the level of expression assessed by SDS PAGE. The position of protein bands for full–length α and truncated α are denoted by arrows.

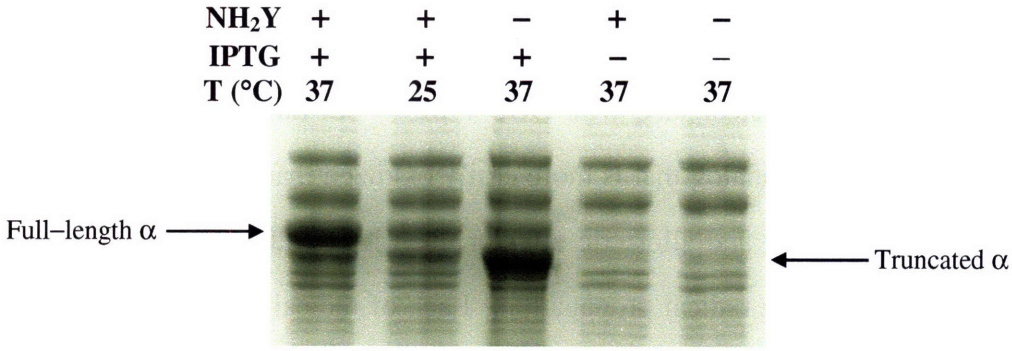

Figure 4–4. Expression of $Y_{730}NH_2Y$–α2. Cells were grown in the presence or absence of IPTG and NH_2Y/DTT and at 25° or 37 °C, as indicated, and the level of expression assessed on a SDS PAGE gel. The position of protein bands for full–length α and truncated α are denoted by arrows.

A control in the absence of CDP and ATP, revealed only Y_{122}• (Figure 4–7, inset). Thus formation of the new signal is controlled by the presence of substrate and effector as previously observed with similar studies on DOPA–β2.[38]

The observed spectrum is a composite of at least two species: unreacted Y_{122}• and the putative NH_2Y_{730}•. To reveal the features of the new radical(s), the spectrum of the Y_{122}•[(14)] with

distinct, well characterized low field features, was subtracted from the composite signal. The resulting nearly isotropic signal (Figure 4–7, red trace) has an apparent g_{av} of 2.0043 and a peak–to–trough width of 24 G.[77] We ascribe this new signal to NH_2Y_{730}•.

Spin quantitation at the 10 s time point revealed that 8 % of total initial spin (relative to starting Y_{122}•) had been lost. Of the remaining spin, 47 % is associated with Y_{122}• and 53 % with the new signal. To further characterize this signal, power saturation studies were carried out. The Y_{122}• is adjacent to the diferric cluster, which dramatically alters its relaxation properties. If the new radical is in fact located within α2, >35 Å removed from the diferric cluster as indicated by the docking model, then its $P_{1/2}$ would be markedly reduced. The results of power dependence experiments are shown in Figure 4–8. The data were fit to Eq. 4–1,[78] where K is a sample and instrument dependent scaling factor, P is the microwave power, b is indicative of homogeneous (b=3) or inhomogeneous (b=1) spectral broadening and $P_{1/2}$ is the microwave power at half saturation of the EPR signal.[78,79] For the Y_{122}•, a $P_{1/2}$ of 28 ± 4 mW was determined, similar to previous measurements.[79,80] The saturation profile of the new signal gave a $P_{1/2}$ of 0.42 ± 0.08 mW consistent with a radical distant from the diiron center.

$$\text{Signal Amplitude} = \frac{K \times (\sqrt{P})}{[1+(P/P_{1/2})]^{0.5\times b}} \qquad (4\text{–}1)$$

Similar experiments have also been carried out with $Y_{731}NH_2Y$–α2. A new signal, the putative NH_2Y_{731}•, is also observed *only* in the presence of CDP/ATP (Figure 4–9). Subtraction of the Y_{122}• spectrum, reveals a spectrum that is similar, but not identical, to that of NH_2Y_{730}• (Figures 4–9 & 4–10). The nearly isotropic signal associated with NH_2Y_{731}• consists of a g_{av} of 2.0044 and a peak–to–trough width of 22 G. At the 10 s time point, 14 % of total initial spin has been lost. Of the remaining spin, 45 % is associated with NH_2Y_{731}• and 55 % with Y_{122}•.

Kinetics of NH_2Y•–α2 formation monitored by SF UV–vis spectroscopy. Pre–steady state experiments were carried out to assess whether NH_2Y•–α2 formation occurs with a rate constant fast enough to be competent in nucleotide reduction in wt RNR. Previous steady state

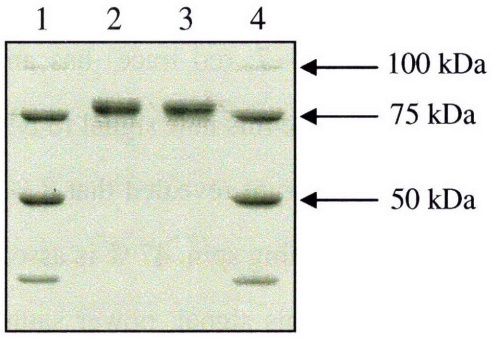

Figure 4–5. SDS PAGE analysis of purified $Y_{730}NH_2Y$–α2. (1) and (4) MW markers; MWs are indicated. (2) Purified $Y_{730}NH_2Y$–α2 (1.5 μg). (3) Purified wt α2 (1.5 μg).

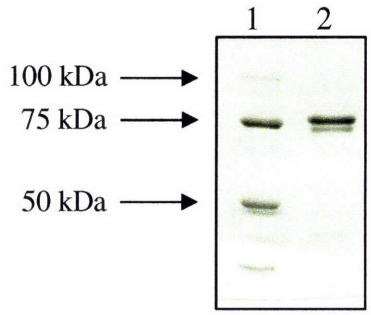

Figure 4–6. SDS PAGE analysis of purified $Y_{731}NH_2Y$–α2. (1) MW markers; MWs are indicated. (2) Purified $Y_{731}NH_2Y$–α2 (1.5 μg).

and pre–steady state kinetic analysis of *E. coli* RNR monitoring nucleotide reduction have shown that radical propagation is preceded by a slow conformation change.[81] This slow physical step masks intermediates that form in the propagation process. In the presence of CDP/ATP, and at concentrations of α2 and β2 used in the present study, the rate constant for this conformational change varies from ~4–17 s^{-1}.[81] The steady state rate constant for dCDP formation is on the order of 2 s^{-1} and is thought to be limited by re–reduction of the active site disulfide that accompanies dCDP formation, or by a conformational change associated with this re–reduction. In previous studies with DOPA–β2, α2 and CDP/ATP, DOPA• formation occurred in two fast kinetic phases (38.0 and 6.8 s^{-1}) and a slow phase (0.7 s^{-1}). Thus, the two fast phases in the

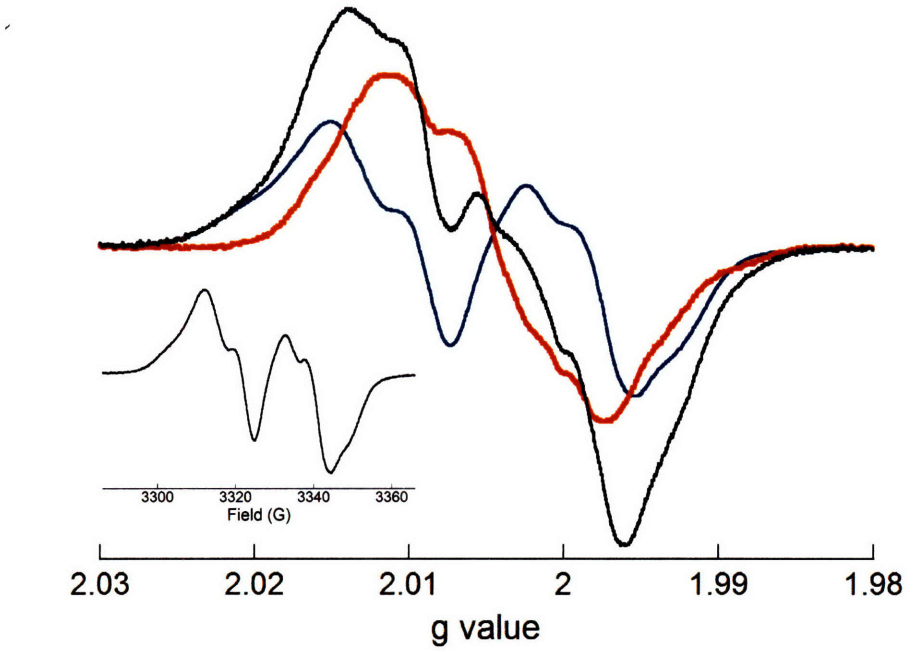

Figure 4–7. Reaction of $Y_{730}NH_2Y$–α2/ATP with wt β2/CDP monitored by EPR spectroscopy. The reaction components were mixed at 25°C to yield final concentrations of 20 μM $Y_{730}NH_2Y$–α2/β2, 1 mM CDP and 3 mM ATP. After 10 s, the reaction was quenched in liquid N_2 and the EPR spectrum (black) subsequently recorded at 77 K. Unreacted Y_{122}• (blue, 47 % of total spin), was subtracted to reveal the spectrum of NH_2Y_{730}• (red, 53 % of total spin). *Inset:* Reaction of $Y_{730}NH_2Y$–α2 with wt β2 in the absence of CDP/ATP.

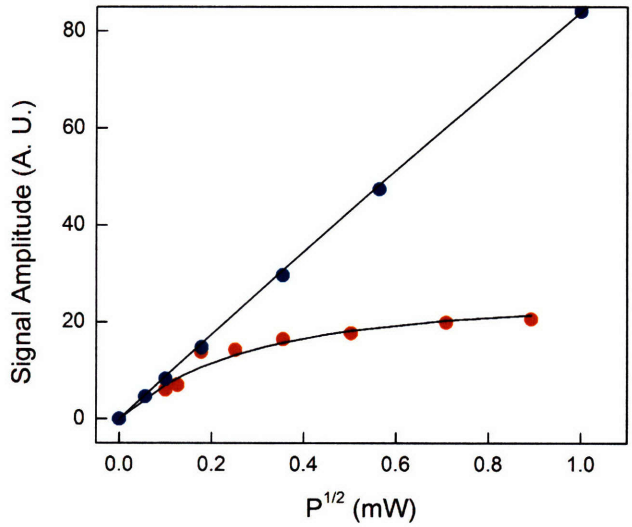

Figure 4–8. Microwave power dependence of Y_{122}• and NH_2Y_{730}• signal intensities. The EPR spectrum of Y_{122}• and NH_2Y_{730}• was recorded as a function of microwave power and the integrated intensity of each signal plotted against the square root of power. Black lines represent fits to the data using Eq. 4–1[78] and yield $P_{1/2}$ of 28 ± 4 mW (b=1.3 ± 0.2) and 0.42 ± 0.08 mW (b=1.2 ± 0.2) for Y_{122}• (blue) and NH_2Y_{730}• (red), respectively.

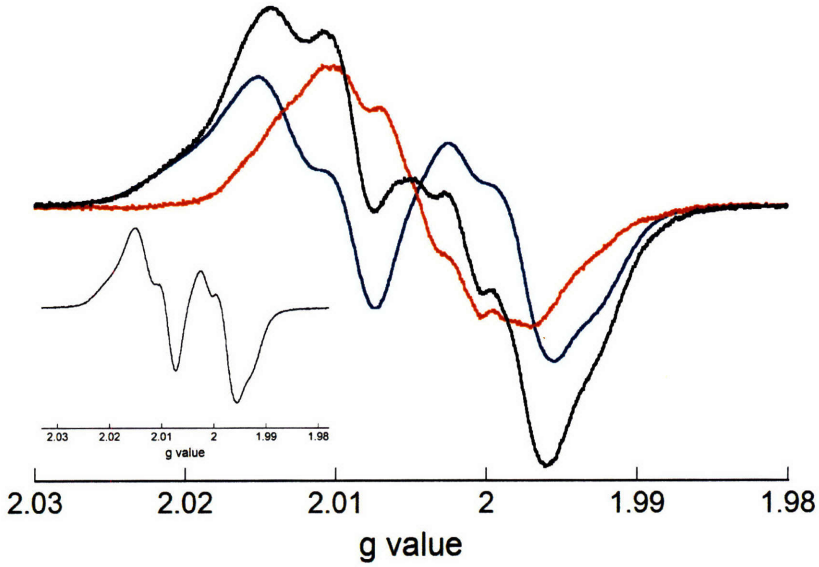

Figure 4–9. Reaction of $Y_{731}NH_2Y$–α2/ATP with wt β2/CDP monitored by EPR spectroscopy. The reaction components were mixed at 25°C to yield final concentrations of 20 μM $Y_{731}NH_2Y$–α2/β2 complex, 1 mM CDP and 3 mM ATP. After 20 s, the reaction was quenched by hand–freezing in liquid N_2 and the EPR spectrum subsequently recorded (black trace) with at 77 K as described in the Methods section. Unreacted Y_{122}• (blue, 55 % of total spin), was subtracted to reveal the spectrum of NH_2Y_{730}• (red, 45 % of total spin). *Inset:* Reaction of $Y_{730}NH_2Y$–α2 with wt β2 in the absence of CDP/ATP.

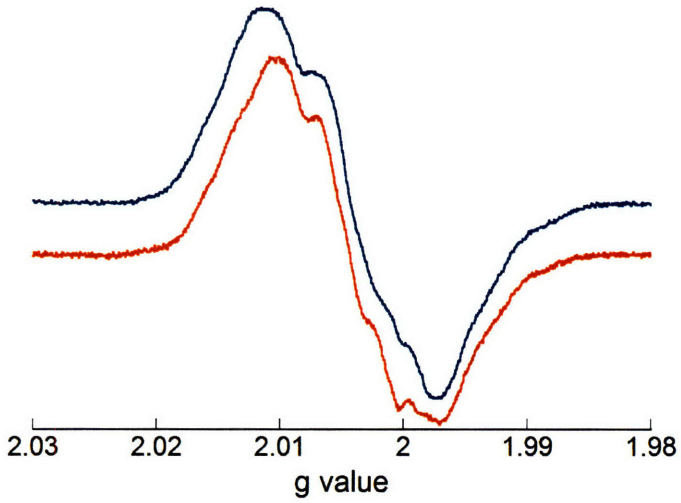

Figure 4–10. Comparison between NH_2Y_{730}• (blue trace) from Fig. 4–7 and NH_2Y_{731}• (red trace) from Fig. 4–9.

DOPA–β2 experiments, and potentially the third phase,[82] were kinetically competent with respect to the conformational change, which limits dCDP formation in the first turnover.[81]

To monitor changes in the concentration of NH_2Y•, its spectrum and extinction coefficient must be determined. Our initial assumption was that its UV–vis spectrum would be similar to that of DOPA• (λ_{max} at 315 nm and ε ~12000 $M^{-1}cm^{-1}$).[38,83] The extinction coefficients associated with Y_{122}• between 310 and 365 nm are low (ε ~ 500–1900 $M^{-1}cm^{-1}$) and can be used in spectral deconvolution.[64,65] Thus, using SF spectroscopy, we carried out a point–by–point analysis of the UV–vis properties of the new radical. $Y_{730}NH_2Y$–α2 (or $Y_{731}NH_2Y$–α2) and ATP in one syringe was mixed with wt β2 and CDP from a second syringe and the absorbance monitored from 305–365 nm in 5 nm intervals. The absorbance change at 1.5 s at each λ, corrected for the absorption by the Y_{122}•,[64,65] was then plotted against the λ. The results are shown in Figure 4–11 and indicate that NH_2Y_{730}• and NH_2Y_{731}• have similar, but distinct absorption profiles. The UV–vis spectrum of NH_2Y_{730}• consists of a broad feature with a λ_{max} at 325 ± 1 nm (ε ~10500 ± 500 $M^{-1}cm^{-1}$). The NH_2Y_{731}• spectrum exhibits a λ_{max} at 320 ± 1 nm (ε ~ 11000 ± 500 M^{-1} cm^{-1}) and a more defined shoulder at 350 nm. The extinction coefficients for NH_2Y•–α2s were determined using ε for Y_{122}• at 410 nm[66] and the assumption that loss of each mole of Y_{122}• leads to formation of one mole of NH_2Y•.

SF UV–vis experiments carried out to monitor the kinetics of loss of Y_{122}• (410 nm) and formation of NH_2Y• (325 nm) are shown in Figure 4–12A for $Y_{730}NH_2Y$–α2. At 410 nm, bi–exponential kinetics with rate constants of 12.0 ± 0.1 s^{-1} and 2.4 ± 0.1 s^{-1} were observed, similar to rate constants obtained for formation of NH_2Y• at 325 nm (13.6 ± 0.1 s^{-1} and 2.5 ± 0.1 s^{-1}). Analogous experiments carried out with $Y_{731}NH_2Y$–α2 showed that loss of Y_{122}• occurred bi–exponentially (17.3 ± 0.2 and 2.3 ± 0.1 s^{-1}) concomitant with formation of NH_2Y_{731}• (21.0 ± 0.1 s^{-1} and 3 ± 0.1 s^{-1}, Figure 4–12B). The rate constants and amplitudes for both reactions are summarized in Table 4–2. A control experiment was carried out in the absence of substrate and effector with $Y_{730}NH_2Y$–α2 (or $Y_{731}NH_2Y$–α2) and β2. As indicated by EPR experiments, no loss of Y_{122}• or formation of NH_2Y• occurred under identical conditions (data not shown).

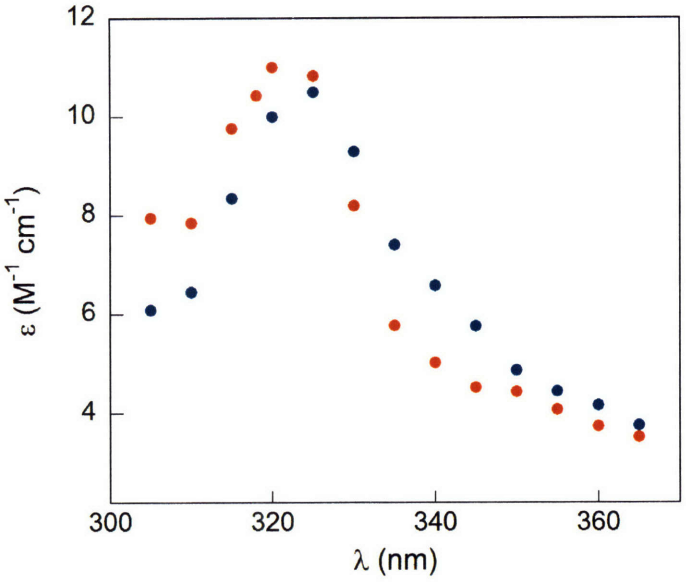

Figure 4–11. Point–by–point reconstruction of the UV–vis spectrum of NH_2Y_{730}• (blue dots) and NH_2Y_{731}• (red dots). Pre–reduced $Y_{730}NH_2Y$–α2 and ATP in one syringe were mixed with wt β2 and CDP from another syringe, yielding final concentrations of 10 μM, 3 mM, 10 μM and 1 mM, respectively. With $Y_{731}NH_2Y$–α2, the reaction was carried out at final concentrations of 9 μM $Y_{731}NH_2Y$–α2β2, 1 mM CDP and 3 mM ATP. The absorption change was monitored in 5 nm intervals; at each λ, 2–4 time courses were averaged and corrected for the absorption of Y_{122}• using previously determined ε in this spectral range.[64,65] The corrected ΔOD was converted to ε,[66] which was then plotted against λ.

As noted above, the fast rate constants observed with the NH_2Y–α2s are kinetically competent in RNR turnover. Thus studies with these mutants provide the first direct evidence for their involvement in radical propagation. The slow rate constant, also observed in the DOPA–β2 experiments, is similar to the steady state rate constant for RNR turnover. A possible explanation for this slow phase is discussed below.

Finally, analysis of the amounts of each radical at 2 s shows that with $Y_{730}NH_2Y$–α2 and $Y_{731}NH_2Y$–α2, 39 % and 35 % of total initial Y_{122}• is consumed, respectively. In contrast with the DOPA–β2, the NH_2Y• is less stable. The instability needs to be assessed in detail and requires kinetic analysis using rapid–freeze quench methods to unravel its mechanistic implications.

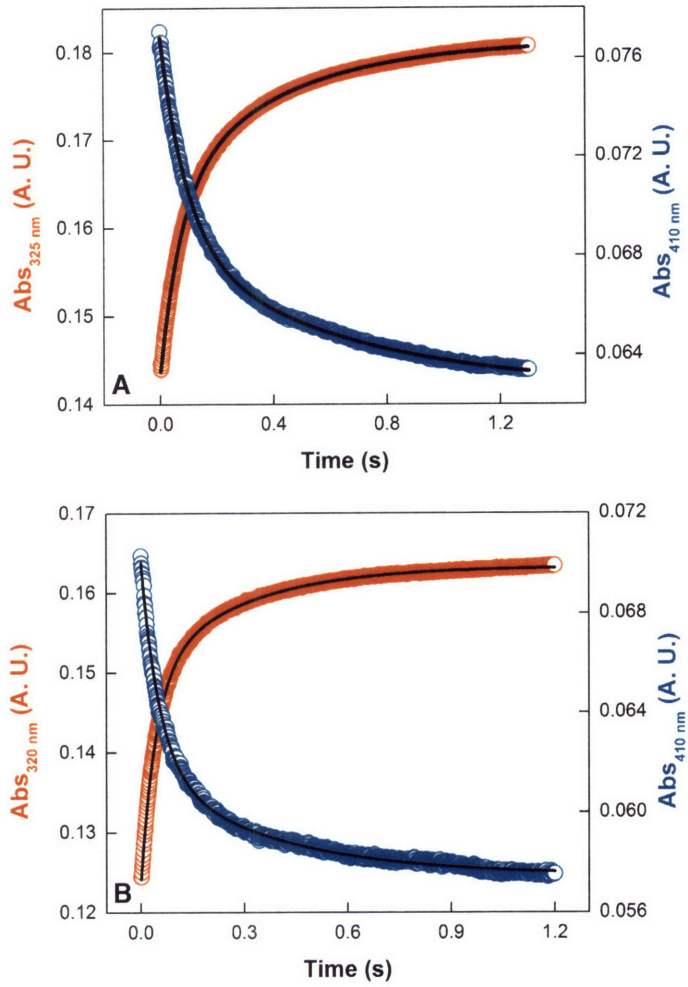

Figure 4–12. Kinetics of formation for NH_2Y_{730}• and NH_2Y_{731}• . (A) Pre–reduced $Y_{730}NH_2Y$–α2 (20 μM) and CDP (2 mM) in one syringe were mixed in a 1:1 ratio with β2 (20 μM) and ATP (3 mM) from another syringe. A total of 7 traces were averaged at each λ. (B) Pre–reduced $Y_{731}NH_2Y$–α2 (18 μM) and CDP (2 mM) in one syringe were mixed in a 1:1 ratio with β2 (18 μM) and ATP (3 mM) from another syringe. A total of 6 traces were averaged at each λ.

Kinetics of NH_2Y•–α2 decay monitored by EPR spectroscopy. We previously examined the stability of the $DOPA_{356}$•–β2 at the subunit interface of α2/DOPA–β2, which revealed a $\tau_{1/2}$ of ~5 min in the presence of CDP/ATP (Chapter 3). The loss of spin was associated with loss of DOPA• and no new DOPA• formed. At the end of the reaction, ~50 % of the total initial spin, which had given rise to DOPA•, was lost. The remaining 50 % of total initial spin was unreacted Y_{122}•. Similar time–dependent EPR experiments were carried out with NH_2Y–α2s to monitor the fate of NH_2Y•–α2 after its generation. For each reaction, EPR spectra

were recorded at several time points over the minute time scale. At each time point, the EPR spectrum was analyzed as described above (Figures 4–7 & 4–9). The $[spin]_{total}$, $[Y_{122}•]$ and $[NH_2Y•]$ was determined at each time point, after formation of the $NH_2Y•$.

Table 4–2. Summary of kinetic data for formation of $NH_2Y•$–α2.

RNR Subunits	CDP/ATP	1st Phase k_{obs} (s^{-1})[a], Ampl[b] (%)	2nd Phase k_{obs} (s^{-1})[a], Ampl[b] (%)
$Y_{730}NH_2Y$–α2β2	NO	–[c]	–[c]
$Y_{730}NH_2Y$–α2β2	YES	12.8 ± 0.8, 20 ± 1	2.5 ± 0.1, 19 ± 1
$Y_{731}NH_2Y$–α2β2	NO	–[c]	–[c]
$Y_{731}NH_2Y$–α2β2	YES	19.2 ± 1.8, 24 ± 1	2.7 ± 0.4, 11 ± 1

[a] The rate constants reported are the averages of those measured at 410 nm (for $Y_{122}•$ loss) and at 320 nm (for $NH_2Y_{731}•$ formation) or 325 nm (for $NH_2Y_{730}•$ formation). The error corresponds to the standard deviation between these two measurements. [b] Ampl, amplitude; the amount of $Y_{122}•$ trapped in each kinetic phase is indicated as a % of total initial $Y_{122}•$. Because the determination of ε for $NH_2Y•$ was based on that of $Y_{122}•$, the amplitudes at 410 nm and 320 or 325 nm are nearly identical. [c] No changes observed.

The decay data is shown in Figure 4–13 for the $Y_{730}NH_2Y$–α2 reaction and Figure 4–14 for the $Y_{731}NH_2Y$–α2 reaction. The data with $Y_{730}NH_2Y$–α2 are similar to those with DOPA–β2. After 11 min ~50 % of total initial $Y_{122}•$ was lost. The decay data can be fit to a mono–exponential function with rate constants of 0.27 ± 0.06, 0.24 ± 0.05 and 0.26 ± 0.09 min^{-1}, for $[spin]_{total}$, $[Y_{122}•]$ and $[NH_2Y_{730}•]$, respectively (Figure 4–13). Accordingly, the decay rate constants of these species are commensurate within error, yielding an average value of 0.26 ± 0.07 min^{-1}, suggesting that a single pathway is responsible for loss of spin, $Y_{122}•$ and $NH_2Y•$.

Loss of spin with $Y_{731}NH_2Y$–α2 was faster than with $Y_{730}NH_2Y$–α2 (Figure 4–14). Decay of $[spin]_{total}$, $[Y_{122}•]$ and $[NH_2Y_{731}•]$ occurred with rate constants of 0.43 ± 0.07, 0.34 ± 0.08 and 0.31 ± 0.1 min^{-1}, respectively (Figures 4–14 B, C, D). The results are similar to the $Y_{730}NH_2Y$–α2 case, in that all three rate constants are commensurate. In contrast to the

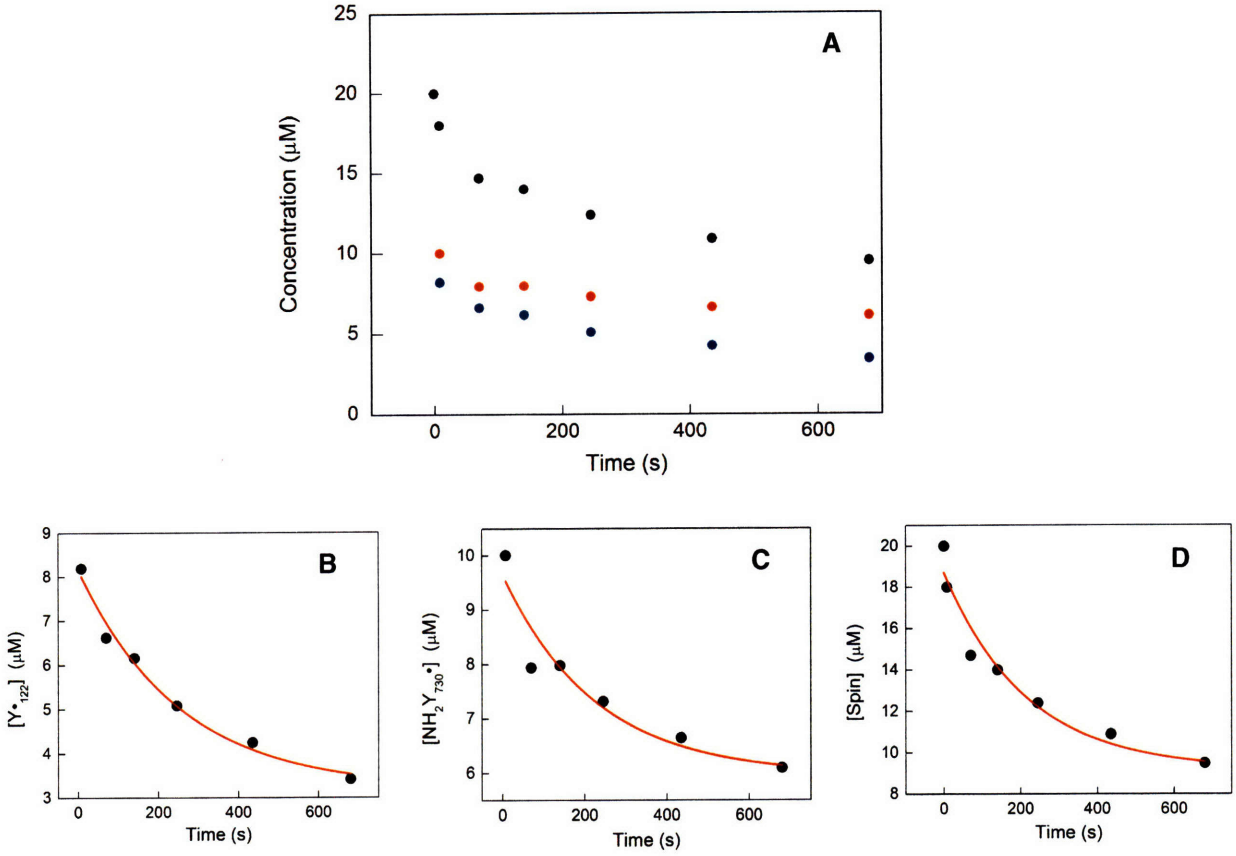

Figure 4–13. Stability of NH_2Y_{730}• probed by EPR spectroscopy. (A) $Y_{730}NH_2Y$–α2 and ATP were mixed with wt β2 (1.0 Y_{122}• / β2) and CDP at 25°C to give final concentrations of 20 μM, 3 mM, 20 μM and 1 mM, respectively. At defined time points, an aliquot was removed, transferred to an EPR tube, frozen in liquid N_2 and its EPR spectrum recorded. The $[spin]_{total}$ (black dots), and its distribution between Y_{122}• (blue dots) and NH_2Y_{730}• (red dots) was determined, after the initial rapid formation of NH_2Y•, and plotted vs. time. Time courses for [Y_{122}•] (B), [NH_2Y_{730}•] (C), and $[spin]_{total}$ (D) are shown with mono–exponenetail fits to the data indicated by red lines. See text for rate constants.

$Y_{730}NH_2Y$–α2 reaction, however, 85 % of initial spin is lost by the ~10 min time point. The disappearance of Y_{122}• was also monitored by UV–vis spectroscopy by recording time–dependent UV–vis spectra after initiation of the reaction and quantitating [Y_{122}•] using the dropline method (Figure 4–14E). This analysis yields a decay rate constant of 0.39 ± 0.03 min^{-1}, in agreement with the EPR measurements. Together, these experiments indicate an average decay rate constant of 0.37 ± 0.07 min^{-1}. These studies report on the stability of NH_2Y_{730}• vs. NH_2Y_{731}• as further discussed below.

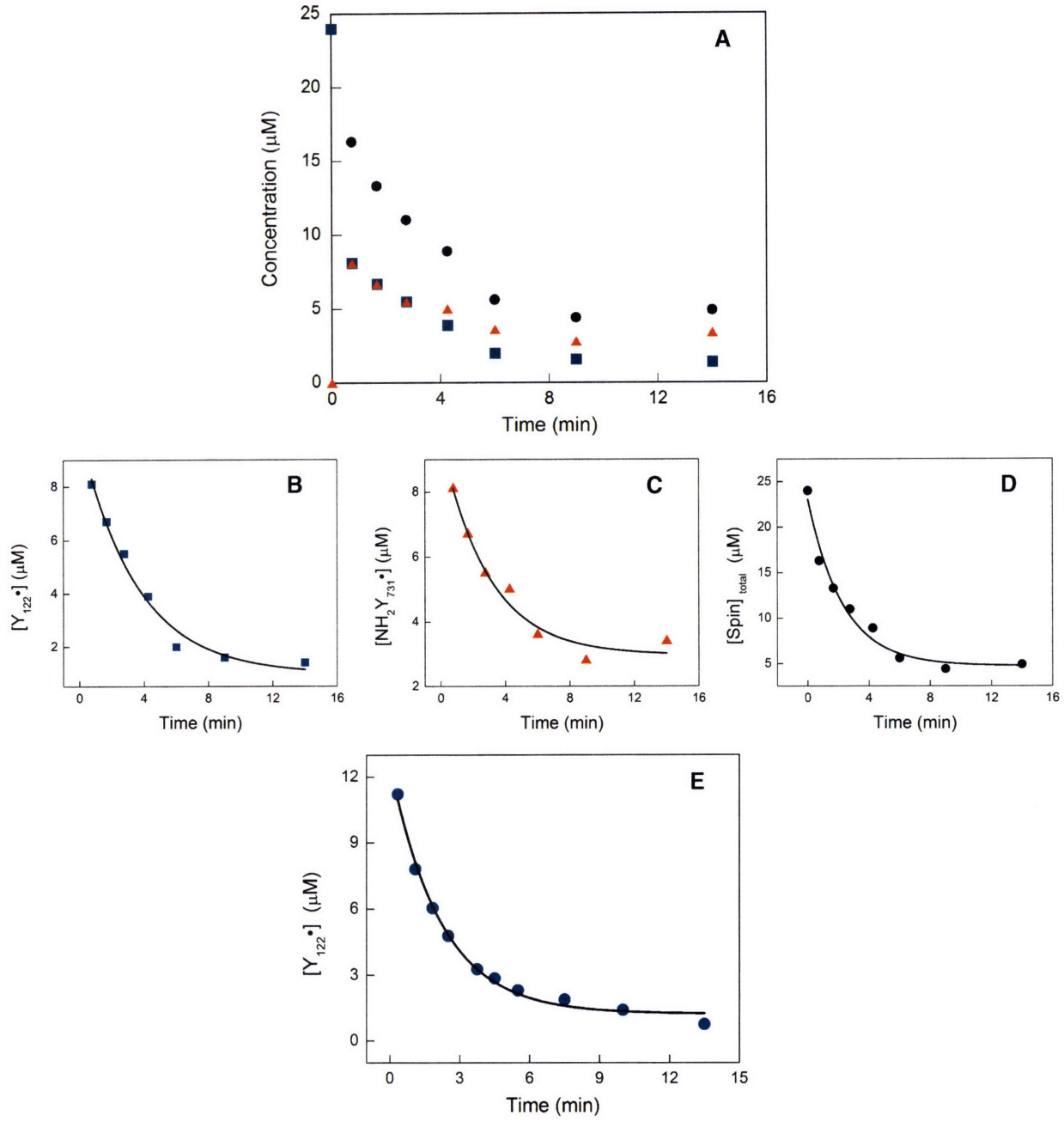

Figure 4–14. Stability of NH_2Y_{731}• probed by EPR and UV–vis spectroscopy. (A) $Y_{731}NH_2Y$–α2 and ATP were mixed with wt β2 (1.2 Y_{122}• / β2) and CDP at 25°C to give final concentrations of 20 μM, 3 mM, 20 μM and 1 mM, respectively. At defined time points, an aliquot was removed, transferred to an EPR tube, frozen in liquid N_2 and the EPR spectrum recorded. The $[spin]_{total}$ (black dots) and its distribution between Y_{122}• (blue squares) and NH_2Y_{731}• (red triangles) was determined, after the initial rapid formation of NH_2Y•, and plotted vs. time. Time courses for [Y_{122}•] (B), [NH_2Y_{731}•] (C), and $[spin]_{total}$ (D) are shown with mono–exponenetail fits to the data indicated by black lines. (E) Time course of Y_{122}• decay measured by UV–vis spectroscopy. The reaction was carried out at 25°C and contained final concentrations of 18 μM $Y_{731}NH_2Y$–α2/β2 (1.2 Y_{122}• / β2), 1 mM CDP and 3 mM ATP. At defined time points a UV–vis spectrum was recorded and the [Y_{122}•] (blue dots) computed using the dropline method. The black line is a mono–exponential fit to the data. See text for k_{obs}s.

Activities of NH_2Y–α2s. Recently, using a series of F_nY_{356}–β2s, we found a correlation between nucleotide reduction activity and the reduction potential of residue 356, when its potential was 80 to 200 mV higher than that of tyrosine.[40,43] The reduction potential of DOPA is 260 mV lower than that of Y (pH 7) and with DOPA–β2,[38] deoxynucleotide formation was below our lower limit of detection. With NH_2Y–α2, the potential of NH_2Y is 190 mV lower than that of Y (pH 7). To test whether this energy barrier would be large enough to shut down radical transfer to C_{439}, and therefore nucleotide reduction, activity assays were performed on NH_2Y–α2s.

Activity was determined by monitoring dCDP formation indirectly (spectrophotometric assay) or directly (radioactive assay). The activities determined using these assays are summarized in Table 4–3. The results show nucleotide reduction activity for $Y_{730}NH_2Y$–α2 and $Y_{731}NH_2Y$–α2 that is 4 % and 7 % that of wt α2, respectively. The observed activity may be inherent to NH_2Y–α2s; on the other hand, it may be ascribed to co–purifying endogenous wt α2 or to wt α2 generated by the host cell as a result of amber codon suppression with Tyr–loaded $mutRNA_{CUA}$ in place of NH_2Y–loaded $tRNA_{CUA}$.

Table 4–3. Monitoring the activity of NH_2Y–α2s by measuring deoxynucleotide and N• formation.

α2 Variant	Spectrophotometric RNR Assay (% wt)[a]	Radioactive RNR Assay (% wt)[a]	N_3ADP Assay (% N• at 20 s,[b] % N• vs. initial Y_{122}•[c])
wt α2	100[a]	100[a]	52
$Y_{730}NH_2Y$–α2	4 ± 0.3	4 ± 0.5	19 ± 2,[b] 15 ± 2[c]
$Y_{731}NH_2Y$–α2	7 ± 1	7 ± 0.5	20 ± 2,[b] 15 ± 2[c]

[a] The activity is reported as % of wt activity, which was 2500 nmol/min•mg. The error is the standard deviation from 3 independent measurements for the spectrophotometric assay and 2 independent measurements for the radioactive assay. [b] The amount of N• is indicated as % of total spin at 20 s; the error is associated with EPR spin quantitation methods. [c] The amount of N• is indicated as % of total initial Y_{122}•; the error is associated with EPR spin quantitation methods.

To distinguish between these two options, assays with N_3ADP were carried out. N_3ADP is a mechanism–based inhibitor of class I RNRs which generates a moderately stable N–centered nucleotide radical (N•) covalently bound to the nucleotide and a cysteine in the active site of α2.[28-31,84] This radical may be used as a reporter of the ability of NH_2Y• to generate a C_{439}• and initiate chemistry on the nucleotide. Previous studies of the inactivation of wt α2/β2 by N_3ADP/dGTP suggest that on a 20 s time scale, 50–60 % of the initial Y_{122}• is lost leading to formation of an equivalent amount of N•.[30,60] Therefore, if the activity observed with NH_2Y–α2s is indicative of wt α2, ~2 % and ~3.5 % of total initial Y_{122}• would be expected to form a N• with $Y_{730}NH_2Y$–α2 and $Y_{731}NH_2Y$–α2, respectively.

Assays with N_3ADP were carried out by mixing each NH_2Y–α2 (or wt α2) and dGTP with wt β2 and N_3ADP. After 20 s the reaction was hand–quenched in liquid N_2. The EPR spectrum obtained for $Y_{730}NH_2Y$–α2 is shown in Figure 4–15. The observed spectrum is a combination of at least three radicals: Y_{122}•, NH_2Y_{730}•, and N•. The spectrum can be deconvoluted using the differences in spectral widths and the unique spectral features within these regions (Figure 4–16). Thus, the data were analyzed by first subtracting the N• spectrum, which contains the broadest of the three signals. The resulting spectrum was then subjected to fractional subtraction of the Y_{122}• component, yielding the NH_2Y_{730}• signal. The concentration of each of the radicals was determined using standard EPR quantitation methods.[63]

The results from this quantitative analysis are shown in Table 4–4. They show that 18 % of the total spin has been lost at the 20 s time point. Of the remaining spin, 19 ± 2 % is associated with N•; 43% is Y_{122}• and 39% is NH_2Y_{730}•. Accounting for the lost spin after 20 s, 15 ± 2 % of total initial Y_{122}• (i.e. at t=0) leads to N• formation. With $Y_{731}NH_2Y$–α2 (Figure 4–17 & Table 4–4), 25 % of the total spin is lost after 20 s with 20 ± 2 % present as N•, 41 % as Y_{122}• and 39 % as NH_2Y_{731}•. Accounting for the lost spin after 20 s, 15 ± 2 % of total initial Y_{122}• leads to formation of N•. Therefore, with both mutants, the amount of N• observed exceeds the 2 % or 3.5 % N• (for $Y_{730}NH_2Y$–α2 and $Y_{731}NH_2Y$–α2, respectively), expected if

the steady state activity was due to contaminating wt α2. These results strongly suggest that NH_2Y–α2s are competent in C_{439}• formation and thus nucleotide reduction.

Kinetics of NH_2Y_{731}• decay in the presence of N_3UDP/ATP monitored by EPR spectroscopy. As noted above, and summarized in Figures 4–15 and 4–17, at the 20 s time point in the reaction of NH_2Y–α2s with N_3ADP, 18–25 % of the total spin is lost. To examine the kinetics of this decay, time–dependent EPR spectra were recoreded with $Y_{731}NH_2Y$–α2/β2 and N_3UDP/ATP. At each time point, the spectrum was deconvoluted, as exemplified above, and the $[spin]_{total}$, $[Y_{122}•]$, $[NH_2Y_{731}•]$ and [N•] were determined. The results of this analysis are shown in Figure 4–18. The disappearance of $[spin]_{total}$ and $[Y_{122}•]$ can be fit to a single exponential decay function yielding rate constants of 0.67 ± 0.15 min^{-1} and 1.07 ± 0.11 min^{-1}, respectively. These decay rate constants are significantly greater than those measured in the presence on CDP/ATP. Therefore, the NH_2Y_{731}•–α2 is less stable when complexed with N_3ADP/dGTP relative to CDP/ATP. The implications of this result will be discussed below.

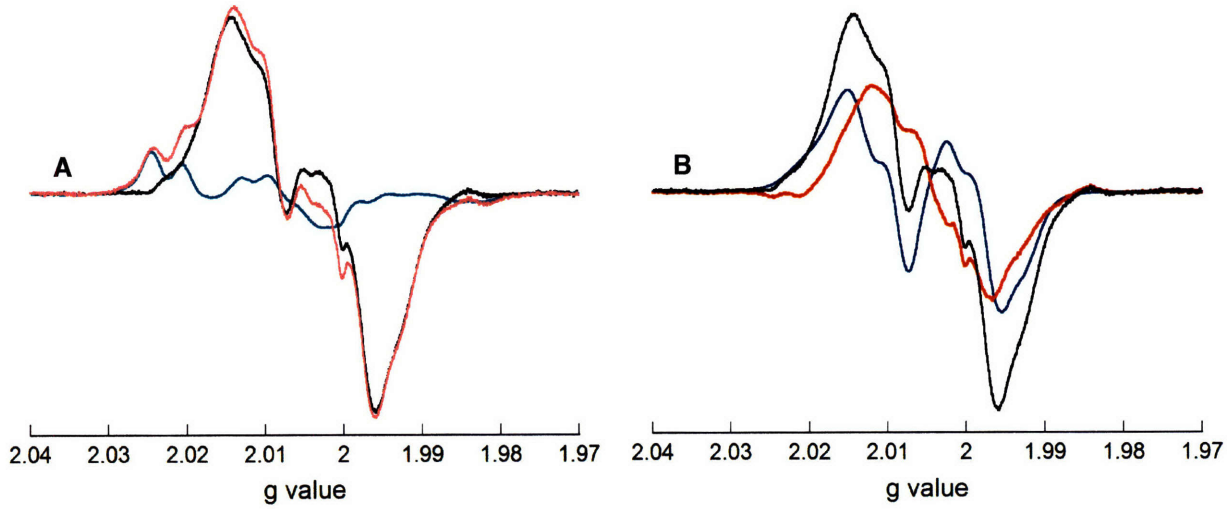

Figure 4–15. N_3ADP assay for $Y_{730}NH_2Y$–α2. The reaction contained final concentrations of 20 μM $Y_{730}NH_2Y$–α2/β2 (1.2 Y_{122}• / β2), 1 mM N_3ADP and 0.25 mM dGTP. After 20 s, it was freeze–quenched in liquid N_2 and its EPR spectrum recorded. (A) Subtraction of N• (aqua, 19 % of total spin) from the observed spectrum (lavender) yields the black trace, which contains the Y_{122}• and NH_2Y_{730}• signals. (B) Subtraction of Y_{122}• (blue, 43 % of total) from the resulting spectrum in (A) reveals the spectrum of NH_2Y_{730}• (red, 39 % of total spin). See Table 4–4 for quantitation of the concentration of each radical species.

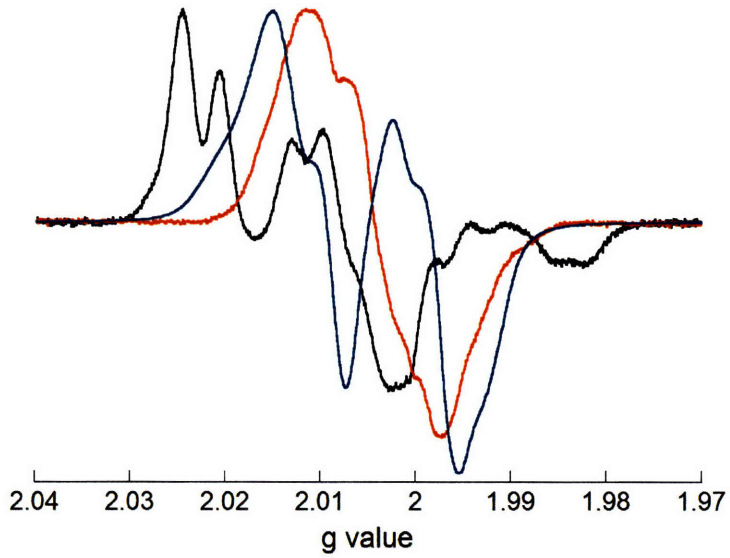

Figure 4–16. EPR spectral comparison of N• (black), Y_{122}• (blue) and NH_2Y_{730}• (red). The distinct features of N• and Y_{122}•, on the low field side of the spectrum, facilitate in deconvolution of the complex spectra in Figures 4–7, 4–9, 4–15 and 4–17.

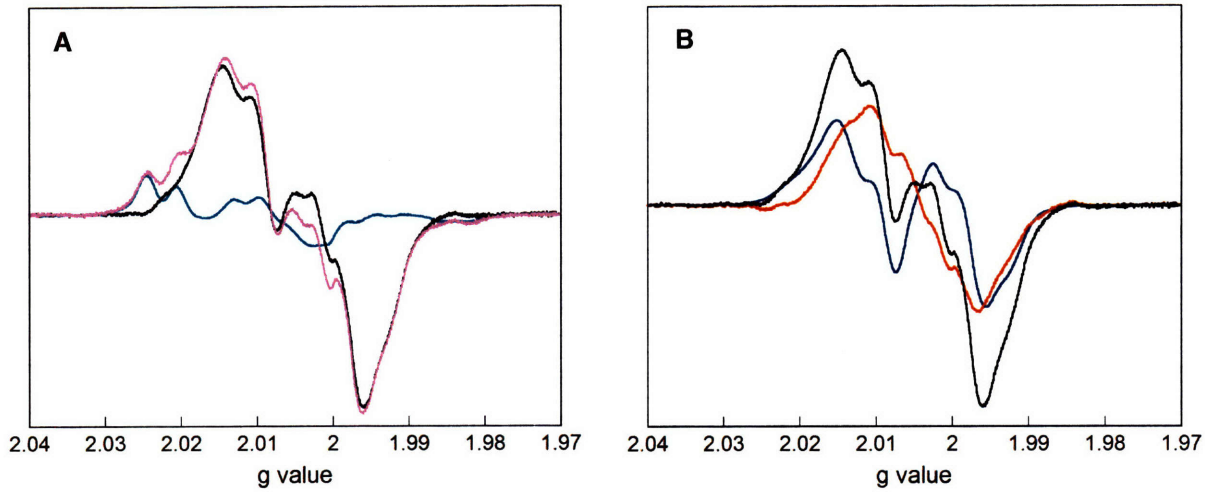

Figure 4–17. N_3ADP Assay for $Y_{731}NH_2Y$–α2. The reaction contained final concentrations of 20 μM $Y_{731}NH_2Y$–α2/β2 (1.2 Y_{122}• / β2), 1 mM N_3ADP and 0.25 μM dGTP. After 20 s, it was freeze–quenched by hand in liquid N_2 and its EPR spectrum recorded. (A) Subtraction of N• (aqua, 20 % of total spin) from the observed spectrum (lavender trace) yields the black trace, which contains Y_{122}• and NH_2Y_{731}• signals. (B) Subtraction of Y_{122}• (blue, 41 % of total) from the resulting spectrum in (A) reveals the spectrum of NH_2Y_{730}• (red, 39 % of total spin). See Table 4–4 for concentration of each of the three component radicals. Note that at the 20 s time point, 18.1 μM spin out of the initial 24 μM remained.

Table 4–4. Analysis of the reaction of wt α2 or NH_2Y–α2s with β2 and N_3ADP/dGTP after 20 s.[a]

α2 Variant	$[Spin]_T$ (μM)[b]	[N•] (μM)	$[Y_{122}•]$ (μM)	$[NH_2Y•]$ (μM)
wt α2	22.9	11.9	11.0	–
$Y_{730}NH_2Y$–α2	19.5	3.7	8.4	7.6
$Y_{731}NH_2Y$–α2	18.1	3.6	7.5	7.1

[a] The error associated with EPR quantitation was ~10 %. [b] In each case, the initial $[Y_{122}•]$ was 24 μM.

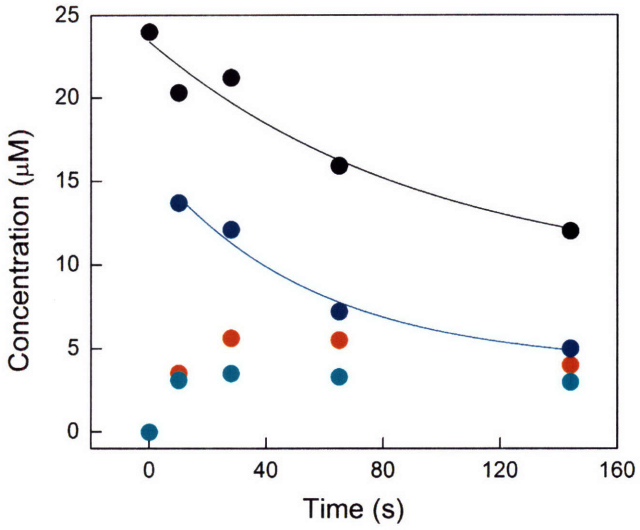

Figure 4–18. Stability of NH_2Y_{731}• in the presence of N_3UDP/ATP probed by EPR spectroscopy. $Y_{731}NH_2Y$–α2 and ATP were mixed with wt β2 (1.2 Y_{122}• / β2) and N_3UDP at 25°C to give final concentrations of 24 μM, 1 mM, 24 μM and 3 mM, respectively. At defined time points, an aliquot was removed, transferred to an EPR tube, frozen in liquid N_2 and the EPR spectrum recorded. The $[spin]_{total}$ (black dots) as well as its distribution between N• (aqua dots), Y_{122}• (blue dots) and NH_2Y_{731}• (red dots) was determined, after the initial rapid formation of NH_2Y•, and plotted vs. time. The black and blue lines indicate mono–exponential fits to $[spin]_{total}$ decay and $[Y_{122}•]$ decay, respectively. See text for rate constants.

DISCUSSION

Generation of $Y_{730}NH_2Y$–α2 and $Y_{731}NH_2Y$–α2. In this study, we have evaluated the proposed roles for residues Y_{730} and Y_{731} in radical propagation, by site–specifically replacing them with NH_2Y (Scheme 4–1). We employed the in vivo suppressor tRNA/RS method, which has been pioneered[46] and developed[47-50] by the Schultz lab and promises to have an immense impact on protein biochemistry. Using this technology, we evolved the desired tRNA/RS pair, which allowed us to generate $Y_{730}NH_2Y$–α2 and $Y_{731}NH_2Y$–α2 in yields of 4–6 mg per g of wet cell paste. The large size of α2 (172 kDa) and the small size difference between NH_2Y and Y have precluded quantitative assessment of NH_2Y incorporation into α2 by direct ESI or MALDI TOF mass spectrometric methods. Analytical methods using LC/MS of tryptic digests of this 172 kDa protein, to evaluate levels of NH_2Y relative to Y in NH_2Y–α2s, are currently being developed. Nevertheless, our studies with the model Z–domain protein indicate that incorporation of NH_2Y is efficient and specific. In addition, evaluation of our NH_2Y–α2 preparations, using N_3ADP and dCDP assays, also suggest presence of low levels of wt α2.

The ability to incorporate NH_2Y site–specifically into proteins will be of general use. Our characterization of the UV–vis and EPR spectroscopic properties of the NH_2Y• should allow NH_2Y to serve as a probe for enzymes that are thought to employ transient Y•s in catalysis or in electron transfer between metal centers. In addition, Francis and colleagues have recently shown that NH_2Y may be derivatized with fluorescent dyes.[85,86] Thus, NH_2Y may also be utilized as a tool for site–specifically appending probes of interest to the target protein.

Structural assignment of the new radical. When NH_2Y–α2s are reacted with β2, in the presence of CDP/ATP, a new EPR–active signal is observed. As noted above, however, neither UV–vis, nor EPR spectral properties of the NH_2Y• had previously been reported. The assignment of our new signal to NH_2Y• is based on SF UV–vis and EPR spectroscopic measurements in conjunction with knowledge of the properties of DOPA, catechol, and *o*–aminophenol radicals.[87,88] First, point–by–point reconstruction of the new radical's UV–vis

spectrum by SF methods reveals an absorption spectrum similar to DOPA•, which is expected based on the structural similarity between these two amino acids. Second, subtraction of the Y_{122}• EPR spectrum from the observed EPR signal, yields a spectrum with a g_{av} of 2.0043 ± 0.0001 which is typical of organic radicals. The small hyperfine couplings (<10 G) from the ring protons and from the amine nitrogen are similar to those previously reported for *o*–aminophenol radicals.[87] Third, information about the location of the new radical relative to the diferric cluster has been obtained by power saturation studies. These studies show that Y_{122}• saturates with a $P_{1/2}$ of 28 mW due to its vicinity to the diferric cluster (4.6 Å to the nearest iron in the cluster).[19] Mechanism based inhibitors that covalently label the active site of α2, >35 Å from the cluster, have $P_{1/2}$ values of 0.16 mW.[80] The new radical has a $P_{1/2}$ of 0.42 ± 0.08 mW consistent with a species distant from the diiron center. These data together strongly suggest that the new radical is NH_2Y• (Scheme 4–1).[89] High field EPR and ENDOR experiments, isotopic labeling studies with ^{15}N and ^{2}H in conjunction with computational studies will be presented in Chapter 5 to further support this assignment.

Kinetics of NH_2Y•–α2 formation. SF kinetic studies give NH_2Y• formation rate constants of 12.8 and 2.5 s^{-1} for $Y_{730}NH_2Y$-α2, and 19.2 and 2.7 s^{-1} for $Y_{731}NH_2Y$–α2. The fast rate constant is indicative of a rate–determining conformational change, which has previously been found to precede radical propagation in wt β2, under single turnover conditions.[81] Thus, formation of NH_2Y• occurs in a kinetically competent fashion at the expense of the Y_{122}•.[38] Further, as with DOPA, NH_2Y acts as a conformational probe and allows direct detection of this physical step, reporting on the regulatory state of the NH_2Y–α2/β2 complex. The slow rate constant observed in these kinetic studies has also been observed when monitoring $DOPA_{356}$• formation (0.4 to 0.8 s^{-1} with different substrate/effector pairs).[38,82] These rate constants are all in the same range, similar to the turnover number of RNR at the protein concentrations used in these experiments. Our previous studies have suggested that in the steady state, re–reduction of the disulfide or a conformational change associated with this process is rate–limiting. If the latter is the case, then this rate constant of 2–3 s^{-1}, might be indicative of the slow conversion of

one form of RNR into the more active form. Alternatively, incorporation of NH_2Y could result in α2 with two conformations of the tyrosine analogue that do not interconvert rapidly or two different conformations of the α2 itself. The separate kinetic phases for $NH_2Y\bullet$ formation indicate that these two conformations do not interconvert on the time scale of the SF experiment. Additional kinetic analysis is required to further assign the nature of the slow rate constant observed.

Activity Assays of NH_2Y–α2s. Steady state turnover measurements show the ability of both mutant proteins to produce dNDPs. As noted above, this activity could be associated with endogenous wt α2, which co–purifies with NH_2Y–α2s, or with wt α2 which is generated by suppression of the amber codon with Tyr–loaded $tRNA_{CUA}$ in place of NH_2Y. Alternatively, the activity may be inherent to NH_2Y–α2s.

To distinguish between these options, experiments with the mechanism–based inhibitor N_3ADP were carried out. The results indicate 15 ± 2 % N• formation with $Y_{730}NH_2Y$–α2 and $Y_{731}NH_2Y$–α2. These values exceed the expected 2 % and 3.5 %, respectively, if the steady state turnover were due to background levels of wt α2. Thus, the results suggest that NH_2Y–α2s are competent in nucleotide production. This implies that the putative $NH_2Y\bullet$ is an intermediate during active radical transport. Detailed kinetic analysis on the ms time scale will further test this proposition. If true, then these observations would mark the first detection of an amino acid radical during long–range hole migration in an RNR variant that is competent in dNDP formation.

Rate of decay of $NH_2Y\bullet$–α2. Further evidence for activity of NH_2Y–α2s requires a detailed kinetic analysis of the decay of $NH_2Y\bullet$, $Y_{122}\bullet$ and total spin during the normal reaction (CDP/ATP) and with the mechanism–based inhibitor (N_3CDP/ATP). Due to lack of availability of N_3CDP, the radical decay kinetics with N_3UDP/ATP was examined instead and compared to that in the presence of CDP/ATP. In these studies, the concentration of each radical species was examined as a function of time *after* the rapid formation of $NH_2Y\bullet$ and loss of $Y_{122}\bullet$.

With $Y_{730}NH_2Y$–α2 in the presence of CDP/ATP, the rate constants for decay of Y_{122}•, NH_2Y• and total spin were similar (0.26 ± 0.07 min^{-1}) indicating that a single pathway is responsible for loss of each species. The Y_{122}• is known to have long life time. Therefore, the data indicate that loss of radical occurs through NH_2Y•. Our model for radical decay is shown in Figure 4–19. In this model, k_1 and k_4 are the radical initiation and nucleotide reduction events with values of ~12 s^{-1} and 500 s^{-1}, respectively.[81] Values of k_2, k_3, k_5, k_6 and k_7 have not been experimentally determined. The observed decay rate constant is a function of k_2 and k_6 and further depends on the ratios of k_2/k_3 and k_6/k_7 (Eq. 4–2). Note that $k_2=k_6$, if product dCDP is released from the NH_2Y–α2/β2 complex after its formation.

$$NH_2Y\bullet \text{ Decay Rate} = k_2 \times [\mathbf{2}] + k_6 \times [\mathbf{6}] \qquad (4\text{–}2)$$

With $Y_{731}NH_2Y$–α2, radical decay also occurs through NH_2Y• with a k_{obs} of 0.37 ± 0.07 min^{-1} as monitored by a combination of EPR and UV–vis spectroscopies. Therefore, NH_2Y_{730}• has a life time that is 40 % longer than that of NH_2Y_{731}•. This may be due to the position of Y_{731} at the subunit interface, which appears to be more exposed and accessible to solution. It is also consistent with the different EPR spectra of NH_2Y_{730}• and NH_2Y_{731}• which demonstrate that each residue is surrounded by a distinct protein environment.

Radical decay kinetics were also determined in the presence of N_3UDP/ATP. Our working model for this reaction is shown in Figure 4–20. This scheme is simplified relative to that with CDP/ATP (Figure 4–19) as radical propagation is unidirectional. It can be shown that k_{obs} is a function of k_A, k_B and k_C as indicated in Eq. 4–3. Importantly, the decay rate constants in this case were 1.07 ± 0.11 min^{-1} and 0.67 ± 0.15 min^{-1} for NH_2Y_{731}• and Y_{122}•, respectively. Faster radical decay with N_3UDP/ATP may be due to greater stability conferred by CDP/ATP than by N_3UDP/ATP. With DOPA–β2, we have previously observed different DOPA• life times as a function of nucleotides bound in the α2 subunit. Alternatively, faster radical decay with N_3UDP/ATP relative to the CDP/ATP case may be indicative of C_{439}• formation by NH_2Y•: it

may be argued, if NH_2Y–α2 did not generate a C_{439}•, then the radical decay constant in the presence of CDP/ATP should be similar to that in the presence of N_3UDP/ATP, as both processes would not proceed past k_1 and k_2 (Figure 4–19) or k_A and k_B (Figure 4–20). At present, we favor the former explanation. However, our working model is that NH_2Y–α2s are competent in nucleotide reduction. Definitive evidence will come from rapid–freeze quench EPR studies which would directly show generation of N• by NH_2Y•, if NH_2Y–α2s are in fact active. The results in this Chapter further suggest that detailed pre–steady state kinetic analysis of the reactions with N_3CDP/ATP and CDP/ATP in conjunction with kinetic modeling are likely to uncover additional rate constants in Figures 4–19 & 4–20. Important in this regard will be the rate constant of for steps k_3/k_5 and k_C in Figures 4–19 & 4–20, respectively. Perhaps the most interesting rate constant is k_3. This step (k_3) is thermodynamically unfavorable and may be rate limiting in Figure 4–19.

$$k_{obs} = \frac{k_A k_B}{k_B + k_C} \qquad (4–3)$$

Implications for mechanism of oxidation. The results above strongly suggest that NH_2Y–α2s are active. Competence in nucleotide reduction has interesting mechanistic implications for radical propagation within $Y_{730}NH_2Y$–α2. Three mechanisms may be envisioned for oxidation of C_{439} by NH_2Y_{730}•: This reaction may occur by (1) a stepwise process, i.e. electron transfer (ET) followed by proton transfer (PT), (2) an orthogonal proton–coupled electron transfer (PCET) or (3) a co–linear PCET (i.e. hydrogen atom transfer – Figure 4–21).[90-92] The option of the stepwise process may be eliminated due to thermochemical bias against formation of high energy charged intermediates in the non–polar α2 active site as well as the insurmountable energy barrier for formation of a cysteine cation radical by the NH_2Y•/NH_2Y^- couple (Figure 4–21A).[91] Orthogonal PCET requires oxidation of C_{439}, which has a solution reduction potential of 1.33 V at pH 7, by a NH_2Y• which has E° of 0.64 V at pH 7 (Figure 4–21B).[1,51] Therefore, the second option would require a thermodynamically uphill process that

is unfavorable by 16 kcal/mol. The hydrogen atom transfer mechanism, however, is thermodynamically more accessible (Figure 4–21C). Its feasibility is based on knowledge of the homolytic bond dissociation energies of R–SH (88–91 kcal/mol) and *o*–aminophenol, calculated to be 78–83 kcal/mol.[1,93-95] Therefore, oxidation of C_{439} by NH_2Y_{730}• by a hydrogen atom transfer mechanism, assuming no perturbations in the protein milieu, is uphill by 'only' 5–13 kcal/mol. Thus, nucleotide reduction activity in $Y_{730}NH_2Y$–α2 would thermodynamically favor a hydrogen atom transfer mechanism for C_{439}• formation by NH_2Y_{730}•.

Interestingly, the bond dissociation energy of catechol (82–83 kcal/mol) is similar to that of *o*–aminophenol.[93] However, $DOPA_{356}$–β2 is inactive in nucleotide reduction. In case of DOPA–β2 orthogonal PCET, the functional mechanism of oxidation at this residue (i.e. similar to Fig. 4–21B), requires matching redox potentials for efficient radical propagation and nucleotide reduction. With, $Y_{730}NH_2Y$–α2, competence in nucleotide reduction, despite unmatched redox potentials (~0.69 V difference), appears to be reconciled due to a different mechanism of oxidation via hydrogen atom transfer, which appears to operate at this residue in the pathway.

In conclusion, we report evolution of a suppressor tRNA/RS pair that is specific for the unnatural amino acid NH_2Y. Site–specific insertion of NH_2Y will be useful for other systems that use Y•s in catalysis and for attaching probes of interest to a target protein. Using this technology we generated $Y_{730}NH_2Y$–α2 and $Y_{731}NH_2Y$–α2 and tested involvement of these residues in long–range radical propagation. The results demonstrate kinetically competent radical transfer from the Y_{122}• in β2 across the subunit interface and trapping of NH_2Y_{730}• or NH_2Y_{731}•. This event is triggered by binding of substrate and effector. Steady state activity assays in conjunction with reactions with the suicide inhibitor N_3ADP indicate that $Y_{730}NH_2Y$–α2 and $Y_{731}NH_2Y$–α2 are competent in nucleotide reduction. This implicates a hydrogen atom transfer mechanism for oxidation of C_{439} by NH_2Y_{730}•. Definitive evidence for activity of NH_2Y–α2s requires a detailed kinetic analysis of the decay of NH_2Y• and formation of N• with the mechanism–based inhibitor N_3NDP.

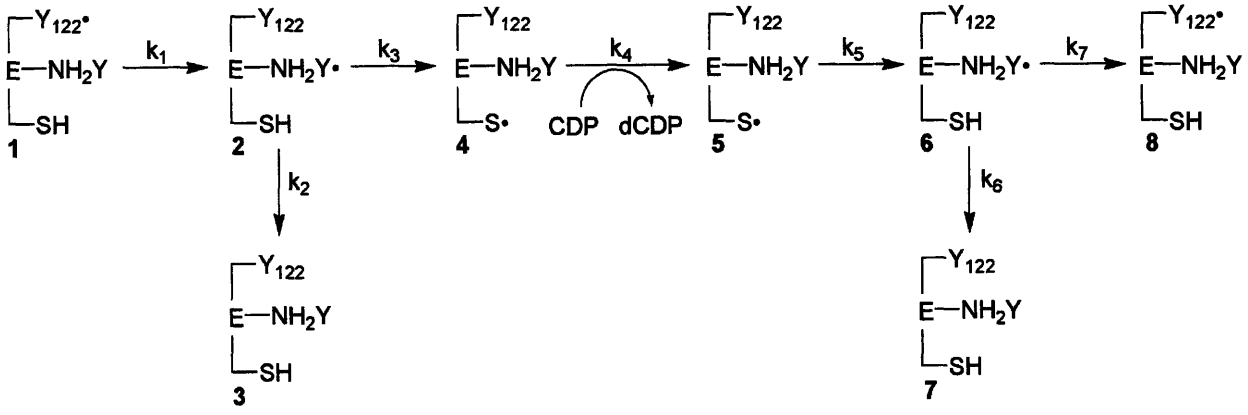

Figure 4–19. Working model for loss of spin during reaction of NH_2Y–α2s with CDP/ATP. Steps k_1, radical initiation, and k_4, nucleotide reduction, occur with rate constants of 2 s^{-1} and 500 s^{-1}, respectively. Reactions k_2 and k_6 lead to loss of radical by consumption of NH_2Y•. Rate constants for the oxidation of C_{439} by NH_2Y• (k_3) or the reverse reaction (k_5) have not been determined. Reverse radical migration is indicated by k_7.

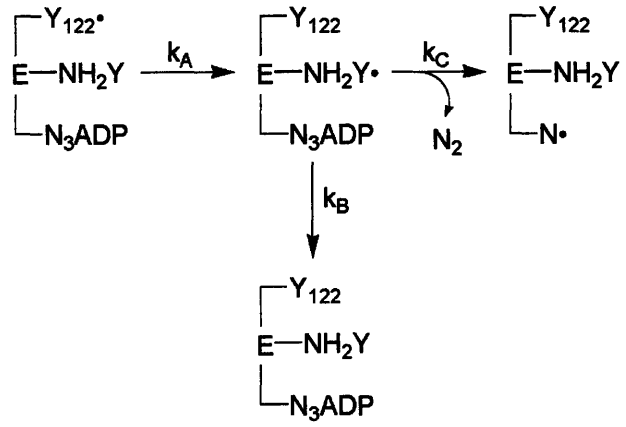

Figure 4–20. Working model for loss of spin during reaction of NH_2Y–α2s with N_3ADP/dGTP. After radical initiation and NH_2Y• formation (k_A), partitioning occurs between C_{439}• formation and subsequent N• formation (k_C) or quenching by yet unknown mechanisms (k_B).

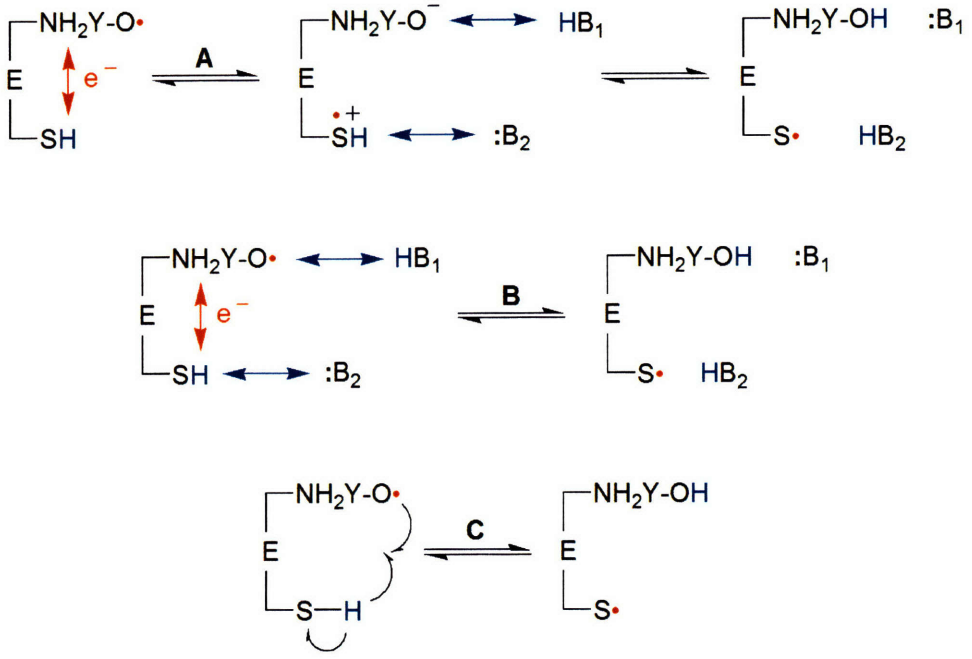

Figure 4–21. Mechanistic options for oxidation of C_{439} by NH_2Y_{730}•. (A) Stepwise ET/PT. The initial ET event generates a distinct intermediate which contains a thiyl cation radical and an 3–aminotyrosinate ($NH_2Y_{730}^-$). Subsequent PT yields a neutral thiyl radical and NH_2Y_{730}. This reaction is highly disfavored (see text). (B) Orthogonal PCET – ET and PT are coupled but the electron and proton have different destinations. The proton of C_{439} is transferred orthogonally to a basic residue, its electron is transferred to NH_2Y_{730}•, thus generating a C_{439}• and NH_2Y_{730}. (C) Co–linear PCET – Hydrogen atom transfer from C_{439} to NH_2Y_{730}•. Proton and electron originate from and arrive at the same moiety.

REFERENCES

(1) Stubbe, J.; van der Donk, W. A. *Chem. Rev.* **1998**, *98*, 705.

(2) Jordan, A.; Reichard, P. *Annu. Rev. Biochem.* **1998**, *67*, 71.

(3) Nordlund, P.; Reichard, P. *Annu. Rev. Biochem.* **2006**, 75, 681.

(4) Stubbe, J. *J. Biol. Chem.* **1990**, *265*, 5329.

(5) Stubbe, J. *Proc. Natl. Acad. Soc. U.S.A.* **1998**, *95*, 2723.

(6) Uhlin, U.; Eklund, H. *Nature* **1994**, *370*, 533.

(7) Licht, S.; Gerfen, G. J.; Stubbe, J. *Science* **1996**, *271*, 477.

(8) Logan, D. T.; Andersson, J.; Sjöberg, B.-M.; Nordlund, P. *Science* **1999**, *283*, 1499.

(9) Jiang, W.; Yun, D.; Saleh, L.; Barr, E. W.; Xing, G.; Hoffart, L. M.; Maslak, M. A.; Krebs, C.; Bollinger J. M. Jr. *Science* **2007**, *316*, 1188.

(10) Brown, N. C.; Reichard, P. *J. Mol. Biol.* **1969**, *46*, 25.

(11) Thelander, L. *J. Biol. Chem.* **1973**, *248*, 4591.

(12) Wang, J.; Lohman, G. J.; Stubbe, J. *Proc. Natl. Acad. Soc. U.S.A.* **2007**, *in press*.

(13) Brown, N. C.; Reichard, P. *J. Mol. Biol.* **1969**, *46*, 39.

(14) Ehrenberg, A.; Reichard, P. *J. Biol. Chem.* **1972**, *247*, 3485.

(15) Sjöberg, B.-M.; Reichard, P.; Gräslund, A.; Ehrenberg, A. *J. Biol. Chem.* **1978**, *253*, 6863.

(16) Reichard, P.; Ehrenberg, A. *Science* **1983**, *221*, 514.

(17) Eriksson, M.; Uhlin, U.; Ramaswamy, S.; Ekberg, M.; Regnstrom, K.; Sjöberg, B.-M.; Eklund, H. *Structure* **1997**, *5*, 1077.

(18) Nordlund, P.; Sjöberg, B.-M.; Eklund, H. *Nature* **1990**, *345*, 593.

(19) Högbom, M.; Galander, M.; Andersson, M.; Kolberg, M.; Hofbauer, W.; Lassmann, G.; Nordlund, P.; Lendzian, F. *Proc. Natl. Acad. Sci.* **2003**, *100*, 3209.

(20) Uppsten, M.; Farnegardh, M.; Domkin, V.; Uhlin U. *J. Mol. Biol.* **2006**, *359*, 365.

(21) Stubbe, J.; Nocera, D. G.; Yee, C. S.; Chang, M. C. Y. *Chem. Rev.* **2003**, *103*, 2167.

(22) Stubbe, J.; Riggs-Gelasco, P. *Trends Biochem. Sci.* **1998**, *23*, 438.

(23) Lawrence, C. C.; Stubbe, J. *Curr. Opin. Chem. Biol.* **1998**, *2*, 650.

(24) Marcus, R. A.; Sutin, N. *Biochim. Biophys. Acta* **1985**, *811*, 265.

(25) Moser, C. C.; Keske, J. M.; Warncke, K.; Farid, R. S.; Dutton, P. L. *Nature* **1992**, *355*, 796.

(26) Gray, H. B.; Winkler, J. R. *Annu. Rev. Biochem.* **1996**, *65*, 537.

(27) Bennati, M.; Weber, A.; Antonic, J.; Perlstein, D. L.; Robblee, J.; Stubbe, J. *J. Am. Chem. Soc.* **2005**, *125*, 14988.

(28) Thelander, L.; Larsson, B.; Hobbs, J.; Eckstein, F. *J. Biol. Chem.* **1976**, *251*, 1398.

(29) Sjöberg, B.-M.; Gräslund, A.; Eckstein, F. *J. Biol. Chem.* **1983**, *258*, 8060.

(30) Salowe, S.; Bollinger, J. M. Jr.; Ator, M.; Stubbe, J.; McCraken. J.; Peisach, J.; Samano, M. C.; Robins, M. J. *Biochemistry* **1993**, *32*, 12749.

(31) Fritscher, J.; Artin, E.; Wnuk, S.; Bar, G.; Robblee, J. H.; Kacprzak, S.; Kaupp, M.; Griffin, R. G.; Bennati, M.; Stubbe, J. *J. Am. Chem. Soc.* **2005**, *127*, 7729.

(32) Bennati, M.; Robblee, J. H.; Mugnaini, V.; Stubbe, J.; Freed, J. H.; Borbat, P. *J. Am. Chem. Soc.* **2005**, *127*, 15014.

(33) Climent, I.; Sjöberg, B.-M.; Huang, C. Y. *Biochemistry* **1992**, *31*, 4801.

(34) Ekberg, M.; Sahlin, M.; Eriksson, M.; Sjöberg, B.-M. *J. Biol. Chem.* **1996**, *271*, 20655.

(35) Ekberg, M.; Birgander, P.; Sjöberg, B.-M. *J. Bacteriol.* **2003**, *185*, 1167.

(36) Yee, C. S.; Seyedsayamdost, M. R.; Chang, M. C.; Nocera, D. G.; Stubbe, J. *Biochemistry* **2003**, *42*, 14541.

(37) Seyedsayamdost, M. R.; Yee, C. S.; Stubbe, J. *Nat. Protoc.* **2007**, *2*, 1225.

(38) Seyedsayamdost, M. R.; Stubbe, J. *J. Am. Chem. Soc.* **2006**, *128*, 2522.

(39) Seyedsayamdost, M. R.; Stubbe, J. *J. Am. Chem. Soc.* **2007**, *129*, 2226.

(40) Seyedsayamdost, M. R.; Reece, S. Y.; Nocera, D. G.; Stubbe, J. *J. Am. Chem. Soc.* **2006**, 128, 1569.

(41) Yee, C. S.; Chang, M. C.; Ge, J.; Nocera, D. G.; Stubbe J. *J. Am. Chem. Soc.* **2003**, *125*, 10506.

(42) Reece, S. Y.; Seyedsayamdost, M. R.; Stubbe, J.; Nocera, D. G. *J. Am. Chem. Soc.* **2006**, *128*, 13654.

(43) Seyedsayamdost, M. R.; Yee, C. S.; Reece, S. Y.; Nocera, D. G.; Stubbe, J. *J. Am. Chem. Soc.* **2006**, *128*, 1562.

(44) Chang, M. C.; Yee, C. S.; Stubbe, J.; Nocera, D. G. *Proc. Natl. Acad. Sci. U.S.A.* **2004**, *101*, 6882.

(45) Reece, S. Y.; Seyedsayamdost, M. R.; Stubbe, J.; Nocera, D. G. *J. Am. Chem. Soc.* **2007**, *129*, 8500.

(46) Wang, L.; Brock, A.; Herberich, B.; Schultz, P. G. *Science* **2001**, *292*, 498.

(47) Wang, L.; Schultz, P. G. *Angew. Chem. Int. Ed. Engl.* **2004**, *44*, 34.

(48) Xie, J.; Schultz, P. G. *Methods* **2005**, *36*, 227.

(49) Wang, L.; Xie, J.; Schultz, P. G. *Annu. Rev. Biophys. Biomol. Struct.* **2006**, *35*, 225.

(50) Xie, J.; Schultz, P. G. *Nat. Rev. Mol. Cell Biol.* **2006**, *7*, 775.

(51) DeFelippis, M. R.; Murthy, C. P.; Broitman, F.; Weinraub, D.; Faraggi, M.; Klapper, M. H. *J. Phys. Chem.* **1991**, *95*, 3416.

(52) Jovanovic, S. J.; Steenken, S.; Tosic, M.; Marjanovic, B.; Simic, M. G. *J. Am. Chem. Soc.* **1994**, *116*, 4846.

(53) Chivers, P. T.; Prehoda, K. E.; Volkman, B. F.; Kim, B.-M.; Markley, J. L.; Raines, R. T. *Biochemistry* **1997**, *36*, 14985.

(54) Russel, M.; Model, P. *J. Bacteriol.* **1985**, *163*, 238.

(55) Salowe, S. P.; Stubbe, J. *J. Bacteriol.* **1986**, *165*, 363.

(56) Santoro, S. W.; Wang, L.; Herberich, B.; King, D. S.; Schultz, P. G. *Nat. Biotechnol.* **2002**, *20*, 1044.

(57) Wang, L.; Zhang, Z.; Brock, A.; Schultz, P. G. *Proc. Natl. Acad. Sci. U.S.A.* **2003**, *100*, 56.

(58) Chin, J. W.; Martin, A. B.; King, D. S.; Wang, L.; Schultz, P. G. *Proc. Natl. Acad. Sci. U.S.A.* **2002**, 99, 11020.

(59) Zhang, Z.; Wang, L.; Brock, A.; Schultz, P. G. *Angew. Chem. Int. Ed. Engl.* **2002**, *41*, 2840.

(60) Salowe, S. P. *Ph.D. Thesis.* Massachusetts Institute of Technology, **1992**.

(61) Ryu, Y.; Schultz, P.G. *Nat. Methods* **2006**, *3*, 263.

(62) Farrell, I.S.; Toroney, R.; Hazen, J. L.; Mehl, R. A.; Chin, J. W. *Nat. Methods* **2005**, *2*, 377.

(63) Palmer, G. *Methods Enzymol.* **1967**, *10*, 595.

(64) Gräslund, A.; Sahlin, M.; Sjöberg, B.-M. *Environ. Health Perspect.* **1985**, *64*, 139.

(65) Nyholm, S.; Thalander, L.; Gräslund, A. *Biochemistry* **1993**, *32*, 11569.

(66) Bollinger Jr., J. M.; Tong, W. H.; Ravi, N.; Huynh, B. H.; Edmondson, D. E.; Stubbe, J. *Methods Enzymol.* **1995**, 258, 278-303.

(67) Wang, L.; Schultz, P. G. *Chem. Biol.* **2001**, *8*, 883.

(68) Liu, D. R.; Schultz, P. G. *Proc. Natl. Acad. Soc. U.S.A.* **1999**, *96*, 4780.

(69) Zhang, Y.; Wang, L.; Schultz, P. G.; Wilson, I. A. *Protein Sci.* **2005**, *14*, 1340.

(70) Turner, J. M.; Graziano, J.; Spraggon, G.; Schultz, P. G. *Proc. Natl. Acad. Soc. U.S.A.* **2006**, *103*, 6483.

(71) Nilsson, B.; Moks, T.; Jansson, B.; Abrahmsen, L.; Elmblad, A.; Holmgren, E.; Henrichson, C.; Jones, T. A.; Uhlen, M. *Protein Eng.* **1987**, *1*, 107.

(72) Fontecave, M.; Mulliez, E.; Logan D. T. *Prog. Nucleic Acid Res. Mol. Biol.* **2002**, *72*, 95.

(73) Rosenkranz, H. S.; Garro, A. J.; Levy, J. A.; Carr, H. S. *Biochim. Biophys. Acta* **1966**, *114*, 501.

(74) Karlsson, M.; Sahlin, M.; Sjöberg, B.-M. *J. Biol. Chem.* **1992**, *267*, 12622.

(75) Jackson, J. C.; Duffy, S. P.; Hess, K. R.; Mehl, R. A. *J. Am. Chem. Soc.* **2006**, *128*, 11124.

(76) Amann, E.; Ochs, B.; Abel, K. J. *Gene* **1987**, *61*, 41.

(77) A more detailed analysis of the new radical species will be presented elsewhere.

(78) Chen-Barrett, Y.; Harrison, P. M.; Treffry, A.; Quail, M. A.; Arosio, P.; Santambrogio, P.; Chasteen, N. D. *Biochemistry* **1995**, *24*, 7847.

(79) Sahlin, M.; Petersson, L.; Gräslund, A.; Ehrenberg, A.; Sjöberg, B.-M.; Thelander, L. *Biochemistry* **1987**, *26*, 5541.

(80) Gerfen, G. J.; van der Donk, W. A.; Yu, G.; McCarthy, J. R.; Jarvi, E. T.; Matthews, D. P.; Farrar, C.; Griffin, R. G.; Stubbe, J. *J. Am. Chem. Soc.* **1998**, *120*, 3823.

(81) Ge, J.; Yu, G.; Ator, M. A.; Stubbe, J. *Biochemisty* **2003**, *42*, 10071.

(82) Rapid chemical quench studies monitoring dCDP formation with intein–generated wt β2, no longer show a burst of dCDP formation (as with wt β2) but exhibit a single rate constant of ~1 s^{-1} (see Chapter 8). Thus, the slow phase observed with DOPA–β2 could also be kinetically competent in turnover.

(83) Craw, M.; Chedekel, M. R.; Truscott, T. G.; Land, E. J. *Photochem. Photobiol.* **1984**, 39, 155-159.

(84) van der Donk, W. A.; Stubbe, J.; Gerfen, G. J.; Bellew, B. F.; Griffin, R. G. *J. Am. Chem.* Soc. **1995**, *117*, 8908.

(85) Hooker, J. M.; Kovacs, E. W.; Francis, M. B. *J. Am. Chem. Soc.* **2004**, *126*, 3718.

(86) Kovacs, E. W.; Hooker, J. M.; Romanini, D. W.; Holder, P. G.; Berry, K. E.; Francis, M. B. *Bioconjug. Chem.* **2007**, *18*, 1140.

(87) Felix, C. C.; Sealy, R. C. *J. Am. Chem. Soc.* **1981**, *103*, 2831.

(88) Neta, P.; Fessenden, R. W. *J. Phys. Chem.* **1974**, *78*, 523.

(89) Previous computational studies on *o*–aminophenol have shown that the BDE of the phenolic hydroxyl group is lower than that of the amine. EPR studies on *o*–aminophenol are in line with these calculations demonstrating the presence of two N–bound protons in the oxidized state (see refs. 88 and 94). Our own preliminary EPR simulations and DFT calculations also suggest that the structure of the radical is that shown in Scheme 4–1 (see Chapter 5).

(90) Cukier, R. I.; Nocera, D. G. *Annu. Rev. Phys. Chem.* **1998**, *49*, 337.

(91) Mayer, J. M.; Rhile, I. J. *Biochim. Biophys. Acta* **2004**, *1655*, 51.

(92) Reece, S. Y.; Hodgkiss, J. M.; Stubbe, J.; Nocera D. G. *Philos. Trans. R. Soc. Lond. B Biol. Sci.* **2006**, *361*, 1351.

(93) Borges dos Santos, R. M.; Martinho Simões, J. A. *J. Phys. Chem. Ref. Data* **1998**, *27*, 707.

(94) Wright, J. S.; Johnson, E. R.; DiLabio, G. A. J. Am. Chem. Soc. **2001**, 123, 1173.

(95) Bakalbassis, E. G.; Lithoxoidou, A. T.; Vafiadis, A. P. *J. Phys. Chem. A* **2006**, *110*, 11151.

CHAPTER 5:

Detailed Kinetic and Spectroscopic Examination of $NH_2Y\bullet$ Formation with $NH_2Y-\alpha 2s$

INTRODUCTION

Ribonucleotide reductases (RNRs) catalyze the conversion of nucleotides to deoxynucleotides, thereby providing the monomeric units required for DNA replication and repair.[1,2] The class Ia RNR from *E. coli* is the best studied RNR to date. It consists of a 1:1 complex of two homodimeric subunits: α2 and β2.[3,4] α2 is the site of nucleotide reduction. It contains the active site as well as binding sites for allosteric regulators, which control the rate and specificity of nucleotide reduction. β2 houses a diiron tyrosyl radical (Y_{122}•) cofactor essential for nucleotide reduction.[5] Each turnover requires radical transfer from Y_{122}• in β2 to C_{439} in α2. The mechanism of this event, the radical initiation, is a major unresolved issue.[6,7]

A structure of the active RNR complex has not been solved. However, based on docking of individual structures of α2 and β2, Uhlin and Eklund made the unusual proposal that a pathway consisting of aromatic amino acids would transport the radical from Y_{122}• in β2 over 35 Å to the active site of α2 (Figure 5–1).[8,9] This was a bold proposition for several reasons. In no other systems are amino acids known to transport radicals over a long distance. All other long range electron transfer pathways contain metal cofactors, which are absent from the proposed pathway in RNR. Additionally, in contrast to the majority of electron transfer pathways, which are irreversible, the radical generation pathway in RNR is reversible.

Nevertheless, evidence from various approaches has accumulated ultimately making a strong case that long range radical transfer mediated by aromatic amino acids is the mechanism of C_{439}• generation in the *E. coli* RNR (see Chapters 2, 3 & 4). Important in this regard were the seminal experiments by Reichard and Ehrenberg, demonstrating that the Y_{122}• participates in catalysis,[5] as well as studies by Stubbe and coworkers, which unraveled a radical nucleotide reduction mechanism and revealed nucleotide radical formation at the expense of Y_{122}• with mechanism–based inhibitors.[10-13]

Initial evidence for the pathway in Figure 5–1 came from site–directed mutagenesis studies, which showed that mutation of any residue in the pathway abrogates nucleotide

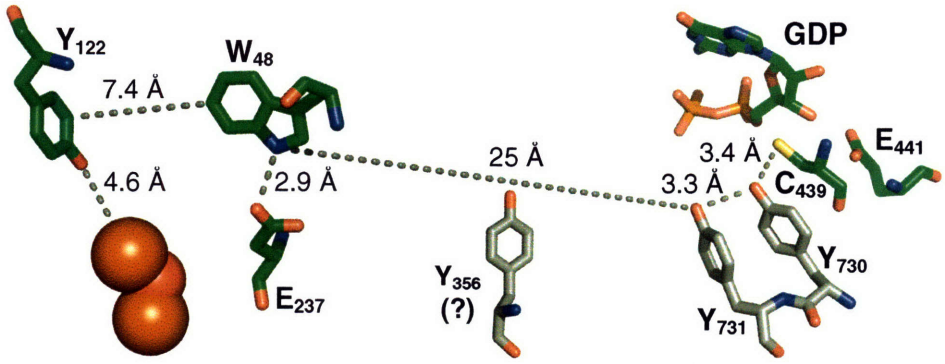

Figure 5–1. The proposed radical initiation pathway within an αβ pair. Residues in grey have been shown to be redox–active using DOPA–β2 and NH_2Y–α2s, respectively. Note that the position of Y_{356} is unknown.

reduction activity.[14,15] Complementation studies subsequently showed that these residues were required in vivo as well as in vitro.[16] These studies implicated involvement of the residues in Figure 5–1 in radical propagation, however, a large conformational change that would reduce the distance between Y_{122}• and C_{439} remained a possibility.

Compelling evidence against such a conformational change and for the docking model has recently been obtained using pulsed electron–electron double resonance (PELDOR) spectroscopy and double quantum coherence (DQC) spectroscopy, which can measure the distance between two paramagnetic species separated by 15–80 Å.[17,18] Studies using the mechanism–based inhibitor 2'–azido–2'–deoxyUDP (N_3UDP), which gives rise to a stable N–centered radical (N•) in the active site of α2, allow the 'diagonal' distance between the Y_{122}• in one αβ pair and the N• in the other αβ pair to be measured. The distance obtained was similar to that calculated from the docking model.[19]

The pathway consists of β2–W_{48} and three tyrosine residues (Y_{356} in β2, Y_{730}/Y_{731} in α2). Evidence for redox activity of residue W_{48} has been obtained from examination of in vitro reconstitution of the diiron Y_{122}• cofactor in apo β2, even before the proposal of long–range radical propagation.[20-22] In these experiments UV–vis, EPR and Mössbauer spectroscopic methods revealed formation of a $W_{48}H^{\bullet+}$ adjacent to a Fe^{III}–Fe^{IV} cluster. Further, under Fe

limiting conditions, oxidation of Y_{122} by $W_{48}H^{\bullet+}$ directly established communication between these residues. These observations have been complemented with Y–W dipeptide model studies, which demonstrate that reversible oxidation of Y by W• is chemically feasible depending on the protonation state of each residue.[23] These results provide chemical precedence for the reversible communication proposed between Y_{122}• and W_{48}.

The involvement of residue Y_{356} in radical propagation has been interrogated by semisynthetic construction of β2.[24,25] The construction method involved intein–mediated site–specific incorporation of unnatural amino acids. The analogues incorporated sterically resemble Tyr, but have altered reduction potentials and pK_as. Incorporation of 3,4–dihydroxyphenylalanine (DOPA), which has a lower reduction potential than Tyr (260 mV lower at pH 7), led to trapping of a $DOPA_{356}$•, its formation requiring binding of substrate and/or effector. Formation of DOPA• occurred concomitantly with disappearance of Y_{122}• in a kinetically competent fashion (see Chapters 2 & 3). Thus these experiments demonstrated direct communication between residues 356 and 122. In a variant of DOPA–β2, DOPA–ββ' (where the β'–monomer lacks the C–terminal 22 residues), this communication was observed in both directions: after formation of $DOPA_{356}$•, reformation of Y_{122}• was accompanied by loss of $DOPA_{356}$•. Incorporation of a series of fluorotyrosine analogues (F_nYs) has provided additional convincing evidence for a redox active role of residue 356 in radical generation and shed light on the mechanism of oxidation of this residue.[26-28]

To investigate the roles of residues Y_{730}/Y_{731} in radical propagation, we recently used the suppressor tRNA/synthetase method, pioneered by Schultz and coworkers, to site–specifically replace each of these residues with the Tyr analogue 3–aminotyrosine (NH_2Y – see Chapter 4).[29,30] This analogue is 190 mV easier to oxidize than Tyr.[31] Examination of NH_2Y–α2 variants demonstrated kinetically competent radical propagation into the α2 subunit and formation of a new radical species, which we proposed was a NH_2Y• based on UV–vis and EPR characterization. In this chapter, we further investigate the structure of the putative NH_2Y• using ^{15}N and ^{2}H isotopic substitution, 9 GHz and 180 GHz EPR spectroscopies, EPR spectral

simulation and density functional theory (DFT) calculations. Our results unambiguously demonstrate that the new signal is associated with the NH_2Y probe, provide insight into the conformation of the NH_2Y• within α2, and yield spin densities for the major nuclei interacting with the unpaired spin. This is the first detailed characterization of an NH_2Y• within an enzyme. The position of the NH_2Y• within the α2/β2 complex is examined using PELDOR spectroscopy. The results give distances between the newly formed NH_2Y•, at residue 730 or 731, in one αβ pair and the remaining Y_{122}• in the other αβ pair, which are consistent with the distances predicted by the docking model. In addition, studies with $Y_{356}F$–β2 show that formation of NH_2Y_{730}• and NH_2Y_{731}• is pathway–dependent. Alternative pathways circumventing Y_{356} do not exist. Finally, X–band EPR and SF UV–vis spectroscopic methods with various substrate/effector combinations reveal a new role for the allosteric effector in catalysis.

MATERIALS AND METHODS

Materials. L–Tyrosine, ^{15}N–HNO_3 (conc: ~10 N, 98 % ^{15}N enrichment), Palladium catalyst on carbon (10 wt % loading), 1,10–phenanthroline, hydroxyurea, Sephadex G–25 and all nucleotides (CDP, GDP, UDP, ADP, ATP, TTP, dGTP) were obtained from Sigma–Aldrich. D_2O (99.8 atom % in D) and Ni–NTA were from VWR and Qiagen, respectively. ^1H and ^{13}C NMR spectra were recorded on a Varian 300 MHz NMR spectrometer at the MIT Department of Chemistry Instrumentation Facility (DCIF). Aqueous samples for ^1H NMR and ^{13}C (^1H–decoupled) NMR were carried out in D_2O with 3–(trimethylsilyl)–propionic acid–d_4 (TSP) and tetramethylsilane as an external standards, respectively. His_6–$Y_{356}F$–β2 was previously prepared by Dr. Cyril Yee and contained 1.0 Y_{122}• per dimer (specific activity $<1/10^5$ that of wt β2). Steady-state absorption spectra were recorded on an Agilent 8453 Diode Array Spectrophotometer.

Synthesis of 3–[^{15}N]–nitrotyrosine, [^{15}N]–NO_2Y. [^{15}N]–HNO_3 (10 N) contained 98 % ^{15}N as determined by mass spectrometry. Synthesis of [^{15}N]–NO_2Y was carried out as previously described with minor modifications.[32] Prior to the synthesis, ^{15}N–HNO_3 was diluted to 7.5 N with water. L–Tyr (7.0 mmol) was added to a 25 mL pear–shaped flask, equipped with a stir bar, and dissolved in 5 mL H_2O at room temperature. The mixture was supplemented with 1.55 mL of [^{15}N]–HNO_3 (11.6 mmol) by dropwise addition over 1 min and stirred for 30 min at room temperature to fully dissolve L–Tyr. The mixture was then cooled by stirring for 15 min in an ice–water bath. Then 4 mL of [^{15}N]–HNO_3 (30 mmol) were added dropwise to the mixture at 4°C over 2 h (8 × 0.5 mL additions of [^{15}N]–HNO_3 in 15 min intervals). The solution was then stirred for an additional 5 h at 4°C and refridgerated overnight, which caused precipitation of [^{15}N]–NO_2Y. The precipitate was isolated and dried by vacuum filtration on a coarse Buchner funnel providing product in 80 % yield (5.6 mmol). The product was analyzed by ^1H and ^{13}C NMR and by UV–vis spectroscopies.

To determine the extinction coefficients, 20–30 mg of the product were weighed out and dissolved in a defined volume of water. UV spectra were acquired on a Cary3 UV–vis Spectro–photometer. Extinction coefficients were then calculated using Beer's Law. A similar procedure was carried out with 'authentic' NO_2Y obtained from Sigma–Aldrich.

^1H NMR (300 MHz, D_2O, 25 °C) δ= 3.18 (dd, 1H, C_β-H_1, 7.4 Hz, 14.8 Hz), 3.30 (dd, 1H, C_β-H_2, 5.8 Hz, 14.8 Hz), 4.24 (dd, 1H, C_α-H, 5.8 Hz, 7.4 Hz), 7.14 (dd, 1H, arom. C-H, 1.1 Hz, 8.7 Hz), 7.54 (dd, 1H, arom. C-H, 2.2 Hz, 8.7 Hz), 8.01 (t, 1H, arom. C-H, 2.2 Hz). ^{13}C NMR (300 MHz, D_2O, 25 °C) δ= 34.7 (s, C_β), 54.2 (s, C_α), 120.4 (d, arom. C_2, 2.1 Hz), 126.1 (d, arom. C_1, 1.6 Hz), 126.8 (d, arom. C_4, 2.4 Hz), 134.2 (d, arom. C_3, 15.2 Hz), 138.2 (s, arom. C_6), 153.1 (d, arom. C_5, 1.2 Hz), 172.1 (s, COOH). UV–vis (H_2O/HCl, pH 2) λ_{max} ~277 nm (ε ~5500 $M^{-1}cm^{-1}$), λ_{max} ~358 nm (ε ~2600 $M^{-1}cm^{-1}$); (H_2O/NaOH, pH 12) λ_{max} ~286 nm (ε ~4100 $M^{-1}cm^{-1}$), λ_{max} ~431 nm (ε ~4100 $M^{-1}cm^{-1}$).

Synthesis of 3–[^{15}N]–aminotyrosine, [^{15}N]–NH_2Y. [^{15}N]–NO_2Y (5.2 mmol) was combined with 18 mL H_2O and 70 mL MeOH in a 250 mL round bottom flask, equipped with a stir bar, at room temperature. The solution was supplemented with 0.52 mmol (550 mg) of Pd/C catalyst. The mixture was evacuated gently and filled with $H_{2(g)}$ several times. It was then stirred for 2 h under H_2 atmosphere using a double $H_{2(g)}$ balloon. After the incubation, the catalyst was removed by filtration using a fine Buchner funnel. The solvent was removed *in vacuo* providing product in quantitative yield. The product was dissolved in a small volume of water, lyophilized to dryness and assessed by ^1H, ^{13}C NMR and UV–vis spectroscopic methods. It was >95 % pure as determined by NMR spectroscopy. Extinction coefficients for the product and 'authentic' NH_2Y (Sigma–Aldrich) were determined as described above for NO_2Y.

^1H NMR (300 MHz, D_2O, 25 °C) δ= 3.12 (m, 2H, C_β-Hs), 3.90 (t, 1H, C_α-H, 6.3 Hz), 6.99 (m, 1H, arom. C-H), 7.19 (m, 2H, arom. C-H). ^{13}C NMR (300 MHz, D_2O, 25 °C) δ= 35.2 (s, C_β), 55.5 (s, C_α), 116.9 (s, arom. C_1), 118.2 (d, arom. C_3, 9.4 Hz), 124.8 (d, arom. C_2, 1.7 Hz), 126.9 (d, arom. C_4, 1.9 Hz), 131.4 (s, arom. C_6), 149.5 (s, arom. C_5), 173.3 (s, COOH). UV–vis

(H_2O/HCl, pH 1) λ_{max} ~275 nm (ε ~1900 $M^{-1}cm^{-1}$); (H_2O, pH 7) λ_{max} ~289 nm (ε ~3200 $M^{-1}cm^{-1}$); (H_2O/NaOH, pH 12) λ_{max} ~303 nm (ε ~4700 $M^{-1}cm^{-1}$).

Growth, expression and purification of [^{15}N]–NH_2Y_{730}–α2. All procedures were carried out as detailed in Chapter 4 without modifications and gave 6 mg of pure [^{15}N]–NH_2Y_{730}–α2 per g of wet cell paste.

Activity assays. The activity of [^{15}N]–NH_2Y_{730}–α2 was determined by the spectrometric assay (Chapter 4).

Reaction of $Y_{730}NH_2Y$–α2 with β2, NDP/(d)NTP monitored by EPR spectroscopy. The reaction of pre–reduced $Y_{730}NH_2Y$–α2 with β2 (1.0 Y_{122}•/dimer, 6200 nmol/min•mg) was carried out with all four substrate effector pairs in parallel. $Y_{730}NH_2Y$–α2 and effector were mixed with β2 and substrate in a final volume of 250 μL to yield final concentrations of 24 μM $Y_{730}NH_2Y$–α2/β2, CDP/ATP (1 mM, 3 mM), GDP/TTP (1 mM, 0.25 mM), UDP/ATP (1.5 mM, 3 mM) or ADP/dGTP (1 mM, 0.12 mM). All four reactions were quenched after 20 s by hand–freezing in liquid N_2. EPR spectroscopy and data processing was carried out as detailed in Chapter 4.

Reaction of [^{15}N]–$Y_{730}NH_2Y$–α2 with β2 and NDP/(d)NTP monitored by EPR spectroscopy. [^{15}N]–NH_2Y_{730}–α2 was pre–reduced as described in Chapter 4. The reaction of pre–reduced [^{15}N]–$Y_{730}NH_2Y$–α2 with β2 (1.2 Y_{122}•/dimer) was carried out with all four substrate/effector pairs in parallel under conditions identical to those described for $Y_{730}NH_2Y$–α2 above.

Reaction of $Y_{730}NH_2Y$–α2 or [^{15}N]–$Y_{730}NH_2Y$–α2 with β2, NDP/(d)NTP in deuterated buffer monitored by EPR spectroscopy. Assay buffer (50 mM Hepes, 15 mM $MgSO_4$, 1 mM EDTA) was prepared in D_2O and its pD adjusted to 8.0. Nucleotides stock solutions were prepared in deuterated assay buffer. $Y_{730}NH_2Y$–α2, [^{15}N]–$Y_{730}NH_2Y$–α2 and β2 were exchanged into deuterated buffer by multiple concentration/dilution cycles at 4°C using a centriprep concentration device and a YM–30 membrane until the solution consisted >99 % of

deuterated buffer. The reaction of $Y_{730}NH_2Y$–α2/β2 (or [^{15}N]–$Y_{730}NH_2Y$–α2) in deuterated buffer with various substrate/effector pairs was carried out as described above.

Preparation of high–field EPR and PELDOR samples. Pre–reduced $Y_{730}NH_2Y$–α2 (or $Y_{731}NH_2Y$–α2) and β2 were combined in an equimolar ratio and concentrated at 4°C in a minicon concentration device (YM–30 membrane) to a final complex concentration of 70–100 μM ($\varepsilon_{280\,nm\,(\alpha2+\beta2)}$ = 320 $mM^{-1}cm^{-1}$). The concentrated sample was divided into 100 μL aliquots and placed in 1.5 mL Eppendorf tubes, flash–frozen in liquid N_2 and shipped on dry ice along with substrate/effector solutions and glycerol–containing buffer to Prof. Marina Bennati at the University of Frankfurt (Germany). High–field EPR and PELDOR samples were prepared by Prof. Marina Bennati by thawing each aliquot on ice and adding 5 μL of a substrate/effector mix to yield final concentrations of CDP/ATP (1 mM, 3 mM) or GDP/TTP (1 mM, 0.25 mM). Each reaction was allowed to proceed for 30 s at room temperature, at which point 15 μL of glycerol buffer (100 mM Hepes, 30 mM $MgSO_4$, 2 mM EDTA, 50 % glycerol, pH 7.6) was added to yield a final glycerol concentration of ~6 %. The reaction was quenched immediately after addition of glycerol buffer by hand–freezing in liquid N_2. High–field (180 GHz) EPR and X–band PELDOR spectra were recorded and analyzed by Dr. Vasyl Denysenkov and Prof. Marina Bennati.

Simulation of X–band EPR spectra. The EPR powder spectra of NH_2Y•–α2 in the presence of CDP/ATP were analyzed using SimFonia software (Brüker) for simulation of anisotropic g– and hyperfine tensors. The g values used were determined by 180 GHz EPR spectroscopy. For all simulations, a Lorentzian/Gaussian ratio of 0.3 was used. Only hyperfine couplings from I=1/2 and I=1 (for [^{14}N]–NH_2Y•) were varied to yield the best fit to the experimental data. For simulation of NH_2Y•–α2 spectra in protonated and deuteratd buffer an isotropic line width parameter of 15.4 and 8.4 MHz were used, respectively. To assess the quality of the simulation, the experimental and simulated spectra were normalized to unit area. χ^2 was then computed using Eq. 5–1, where y_i and y'_i are the data for the experimental and the

simulated spectrum, respectively.[33] Iterative rounds of simulation and calculation of χ^2 were performred until χ^2 was optimized.

$$\chi^2 = \sum (y_i - y'_i)^2 \qquad (5\text{–}1)$$

Computational studies. DFT calculations were performed by Dr. Jörg Fritscher and Prof. Marina Bennati at the University of Frankfurt. The simulation in Figure 5–8C was carried out by Dr. Debora Martino using an in–house program written in MatLab.

Reaction of $Y_{731}NH_2Y$–α2 with β2, NDP/(d)NTP monitored by EPR spectroscopy. The reaction of pre–reduced $Y_{731}NH_2Y$–α2 with β2 (1.2 Y_{122}•, 7800 nmol/min•mg) was carried out with all four substrate effector pairs in parallel. $Y_{731}NH_2Y$–α2 and effector were mixed with β2 and substrate to yield final concentrations of 20 μM $Y_{731}NH_2Y$–α2/β2, CDP/ATP (1 mM, 3 mM), GDP/TTP (1 mM, 0.25 mM), UDP/ATP (1.5 mM, 3 mM) and ADP/dGTP (1 mM, 0.12 mM). All four reactions were quenched after 20 s by hand–freezing in liquid N_2. EPR spectroscopy and data processing was carried out as detailed in Chapter 4.

Reaction of $Y_{730}NH_2Y$–α2 (or $Y_{731}NH_2Y$–α2) with His_6–$Y_{356}F$–β2 monitored by EPR spectroscopy. Pre–reduced $Y_{730}NH_2Y$–α2 (or $Y_{731}NH_2Y$–α2) and ATP were mixed with His_6–$Y_{356}F$–β2 and CDP to yield final concentrations of 15 μM, 3 mM, 15 μM and 1 mM, respectively. The reaction was quenched at 20 s or 2 min by hand–freezing in liquid N_2. A similar reaction under identical conditions was carried out with GPD/TTP with final concentrations of 1 mM and 0.2 mM, repsectively. For a direct comparison, a reaction was also carried out with wt β2 in the presence of CDP/ATP in parallel. Acquisition of EPR spectra and spin quantitation were described in Chapter 4. Note that the pre–reduction procedure removes the Y_{122}• of copurifying wt β2 in the NH_2Y–α2 preparations.

SF UV–vis spectroscopy of NH_2Y–α2/β2 with various NDP/(d)NTP pairs. All reactions were carried out in assay buffer (50 mM Hepes, 15 mM $MgSO_4$, 1 mM EDTA, pH 7.6). In all cases $Y_{730}NH_2Y$–α2 (or $Y_{731}NH_2Y$–α2) and effector (if present) in one syringe were combined with β2 and substrate (if present) from a second syringe to yield 5 μM NH_2Y–α2/β2.

The following substrate and/or effector combinations (final concentrations) were studied: CDP/ATP (1 mM, 3 mM), GDP/TTP (1 mM, 0.2 mM), UDP/ATP (1 mM, 3 mM), ADP/dGTP (1 mM, 0.2 mM), CDP (1 mM), GDP (1 mM), UDP (1 mM), ADP (1 mM), ATP (3 mM), TTP (0.2 mM) and dGTP (0.2 mM). The reactions were monitored at 325 nm for $Y_{730}NH_2Y\bullet$–α2, (ε ~10500 $M^{-1}cm^{-1}$) and 320 nm for $Y_{731}NH_2Y\bullet$–α2 (ε ~11000 $M^{-1}cm^{-1}$). In each experiment, 5–7 were traces were averaged and kinetic parameters obtained by curve fitting using OriginPro or KaleidaGraph Software. Iterative rounds of fitting and calculation of a residual plot and the R^2 correlation value were carried out until both were optimized. All the fits shown had satisfactory residuals throughout the time course, i.e. randomized scatter at Abs~0, and R^2 values ≥0.99.

Temperature–dependent SF UV–vis spectroscopy of $Y_{730}NH_2Y$–α2/β2 with CDP/ATP. Temperature–dependent SF UV–vis experiments were carrid out between 23°C and 36°C. The final concentrations were 4 μM $Y_{730}NH_2Y$–α2/β2, 1 mM CDP, 3 mM ATP in assay buffer (50 mM Hepes, 15 mM $MgSO_4$, 1 mM EDTA, pH 7.6). The instrument was equilibrated at each temperature (23, 25, 28, 34, 36°C) for 10–15 min before acquisition of kinetic traces. The internal instrument temperature reading was within 0.4–0.8°C of the temperature setting used on the circulating water bath. At each temperature, formation of $NH_2Y_{730}\bullet$ was monitored by averaging 5–7 individual traces at 325 nm. Kinetic parameters were obtained by fitting to double–exponential curves using OriginPro Software. To obtain thermodynamic parameters, Eyring analysis was performed by plotting $\ln(k_{obs}/T)$ vs. 1/T and fit to Eq. 5–2, where k_{obs} is the observed fast or slow rate constant for $NH_2Y\bullet$ formation, T is the tempterature (from the circulating water bath), k_B is the Boltzman constant, h is Planck's constant, R is the universal gas constant, $\Delta H^{\ddagger}$ is the enthalpy of activation and $\Delta S^{\ddagger}$ is the entropy of activation. Using the $\Delta H^{\ddagger}$ and $\Delta S^{\ddagger}$ values obtained from this analysis, the free energy of activation for the reaction ($\Delta G^{\ddagger}$) at 25°C was computed using Eq. 5–3.

$$\ln(k_{obs}/T) = \ln(k_B/h) + \frac{DH^{\ddagger}}{RT} + \frac{DS^{\ddagger}}{RT} \qquad (5\text{–}2)$$

$$\Delta G^{\ddagger} = \Delta H^{\ddagger} - T\times\Delta S^{\ddagger} \qquad (5\text{–}3)$$

RESULTS

Isotope labeling of NH_2Y to examine the new signal with NH_2Y–α2s by EPR spectroscopy. To assess the involvement of residues Y_{730} and Y_{731} in radical propagation, we recently reported efficient site–specific incorporation of NH_2Y into α2 using the amber suppressor tRNA/ aminoacyl–tRNA synthetase method developed by the Schultz lab. We demonstrated formation of a putative NH_2Y• based on UV–vis, EPR and EPR power saturation studies, only in the presence of CDP/ATP. Further assignment of the new EPR spectrum requires isotopic substitution studies coupled with EPR and ENDOR spectroscpies, simulation of the spectra and computational methods.

To support our assignment and obtain information about the orientation of the β–protons, spin density distribution and H–bonding interactions, isotopic substitution studies have been carried out. As noted in Chapter 4, no EPR spectrum of NH_2Y• has been reported. However, the *o*–aminophenol radical, an excellent surrogate for NH_2Y•, has been examined in detail. These studies have shown that the *o*–aminophenol radical has significant hyperfine coupling to the ^{14}N nucleus (I=1) and the exchangeable amine protons (I=1/2), although spin densities have not been reported. A summary of the EPR parameters obtained for the *o*–aminophenol radical generated by numerous laboratories using different oxidants is summarized in Table 5–1.[34-39] The variability of data in Table 5–1 is due to different oxidants or solvents in which the radical was generated. In case of metal oxidants, such as Ce^{IV} or Co^{II} the structure of the radical was not described. The *o*–aminophenol radical may be coordinated to the metal oxidant making comparison with our NH_2Y• inappropriate (Table 5–1, entries 2, 8, 9). In case of the organotin oxidant, the structure of the resulting radical was analyzed. The *o*–aminophenol radical was found to be coordinated to Sn; a Sn hyperfine constant of 160 MHz was reported (Table 5–1, entry 7). In entry 4, a complicated oxidation mechanism involving hydrogen azide was used, but the pH of the reaction was not reported. In entry 3, Dixon et al. have suggested a reassignment of the data by Neta et al. (entry 1) based on analysis of their own spectra in entry 4 (Table 5–1).

However, this reassignment is not consistent with earlier work by Dixon et al. (Table 5–1, entry 2) or with parameters provided by other groups (Table 5–1, entries 5–9). The data in entries 5 and 6 were acquired in CH_2Cl_2/THF and MeOH at –61°C and –75°C, respectively. These low dielectric solvents may better simulate the environment in the protein interior, although the dielectric at residues Y_{730} and Y_{731} is not known. It appears the data in entries 1, 5, and 6 provide the best models for comparison with our NH_2Y• as the radicals were generated by standard radiolysis or photolysis methods and are not complicated by the presence of metal oxidants.

According to these entries in Table 5–1, substitution of [^{14}N]–NH_2Y with [^{15}N]–NH_2Y would be expected to change its EPR spectrum by removing the triplet pattern produced by ^{14}N (I=1) and replacing it with a doublet pattern arising from the I=1/2 nucleus of ^{15}N. Due to the similar gyromagnetic raios of ^{14}N and ^{15}N (^{15}N/^{14}N=1.4), the strengths of hyperfine coupling is not expected to change significantly.

The results in Table 5–1 also show that the exchangeable aromatic amine protons of NH_2Y have significant hyperfine interaction with the unpaired spin. Thus, replacement of these protons may be used to interrogate the identity of the new signal. Replacement of ^{1}H (I=1/2) with ^{2}H (I=1) would be expected to change its EPR spectrum based on the change in the nuclear spin quantum number. However, due to the smaller gyromagnetic ratio of ^{2}H compared to ^{1}H (^{1}H/^{2}H=6.5), the splitting by ^{2}H would be too small to be resolved in our frozen solution spectra. Thus, replacement of ^{2}H with ^{1}H would effectively eliminate hyperfine splitting from the exchangeable amine protons in deuterated buffer. It would also eliminate weakly coupled matrix protons or H–bond interactions that may be present and result in a trace with a narrower spectral width.

The data in Table 5–1 also indicate a significant hyperfine splitting from the C_4–proton (Figure 5–1). This indicates a substantial spin density at C_4. Consequently, we would expect a significant hyperfine interaction from the β–protons in NH_2Y• via a hyperconjugation mechanism, the basis of which has previously been described.

Table 5–1. Summary of EPR parameters (in MHz)[a] previously reported for an *o*–amino–phenol radical.[b]

Entry	Reference	g factor	$^{b}A_3^H$	$^{b}A_4^H$	$^{b}A_5^H$	$^{b}A_6^H$	$^{b}A^N$	$^{b}A^{N\text{-}H}$
1	Neta *et al.*[c]	2.00372	<0.28	12.1	2.8	8.2	13.3	14.8 (2)[m]
2	Dixon *et al.*[d]	nr[l]	-2.52	18.5	4.2	7.3	18.5	22.8
3	Dixon *et al.*[e]	nr[l]	0	12.1	8.2	2.8	13.3	14.8 (2)[m]
4	Dixon *et al.*[f]	nr[l]	1.4	11.9	7.1	2.9	14.1	17.0
5	Loth *et al.*[g]	nr[l]	1.29	6.5	1.5	6.1	12.4	21.3/16.2
6	Loth *et al.*[h]	nr[l]	0.28	8.4	3.9	7.0	12.6	19.3/15.4
7	Sur *et al.*[i]	2.0025	4.82	9.6	4.8	<0.28	14.4	19.3
8	Simandi *et al.*[j]	2.0041	2.13	11.8	2.1	5.9	12.7	18.2 (2)[m]
9	Simandi *et al.*[k]	2.0047	2.13	11.8	2.1	5.9	12.7	2.8 (2)[m]
	Range	2.0037 – 2.0047	0 – 4.82	6.5 – 18.5	1.5 – 8.2	<0.28 – 8.2	12.4 – 18.5	14.8 – 22.8

[a] Hyperfine coupling constants were reported in Gauss, they have been converted to MHz as per 1 G=2.8 MHz. [b] See Figure 5–2 for numbering scheme of *o*-aminophenol radical. A_x^H is the hyperfine coupling constant from the proton attached to C_x of the *o*-aminophenol radical. A^N is the coupling from the N–nucleus, $A^{N\text{-}H}$ is the coupling from the amine protons. [c] Generated by in situ radiolysis/EPR spectroscopy in water at room temperature (Ref. 34). [d] Generated by reaction of *o*-aminophenol in water with Ce^{IV} and monitored by flow EPR at RT (Ref. 36). [e] Suggested assignment by Dixon et al of the data in Neta et al (Ref. 35). [f] Auto-oxidation in water in the presence of hydrogen azide and *p*-benzoquinone at RT. [g] Spectra obtained in CH_2Cl_2/THF at –61°C (Ref. 39). [h] Spectra obtained in CH_3OH at –75°C (Ref. 39). [i] Data are for a 4–t–butyl–2–aminophenoxyl radical complexed to triphenyltin – generated by in situ irradiation at RT (Ref. 38). [j] Oxidation mediated by Co^{II} in CH_3OH, monitored at 25°C (Ref. 37). [k] Oxidation mediated by Co^{II} in CD_3OD, monitored at 25°C (Ref. 37). [l] nr, not reported. [m] Two protons with identical hyperfine splitting constants.

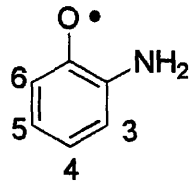

Figure 5–2. Numbering scheme for *o*–aminophenol radical data in Table 5–1. Accordingly, A_3^H in Table 5–1 corresponds to the hyperfine coupling constant from the proton attached to C_3.

Preparation of [^{15}N]–NH_2Y. To test these predictions, [^{15}N]–NH_2Y was prepared according to the synthetic route in Scheme 5–1 in 80 % yield with 98 % [^{15}N] isotopic enrichment (see Materials). As expected, the nuclear coupling from ^{15}N to ^{13}C was observed in ^{1}H–decoupled ^{13}C NMR and in ^{1}H NMR spectra of [^{15}N]–NH_2Y. Interestingly, in case of [^{15}N]–NO_2Y, ^{1}J, ^{2}J and ^{3}J couplings were observed in the ^{13}C NMR spectrum on the order of 15.2 Hz, 2.3 Hz and 1.4 Hz, respectively (Figure 5–3). With [^{15}N]–NH_2Y, only the ^{1}J and ^{2}J couplings are present in the ^{13}C NMR spectrum at 9.4 Hz and 1.8 Hz, respectively (Figure 5–3). Previous NMR studies with aniline have shown ^{1}J, ^{2}J and ^{3}J ^{15}N–^{13}C couplings on the order of 13.9–14.8, 2–4 and 0–1.5 Hz, respectively, depending on the solvent and concentration.[40]

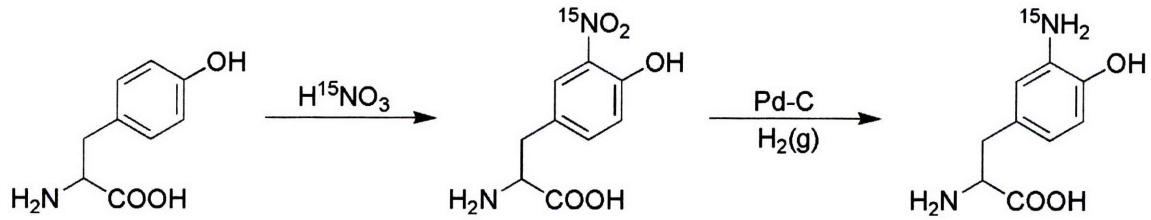

Scheme 5–1. Synthetic scheme used for preparation of ^{15}N–NH_2Y. See Methods for details.

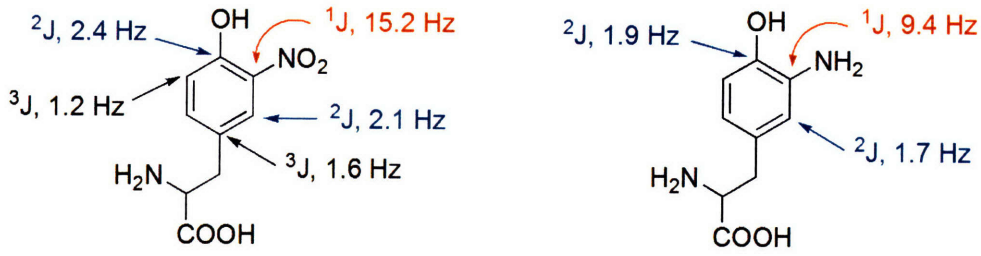

Figure 5–3. ^{15}N–^{13}C J–couplings observed with [^{15}N]–NO_2Y (left) and [^{15}N]–NH_2Y (right). The strength of ^{1}J, ^{2}J and ^{3}J couplings from the ^{1}H–decoupled ^{13}C NMR spectrum are shown.

To further confirm the identity of the product, pH–dependent UV–vis spectra were acquired. The λ_{max} and ε for 3–ammoniumtyrosine, 3–aminotyrosine and 3–aminotyrosinate were determined with authentic NH_2Y (from Sigma–Aldrich) at low, neutral and high pH, respectively (Scheme 5–2). This data is summarized in Table 5–2. Measurement of these values for our synthetic [^{15}N]–NH_2Y showed a very similar trend (Table 5–2). Thus, the ^{1}H, ^{13}C and UV–vis analyses confirm that the product is in fact [^{15}N]–NH_2Y.

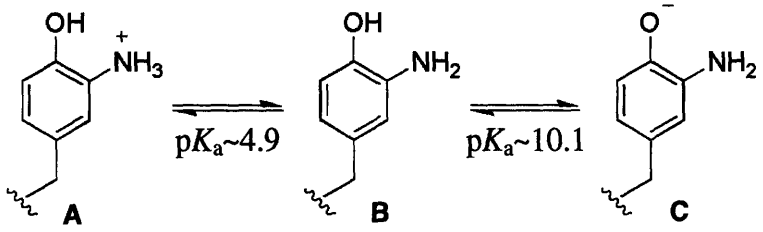

Scheme 5–2. Different protonation states and pK_as of NH_2Y. Species A, B, and C have absorption maxima at 275, 289, and 303 nm, respectively. The pK_as for conversion of A to B and B to C are from Refs. 31 and 32.

Table 5–2. UV spectral properties of authentic ^{14}N–NH_2Y[a] and synthetic ^{15}N–NH_2Y determined in H_2O at 25°C.

Protonation Form	Authentic NH_2Y λ_{max} (nm)[b], ε ($M^{-1}cm^{-1}$)[c]	Synthetic ^{15}N–NH_2Y λ_{max} (nm), ε ($M^{-1}cm^{-1}$)[c]
H_3N^+–Y	275 ± 1, 2150 ± 150	275 ± 1, 1900 ± 130
H_2N–Y	289 ± 1, 3200 ± 220	289 ± 1, 3200 ± 220
H_2N–Y^-	303 ± 1, 5100 ± 360	303 ± 1, 4700 ± 330

[a] "Authentic" ^{14}N–NH_2Y was obtained from Sigma-Aldrich. [b] Estimated error based on accuracy of spectrophotometer. [c] Estimated error based on accuracy of spectrophotometer and microbalance weight measurements.

Preparation of [^{15}N]–NH_2Y–α2. [^{15}N]–NH_2Y was incorporated into α2 as described for [^{14}N]–NH_2Y. Purification by dATP chromatography gave 6 mg ^{15}N–labeled $Y_{730}NH_2Y$–α2 with 98 % ^{15}N enrichment per g of wet cell paste. The product was >95 % pure by SDS PAGE. Spectrophotometric assays revealed that nucleotide reduction occurred at 115 ± 12 nmol/min•mg. This is similar to the activity of 100 ± 8 nmol/min•mg observed with $Y_{730}NH_2Y$–α2 (Chapter 4).

Generation of [^{14}N]–NH_2Y_{730}• and [^{15}N]–NH_2Y_{730}• with various NDP/(d)NTP pairs. The availability of [^{14}N]– and [^{15}N]–$Y_{730}NH_2Y$–α2 allows us to examine the effect of [^{15}N] incorporation on the EPR spectra of NH_2Y• and to test the generality of the effect of [^{15}N] by carrying out the reaction with all substrate/effector paris, CDP/ATP, GDP/TTP, UDP/ATP and ADP/dGTP. Pre–reduced [^{14}N]–$Y_{730}NH_2Y$–α2 or [^{15}N]–$Y_{730}NH_2Y$–α2 and effector were mixed with wt β2 and substrate. The reaction was hand–quenched after 20 s in liquid N_2 and its EPR spectrum recorded. This reaction time was chosen as the [NH_2Y•] was found to be maximal in the presence of CDP/ATP (Chapter 4). To investigate the effect of the exchangeable amine protons on the EPR spectrum, the reaction of [^{14}N]–$Y_{730}NH_2Y$–α2 and [^{15}N]–$Y_{730}NH_2Y$–α2 with β2, substrate and effector were also performed in deuterated buffer (see Methods). Care was taken to exchange both subunits into deuterated buffer by concentration/dilution cycles prior to the reaction.

All spectra were composites of Y_{122}• and NH_2Y• signals. The NH_2Y• were obtained by subtracting the Y_{122}• contribution as described in detail in Chapter 4. The results are presented in Figure 5–4. Spectral widths, g values and the yield of NH_2Y• for [^{14}N]–$Y_{730}NH_2Y$–α2 in protonated buffer are shown in Table 5–3. The spectra of [^{14}N]–NH_2Y_{730}• in protonated buffer in the presence of CDP/ATP, GDP/TTP and UDP/ATP are similar, but different from that with ADP/dGPT (Figure 5–4). The distinct features with ADP/dGTP may be explained by subtle changes in the dihedral angle of one of the β–protons, as we suggested in the case of DOPA–β2 (Chapter 2). With CDP/ATP, GDP/TTP and UDP/ATP, 18–19 μM of total spin have remained after 20 s reaction time. With ADP/dGTP, however, ~60 % of the initial spin has been lost. Therefore, the data in Table 5–3 suggest that the stability of the NH_2Y• is dependent on the

substrate and effector bound in the active site of α2. Observation of an EPR–active signal with all four substrate/effector pairs is consistent with the proposed roles for Y_{730} as an intermediate during radical initiation.

Spectra of [^{15}N]–NH_2Y_{730}• in protonated buffer establish that ^{15}N incorporation has an effect on the EPR spectrum (Figure 5–4). However, the effect is difficult to describe because of superposition of hyperfine splittings, presumably from the exchangeable amine protons and the β–protons. Simulation of these spectra is necessary to uncover the effect of ^{15}N incorporation (see below).

The spectra of [^{14}N]–NH_2Y_{730}• and [^{15}N]–NH_2Y_{730}• in deuterated buffer, show a marked perturbation relative to those in protonated buffer (Figure 5–4). Both spectra are sharper relative to those in protonated buffer presumably due to elimination of hyperfine interaction from matrix protons. The marked change from protonated to deuterated buffer indicates that the exchangeable amine protons have significant hyperfine interaction with the unpaired spin. The spectrum of [^{14}N]–NH_2Y_{730}• appears as a doublet of doublets with a large and a small hyperfine splitting constant. The spectrum of [^{15}N]–NH_2Y_{730}• has collapsed to an apparent anisotropic triplet spectrum, clearly demonstrating the effect of ^{15}N incorporation. Qualitatively, it appears that the amine nitrogen displays anisotropic hyperfine interaction as the ^{15}N hyperfine coupling affects the spectrum only on the low field side. A more quantitative analysis of these traces requires spectral simulations, which will be presented below. Together, these isotope–dependent spectral shifts upon ^{15}N incorporation or deuteration validate our hypothesis that the new signal is associated with the NH_2Y probe.

As noted above, the features of the NH_2Y_{730}• in protonated buffer in the presence of ADP/dGTP are different from those of the remaining three pairs. In deuterated buffer, however, this trend appears to have disappeared (Figure 5–4). This perhaps indicates that the different features in protonated buffer arise from modulation of a hydrogen bond to the NH_2Y_{730}• as a function of substrate/effector pairs in α2. Alternatively, the D_2O environment may 'fix' the dihedral angle of C_β–H, so that spectra in D_2O are identical regardless of the substrate/effector

bound in α2. At this point a distinction cannot be made. However, we have proposed that at this junction in the radical transfer pathway proton and electron move together as an H atom.[6] Thus, detection of a hydrogen bond at NH_2Y_{730}• would have important implication for catalysis and the role of proton–coupled electron transfer in hole migration. This requires detailed structural analysis of the NH_2Y_{730}• by various spectroscopic and computational methods as well as experimental determination of the anisotropic g factors of NH_2Y•.

Table 5–3. Yield of NH_2Y• and total spin after reacting $Y_{730}NH_2Y$–α2 with β2 and various NDP/(d)NTP pairs for 20 s.

Substrate/Effector	g value[a]	Spectral width (G)[b]	[NH_2Y•] (μM)[c]	Total Spin Remaining (μM)[d]
CDP/ATP	2.0043	24.0 ± 1	9.7	18.2
GDP/TTP	2.0044	25.0 ± 1	10.1	19.4
UDP/ATP	2.0043	22.3 ± 1	9.3	18.2
ADP/dGTP	2.0041	22.1 ± 1	2.4	9.8

[a] The error in the g value measurements is ± 0.0001. [b] The peak-to-trough spectral widths are reported from a single measurement. [c] [NH_2Y•] after 20 s reaction time. [d] Total spin remaining at 20 s relative to total spin at t=0, which was 24 μM in these experiments.

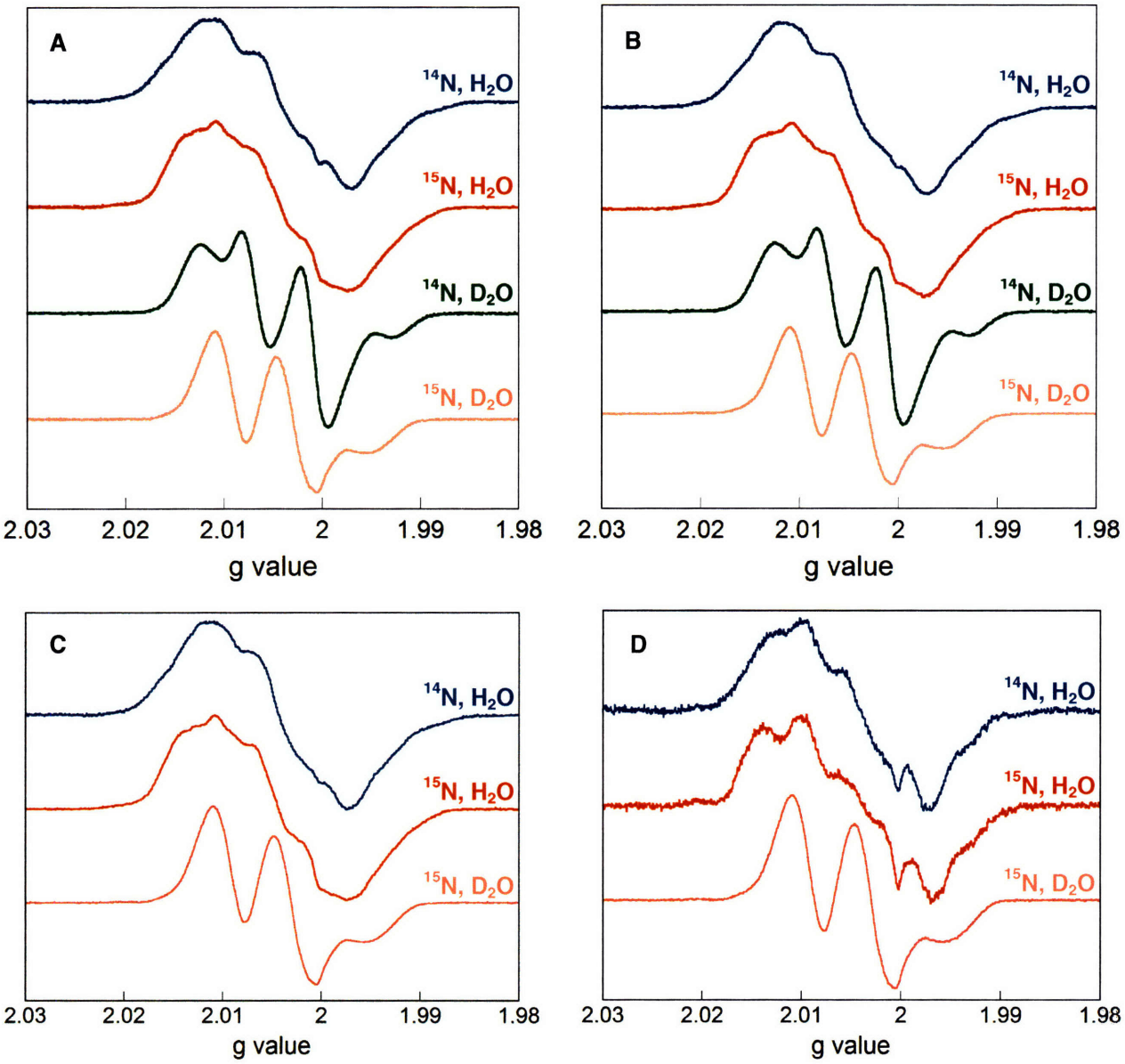

Figure 5–4. Normalized EPR spectra of isotopically substituted NH_2Y_{730}•. Spectra were acquired with $Y_{730}NH_2Y$–α2/β2 containing [^{14}N]–NH_2Y or [^{15}N]–NH_2Y in protonated or deuterated buffer in the presence of CDP/ATP (A), GDP/TTP (B), UDP/ATP (C) or ADP/dGTP (D). Note that spectra of [^{14}N]–NH_2Y_{730}• in deuterated buffer in the presence of UDP/ATP and ADP/dGTP have not been collected. See Table 5–3 for further analysis of the spectra of [^{14}N]–NH_2Y_{730}• in protonated buffer.

Analysis of NH_2Y_{730}• by 180 GHz EPR spectroscopy. To obtain the g anisotropy for NH_2Y_{730}• necessary for spectral simulation and further characterization of the radical, high field EPR spectra were acquired. $Y_{730}NH_2Y$–α2 and β2 were concentrated to 80 μM, and NH_2Y• formation was initiated by addition of CDP/ATP. The reaction was hand–quenched in liquid N_2 after 30–45 s. EPR spectra at 180 GHz and at 6 K or 70 K are shown in Figure 5–5. At 6 K, the spectrum is a composite of Y_{122}• and NH_2Y•. However, at 70 K, the signal associated with Y_{122}• adjacent to the diferric cluster is not observed and only the NH_2Y• is apparent. The g values obtained from analysis of this spectrum reveal its anisotropy: g_x=2.00520, g_y=2.00420, g_z=2.00220 with an accuracy of ± 0.0001.

The value of g_z is close to the free–electron g value (g_e) of 2.002319. The g_x and g_y values, however, significantly depart from g_e. These results are consistent with the Stone g matrix theory and will be further discussed below.[41,42] The principal axes of the g matrix for NH_2Y• are defined in Figure 5–6A. Accordingly, g_x is paralled to the C_4–O bond, g_z is perpendicular to the aromatic plane and g_y is perpendicular to g_x and g_z.

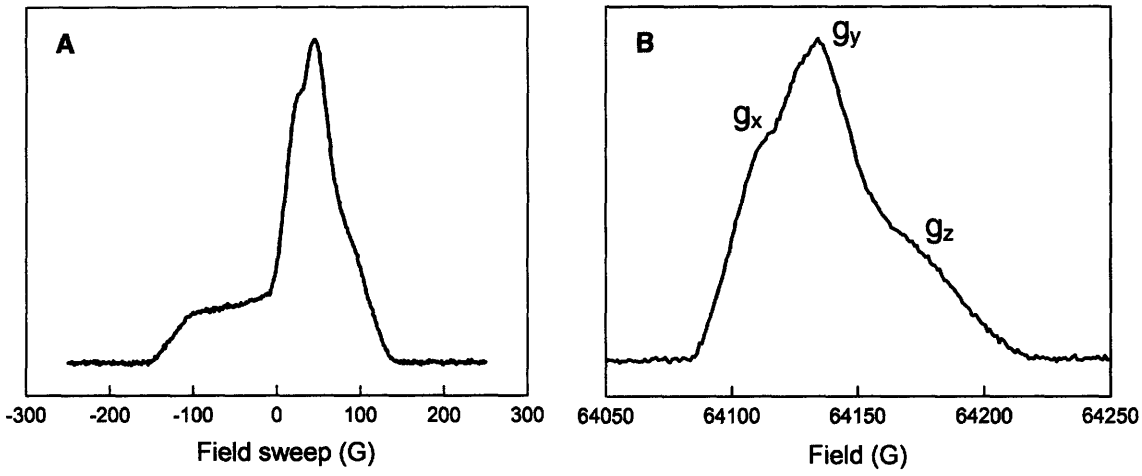

Figure 5–5. EPR spectra of NH_2Y_{730}• at 180 GHz in the presence of CDP/ATP. (A) Spectrum at 6 K containing β2/NH_2Y_{730}•. This spectrum is a composite of Y_{122}• and NH_2Y• signals. (B) Spectrum at 70 K containing only the NH_2Y_{730}• signal with g values of g_x=2.00520, g_y=2.00420 and g_z=2.00220. The error in these measurements was ± 0.0001.

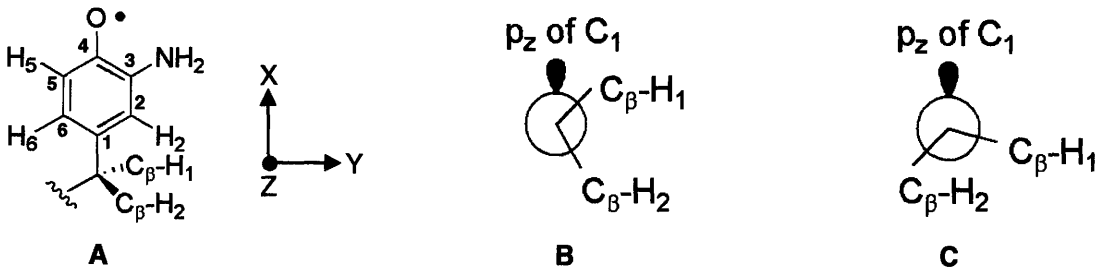

Figure 5–6. Numbering scheme, g tensor axis orientation and conformations of $NH_2Y•$. (A) Numbering scheme and axis orientations used for $NH_2Y•$ in DFT calculations and simulations (see Tables 5–4, 5–5 & 5–6). Note that the z–axis is perpendicular to the molecular plane. (B) Dihedral angle of C_β–protons used in the DFT calculation in Table 5–4. In this case, the calculations show a strong hyperfine coupling constant to only one of the two C_β–protons. (C) Dihedral angle of C_β–protons used in the DFT calculation in Table 5–5. In this case, the calculations show a strong hyperfine coupling constant to both C_β–protons.

Spectral simulations. The availability of g values for $NH_2Y_{730}•$ facilitates simulation of the EPR spectra in Figure 5–4. To guide in spectral assignment of our spectra, DFT calculations were performed at the B3LYP level to predict the hyperfine coupling constants in the $NH_2Y•$ system. These calculations were carried out on two conformations of $NH_2Y•$, in which the dihedral angels between the β–protons and the plane of the aromatic ring were different, to assess their effect on the hyperfine interaction. The results are summarized in Tables 5–4 and 5–5. They show that in one conformation (Table 5–4 and Figure 5–6B), major hyperfine coupling constants are expected from the ring proton *ortho* to the hydroxyl group (–11.08 MHz), only one of the C_β–protons (15.94 MHz), the aromatic NH_2 moiety (4.16 MHz with a major z–component) and its exchangeable protons (–12.32 and –12.78 MHz). In another conformation (Table 5–5 and Figure 5–6C), where the dihedral angle between the β–protons and the plane of the aromatic ring has been changed by rotation about the C_β–C_1 bond, major hyperfine interactions are expected from the ring–proton *ortho* to the hydroxyl group (–10.25 MHz), both

C_β–protons (30.11 and 29 MHz), the aromatic NH_2 group (4.22 MHz with a major *z*–component) and its exchangeable protons (–12.54 and –13.01 MHz). Thus, depending on the conformation of the NH_2Y_{730}• within α2, one or both β–protons may show strong hyperfine interactions. The strength of coupling will depend on the dihedral angle between the C_β–$C_\beta H$ bond and the plane of the aromatic ring.

Table 5–4. Hyperfine coupling constants (in MHz) calculated for NH_2Y•. See Figures 5–6A and 5–6B for numbering scheme and conformation of NH_2Y•.

Nucleus	A_x	A_y	A_z	A_{iso}
N	–3.89	–3.53	19.9	4.16
N–H_1	–17.64	–16.67	–21.99	–12.32
N–H_2	23.34	–15.57	0.56	–12.78
β–H_1	14.16	14.42	19.21	15.94
β–H_2	1.65	1.8	5.88	3.11
ring–H_2	1.95	4.22	8.21	4.8
ring–H_5	–16.23	–13.33	–3.63	–11.08
ring–H_6	–2.9	–2.17	3.06	–0.67

Table 5–5. Hyperfine coupling constants (in MHz) calculated for NH_2Y• in an alternative conformation. See Figure 5–6A and 5–6C for numbering scheme and the alternative conformation of NH_2Y•.

Nucleus	A_x	A_y	A_z	A_{iso}
N	–3.97	–3.6	20.23	4.22
N–H_1	–18.03	–16.93	–2.65	–12.54
N–H_2	–23.73	–15.83	0.54	–13.01
β–H_1	28.04	28.94	33.34	30.11
β–H_2	26.95	27.81	32.24	29
ring–H_2	1.88	4.16	8.27	4.77
ring–H_5	–15.05	–12.5	–3.2	–10.25
ring–H_6	–3.37	–2.84	2.82	–1.13

Simulation of EPR spectra of $[^{15}N]$–NH_2Y_{730}• acquired in deuterated buffer was attempted first. In this case, hyperfine coupling to the exchangeable deuterons is very small thus facilitating the simulations by lowering the number of unknown hyperfine coupling constants. Consequently, only the N–nucleus of the amine group, the ring proton *ortho* to the hydroxyl and one or two C_β–protons need be included in the simulations. The g values determined by EPR spectroscopy at 180 GHz were used in the simulations. Previous experiment and theoretical studies with Y•s have shown that the hyperfine interaction with the ring proton is anisotropic.[43,44] Thus, in case of the ring proton, an anisotropic hyperfine splitting was simulated. On the other hand, C_β–proton hyperfine interactions have been shown to be isotropic or nearly isotropic in several Y•–containing systems.[45] There is not much precedence for simulation of an aromatic N–nucleus containing amino acid radical within a protein. However, studies on a tryptophan cation radical in cytochrome c peroxidase by Hoffman and colleagues[46] and on a neutral tryptophan radical in RNR by Lassman and coworkers[47] demonstrate that the N–nucleus of an aromatic amine group is axially coupled to the unpaired spin with a major z–component. These studies are consistent with the DFT calculations in Tables 5–4 and 5–5, which show isotropic, axial and anisotropic hyperfine interactions with the C_β–proton(s), the aromatic N–nucleus and the ring proton *ortho* to the hydroxyl group, respectively. With these guidelines for the symmetry of hyperfine interactions in mind, iterative rounds of simulation and calculation of χ^2 (see Methods) were performed until additional changes in the simulated parameters yielded no further decrease in χ^2. Approximately 100 iterations were carried out with 5–12 unknown hyperfine coupling constants from 3–4 nuclei (one or two C_β–protons, the N–nucleus and one ring proton). The best solution consisted of an isotropic hyperfine splitting by the C_β–proton ($A_x=A_y=A_z$), axial hyperfine splitting by the N–nucleus ($A_x=A_y \neq A_z$) and anisotropic hyperfine interaction from the ring proton *ortho* to the hydroxyl group ($Ax \neq Ay \neq Az$). The axial symmetry of the ^{14}N hyperfine interacation shows that the axis of the largest ^{14}N or ^{15}N hyperfine tensor, A_z, is parallel to g_z. As shown in Figure 5–6A, the g_z–axis is perpendicular to the

molecular plane. This orientation is found for most π radicals with planar π systems and is also anticipated by theory.[46]

The best simulation of the EPR spectrum of [^{15}N]–NH_2Y_{730}• in deuterated buffer is shown in Figure 5–7A. The simulated parameters are summarized in Table 5–6. The data show that a single C_β–proton is sufficient to yield a good simulation with a low χ^2 value. This sets a constraint on the dihedral angle between each C_β proton and the plane of the aromatic ring.

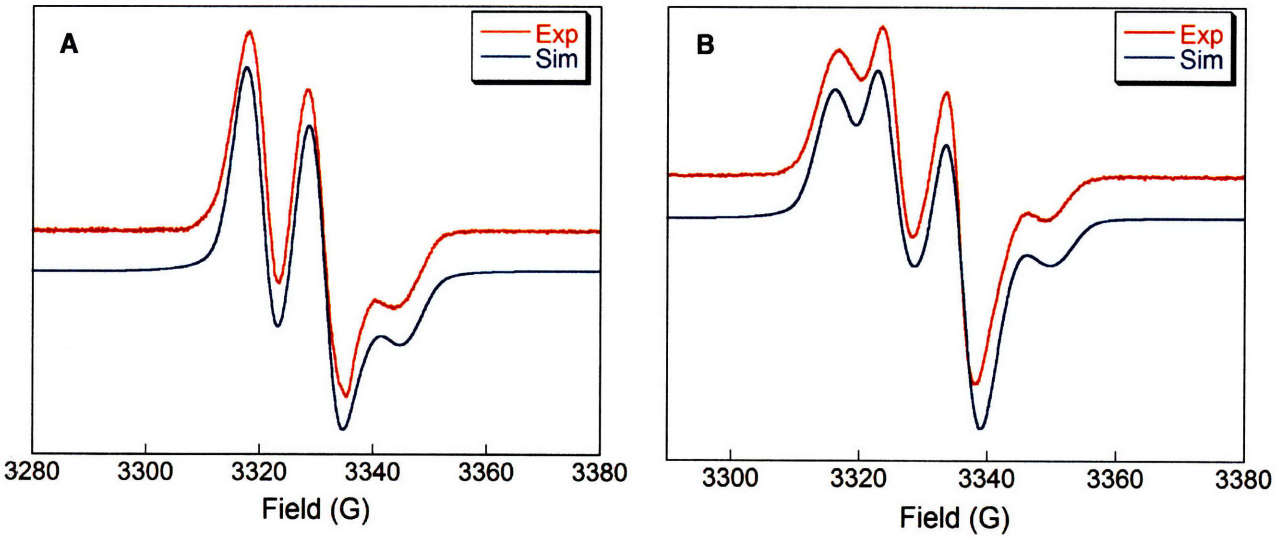

Figure 5–7. Simulation of [^{15}N]–NH_2Y_{730}• EPR spectra in deuterated assay buffer. (A) Experimental and simulated spectra of [^{15}N]–NH_2Y_{730}• in the presence of CDP/ATP. (B) Experimental and simulated spectra of [^{14}N]–NH_2Y_{730}• in the presence of CDP/ATP. In this case the parameters were identical to those in (A) except that the nuclear parameters for ^{15}N were replaced with those of ^{14}N. The parameters for these simulations are summarized in Tables 5–6.

Table 5–6. Parameters (in MHz) used for simulation of [^{14}N]–NH_2Y_{730}• and [^{15}N]–NH_2Y_{730}• EPR spectra in protonated or deuterated buffer.[a]

Nucleus	A_x	A_y	A_z	A_{iso}
		$^{15}NH_2Y - D_2O$		
C_β–H	30.8	30.8	30.8	30.8
^{15}N	5.04	5.04	44.2	11.4
ring–H_5[b]	3.0	4.5	8.5	–5.3
		$^{14}NH_2Y - D_2O$		
C_β–H	30.8	30.8	30.8	30.8
^{14}N	3.6	3.6	31.5	8.1
Ring–H_5[b]	3.0	4.5	8.5	–5.3
		$^{15}NH_2Y - H_2O$		
C_β–H	30.8	30.8	30.8	30.8
^{15}N	5.04	5.04	44.2	11.4
Ring–H_5[b]	3.0	4.5	8.5	–5.3
^{15}N–H_1	14.8	14.8	19.0	–16.2
^{15}N–H_2	19.6	13.7	4.2	–9.7
		$^{14}NH_2Y - H_2O$		
C_β–H	30.8	30.8	30.8	30.8
^{15}N	3.6	3.6	31.5	8.1
Ring–H_5[b]	3.0	4.5	8.5	–5.3
^{15}N–H_1	14.8	14.8	19.0	–16.2
^{15}N–H_2	19.6	13.7	4.2	–9.7
		$^{14}NH_2Y - H_2O$		
C_β–H	25.4	25.4	33.0	27.9
^{15}N	3.6	3.6	26.8	6.5
Ring–H_5[b]	4.6	4.6	8.0	–5.7
^{15}N–H_1	9.4	9.4	3.6	–7.5
^{15}N–H_2	9.4	9.4	3.6	–7.5

[a] See Figures 5–7 & 5–8 for simulations. [b] See Figure 5–6A for numbering scheme and the g tensor axis for NH_2Y•.

The simulation of [^{14}N]–NH_2Y_{730}• in deuterated buffer is shown in Figure 5–7B. The parameters used in this simulation are summarized in Table 5–6. In this case, the simulated spectrum is identical to that in Figure 5–7A, except that the N–nucleus hyperfine constants have been divided by 1.4 – based on the difference in the gyromagnetic ratios of ^{14}N and ^{15}N – and the nuclear parameter I=1/2 for ^{15}N is replaced with I=1 for ^{14}N. The hyperfine constants for the ring proton *ortho* to the hydroxyl and the C_β–proton have not been changed. The fact that a simple substitution of the ^{15}N simulation with ^{14}N nuclear parameters generates an excellent fit to the [^{14}N]–NH_2Y_{730}• data provides further strong support that the new signal is associated with NH_2Y. Note that the quadrupolar coupling generated by the ^{14}N nucleus has not been simulated here. The quadrupole moment of the ^{14}N nucleus is sufficiently small that it yields quadrupolar coupling constants on the order of 1 G or 2.8 MHz.[47] This is within the line width of the X–band EPR spectra. It may, however, contribute to spectral broadening of the $^{14}NH_2Y$• signal.

The best simulation of the [^{15}N]–NH_2Y_{730}• spectrum in protonated buffer is shown in Figure 5–8A. In this case, the simulated and experimental spectra have been overlaid, rather than offset as in Figure 5–7, because they do not completely overlap. The parameters obtained from simulation of spectra in deuterated buffer were not changed and the simulations were carried out by only considering the additional hyperfine interactions due to the exchangeable aromatic amine protons (Table 5–6).

The best simulation for [^{14}N]–NH_2Y_{730}• in protonated buffer is shown in Figure 5–8B. In simulating this spectrum, only the nuclear spin quantum number has been changed and the hyperfine coupling constants divided by 1.4 relative to the parameters obtained for [^{15}N]–NH_2Y_{730}• in protonated buffer.

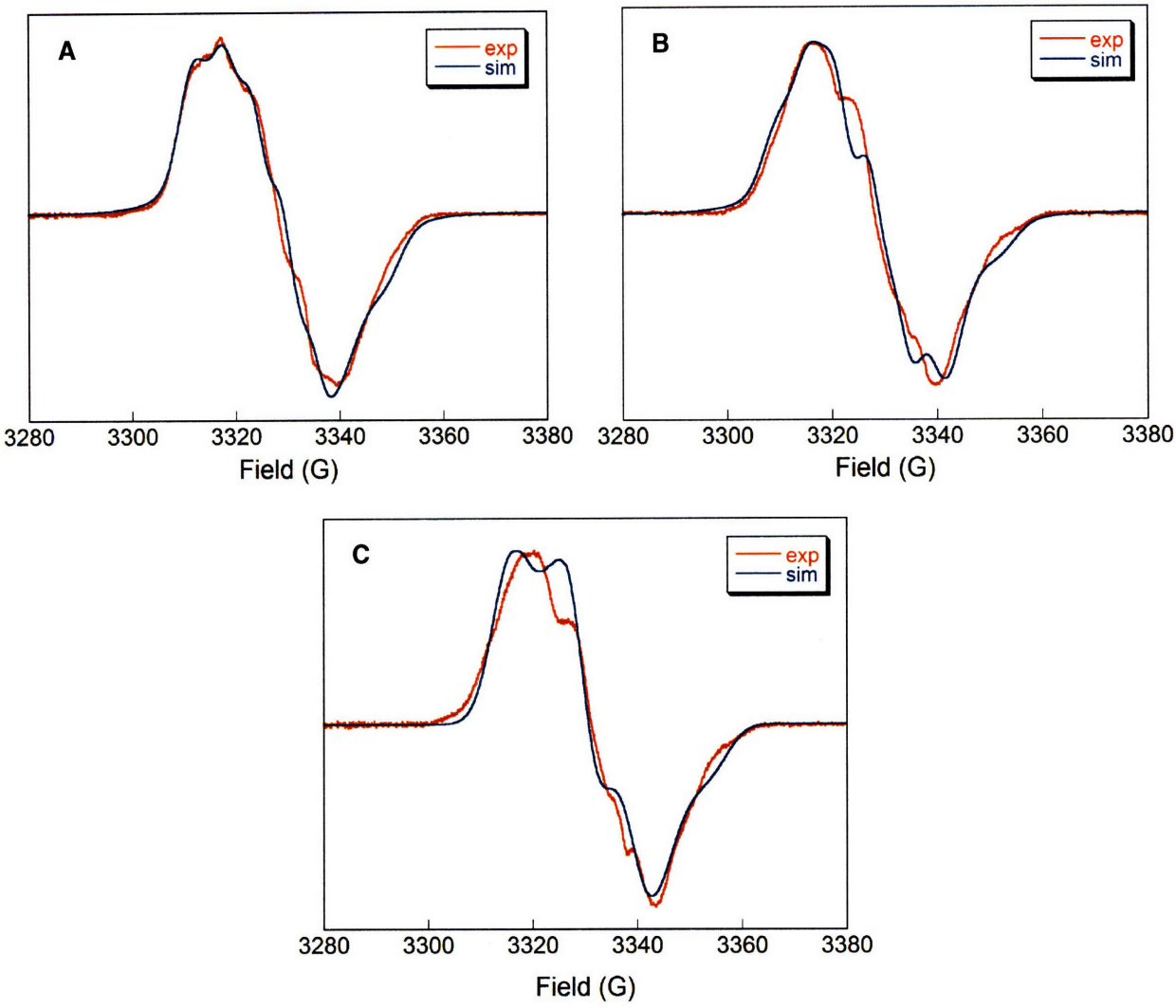

Figure 5–8. Simulation of NH_2Y_{730}• EPR spectra in protonated assay buffer. (A) Experimental and simulated spectra of [^{15}N]–NH_2Y_{730}• in the presence of CDP/ATP. (B) Experimental and simulated spectra of [^{14}N]–NH_2Y_{730}• in the presence of CDP/ATP. In this case the parameters were identical to those in (A) except that the nuclear parameters for ^{15}N were replaced with those of ^{14}N (see Table 5–6). (C) Experimental and 'fit' spectra of [^{14}N]–NH_2Y_{730}• using a program in MatLab. In this case the hyperfine constants for the two exchangeable amine protons were identical (see Table 5–6).

The poor simulations obtained with NH_2Y_{730}• in protonated buffer may be due to an internal H–bond within NH_2Y• that is not captured in the simulations (Scheme 5–3). It is important to uncover whether such an interaction exists, as it would have implications for hydrogen atom transfer reactions of NH_2Y_{730}• with residues Y_{731} and C_{439}. Preliminary

computational studies by Loth et al. suggest that the H–bonded conformation is 1–6 kcal/mol more stable than all other conformations without an internal H–bond (Scheme 5–3).[39] For the two conformation shown in Scheme 5–3, the H–bonded structure has been estimated to be 1.5–2 kcal/mol more stable than the other conformation. Detection of internal H–bonding in NH_2Y_{730}• requires ENDOR spectroscopy in protonated and deuterated buffer with [^{14}N]– and [^{15}N]–$Y_{730}NH_2Y$–α2/β2.

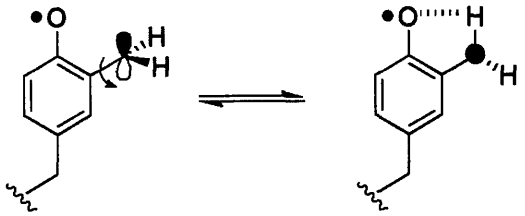

Scheme 5–3. Rotation about the C_3–N bond in NH_2Y•. The nitrogen has been left out of the figure for clarity. The N–orbital carrying the lone pair electrons is shown at the N–nucleus in both conformations. When this N–orbital is coplanar with the aromatic ring, H–bonding is not optimal, as shown in conformation (A). Rotation about the C_3–N bond, indicated by the red arrow, results in a conformation in which the lone pair orbital is perpendicular to the plane of the aromatic ring. In this conformation, one of the amine protons is coplanar with the aromatic ring and in a H–bonding orientation. The O–orbitals are not shown, but an ideal orientation results when one of the two O–orbitals are also coplanar with the aromatic ring. The H–bond is indicated by the dashed line.

Alternatively, the poor simulation obtained with NH_2Y_{730}• in protonated buffer, relative to those in deuterated buffer, may be due to a small structural change as a result of changing the environment from D_2O to H_2O, or to poor simulation of the additional six parameters for the exchangeable amine protons. In the former case, a better simulation would require re–assigning the hyperfine coupling constants for C_β–H, the aromatic N–nucleus and the aromatic ring proton. In the latter case, a better simulation would require fitting rather than reproducing the data. With *o*–aminophenol radicals, previous investigators have used identical hyperfine coupling constants for both amine protons when the radical was generated in H_2O (Table 5–1). However, different

coupling constants for the two amine protons were required for the simulations when the radical was generated in CH_3OH or in CH_2Cl_2. Extrapolating to NH_2Y•s, the relative polarity of solvent and protein residues surrounding the NH_2Y• may induce conformational changes that can change the hyperfine coupling constant from each of the two amine protons. In Figure 5–8B, the simulations were performed assuming distinct hyperfine splitting for each amine proton. The simulation in Figure 5–8C assume identical hyperfine interaction. In addition, the spectrum in Figure 5–8C has been fit, rather than simulated, using an in–house written MatLab program. Nevertheless, both attempts yield simulated spectra that do not capture all the features in the observed spectra. Additional studies are required to obtain more satisfactory simulations of the NH_2Y_{730}• spectra in protonated buffer.

It is important to note that the simulations do not provide the sign of the hyperfine interaction matrix. ENDOR studies are required to measure the sign of these constants. In Table 5–6 the isotropic hyperfine constants have been calculated by adopting the signs from the computational studies from Table 5–4. While DFT calculations are not powerful enough to 'predict' g values and hyperfine coupling constants, they can predict the symmetry and therefore sign of hyperfine interactions with ease.

The spectra and simulations presented in this section yield isotropic hyperfine constants, which allow calculation of spin densities at C_1, C_5 and the aromatic N–nucleus and elucidation of the dihedral angles between the C_β–protons and the aromatic ring. The calculations to obtain this structural information will be presented below.

Formation of NH_2Y_{731}• with other substrate/effector pairs. In Chapter 4, we presented the EPR spectrum of NH_2Y_{731}• in the presence of CDP/ATP. This spectrum contained features distinct from that of NH_2Y_{730}•. To further characterize NH_2Y_{731}•, its spectrum has been recorded in the presence of the other substrate/effector pairs. All spectra were composites of Y_{122}• and NH_2Y•. Subtraction of the Y_{122}• component yields the spectra shown in Figure 5–9. The peak–to–trough spectral widths, g values, total spin and yield of NH_2Y• at the 20 s time point are summarized in Table 5–7.

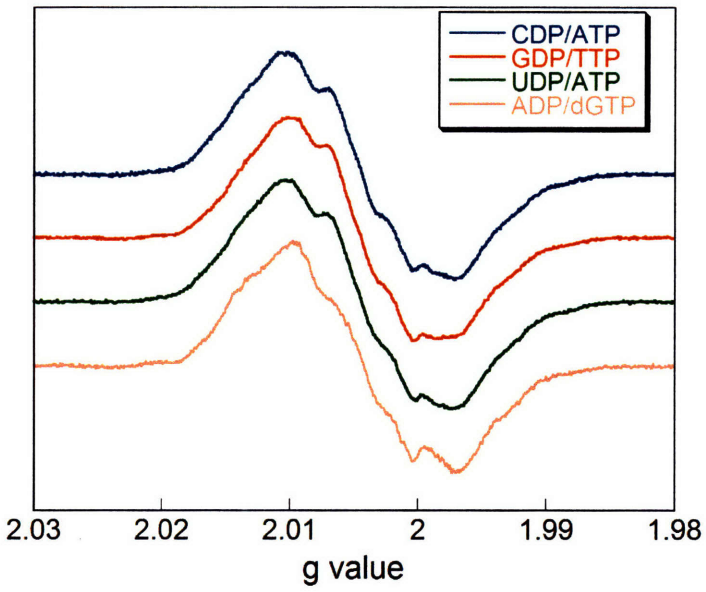

Figure 5–9. EPR spectra of NH_2Y_{731}• in the presence of various NDP/(d)NTPs. Spectra subsequent to subtraction of the Y_{122}• are shown. See Table 5–7 for summary of spectral parameters.

Observation of an NH_2Y• with all four substrate/effector pairs is consistent with the proposed redox–active role of Y_{731} in radical propagation, which we postulated on the basis of results in Chapter 4. As with NH_2Y_{730}•, the traces in the presence of CDP/ATP, GDP/TTP and UDP/ATP are similar, but different from that in the presence of ADP/dGTP (Figure 5–9). This may be due to a variation in the C_β–proton dihedral angles or a result of distinct H–bonding interactions. In addition, the yield of total spin and NH_2Y_{731}• at the 20 s time point are similar for CDP/ATP, GDP/TTP and UDP/ATP, but different from that with ADP/dGTP. With ADP/dGTP, NH_2Y_{731}• is more stable and present in a lower yield compared with other substrate/effector pairs (Table 5–7).

Table 5–7. Yield of NH_2Y• and total spin after reacting $Y_{731}NH_2Y$–α2 with β2 and various NDP/(d)NTP pairs for 20 s.

Substrate/Effector	g value[a]	Spectral width (G)[b]	[NH_2Y•] (μM)[c]	Total Spin Remaining (μM)[d]
CDP/ATP	2.0044	20.2	7.7	17.0
GDP/TTP	2.0044	19.4	7.4	18.0
UDP/ATP	2.0044	21.8	7.6	16.8
ADP/dGTP	2.0042	21.3	5.5	21.1

[a] Note that the error in the g value measurements is ± 0.0001. [b] The peak-to-trough spectral widths are reported from a single measurement. [c] [NH_2Y•] after 20 s reaction time. [d] Total spin remaining at 20 s relative to total spin at t=0, which was 24 μM in these experiments.

Comparison of the data in Table 5–3 for NH_2Y_{730}• vs. those in Table 5–7 for NH_2Y_{731}• show that the spectra at residue 731 are narrower than those at 730, though the observed g values are similar. The yield of the NH_2Y• and its stability also depend on the position of the probe. With CDP/ATP, GDP/TTP, and UDP/ATP, the NH_2Y• is more stable and present at higher concentrations at residue 730 than at 731 (Tables 5–3 & 5–7). This may be related to the position of Y_{731} in the α2/β2 complex, which is more solvent–exposed than Y_{730}. The ADP/dGTP pair is an outlier in this regard, as the NH_2Y• is more stable at residue 731 relative to 730.

The NH_2Y_{731}• was also studied by 180 GHz EPR spectroscopy. Samples were prepared and analyzed as described for NH_2Y_{730}•. The results are shown in Figure 5–10. Analysis of these spectra reveals the anisotropy for NH_2Y_{731}•: g_x=2.0052, g_y=2.0042, g_z=2.0022. These are identical to the g values measured for NH_2Y_{730}• as indicated by the g values measured by X–band EPR spectroscopy (Tables 5–3 & 5–7). Incorporation of [^{15}N]–NH_2Y into residue 731 and acquisition of EPR spectra in deuterated buffer, and their analysis, will be required to study the structure NH_2Y_{731}• in more detail.

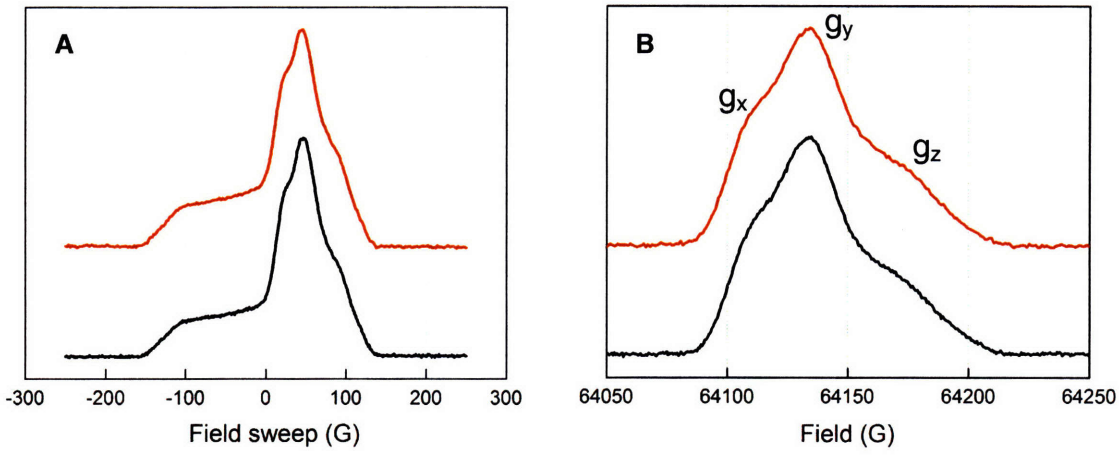

Figure 5–10. EPR spectra of NH_2Y_{731}• at 180 GHz. (A) Spectra at 6 K containing β2/NH_2Y_{731}• in the presence of CDP/ATP (black trace) or GDP/TTP (red trace). These spectra are composites of Y_{122}• and NH_2Y• signals. (B) Spectra at 70 K containing only the signal from NH_2Y_{731}• in the presence CDP/ATP (black) or GDP/TTP (red). Both spectra yield g values of g_x=2.00520, g_y=2.00420 and g_z=2.00220. The error in the g values was ± 0.0001.

Distance measurements using PELDOR spectroscopy with NH_2Y–α2s. Having examined the structure of NH_2Y•, we next sought to investigate its position within the α2/β2 complex. While Y_{730} and Y_{731} have been proposed to participate in radical transfer, their position within the pathway has remained undetermined. Direct spectroscopic analysis of these residues has been hampered by the conformational change that masks radical initiation.[48] However, the emergence of the NH_2Y probe allows a direct measurement between the newly formed NH_2Y• in one α/β pair of the radical transfer pathway with the remaining Y_{122}• in the other α/β pair. The results of similar experiments were presented in Chapters 2 & 3 for DOPA–β2 and DOPA–ββ', respectively, which provided the first distance constraints regarding the position of residue 356 in the radical transfer pathway.

PELDOR samples were prepared by first concentrating pre–reduced NH_2Y–α2 and β2 (1.2 Y_{122}•/dimer) to 80 μM. Formation of NH_2Y• was induced by addition of GDP/TTP followed by hand–quenching each sample in liquid N_2. The resulting spectra are shown in

Figure 5–11. Figure 5–11A (black trace) shows the X–band spin–echo detected absorption spectrum of this reaction for $Y_{731}NH_2Y$–α2 along with the pump and detect frequencies used in the four–pulse DEER sequence.[49] The spectrum is a composite of NH_2Y_{731}• and Y_{122}• signals. Subtraction of the Y_{122}• component (blue, 59 %) yields the NH_2Y_{731}• (red, 41 %). Figure 5–11B shows the echo modulation trace for NH_2Y_{731}• recorded at the detection frequency after subtraction of a mono–exponential signal decay function. The modulation frequency of this spectrum is indicative of the distance between Y_{122}•–NH_2Y_{731}•, the modulation depth is a function of the concentration of radical pairs. Analysis of this trace using the distance–domain Tikhonov regularization procedure[50] results in the distance distribution profile in Figure 5–11C (red), which indicates a distance of 38.1 ± 1.2 Å between Y_{122}• and NH_2Y_{731}•. A small peak corresponding to the Y_{122}•–Y_{122}• pair is also observed.[17]

A similar analysis has been carried out with $Y_{730}NH_2Y$–α2. In this case, the echo modulation spectrum shown in Figure 5–11B (green) is obtained. Analysis of this trace yields a distance of 38.7 ± 1.8 Å along with a peak related to unreacted Y_{122}•–Y_{122}•. The basis for residual Y_{122}•–Y_{122}• is related to differences in the formation rate constant and stability of NH_2Y• at residue 730 vs. 731 (see Chapter 4).

In the PELDOR spectra in Figure 5–11, a coupling between NH_2Y•–NH_2Y• distance is not detected (though a lower limit has not been set). This is consistent with recent findings of half–sites reactivity in the α2/β2 complex, which contains two radical transfer pathways, structurally related by C_2–symmetry (Figure 5–12). In the first turnover, radical transfer occurs within only one of these pathways. In case of NH_2Y–α2s, radical transfer results in formation of a new NH_2Y• at the expense of Y_{122}• in one α/β pair. The Y_{122}• within the other αβ pair, where radical initiation does not occur, is preserved thus allowing distance measurements diagonally across the α2/β2 complex between these two radicals. The measured distance by PELDOR presented here and the distances predicted by the docking model are summarized in Figure 5–12. The implications of these measurements will be discussed below.

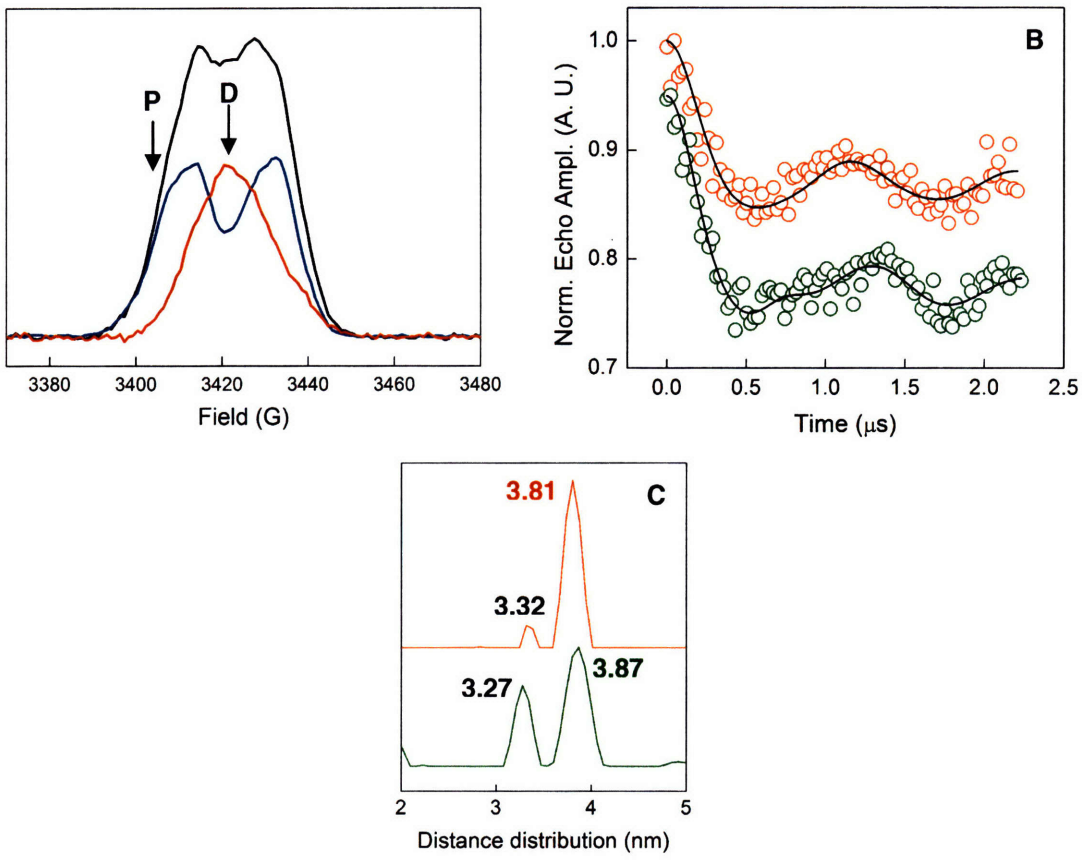

Figure 5–11. PELDOR spectroscopy with NH_2Y–α2s. (A) Spin–echo detected EPR spectrum after reaction of $Y_{731}NH_2Y$–α2/β2 with GDP/TTP. The spectrum of unreacted Y_{122}• (blue) has been subtracted from the observed spectrum (black) yielding the NH_2Y_{731}• spectrum (red). Pump (P) and detect (D) frequencies are indicated by arrows. (B) Normalized four–pulse DEER at 6 K for $Y_{731}NH_2Y$–α2/β2 (red) and $Y_{731}NH_2Y$–α2/β2 (green) with GDP/TTP. The black lines describe fits using the Tikhonov regularization procedure. (C) Resulting distance distributions obtained from the analysis in (B) are shown for each NH_2Y–α2. The distances of 3.32 and 3.27 nm (black) are related to the Y_{122}•–Y_{122}• pair.

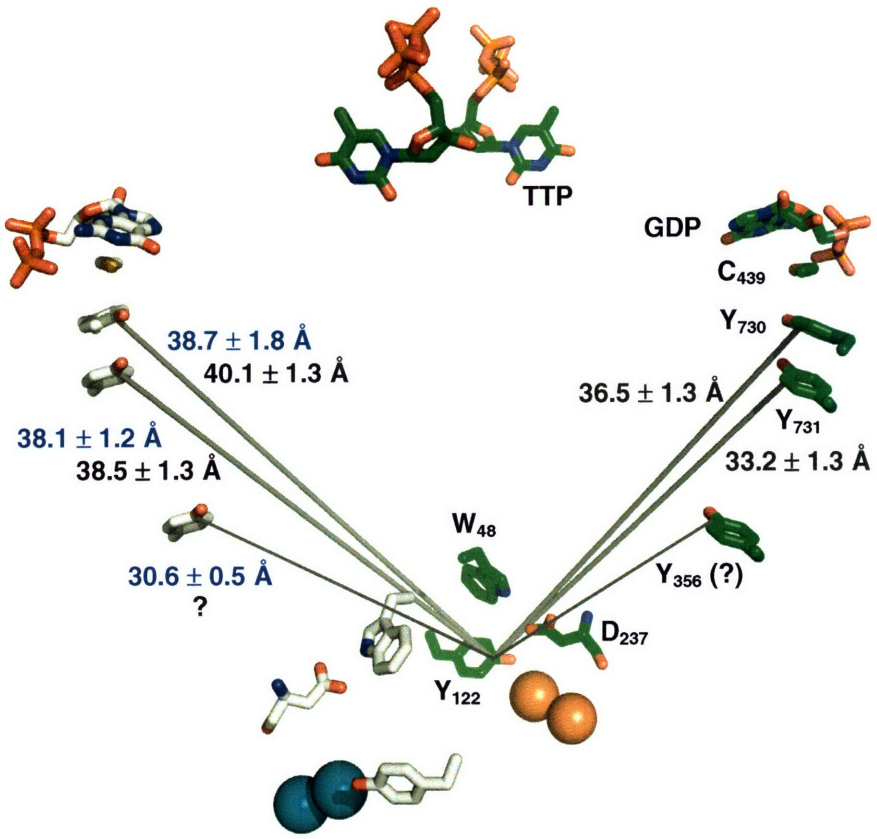

Figure 5–12. Distances between Y_{122}• and other residues in the radical transfer pathway. Diagonal and linear distances predicted by the docking model (black) and measured diagonal distances obtained by PELDOR in this study (blue). The residues constituting a pathway in one α/β pair are colored in light grey (Fe shown in teal); residues in the second pathway are shown in green (Fe shown in orange). For clarity, the residues and ligands in only one pathway (right) have been labeled. Distances from the model (black) represent averages from both pathways in the complex and have been measured from the aromatic C_4 atom of each Tyr residue. The position of Y_{356} is unknown. The distance between residue 356 and Y_{122}• was obtained from PELDOR studies with DOPA–β2 (Chapter 2).

Reaction of NH_2Y–α2 with $Y_{356}F$–β2. Having identified the structure of the NH_2Y• and established its position in the α2/β2 complex using PELDOR spectroscopy, we next addressed the pathway dependence of its formation. To do so, we used the His_6–$Y_{356}F$–β2. In this mutant, radical transfer into α2 does not occur because the pathway is blocked at residue 356. Thus, if formation of NH_2Y_{730}• or NH_2Y_{731}• requires a redox–active Y_{356} residue, then no NH_2Y• should be observed. If however, alternative pathways exist that can lead to NH_2Y_{730}• or

NH_2Y_{731}• formation, then an NH_2Y• may be observed. The results of these experiments are shown in Figure 5–13. The reaction was quenched at 20 s and at 2 min. The EPR spectra reveal that no NH_2Y• had been formed in either experiment; only the well–characterized Y_{122}• signal is observed. In addition, spin quantitation reveals no significant loss of spin at the 20 s or the 2 min time points consistent with a requirement for Y_{356} in radical hopping into α2. In contrast, in a parallel control experiment, when $Y_{356}F$–β2 is replaced with wt β2, the composite spectrum described in Chapter 4 is obtained with both NH_2Y–α2s. Therefore, a redox–active Y_{356} is a prerequisite for hole migration into subunit α2.

Recently, Clement Chan has performed an experiment with a double α2 mutant, $Y_{731}F/Y_{730}NH_2Y$–α2. As with the His_6–$Y_{356}F$–β2 mutant, no NH_2Y• is observed in the presence of substrate and effector and no loss of spin had occurred. These results suggest that formation of an NH_2Y_{730}• requires a redox–active Y_{356} and Y_{731} in the α2/β2 complex.

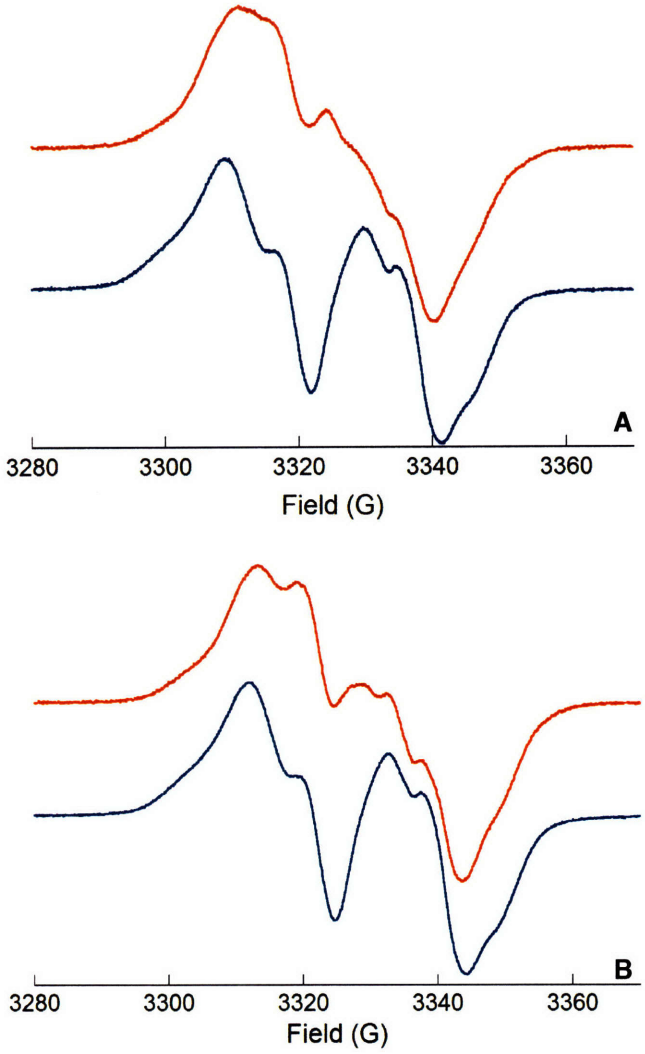

Figure 5–13. Pathway dependence for $NH_2Y\bullet$ formation. (A) EPR spectra of $Y_{730}NH_2Y$–α2 in the presence of CDP/ATP with wt β2 (red) or His_6–$Y_{356}F$–β2 (blue) after a 20 s reaction time. (B) EPR spectra of $Y_{731}NH_2Y$–α2 in the presence of CDP/ATP with wt β2 (red) or His_6–$Y_{356}F$–β2 (blue) after a 20 s reaction time.

SF UV–vis spectroscopy of NH_2Y–α2/β2 with various NDP/(d)NTP combinations. The kinetics of $NH_2Y\bullet$ formation with CDP/ATP was described in Chapter 4 for $Y_{730}NH_2Y$–α2 and $Y_{731}NH_2Y$–α2. The results showed formation of an $NH_2Y\bullet$ in a kinetically competent manner. However, a slow rate constant of ~2–3 s^{-1} was also observed, the physical nature of

which is undetermined. To investigate the effect of nucleotides on the kinetics and extent of radical transfer, additional reactions have been carried out with GDP/TTP, UDP/ATP, ADP/dGTP, all four substrates alone (CDP, GDP, UDP, ADP) and three effectors alone (ATP, TTP, dGTP). Representative data and fits for a reaction containing only GDP or TTP are shown for $Y_{730}NH_2Y$–α2 in Figure 5–14. The results for all substrate and effector combinations are summarized in Table 5–8. Representative data and fits for the reaction of $Y_{731}NH_2Y$–α2 with GDP or ADP alone, and with TTP or dGTP alone are shown in Figure 5–15, with the kinetic parameters of the complete set summarized in Table 5–9. Analysis of kinetic data was carried out by iterative rounds of fitting and calculation of the R^2 correlation value and residual plot until the R^2 value was maximized and the residual plot was randomly scattered around zero.

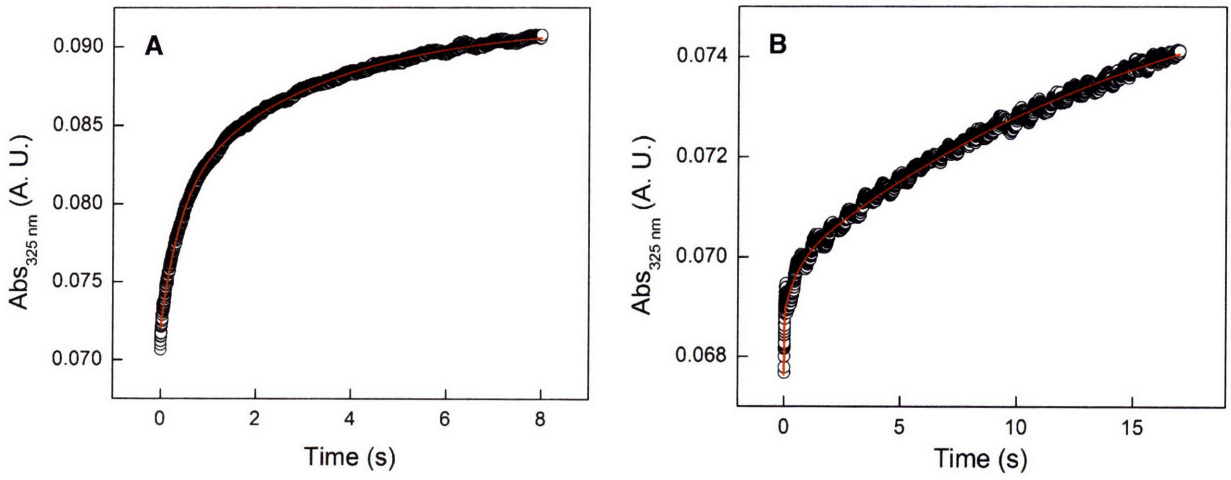

Figure 5–14. Kinetics of NH_2Y_{730}• formation monitored by SF UV–vis spectroscopy. Kinetics of NH_2Y• formation in the reaction of $Y_{730}NH_2Y$–α2/β2 in the presence of GDP alone (A) or TTP alone (B). Both experiments were carried out at a final complex concentration of 5 μM. Nucleotide concentrations were 1 mM GDP or 0.2 mM TTP. Red lines describe fits to data. See Table 5–8 for kinetic parameters. All fits had satisfactory residuals and R^2 correlation values of ≥0.99.

Table 5–8. Summary of kinetic parameters for reaction of $Y_{730}NH_2Y$–α2 with β2 and various substrate/effector combinations at 25°C.

Nucleotides	1st Phase		2nd Phase		3rd Phase	
	k_{obs} (s^{-1})	Amp (% Y_{122}•)	k_{obs} (s^{-1})	Amp (% Y_{122}•)	k_{obs} (s^{-1})	Amp (% Y_{122}•)
CDP	5.2 ± 0.5	9 ± 1	0.8 ± 0.1	19 ± 2		
CDP/ATP	12 ± 1	20 ± 2	2.4 ± 0.2	19 ± 2		
ATP	27 ± 3	2 ± 1				
UDP	1.4 ± 0.2	5 ± 1	0.2 ± 0.1	19 ± 2		
UDP/ATP	4.5 ± 0.2	20 ± 2	0.64 ± 0.03	15 ± 2		
GDP	2.5 ± 0.1	12 ± 1	0.3 ± 0.1	16 ± 2		
GDP/TTP	18 ± 2	15 ± 2	2.3 ± 0.2	16 ± 2		
TTP	120 ± 10	2 ± 1	1.8 ± 0.2	2 ± 1	0.06 ± 0.01	10 ± 1
ADP	50 ± 5	2 ± 1	6.5 ± 0.7	2 ± 1	0.06 ± 0.01	3 ± 1
ADP/dGTP	39 ± 2	8 ± 1	3.7 ± 0.2	7 ± 1		
dGTP	48 ± 3	3 ± 1	1.1 ± 0.1	3 ± 1	0.11 ± 0.01	17 ± 2

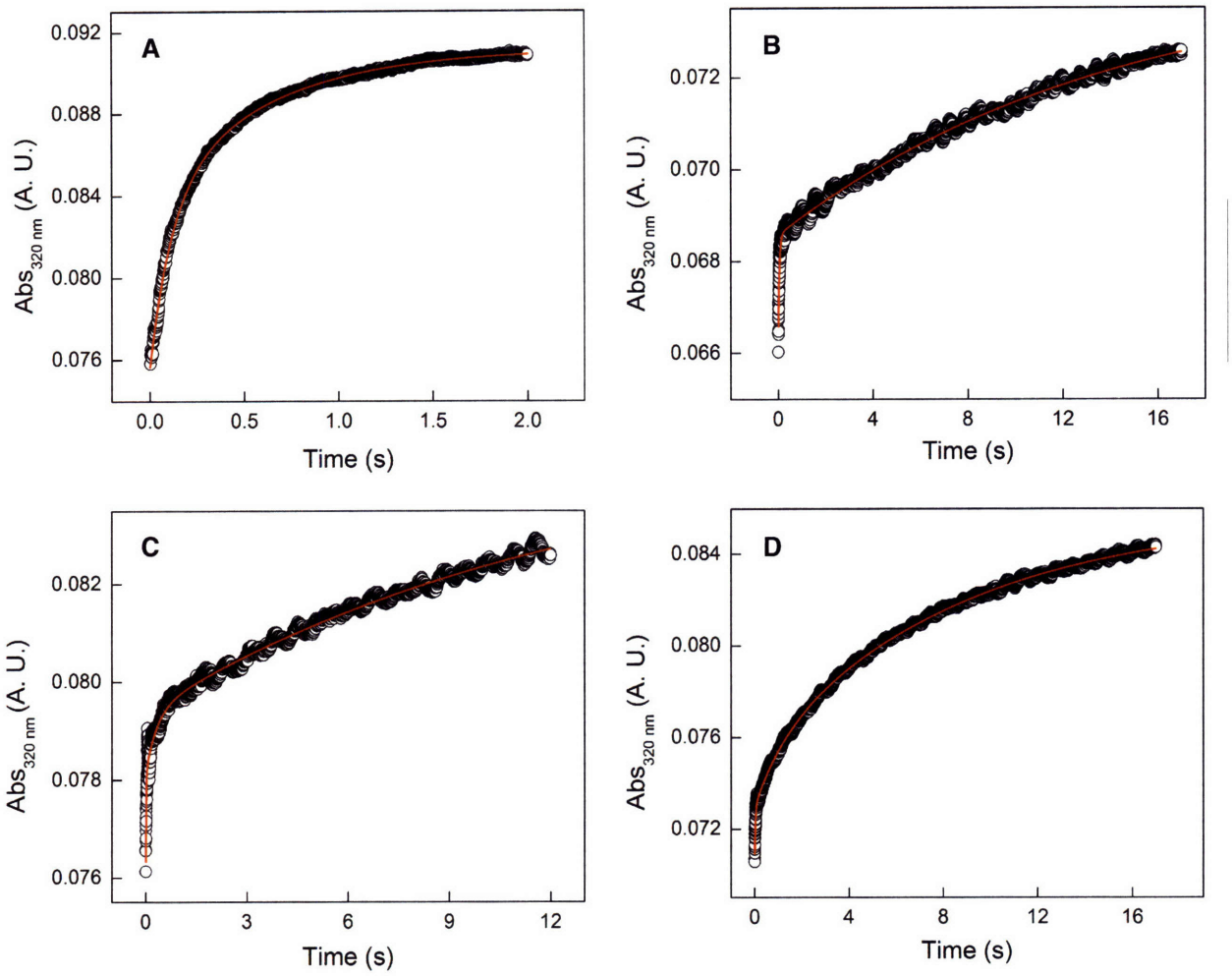

Figure 5–15. Kinetics of NH_2Y_{731}• formation monitored by SF UV–vis spectroscopy. Kinetics of NH_2Y• formation in the reaction of $Y_{731}NH_2Y$–α2/β2 in the presence of GDP alone (A), TTP alone (B), ADP alone (C) or dGTP alone (D). All experiments were carried out at a final complex concnentration of 5 μM. Nucleotide concentrations were 1 mM GDP, 0.2 mM TTP, 1 mM ADP, or 0.2 mM dGTP. Red lines describe fits to data. See Table 5–9 for kinetic parameters. All fits had satisfactory residuals and R^2 correlation values of ≥0.99.

Table 5–9. Summary of kinetic parameters for reaction of $Y_{731}NH_2Y$–α2 with β2 and various substrate/effector combinations at 25°C.

Nucleotides	1st Phase k_{obs} (s^{-1})	1st Phase Amp (% Y_{122}•)	2nd Phase k_{obs} (s^{-1})	2nd Phase Amp (% Y_{122}•)	3rd Phase k_{obs} (s^{-1})	3rd Phase Amp (% Y_{122}•)
CDP	10.8 ± 1.1	9 ± 1	1.3 ± 0.1	16 ± 2		
CDP/ATP	18 ± 2	22 ± 2	2.5 ± 0.3	10 ± 1		
ATP	0.05 ± 0.01	8 ± 1				
UDP	4.4 ± 0.2	11 ± 1	0.8 ± 0.1	15 ± 2		
UDP/ATP	7.1 ± 0.6	16 ± 2	1.2 ± 0.1	13 ± 1		
GDP	7.7 ± 0.8	13 ± 1	1.4 ± 0.2	10 ± 1		
GDP/TTP	28 ± 3	22 ± 2	2.3 ± 0.3	9 ± 1		
TTP	20 ± 1	3 ± 1	0.07 ± 0.01	8 ± 1		
ADP	70 ± 4	3 ± 1	3 ± 0.3	2 ± 1	0.08 ± 0.01	8 ± 1
ADP/dGTP	25 ± 2	13 ± 1	2.3 ± 0.2	5 ± 1		
dGTP	35 ± 4	3 ± 1	0.9 ± 0.1	3 ± 1	0.1 ± 0.01	19 ± 2

Inspection of the data in Table 5–8 reveals that NH_2Y• formation is fast and efficient with CDP/ATP, GDP/TTP and UDP/ATP. In these cases biphasic kinetics are observed with a fast phase of 4.5–18 s^{-1}, which is similar to the rate constant measured by pre–steady state experiments monitoring dCDP formation (4–17 s^{-1}), and a slow phase of 0.64–2.4 s^{-1}, which is similar to the turnover number (~2 s^{-1}). The yield of the reaction is also similar with these pairs, ranging from 31–39 % (Table 5–8). With ADP/dGTP, trapping of NH_2Y• is fast and biphasic with rate constants of 39 and 3.7 s^{-1}, but it is ~2–fold less efficient than with the other three NDP/(d)NTP pairs. This trend is similar to that observed in the EPR spectra of NH_2Y•, where spectra in the presence of CDP/ATP, GDP/TTP and UDP/ATP were qualitatively similar but distinct from the spectrum obtained in the presence of ADP/dGTP.

A similar conclusion is reached when examining the kinetics of NH_2Y• with $Y_{731}NH_2Y$–α2. Here, biphasic rate constants of 7.1–28 s^{-1} and 1.2–2.5 s^{-1} are observed with CDP/ATP, GDP/TTP and UDP/ATP (Table 5–9). With ADP/dGTP, rate constants of NH_2Y• are within the range of those with the other NDP/(d)NTP pairs (25 s^{-1} and 2.3 s^{-1}), but the yield of the reaction is ~2–fold lower. Interestingly, the rate constants for NH_2Y• formation with $Y_{731}NH_2Y$–α2 are always faster than with $Y_{730}NH_2Y$–α2 in the presence of CDP/ATP, GPD/TTP and UDP/ATP.

Comparison of the outcome of the reaction with substrate alone and effector alone may suggest a role for each of these in radical transfer. In the case of $Y_{730}NH_2Y$–α2 with effector alone, NH_2Y• formation does occur, albeit in an inefficient and slow fashion. With ATP and TTP, only 2 and 14 % of initial Y_{122}• give rise to an NH_2Y•, respectively. In case of TTP, the majority of the reaction (10 of 14 %) occurs with a rate constant of 0.06 s^{-1}, which clearly cannot support turnover. With dGTP, 23 % of initial Y_{122}• generates a NH_2Y•, however, the majority of this reaction (17 of 23 %) occurs with a k_{obs} of 0.11 s^{-1}. It should be noted that with effector alone, the k_{obs}s in other kinetic phases are significantly faster than that measured by Ge et al, although the yield of NH_2Y• associated with these kinetic phases is low. With ATP, TTP and dGTP alone, fast k_{obs}s of 27, 120 and 48 s^{-1} with NH_2Y• yields of 2, 2, and 3 % of total initial Y_{122}• are observed, respectively (Table 5–8). The nature of these fast conformational changes is at present not understood.

A similar trend is obtained with $Y_{731}NH_2Y$–α2, that is, effectors are competent in NH_2Y• production, however, the yield is lower than with substrate/effector or with substrate alone and the rate constants for the majority of the total change are too slow to support turnover (Table 5–9). With ATP, TTP and dGTP, 8, 11, and 25 % of initial Y_{122}• forms an NH_2Y•. With TTP and dGTP, the majority of this change (8 of 11 % and 19 of 25 %) occurs with slow rate constant of 0.07 and 0.1 s^{-1}, respectively. In addition, with $Y_{731}NH_2Y$–α2, the k_{obs}s with (d)NTPs alone are slower than those with $Y_{730}NH_2Y$–α2. NH_2Y• formation with ATP is mono–phasic with k_{obs} of 0.05 s^{-1} (compared to 27 s^{-1} with $Y_{730}NH_2Y$–α2). With TTP, a rate constant of 20 s^{-1} is

observed, which is similar to the rate constant for the rate–limiting physical change measured by Ge et al, and slower than that measured with $Y_{730}NH_2Y$–α2 (120 s^{-1}). With dGTP, a k_{obs} of 35 s^{-1} is detected, which is slower than that with $Y_{730}NH_2Y$–α2 (48 s^{-1}).

With substrate alone, NH_2Y• formation is fast and efficient, however, less so than in the presence of substrate and effector together. With $Y_{730}NH_2Y$–α2 and $Y_{731}NH_2Y$–α2 in the presence of CDP/ATP, GDP/TTP and UDP/TTP, it appears that substrate is providing the main conformational trigger, as reactions with substrate alone trap nearly as much NH_2Y• with a similar rate constant to those with substrate and effector. However, the presence of effector does increase both the rate constant for and extent of radical transfer. Importantly, the presence of effector increases the extent of NH_2Y• formation in the fast phase, while decreasing the extent of NH_2Y• formation in the slow phase. Examining the reaction of $Y_{730}NH_2Y$–α2/β2 with CDP/ATP vs. CDP alone, shows that in the former case 20 % is trapped rapidly, with 19 % trapped with a slow k_{obs}. With substrate alone, only 9 % is trapped rapidly and 19 % is trapped with a slow k_{obs}. This trend is also seen with UDP/ATP vs. UDP alone. In the former case 20 % and 15 % of total initial Y_{122}• are trapped with a fast and a slow k_{obs}, respectively. With UDP alone, the yield of NH_2Y• in the fast phase has decreased to 5 %, while that in the slow phase has increased to 19 %. A similar analysis can be applied to reactions with GDP/TTP vs. GDP alone. This shows that 18 % of initial Y_{122}• is trapped rapidly with GPD/TTP, whereas only 2 % is trapped rapidly with GDP alone (Table 5–8).

This trend holds when examining the kinetics of NH_2Y• with $Y_{731}NH_2Y$–α2 and NDP/(d)NTP vs. NDP alone. For example, with CDP/ATP, the extent of NH_2Y• formation with a fast and slow k_{obs} are 22 % and 10 %. Removing ATP from this reaction, decreases the former to 9 % and increases the latter to 16 % (Table 5–9). This trend also holds with UDP/ATP and GDP/TTP. The kinetics in the presence of ADP/dGTP with $Y_{730}NH_2Y$–α2 and $Y_{731}NH_2Y$–α2 are also consistent with this trend. In these cases, the reaction with ADP alone is triphasic, whereas those with ADP/dGTP are biphsic. The additional phase with ADP alone occurs with a k_{obs} of 0.06 and 0.08 s^{-1} with $Y_{730}NH_2Y$–α2 and $Y_{731}NH_2Y$–α2, respectively. Therefore, in

these cases, the absence of effector is responsible for appearance of a slow phase, which cannot support turnover and accounts for a significant portion of the overall change.

To summarize, in almost all cases with substrate alone, more $NH_2Y\bullet$ is formed with a slow rate constant than with the fast rate constant. However, when the reaction is supplemented with effector, more $NH_2Y\bullet$ is formed with a fast rate constant, compatible with turnover, than with a slow rate constant. Thus, the results seem to suggest that the role of the effector is to redistribute a larger population of the complex into a conformation, which generates a $NH_2Y\bullet$ more rapidly. While substrate provides the main conformational trigger, it requires the presence of effector to arrange the complex into a state that initiates radical transfer in a more rapid fashion, compatible with turnover.

Temperature dependence in formation of $NH_2Y_{730}\bullet$. To further characterize the conformational changes that gives rise to formation of the $NH_2Y\bullet$, temperature–dependent SF UV–vis studies were performed. A representative time course is shown in Figure 5–16A at 34°C. Kinetics were recorded at five different temperatures and the data are summarized in Table 5–10. At all temperatures, the kinetics were bi–phasic with a fast and a slow rate constant. The data reveal that the extent of $NH_2Y\bullet$ formation is temperature–independent ranging from 22–29 % and 11–16 % in the fast and slow kinetic phases, respectively (Table 5–10). This lack of temperature dependence of the equilibrium constant for formation of $NH_2Y\bullet$ suggests that the $\Delta H°\sim 0$ according to van't Hoff analysis (Eq. 5–4). This further suggests that ln(K) may be used to estimate an $\Delta S°$ for formation of $NH_2Y\bullet$ (Eq. 5–4). However, as noted in Chapter 4, due to the set of reactions that ensue upon $NH_2Y\bullet$ generation, it is unclear whether or not formation of $NH_2Y\bullet$ is at equilibrium within the time scale of the current experiment.

$$\ln(K) = -\frac{\Delta H°}{RT} + \frac{\Delta S°}{R} \qquad (5–4)$$

Both rate constants for trapping the $NH_2Y\bullet$ vary with temperature according to the Arrhenius model for temperature dependence of chemical reactions (Table 5–10). Comparing

the k_{obs} at 23°C and at 36°C, shows a ~2–fold and a 2.3–fold increase for the k_{obs} in the fast and slow kinetic phases, respectively. The data were analyzed using the Eyring equation (Eq. 5–2) by plotting $\ln(k_{obs}/T)$ for each phase vs. 1/T. This analysis for the fast and slow rate constant is shown in Figure 5–16B & 5–16C, respectively. Accordingly, thermodynamic parameters of $\Delta H^{\ddagger}$ = +13.1 kcal/mol and $\Delta S^{\ddagger}$ = –9.5 kcal/mol were obtained for the fast conformational change and $\Delta H^{\ddagger}$ = +11.8 and $\Delta S^{\ddagger}$ = –17.5 kcal/mol for the slow conformational change. Using Eq. 5–3, these parameters yield a $\Delta G^{\ddagger}_{298\,K}$ of –15.9 kcal/mol and –17 kcal/mol, for the fast and slow conformational change, respectively (Table 5–11).

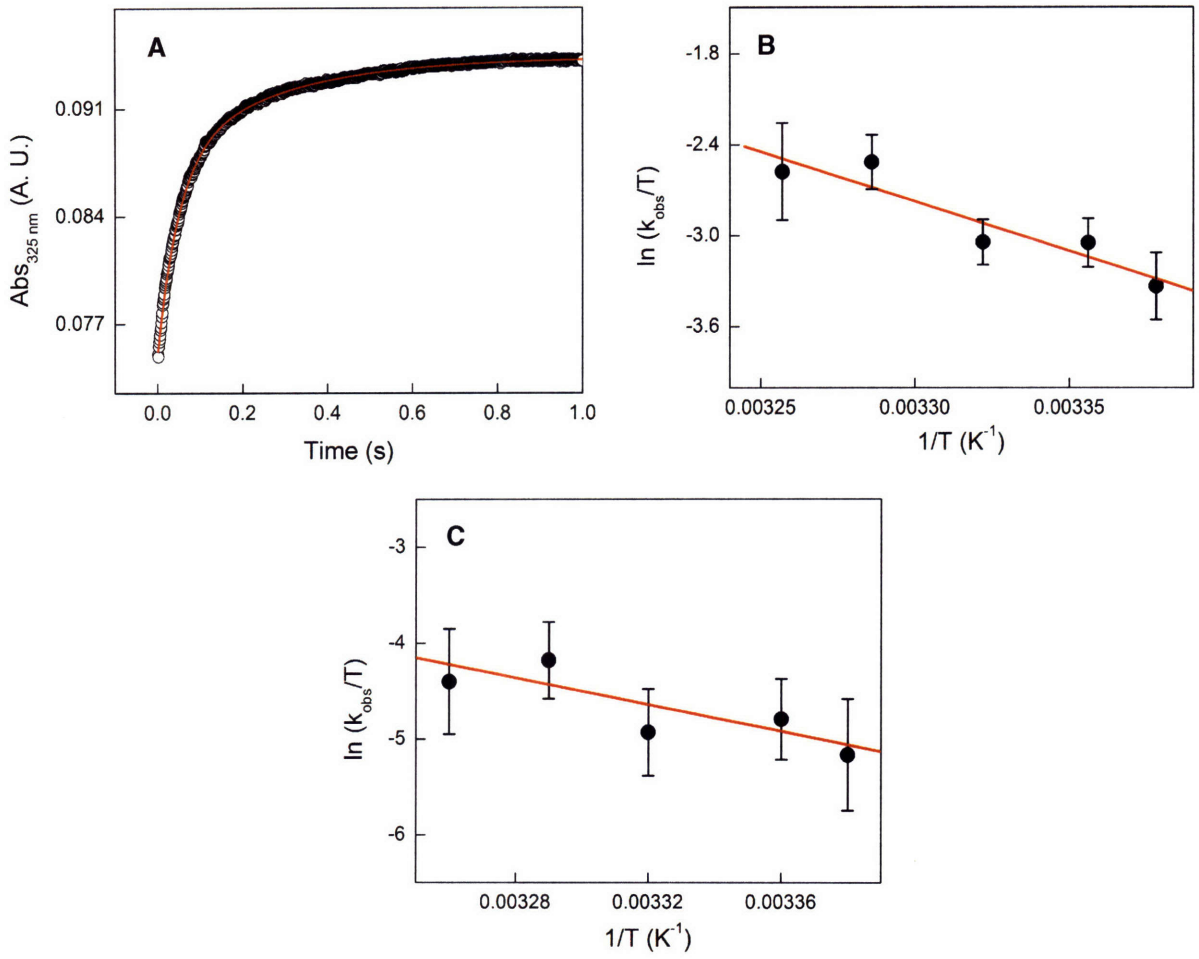

Figure 5–16. Temperature–dependence of NH_2Y_{730}• formation. (A) Representative time course at 34°C in the reaction of $Y_{730}NH_2Y$–α2/β2 with CDP/ATP. The red line describes a bi–exponential fit to the data. See Table 5–9 for kinetic parameters at various temperatures. (B) Eyring plot and linear fit according to Eq. 5–2 for the fast rate constant observed in NH_2Y_{730}• formation. (C) Eyring plot and linear fit according to Eq. 5–2 for the slow rate constant observed in NH_2Y_{730}• formation.

Table 5–10. Summary of kinetic parameters for the reaction of $Y_{730}NH_2Y$–α2/β2 with CDP/ATP as a function of temperature.

T (°C)	1st Phase k_{obs} (s^{-1})	1st Phase Amp (% Y_{122}•)	2nd Phase k_{obs} (s^{-1})	2nd Phase Amp (% Y_{122}•)
23.0	10.5 ± 1.1	26 ± 2	1.7 ± 0.2	13 ± 1
25.0	14.1 ± 1.3	26 ± 2	2.4 ± 0.2	14 ± 1
28.0	14.3 ± 1.0	29 ± 2	2.3 ± 0.2	11 ± 1
34.0	23.3 ± 1.3	22 ± 2	4.6 ± 0.4	16 ± 1
36.0	20.3 ± 2.7	24 ± 3	3.9 ± 0.5	14 ± 2

Table 5–11. Summary of thermodynamic parameters for NH_2Y• formation with $Y_{730}NH_2Y$–α2 in the presence of CDP/ATP.

Rate Constant	$\Delta H^{\ddagger}$ (kcal/mol)	$\Delta S^{\ddagger}$ (kcal/mol)	$\Delta G^{\ddagger}_{298\ K}$ (kcal/mol)
Fast k_{obs}	13.1 ± 2.3	–9.5 ± 1.7	15.9 ± 2.8
Slow k_{obs}	11.8 ± 2.1	–17.5 ± 3.1	17.0 ± 3.0

DISCUSSION

In Chapter 4, we established the application of a suppressor tRNA/aminoacyl–tRNA synthetase pair to site–specifically incorporate NH_2Y into residues 730 and 731 of α2. Using these constructs we demonstrated a new intermediate, NH_2Y•, that we characterized by EPR and UV–vis spectroscopies. We also showed that generation of NH_2Y• required the presence of substrate and effector and described the kinetics of its formation and decay in the presence of CDP/ATP. In this Chapter, additional studies have been carried out to address the structure of the NH_2Y•, its position in the α2/β2 complex, the pathway–dependence of its formation and the role of substrate and effector in its formation.

Examination of the structure of NH_2Y_{730}•. To study the structure of the NH_2Y•, isotopic substitution with ^{15}N and solvent ^{2}H were carried out and the resulting radical examined by 9 GHz and 180 GHz EPR spectroscopy, spectral simulation and DFT calculations. Importantly, in these studies the g values were experimentally determined with [^{14}N]–NH_2Y_{730}• by EPR spectroscopy at 180 GHz. The g values of an aromatic radical can be informative in regard to its local environment. According to the Stone model for g factor perturbation,[41,42,51] the g component perpendicular to the aromatic π radical plane, g_z, is equal to the free–electron g value, g_e, whereas the g components within the aromatic plane, g_x and g_y, have higher g values than g_e. The g anisotropy in organic radicals, which have significant spin density on a heteroatom, such as O or N, originates from a larger spin orbit coupling of these atoms, relative to C, and from presence of electrons that occupy nonbonding orbitals. Therefore, hydrogen bonds or the solvent dielectric or other near by residues which effect the electrostatic environment, will change the g values. Recent DFT calculations by Un and coworkers on model Y•s in solution and on the Y_{122}• in *E. coli*, have validated the work by Stone.[52] They show that the g_x value is inversely proportional to hydrogen bonding and solvent dielectric, i.e. the presence of a hydrogen bond will decrease the g_x value and the higher the dielectric constant, the lower g_x. In the class I RNRs, determination of g_x and X–ray crystal structures of β2s from

various organisms have shown that the g_x value is a diagnostic for the presence of a hydrogen bond.[45] Therefore, it is likely that the g values measured with NH_2Y_{730}• and NH_2Y_{731}• will be more informative in the near future, as more experiments are carried out with NH_2Y•s in other systems.

A key issue regarding the application of NH_2Y to other systems will be its ability to form an internal H–bond upon oxidation. As noted above and demonstrated in Scheme 5–3, the amine group may adopt an orientation in which it is H–bonded to a lone pair on the O–atom. Preliminary computational studies by Loth et al. in the 1960s with *o*–aminophenol radical indicated that the H–bonded conformation is 1–7 kcal/mol more stable than other structures without an internal H–bond.[39] Specifically, for the two structures shown in Scheme 5–3, the H–bonded conformation was found to be 1.5–2 kcal/mol more stable. Additional theoretical and experimental studies using more advanced methods will be necessary to assess these predictions. If an internal H–bond does form, it would interfere, although it is unclear to what extent, with the chemistry of hydrogen atom transfer at that residue. Orthogonal proton–coupled electron transfer reactions would be less affected. In α2, we have proposed that Y_{730} and Y_{731} are involved in a hydrogen atom transfer network with C_{439}. In Chapter 4, we postulated that the NH_2Y–α2s were competent in C_{439}• generation. At this point it is unclear whether the ability to generate C_{439}• is due to a lack of an internal H–bond formation in NH_2Y•–α2s, or whether this H–bond does form but does not interfere significantly with redox reactions at residues 730 and 731.

The isotopic replacement studies and spectral simulations in this Chapter have yielded hyperfine coupling constants that may be used to obtain unpaired spin densities in NH_2Y•. Proton hyperfine interactions consist of an isotropic term and an anisotropic term due to direct dipolar coupling. For an α–proton, i.e. a proton, such as H_5, that is directly bound to the aromatic ring (see Table 5–6 & Figure 5–6A), the isotropic term is proportional to the spin density at the carbon nucleus to which it is attached to. Quantitatively, this is described by the McConnell relation (Eq. 5–5), where A_H is the isotropic hyperfine constant, and Q_{CH} is related to

the σ–π electron interactions in a C–H bond and can be calculated with good accuracy from first principles.[53,54] Empirically Q_{CH} varies between –56 and –84 MHz with a value of –69.7 MHz being used by most investigators.[55] Finally, ρ_C is the spin density at the C–nucleus to which the proton is attached. Using this relation we obtain a spin density of 0.08 at C_5 (Figure 5–6).

$$A_H = Q_{CH} \times \rho_C \qquad (5–5)$$

Proton hyperfine coupling constants from a β–proton, i.e. a proton not directly connected to the aromatic ring, are usually as strong as those from an α–proton. This interaction is in general described by a hyperconjugation mechanism between the β proton and the *p* orbital of the aromatic ring. The strength of this interaction is dependent on the dihedral angle, θ, between the C_β–H bond and the p_z orbital at C_1 of the aromatic ring.[53] The total hyperfine interaction, consisting of dipolar and isotropic components, is given by Eq. 5–6, where A_T is the total hyperfine interaction, A_H is the isotropic component and D_C is the dipolar component between C_1 and the β–proton, which does not correlate with the spin density at C_1.

$$A_T = A_H + D_C \qquad (5–6)$$

The isotropic component is defined by Eq. 5–7, where B_0 is not associated with hyperconjugation and is neglected because it is small relative to the second factor.[53,56] B_1 accounts for the contribution by hyperconjugation and has a value of 140–162 MHz.[57] Using our experimentally determined value of 30.8 MHz and 0 MHz for C_β–H_1 and C_β–H_2, respectively, $B_0 = 0$, and $\theta_1 + \theta_2 = 120°$ we obtain a spin density of 0.25–0.29 at C_1 and θ angles of –30° and 90°. A Newman projection that shows these θ angles relative to the p_z of C_1 is shown in Figure 5–17A. Note that a second C_β–H was not required for the simulations, therefore a coupling of 0 MHz was used for C_β–H_2.

$$A_H = (B_0 \times \rho_C) + (B_1 \times \rho_C \times \cos^2 \theta) \qquad (5\text{–}7)$$

Obtaining spin density at the N–atom of the amine substituent is not as straight forward because theoretical and experimental studies on aromatic C–N systems have not been as prevalent as those described above for α–protons and β–protons, or ^{13}C and ^{17}O hyperfine interactions in aromatic radicals. Hoffman and coworkers used ^{13}C, and $^{14}N/^{15}N$ ENDOR to arrive at the spin density of the aromatic N–nucleus in a tryptophan cation radical of cytochrome c peroxidase.[46] Lassman and colleagues have determined the spin density of a W• in *E. coli* $Y_{122}F$–β2 using the anisotropic hyperfine constants, which they obtained by simulation of their EPR spectra.[47] In their studies, the N–nucleus hyperfine tensor was axially symmetric. Because, ENDOR studies have not been carried out and because our simulations show axial symmetry for the N–hyperfine tensor, N spin densities are derived based on the approach used by Lassman and coworkers. Accordingly, Eq. 5–8 was used, where A_e is the effective hyperfine constant, A_z is the *z*–component of the hyperfine tensor, A_{iso} is the isotropic coupling constant (see Table 5–6) and B has been empirically determined to be 47.8 MHz. This analysis yields a spin density of ([31.5 – 8.1]/2 / 47.8=) 0.24 at the p_z orbital of the N–nucleus.

$$A_e = A_z - A_{iso} = 2B \qquad (5\text{–}8)$$

Alternatively, the isotropic ^{14}N hyperfine splitting constant may be related to the spin density at the N– and adjacent C–nucleus using Eqs. 5–9 and 5–10, which have been derived semi–empirically using a series of aromatic N–heterocyclic radicals (such as pyridine, pyrazine, methylpyridine, etc.).[58-62] Eq. 5–9 may be used to determine the spin density at the N–nucleus. Here, A_N is the isotropic ^{14}N hyperfine coupling constant and Q_N has a value of 42 MHz. Use of this equation, yields a spin density of (8.1/42=) 0.2 at the N–nucleus in NH_2Y_{730}•. It has been suggested that the theory for ^{13}C or ^{17}O hyperfine interaction can be applied to ^{14}N as described in Eq. 5–10. Here ρ_N and ρ_C represent the spin density at the N–nucleus and the neighboring

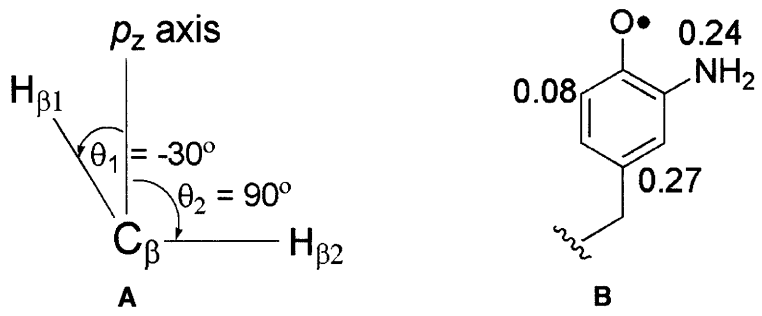

Figure 5–17. Structure of the NH_2Y_{730}•. (A) Dihedral angles from measurement of C_β–H hyperfine constants. The dihedral angles are shown relative to the p_z of C_1, labeled as p_z axis. (B) Summary of spin densities at C_1 (0.27), N (0.24), and C_5 (0.08) determined in this study. The remainder of spin density is attributed to the O–nucleus of the hydroxyl group and the C_3–nucleus of the aromatic ring.

C–nucleus, respectively, Q_{NC} represents the electron spin polarization in the *s* orbitals of ^{14}N due to spin density in the *p* orbital of the N–atom, and Q_{CN} represents the polarization due to the spin density at C_3. In the literature, the values for Q_{NC} and Q_{CN} vary from 53.5 to 86.5 MHz, and –4.8 to 19.6 MHz, respectively.[58-62] Nanda et al. have treated this topic most recently and have determined Q_{CN} and Q_{NC} values of 53.5 and –4 MHz, respectively.[60] Using these values, and a ρ_N of 0.2, which was obtained from application of Eq. 5–9, a ρ_C of 0.23 is obtained for C_3. This would yield a ρ_O of 0.22 for the hydroxyl oxygen in NH_2Y_{730}•. However, we stress that these Q values were obtained from sp^2 hybridized N–heterocycles. As previously pointed out,[58] Q values can only be considered constants in a series of compounds in which the state of hypridization of the C– and N–nuclei does not vary. In NH_2Y, the amine moiety is clearly sp^3 hybridized. Therefore, we prefer the determination of ^{14}N spin densities using the anisotropic hyperfine splitting constants as discussed above.

$$A_N = Q_N \times \rho_N \qquad (5–9)$$

$$A_N = (Q_{NC} \times \rho_N) + (Q_{CN} \times \rho_C) \qquad (5–10)$$

From the discussion above, 0.57 to 0.61 of the total spin density is accounted for, leaving 0.43 – 0.39 (Fig. 5–17B). Based on previous studies, the majority of this will be associated with the O–atom, the C_3 and the C_4 of the aromatic ring, which in Y•s, have spin densities of 0.26, 0.23, and 0.05 respectively. In catechol, the spin density at each of the oxygens was determined to be 0.16.[63] In NH_2Y•, the spin density of the hydroxyl group should be between 0.16 and 0.26, but greater than that of the N–nucleus as O has a larger spin–orbit coupling constant, 76 cm^{-1} and 151 cm^{-1}, respectively. Because C_4 densities are typically small, we assign ($O+C_3$) with the remainder of the density.

The isotopic substitution studies described herein have established that the new signal is a NH_2Y•, as we postulated in Chapter 4. Spectral simulation, 9 GHz and 180 GHz EPR spectroscopy and DFT calculations have revealed the dihedral angels of the β–protons and spin densities within the NH_2Y• at the N–nucleus and at C_1 and C_5 (Figure 5–17). Additional ENDOR and EPR studies will be necessary to assess the presence of an internal H–bond in NH_2Y•, which will have important implications for the mechanism of radical transfer at this juncture in the pathway. ^{13}C and ^{17}O studies will be required to determine how the remainder of the spin density is distributed between the O–nucleus of the hydroxyl group and C_3.

Positions of NH_2Y_{730}• and NH_2Y_{731}• within the radical transfer pathway. To examine the positions of residues 730 and 731 within the α2/β2 complex, PELDOR studies with $Y_{730}NH_2Y$–α2 and $Y_{731}NH_2Y$–α2 in the presence of β2 and GDP/TTP were performed in this Chapter. These studies have yielded diagonal distances of 38.7 Å and 38.1 Å between Y_{730}•–Y_{122}• and Y_{731}•–Y_{122}•, respectively. To analyze these distances, we consider the docking model, generated from the individual structures of α2 and β2 based on shape and charge complementarities and conserved residues (Figure 5–12). Based on this model, the diagonal distance across the α2/β2 dimer interface for the Y_{122}–Y_{731} and Y_{122}–Y_{730} pairs are 38.6 ± 1.3 Å and 40.1 ± 1.3 Å, respectively. Within error, these distances are similar to the 38.1 and 38.7 Å that we have reported here. Accordingly, our studies establish the positions of the critical Tyr

pathway residues in the α2/β2 complex, as presaged by the docking model, and also support a long–range radical transfer mechanism for C_{439}• formation.

An important insight may be provided by the width of the distance distribution for the Y_{122}•–Y_{731}• and Y_{122}•–Y_{730}• pairs, shown in Figure 5–11C. PELDOR spectroscopy was presented with DOPA–β2/α2 in the presence of all four substrate/effector pairs in Chapter 2. In these cases, the half–peak width of the distance distribution was 0.5 Å. The half–peak widths measured with NH_2Y–α2s are considerably larger than those with DOPA–β2, 1.2 Å and 1.8 Å, for $Y_{731}NH_2Y$–α2 and $Y_{730}NH_2Y$–α2, respectively. DOPA–β2 is unable to generate a C_{439}•, whereas with NH_2Y–α2s we have proposed competence in nucleotide reduction. The larger distribution with NH_2Y–α2s may be due to a distribution of conformations of the β–monomer that contains the Y_{122}•. We hypothesize that this distribution is due to two populations of NH_2Y–α2: a population which has formed deoxynucleotide and generated NH_2Y• upon reverse radical transfer, and another population that has not formed deoxynucleotide and trapped NH_2Y• during forward radical transfer. As we proposed in Chapter 3, formation of deoxynucleotide within one pathway results in a conformational change in the active site and promotes radical transfer into the second α active site. Therefore, we suggest that the distribution represents populations of NH_2Y–α2, which have undergone the conformational changes, as a result of deoxynucleotide formation, and thus have a slightly different diagonal distance than the population that traps NH_2Y• in forward radical transfer. NH_2Y• formation is biphasic in the presence of CDP/ATP or GDP/TTP. Thus, the two populations may correspond to those that generate NH_2Y• with a fast k_{obs} (~12 s^{-1}) and those that generate NH_2Y• with a slow k_{obs} (~2 s^{-1})

This proposal is consistent with two lines of evidence. First, with DOPA–β2 and DOPA–ββ' an identical distance and distance distribution is obtained in the presence of all four substrate/effector pairs. Both constructs are inactive in nucleotide reduction. Therefore, the conformational change associated with active site disulfide formation does not occur (Chapter 3) and the distribution for the Y_{122}•–$DOPA_{356}$• distance is narrow relative to the distributions observed with NH_2Y–α2s. Second, with N_3UDP, an N–centered radical (N•) is formed in the

active site, which is stable for several minutes. The mechanistic models for N• formation do not include active site disulfide generation. Based on our model, this would indicate a narrow distance distribution. Consistent with this idea, experiments have provided the diagonal distance between Y_{122}•–N• with a distribution similar to that observed with DOPA–β2 or DOPA–ββ'.

In summary, PELDOR studies with NH_2Y–α2s have established the position of Y_{730} and Y_{731} in an active α2/β2 complex. The studies reported set the stage for further X–band PELDOR experiments with other substrate/effector pairs and high field PELDOR experiments which could be used to measure the angle between paramagnets and ultimately the important distance from Y_{356} to Y_{731}. Time–resolved PELDOR experiments with NH_2Y–α2s, or PELDOR experiments with ββ' and NH_2Y–α2s will provide further insight into the model proposed above to explain the conformational distribution observed herein.

Kinetics of NH_2Y• formation with various NDP/(d)NTP combinations. In this chapter, the kinetics of NH_2Y_{730}• and NH_2Y_{731}• formation was examined as a function of substrate/effector pairs bound in α2 using SF UV–vis spectroscopy. The results have provided insight into the role of each nucleotide in triggering of radical initiation across the α2/β2 subunit interface.

In Chapter 2, we presented the kinetics of DOPA• formation as a function of substrate/ effector combination. Considering the reactions in the presence of the four NDP/(d)NTP pairs, there are several main features that need be discussed when comparing the results in Chapter 2 with those in this chapter. First, with DOPA–β2, tri–phasic kinetics is observed in the presence of CDP/ATP, UDP/ATP and ADP/dGTP; with GDP/TTP the kinetics are biphasic. With NH_2Y–α2s, only biphasic kinetics is observed with all NDP/(d)NTP pairs. The nature of the third kinetic phase in DOPA–β2 is at this point unclear. It is likely related to the additional mutations ($V_{353}G/S_{354}C$) present in all semisynthetic β2s. In Chapter 8, we will show that these mutations have a marked effect on the pre–steady state kinetics of dCDP formation. Experiments with intein wt β2 and NH_2Y–α2s will be useful in demonstrating whether the additional kinetic phase is in fact associated with the mutations in semisynthetic β2. Second, the

rate constant for the fast kinetic phase depends on the position of the radical trap. The k_{obs} increases in the order $Y_{730}NH_2Y$–α2 < $Y_{731}NH_2Y$–α2 < Y_{356}DOPA–β2; e.g. with CDP/ATP, the k_{obs} for the fast phase is 12, 18 and 38 s^{-1}, respectively. This observation is surprising as in all cases, radical trapping is limited by the conformational change that precedes radical initiation. Thus, it is difficult to explain how the rate constant for NH_2Y• or DOPA• formation can vary with the position of the trap in the pathway. Additional experiments are needed to illuminate this issue. Third, the yield of DOPA• formation is different from that of NH_2Y•. With DOPA–β2, 48 ± 4 % of total initial Y_{122}• generates a DOPA•. With $Y_{730}NH_2Y$–α2 and $Y_{731}NH_2Y$–α2, 30 ± 9 % and 28 ± 6 % of total initial Y_{122}• is involved in NH_2Y• formation, respectively. This difference likely reflects the stability of NH_2Y• and its ability to generate a C_{439}•. With DOPA–β2, nucleotide reduction, and thus C_{439}• formation, does not occur.

Comparison of DOPA• formation kinetics in Chapter 2 led us to conclude that substrate binding provided the main conformational determinants for triggering radical propagation, that effector alone was capable of triggering radical propagation, although in a slow and inefficient manner, and that the yield of DOPA• formation was highest when both substrate and effector were present. All these conclusions apply to the experiments with NH_2Y–α2s presented here. In these cases, substrate is the main signal for radical propagation across the subunit interface and concomitant NH_2Y• formation. Further, as with DOPA–β2, NH_2Y• is observed with NH_2Y–α2s in the presence of effector alone, although this process is slow and low–yielding. However, in contrast to the studies with DOPA–β2, an additional important insight is provided by the studies in this Chapter. Comparison of kinetics in the presence of substrate with those in the presence of substrate and effector shows that in the latter case more NH_2Y• is formed with a fast k_{obs}, whereas in the former case, more NH_2Y• is formed with a slow k_{obs}. Thus, the presence of effector increases the yield of NH_2Y• in the fast phase, while decreasing it in the slow phase, which is not kinetically competent based on results of Ge et al.[47] This suggests that the role of the effector is to redistribute a larger population of the complex into a conformation, which generates a NH_2Y• with a faster k_{obs} that is competent in turnover. Accordingly, the effector

plays an important role in changing the conformation of the complex from an inactive into an active state. Steady state experiments show that in the presence of substrate alone, k_{cat} is 2–10 fold lower than that in the presence of substrate and effector. The current results indicate that the rate of nucleotide formation is similar in the presence of substrate and substrate/effector, however, a smaller population is productive in product formation in the presence of substrate alone vs. in the presence of substrate and effector together. This results in an apparent lower specific activity in the presence of substrate alone.

In summary, the kinetics of NH_2Y• formation have provided important insights regarding the role of nucleotides in radical propagation. NH_2Y is an excellent probe for examining the state of the α2/β2 complex as a function of nucleotides and will be useful in re–investigating the model of allosteric regulation proposed by Reichard and coworkers. One prediction that this model makes, is that the combination of ATP/TTP results in an inactive complex.[64] It could, however, not be tested using activity assays, because the presence of substrate affects the regulatory state of the complex. In addition, a role for dATP in activation and inhibition of RNR has been suggested, which may be tested using NH_2Y–α2s.

REFERENCES

(1) Stubbe, J.; van der Donk, W. A. *Chem. Rev.* **1998**, *98*, 705.

(2) Jordan, A.; Reichard, P. *Annu. Rev. Biochem.* **1998**, *67*, 71.

(3) Brown, N. C.; Canellakis, Z. N.; Lundin, B.; Reichard, P.; Thelander, L. *Eur. J. Biochem.* **1969**, *9*, 561.

(4) Thelander, L. *J. Biol. Chem.* **1973**, *248*, 4591.

(5) Ehrenberg, A.; Reichard, P. *J. Biol. Chem.* **1972**, *247*, 3485.

(6) Stubbe, J.; Nocera, D. G.; Yee, C. S.; Chang, M. C. Y. *Chem. Rev.* **2003**, *103*, 2167.

(7) Stubbe, J.; Riggs-Gelasco, P. *Trends Biochem. Sci.* **1998**, *23*, 438.

(8) Uhlin, U.; Eklund, H. *Nature* **1994**, *370*, 533.

(9) Nordlund, P.; Sjöberg, B.-M.; Eklund, H. *Nature* **1990**, *345*, 593.

(10) van der Donk, W. A.; Yu, G.; Pérez, L.; Sanchez, R. J.; Stubbe, J. *Biochemistry* **1998**, *37*, 6419.

(11) van der Donk, W. A.; Yu, G.; Silva, D. J.; Stubbe, J. *Biochemistry* **1996**, *35*, 8381.

(12) Thelander, L.; Larsson, B.; Hobbs, J.; Eckstein, F. *J. Biol. Chem.* **1976**, *251*, 1398.

(13) Salowe, S. P.; Ator, M. A.; Stubbe, J. *Biochemistry* **1987**, *26*, 3408.

(14) Climent, I.; Sjöberg, B. M.; Huang, C. Y. *Biochemistry* **1992**, *26*, 4801.

(15) Ekberg, M.; Sahlin, M.; Eriksson, M.; Sjöberg, B.-M. *J. Biol. Chem.* **1996**, *271*, 20655.

(16) Ekberg, M.; Birgander, P.; Sjoberg, B.-M. *J. Bacteriol.* **2003**, *185*, 1167.

(17) Bennati, M.; Weber, A.; Antonic, J.; Perlstein, D. L.; Robblee, J.; Stubbe, J. *J. Am. Chem. Soc.* **2003**, *125*, 14988.

(18) Schiemann, O.; Prisner, T. F. *Q. Rev. Biophys.* **2007**, *40*, 1.

(19) Bennati, M.; Robblee, J. H.; Mugnaini, V.; Stubbe, J.; Freed, J. H.; Borbat, P. *J. Am. Chem. Soc.* **2005**, *127*, 15014.

(20) Bollinger, J. M., Jr.; Tong, W.-H.; Ravi, N.; Huynh, B.-H.; Edmonson, D. E.; Stubbe, J. *J. Am. Chem. Soc.* **1994**, *116*, 8015.

(21) Bollinger Jr., J. M.; Tong, W. H.; Ravi, N.; Huynh, B. H.; Edmondson, D. E.; Stubbe, J. *J. Am. Chem. Soc.* **1994**, *116*, 8024.

(22) Ravi, N.; Bollinger Jr., J. M.; Huynh, B. H.; Edmondson, D. E.; Stubbe, J. *J. Am. Chem. Soc.* **1994**, *116*, 8007.

(23) Reece, S. Y.; Nocera, D. G.; Stubbe, J. *Biochim. Biophys. Acta* **2005**, *1706*, 232.

(24) Yee, C. S.; Chang, M. C. Y.; Ge, J.; Nocera, D. G.; Stubbe, J. *J. Am. Chem. Soc.* **2003**, *125*, 10506.

(25) Yee, C. S.; Seyedsayamdost, M. R.; Chang, M. C. Y.; Nocera, D. G.; Stubbe, J. *Biochemistry* **2003**, *42*, 14541.

(26) Seyedsayamdost, M. R.; Reece, S. Y.; Nocera, D. G.; Stubbe, J. *J. Am. Chem. Soc.* **2006**, *128*, 1569.

(27) Seyedsayamdost, M. R.; Stubbe, J. *J. Am. Chem. Soc.* **2006**, *128*, 2522.

(28) Seyedsayamdost, M. R.; Yee, C. S.; Stubbe, J. *Nat. Protoc.* **2007**, *2*, 1225.

(29) Xie, J.; Schultz, P. G. *Methods* **2005**, *36*, 227.

(30) Xie, J.; Schultz, P. G. *Nat. Rev. Mol. Cell Biol.* **2006**, *7*, 775.

(31) DeFelippis, M. R.; Murthy, C. P.; Broitman, F.; Weinraub, D.; Faraggi, M.; Klapper, M. H. *J. Phys. Chem.* **1991**, *95*, 3416.

(32) Skawinski, W.; Flisak, J.; Chung, A. C.; Jordan, F.; Mendelsohn, R. *J. Labelled Comp. Radiopharm.* **1990**, *28*, 1179.

(33) van der Donk, W. A.; Gerfen, G. G.; Stubbe, J. *J. Am. Chem. Soc.* **1998**, *120*, 4252.

(34) Neta, P.; Fessenden, R. W. *J. Phys. Chem.* **1974**, *78*, 523.

(35) Dixon, W. T.; M., M.; Murphy, D. *J. Chem. Soc. Faraday II* **1974**, *70*, 1713.

(36) Dixon, W. T.; Hoyle, P. M.; Murphy, D. *J. Chem. Soc. Faraday II* **1978**, *74*, 2027.

(37) Simandi, L. I.; Barna, T. M.; Korecz, L.; Rockenbauer, A. *Tetrahedron Lett.* **1993**, *34*, 717.

(38) Sur, S. K.; Colpa, J. P. *Organometallics* **1989**, *8*, 2749.

(39) Loth, K.; Graf, F. *Helvetica. Chim. Acta* **1981**, *64*, 1910.

(40) Wasylishen, R. E. *Can. J. Chem.* **1976**, *54*, 833.

(41) Stone, A. J. *Proc. R. Soc. Chem.* **1963**, *A271*, 424.

(42) Stone, A. J. *Mol. Phys.* **1963**, *6*, 509.

(43) McConnell, H. M.; Heller, C.; Cole, T.; Fessenden, R. W. *J. Am. Chem. Soc.* **1960**, *82*, 766.

(44) Kwiram, A. L. *J. Phys. Chem.* **1968**, *49*, 2860.

(45) Pesavento, R. P.; van der Donk, W. A. *Adv. Prot. Chem.* **2001**, *58*, 317.

(46) Huyett, J. E.; Doan, P. E.; Gurbiel, R.; Houseman, A. L. P.; Sivaraja, M.; Goodin, D. B.; Hoffman, B. M. *J. Am. Chem. Soc.* **1995**, *117*, 9033.

(47) Lendzian, F. e. a. *J. Am. Chem. Soc.* **1996**, *118*, 8111.

(48) Ge, J.; Yu, G.; Ator, M. A.; Stubbe, J. *Biochemistry* **2003**, *42*, 10071.

(49) Jeschke, G.; Bender, A.; Paulsen, H.; Zimmermann, H.; Godt, A. *J. Magn. Reson.* **2004**, *169*, 1.

(50) Chiang, J. W.; Borbat, P. P.; Freed, J. H. *J. Magn. Reson.* **2005**, *172*, 279.

(51) Un, S.; Gerez, C.; Elleingand, E.; Fontecave, M. *J. Am. Chem. Soc.* **2001**, *123*, 3048.

(52) Un, S. *Magn. Reson. Chem.* **2005**, *43*, S229.

(53) McConnell, H. M. *J. Chem. Phys.* **1956**, *24*, 764.

(54) McConnell, H. M.; Chestnut, D. B. *J. Chem. Phys.* **1958**, *28*, 107.

(55) Bender, C. J.; Sahlin, M.; Babcock, G. T.; Barry, B. A.; Chandrashekar, T. K.; Salowe, S. P.; Stubbe, J.; Lindstrom, B.; Petersson, L.; Ehrenberg, A.; Sjöberg, B.-M. *J. Am. Chem. Soc.* **1989**, *111*, 8076.

(56) Heller, C.; McConnell, H. M. *J. Chem. Phys.* **1960**, *32*, 1535.

(57) Fessenden, R. W.; Schuler, R. H. *J. Chem. Phys.* **1963**, *39*, 2147.

(58) Henning, J. C. M. *J. Chem. Phys.* **1966**, *44*, 2139.

(59) Talcott, C. L.; Myers, R. J. *Mol. Phys.* **1967**, *12*, 549.

(60) Nanda, D. N.; Narasimhan, P. T. *Theoret. Chim. Acta* **1974**, *32*, 321.

(61) Ward, R. L. *J. Am. Chem. Soc.* **1962**, *84*, 332.

(62) Geske, D. H.; Padmanabhan, G. R. *J. Am. Chem. Soc.* **1965**, *87*, 1651.

(63) Felix, C. C.; Sealy, R. C. *J. Am. Chem. Soc.* **1982**, *104*, 1555.

(64) Brown, N. C.; Reichard, P. *J. Mol. Biol.* **1969**, *46*, 39.

CHAPTER 6:

Mono–, Di–, Tri–, and Tetra–Substituted Fluorotyrosines: New Probes for Enzymes that Use Tyrosyl Radicals in Catalysis

Adapted from: Seyedsayamdost, M. R.; Reece, S. Y.; Nocera, D. G.; Stubbe, J. *J. Am. Chem. Soc.* **2006**, *128*, 1569.

INTRODUCTION

Electron transfer (ET) has been the focus of most studies of charge transport in biology. Proteins modified with redox active donors and acceptors,[1-5] protein partners,[6-10] and DNA bioconjugates[11-14] reveal that electrons transfer over long distances according to Marcus' theory of ET,[15] augmented by considerations for electron tunneling.[16,17] In functioning enzymes, however, the occurrence of isolated ET is uncommon. Many primary metabolic steps involving charge transport rely on amino acid radicals in which ET is coupled to proton transfer (PT).[18-21] For such charge transport reactions, the problem is intrinsically more complicated because both the electron and proton tunnel and these tunneling events can be coupled to one another.[22,23] As the electron moves, the pK_a of the oxidized cofactor will change; but to predict kinetics, knowledge of the driving forces for the ET and PT reactions is insufficient. The reorganization energy will be affected by the charge redistribution resulting from electron and proton motion.[24-27] In addition, the electronic coupling will change parametrically with the proton coordinate.

Of the amino acid radicals participating in biological charge transfer processes, the tyrosyl radical (Y•) is pre–eminent.[20,21,28] This one–electron, protein–based oxidant has been identified as both a stable cofactor in deoxynucleotide biosynthesis[29] and as a transient intermediate with directed reactivity in photosynthetic O_2 evolution,[30] prostaglandin biosynthesis,[31] and disproportionation of hydrogen peroxide.[32] Despite extensive knowledge about the structure of the Y•s in these systems and the ever increasing number of Y•s identified in other proteins,[33-35] the precise mechanism of their formation and reactivity at a functional biological level has for the most part remained unknown. However, at a mechanistic level, it is well established that oxidation of tyrosine under physiological conditions requires the loss of both a proton and an electron, implicating proton–coupled electron transfer (PCET) in the radical forming mechanism.[18,30,36] Therefore, the study of Y•s in the initiation and propagation of charge in biology will necessarily demand that new tools are needed to control both the electron and

proton for Y• formation within the enzyme. This is especially pertinent to our studies of class I ribonucleotide reductase (RNR) where reversible radical transfer is proposed to occur between a stable Y_{122} radical (Y_{122}•) on the β2 subunit and C_{439} on the α2 subunit.[18,37] Radical migration over this unprecedented distance has been suggested to involve a radical hopping pathway spanning both subunits with three other tyrosine residues, Y_{356} (β2), 731 (α2) and 730 (α2), leading into the α2 active site. Moreover, the mechanism of formation of the stable Y_{122}•, which involves a putative di–iron, Fe^{III}/Fe^{IV} intermediate as the oxidant, also remains unknown.[38-42]

Substitution of tyrosine with other redox active amino acids can provide insight into the mechanism of charge transport in enzymes. However, only the natural amino acids of tryptophan and cysteine have reduction potentials close to that of tyrosine and they are poor structural substitutes. For this reason, we have turned our attention to unnatural amino acids, specifically, fluorotyrosines because they offer minimal structural perturbations compared to tyrosine. They are isosteric with tyrosine and the van der Waals radius of fluorine is only 0.15 Å larger than that of hydrogen, thus representing the most conservative substitution barring isotopic replacement. Fluorination at various points on the phenol ring affects a large range of pK_a values for the unprotected amino acid (F_nYs).[43] A similar variation in the tyrosyl radical reduction potentials upon fluorine substitution would provide a systematic variation in $\Delta G°_{ET}$ and $\Delta G°_{PT}$, the factors that control the thermodynamics of PCET reactions.

In this paper we report the synthesis and physical characterization of the N– and C–protected fluorotyrosines, Ac–F_nY–NH_2s, shown in Scheme 6–1. We also develop the methodologies for determining the $\Delta G°_{ET}$ and $\Delta G°_{PT}$ for the half of the PCET reaction involving fluorotyrosine oxidation by measuring the reduction potentials for the radical and the pK_a of the phenolic protons for Ac–F_nY–NH_2s, the latter of which is shown to vary by >4 pK_a units. Furthermore, we report the spectroscopic properties of the F_nY•s, both EPR spectra and UV/Vis absorbance spectra using transient laser absorption spectroscopy. To demonstrate the efficacy of the fluorotyrosine method in unraveling charge transport in biological systems of complexity, we

report the global substitution of tyrosine by 3–fluorotyrosine (3–FY) in β2, and present the EPR spectrum of the $3\text{–}FY_{122}$•, along with its simulation.

Scheme 6–1. Fluorotyrosine analogues prepared in this study.

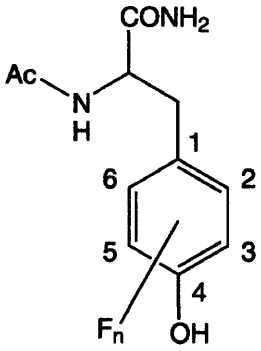

n = 0: Ac-Y-NH_2

n = 1: Ac-3-FY-NH_2

n = 2: Ac-2,3-F_2Y-NH_2, Ac-3,5-F_2Y-NH_2

n = 3: Ac-2,3,5-F_3Y-NH_2, Ac-2,3,6-F_3Y-NH_2

n = 4: Ac-2,3,5,6-F_4Y-NH_2

MATERIALS AND METHODS

Materials. All fluorinated phenols, pyruvic acid, pyridoxal–5′–phosphate (PLP), N–acetyl–L–tryosinamide, 3–fluoro–L–tyrosine, trifluoroacetic acid (TFA), thionyl chloride, acetic anhydride, triethylamine, gaseous ammonia, 1–(3–dimethylamino–propyl)–3–ethylcarbodiimide hydrochloride (WSC•HCl) and N–methylmorpholine (NMM) were purchased from Sigma–Aldrich. L–Tyrosine methyl ester hydrochloride (Y–OMe•HCl) and 4–benzoyl–N–[(1,1–dimethylethoxy) carbonyl]–L–phenylalanine (Boc–BPA–OH) were from Advanced ChemTech. 1–Hydroxybenzotriazole (HOBt) was obtained from NovaBiochem. All chemicals were used as received.

Synthesis of F_nYs. The plasmid, pTZTPL, encoding the enzyme tyrosine phenol lyase (TPL), was a generous gift of Prof. Robert Phillips. TPL purifications were carried out as described.[44] F_nYs were synthesized by stirring a 1 L solution of 30 mM ammonium acetate, pH 8.0, 10 mM of the appropriate fluorophenol, 60 mM sodium pyruvate, 5 mM β–mercaptoethanol, 40 μM PLP and 30 U of TPL at room temperature for 3 – 4 days in the dark. Synthesis of 2,3,5,6–tetrafluorotyrosine required 300 U of TPL and a 3 – 4 week incubation period, with additional 20 U TPL and 1 mM tetrafluorophenol added every week. It was important to keep the phenol concentration at 10 mM or lower, as higher concentrations resulted in enzyme denaturation. After the incubation period, the mixture was acidified to pH = 3.0 with conc. HCl. The precipitated protein was removed by filtering the mixture through a 2 – 3 cm thick Celite pad. The filtrate was extracted once with 0.5 volumes of ethyl acetate. The aqueous layer was loaded onto a 200 mL (4 × 17 cm) AG50W–X8 (50 – 100 mesh) cation exchange resin in the protonated state. After loading, the column was washed with 10 volumes water. The F_nY analogue was then eluted with a 10% ammonium hydroxide solution. Fractions that gave positive ninhydrin tests (purple stain after heating, see below) were pooled, concentrated *in vacuo*, lyophilized to dryness and stored at 4 °C. Yields ranged from 50 – 80% based on the phenol as

the limiting reagent. The ninhydrin solution consisted of 0.19% w/v ninhydrin, 95% v/v η–butanol, 0.5% v/v acetic acid and 4.5% v/v water.

3,5–F_2Y: ^{1}H NMR (300 MHz, D_2O) δ = 3.0 (dd, 1H, C_β-H_1, 8.2 Hz, 14.7 Hz) 3.18 (dd, 1H, C_β-H_2, 5.1 Hz, 14.6 Hz) 3.93 (dd, 1H, C_α-H, 5 Hz, 8 Hz), 6.88 (m, 2H, arom. C-H). ^{19}F NMR (300 MHz, D_2O) δ = 26.9 (d, 2F, 8.3 Hz).

2,3–F_2Y: ^{1}H NMR (300 MHz, D_2O) δ = 2.74 (dd, 1H, C_β-H_1, 7.7 Hz, 13.8 Hz), 2.92 (dd, 1H, C_β-H_2, 5.8 Hz, 13.8 Hz), 3.43 (dd, 1H, C_α-H, 5.8 Hz, 7.7 Hz), 6.46 (m, 1H, arom. C-H), 6.71 (m, 1H, arom. C-H). ^{19}F NMR (300 MHz, D_2O) δ = –3.50 (dd, 1F, 8.3 Hz, 19 Hz) 16.8 (dd, 1F, 8.3 Hz, 19.8 Hz).

2,3,5–F_3Y: ^{1}H NMR (300 MHz, D_2O) δ = 2.73 (dd, 1H, C_β-H_1, 7.5 Hz, 13.9 Hz), 2.89 (dd, 1H, C_β-H_2, 5.9 Hz, 13.9 Hz), 3.43 (dd, 1H, C_α-H, 5.8 Hz, 7.4 Hz), 6.66 (m, 1H, arom. C-H). ^{19}F NMR (300 MHz, D_2O) δ = 0.28 (dd, 1F, 16.6 Hz, 19.4 Hz) 12.55 (m, 1F) 19.7 (m, 1F).

2,3,6–F_3Y: ^{1}H NMR (300 MHz, D_2O) δ = 3.08 (dd, 1H, C_β-H_1, 8.2 Hz, 15 Hz), 3.24 (dd, 1H, C_β-H_2, 5.7 Hz, 9.2 Hz) 3.9 (dd, 1H, C_α-H, 5.7 Hz, 8.1 Hz) 6.42 (m, 1H, arom. C-H). ^{19}F NMR (300 MHz, D_2O) δ = –7 (m, 1F), 19.07 (d, 1F, 22.2 Hz), 38.13 (t, 1F, 11.1 Hz).

2,3,5,6–F_4Y: ^{1}H NMR (300 MHz, D_2O) δ = 3.12 (dd, 1H, C_β-H_1, 8.3 Hz, 14.9 Hz) 3.27 (dd, 1H, C_β-H_2, 5.4 Hz, 14.9 Hz) 3.9 (dd, 1H, C_α-H, 5.5 Hz, 8 Hz). ^{19}F NMR (300 MHz, D_2O) δ = –5.14 (dd, 2F, 11.1 Hz, 27.8 Hz) 11.81 (dd, 2F, 11.1 Hz, 27.7 Hz).

Synthesis of F_n–tyrosine methyl ester hydrochloride (F_nY–OMe·HCl). In a typical synthesis, the diammonium salt of the F_nY (0.597 mmol) was combined with 20 mL of methanol in a 50 mL round bottom flask. Thionyl chloride (400 μL) was added dropwise and the solution was stirred for three days at room temperature. The solvent was removed *in vacuo* and the resulting white solid was dissolved in a minimal amount of methanol. The undissolved NH_4Cl was removed by filtration and ether was added dropwise to the filtrate to induce crystallization. After cooling to –20°C, the white crystals were isolated by filtration and dried *in vacuo* providing product in 70 – 88% yield.

3–FY–OMe•HCl: ^{1}H NMR (300 MHz, $(CD_3)_2SO$, 25 °C) δ= 3.02 (m, 2H, C_β-H), 3.68 (s, 3H, -OCH_3), 4.22 (m, 1H, C_α-H), 6.80 (m, 1H, arom. C-H), 6.90 (m, 1H, arom. C-H), 7.02 (m, 1H, arom. C-H), 8.56 (b.s., 3H, -NH_3), 9.88 (b.s., 1H, PhO-H). ^{19}F NMR (300 MHz, $(CD_3)_2SO$, 25 °C) δ= 27.3 (t, 1F, 11.1 Hz).

3,5–F_2Y–OMe•HCl: ^{1}H NMR (300 MHz, $(CD_3)_2SO$, 25 °C) δ= 3.05 (m, 2H, C_β-H), 3.70 (s, 3H, -OCH_3), 4.27 (m, 1H, C_α-H), 6.94 (d, 2H, arom. C-H, 8.8 Hz), 8.63 (b.s., 3H, -NH_3), 10.15 (s, 1H, PhO-H). ^{19}F NMR (300 MHz, $(CD_3)_2SO$, 25 °C) δ= 32.1 (d, 2F,11.1 Hz).

2,3–F_2Y–OMe•HCl: ^{1}H NMR (300 MHz, $(CD_3)_2SO$, 25 °C) δ= 3.09 (m, 2H, C_β-H), 3.65 (s, 3H, -OCH_3), 4.14 (m, 1H, C_α-H), 6.78 (m, 1H, arom. C-H), 6.89 (m, 1H, arom. C-H), 8.64 (b.s., 3H, -NH_3), 10.51 (s, 1H, PhO-H). ^{19}F NMR (300 MHz, $(CD_3)_2SO$, 25 °C) δ= –0.5 (d, 1F, 22.2 Hz), δ= 19.5 (d, 1F, 22.2 Hz).

2,3,5–F_3Y•HCl: ^{1}H NMR (300 MHz, $(CD_3)_2SO$, 25 °C) δ= 3.12 (m, 2H, C_β-H), 3.69 (s, 3H, -OCH_3), 4.22 (m, 1H, C_α-H), 7.10 (m, 1H, arom. C-H), 8.70 (b.s., 3H, -NH_3), 10.83 (b.s., 1H, PhO-H). ^{19}F NMR (300 MHz, $(CD_3)_2SO$, 25 °C) δ= 5.5 (d, 1F, 16.7 Hz), 15.8, (s, 1F), 24.5 (s, 1F).

2,3,6–F_3Y•HCl: ^{1}H NMR (300 MHz, $(CD_3)_2SO$, 25 °C) δ= 3.07 (m, 2H, C_β-H), 3.64 (s, 3H, -OCH_3), 4.07 (m, 1H, C_α-H), 6.73 (m, 1H, arom. C-H), 8.70 (b.s., 3H, -NH_3), 11.13 (s, 1H, PhO-H). ^{19}F NMR (300 MHz, $(CD_3)_2SO$, 25 °C) δ= –4.8 (s, 1F), 22.3, (d, 1F, 22.2 Hz), 40.9 (m, 1F).

2,3,5,6–F_4Y•HCl: ^{1}H NMR (300 MHz, $(CD_3)_2SO$, 25 °C) δ= 3.16 (m, 2H, C_β-H), 3.66 (s, 3H, -OCH_3), 4.14 (m, 1H, C_α-H), 8.75 (b.s., 3H, -NH_3), 11.56 (b.s., 1H, PhO-H). ^{19}F NMR (300 MHz, $(CD_3)_2SO$, 25 °C) δ = –0.6 (d, 2F, 16.7 Hz), 16.2, (d, 1F, 22.2 Hz), δ= 40.9 (m, 1F)

Synthesis of N–acetyl–F_n–tyrosinamide (Ac–F_nY–NH_2). In a typical synthesis, 460 μmol of F_nY–OMe in 5.2 mL MeCN were stirred with 4 equiv. of triethylamine and 3 equiv. of acetic anhydride. The reaction was monitored by TLC (20:1 $CHCl_3$/MeOH). After 2 h, the solvent was removed *in vacuo*. The product was redissolved in MeOH followed by removal of MeOH *in vacuo* (2×). The N–acetylated, methyl ester derivative was converted to the amide by

stirring the compound at a concentration of 100 mM in $NH_{3(g)}$–saturated MeOH. The reaction was complete after 3 days. The solvent was removed *in vacuo* and the product purified by silica gel chromatography with 15:1 CH_2Cl_2/MeOH as the eluant. The product was characterized by ^1H and ^{19}F NMR as well as by LR–ESI–MS. Yields of 80 – 95% were obtained for all analogues.

Ac–3–FY–NH_2: ^1H–NMR (300 MHz, CD_3OD) δ = (s, 3H, Ac), (dd, 1H, C_β-H_1, 8.8 Hz, 14.0 Hz), (dd, 1H, C_β-H_2, 5.8 Hz, 14.0 Hz), (dd, 1H, C_α-H, 5.8 Hz, 8.8 Hz), (m, 1H, arom. C-H). ^{19}F NMR (300 MHz, CD_3OD) δ = (dd, 1F, 8.3 Hz, 19.4 Hz) (dd, 1F, 8.3 Hz, 19.4 Hz). LR–ESI–MS: *m/z* (–H) calc. 239.0, obs. 238.9.

Ac–3,5–F_2Y–NH_2: ^1H–NMR (300 MHz, CD_3OD) δ = 1.92 (s, 3H, Ac), 2.75 (dd, 1H, C_β-H_1, 9.2 Hz, 13.9 Hz), 3.03 (dd, 1H, C_β-H_2, 5.5 Hz, 13.9 Hz), 4.55 (dd, 1H, C_α-H, 5.7 Hz, 9.2 Hz), 6.83 (m, 2H, arom. C-H). ^{19}F NMR (300 MHz, CD_3OD) δ = 25.2 (d, 2F, 8.3 Hz). LR–ESI–MS: *m/z* (–H) calc. 257.0, obs. 256.9.

Ac–2,3–F_2Y–NH_2: ^1H–NMR (300 MHz, CD_3OD) δ = 1.90 (s, 3H, Ac), 2.85 (dd, 1H, C_β-H_1, 8.8 Hz, 14.0 Hz), 3.12 (dd, 1H, C_β-H_2, 5.8 Hz, 14.0 Hz), 4.61 (dd, 1H, C_α-H, 5.8 Hz, 8.8 Hz), 6.83 (m, 1H, arom. C-H). ^{19}F NMR (300 MHz, CD_3OD) δ = –3.12 (dd, 1F, 8.3 Hz, 19.4 Hz) 17.3 (dd, 1F, 8.3 Hz, 19.4 Hz). LR–ESI–MS: m/z (–H) calc. 257.0, obs. 256.9.

Ac–2,3,5–F_3Y–NH_2: ^1H–NMR (300 MHz, CD_3OD) δ = 1.93 (s, 3H, Ac), 2.78 (dd, 1H, C_β-H_1, 8.4 Hz, 14.1 Hz), 3.03 (dd, 1H, C_β-H_2, 6 Hz, 14.3 Hz), 4.53 (dd, 1H, C_α-H, 5.7 Hz, 8.2 Hz), 6.56 (m, 1H, arom. C-H). ^{19}F NMR (300 MHz, CD_3OD) δ = –0.95 (t, 1F, 19.4 Hz) 10.48 (m, 1F) 19.05 (dd, 1F, 11.1 Hz, 27.7 Hz). LR–ESI–MS: m/z (–H) calc. 275, obs. 274.9.

Ac–2,3,6–F_3Y–NH_2: ^1H –NMR (300 MHz, CD_3OD) δ = 1.94 (s, 3H, Ac), 2.93 (dd, 1H, C_β-H_1, 8.8 Hz, 14 Hz), 3.17 (dd, 1H, C_β-H_2, 5.5 Hz, 13.8 Hz), 4.65 (dd, 1H, C_α-H, 5.7 Hz, 13.8 Hz), 6.51 (m, 1H, arom. C-H). ^{19}F NMR (300 MHz, CD_3OD) δ = –10.4 (m, 1F) 17.4 (d, 1F, 21 Hz) 36.2 (t, 1F, 12 Hz). LR–ESI–MS: *m/z* (–H) calc. 275, obs. 274.9.

Ac–2,3,5,6–F_4Y–NH_2: ^1H–NMR (300 MHz, CD_3OD) δ = 1.92 (s, 3H, Ac), 2.96 (dd, 1H, C_β-H_1, 8.4 Hz, 14.4 Hz), 3.2 (dd, 1H, C_β-H_2, 6 Hz, 14.4 Hz), 4.64 (dd, 1H, C_α-H, 6 Hz, 8.4 Hz).

LR–ESI–MS: calc 293, obs 293. ^{19}F NMR (300 MHz, CD_3OD) δ = –5.0 (dd, 2F, 6 Hz, 22.5 Hz) 12.6 (dd, 2F, 6 Hz, 22.5 Hz). LR–ESI–MS: *m/z* (–H) calc. 293, obs. 292.9.

Synthesis of 4–Benzoyl–L–phenylalanyl–F_nY methyl ester trifluoroacetic acid (BPA–F_nY–OMe•CF_3COOH). F_nY–OMe (0.432 mmol, 1.0 eq), BPA–OH (160 mg, 0.432 mmol, 1.0 eq), N–ethyl–N'–(3–dimethylaminopropyl)carbodiimide hydrochloride (WSC•HCl) (91 mg, 0.475 mmol, 1.1 eq), and 1–hydroxybenzotriazole (HOBt) (64 mg, 0.475 mg, 1.1 eq) were combined in a 50 mL round bottom flask with 20 mL of methylene chloride. *N*–methylmorpholine (NMM) (175 µL, 1.73 mmol, 4 eq) was added and the solution was stirred overnight at room temperature. The solution was diluted to 75 mL with methylene chloride and washed with 2 × 30 mL of 10% citric acid solution. The organic layer was dried over $MgSO_4$ and the solvent removed *in vacuo*. The resulting clear oil was dissolved in a few mLs of methylene chloride and loaded onto a 1 mm thick silica gel Chromatotron plate. The product was eluted with 3% methanol/methylene chloride and the solvent was removed *in vacuo*. The resulting clear oil was dissolved in 1:1 TFA:CH_2Cl_2 and stirred for 20 min at room temperature. The solvents were then evaporated under a stream of $N_{2(g)}$ and the resulting clear oil was dried under high vacuum. Trituration with CH_2Cl_2 followed by the dropwise addition of ether resulted in the formation of white crystals, which were cooled to –20 °C and isolated by filtration. Synthesis of these dipeptides was carried out by Steven Reece.

BPA–Y–OMe•CF_3COOH: ^1H NMR (300 MHz, $(CD_3)_2CO$, 25 °C) δ = 2.88–3.18 (m, 2H, C_β-H), 3.37 (m, 2H, C_β-H), 3.68 (s, 3H, -OCH_3), 4.62 (m, 1H, C_α-H), 4.88 (m, 1H, C_α-H), 6.78 (m, 2H, phenol-H), 7.15 (m, 2H, phenol-H), 7.30 (d, 2H, $C_6H_4OC_6H_5$, 7.7 Hz), 7.55 (m, 2H, $C_6H_4OC_6H_5$), 7.67 (m, 3H, $C_6H_4OC_6H_5$), 7.76 (m, 2H, $C_6H_4OC_6H_5$).

BPA–3–FY–OMe•CF_3COOH: ^1H NMR (300 MHz, $(CD_3)_2CO$, 25 °C) δ = 2.90 – 3.20 (m, 2H, C_β-H), 3.32–3.48 (m, 2H, C_β-H), 3.69 (s, 3H, -OCH_3), 4.63 (m, 1H, C_α-H), 4.96 (m, 1H, C_α-H), 6.85 – 7.04 (m, 2H, phenol-H), 7.14 (m, 1H, phenol-H), 7.32 (m, 2H, $C_6H_4OC_6H_5$), 7.50 – 7.82 (m, 7H, $C_6H_4OC_6H_5$) ^{19}F NMR (300 MHz, $(CD_3)_2CO$, 25 °C) δ = 27.17 (m, 1F), 89.76 (s, 3F).

BPA–3,5–F_2Y–OMe•CF_3COOH: ^{1}H NMR (300 MHz, $(CD_3)_2CO$, 25 °C) δ = 2.89–3.25 (m, 2H, Cβ-H), 3.38 (m, 2H, Cβ-H), 3.70 (s, 3H, -OCH_3), 4.65 (m, 1H, Cα-H), 4.95 (m, 1H, Cα-H), 7.03 (m, 2H, phenol-H), 7.33 (d, 2H, $C_6H_4OC_6H_5$, 8.3 Hz), 7.56 (m, 2H, $C_6H_4OC_6H_5$), 7.62–7.85 (m, 5H, $C_6H_4OC_6H_5$). ^{19}F NMR (300 MHz, $(CD_3)_2CO$, 25 °C) δ = 26.6 (s, 2F), 85.6 (s, 3F).

BPA–2,3–F_2Y–OMe•CF_3COOH: ^{1}H NMR (300 MHz, $(CD_3)_2CO$, 25 °C) δ = 2.93 – 3.49 (m, 4H, Cβ-H), 3.69 (s, 3H, -OCH_3), 4.68 (m, 1H, Cα-H), 4.95 (m, 1H, Cα-H), 6.80 (m, 1H, phenol-H), 7.01 (m, 1H, phenol-H), 7.39 (d, 2H, $C_6H_4OC_6H_5$, 7.7 Hz), 7.56 (m, 2H, $C_6H_4OC_6H_5$), 7.63 – 7.86 (m, 5H, $C_6H_4OC_6H_5$). ^{19}F NMR (300 MHz, $(CD_3)_2CO$, 25 °C) δ = –1.7 (m, 1F), 18.3 (m, 1F), 85.6 (s, 3F).

BPA–2,3,5–F_3Y–OMe•CF_3COOH: ^{1}H NMR (300 MHz, $(CD_3)_2CO$, 25 °C) δ = 2.93–3.51 (m, 4H, Cβ-H), 3.70 (s, 3H, -OCH_3), 4.68 (m, 1H, Cα-H, 5.04 (m, 1H, Cα-H), 7.11 (m, 1H, phenol-H), 7.41 (d, 2H, $C_6H_4OC_6H_5$, 7.7 Hz), 7.55 (m, 2H, $C_6H_4OC_6H_5$), 7.62 – 7.85 (m, 5H, $C_6H_4OC_6H_5$). ^{19}F NMR (300 MHz, $(CD_3)_2CO$, 25 °C) δ = 7.93 (d, 1F, 22.2 Hz), 18.56 (m, 1F), 26.1 (s, 1F), 89.9 (s, 3F).

BPA–2,3,6–F_3Y–OMe•CF_3COOH: ^{1}H NMR (300 MHz, $(CD_3)_2CO$, 25 °C) δ = 3.00–3.26 (m, 2H, Cβ-H), 3.44 (m, 2H, Cβ-H), 3.67 (s, 3H, -OCH_3), 4.66 (m, 1H, Cα-H), 5.12 (m, 1H, Cα-H), 6.76 (m, 1H, phenol-H), 7.41–7.85 (m, 9H, $C_6H_4OC_6H_5$). ^{19}F NMR (300 MHz, $(CD_3)_2CO$, 25 °C) δ = –1.86 (m, 1F), 25.2 (d, 1F, 22.2 Hz), 44.1 (m, 1F), 90.0 (s, 3F).

BPA–2,3,5,6–F_4Y–OMe•CF_3COOH: ^{1}H NMR (300 MHz, $(CD_3)_2CO$, 25 °C) δ = 3.10 – 3.52 (m, 4H, Cβ-H), 3.68 (s, 3H, -OCH_3), 4.65 (m, 1H, Cα-H), 5.05 (m, 1H, Cα-H), 7.46 – 7.85 (m, 9H, $C_6H_4OC_6H_5$). ^{19}F NMR (300 MHz, $(CD_3)_2CO$, 25 °C) δ = –2.42 (d, 2F, 22.2 Hz), 14.6 (d, 2F, 22.2 Hz), 85.6 (s, 3F).

Physical measurements. ^{1}H and ^{19}F NMR spectra were recorded on a Varian 300 MHz NMR at the MIT Department of Chemistry Instrumentation Facility (DCIF). Aqueous samples for ^{1}H NMR and ^{19}F NMR were carried out in D_2O with 3–(trimethylsilyl)–propionic acid–d_4 (TSP) as an internal standard and $CFCl_3$ as an external standard, respectively. Nonaqueous ^{1}H

and ^{19}F NMR were externally referenced to tetramethylsilane and $CFCl_3$, respectively. Steady–state absorption spectra were recorded on an Agilent 8453 Diode Array Spectrophotometer.

pK_a determination of Ac–F_nY–NH_2 analogues using UV spectroscopy and ^{19}F NMR spectroscopy. The pHs of several buffer solutions (10 mM Potassium phosphate, 200 mM KCl) were adjusted using either KOH or HCl spanning a pH range of 2 – 13 at 0.3 – 0.5 pH unit intervals. The blocked F_nY was diluted into each buffer and the pH remeasured before and after acquisition of the UV spectrum. The absorption at $\lambda_{max}(Y^-)$, the wavelength of maximum absorption for the deprotonated phenolate form, was plotted vs. pH and the data fit Eq. 6–1:

$$\frac{A(\text{pH}) - A(\text{pH}=2)}{A(\text{pH}=13) - A(\text{pH}=2)} = f_Y = \frac{10^{(\text{pH} - \text{p}K_a)}}{1 + 10^{(\text{pH} - \text{p}K_a)}} \qquad (6\text{–}1)$$

where A is absorbance at λ_{max}(Ac–Y^-–NH_2) and f_Y represents the fraction of the amino acid in the phenolate form.

To determine the pK_a of free 2,3–F_2Y by ^{19}F NMR, the samples were prepared in a similar fashion as described above for the pK_a determinations by UV spectroscopy. After preparation of the sample in an Eppendorf tube, the pH was measured again and the sample transferred to an NMR tube. Spectra were externally referenced to $CFCl_3$ and ^{19}F NMR recorded at different pH values. The change in chemical shift of each fluorine nucleus was plotted against pH and fit to Eq. 6–2:

$$\frac{\delta(\text{pH}) - \delta(\text{pH}=5.3)}{\delta(\text{pH}=9.4) - \delta(\text{pH}=5.3)} = f_Y = \frac{10^{(\text{pH} - \text{p}K_a)}}{1 + 10^{(\text{pH} - \text{p}K_a)}} \qquad (6\text{–}2)$$

Differential pulse voltammetry (DPV). The buffer used for pK_a measurements (10 mM Potassium phosphate, 200 mM KCl) was also used for electrochemical experiments. DPV was performed on the N–acetyl, C–amide–protected amino acids, using a CV–50W instrument from Bioanalytical Systems as previously described.[45] Briefly, measurements were performed in a

three–electrode glass cell, with a glassy carbon working electrode, a platinum wire counter–electrode and a Ag/AgCl/3M NaCl reference electrode. The glassy carbon electrode was polished with a water/alumina slurry and sonicated for ~1 min prior to each measurement. Typically, the solution contained 150 – 200 μM protected Ac–F_nY–NH_2 analogue in 10 mM potassium phosphate buffer with 200 mM KCl as the supporting electrolyte. The pH of several buffer solutions was adjusted with 1 M HCl or 1 M KOH prior to addition of the analyte and spanned a range of 1 – 13 at 0.3 – 0.5 pH unit intervals. After addition of the analyte to the solution and immediately before each measurement, the pH was measured with a pH meter, and the solution degassed by Ar sparging for 2 min. Measurements were made with the ferricyanide/ferrocyanide couple as an internal standard (0.436 V vs. NHE). DPV parameters were as follows: scan rate, 10 mV/s; sample width, 17 ms; pulse amplitude, 50 mV; pulse width, 50 ms; pulse period, 200 ms; quiet time, 4 s; sensitivity, 100 μA/V; temperature, 25 °C.

Generation of oxidized F_nYs and EPR measurements. A 10 – 15 mM solution of each free F_nY was prepared and the pH adjusted to 11 with NaOH. The sample was transferred to an EPR tube and the solution bubbled with Ar for 15 min. The tube was then sealed under Ar pressure and quick–frozen in liquid N_2. The tube was immersed in liquid N_2 in a quartz finger dewar and irradiated for 5 min using the unfiltered light from a 1000 W high pressure Xe arc lamp. The photolyzed product was never allowed to warm above 77 K and the EPR spectra were subsequently recorded on a Bruker ESP–300 X–band (9.4 GHz) spectrometer equipped with an Oxford liquid He cryostat at 77 K. The EPR parameters were as follows: power = 0.2 mW; modulation frequency = 100 kHz; modulation amplitude = 1.5 G, time constant = 5.12 ms and conversion time = 20.48 ms. The resulting EPR spectra remained unchanged after storage of the photolysed product for one month at 77 K in the dark. The EPR spectra of 3–FY–β2 and wt β2 (vide infra) were obtained at 25 K using the same parameters listed above, except with a modulation amplitude = 2 G. The 3–FY–β2 spectrum was simulated by Dr. Stoyan Smoukov and Prof. Brian Hoffman using SIMPIP and QPOW obtained from the Illinois EPR Research Center.

Transient absorption (TA) spectroscopy. Pump light for TA measurements was provided by an Infinity Nd:YAG laser (Coherent) running at 20 Hz. The set–up of the instrument was slightly modified from that previously described.[46] The third harmonic (355 nm, 200 mJ per pulse) was used to pump a Type II XPO (Coherent). The 600 nm signal beam was isolated and frequency doubled in a XPO–UV frequency doubling crystal (Coherent) to produce a slightly divergent 300 nm beam with a ~5 ns pulse width and a pulse energy of ~500 μJ. This beam was then passed through a slow focusing lense and through the sample at a ~160°, producing a beam spot of 2 mm diameter on the sample. A 75 W Xe arc lamp (unpulsed, PTI) provided the probe light, which was focused onto the sample, overlapped with the pump beam, recollimated after the sample, and focused onto the entrance slit of a Triax 320 spectrometer. The probe beam was dispersed by a 300 × 500 blazed grating and collected with either an intensified gated CCD camera (ICCD, Andor Technology, 1024 × 256 pixels, 26 μm^2) for TA spectra or a photomultiplier tube (PMT) for TA kinetics at a single wavelength. PMT outputs were collected and averaged with a 1 GHz oscilloscope (LeCroy 9384CM). To produce a TA spectrum, a series of four spectra were taken: I_F (pump on/probe off), I (pump on/probe on), I_B (pump off/probe off), and I_0 (pump off/probe on). Uniblitz shutters driven by delay generators (DG535, Stanford Research Systems) and T132 Uniblitz shutter drivers were used to block the pump and probe light in this sequence using a TTL trigger from the Q–switch of the laser. Transient spectra were corrected for fluorescence and background light using these spectra and the equation: $\Delta OD = \log[(I_0 - I_B)/(I - I_F)]$. Spectra reported are the average of 1250 of the four–spectra sequences. The instrument control and data analysis were performed by software written in LabView. Aqueous BPA–F_nY–OMe samples were prepared at 200–500 μM concentrations in deionized water buffered to pH 4 with 20 mM succinic acid. All TA measurements were performed in a 2 mm quartz optical cell. For BPA–3–FY–OMe, 266 nm pump light was used as described previously,[47] and the sample was flowed through a 2 mm cell to ensure fresh sample for each laser shot. T. A. spectroscopy was carried out by Steven Reece.

Computational methods. Density functional theory calculations (DFT) were performed using the Amsterdam Density Functional (ADF2002.02) program[48,49] a home–built Linux cluster comprising 60 Intel processors organized in groups of 12 running in parallel. The generalized gradient approximation was used as implemented in ADF by the Becke–88 functional for exchange,[50] and the Perdew–Wang–91functional for correlation.[51] A basis set of triple–ζ Slater–type functions augmented by a polarization set (TZP) was used for all atoms; spin restriction was lifted for all Ac–F_nY•–NH_2 radicals. Energies reported are gas–phase internal energies at 0 K, without zero–point vibrational energy, of the geometry optimized structure. Each structure was optimized from the same amino acid backbone configuration, which was kept nearly constant throughout the calculation. Orbital energies, Cartesian coordinates and atom numbering schemes for each of the protonated, deprotonated and radical Ac–F_nY–NH_2s are provided in the Supporting Information. Computational studies were carried out by Steven Reece.

Global incorporation of 3–FY into β2. Competent BL21(DE3) cells were transformed with pTB2, an β2 overexpression plasmid, and grown on an LB agar plate containing 100 mg/L ampicillin. A single colony from the plate was used to seed a 200 mL culture containing 100 mg/L ampicillin. The culture was grown overnight and then centrifuged at 10,000 g for 10 min. The cell pellet was resuspended in 50 mL of minimal medium containing no L–tyrosine and 100 mg/L ampicillin (details of the medium have been reported).[52] The doubling time of the cells was typically ~40 min and at $A_{600\ nm}$ of 0.6, 1 g/L of 3–FY was added to the culture. IPTG (0.5 mM) was added to the culture 15 min after the addition of 3–FY. The cells were grown to $A_{600\ nm}$ of 1.4 – 1.6 and harvested ~4 h after induction. The yield was 5 g/L, similar to yields obtained for wt β2 culture growths. 3–FY–β2 was purified using published procedures.[53]

Extent of incorporation of 3–FY into β2. The 3–FY content of β2 was analyzed by the MIT Biopolymer Laboratory using the following procedure: The purified 3–FY–β2 (200 – 2000 pmol) was lyophilized to dryness in a Speedvac and hydrolyzed in 200 μL of 6 N HCl (Pierce Sequence Grade) at 150 °C for 1 h or 110 °C for 22 h under N_2 with norleucine (1000 pmol) added as an internal standard. The samples were then dried *in vacuo*, treated with 2%

borane/diisopropyl ethylamide complex solution (40 μL) to reduce methionine oxidation and allowed to air–dry for 2 h. The samples were then dissolved in 0.3 M sodium acetate buffer (pH 5.5) containing 0.025 % w/v potassium EDTA, mixed rigorously, and centrifuged at 15,000 rpm on a tabletop centrifuge for 5 min to remove particulate matter. Aliquots (30 μL) were then loaded onto an Applied Biosystem Model 420A Derivatizer using phenyl isothiocyanate as the derivatizing agent, followed by automatic injection onto an Applied Biosystem 130A Separation System, which uses a Spheri–5 PTC 5 micron, 220 × 2.1 mm column from Perkin–Elmer Brownlee. A series of pure amino acid standards including 3–FY (500 pmol) were also derivatized and analyzed to determine the retention time of each amino acid and for quantitation purposes. The data was collected and analyzed using a Perkin–Elmer Applied Biosystem 610A Data Analysis program. Global incorporation of 3–FY and determination of its extent were performed by Dr. Hiep-Hoa Nguyen.

RESULTS AND DISCUSSION

pK_a determination of F_nYs by UV and ^{19}F NMR spectroscopy. A slightly modified method from that of Kim and Cole[43] and Phillips and coworkers[54] yields the free F_nYs in good yields and high purity. The amine and acid functionalities of the free amino acids were protected by acetylation and amidation to avoid complications arising from different protonation states of these groups. Figure 6–1 presents the absorption spectra of phenol and phenolate forms of the Ac–F_nY–NH_2 amino acids presented in Scheme 6–1. Substitution of the aromatic protons of tyrosine with fluorine results in a blue–shift of the λ_{max} associated with the $\pi \rightarrow \pi^*$ transition (Figure 6A), which red shifts upon deprotonation (Figure 6B). This observed bathochromic shift with deprotonation of the phenol group allows for the measurement of pK_a by UV spectroscopy.

The typical absorbance changes for Ac–F_nY–NH_2s induced by changes in pH are shown in Figure 6–2 for the Ac–2,3–F_2Y–NH_2 derivative. The pK_a values were determined by plotting f_{Y^-} as a function of pH, and fitting the data to Eq. 6–1 (see inset). The pK_a values listed in Table 6–1 for the protected Ac–F_nY–NH_2 amino acids differ significantly from those previously determined for the unprotected F_nY analogues.[43] N–acetyl and C–amide protected derivatives allow us to monitor acid/base equilibria resulting only from the fluorophenol moiety; therefore the pK_a values obtained on these blocked derivatives better approximate the pK_a that these residues would have in a solvent–exposed, simple polypeptide chain. The pK_a values of F_nY derivatives may be independently determined by ^{19}F NMR. Figure 6–3 shows the pH dependence of the two fluorine signals of free (i.e. unprotected) 2,3–F_2Y; as the pH is decreased, these signals shift downfield. When the chemical shift is plotted as a function of pH and fit to Eq. 6–2, pK_as of 7.53 (using the lower field ^{19}F nucleus) and 7.59 (using the higher field ^{19}F nucleus) are obtained, in good agreement with that previously reported for the unprotected amino acid (pK_a = 7.6).[43] Within a protein environment, the determination of pK_a values of F_nY by the ^{19}F NMR method may be easier to implement since large UV absorptions from intra–protein Y and W

residues will obscure the bathochromic shift of F_nY residues incorporated into the protein. Indeed, ^{19}F NMR signals of non–natural F_nY amino acids have been used in small proteins to probe changes in the environment of specific residues upon domain movements.[55]

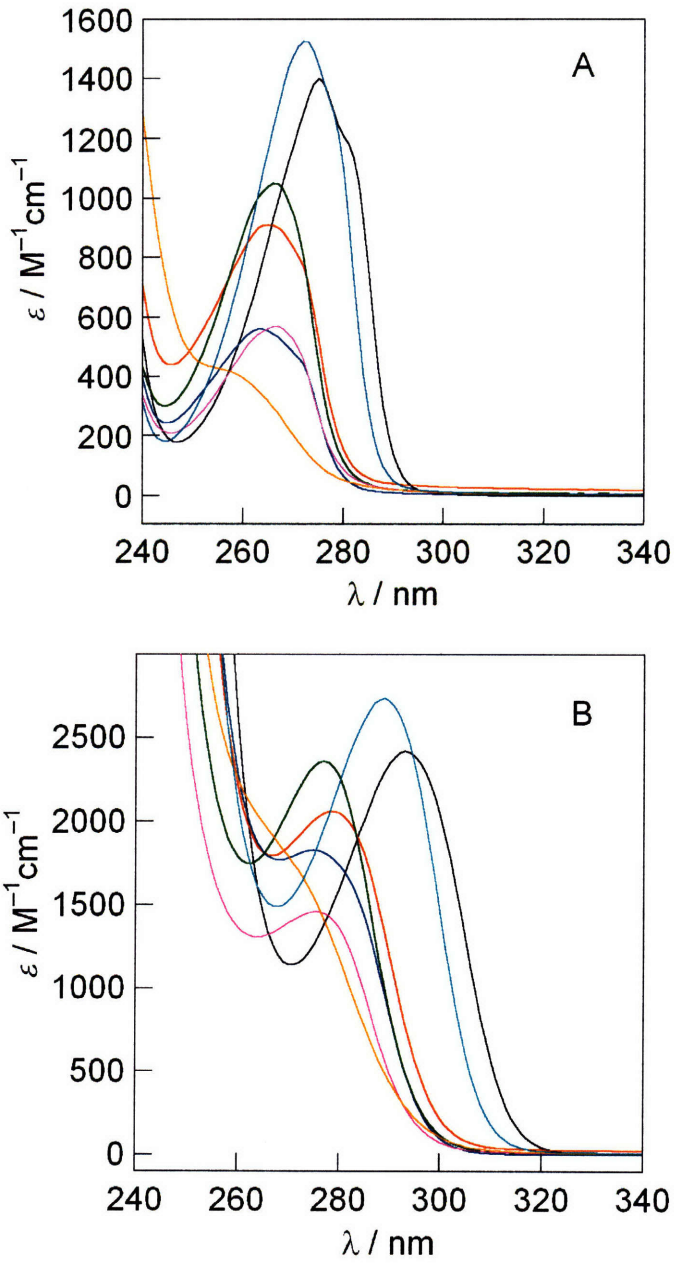

Figure 6–1. UV spectra of phenol and phenolate forms of Ac–F_nY–NH_2Ys. The UV spectra of phenol (A) and phenolate (B) forms are shown for (—) Ac–Y–NH_2, (—) Ac–3–FY–NH_2, (—) Ac–3,5–F_2Y–NH_2, (—) Ac–2,3–F_2Y–NH_2, (—) Ac–2,3,6–F_3Y–NH_2, (—) Ac–2,3,5–F_3Y–NH_2, and (—) Ac–F_4Y–NH_2.

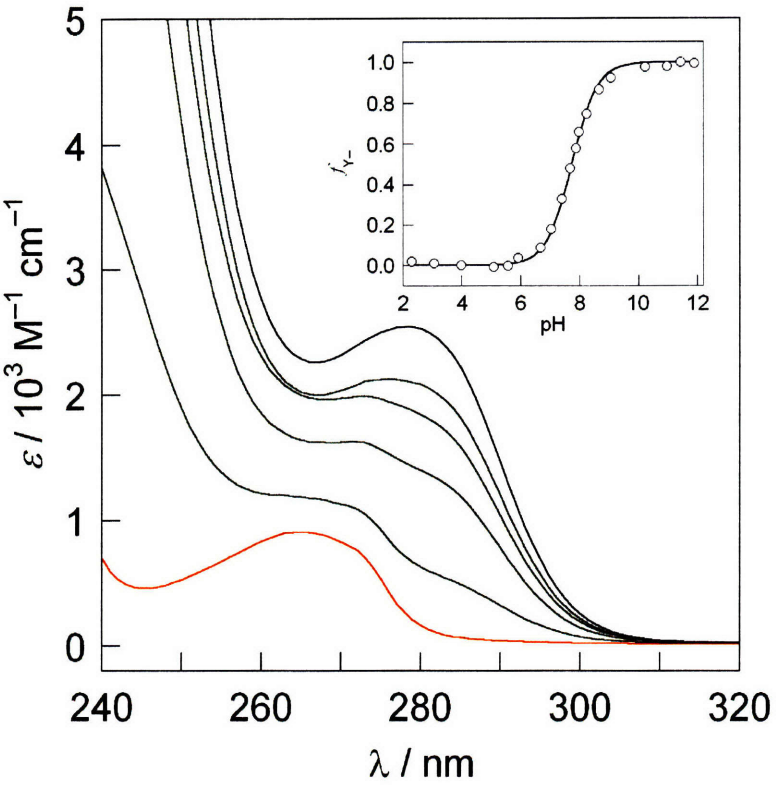

Figure 6–2. UV spectra of Ac–2,3–F_2Y–NH_2 as a function of pH. Changes in the absorption profile of Ac–2,3–F_2Y–NH_2 at aqueous solution pH of 5.1 (—), 7.0, 7.7, 8.0, 8.3 and 9.1(—). Inset: Fraction of Ac–2,3–F_2Y^- –NH_2 vs. pH (○) and fit (—) as described by Eq. 6–1.

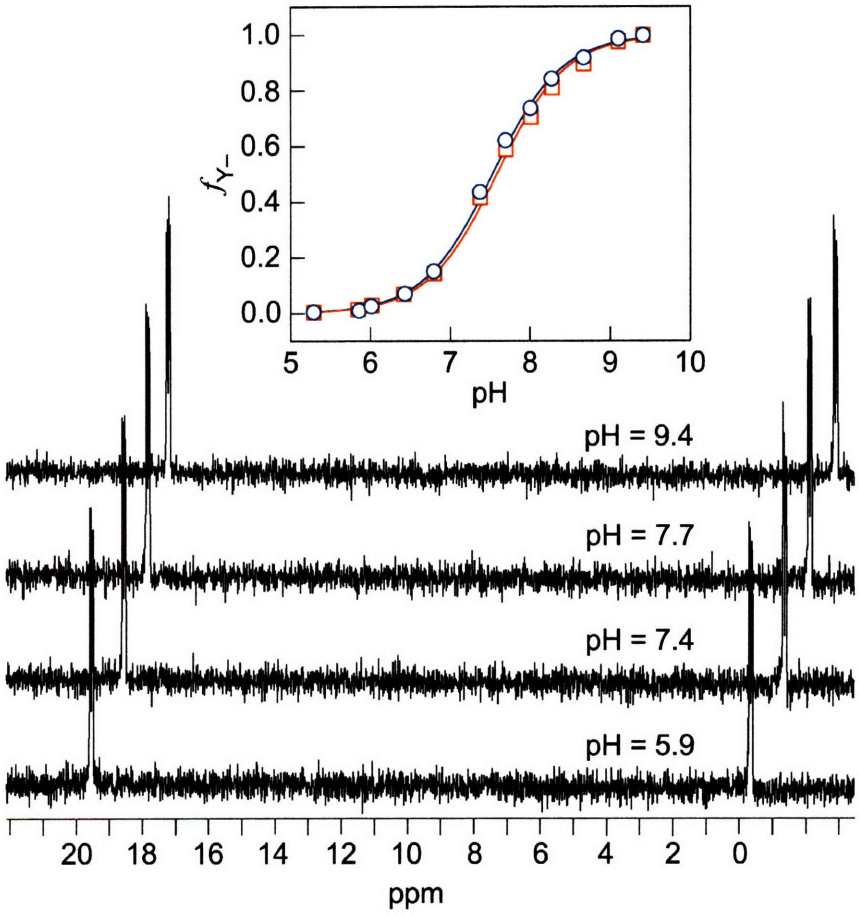

Figure 6–3. Dependence of ^{19}F NMR chemical shifts on pH. ^{19}F NMR spectra of free 2,3–F_2Y at various pH values (bottom) and fraction of 2,3–F_2Y^- as a function pH fit to Eq. 6–2 (top inset). Blue data points represent signal of the higher field ^{19}F nucleus, red data points represent that of the lower field ^{19}F nucleus.

Table 6–1. Physical data for tyrosine and fluorotyrosine derivatives.

Derivative	$\lambda_{max}(F_nY)$ / nm (ε / M^{-1} cm^{-1})	$\lambda_{max}(F_nY^-)$ / nm (ε / M^{-1} cm^{-1})	$\lambda_{max}(F_nY\bullet)$/ nm	pK_a[a]	pK_a[b]	pK_a[c]	$E_p(Y\bullet/Y^-)$/ mV[d]	δ(O–H)/ ppm[e]
Y	275 (1400)	293 (2420)	407	10	–	9.9	642	9.44
3–FY	272 (1530)	289 (2740)	400	8.4	8.4	8.4	705	9.88
3,5–F_2Y	263 (560)	275 (1830)	395	6.8	7.2	7.2	755	9.88
2,3–F_2Y	265 (910)	279 (2060)	408	7.6	7.7	7.8	810	10.51
2,3,5–F_3Y	267 (570)	276 (1460)	400	6.1	6.4	6.4	853	10.83
2,3,6–F_3Y	266 (1050)	277 (2360)	415	6.6	6.9	7.0	911	11.13
F_4Y	~257 (420)	~273 (1660)	411	5.2	5.6	5.6	968	11.56

[a] F_nY pK_a as reported in ref. 43. [b] Ac–F_nY–NH_2 pK_a as determined by the UV–Vis absorption titration method. [c] Ac–F_nY–NH_2 pK_a as determined by the DPV method. [d] DPV peak potential vs. NHE for the Ac–$F_nY\bullet$–NH_2/Ac–F_nY^-–NH_2 couple. [e] F_nY–OMe ^1H NMR in $(CD_3)_2SO$.

pH Dependent oxidation of Ac–F_nY–NH_2s. Oxidation of Y is an irreversible one–electron event[56] and thus only peak potentials, E_p, may be obtained, most accurately by DPV.[45] We have determined E_ps for each F_nY as a function of pH. A differential pulse volatmmogram for the Ac–F_nY^-–NH_2Y/Ac–F_nY•–NH_2 couple is shown in Figure 6–4 indicating that fluorination of the phenol ring leads to an increase in E_p. Plots of E_p vs. pH for the Ac–F_nY–NH_2 amino acids are shown in Figure 6–5. At pH values exceeding the pK_a of each Ac–F_nY–NH_2, a pH–independent peak potential is observed, indicative of the Ac–F_nY•–NH_2/Ac–F_nY^-–NH_2 couple, and these values are listed in Table 6–1. As the pH is decreased below the pK_a, the peak potential increases at 59 mV per pH unit corresponding to the Ac–F_nY•–NH_2/Ac–F_nY–NH_2 redox couple in which tyrosine oxidation is accompanied by proton loss. The pH dependence of E_p is in accordance with the Nernst equation (Eq. 6–3),

$$E_p = E_p(\text{Ac–Y•–NH}_2\text{/Ac–Y}^-\text{–NH}_2) + 2.3\ RT/nF \log (1 + 10^{-pH}/10^{-pK_a}) \qquad (6\text{–}3)$$

where E_p(Ac–Y•–NH_2/Ac–Y^-–NH_2) is the peak potential of the deprotonated tyrosinate and the pK_a accounts for the Ac–Y–NH_2 → Ac–Y^-–NH_2 + H^+ reaction. A fit of the E_p vs. pH curves in Figure 6–5 to Eq. 6–3 yields pK_as for Ac–F_nY–NH_2s that are in good agreement with those obtained using the UV titration method already described (see Table 6–1). The pK_a of the oxidized $[F_nY•]^+$ radicals cannot be determined from Eq. 6–3 because the aqueous solution is oxidized at potentials below that needed for the electrochemical generation of $[F_nY•]^+$ at low pHs.

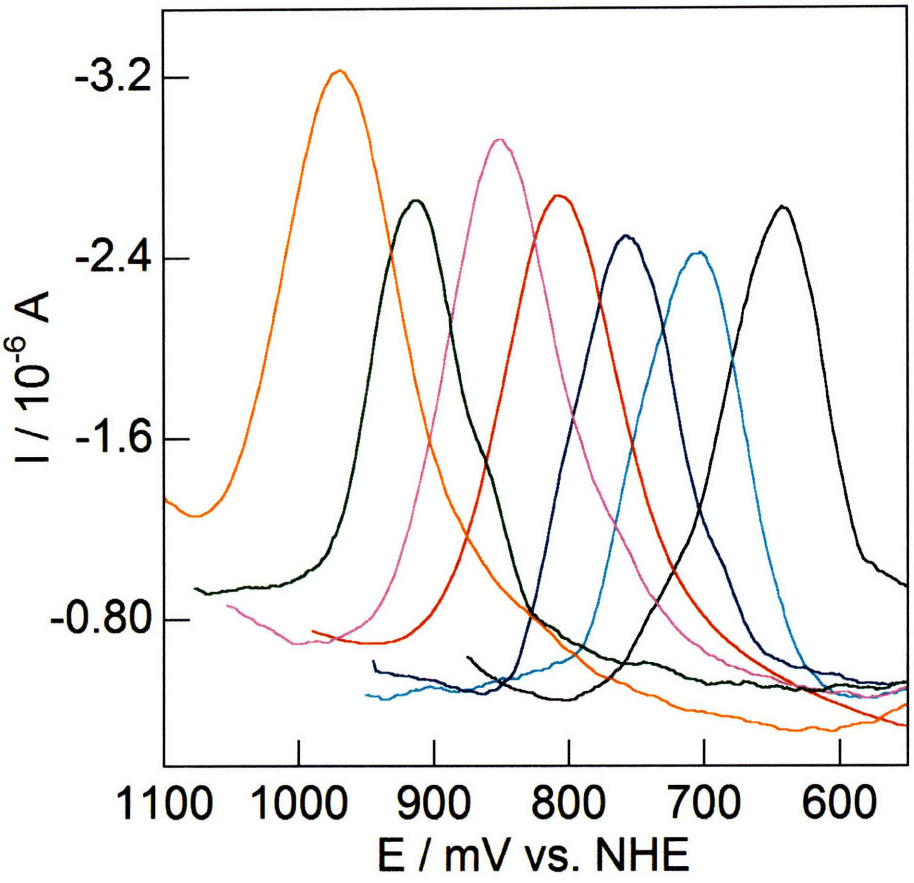

Figure 6–4. Differential pulse voltammogram for Ac–F_nY^-–NH_2/Ac–F_nY•–NH_2s. Traces shown are for: (—) Ac–Y–NH_2, (—) Ac–3–FY–NH_2, (—) Ac–3,5–F_2Y–NH_2, (—) Ac–2,3–F_2Y–NH_2, (—) Ac–2,3,5–F_3Y–NH_2, (—) Ac–2,3,6–F_3Y–NH_2 and (—) Ac–F_4Y–NH_2.

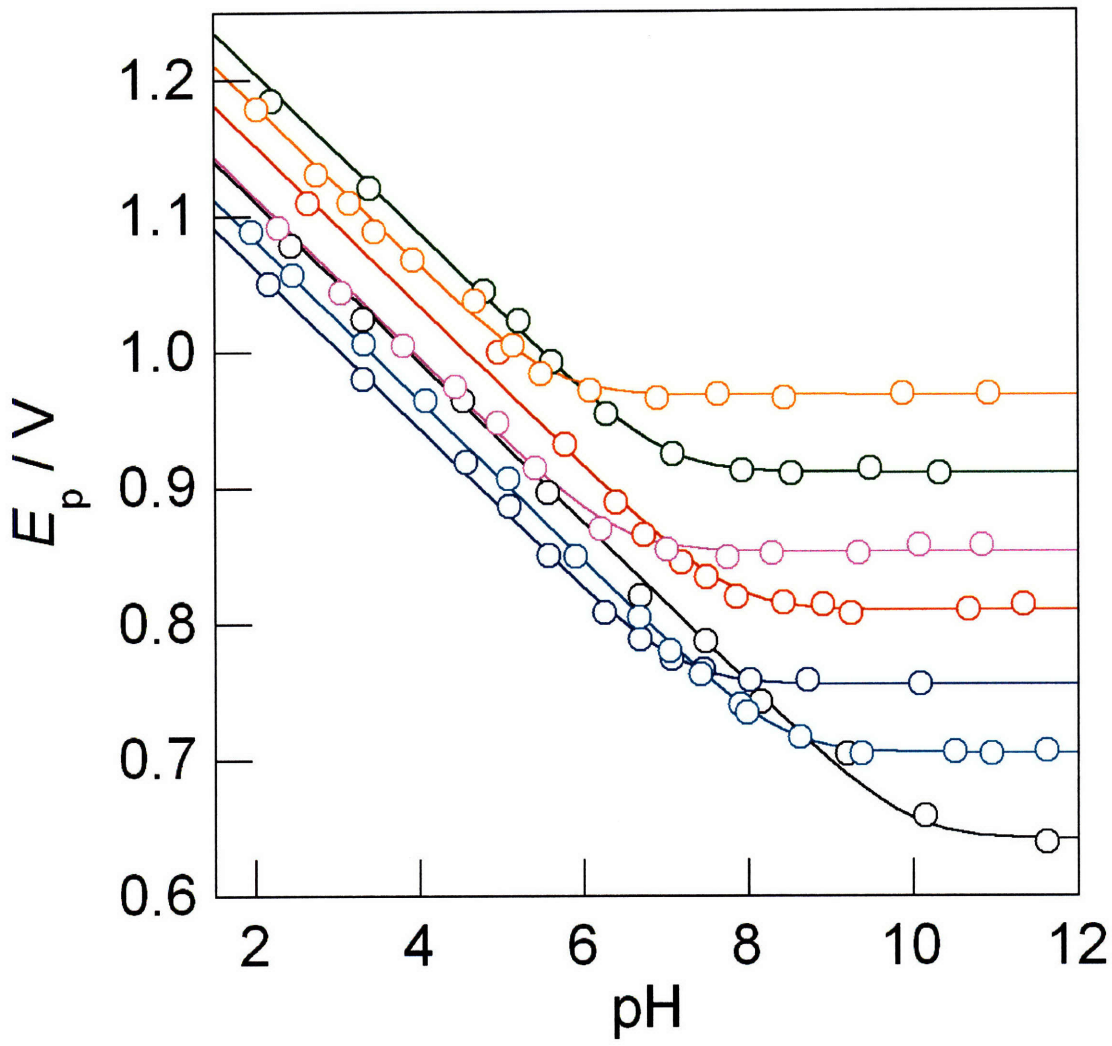

Figure 6–5. Reduction potential vs. NHE as a function of pH for Ac–F_nY–NH_2 derivatives. Data points are for: (○) Ac–Y–NH_2, (○) Ac–3–FY–NH_2, (○) Ac–3,5–F_2Y–NH_2, (○) Ac–2,3–F_2Y–NH_2, (○) Ac–2,3,5–F_3Y–NH_2, (○) Ac–2,3,6–F_3Y–NH_2 and (○) Ac–F_4Y–NH_2. Lines describe fits according to Eq. 6–3. See Table 6–1 for parameters obtained from these fits.

Electronic structure calculations of Ac–F_nY–NH_2s. The Ac–F_nY•–NH_2/Ac–F_nY^-–NH_2 redox couple was found to generally increase with the number of fluorine substituents on the phenol ring. Within the series of di– and trifluorotyrosines, the couples follow a trend: Ac–2,3–F_2Y–NH_2 > Ac–3,5–F_2Y–NH_2 and Ac–2,3,6–F_3Y–NH_2 > Ac–2,3,5–F_3Y–NH_2 that is captured computationally. Geometry optimizations on Ac–F_nY–NH_2, Ac–F_nY•–NH_2, and Ac–F_nY^-–NH_2 were performed while keeping the amino acid backbone in the same conformation. Figure 6–6 (top) compares the difference in total bonding energy between the Ac–F_nY•–NH_2 and Ac–F_nY^-–NH_2 redox states as calculated by DFT to the experimentally determined E_ps (Ac–F_nY•–NH_2/Ac–F_nY^-–NH_2). The linear correlation between observed and calculated results validates the quality of the computation. The electronic structure calculation summarized in Figure 6–7 shows that the observed trend in the reduction potential arises from primarily stabilization of the HOMO and HOMO–1 orbitals of the phenolate with increasing fluorination of the aromatic ring of tyrosine. This stabilization of HOMO and HOMO–1 levels is most pronounced for Ac–F_nY^-–NH_2; these levels exhibit only a modest shift for Ac–F_nY•–NH_2 (and Ac–F_nY–NH_2) (data not shown). The Kohn–Sham representations of the frontier molecular orbitals, shown for tyrosinate in Figure 6–7, reveals that the HOMO orbital carries significant π–electron density at the 3 and 5 positions of the aromatic ring whereas the HOMO–1 has π–electron density localized on the orbital of the oxygen of the phenol, in an in–plane antibonding interaction with the aromatic ring. The interaction of the HOMO and HOMO–1 ring orbitals with the pπ–orbitals of the fluorine atom substituents allows subtle variations in the reduction potential among members of the phenolate series to be understood. For instance, substitution of fluorine at the 2,3 vs 3,5 ring positions results in a 65 mV increase in the reduction potential of the radical. The HOMO, which is presented in the framed box of Figure 6–7, exhibits an antibonding interaction between the π–orbitals of the fluorine atoms and the 3,5–carbon pπ orbitals of the aromatic ring. By moving a fluorine from a 5– to a 2–position, this antibonding interaction is relaxed significantly, resulting in stabilization of the HOMO. A similar effect is observed for 2,3,5– and 2,3,6–trifluorotyrosines.

A parallel calculation was performed to assess the difference between the observed ln(K_a) and the total bonding energy difference of protonated and deprotonated Ac–F_nY–NH_2s. The calculation predicts the general trend that increasing the number of fluorine substituents decreases the pK_a of the phenolic proton (Figure 6–6, bottom), however a poorer correlation is observed as compared to that for the reduction potentials. The anomaly is most obvious for Ac–2,3–F_2Y–NH_2 and Ac–3,5–F_2Y–NH_2, which are calculated to have similar pK_as despite an observed difference of 0.6 pK_a units. We believe that such deviations arise from the deficiency of gas phase DFT calculations in modeling specific hydrogen bonding interactions that are important in determining the overall pK_a of the fluorotyrosines.[57-59]

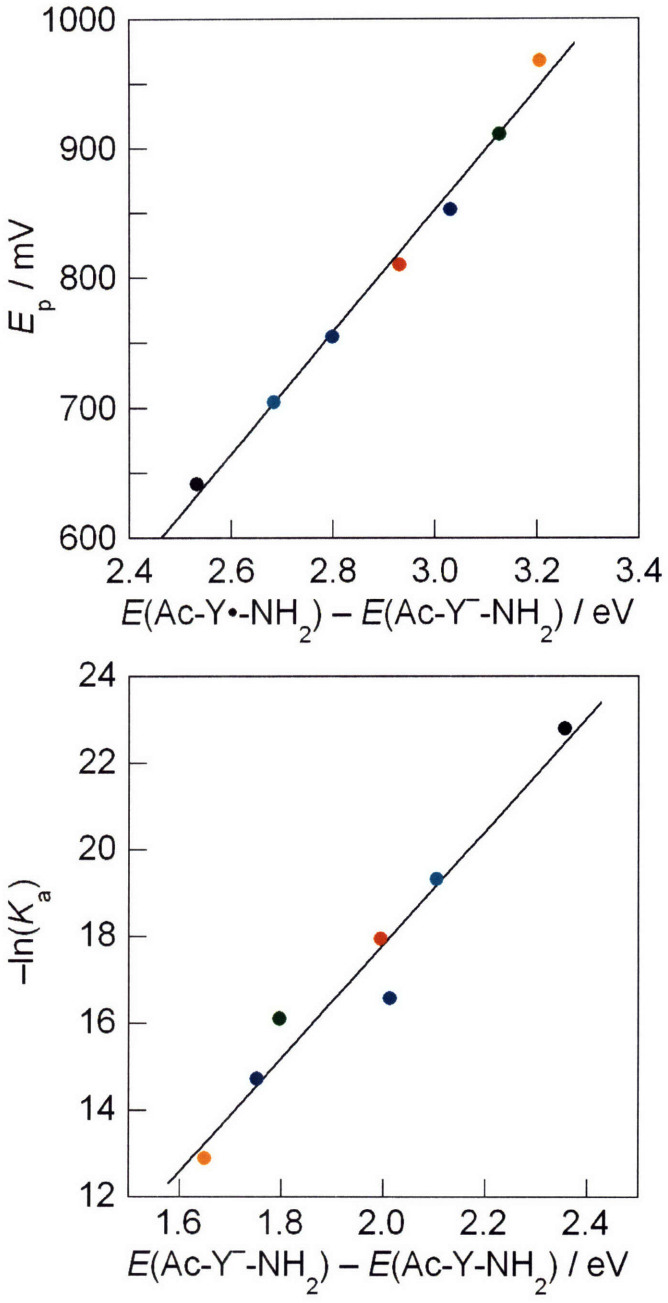

Figure 6–6. DFT calculations for E_ps and pK_as of Ac–F_nY–NH_2Ys. (Top) Plot of E_P(Ac–F_nY•–NH_2/Ac–F_nY$^-$–NH_2) vs. E(Ac–F_nY•–NH_2) – E(Ac–F_nY$^-$–NH_2), the total bonding energy difference between Ac–F_nY•–NH_2 and Ac–F_nY$^-$–NH_2 as calculated by DFT, with linear fit (—). (Bottom) Plot of –ln(K_a) vs. E(Ac–F_nY$^-$–NH_2) – E(Ac–F_nY–NH_2), the total bonding energy difference between Ac–F_nY$^-$–NH_2 and Ac–F_nY–NH_2 as calculated by DFT, with linear fit (—). Color coded points correspond to data for (●) Ac–Y–NH_2, (●) Ac–3–FY–NH_2, (●) Ac–3,5–F_2Y–NH_2, (●) Ac–2,3–F_2Y–NH_2, (●) Ac–2,3,5–F_3Y–NH_2, (●) Ac–2,3,6–F_3Y–NH_2, (●) Ac–F_4Y–NH_2.

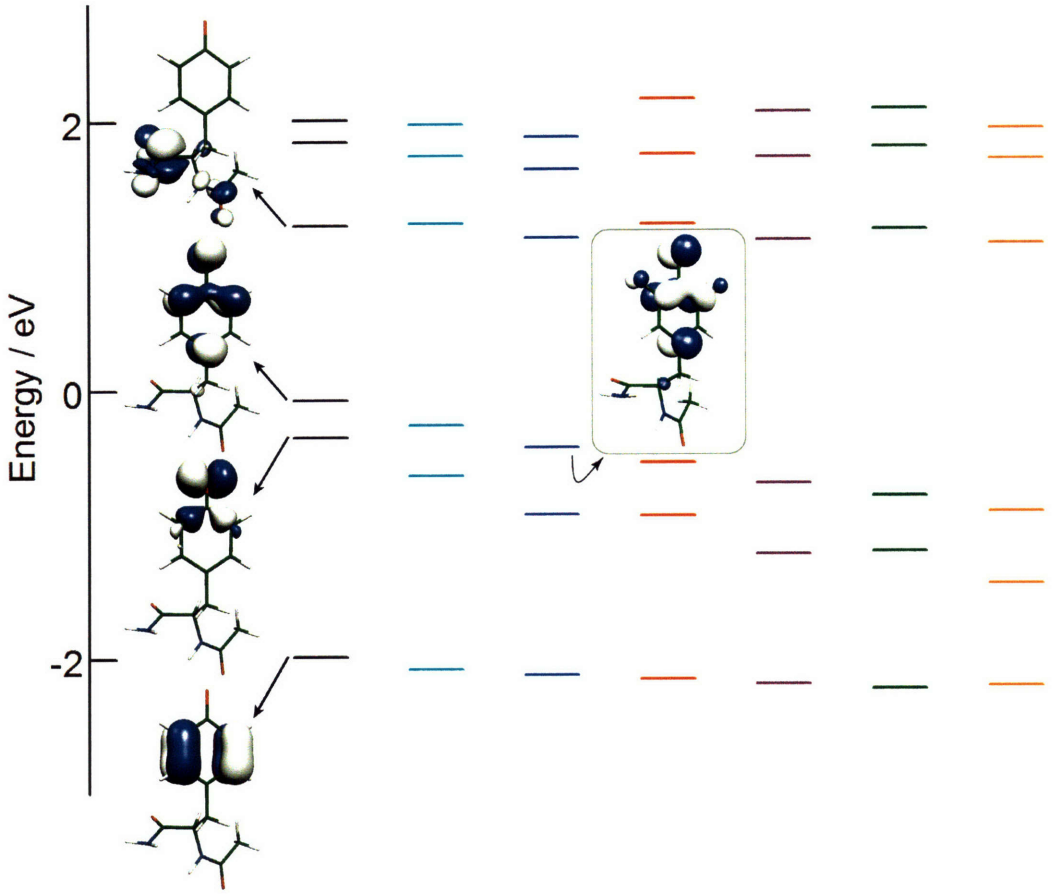

Figure 6–7. Energy level diagram for frontier molecular orbitals of the phenolates of Ac–F_nY–NH_2s. Shown are (—) Ac–Y^-–NH_2, (—) Ac–3–FY^-–NH_2, (—) Ac–3,5–F_2Y^-–NH_2, (—) Ac–2,3–F_2Y^-–NH_2, (—) Ac–2,3,5–F_3Y^-–NH_2, (—) Ac–2,3,6–F_3Y^-–NH_2 and (—) Ac–F_4Y^-–NH_2. Selected Kohn–Sham representations of orbitals for the tyrosine analogue are shown at the 95% probability level. The Kohn–Sham representation of the HOMO orbital for Ac–3,5–F_2Y^-–NH_2 is presented in the frame.

Spectroscopic characterization of F_nY•s. Having determined the pK_a and E_p for each Ac–F_nY–NH_2, we next assessed the EPR and UV–vis properties of their oxidized forms. For EPR studies, the oxidized species were generated by the method of Hulsebosch et al.[60] using UV photolysis at 77 K. The spectra obtained are shown in Figure 6–8; the signal was stable for at least 1 month at 77 K. All F_nY•s display broader signals than Y•; lower modulation amplitudes and larger sweep widths did not uncover any additional hyperfine interactions. Qualitatively, the

spectra of 2,3,5–F_3Y•, 2,3,6–F_3Y• and 2,3,5,6–F_4Y• are similar, whereas those of 3–FY•, 2,3–F_2Y• and 3,5–F_2Y• are distinctly different.

Attempts to simulate the EPR spectra displayed in Figure 6–8 by several methods were unsuccessful. Both standard programs as well as DFT–based simulations were unsatisfactory, as has been previously observed with 3–FY• (David Britt, personal communication). These results suggest that frozen glasses of F_nY• contain a wide distribution of dihedral angles of the β–methylene hydrogen atoms. In Y•, one of these hydrogen atoms is responsible for the strongest hyperfine coupling to the unpaired electron.[60] Since the strength of this interaction varies as $\cos^2\theta$, where θ is the dihedral angle between the plane of the aromatic ring and the β–methylene hydrogen, a distribution over these angles can broaden the spectra. Nevertheless, these spectra show that F_nY•s have distinct EPR properties useful for the study of proteins with multiple Y•s. Further, incorporation of these analogues into enzymes will fix the θ dihedral angle for the C_β–protons and reveal more resolved spectra.

The absorption spectra of the F_nY• were obtained using the flash photolysis technique with benzophenone as the photo–oxidant of Y. The triplet excited state of benzophenone has been shown to be a competent, bimolecular oxidant of tyrosine with an excited state reduction potential of 1.69 V vs. NHE and bimolecular rate constant for reaction with Y of $2.6 \pm 0.2 \times 10^9$ $M^{-1}s^{-1}$. [61] Moreover, the absorption spectrum of the benzophenone ketyl radical, produced upon Y photo–oxidation, does not significantly overlap with that of the F_nY•.

The photosensitized oxidation of tyrosine by benzophenone was accomplished by designing a unimolecular ET within the dipeptide pair formed from the catenation of the unnatural amino acid, 4–benzoyl–L–phenylalanine, BPA, to the F_nY–OMe amino acids. Excitation of a solution of BPA–Y–OMe dipeptide at pH 4.0 with a 300 nm nanosecond laser pulse produces a species with the transient absorption spectrum shown in Figure 6–9 at 100 ns. The strong, sharp peak with λ_{max} = 334 nm and broad peak at λ_{max} = 547 nm with a shoulder to the blue are the spectral signatures of the reduced benzophenone ketyl radical[62] ($\varepsilon_{550\ nm}$(BPK•) = 3300 ± 700 $M^{-1}cm^{-1}$ in cyclohexane),[63] whereas the absorption bands at λ_{max} = 390 and 407 nm

are characteristic of Y• (ε_{410}(Y•) = 2750 ± 200).[64] The Y• peaks are slightly blue–shifted from that of free Y• owing to their overlap with the tailing absorption of the 334 nm band of the ketyl radical of BPA (BPA•). The subsequent gray traces recorded at 400 ns and 1 μs show that the overall profile shape does not change with time. The transient signals decayed concomitantly with a rate constant of 5.6×10^6 s^{-1}; single λ kinetics data recorded at 547 nm is shown in the inset of Figure 6–9. This unimolecular decay is consistent with charge recombination between BPA• and Y•. The kinetics were unaffected by the presence or absence of oxygen in solution. A minor residual absorbance (<10%), which persists for tens of microseconds, is likely due to a small fraction of ET product formed in the bimolecular reaction between ^{3}BPA–Y–OMe and ground state BPA–Y–OMe. This reaction is favored at the high concentrations of dipeptide required for the TA experiment.

Figure 6–10 shows the TA spectra obtained 100 ns after 300 nm excitation of each of the BPA–F_nY–OMe dipeptides. The amount of BPA•–F_nY•–OMe produced in each experiment varies due to changes in pump–probe beam overlap and sample concentration. Therefore, to allow for comparison of the fluorotyrosyl radical absorption maxima between experiments, the spectra in Figure 6–10 are normalized to the 547 nm peak of the BPA•. The absorbance maximum of the BPA• species is invariant for each of the dipeptides whereas the absorption band of the F_nY• species varies in its maximum between 395 and 415 nm. The values of λ_{max} for each of the F_nY•s are listed in Table 6–1. An interesting comparison can be made between the F_nY•s and Y• absorbance features. The 2,3–F_2Y•, 2,3,6–F_3Y• and F_4Y• all have the familiar double hump absorbance feature of Y•, though they are slightly broader and red–shifted. The spectrum of 3–FY• also contains the double hump feature, though its λ_{max} is now blue–shifted by 7 nm. Of particular note are the single peaks at 395 and 400 nm for 3,5–F_2Y• and 2,3,5–F_3Y•, respectively, which are significantly blue–shifted from the larger 407 nm absorbance peak of Y•.

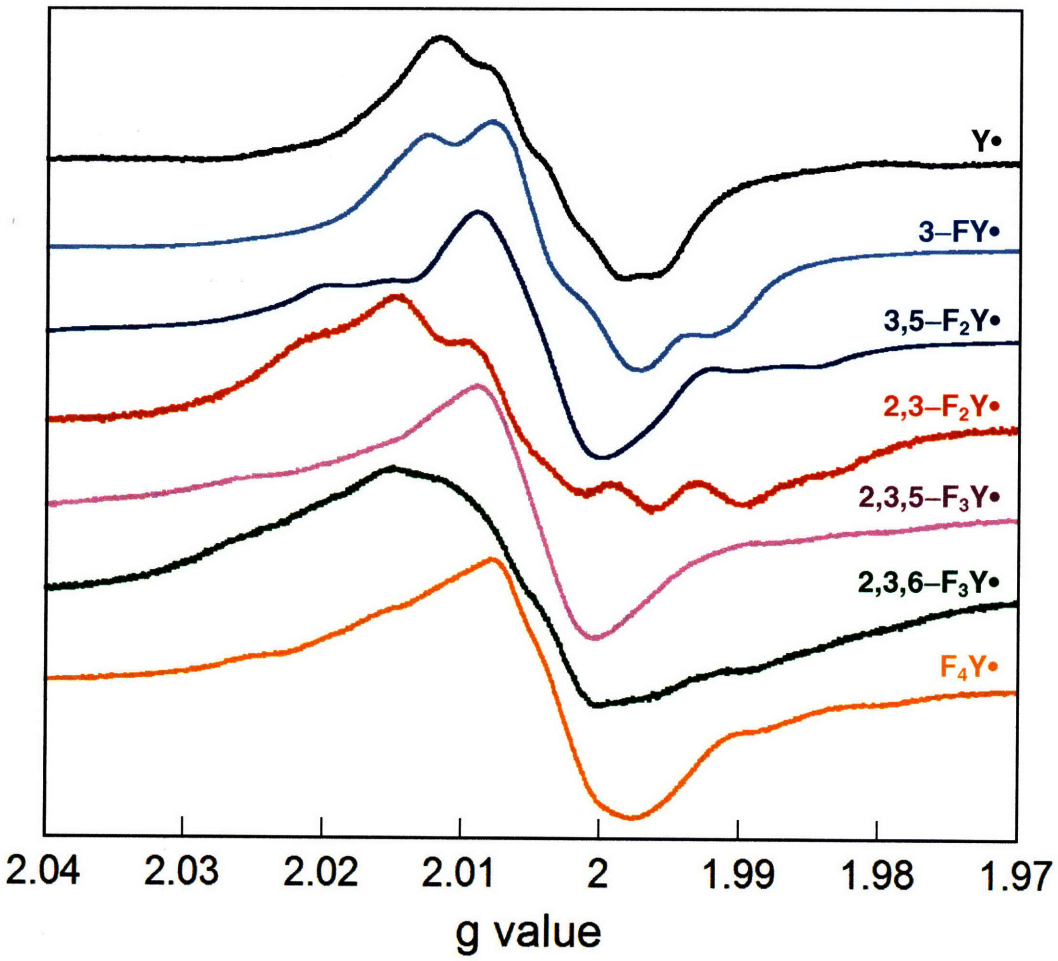

Figure 6–8. Normalized EPR spectra of F_nY•s. The oxidized product was formed by UV photolysis of a pH 11 solution of each F_nY at 77 K (see Methods).

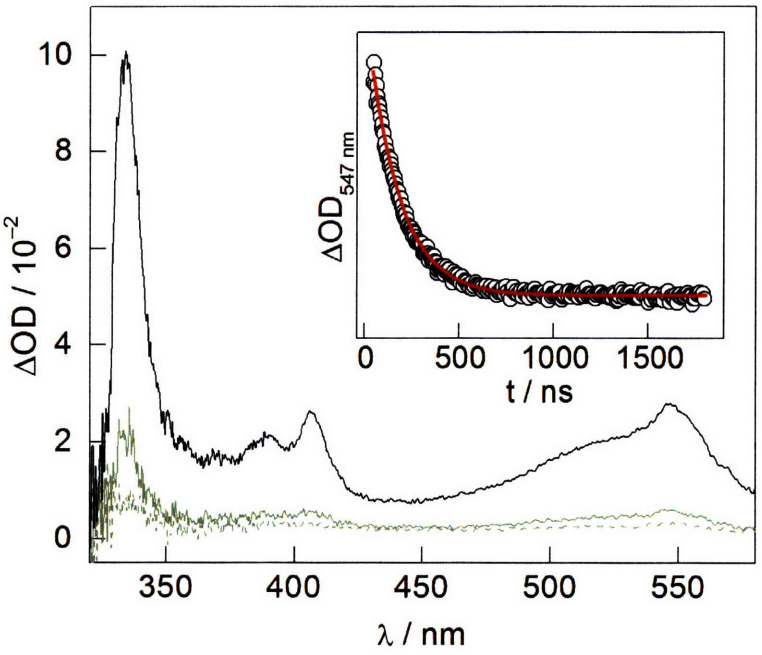

Figure 6–9. TA spectroscopy with BPA–Y–OMe. Spectra shown were recorded at (—) 100 ns, (—) 400 ns, and (—) 1 μs following a 300 nm, 5 ns excitation of a 500 μM solution of BPA–Y–OMe buffered to pH 4.0 with 20 mM succinic acid. Inset: Single l kinetics of the 547 nm absorption (○) and a mono–exponential decay fit (—) to the data.

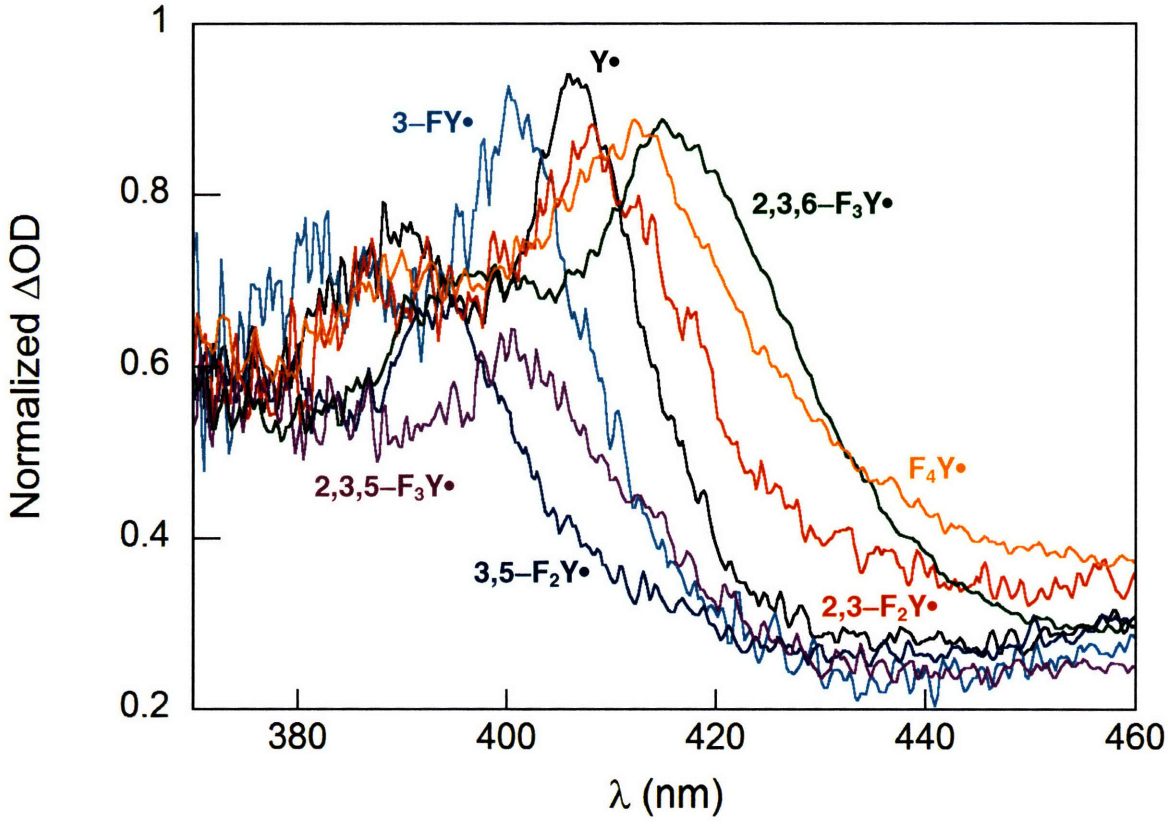

Figure 6–10. UV–vis spectra of BPA–F_nY•–OMe derivatives. Spectra have been normalized to the 547 nm peak of BPA• 100 ns after excitation of each BPA–F_nY–OMe.

Incorporation of 3–FY into β2. To demonstrate the ability of F_nYs as spectroscopic probes of Y sites in biological systems, we replaced all Ys in β2 with 3–FY using global incorporation methods. The successful procedure required growth of the bacteria in minimal media from which L–tyrosine was omitted and replaced by 3–FY. Under these conditions the doubling time of the bacteria was 40 min. SDS–PAGE analysis of whole cells subsequent to induction with IPTG suggests that expression level of the 3–FY–β2 is quite similar to that observed for wt β2, which has a monomeric MW of ~ 43 kDa (Figure 6–11, lane 1). 3–FY–β2 was isolated using the standard isolation procedure for wt β2. Visual inspection of the gel of purified 3–FY–β2 (Figure 6–11, lane 4) shows that the isolated protein is ~95 % homogeneous and amino acid analysis of purified 3–FY–β2 indicates ~90 % incorporation of 3–FY. The excellent yield of labeled protein and the similarities in its purification relative to wt β2, suggest that the 3–FY–β2 is folded. The amount of radical per 3–FY–β2 was established by EPR integration using wt *E. coli* β2 as a standard.[65] The 3–FY–β2 was determined to contain 0.6 – 0.8 Y_{122}•s/dimer as isolated. The absorption spectrum of the 3–FY_{122}• (data not shown) shows that λ_{max} blue–shifts to 402 nm (wt Y_{122}• has a λ_{max} of 411 nm), consistent with the results from the TA experiments described above.

The EPR spectrum of wt β2 from *E. coli* has previously been characterized at 9, 35, 140, 195, 245, 280 GHz and has anisotropic g values of g_x = 2.00912 – 2.00868, g_y = 2.00457 – 2.0043 and g_z = 2.00225 – 2.00208.[28] The X–band EPR spectrum of wt β2 is dominated by the well–resolved, nearly isotropic, coupling to one of its β–Hs (A_x = 61.2, $A_y = A_z$ = 53.7 MHz).[66] The second β–H coupling is much smaller and is usually lost in the EPR linewidth. This study presents the first observation of the magnetic properties of a 3–FY• in a protein. The X–band EPR spectrum of this radical, along with the simulation, is shown in Figure 6–12. Table 6–2 presents the A–tensors of the nuclei with significant hyperfine couplings to the unpaired electron. The splitting due to coupling to the β–H is similar to that observed for the Y_{122}• in wt β2. However, a strongly split doublet of doublets, demarcated by brackets in Figure 6–12, is apparent at the extremes of the spectrum due to coupling to the fluorine nucleus. Together the results

above show that 3–FY can be incorporated at high efficiency into β2, yielding 3–FY–β2 with high radical content and activity. Further, the EPR spectrum shows that the 3–FY_{122}• has well–resolved hyperfine interactions that can be simulated, supporting our contention that the F_nY• EPR spectra of Figure 6–8 are broad due to a distribution in the dihedral angles of β–methylene hydrogens.

RNR activity is preserved with global substitution of the 14 Y residues of β2. The activity of the 3–FY–β2/α2 complex was measured by a coupled spectrophotometric assay using TR/TRR/NADPH as the reductant.[65] The specific activity obtained was ~65 % that of wt β2, suggesting that substitution of the 14 Y residues in β2 with 3–FY minimally perturbs the tertiary structure of 3–FY–β2.

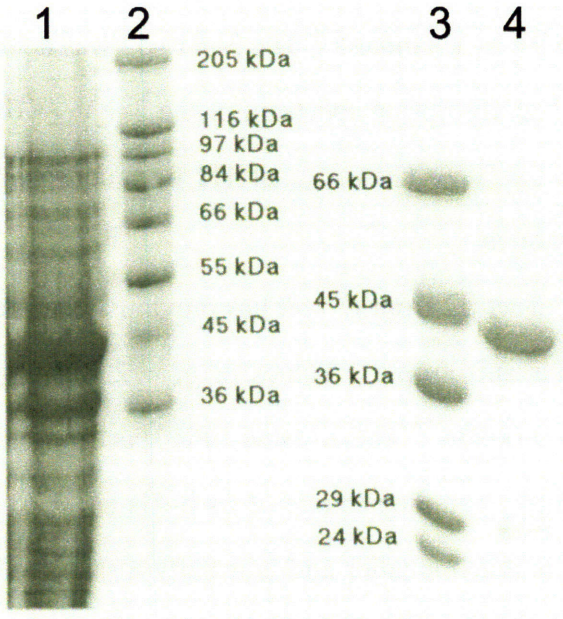

Figure 6–11. SDS PAGE analysis of 3–FY–β2. (1) overexpression of 3–FY–β2, (2) high range molecular weight marker, (3) low range molecular weight marker, (4) purified 3–FY–β2.

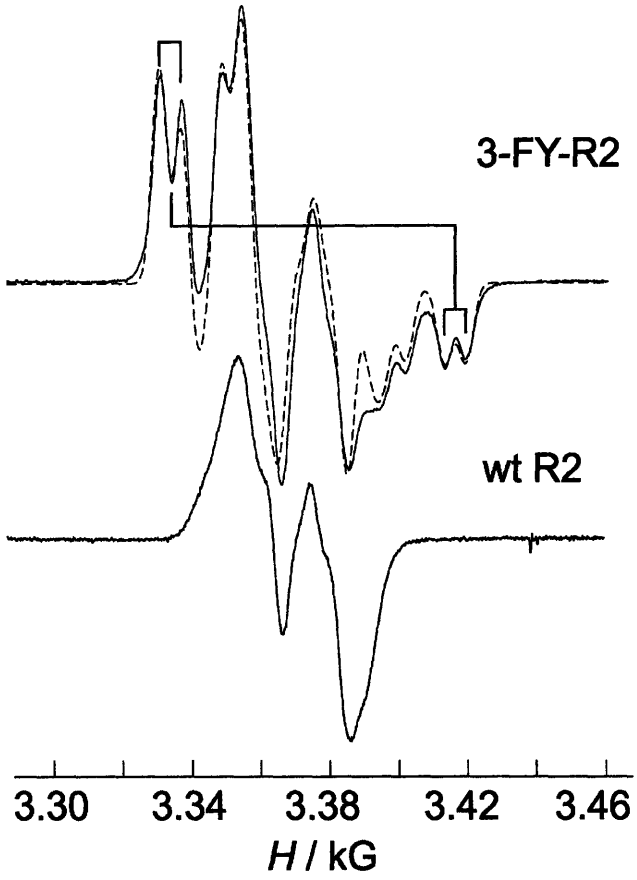

Figure 6–12. EPR spectrum and simulation of 3–FY_{122}•–β2. (Top) EPR spectrum (solid line) and simulation (dotted line) of 3–FY_{122}•–β2 at 25 K. The values used for the simulation are listed in Table 6–2. (Bottom) EPR spectrum of wt–β2 under the same conditions.

Table 6–2. A–tensors of nuclei with significant hyperfine interaction in 3–FY_{122}•–β2.

Nucleus	A_x (MHz)	A_y (MHz)	A_z (MHz)	ϕ^a
3–F	–15 (6)	–3 (4)	180 (2)	0
β–H_1	48 (6)	54 (4)	50 (2)	0
5–H	–25 (1)	–8 (1)	–17 (1)	25
2,6–H	3	9	6	65

[a] φ angles describe rotation about the axis normal to the plane of the phenol ring between the *g* tensor and hyperfine tensors.

CONCLUSIONS

The mechanistic complexity arising from the coupling of electron and proton transfers in charge transport processes involving amino acid radicals requires the development of new tools and methods for their study. We show here that F_nYs will be useful in the study of biological charge transport mechanisms involving tyrosine for the following reasons. (1) They provide a range of pK_a for the phenolic proton and E_p for the Y•/Y couple, which allows for tuning of the $\Delta G°_{PT}$ and $\Delta G°_{ET}$ for the PCET reaction. UV–Vis and ^{19}F NMR spectroscopic studies in conjunction with DPV illustrate that the Ac–F_nY–NH_2s offer a range of almost 5 units in pK_a and 320 mV in redox potential within the pH range of 6–9 where proteins are usually stable. (2) The oxidized forms of F_nY•s possess unique spectral signals allowing a distinction between Y• and F_nY• in the same system. The EPR spectra of F_nY•s and time–resolved UV–vis spectra of BPA–F_nY–OMe dipeptides show that the EPR properties are altered and the λ_{max} for F_nY• absorption can be shifted by ~10 nm relative to Y•. (3) In addition to glutathione transferase[67,68] and other proteins,[69-74] 3–FY can be incorporated into RNR with relatively minimal structural perturbation, as demonstrated by the preserved activity of the β2 subunit of class I *E. coli* RNR in which 14 Y residues were globally replaced by 3–FY.

The F_nYs will be useful for a variety of mechanistic studies in biology, in which tyrosine is integral to radical initiation and transport. We demonstrate one example of this utility in the next Chapter in which Y_{356} of β2 is site–specifically replaced with the F_nYs presented in this study. A study of the pH dependent activity of each of these new semi–synthetic enzymes cast with the backdrop of the Ac–F_nY–NH_2s pK_a and Ac–F_nY•–NH_2s reduction potential data reported herein, allow for mechanistic details of the PCET reactivity at this site to be unveiled.

REFERENCES

(1) *Electron Transfer in Chemistry*; Balzani, V. Ed.; Wiley-VCH: Weinheim, Germany, 2001; Vol. 3, Part 1.

(2) Gray, H. B.; Winkler, J. R. *Annu. Rev. Biochem.* **1996**, *65*, 537.

(3) Gunner, M. R.; Robertson, D. E.; Dutton, P. L. *J. Phys. Chem.* **1986**, *90*, 3783.

(4) Farver, O.; Pecht, I. *Biophys. Chem.* **1994**, *50*, 203.

(5) Namslauer, A.; Braenden, M.; Brzezinski, P. *Biochemistry* **2002**, *41*, 10369.

(6) Tollin, G. In *Electron Transfer in Chemistry*; Balzani, V. Ed.; Wiley-VCH: Weinheim, Germany, 2001; Vol. 4, Part 1, p 202.

(7) Davidson, V. L. *Acc. Chem. Res.* **2000**, *33*, 87.

(8) McLendon, G.; Hake, R. *Chem. Rev.* **1992**, *92*, 481.

(9) Millett, F.; Durham, B. *Biochemistry*, **2002**, *41*, 11315.

(10) Nocek, J. M.; Zhou, J. S.; Forest, S. D.; Priyadarshy, S.; Beratan, D. N.; Onuchic, J. N.; Hoffman, B. M. *Chem. Rev.* **1996**, *96*, 2459.

(11) Lewis, F. D. Electron Transfer and Charge Transport in DNA. In *Electron Transfer in Chemistry*; Balzani, V. Ed.; Wiley-VCH: Weinheim, Germany, 2001; Vol. 3, Part 5, p 105.

(12) Boon, E. M.; Barton, J. K. *Curr. Opin. Struct. Biol.* **2002**, *12*, 320.

(13) Giese, Bernd. *Curr. Opin.Chem. Biol.* **2002**, *6*, 612.

(14) Jortner, J.; Bixon, M.; Langenbacher, T.; Michel-Beyerle, M. E. *Proc. Natl. Acad. Sci. U.S.A.* **1998**, *95*, 12759.

(15) Marcus, R. A.; Sutin, N. *Biochim. Biophys. Acta* **1985**, *811*, 265.

(16) Hopfield, J. J. *Proc. Natl. Acad. Sci. U.S.A.* **1974**, *71*, 3640.

(17) Levich, V. G. *Adv. Electrochem. Electrochem. Eng.* **1966**, *4*, 249.

(18) Stubbe, J.; Nocera, D. G.; Yee, C. S.; Chang, M. C. Y. *Chem. Rev.* **2003**, *103*, 2167.

(19) Chang, C. J.; Chang, M. C. Y.; Damrauer, N. H.; Nocera, D. G. *Biophys. Biochim. Acta* **2004**, *1655*, 13.

(20) Stubbe, J.; van der Donk, W. A. *Chem. Rev.* **1998**, *98*, 705.

(21) Stubbe, J. *Chem. Comm.* **2003**, *20*, 2511.

(22) Cukier, R. I.; Nocera, D. G. *Annu. Rev. Phys. Chem.* **1998**, *49*, 337.

(23) Hammes-Schiffer, S. *Acc. Chem. Res.* **2001**, *34*, 273.

(24) Cukier, R. I. *J. Phys. Chem.* **1995**, *99*, 16101.

(25) Cukier, R. I. *J. Phys. Chem. A* **1999**, *103*, 5989.

(26) Soudackov, A. V.; Hammes-Schiffer, S. *J. Chem. Phys.* **1999**, *111*, 4672.

(27) Soudackov, A.; Hammes-Schiffer, S. *J. Chem. Phys.* **2000**, *113*, 2385.

(28) Pesavento, R. P.; van der Donk, W. A. *Adv. Protein Chem.* **2001**, *58*, 317.

(29) Jordan, A.; Reichard, P. *Annu. Rev. Biochem.* **1998**, *67*, 71.

(30) Tommos, C.; Babcock, G. T. *Biochim. Biophys. Acta* **2000**, *1458*, 199.

(31) Karthein, R.; Nastainczyk, W.; Ruf, H. H. *Eur. J. Biochem.* **1987**, *166*, 173.

(32) Chouchane, S.; Girotto, S.; Yu, S.; Magliozzo, R. S. *J. Biol. Chem.* **2002**, *277*, 42633.

(33) Su, C.; Sahlin, M.; Oliw, E. H. *J. Biol. Chem.* **1998**, *273*, 20744.

(34) Ivancich, A.; Dorlet, P.; Goodin, D. B.; Un, S. *J. Am. Chem. Soc.* **2001**, *123*, 5050.

(35) Aubert, C.; Mathis, P.; Eker, A. P. M.; Brettel, K. *Proc. Natl. Acad. Sci. U.S.A.* **1999**, *96*, 5423.

(36) Sjödin, M.; Styring, S.; Wolpher, H.; Xu, Y.; Sun, L.; Hammarström, L. *J. Am. Chem. Soc.* **2005**, *127*, 3855.

(37) Stubbe, J.; Riggs-Gelasco, P. *Trends Biochem. Sci.* **1998**, *23*, 438.

(38) Bollinger, Jr., J. M.; Edmonson, D. E.; Huynh, B. H.; Filley, J.; Norton, J. R.; Stubbe, J. *Science* **1991**, *253*, 292.

(39) Bollinger, Jr., J. M.; Tong, W. H.; Ravi, N.; Huynh, B. H.; Edmonson, D. E.; Stubbe, J. *J. Am. Chem. Soc.* **1994**, *116*, 8015.

(40) Bollinger, Jr. J. M.; Tong, W. H.; Ravi, N.; Huynh, B. H.; Edmondson, D. E.; Stubbe, J. *J. Am. Chem. Soc.* **1994** *116*, 8024.

(41) Baldwin, J.; Krebs, C.; Ley, B. A.; Edmondson, D. E.; Huynh, B. H.; Bollinger, Jr., J. M. *J. Am. Chem. Soc.* **2000** *122*, 12195.

(42) Krebs, C.; Chen, S.; Baldwin, J.; Ley, B.A.; Patel, U.; Edmondson, D. E.; Huynh, B. H.; Bollinger, Jr., J. M. *J. Am Chem. Soc.* **2000** *122*, 12207.

(43) Kim, K.; Cole, P. A. *J. Am. Chem. Soc.* **1998**, *120*, 6851.

(44) Chen, H.; Gollnick, P.; Phillips, R. S. *Eur. J. Biochem.* **1995**, *229*, 540.

(45) Tommos, C.; Skalicky, J. J.; Pilloud, D. L.; Wand, A. J.; Dutton, P. L. *Biochemistry* **1999**, *38*, 9495.

(46) Loh, Z.-H.; Miller, S. E.; Chang, C. J.; Carpenter, S. D.; Nocera, D. G. *J. Phys. Chem. A* **2002**, *106*, 11700.

(47) Reece, S. Y.; Stubbe J.; Nocera, D. G. *Biophys. Biochim. Acta* **2005**, *1706*, 232.

(48) te Velde, G.; Bickelhaupt, F. M.; van Gisbergen, S. J. A.; Fonseca Guerra, C.; Baerends, E. J.; Snijders, J. G.; Ziegler, T. *J. Comput. Chem.* **2001**, *22*, 931.

(49) Fonseca Guerra, C.; Snijders, J. G.; te Velde, G.; Baerends, E. J. *Theor. Chem. Acc.* **1998**, *99*, 391.

(50) Becke, A. D. *Phys. Rev. A* **1988**, *38*, 3098.

(51) Perdew, J. P.; Chevary, J. A.; Vosko, S. H.; Jackson, K. A.; Pederson, M. R.; Singh, D. J.; Fiolhais, C. *Phys. Rev. B* **1992**, *46*, 6671.

(52) Seyedsayamdost, M. R.; Reece, S. Y.; Nocera, D. G.; Stubbe, J. *J. Am. Chem. Soc.* **2006**, *128*, 1569.

(53) Ge, J.; Yu, G.; Ator, M. A.; Stubbe, J. *Biochemistry* **2003**, *42*, 10071.

(54) Phillips, R. S.; Ravichandran, K.; Von Tersch, R. L. *Enzyme and Microbial Technology* **1989**, *11*, 80.

(55) Bonaccio, M.; Ghaderi, N.; Borchardt, D.; Dunn, M. F. *Biochemistry*, **2005**, *44*, 7656.

(56) Harriman, A. *J. Phys. Chem.* **1987**, *91*, 6102.

(57) Baker, A.W.; Kaeding, W.W. *J. Am. Chem. Soc.* **1959**, *81*, 5904.

(58) West, R.; Powell, D. L.; Whatley, L. S.; Lee, M. K. T.; Schleyer, P. von R. *J. Am. Chem. Soc.* **1962**, *84*, 3221.

(59) Carosati, E.; Sciabola, S.; Cruciani, G. *J. Med. Chem.* **2004**, *47*, 5114.

(60) Hulsebosch, R. J.; van den Brink, J. S.; Nieuwenhuis, S. A. M.; Gast, P.; Raap, J.; Lugtenburg, J.; Hoff, A. J. *J. Am. Chem. Soc.* **1997**, *119*, 8685.

(61) Canonica, S. H., B.; Wirz, J. *J. Phys. Chem. A.* **2000**, *104*, 1226.

(62) Kajii, Y. I., H.; Shibuya, K.; Obi, K. *J. Phys. Chem.* **1992**, *96*, 7244.

(63) Johnston, J. L.; Lougnot, D. J.; Wintgens, V.; Scaiano, J. C. *J. Am. Chem. Soc.* **1988**, *110*, 518.

(64) Feitelson, J.; Hayon, E. *J. Phys. Chem.* **1973**, *77*, 10.

(65) Ge, J.; Perlstein, D. L.; Nguyen, H.-H.; Bar, G.; Griffin, R. G.; Stubbe, J. *Proc. Nat. Acad. U.S.A.* **2001**, *98*, 10067.

(66) Bender, C. J.; Sahlin, M.; Babcock, G. T.; Barry, B. A.; Chandrashekar, T. K.; Salowe, S. P.; Stubbe, J.; Lindström, B.; Petersson, L.; Ehrenberg, A.; Sjöberg, B.-M. *J. Am. Chem. Soc.* **1989**, *111*, 8076.

(67) Parsons, J. F.; Armstrong, R. N. *J. Am. Chem. Soc.* **1996**, *118*, 2295.

(68) Xiao, G.; Parsons, J. F.; Armstrong, R. N.; Gilliland, G. L. *J. Am. Chem. Soc.* **1997**, *119*, 9325.

(69) Hull, W. E.; Sykes, B. D. *Biochemistry* **1976**, *15*, 1535.

(70) Kimber, B. J.; Griffths, D. V.; Birdsall, B.; King, R. W.; Scudder, P.; Freeney, J.; Roberts, G. C. K.; Burgen, A. S. V. *Biochemistry* **1977**, *16*, 3492.

(71) Sixl, F.; King, R. W.; Bracken, M.; Feeney, J. *Biochem. J.* **1990**, *266*, 545.

(72) Eccleston, J. F.; Molloy, D. P.; Hinds, M. G.; King, R. W.; Feeney, J. *Eur. J. Biochem.* **1993**, *278*, 1041.

(73) Lui, S. M.; Cowan, J. A. *J. Am. Chem. Soc.* **1994**, *116*, 4483.

(74) Pal, P. P.; Bae, J. H.; Azim, M. K.; Hess, P.; Friedrich, R.; Huber, R.; Moroder, L.; Budisa, N. *Biochemistry* **2005**, *44*, 3663.

CHAPTER 7:

pH Rate Profiles of F_nY_{356}–β2s (n = 2, 3, 4) in *E. coli* Ribonucleotide Reductase: Further Evidence that Y_{356} is a Redox–Active Amino Acid Along the Radical Propatation Pathway and Elucidation of its Mechanism of Oxidation

Adapted from: Seyedsayamdost, M. R.; Yee, C. S.; Reece, S. Y.; Nocera, D. G.; Stubbe, J. *J. Am. Chem. Soc*, **2006**, 128, 1562.

INTRODUCTION

Class I *E. coli* ribonucleotide reductase (RNR) plays a crucial role in DNA replication and repair by catalyzing the reduction of nucleoside diphosphates (NDPs) to deoxynucleoside diphosphates (dNDPs).[1,2] It is composed of two homodimeric subunits designated α2 and β2. A complex between α2 and β2 is required for activity.[3] α2 houses the NDP binding sites and the binding sites for the effectors that control the specificity and rate of nucleotide reduction.[3-5] β2 harbors the diferric tyrosyl radical (Y_{122}•) cofactor proposed to initiate nucleotide reduction by generating a transient thiyl radical (C_{439}•) in the active site of α2.[6] The crystal structures of both α2 and β2 have been solved independently.[7-9] A docking model of the two proteins has been generated using these structures based on their shape complementarity and on knowledge of conserved residues. This model, a 1:1 complex of the α2 and β2 homodimers, places the Y• on β2 at a distance >35 Å away from the terminal site of oxidation on α2, the C_{439} residue. Electron tunneling between these residues based on Marcus theory ($k_{ET} = 10^{-6}$ s^{-1} for $\beta = 1.2$ Å^{-1} under activationless conditions) is too slow to account for a k_{cat} of ~2–10 s^{-1}.[10] Thus, the radical generation process has been proposed to occur via a hopping mechanism involving aromatic amino acid radical intermediates as shown in Figure 7–1.[7,11] As we showed in Chapters 2 & 3, mounting evidence is calling into question the symmetry of the docking model.[12,13] However, a strong case can be made for involvement of the residues on this pathway, specifically Y_{356} on β2 and Y_{731} and Y_{730} on α2. They are the only absolutely conserved residues that are not involved in assembly of the di–iron cofactor or in the nucleotide reduction process.[13,14]

Efforts to examine this pathway model experimentally and identify the mechanism(s) for radical propagation have heretofore relied on site–directed mutagenesis of each amino acid within the pathway on both the *E. coli* and mouse RNRs.[15-18] More recently, *in vivo* complementation studies in *E. coli* using pathway mutants to investigate radical migration have been reported.[19] These studies demonstrate the requirement for these residues (Figure 7–1) in

nucleotide reduction. However, they are not amenable to addressing the mechanism of the radical propagation process or the intermediacy of amino acid radicals as the proteins are "inactive". Investigation of the radical propagation process is further complicated by results from steady–state and pre–steady state kinetic analyses of *E. coli* RNR that suggest that radical propagation and nucleotide reduction are preceded by a slow physical step and that binding of substrate and effector trigger this physical step.[13] This conformational gating makes the electron transfer (ET) step kinetically invisible and thus impossible to study. One way to gain insight into the propagation reaction therefore is to change the rate–limiting step from this physical step to ET by altering the reduction potential of a residue within the pathway.

The limited repertoire of natural amino acids does not allow an informative perturbation to be made and thus we have recently turned to site–specific insertions of unnatural amino acids into β2 at Y_{356} using protein ligation methods.[20] A 3–NO_2Y_{356}–β2 construct has allowed us to measure the pK_a of a single amino acid residue in a putative 260 kDa α2/β2 complex.[21] A 2,3–F_2Y_{356}–β2 provided the first clues that the phenolic proton at 356 in β2 is not required for conformational gating of turnover.[22] Results from studying the aniline amino acid, $Y_{356}PheNH_2$–β2 construct,[23] suggested that the rate of radical transfer through position 356 is affected mainly by the reduction potential of the residue at that position and not controlled by hydrogen–bonding or proton transfer. In addition, studies with DOPA–β2 and NH_2Y–α2s in Chapters 2–5 have provided compelling evidence for a redox–active role of these residues in radical propagation and have suggested a hydrogen atom transfer mechanism between Y_{730} and C_{439}.

To assess the interplay between the electron and proton transfer events requires the systematic variation of the radical reduction potential and phenolic pK_a at Y_{356}, the proposed gate keeper for radical transport between the α2 and β2 subunits. In Chapter 6,[24] we reported the synthesis and characterization of a number of unnatural, N–acetyl and C–amide protected fluorotyrosine analogues, Ac–F_nY–NH_2 (Table 7–1). These derivatives have radical peak reduction potentials that vary from –50 to +270 mV relative to Ac–Y•–NH_2 in the pH region in which RNR activity can be measured and pK_as that range from 5.6 to 7.8. We suggested that

these analogues would be useful in probing the mechanism(s) of proton–coupled electron transfer (PCET) in systems that involve redox active tyrosines.

We now present the semisynthesis of β2 in which Y_{356} has been replaced with fluorinated tyrosine derivatives of Table 7–1. These β2 analogues have allowed us to study the role of Y_{356} in the radical propagation process of *E. coli* RNR. The results suggest that an increase in the peak reduction potential of the F_nY analogue relative to Y by 80 mV results in a change in the rate–limiting step from a conformational change to the radical propagation process. These studies support the proposal that the protonation state of the phenol of this residue is not important in conformational gating, that the proton can be lost from this pathway without affecting the overall enzymatic activity, and that Y_{356} is a redox–active amino acid on the radical propagation pathway. Additionally, the rigorous assessment of the enzymatic activity afforded by the F_nY_{356}–β2 series establishes that the energetics of radical hopping through Y_{356} is finely tuned in wt class I RNR and can only operate within a ~130 mV window for the Y•/Y redox couple.

Table 7–1. Fluorotyrosine derivatives used to substitute Y_{356} of β2 and their physical properties.

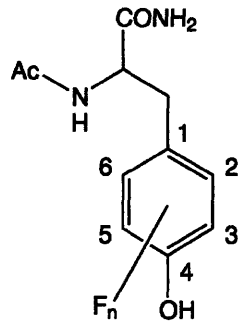

Fluorotyrosine	pK_a	$E_p(Y^{\bullet}/Y^{-})$ / mV
Ac–Y–NH_2	9.9	642
Ac–3,5–F_2Y–NH_2	7.2	755
Ac–2,3–F_2Y–NH_2	7.8	810
Ac–2,3,5–F_3Y–NH_2	6.4	853
Ac–2,3,6–F_3Y–NH_2	7.0	911
Ac–F_4Y–NH_2	5.6	968

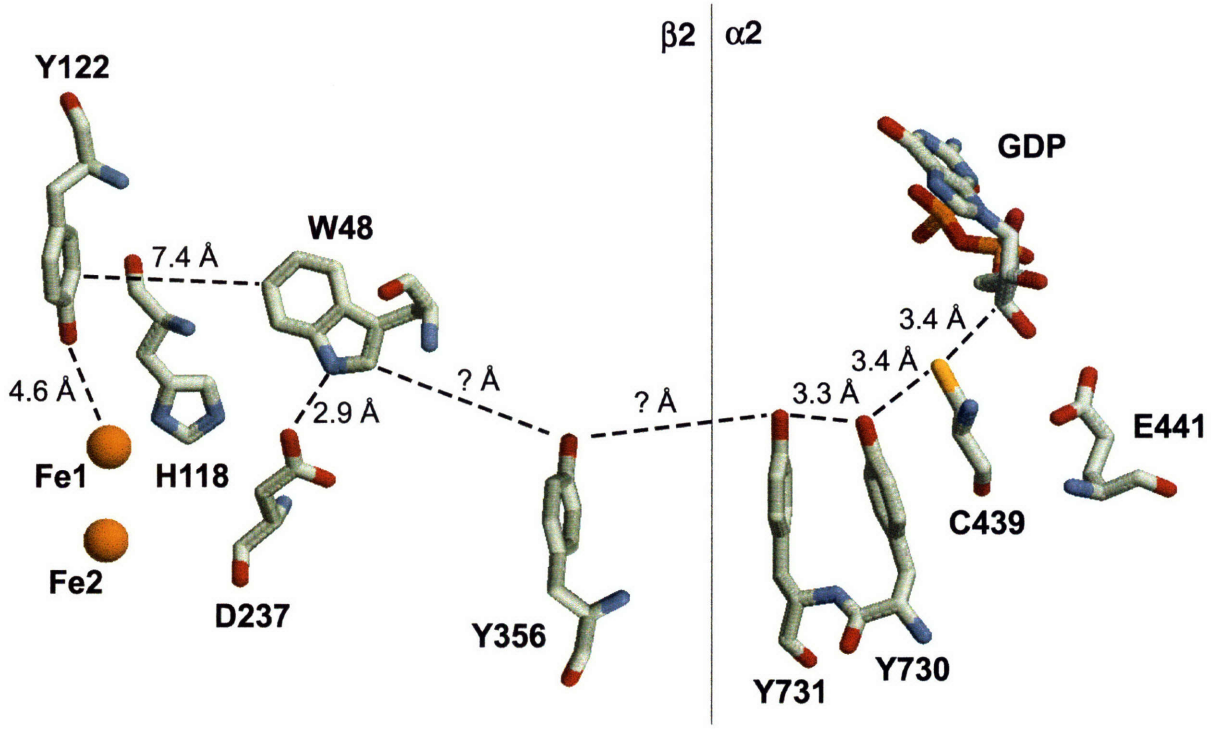

Figure 7–1. Putative PCET pathway of *E. coli* RNR based on the docking model (Ref 7). Y_{356} is not visible in the crystal structure of β2; it is proposed to propagate the radical between W_{48} on β2 and Y_{731} on α2. Distances on the β2 side are taken from the crystal structure of oxidized β2 at 1.4 Å resolution (Ref. 9).

MATERIALS AND METHODS

Materials. ATP, cytidine–5'–diphosphate (CDP), reduced β–nicotinamide adenine dinucleotide phosphate (NADPH), N–hydroxyurea, trifluoroacetic acid (TFA), 2–mercaptoethanesulfonic acid (Mesna), Fmoc–succinimide, Sephadex G–25 resin, DNase I (10 U/μL) and Triton X–100 were purchased from Sigma–Aldrich. BL21 (DE3) RIL Codon+ competent cells were obtained from Stratagene. Calf–intestine alkaline phosphatase (20 U/μL) was purchased from Roche. All amino acid derivatives were purchased from Novabiochem, Fmoc–L–Leu–PEG–PS resin and all other chemicals required for peptide synthesis were obtained from Applied Biosystems. [2–^{14}C]–CDP was purchased from Moravek Biochemicals. *E. coli* thioredoxin (TR, SA of 40 U/mg) and *E. coli* thioredoxin reductase (TRR, SA of 1800 U/mg) were isolated as previously described.[13]

Physical measurements. ^{1}H NMR spectra were recorded on a Varian 300 MHz NMR spectrometer at the MIT Department of Chemistry Instrumentation Facility. NMR samples were internally referenced to tetramethylsilane. pH measurements were performed with an Orion microelectrode. Absorption spectra were recorded on an Agilent 8453 Diode Array Spectrophotometer. EPR spectra were recorded at 77 K on a Bruker ESP–300 X–band (9.4 GHz) spectrometer equipped with an Oxford liquid helium cryostat.

Synthesis of Fmoc–F_nYs. Fmoc–F_nYs were synthesized by the method of Lapatsanis *et al.* with minor modifications.[25] The tyrosine analogue (700 μmol) was dissolved in 2.4 mL of 10% Na_2CO_3 and mixed with Fmoc–succinimide (970 μmol) in 2.5 mL of dioxane at 4 °C. The reaction was warmed to room temperature and reacted for 20 min to 2 h (F_nYs with higher fluorine substitution required longer reaction times). The reaction was monitored via TLC using 10:1 $CHCl_3$/MeOH as the mobile phase. After completion, the reaction was quenched with 25 mL water and extracted twice with 10 mL of EtOAc to remove Fmoc–succinimide. The pH was then lowered to 2–3 with 2 N HCl and the solution extracted with EtOAc (10×, 10 mL). The

organic layer was washed with saturated NaCl (3×, 3 mL), water (2×, 3 mL) and finally dried over $MgSO_4$. The solvent was removed *in vacuo* and the product purified by silica gel chromatography (16 g, 1.5 × 28 cm) using isocratic elution. The solvent system, R_f, and yield for each analogue have been reported (Table 7–2).[26]

Fmoc–L–3,5–F_2Y: ^{1}H–NMR (300 MHz, CD_3OD) δ = 2.85 (dd, 1H, C_β-H_1, 9.7 Hz, 14.3 Hz), 3.12 (dd, 1H, C_β-H_2, 5.7 Hz, 14.3 Hz), 4.2 (m, 3H, fluorenyl C-H and C-H_2), 4.37 (dd, 1H, C_α-H, 5.7 Hz, 10 Hz), 6.82 (m, 2H, PhOH C-H), 7.35 (dt, 4H, arom. fluorenyl C-H, 7.6 Hz, 26.7 Hz), 7.62 (d, 2H, arom. fluorenyl C-H, 7.5 Hz), 7.8 (d, 2H, arom. fluorenyl C-H, 7.1 Hz).

Fmoc–L–2,3–F_2Y: ^{1}H–NMR (300 MHz, CD_3OD) δ = 2.9 (dd, 1H, C_β-H_1, 9.6 Hz, 14.6 Hz), 3.23 (dd, 1H, C_β-H_2, 4.8 Hz, 14.2 Hz), 4.24 (m, 3H, fluorenyl C-H and C-H_2), 4.4 (dd, 1H, C_α-H, 5 Hz, 9.7 Hz), 6.61 (m, 1H, PhOH C-H_5), 6.82 (m, 1H, PhOH C-H_6), 7.28 (m, 2H, arom. fluorenyl C-H), 7.38 (t, 2H, arom. fluorenyl C-H, 7.4 Hz), 7.6 (d, 2H, arom. fluorenyl C-H, 7.4 Hz), 7.77 (d, 2H, arom. fluorenyl C-H, 7.4 Hz).

Fmoc–L–2,3,6–F_3Y: ^{1}H–NMR (300 MHz, CD_3OD) δ = 3.02 (dd, 1H, C_β-H_1, 9.3 Hz, 14 Hz), δ = 3.2 (dd, 1H, C_β-H_2, 5.7 Hz, 13.9 Hz), 4.2 (m, 3H, fluorenyl C-H and C-H_2), 4.41 (dd, 1H, C_α-H, 5.7 Hz, 9.4 Hz), 6.46 (m, 1H, PhOH C-H), 7.33 (dt, 4H, arom. fluorenyl C-H, 7.1 Hz, 26.7 Hz), 7.6 (d, 2H, arom. fluorenyl C-H, 7 Hz), 7.78 (d, 2H, arom. fluorenyl C-H, 9 Hz).

Fmoc–L–2,3,5–F_3Y: ^{1}H–NMR (300 MHz, CD_3OD) δ = 2.9 (dd, 1H, C_β-H_1, 9.6 Hz, 13.5 Hz), 3.25 (dd, 1H, C_β-H_2, 4.2 Hz, 13.8 Hz), 4.25 (m, 3H, fluorenyl C-H and C-H_2), 4.43 (dd, 1H, C_α-H, 4.7 Hz, 9.2 Hz), 6.82 (m, 1H, PhOH C-H), 7.32 (dt, 4H, arom. fluorenyl C-H, 7.2 Hz, 26.7 Hz), 7.58 (d, 2H, arom. fluorenyl C-H, 7.2 Hz), 7.75 (d, 2H, arom. fluorenyl C-H, 7.2 Hz).

Fmoc–L–2,3,5,6–F_4Y: ^{1}H–NMR (300 MHz, CD_3OD) δ = 3.06 (dd, 1H, Cb-H1, 9.2 Hz, 14.2 Hz), δ = 3.26 (dd, 1H, Cb-H2, 5.4 Hz, 14.2 Hz), δ = 4.23 (m, 3H, non–arom. fluorenyl-H), δ = 4.38 (dd, 1H, Ca-H, 5.4 Hz, 9.3 Hz), δ = 7.34 (dt, 4H, arom. fluorenyl-H, 7.7 Hz, 27 Hz), δ = 7.61 (d, 2H, arom. fluorenyl-H, 7.2 Hz), δ = 7.78 (d, 2H, arom. fluorenyl-H, 7.5 Hz).

Peptide synthesis. The β2 C–terminal peptide CSF_nYLVGQIDSEVDTDDLSNFQL was synthesized by a combination of standard solid phase and solution phase peptide synthesis

methods as previously described.[21] The first 19 residues were added using a Pioneer Peptide Synthesizer from Applied Biosystems. The remaining three amino acids (positions 20–22 on the peptide) were coupled manually. The manual coupling reaction of Fmoc–F_nYs were carried out for 1 h and a typical reaction contained 4 equiv of Fmoc–F_nY, 3.6 equiv of O–(7–azabenzotriazole–1–yl)–N,N,N'N'–tetramethyluronium hexafluorophosphate (HATU) and 8 equiv of diisopropyl ethylamine (DIPEA) in DMF. The purified peptides were characterized by RP–HPLC and MALDI–TOF MS. The results are summarized in Table 7–3.

Table 7–2. Purification and yield of Fmoc–F_nY–COOH.

F_nY Analogue	Solvent System for Silica Gel Purification	R_f	Yield (%)
Fmoc–2,3–F_2Y	20:1 $CHCl_3$/MeOH	0.3	95
Fmoc–3,5–F_2Y	10:1 $CHCl_3$/MeOH	0.4	85
Fmoc–2,3,5–F_3Y	10:1 $CHCl_3$/MeOH	0.2	50
Fmoc–2,3,6–F_3Y	10:1 $CHCl_3$/MeOH	0.25	51
Fmoc–F_4Y	20:1 $CHCl_3$/MeOH	0.2	82

Semisynthesis of β2 and F_nY_{356}–β2s. Culture growth, ligation and protein purification were carried out as previously described[21] with minor modifications. After Mesna–mediated cleavage of β2(1–353) from the chitin resin, excess Mesna was removed using a Sephadex G–25 column (200 mL, 3 × 30 cm) equilibrated in cleavage buffer (50 mM Hepes, pH 7.6, 500 mM NaCl). Furthermore, prior to purification by MonoQ anion exchange chromatography, unbound peptide was removed by concentration/dilution cycles using a YM–30 membrane. MonoQ purifications were performed under reducing conditions with 1.5 mM DTT. Each F_nY_{356}–β2 was judged to be >95% pure on the basis of SDS–PAGE analysis. Each β2 was further characterized by ESI–MS, and the tyrosyl radical was quantitated by UV–Vis and EPR spectroscopic methods (Table 7–4).

Table 7–3. RP–HPLC and MALDI–TOF MS characterization of F_nY–22mers[a].

F_nY–22mer	RP–HPLC R_t (min)	MS of (^{t}Buthio)–protected F_nY–22mer m/z $[M–H]^-$ calcd (obs)	MS of deprotected F_nY–22mer m/z $[M–H]^-$ calcd (obs)
Y–22mer	19	2548.6 (2548.2)	2460.6 (2460.1)
2,3–F_2Y–22mer	19	2584.6 (2585.2)	2496.6 (2495.6)
3,5–F_2Y–22mer	18.5	2584.6 (2584.0)	2496.6 (2495.8)
2,3,6–F_3Y–22mer	19	2602.6 (2601.9)	2552.6 (2551.6)[c]
2,3,5–F_3Y–22mer	21.5	2602.6 (2601.5)	2552.6 (2551.6)[c]
F_4Y–22mer	18	2642.6 (2641.4)[b]	2570.6 (2570.3)[c]

[a] See ref 21 for detailed description of HPLC and MALDI–TOF methods. [b] $[M – 2H + Na]^-$. [c] $[M – 2H + K]^-$

Table 7–4. Physical and biochemical characterization of F_nY_{356}–β2s.

F_nY_{356}–β2	Yield (mg)[a]	ESI–MS m/z $[M + H]^+$ calcd (obs)	Radical Content[b] (Y_{122}•/dimer)	Maximal Specific Activity (nmol/min mg)[c]	K_m for α2 (μM)
Y–β2	14.3	43360 (43360)	0.34	450	0.55 ± 0.18
2,3–F_2Y_{356}–β2	15	43396 (43399)	0.33	370	0.62 ± 0.11
3,5–F_2Y_{356}–β2	20	43396 (43392)	0.31	450	nd[d]
2,3,5–F_3Y_{356}–β2	13	43414 (43410)	0.42	365	0.65 ± 0.15
2,3,6–F_3Y_{356}–β2	10.5	43414 (43413)	0.41	95	nd[d]
F_4Y_{356}–β2	10	43432 (43434)	0.42	30	0.59 ± 0.2
$V_{353}G/ S_{354}C$–β2[e]	—	—	1.1	1420	0.55 ± 0.21

[a] Amount recovered from incubation with 45 mg of Mesna–activated β2. [b] Measured by the dropline correction method and quantitative EPR methods using recombinant wt–β2 as standard. [c] Activity of intein–generated F_nY_{356}–β2s is normalized for radical content of Y–β2. [d] nd = not determined. [e] Made by recombinant methods.

Purification of α2 and removal of contaminating β2. α2 (S.A. 1900 nmol/min/mg) was purified as previously described.[27] To reduce α2 and the Y• of contaminating β2 which co–purifies with α2, α2 (~40 μM) was incubated with 30 mM DTT for 25 min at room temperature. Hydroxyurea, ATP, and CDP were then added to final concentrations of 30 mM, 3 mM and 1 mM, respectively, and the incubation was continued for an additional 20 min at room temperature. α2 was then isolated using a Sephadex G–25 column (~35 mL, 1.5 x 23 cm), which had been equilibrated in assay buffer (50 mM Hepes, 15 mM $MgSO_4$, 1 mM EDTA, pH 7.6).

Determination of pH rate profiles of F_nY_{356}–β2s. 2–[N–morpholino]ethanesulfonic acid (Mes), N–2–hydroxethylpiperazine–N'–2–ethanesulfonic acid (Hepes), N–[Tris(hydroxyl-methyl)methyl]–3–aminopropanesulfonic acid (Taps) and 2–[cyclohexylamino]–ethanesulfonic acid (Ches) were used for the pH rate profiles. Each buffer was adjusted to the desired pH with either KOH or HCl. Each reaction contained in a volume of 230 μL: 50 mM Hepes (or Mes, Taps, Ches), 15 mM $MgSO_4$, 1 mM EDTA, 3 mM ATP, 1 mM [2–^{14}C]–CDP ($6 \times 10^6 - 1.5 \times 10^7$ cpm/μmol), 30 μM TR, 0.5 μM TRR, 1 mM NADPH, 3 μM α2 and 3 μM F_nY_{356}–β2. For each reaction, nucleotides, TR, TRR and α2 were incubated at 25 °C for ~1.5 – 2 min. The reaction was then initiated by addition of F_nY_{356}–β2 and NADPH. At defined time points, 40 μL were withdrawn and quenched with 25 μL of 2 % perchloric acid. At the end of the time course, the reactions were neutralized with 20 μL of 0.5 M KOH. Each sample was incubated at –20 °C overnight to ensure complete precipitation of potassium perchlorate. The samples were then spun down for 3 min in a tabletop centrifuge. Each supernatant was transferred to a 1.5 mL screw top microfuge tube, to which was added 14 U of calf intestine alkaline phosphatase, 120 nmol of carrier deoxycytidine (dC) and Tris–EDTA buffer (pH 8.5) to a final concentration of 75 mM and 0.15 mM, respectively. The amount of dC was then quantitated by the method of Steeper and Steuart.[28]

RESULTS

Synthesis and characterization of $F_nY_{356}/V_{353}G/S_{354}C$–β2s. β2 is a homodimer containing 375 amino acids per monomer, which can be prepared semisynthetically by intein methods.[21] Residues 1–353 of β2 with its C–terminus fused to the *VmaI* intein and a chitin–binding domain were made via molecular biological methods. Residues 357 to 375 were synthesized by automated solid phase peptide synthesis with residues 354, 355 and 356 being added manually.[21-23] A number of minor changes have been made from our initially reported procedure to enhance recoveries of β2 and in efforts to increase the amount of Y_{122}• per β2. In general, C354 of the C–terminal tail of β2 can form a disulfide with the excess peptide used in the ligation reaction to generate full length β2. Removal of the peptide is essential for accurate quantitation of RNR activity as the peptide is a competitive inhibitor of the nucleotide reduction process.[29] The final purification steps therefore used concentration/dilution cycles to remove non–covalently bound peptide as well as anion exchange chromatographay on a MonoQ column with DTT in all the buffers to reduce the peptide–β2 disulfide bond and remove the peptide. While DTT has previously been shown to reduce the Y_{122}• in β2,[30] the minimal time required for this purification step, ensures that this side reaction does not occur. A summary of the recovery of semi–synthetic β2s, their characterization by ESI–MS, the amount of Y_{122}• per β2, and the maximum specific activity of each β2, are presented in Table 7–4. The amount of Y_{122}• radical was quantified by X–band EPR spectroscopy and by the dropline correction method using the UV–vis spectrum.[31,32]

Over the past few years we have continually modified various aspects of the semi–synthesis of β2 in order to improve yields and amounts of Y_{122}• recovered. We have performed all of the ligation reactions described here, with the exception of the 2,3–F_2Y–peptide, on the same batch of β2–thioester. As a control for all of our experiments, wt–β2 made by the intein procedure (containing $V_{353}G/S_{354}C/Y_{356}$ and from here on referred to as Y–β2) was generated

from the same batch and is reported in Table 7–4. Its specific activity is identical to the double mutant made by site directed mutagenesis after normalization for the amount of Y•.

Problems encountered in the RNR activity assay. Because we wished to set lower limits of detection on the rates of deoxynucleotide formation with the mutant RNRs, we made two changes to the standard assays.[21] First, α2 (specific activity of 1.9 μmol/min/mg) as isolated, always co–purifies with a small amount of β2 (estimated to be <1% by SDS PAGE). We therefore inactivated this contaminating β2 by reduction of its Y_{122}• with hydroxyurea in the presence of DTT, ATP, and CDP and showed with control experiments in the absence of the β2 mutant, that no dNDP was detectable within the time frame of the assay (data not shown). Second the peptide used to generate semi–synthetic β2 is a known competitive inhibitor of β2's interaction with α2. An additional purification step for β2 mutants was thus added to the protocol to ensure that all of the peptide (covalently and non–covalently bound to β2) was removed. In each β2, there is now a cysteine at position 354 in place of the serine of the wt–β2. β2 mutants containing this cysteine are inactivated in the presence of α2, CDP and ATP in a slow, time–dependent, reaction.[21] This inactivation presumably results from an uncoupling of the radical propagation pathway, resulting in the reduction of Y_{122}•. Control experiments showed that this uncoupling did not occur to any significant extent under the conditions of the assays (data not shown). Finally, to ensure that the single amino acid substitution does not effect the interaction between the α2 and β2, the K_m values for several of the mutants were determined and found to be identical to Y–β2 as listed in Table 7–4.

pH rate profiles for wt and F_nY_{356}–β2s. Kinetic assays for nucleotide reduction over the RNR accessible pH range from 6.5 to 9 were carried out to determine if direct evidence for the role of Y_{356} as a redox–active amino acid on a pathway between α2 and β2 could be obtained. The results of our kinetic assays for the various F_nY_{356}–β2s are shown in Figure 7–2 and are quite dramatic. First, all of the F_nY_{356}–β2s are active between pH 6.5 to 8.5 and the activity is relatively high despite the complexity of the semisynthetic procedure for β2 generation (Table 7–4). Second, the activities of 2,3–F_2Y_{356}–β2, 3,5–F_2Y_{356}–β2 and 2,3,5–

F_3Y_{356}–β2 are very close to that of Y–β2 in the pH range from 6.5 to 7.6. On the alkaline side, the activity drops off for all F_nY derivatives with the drop–off beginning at a lower pH for the 2,3,5–F_3Y_{356}–, 2,3,6–F_3Y_{356}– and 2,3,5,6–F_4Y_{356}–β2s. With 2,3,6–F_3Y_{356}–β2 and 2,3,5,6–F_4Y_{356}–β2 the activity relative to Y–β2 is substantially reduced throughout the entire pH rate profile. At pH values greater than 8.5, the activity is below the lower limit of detection of our assay method.

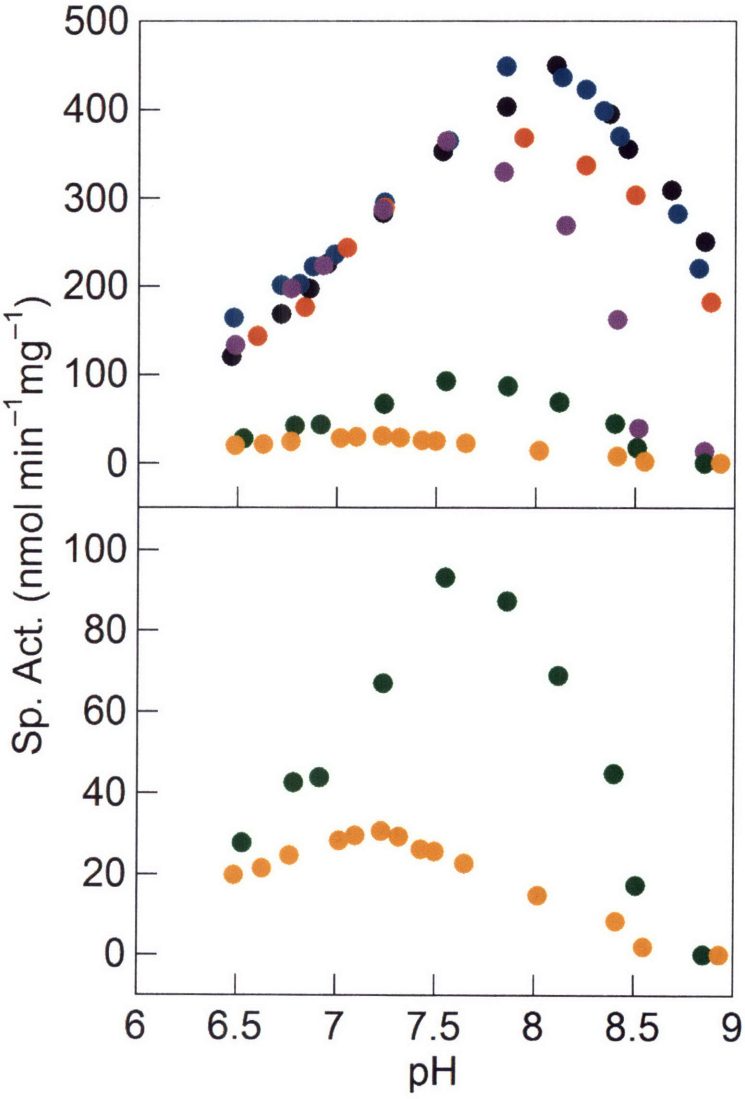

Figure 7–2. pH rate profiles of F_nY_{356}–β2s. The top panel shows an overlay of the pH rate profiles of Y–β2 and F_nY_{356}–β2s used in this study. The bottom panel shows a blow–up of the profiles of 2,3,6–F_3Y_{356}–β2 and F_4Y_{356}–β2. Each point represents an average of two independent measurements. The error was within 15 % for all points: (•) Y_{356}–β2, (•) 3,5–F_2Y_{356}–β2, (•) 2,3–F_2Y_{356}–β2, (•) 2,3,5–F_3Y_{356}–β2, (•) 2,3,6–F_3Y_{356}–β2, and (•) F_4Y_{356}–β2.

DISCUSSION

The F_nYs in Table 7–1 were incorporated into β2 by the intein procedure. They were chosen to perturb the protonation state and reduction potential of residue 356 in an effort to examine its role in the radical propagation process. For each mutant β2 the ability to make deoxynucleotides was measured over the accessible pH range for RNR (6.5 to 9). The results, Figure 7–2, reveal that the F_nYs markedly perturb the activity suggesting that these mutants will be useful for examining radical propagation.

The observed drop in RNR activity of F_nY–β2 mutants relative to Y–β2 may be related to changes in their reduction potentials. Unfortunately, one cannot measure the reduction potentials of these F_nYs within β2. We can, however, measure the peak reduction potentials of Ac–F_nY–NH_2 derivatives. These values were determined in the pH range in which RNR activity can be measured (6.5 and 9, Figure 7–3) using differential pulse voltammetry (DPV, see Chapter 6). Previous work has shown that the peak potential for the Y• as measured by DPV is very similar to its reduction potential measured by cyclic voltammetry and pulse radiolysis.[33] The data in Figure 7–3 show that the fluorinated tyrosine derivatives have potentials that vary from –50 mV to +270 mV relative to tyrosine.

To gain insight into the relationship between RNR activity and the reduction potential of residue at 356, Figure 7–4 was generated. In this Figure, the activity data of each mutant relative to that of Y–β2 is plotted against the peak reduction potential difference between Ac–F_nY–NH_2 and Ac–Y–NH_2. Analysis of the data in this fashion allows removal of the pH dependent activity inherent to Y–β2 and assumes that all of the mutants have the same inherent pH dependence. The basis of this pH dependence is not understood. The construction of Figure 7–4 also assumes that the reduction potential of Y_{356}• and F_nY_{356}• varies 59 mV/pH unit, as with E_p(Ac–F_nY•–NH_2/Ac–F_nY–NH_2) and requires proton loss to bulk solution concomitant with oxidation. Furthermore, we assume that if the protein environment perturbs the reduction potential for Y in

Y–β2, it has the same relative effect on each F_nY in the corresponding F_nY_{356}–β2. We note that the data in Figure 7–4 reveal some scatter, which we attribute in part to the difficulties with making β2 semi–synthetically. Moreover, fluorine substitution may affect the conformation of residue 356 and its interactions with its environment. Four fluorines certainly have altered steric properties relative to four hydrogens, stemming from the slightly larger van der Waals radius of F vs. H (1.2 Å vs 1.35 Å, respectively) and the longer C–F bond vs the C–H bond (1.38 Å and 1.09 Å, respectively). Finally, using the pK_a of Ac–F_nY–NH_2 as a benchmark for F_nY_{356}, a difference in charge of this residue may result owing to the pK_a differences of each of these fluorinated tyrosines. Given the incongruities that may be engendered by fluorine substitution, the data in Figure 7–4 are quite striking.

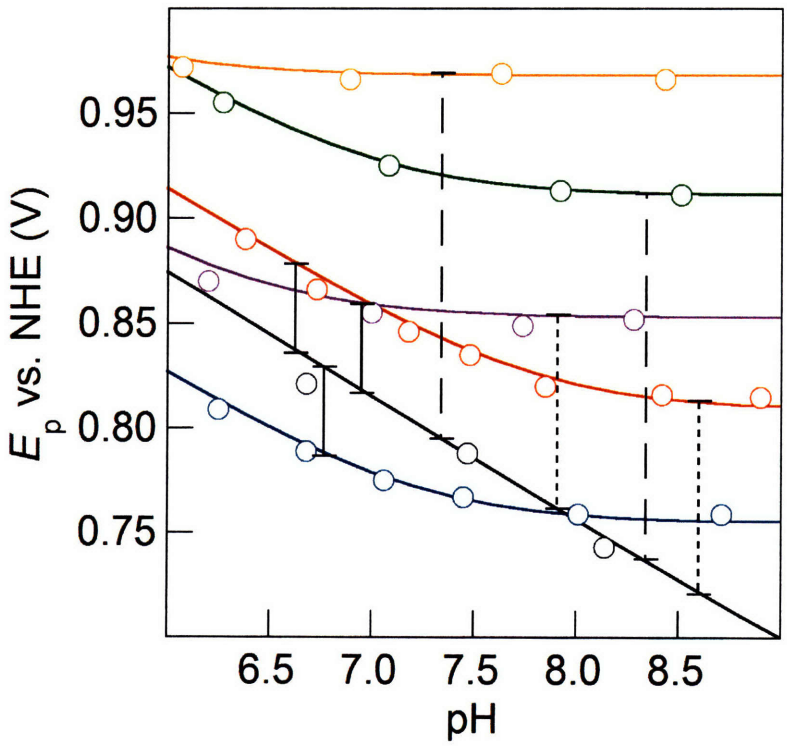

Figure 7–3. Peak reduction potential of Ac–F_nY•–NH_2s as a function of pH. The E_p vs. pH for reduction of (—) Ac–Y•–NH_2, (—) Ac–3,5–F_2Y•–NH_2, (—) Ac–2,3–F_2Y•–NH_2, (—) Ac–2,3,5–F_3Y•–NH_2, (—) Ac–2,3,6–F_3Y•–NH_2, and (—) Ac–F_4Y•–NH_2[24] in the pH range accessible to RNR are shown. The lines indicate peak reduction potential differences of ±40 mV (solid), 90 mV (short dash) and 180 mV (long dash) relative to that for Ac–Y•–NH_2.

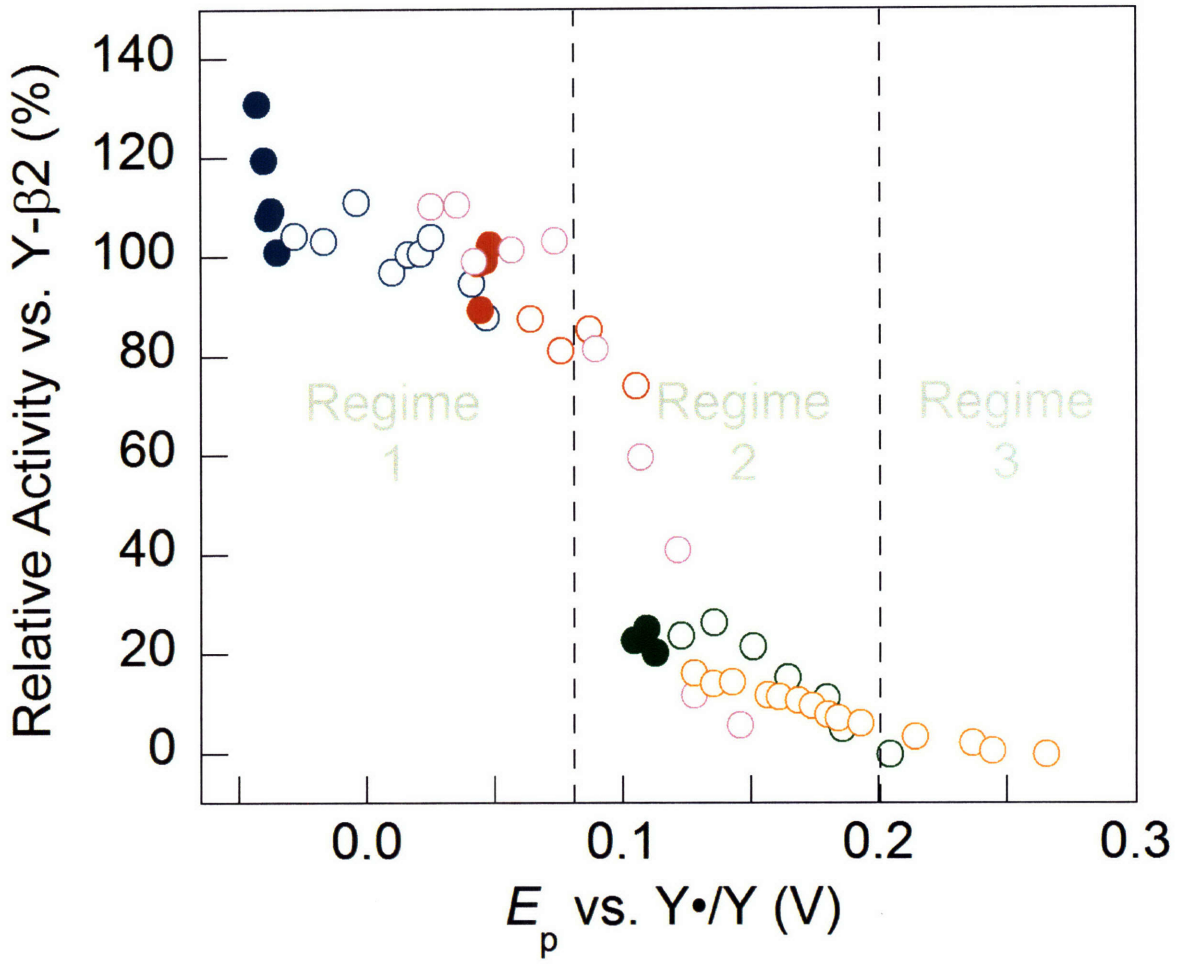

Figure 7–4. Redox potential regimes of RNR activity. Relative activities of F_nY_{356}–β2s vs. Y–β2, obtained from Figure 7–2, and plotted as a function of peak reduction potential difference between the corresponding Ac–F_nY•–NH_2 and Ac–Y•–NH_2[24]: (●,○) 3,5–F_2Y_{356}–β2, (●,○) 2,3–F_2Y_{356}–β2, (○) 2,3,5–F_3Y_{356}–β2, (●,○) 2,3,6–F_3Y_{356}–β2, and (○) F_4Y_{356}–β2. Filled circles represent data points where pH < pK_a of the corresponding F_nY; open circles represent data points where pH > pK_a of the corresponding F_nY. The three different regimes of RNR activity are highlighted as either gated by a physical/conformational change (regime 1), rate–limited by radical transport (regime 2), or reduced to background levels (regime 3) depending on the peak reduction potential difference between the corresponding Ac–F_nY•–NH_2 and Ac–Y•–NH_2.

Three distinct activity regimes emerge from Figure 7–4. When peak reduction potential differences are –50 mV to 80 mV (regime 1), nucleotide reduction activity falls within the range of that observed for Y–β2; both 2,3–F_2Y_{356}–β2 and 3,5–F_2Y_{356}–β2 exhibit 90 to 120% of the activity obtained for Y–β2. As the difference in peak reduction potential increases from 80 to 200 mV (regime 2), the RNR activity drops off dramatically. At >200 mV difference (regime 3), no detectable activity of RNR is observed. 2,3,5–F_3Y_{356}–β2 spans the potential range from ~ 25 to 145 mV, whereas 2,3,6–F_3Y_{356}–β2 and F_4Y_{356}–β2 have very low activities and high peak reduction potential differences at all pHs accessible to RNR.

Our interpretation of these data is summarized by the three activity regimes marked with the dashed lines in Figure 7–4. When the reduction potential difference is within the range of –50 to 80 mV (regime 1), the rate of nucleotide reduction in the F_nY_{356}–β2s is governed by the same factors as nucleotide reduction by Y–β2. Pre–steady state experiments have shown that the rate limiting step in *E. coli* RNR is a physical step or steps prior to the radical propagation process that is gated by binding of substrate and allosteric effector.[13] In the steady state, the rate–determining step is proposed to be the same physical step or alternatively a step involved in re–reduction of α2 or a conformational change associated with this re–reduction, subsequent to dNDP formation and re–generation of the Y•.[21] In either case, the rate of nucleotide reduction should be independent of Y_{356}• reduction potential, leading us to assign regime 1 to the physically/conformationally gated step. The peak reduction potential of Ac–3,5–F_2Y•–NH_2 falls effectively in the conformationally gated regime over all pHs, whereas the potentials of Ac–2,3–F_2Y•–NH_2 and Ac–2,3,5–F_3Y•–NH_2 falls within this regime for pH <~8.4 and pH <~7.5, respectively. At a pH of 6.81 (solid line, Figure 7–3), the peak reduction potential difference between Ac–3,5–F_2Y•–NH_2 and Ac–Y•–NH_2 is –40 mV. Similarly, at pHs of 6.6 and 6.93 (solid lines, Figure 7–3) the peak reduction potentials of Ac–2,3–F_2Y•–NH_2 and Ac–2,3,5–F_3Y•–NH_2, respectively, are ~ 40 mV higher than that of Ac–Y•–NH_2. The relative activities are all identical within error (108, 99 and 100 % of Y–β2, respectively, for 3,5–F_2Y_{356}–β2, 2,3–F_2Y_{356}–β2 and 2,3,5–F_3Y_{356}–β2).

When the driving force for Y_{356} oxidation exceeds 80 mV but is less than 200 mV relative to Y, the rate of nucleotide reduction correlates with the difference in peak reduction potential, suggesting that there has been a change in the rate limiting step to one involving radical transport through F_nY_{356}. This point is demonstrated for 2,3–F_2Y_{356}–β2 and 2,3,5–F_3Y_{356}–β2. The short dashed lines in Figure 7–3 indicate two pH values (8.6 and 7.8) at which the peak reduction potential difference between Ac–2,3–F_2Y•–NH_2 and Ac–Y•–NH_2, and between Ac–2,3,5–F_3Y•–NH_2 and Ac–Y•–NH_2 is ~ 90 mV. If activity is determined solely by the reduction potential, then the relative activity of 2,3–F_2Y_{356}–β2 at pH 8.5 should approximate that of 2,3,5–F_3Y_{356}–β2 at pH 7.8. The relative activities observed are 85 % and 81 %, respectively.

At potentials differences greater than 150 mV (regime 3), the rate of radical transfer appears to become so slow that nucleotide reduction is minimal and for potential differences >200 mV activity is abolished. Note that the relative activities of 2,3,6–F_3Y_{356}–β2 at pH 8.4 and that of F_4Y_{356}–β2 at pH 7.4, where the peak reduction potential difference between these corresponding Ac–F_nY•–NH_2s and Ac–Y•–NH_2 is 180 mV (long dashed lines, Figure 7–3), are 11% and 8%, respectively. The direct correlation between activity and peak reduction potential strongly suggests that Y_{356} is a redox–active amino acid on the pathway.

We also examined whether the protonation state of the F_nYs at position 356 affects RNR activity. Our previous studies with NO_2Y_{356}–β2[21] showed that the pK_a of this residue at the α2/β2 interface is unperturbed relative to that of Ac–NO_2Y–NH_2 in solution. Similar measurements of the pK_as of the F_nYs within β2 cannot be made because these phenolates do not absorb in the visible region of the spectrum as does 3–NO_2Y^-. We have thus assumed that the pK_as of the Ac–F_nY–NH_2 are indicative of those within the α2/β2 complex. We have incorporated this information into Figure 7–4 in an effort to determine if the protonation state of the F_nY has any correlation with RNR activity: the filled circles in Figure 7–4 represent data points where pH < pK_a of the corresponding F_nY; conversely open circles represent data points where pH > pK_a of the corresponding F_nY. This analysis reveals that most of the F_nYs used in

this study are deprotonated or exhibit changes in protonation state, whereas Y because of its higher pK_a, remains protonated throughout the range where the activity of RNR can be measured. In contrast with the peak potential data, no clear correlation exists between the protonation state of the F_nY_{356} and the activity of the corresponding mutant.

Our results do not provide any insight about the destination of the proton from Y_{356} in Y–β2 in the forward PCET event or its delivery in the back PCET event. Comparison of sequences of the disordered C–terminal tails of over 160 β2s suggest that, while there are no absolutely conserved residues, E_{350} is present in 129 of 162 β2 sequences.[34] Thus, it is possible that this residue functions as a proton acceptor in the forward PCET reaction and a proton donor in the reverse reaction. The importance of this residue is supported by mutagenesis studies carried out on many of the residues within the C–terminus of β2. Individual substitution of Y_{356} and E_{350} with alanine was found to affect activity. In the former case, β2 was inactive and in the latter case the rate was reduced 250 fold.[35]

The mechanistic details for radical transport involving a tyrosyl radical at this position are important to consider. Radical transport involving the deprotonated fluorotyrosines can proceed by simple ET (Eq. 7–1). Conversely, a stepwise ET/PT reaction of a protonated tyrosine confronts a large thermochemical bias because ΔG° for the initial ET or PT event is high.[36-39] Accordingly, these thermodynamic constraints implicate proton–coupled electron transfer (PCET) for radical propagation (Eq. 7–2).[40-43]

$$F_nY\bullet + e^- \rightarrow F_nYO^- \qquad (7\text{–}1)$$

$$Y\bullet + e^- + H^+ \rightarrow YOH \qquad (7\text{–}2)$$

In Y–β2, therefore, the proton must be lost concomitant with Y_{356} oxidation via PCET.

Assuming the radical propagation pathway shown in Figure 7–1, our results with the F_nY_{356}–β2s suggest that hole migration between the W_{48}–β2–Y_{356}–β2 pair and the Y_{356}–β2–Y_{731}–α2 does not occur by an obligatory hydrogen atom transfer as phenolates of the F_nY_{356}–β2s

are active. Furthermore, this activity for the phenolates is inconsistent with the models based on site–directed mutagenesis studies[15] and theory[44] that W_{48}, Y_{356}, and Y_{731} are connected by way of a hydrogen–bonding network that is required for conformational gating of the radical propagation process. The turnover number of 2,3,5–F_3Y_{356}–β2 at pH 7.6, for example, is identical to that of Y–β2, where it is deprotonated if one assumes that the pK_a is not perturbed from that of Ac–2,3,5–F_3Y–NH_2, as indicated by our studies on NO_2Y_{356}–β2.[21] W_{48} and Y_{731} must therefore communicate by ET involving the 2,3,5–F_3Y^-/2,3,5–F_3Y• couple. Insertion of a negative charge at the α2/β2 interface apparently does not affect overall RNR activity. These results, taken together with our preliminary studies,[22,23] lead us to conclude that the proton from Y_{356} in the wild type enzyme is transferred (off pathway) to solvent, either directly or via a base or bases in β2 or α2.

CONCLUSION

A major unresolved issue in class I RNRs is the mechanism of radical propagation – how does Y_{122}• on β2, transiently and reversibly generate a C_{439}• on α2 proposed to be >35 Å away. This problem is different from most ET reactions in biology studied to date, which typically occur over a distances of 10–15 Å by a tunneling mechanism and consequently do not involve aromatic amino acid radical intermediates.[45-57] The participation of tyrosine in the radical initiation pathway of RNR steps beyond simple ET because management of proton and electron inventories is required for charge transport involving the amino acid. In Chapter 6, we have shown that fluorotyrosine derivatives have radical peak reduction potentials from –50 to +270 mV relative to Y and pK_as that range from 5.6 to 7.8. By exploiting these properties for F_nYs substituted at Y_{356}, our data strongly suggest that this residue in β2 is a redox–active amino acid on the radical propagation pathway in the class I RNRs. This result is important, as Y_{356} is the only residue on the pathway that is not observable structurally. Different activity regimes of RNR may be accessed by tuning the reduction potential of F_nY_{356}• such that radical transport becomes rate limiting in nucleotide reduction. Future experiments using pre–steady state kinetic analyses will focus on establishing that the radical propagation process does, in fact, become rate limiting at peak reduction potential differences >80 mV as proposed based on our reported data, as well as on detection of radical amino acid intermediates during turnover. Studies reported herein, further strongly suggest that hole migration between the β2–W_{48}–β2–Y_{356} and the β2–Y_{356}–α2–Y_{731} pairs does not occur by hydrogen atom transfer, as phenolates of the F_nY_{356}–β2s are active. The obligation of protons to the pathway from Y_{122} to Y_{356} in β2 and from Y_{731}

into C_{439} at the active site of α2 remains an open question and needs to be investigated, most efficiently by direct kinetic analysis of the radical intermediates.

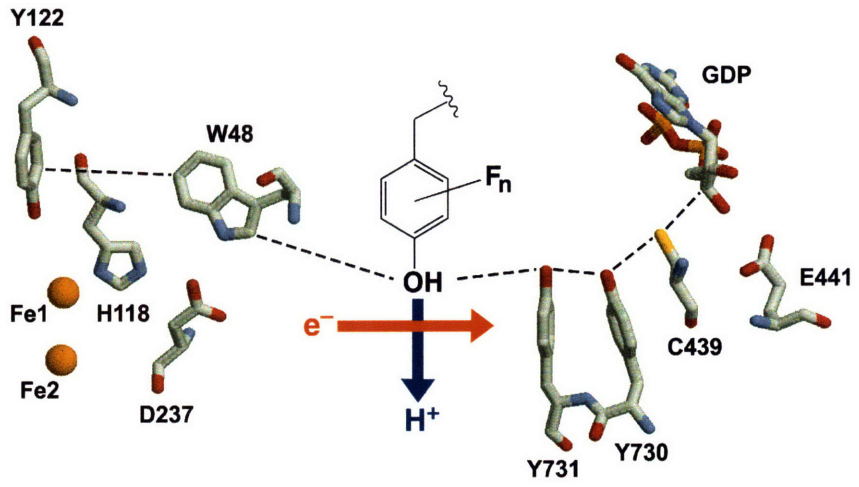

Figure 7–5. Mechanism of Y_{356} oxidation during radical transfer. Y_{356} is oxidized by an orthogonal PCET methanism, where movement of the phenolic electron and proton are coupled. The proton is transferred off–pathway perhaps to residue E_{350}, the electron is transferred to residue 48 or 731 depending on the direction of radical transfer.

REFERENCES

(1) Jordan, A.; Reichard, P. *Annu. Rev. Biochem.* **1998**, *67*, 71.

(2) Stubbe, J.; van der Donk, W. A. *Chem. Rev.* **1998**, *98*, 705.

(3) Thelander, L. *J. Biol. Chem.* **1973**, *248*, 4591.

(4) Kashlan, Ossama B.; Scott, Charles P.; Lear, James D.; Cooperman, Barry S. *Biochemistry* **2002**, *41*, 462.

(5) Kashlan, O. B.; Cooperman, B. S. *Biochemistry* **2003**, *42*, 1696.

(6) Stubbe, J.; Riggs-Gelasco, P. *Trends Biochem. Sci.* **1998**, *23*, 438.

(7) Uhlin, U.; Eklund, H. *Nature* **1994**, *370*, 533.

(8) Nordlund, P.; Sjöberg, B.-M.; Eklund, H. *Nature* **1990**, *345*, 593.

(9) Högbom, M.; Galander, M.; Andersson, M.; Kolberg, M.; Hofbauer, W.; Lassmann, G.; Nordlund, P.; Lendzian, F. *Proc. Natl. Acad. Sci.* **2003**, *100*, 3209.

(10) Marcus, R. A.; Sutin, N. *Biochim. Biophys. Acta* **1985**, *811*, 265.

(11) Stubbe, J.; Nocera, D. G.; Yee, C. S.; Chang, M. C. Y. *Chem. Rev.* **2003**, *103*, 2167.

(12) Erickson, H. K. *Biochemistry* **2001**, *40*, 9631.

(13) Ge, J.; Yu, G.; Ator, M. A.; Stubbe, J. *Biochemistry* **2003**, *42*, 10071.

(14) Eklund, H.; Uhlin, U.; Farnegardh, M.; Logan, D. T.; Nordlund, P. *Prog. Biophys. Mol. Biol.* **2001**, *77*, 177.

(15) Ekberg, M.; Sahlin, M.; Eriksson, M.; Sjöberg, B. M. *J. Biol. Chem.* **1996**, *271*, 20655.

(16) Ekberg, M.; Potsch, S.; Sandin, E.; Thunnissen, M.; Nordlund, P.; Sahlin, M.; Sjöberg, B. M. *J. Biol. Chem.* **1998**, *273*, 21003.

(17) Rova, U.; Goodtzova, K.; Ingemarson, R.; Behravan, G.; Gräslund, A.; Thelander, L. *Biochemistry* **1995**, *34*, 4267.

(18) Rova, U.; Adrait, A.; Potsch, S.; Gräslund, A.; Thelander, L. *J. Biol. Chem.* **1999**, *274*, 23746.

(19) Ekberg, M.; Birgander, P.; Sjöberg, B.-M. *J. Bacteriol.* **2003**, *185*, 1167.

(20) Muir, T. W. *Annu. Rev. Biochem.* **2003**, *72*, 249.

(21) Yee, C. S.; Seyedsayamdost, M. R.; Chang, M. C.; Nocera, D. G.; Stubbe, J. *Biochemistry* **2003**, *42*, 14541.

(22) Yee, C. S.; Chang, M. C.; Ge, J.; Nocera, D. G.; Stubbe, J., *J. Am. Chem. Soc.* **2003**, *125*, 10506.

(23) Chang, M. C. Y.; Yee, C. S.; Nocera, D. G.; Stubbe, J. *J. Am. Chem. Soc.* **2004**, *126*, 16702.

(24) Seyedsayamdost, M. R.; Reece, S. Y.; Nocera, D. G.; Stubbe, J. *J. Am. Chem. Soc.* **2006**, *128*, 1569.

(25) Lapatsanis, L.; Milias, G.; Froussios, K.; Kolovos, M. *Synthesis* **1983**, 671.

(26) Seyedsayamdost, M. R.; Yee, C. S.; Reece, S. Y.; Nocera, D. G.; Stubbe, J. *J. Am. Chem. Soc.* **2006**, *128*, 1562.

(27) Salowe, S.; Bollinger, J. M., Jr.; Ator, M.; Stubbe, J.; McCraken, J.; Peisach, J.; Samano, M. C.; Robins, M. J. *Biochemistry* **1993**, *32*, 12749.

(28) Steeper, J. R.; Steuart, C. D. *Anal. Biochemistry* **1970**, *34*, 123.

(29) Climent, I; Sjöberg, B. M; Huang, C. Y. *Biochemistry* **1991**, *31*, 5164.

(30) Fontecave, M.; Gerez, C.; Mansuy, D.; Reichard, P. *J. Biol. Chem.* **1990**, *265*, 10919.

(31) Bollinger Jr., J. M. *Ph.D. Thesis.* Massachusetts Institute of Technology, **1993**.

(32) Bollinger, J. M. Jr.; Tong, W. H.; Ravi, N.; Huynh, B. H.; Edmondson, D. E.; Stubbe, J. *Methods Enzymol.* **1995**, *258*, 278.

(33) Tommos, C.; Skalicky, J. J.; Pilloud, D. L.; Wand, A. J.; Dutton, P. L. *Biochemistry* **1999**, *38*, 9495.

(34) Ge, J., *Ph.D. Thesis.* Massachusetts Institute of Technology, **2003**.

(35) Climent, I.; Sjöberg, B. M.; Huang, C. Y. *Biochemistry* **1992**, *31*, 4801.

(36) Mayer, J. M.; Rhile, I. J. *Biochim. Biophys. Acta* **2004**, *1655*, 51.

(37) Sjödin, M.; Ghanem, R.; Polivka, T.; Pan, J.; Styring, S.; Sun, L.; Sundström, V.; Hammarström, L. *Phys. Chem. Chem. Phys.* **2004**, *6*, 4851.

(38) Sjödin, M.; Styring, S.; Wolpher, H.; Xu, Y.; Sun, L.; Hammarström, L. *J. Am. Chem. Soc.* **2005**, *127*, 3855.

(39) Reece, S. Y.; Nocera, D. G. *J. Am. Chem. Soc.* **2005**, *127*, 9448.

(40) Chang, C. J.; Chang, M. C. Y.; Damrauer, N. H.; Nocera, D. G. *Biophys. Biochim. Acta* **2004**, *1655*, 13.

(41) Cukier, R. I.; Nocera, D. G. *Annu. Rev. Phys. Chem.* **1998**, *49*, 337.

(42) Cukier, R. I. *Biochim. Biophys. Acta* **2004**, *1655*, 37.

(43) Hatcher, E.; Soudackov, A. V.; Hammes-Schiffer, S. *J. Am. Chem. Soc.* **2004**, *126*, 5763.

(44) Himo, F.; Siegbahn, P. E. M. *Chem. Rev.* **2003**, *103*, 2421.

(45) Page, C. C.; Moser, C. C.; Chen, X.; Dutton, P. L., *Nature* **1999**, *402*, 47.

(46) *Electron Transfer in Chemistry*; Balzani, V. Ed.; Wiley-VCH: Weinheim, Germany, 2001; Vol. 3, Part 1.

(47) Gray, H. B.; Winkler, J. R. *Annu. Rev. Biochem.* **1996**, *65*, 537.

(48) Gunner, M. R.; Robertson, D. E.; Dutton, P. L. *J. Phys. Chem.* **1986**, *90*, 3783.

(49) Farver, O.; Pecht, I. *Biophys. Chem.* **1994**, *50*, 203.

(50) Namslauer, A.; Braenden, M.; Brzezinski, P. *Biochemistry* **2002**, *41*, 10369.

(51) Tollin, G. In *Electron Transfer in Chemistry*; Balzani, V. Ed.; Wiley-VCH: Weinheim, Germany, 2001; Vol. 4, Part 1, p 202.

(52) Davidson, V. L. *Acc. Chem. Res.* **2000**, *33*, 87.

(53) McLendon, G.; Hake, R. *Chem. Rev.* **1992**, *92*, 481.

(54) Millett, F.; Durham, B. *Biochemistry*, **2002**, *41*, 11315.

(55) Nocek, J. M.; Zhou, J. S.; Forest, S. D.; Priyadarshy, S.; Beratan, D. N.; Onuchic, J. N.; Hoffman, B. M. *Chem. Rev.* **1996**, *96*, 2459.

(56) Lewis, F. D. Electron Transfer and Charge Transport in DNA. In *Electron Transfer in Chemistry*; Balzani, V. Ed.; Wiley-VCH: Weinheim, Germany, 2001; Vol. 3, Part 5, p 105.

(57) Boon, E. M.; Barton, J. K. *Curr. Opin. Struct. Biol.* **2002**, *12*, 320.

CHAPTER 8:

Switching the Rate–Determining Step from a Conformational Change to Radical Propagation with 2,3,5–F_3Y–β2 of *E. coli* Ribonucleotide Reductase

INTRODUCTION

Inside the cell, ribonucleotide reductases (RNRs) are responsible for reduction of all four nucleotides to 2'–deoxynucleotides, which are essential for DNA replication and repair.[1-3] The *E. coli* RNR is the best RNR studied to date and consists of two homodimeric protein subunits, α2 and β2. α2 harbors the active site, in which thiyl radical–mediated (C_{439}•) nucleotide reduction occurs.[4] It also contains binding sites for allosteric effectors, which control the rate and specificity of catalysis. β2 is the radical initiator subunit and carries a diiron tyrosyl radical (Y_{122}•) cofactor.[5,6] Each turnover requires oxidation of C_{439} in α2 by Y_{122}• in β2. A mechanism for this reaction, the radical propagation event, has only recently emerged.

A structure of the active α2/β2 complex does not exist. However, Uhlin and Eklund have generated a docking model for how these two subunits interact, using shape and charge complementarity.[7-9] Based on this model, the radical transfer pathway shown in Figure 8–1 has been proposed, in which the distance between Y_{122}• and C_{439} is >35 Å. This pathway is unusual as it consists of only aromatic amino acid radicals which catalyze reversible long–range charge transport between Y_{122}• and C_{439}. Mutagenesis studies have shown that the residues in Figure 8–1 are essential for catalysis.[10] However, all site–directed mutants of the aromatic

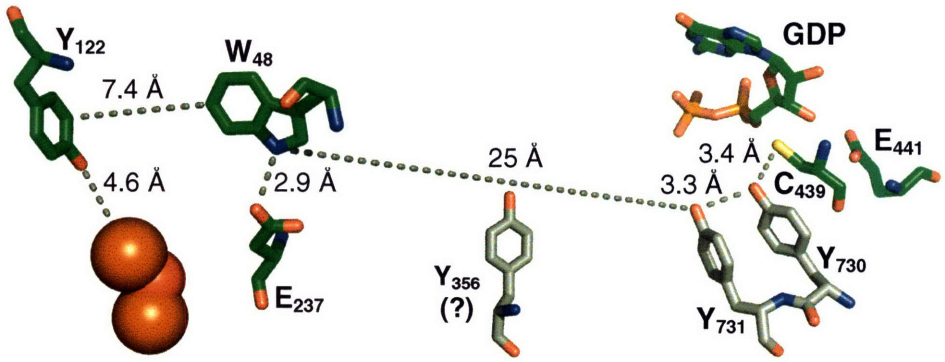

Figure 8–1. The proposed radical initiation pathway within an αβ pair. Residues in grey have been shown to be redox–active using DOPA–β2 and NH_2Y–α2s, respectively. Note that the position of Y_{356} is unknown

pathway–residues generated thus far are inactive in catalysis thus preventing mechanistic studies. Consequently, examination of this pathway requires more subtle and direct perturbations.[11,12]

To explore the pathway in Figure 8–1, we have taken a focused approach of incorporating unnatural Y analogues into residues Y_{356} in β2 and Y_{731}/Y_{730} in α2 using various approaches. The analogues that have been inserted are structural homologues of Y; however, they have altered reduction potentials and/or pK_as. These analogues have taught us a great deal regarding the pathway and the mechanism attendant to long–range hole migration. In chapter 2, we replaced residue Y_{356} with 3,4–dihydroxyphenylalanine (DOPA) using expressed protein ligation methods. Characterization of DOPA–β2 revealed kinetically competent formation of a DOPA radical (DOPA•) which we examined by UV–vis and EPR spectroscopies. In chapter 3 we generated and characterized heterodimeric DOPA–β2, DOPA–ββ', in which the β'–monomer was missing the C–terminal 22 residues. We presented kinetically competent DOPA• formation and reformation of Y_{122}• by DOPA•. The insights gained with DOPA–β2 and DOPA–ββ' have been important as residue 356 lies on the C–terminal tail of β2 and has not been resolved in any structure of β2 solved to date. In addition, they have supported the model in Figure 8–1 by demonstrating that residue 356 is redox–active and have established connectivity between Y_{122}• and residue 356 in both directions.

In chapter 4, we incorporated 3–aminoY (NH_2Y) into residues Y_{730} and Y_{731} of α2 using an evolved suppressor tRNA/aminoacyl–tRNA synthetase pair. Our studies using SF UV–vis and EPR spectroscopies revealed kinetically competent NH_2Y radical (NH_2Y•) formation. They also showed that both NH_2Y–α2s are active in nucleotide reduction, suggesting that the NH_2Y•s observed are transient and competent radical intermediates during long–range hole propagation. In chapter 5, we employed isotopic substitution of NH_2Y using ^{15}N and ^{2}H, multi–frequency EPR spectroscopies, spectral simulations and theoretical studies to provide a detailed structure of the NH_2Y_{730}•, to establish the positions of residues 730/731 in the α2/β2 complex using PELDOR spectroscopy and to demonstrate pathway dependence for NH_2Y_{730}• and NH_2Y_{731}•

formation. Together the studies with DOPA and NH_2Y traps have provided compelling evidence for the redox–active roles of residues Y_{356}, Y_{731} and Y_{730} in radical propagation.

To further examine the mechanism of Y oxidation at residue 356, we demonstrated the usefulness of fluorotyrosines (F_nYs) by presenting their synthesis and detailed physical characterization in Chapters 6. Subsequently, we generated a series of F_nY–β2s (n=2, 3, 4) which we used to interrogate the mechanism of involvement of residue 356 in radical transfer (Chapter 7).

The results in Chapter 7 suggest that substitution of Y_{356} with a series of F_nYs (n=2, 3, or 4) has a marked affect on the pH rate profile for nucleotide reduction. Three activity regimes are observed. In the first regime, where the reduction potential difference between F_nY and Y is –50 to 80 mV, the rate–limiting step in turnover is a conformational change that precedes radical transfer. In this regime the mutant RNRs have specific activities similar to that of intein wt RNR. In the second regime, where the reduction potential difference is between 80 and 200 mV higher than that of Y, we have proposed a shift in the rate–limiting step from a conformational change to radical transfer. In this range, the specific activities of mutant RNRs decrease as a function of the reduction potential difference between F_nY and Y. Finally, in the third regime, where the reduction potential difference exceeds 200 mV, radical transfer is completely shut down resulting in absence of nucleotide reduction activity. Importantly, one analogue, 2,3,5–F_3Y, spans almost the entire reduction potential difference range, from +25 mV at pH 6.5 to +145 mV at pH ~9. In this chapter, we experimentally assess whether radical transfer has in fact become rate–determining with 2,3,5–F_3Y–β2, as we proposed in Chapter 7, and suggest a kinetic model for its turnover.

Kinetic models for the steady state and pre–steady state reactions of wt RNR have been examined before in detail.[13] A main experimental observation in these studies, has been that disappearance of Y_{122}• is never observed under various conditions, i.e. in the temperature range of 2–25°C, with various substrate or substrate/effector combinations, with 3'–[^{2}H]–CDP, at lower reaction pH (6.6) or in deuterated buffer. The results have also revealed a burst of dCDP

suggesting that a step or steps subsequent to dCDP formation is rate–limiting in turnover. This burst phase corresponds to a conformational change that precedes radical transfer and occurs with a k_{obs} of 4–16 s^{-1}. The model that has emerged from these kinetic studies of wt RNR is shown in Figure 8–2. The K_d for CDP[14] and dCDP[15] have previously been measured. Pre–steady state kinetics have determined a rate constant of 4–17 s^{-1} for a physical step that precedes radical transfer, as noted above. This step has been labeled 2–10 s^{-1} in Figure 8–2. The remainder of the rate constants in Figure 8–2 were obtained from kinetic modeling of the catalytic cycle and have been chosen to recapitulate the lack of observable intermediates during forward or reverse radical propagation. This has required fast C_{439}• formation (≥200 s^{-1}), fast active site chemistry (500 s^{-1}) and even faster reverse radical transfer (≥1000 s^{-1}). The kinetic model in Figure 8–2 provides a frame work for the models that will be introduced in the current Chapter.

If a step during radical transfer has in fact become rate–limiting, as a result of F_nY insertion in our F_nY–β2s (Chapter 7), then we may expect buildup of an intermediate during this process, which could be examined by stopped flow (SF) UV–vis or rapid freeze quench (RFQ) EPR spectroscopies. In addition, rapid chemical quench (RCQ) studies would be useful to show

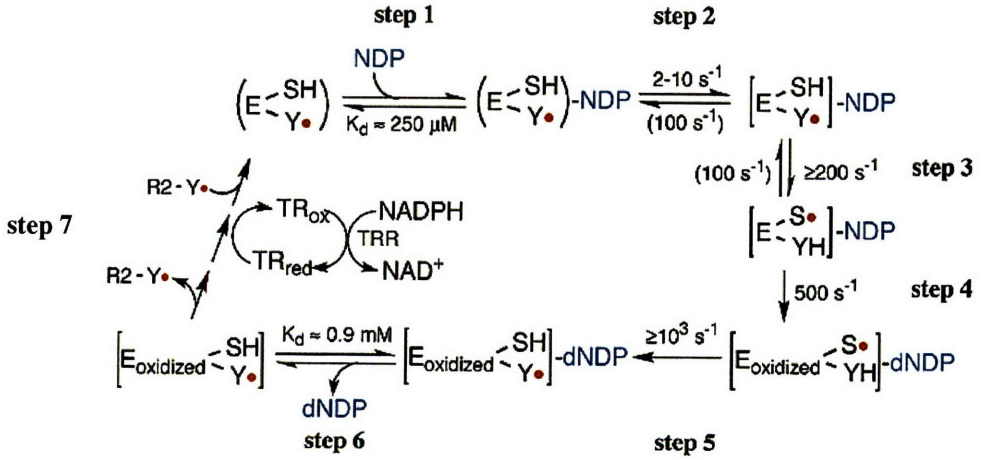

Figure 8–2. Kinetic model for the reaction of wt RNR. The K_d for CDP (step 1) and dCDP (step 6), the conformational change preceding radical transfer (step 2) and re–reduction of active site disulfides (step 7) have previously been measured. The rate constants for forward radical transfer (step 3), active site chemistry (step 4) and reverse radical transfer (step 5) are modeled based on results by Ge *et al.*[13]

whether the intermediate occurs during forward or reverse radical transfer. If it occurs during forward radical transfer, then we may expect to see linear formation of dCDP, rather than a burst. If, however, it occurs during reverse radical propagation, we would still expect to see a burst of dCDP. A major complication of the kinetics with F_nY–β2s is that the expressed protein ligation method used to generate the mutants requires 2 mutations in addition to the Y→F_nY change: $V_{353}G$ and $S_{354}C$.[16,17] Steady state assays have shown that the latter does not affect the specific activity, however, the former results in a 3–4× lower activity. As will be shown, this affects the rate constant for the conformational change that gates radical transfer and thus the likelihood of an intermediate buildup during this process.

The results in this Chapter show that no intermediates are observed by SF UV–vis or RFQ EPR spectroscopies in the reaction of 2,3,5–F_3Y–β2 with wt α2, CDP and ATP at high pH, where radical transfer is proposed to be rate–limiting. Kinetic simulations show that forward or forward and reverse radical transfer may be slow in turnover without generating a build–up of intermediates. RCQ experiments are in line with this model, in that no burst of dCDP is observed, which is predicted by the simulations. Most convincingly, in experiments with NH_2Y–α2s and 2,3,5–F_3Y–β2, the pre–steady state pH rate profile for NH_2Y• formation is similar to the steady state pH rate profile of 2,3,5–F_3Y–β2 for dCDP production (Chapter 7). This holds for $Y_{730}NH_2Y$–α2 and $Y_{731}NH_2Y$–α2. These results strongly suggest that our interpretation of the results in Chapter 7 has been correct. Substitution of F_nYs into the radical transfer pathway provides the required change in reduction potential to slow hole migration. However, the slow conformational change that precedes radical transfer and rapid reformation of Y_{122}• avoid build–up of any intermediates.

MATERIALS AND METHODS

Materials. [2–^{14}C]–CDP (50 μCi/mL) was purchased from Moravek, calf–intestine alkaline phosphatase (20 U/μL) was obtained from Roche. *E. coli* thioredoxin (TR, 40 U/mg) and TR reductase (TRR, 1800 U/mg) were isolated as previously described. 2–[N–morpholino]–ethanesulphonic acid (Mes), N–2–hydroxethylpiperazine–N'–2–ethanesulphonic acid (Hepes), N–[Tris(hydroxylmethyl)methyl]–3–aminopropanesulfonic acid (Taps) 2–[cyclohexylamino]–ethanesulphonic acid (Ches) and Emusifier–Safe scintillation liquid were obtained from EMD Bioscience.

Semisynthesis of F_nY–β2 and F_nY–ββ'. Growth and expression of β2–intein–CBD, ligation to F_nY–22mer and separation of F_nY–β2 from F_nY–ββ' using MonoQ chromatography were carried out as detailed in Chapter 7.

Growth, expression and purification of His_6–$V_{353}G/S_{354}C$–β2. Growth and expression of His_6–$V_{353}G/S_{354}C$–β2 was carried out on a 10 L scale as previously described (Chapter 2). This procedure yields 3 g of wet cell paste per L culture. Purification using Ni–NTA chromatography was carried out as reported yielding 20 mg of pure His_6–$V_{353}G/S_{354}C$–β2 with 1.1 Y_{122}• per dimer by the dropline procedure.

Monitoring dCDP formation by RCQ studies. RCQ studies were carried out on a KinTek Model RQF–3 Chemical Quench Flow instrument equipped with a Lauda RM6 circulating water bath. All experiments were carried out at 25 °C by mixing pre–reduced α2, β2 variant and TRR in syringe A in a 1:1 ratio with TR, NADPH, ATP and [2–^{14}C]–CDP (12600 or 14100 cpm/nmol) from syringe B. In all experiments, the final concentrations were 10 μM α2, 10 μM β2 variant, 1 mM [2–^{14}C]–CDP, 3 mM ATP, 60 μM TR, 1.2 μM TRR and 3 mM NADPH. Reactions were carried out at in assay buffer (50 mM Goods buffer, 15 mM $MgSO_4$, 1 mM EDTA) at pH 6.8 with Mes, pH 7.6 with Hepes or pH 8.4 with Taps (see Chapter 7). The zero time point was generated by replacing the contents of syringe A with buffer. Triplicate runs were performed for each time point in a randomized fashion. For each time point, 28 μL from

each syringe were mixed, allowed to react for a defined time period, ranging from 50 ms to 60 s, and quenched by combining with 198 μL of 2 % perchloric acid. After quenching, the sample was briefly spun down in a centrifuge and the reaction mixture neutralized to pH 7.5 by addition of 150 μL of 0.5 N KOH. Samples were maintained on ice until completion of the entire time course. At that point, the samples were incubated at −20°C overnight to allow for complete precipitation of potassium perchlorate. Each sample was then thawed on ice, spun down in a table top centrifuge, transferred to a new eppendorf tube and combined with calf intestine alkaline phosphatase (20 U) and carrier deoxycytidine (150 nmol) in 120 mM Tris, 0.24 mM EDTA, pH 8.5. The mixture was incubated at 37°C for 2–2.5 h. For each sample, cytidine was separted from deoxycytidine on a Dowex−1 borate column according to the procedure of Steeper and Steuart. The amount of [^{14}C]–deoxycytidine was then quantitated on a Beckman LS 6500 Scintillation Counter by mixing 1.8 mL of the 8 mL eluant (from the Dowex−1 borate column) with 10 mL of Emulsifier–Safe scintillation fluid.

Data analysis of RCQ experiments. Curve fitting to linear and lag phase functions was carried out with KaleidaGraph Software. Observed lag phases were fit to Eq. 8–1 using DynaFit or KaleidaGraph, where $dCDP_t$ is the nmol of product formed as a function of time, V_{cat} is the steady state rate (nmol/s), t is time, and k_{lag} is the lag phase rate constant (s^{-1}).[18]

$$dCDP_t = V_{cat}\left\{t - \frac{1}{k_{lag}} \times [1-\exp^{(-k_{lag} \times t)}]\right\} \qquad (8-1)$$

Generation of apo Y–β2, 2,3,5–F_3Y–β2 or 2,3,5–F_3Y–ββ' with lithium 8–hydroxy-quinoline–6–sulfonate. The apo β2 variant was generated as described in Chapter 2 according to a modification of the procedure reported by Atkin et al.[19] Briefly, a solution of 2.5 mL of β2 variant (~20 mg, 90 μM) was dialyzed against 500 mL of chelator solution consisiting of 1 M imidazole, 30 mM NH_2OH, 50 mM 8–hydroxyquinoline–6–sulfonate (pH 7.0) in a 3 mL Slide–a–lyzer cassette for 3 h. The chelator was then removed by dialysis against 4 L Hepes buffer (50 mM Hepes, 5 % glycerol, pH 7.6) for 3 h and further by desalting on a Sephadex

G–25 column (1.5 × 23, 40 mL), which had been equilibrated in Hepes buffer. This procedure delivers apo β2 in 80–95 % yield. The concentration of apo β2 or ββ' variant was determined using $\varepsilon_{280\,nm} = 120\ mM^{-1}cm^{-1}$.

Reconstitution of apo F_nY–β2. Apo β2 variants were reconstituted as described in detail in Chapter 2. This procedure yields radical contents of ~1.2 Y_{122}•/β2 as determined by the dropline procedure (see Chapter 2).

Spectrophotometric and radioactive RNR Assay. RNR activity assays were performed as described in detail in Chapter 2. The final concentration of α2 and β2 variant in these assays were 3 μM each. The specific activity of [2–^{14}C]–CDP was 3800 cpm/nmol.

Single wavelength and diode array SF UV–vis spectroscopy. SF UV–vis experiments were carried out at 25°C as described in detail in Chapter 2. Single wavelength kinetics experiments utilized PMT detection at 410 nm (λ_{max} of Y_{122}• with $\varepsilon = 3700\ M^{-1}cm^{-1}$), 510 nm ($\lambda_{max}$ of W• with $\varepsilon = 2200\ M^{-1}cm^{-1}$) and 560 nm ($\lambda_{max}$ of $WH^{\bullet+}$ with $\varepsilon = 3000\ M^{-1}cm^{-1}$).[20] Typically, pre–reduced α2 (50–70 μM) and ATP (6 mM) in one syringe were mixed with 2,3,5–F_3Y–β2 or 2,3,5–F_3Y–ββ' (50–70 μM) and CDP (2 mM) in a 1:1 ratio in 50 mM Taps, 15 mM $MgSO_4$, 1 mM EDTA, pH 8.4. Time courses shown are the average of at least 5 individual traces. Diode array SF UV–vis spectroscopy was carried out with an Applied Photophsysics PDA.1 Photodiode Array detector. The concentration of reaction components were the same as those monitored by single λ kinetics. The reaction time before each rapid scan spectrum is listed in the Figure legends. Note that the pre–reduction procedure removes the Y_{122}• of contaminating wt β2, which is present in α2 preparations.

RFQ–EPR spectroscopy. The instrument for preparation of RFQ EPR samples was described in detail in Chapter 3. Typically, pre–reduced α2 (50–70 μM) and ATP (6 mM) in one syringe were mixed in a 1:1 ratio with 2,3,5–F_3Y–β2 or 2,3,5–F_3Y–ββ' (50–70 μM) and CDP (2 mM) from a second syringe in 50 mM Taps, 15 mM $MgSO_4$, 1 mM EDTA, pH 8.4. Assembly, operation and quenching of samples were performed as described in Chpater 3. EPR spectra were recorded at the Department of Chemistry Instrumentation Facility on a Bruker

ESP–300 X–band (9.4 GHz) spectrometer. Spectra at 77 K were recorded with a quartz finger dewar filled with liquid N_2; spectra at 15 or 20 K were acquired with an Oxford liquid helium cryostat and an Oxford ITC 503 temperature controller. Unless noted otherwise, EPR parameters were as follows: Power = 50 μW, modulation amplitude = 1.5 G, modulation frequency = 100 kHz, time constant = 5.12 ms and scan time = 41.9 s.

Kinetic simulations. Kinetc Simulations were carried out using KinSim, available free of charge from the web (http://www.biochem.wustl.edu/cflab/message.html). The kinetic schemes used for kinetic modeling are shown in Figures 8–14 to 8–18.

pH rate profile for NH_2Y• formation in the reaction of 2,3,5–F_3Y–β2 with NH_2Y–α2s and CDP/ATP monitored by SF UV–vis spectroscopy. NH_2Y–α2 was prepared and pre–reduced as detailed in Chapter 4. In all experiments, pre–reduced NH_2Y–α2 and ATP were mixed with 2,3,5–F_3Y–β2 and CDP to yield final concentrations of 4 μM, 3 mM, 4 μM and 1 mM, respectively. Single wavelength kinetics were monitored using PMT detection at 320 nm (λ_{max} of NH_2Y_{731}• with ε = 11000 $M^{-1}cm^{-1}$) or 325 nm (λ_{max} of NH_2Y_{730}• with ε = 10500 $M^{-1}cm^{-1}$). The temperature was maintained at 25°C with a Lauda RE106 circulating water bath. Reactions were carried out in Mes (pH 6.5–7), Hepes (pH 7–8), Taps (pH 8–8.8) or Ches (pH 8.8–9.2) buffer, which consisted of 50 mM Goods Buffer, 15 mM $MgSO_4$, 1 mM EDTA adjusted to the desired pH. Syringes and reaction lines were equilibrated in the desired buffer prior to the experiment. At each pH, a minimum of 5 traces were averaged and analyzed using OriginPro Software.

RESULTS

Rationale for pre–steady state experiments. Kinetic investigations of the radical initiation pathway have shown that the aromatic amino acid radicals, which carry the oxidizing equivalents from the Y_{122}• in β2 into the active site of α2, are masked by a conformational change. Thus, examination of the mechanism of long–range hole propagation requires that the rate constant for this process is diminished relative to the conformational step. The results in Chapter 7 indicate that the F_nYs inserted site–specifically at residue 356 may provide the necessary change in the driving force by increasing the reduction potential to alter the rate–determining step. However, direct experimental validation that radical propagation has become rate–determining in turnover has been missing.

Previous pre–steady state examination of wt RNR has shown that production of dCDP in the first turnover is limited by a conformational change that precedes radical transfer. Recently, we have, for the first time, directly monitored this conformational change by measuring the rate constant for DOPA• and NH_2Y• formation in DOPA–β2 and NH_2Y–α2, respectively (Chapters 2 & 4). In wt RNR, at low concentrations (<3 μM), the conformational step remains rate–limiting during multiple turnovers. At high concentrations of RNR (~15 μM), however, re–reduction or a step associated with re–reduction has been proposed to become rate–limiting under multiple turnover conditions. Importantly, at low and high concentrations of RNR, a burst of dCDP formation is observed in the first turnover, with rate constants of 4.4–16.5 s^{-1} and amplitudes of 1.4–2.2 dCDP per α2 or 1.2–1.8 dCDP per Y_{122}•.[13]

To test the prediction, that radical transfer becomes rate–determining with F_nY–β2s, pre–steady state experiments have been carried out with 2,3,5–F_3Y–β2 and F_4Y–β2. Radical transfer could be rate–determining in the forward or reverse PCET processes. If reverse radical transfer has become rate–limiting, then a burst of dCDP would be expected in the first turnover with a rate constant similar to the conformational step and an amplitude similar to those with wt RNR. If, however, forward radical transfer has become rate–determining, then kinetic

simulations show that linear or lag kinetics in dCDP formation would be expected (see below). This also holds for the case, in which forward and reverse radical transfer are rate–determining. The mutations required for semisynthesis of β2, result in a 3–4× diminishment of k_{cat} relative to wt RNR. It is unclear which elementary step in the kinetics of RNR is affected by these mutations.

Pre–steady state analysis of His_6–$V_{353}G/S_{354}C$–β2 by RCQ. To examine the kinetics of dCDP formation, RCQ experiments have been performed. As a control for RCQ experiments, His_6–$V_{353}G/S_{354}C$–β2 was examined first. This variant is prepared by recombinant expression and has a specific activity that is 3–4× lower than that of wt β2. A time course of dCDP formation with this variant is shown in Figure 8–3 at pH 7.6 and 6.8. Surprisingly, the burst of dCDP formation observed with wt RNR, is absent in this double mutant. Qualitatively, this appears to be consistent with a slower rate constant for the conformational change that precedes radical transfer. Thus, the mutations required for semisynthesis of β2 may in fact have inadvertently decreased the likelihood of observing intermediates during radical transfer, as formation of potential radical intermediates is now 3–4× fold slower than in wt RNR.

At pH 6.8, the data can be fit to a linear rate of dCDP formation indicating that the conformational change is slow during multiple turnover, even at these high protein concentrations (Figure 8–3A). This result contrasts with those obtained with wt RNR, where the conformational step is slow during multiple turnover only at low [RNR] and re–reduction or a process associated with re–reduction is likely rate–limiting at high [RNR]. A magnified view of the first 3 s shows that a linear fit describes the data well (Figure 8–3B). The specific activity obtained from this experiment, 380 nmol/min•mg, agrees well with that from steady state nucleotide reduction assays monitoring [^{14}C]–dCDP. Wt RNR has a specific activity of ~1600 nmol/min•mg at this pH.

At pH 7.6, a lag phase appears to precede dCDP formation in the first turnover (Figure 8–3C), which is more easily discerned in a blow–up of the initial 3 s of the reaction (Figure 8–3D). Analysis of this trace indicates that a single lag phase, with a rate constant of 0.21 s^{-1}, is

sufficient to describe the data. The nature of this lag phase is at present not understood. It may be related to reorganization of $\alpha 2$, $\beta 2$ or $\alpha 2/\beta 2$ into an active form. The lag phase is followed by a steady state nucleotide reduction rate of 600 nmol/min•mg, which is similar to activities obtained by steady state assays. Wt RNR has a specific activity of 3500 nmol/min•mg at this pH.

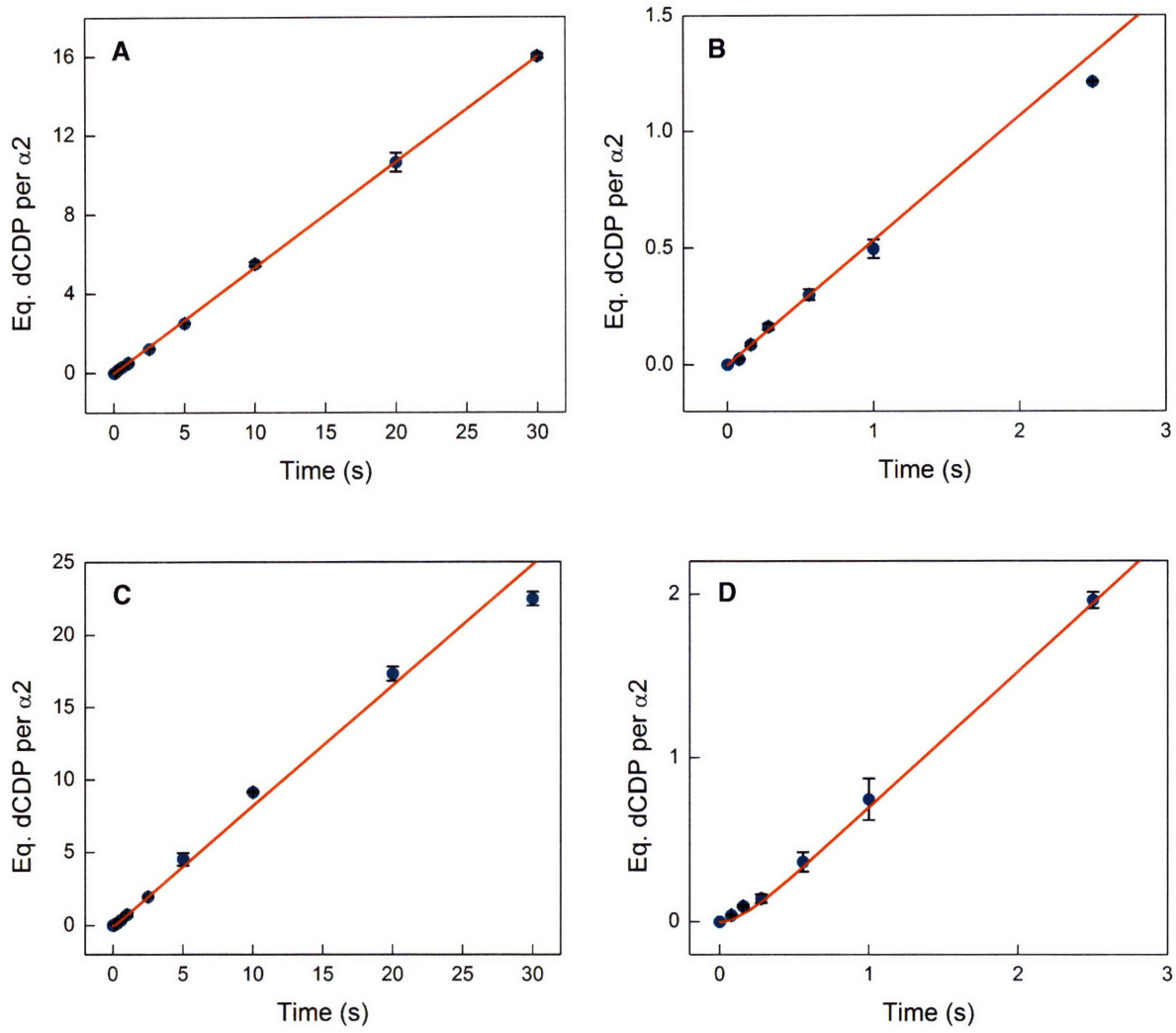

Figure 8–3. RCQ analysis of [^{14}C]–dCDP formation with His_6–$V_{353}G/S_{354}C$–β2 (1.1 Y_{122}•/dimer). Reactions were carried out at pH 6.8 (A, B) and pH 7.6 (C, D). The experimental set up and the final concentration of each component were described in the Methods Section. (A) A background count of 180 cpm, which was determined from triplicate reactions of syringe B against buffer (see Methods), was subtracted from each time point. The counts for the first three time points were an average of ~100 cpm above background. The red line describes a linear fit to the data giving a specific activity of 380 ± 60 nmol/min•mg. (B) Magnified view of the initial 3 s of the reaction at pH 6.8. (C) A background of 250 cpm, determined in a similar fashion as in (A), was subtracted from each time point. The counts for the first three time points were an average of ~120 cpm above background. The data have been fit to Eq. 8–1 (red line) giving a lag phase of 0.21 ± 0.04 s^{-1} and linear rate of 600 ± 120 nmol/min•mg. (D) Magnified view of the initial 3 s of the reaction at pH 7.6.

Pre–steady state analysis of F_nY–β2s by RCQ. Next, we examined pre–steady state dCDP formation with intein wt β2, Y–β2, which was made by the same procedure as F_nY–β2s (Figure 8–4). This construct contains 0.3 Y_{122}• per Y–β2, similar to the radical content of F_nY–β2s. The data can be fit with a single lag phase of 0.2 s^{-1} followed by a steady state turnover of 173 nmol/min•mg. It is important to note that a burst of dCDP would be observable, even with the low radical content of semisynthetic β2s. With the specific activity of dCDP used in these experiments, a burst of dCDP corresponding to 1.2 dCDP per Y_{122}• would yield a count of 600 cpm, which is 3× above background levels of dCDP (~200 cpm).

Similar experiments were carried out with 2,3,5–F_3Y–β2 at pH 6.8 and 8.4, and with F_4Y–β2 at pH 6.8 and 7.6. In case of 2,3,5–F_3Y–β2, the change in pH from 6.8 to 8.4 is proposed to correspond with a change in the rate–determining step in turnover. The pH rate profiles in Chapter 7 indicate that at pH 6.8, the conformational change preceding radical transfer is the slowest step in turnover, whereas at pH 8.4, radical transfer itself has become

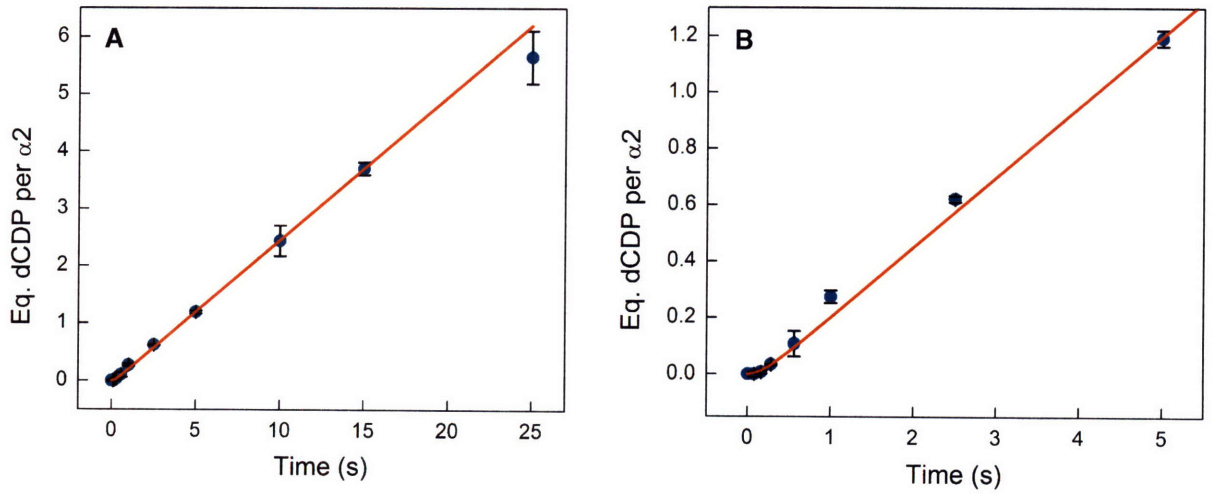

Figure 8–4. RCQ analysis of [^{14}C]–dCDP formation with Y–β2 (0.35 Y_{122}•/dimer) at pH 6.8. (A) The experimental set up and the final concentration of each component were described in the Methods Sections. A background count of 130 cpm which was determined from triplicate reactions of syringe B against buffer (see Methods), was subtracted from each time point. The counts for the first three time points were an average of ~45 cpm above background. The red line describes a fit to Eq. 8–1 yielding a lag phase of 0.20 ± 0.03 s^{-1} followed by a linear phase at 173 ± 26 nmol/min•mg. (B) Magnified view of the initial 5 s.

rate–determining. Y–β2 and 2,3,5–F_3Y–β2 have specific activities of 200 and 205 nmol/min•mg at pH 6.8 and 390 and 150 nmol/min•mg at pH 8.4, respectively (Chapter 7).

The pre–steady state formation of dCDP with 2,3,5–F_3Y–β2 is shown in Figure 8–5. At pH 6.8, linear dCDP formation is observed with a specific activity of 254 nmol/min•mg, similar to activities measured in Chapter 7 (Figure 8–5A/B). At pH 8.4, a single lag phase, which is clearly discernibly in a magnified view of the initial 5 s of the reaction, with a rate constant of 0.29 s^{-1}, precedes steady state formation of dCDP, which occurs at 221 nmol/min•mg (Figure 8–5C/D). The specific activity of 2,3,5–F_3Y–β2 at pH 8.4 is significantly higher than expected based on results in Chapter 7. This may be due to small differences in the reaction pH. In the pH range of 8.2–8.5, the activity of 2,3,5–F_3Y–β2 is strongly dependent on the pH. The specific activities at pH 8.2 and 8.5 are 270 and 40 nmol/min•mg, indicating that even small changes in the reaction pH could have a marked effect on activity.

With F_4Y–β2, a drastic drop of activity was observed relative to Y–β2, throughout the pH range (Chapter 7). This is consistent with the large reduction potential difference of 130–270 mV between F_4Y and Y between pH 6.5 and 9.0. Therefore, we proposed that radical transfer was rate–determining throughout the pH range. Consequently, with F_4Y–β2, similar pre–steady state dCDP formation profiles are expected at pH 6.8 and 7.6. However, experiments with F_4Y–β2 are complicated by the very low activity of this construct. In chapter 7, specific activities of 26 and 22 nmol/min•mg were measured for F_4Y–β2 at pH 6.8 and 7.6, respectively, at final concentrations of 3 μM α2/F_4Y–β2. Pre–steady state formation of dCDP at pH 6.8 is shown in Figure 8–6A. This data set suffers from a low signal/noise, because the data points up to 4 s have similar counts as the zero time point, due to low specific activity of this variant. To illustrate the low signal/noise, counts, rather than conversion of the data to equivalents of α2, have been plotted. A linear fit seems to describe the data best, which is shown in Figure 8–6A/B and yields a specific activity of 16 nmol/min•mg. Fitting the data with one or two lag phases leads to a lower R^2 correlation value between the data and the fit. Additional experiments, with higher radical content in F_4Y–β2 are required to illuminate the pre–steady state kinetics

with this mutant. At pH 7.6, the background (i.e. t=0) counts were low and lag phase kinetics are observed (Figure 8–6C/D). The fit to Eq. 8–1 yields a lag phase rate constant of 1.6 s^{-1} and a specific activity of 24 nmol/min•mg, similar to the activity measured in chapter 7.

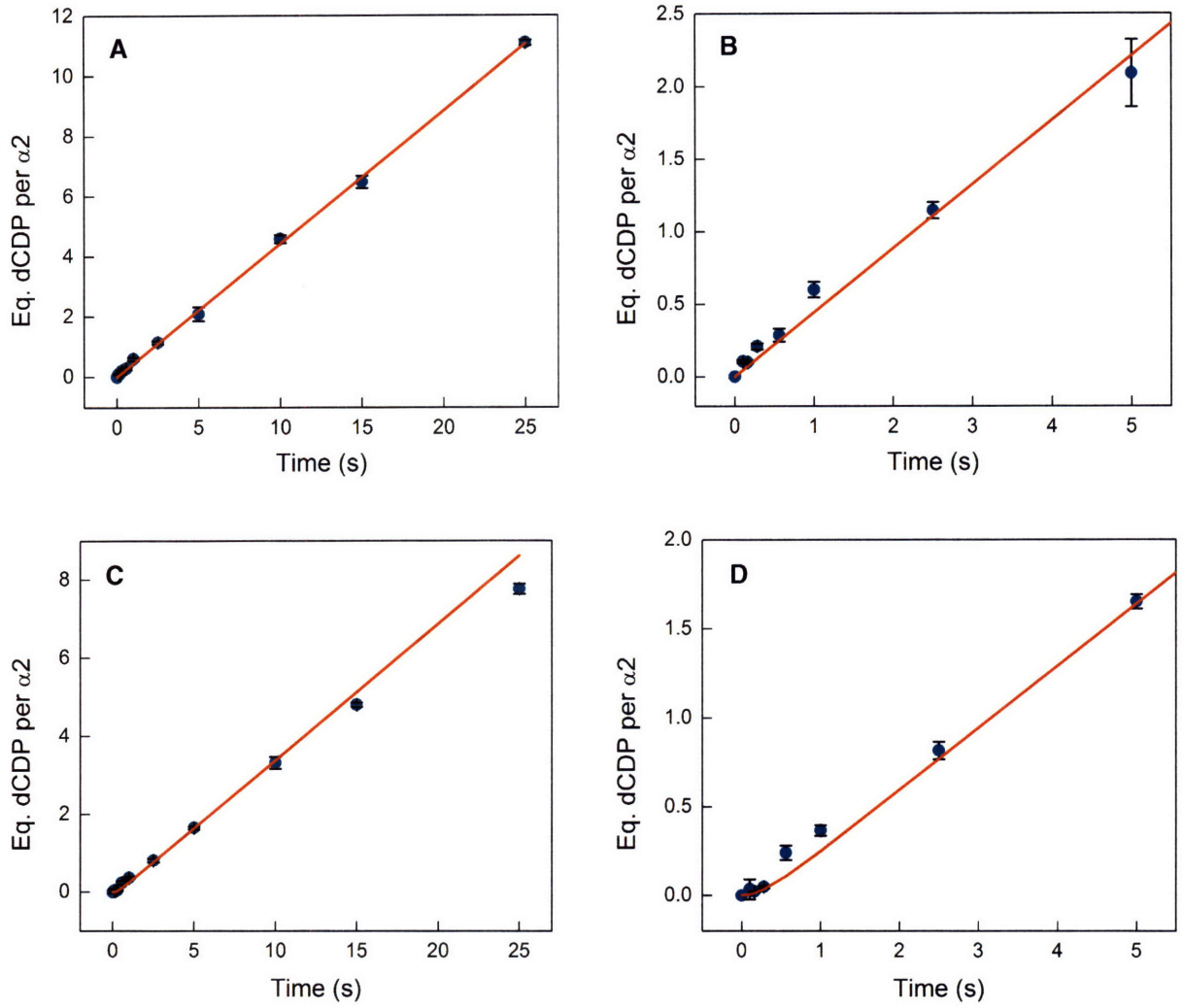

Figure 8–5. RCQ analysis of [^{14}C]–dCDP formation with 2,3,5–F_3Y–β2 (0.4 Y_{122}•/dimer). Reactions were carried out at pH 6.8 (A, B) and 8.4 (C, D). The experimental set up and the final concentration of each component were described in the Methods Sections. (A) A background count of 75 cpm, which was determined from triplicate reactions of syringe B against buffer (see Methods), was subtracted from each time point. The counts for the first three time points were an average of ~70 cpm above background. The red line describes a linear fit to the data giving a specific activity of 254 ± 23 nmol/min•mg. (B) Magnified view of the initial 3 s of the reaction at pH 6.8. (C) A background of 310 cpm, determined in a similar fashion as in (A), was subtracted from each time point. The counts for the first three time points were an average of ~80 cpm above background. The red line is a fit to Eq. 8–1 yielding a lag phase of 0.29 ± 0.06 s^{-1} and a linear phase of 221 ± 44 nmol/min•mg. (D) Magnified views of the initial 5 s at pH 8.4.

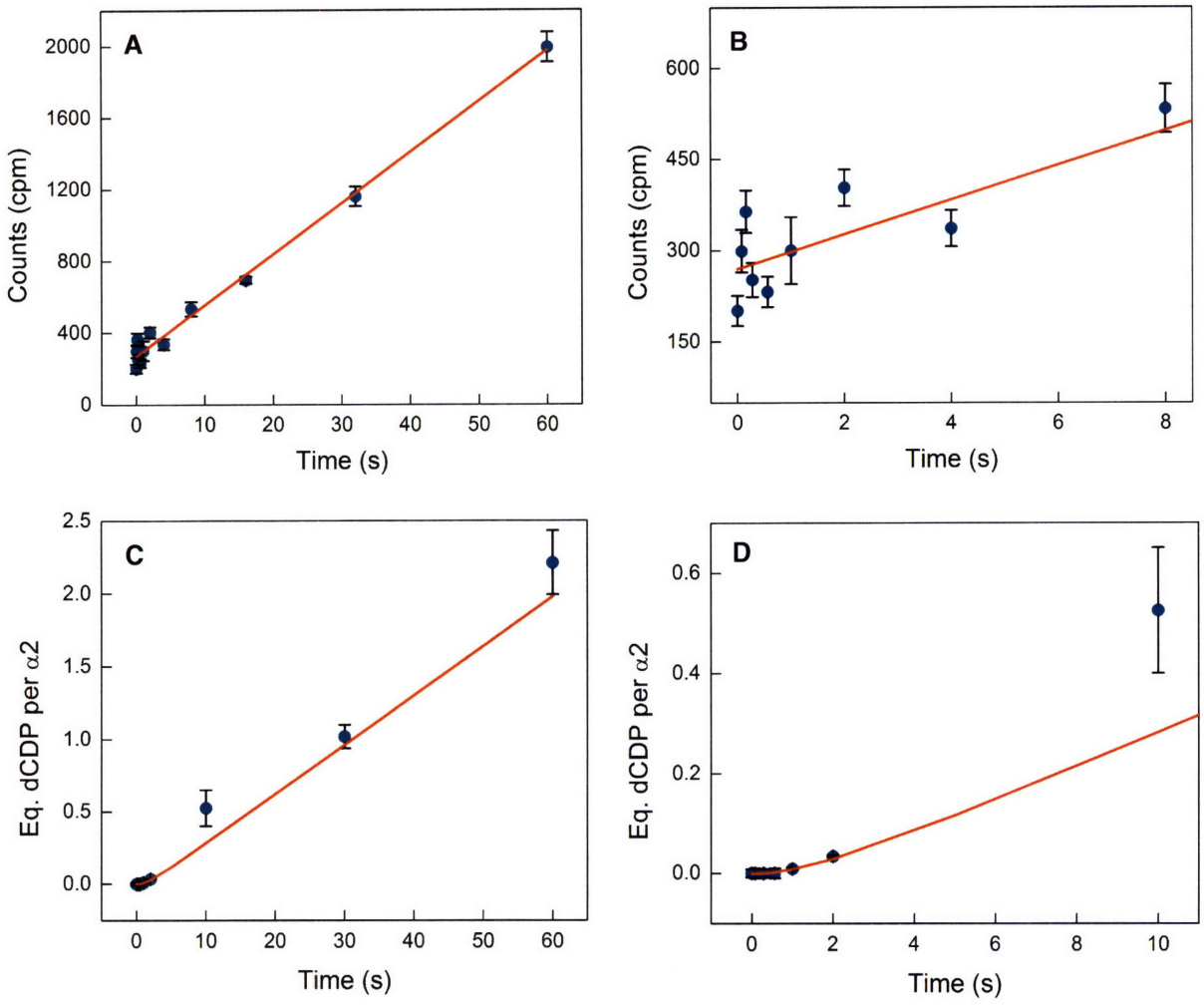

Figure 8–6. RCQ analysis of [^{14}C]–dCDP formation with F_4Y–β2 (0.37 Y_{122}•/dimer). Reactions were carried out at pH 6.8 (A, B) and 7.6 (C, D). The experimental set up and the final concentration of each component were described in the Methods Sections. (A) A background count of 170 cpm, which was determined from triplicate reactions of syringe B against buffer (see Methods), was subtracted from each time point. The counts for the first three time points were an average of ~100 cpm above background. The red line described a linear fit to the data giving a specific activity of 16 ± 5 nmol/min•mg. (B) Magnified view of the initial 8 s of the time course at pH 6.8. (C) A background of 200 cpm, determined in a similar fashion as in (A), was subtracted from each time point. The counts for the first three time points were an average of ~25 cpm above background. The red line is a fit to the data, according to Eq. 8–1, and yields a lag phase of 1.6 ± 0.4 s^{-1} and a linear phase of 24 ± 6 nmol/min•mg. (D) Magnified view of the initial 10 s of the reaction at pH 7.6.

The data from RCQ experiments with the various β2 analogues are summarized in Table 8–1. Importantly, no burst of dCDP is observed in any of these cases. In all cases linear or lag kinetics in dCDP production are observed, which is consistent with a slower conformational step prior to radical transfer. In the case of His–$V_{353}G/S_{354}C$–β2 and Y–β2, we conclude that the 3–4× lower activities observed are due to a 3–4× slower conformational gating step. This in turn, lowers the likelihood of intermediate buildup during radical transport. In the case of 2,3,5–F_3Y–β2 and F_4Y–β2, we propose that reverse radical transfer cannot be solely rate–limiting in turnover, as this would have resulted in a burst of dCDP, although kinetic simulations are required to assess this proposition (see below). Additional experiments with F_nY–β2 containing greater Y_{122}• contents at different pHs are necessary to fully examine the pre–steady state kinetics of F_nY–β2s. Nevertheless, any kinetic model must reproduce the linear or lag phase kinetics in the pre–steady state formation of dCDP with 2,3,5–F_3Y–β2 or F_4Y–β2. Kinetic models for the catalytic cycle of 2,3,5–F_3Y–β2 will be discussed below.

Table 8–1. Summary of kinetic parameters from RCQ experiments monitoring [^{14}C]–dCDP formation.

β2 Variant	pH	Lag Phase (s^{-1})	Linear Phase (nmol/min•mg)
$V_{353}G/S_{354}C$–β2	6.8	–	380 ± 80
$V_{353}G/S_{354}C$–β2	7.6	0.21 ± 0.04	600 ± 120
Y–β2	6.8	0.20 ± 0.03	173 ± 26
2,3,5–F_3Y_{356}–β2	6.8	–	254 ± 23
2,3,5–F_3Y_{356}–β2	8.4	0.29 ± 0.06	221 ± 44
F_4Y–β2	6.8	–	16 ± 5
F_4Y–β2	7.6	1.6 ± 0.4	24 ± 6

Increasing the radical content of semisynthetic F_nY–β2s. To further test the proposal that the rate–determining step shifts from a physical step to the radical transfer step with F_nY–β2s, additional pre–steady state experiments were carried out. Qualitatively, the data above are consistent with a model in which forward radical transfer is slow during turnover. Consequently, W_{48}•, the residue proposed to oxidize F_nY_{356} may build up in this process, which may be observed by SF UV–vis and RFQ EPR experiments. To maximize our chances of detecting low levels of radicals, we decided to invest some time to elevate the amount of Y_{122}• in our semisynthetic β2s.

To increase the radical content of semisynthetic β2s, the method of Atkins et al. was employed. This method failed to increase Y_{122}• levels of DOPA–β2, presumably due to participation of $DOPA_{356}$ in the in vitro reconstitution reaction. However, in the present case, with intein–generated wt β2 (Y–β2), this procedure yields 1.1–1.2 Y_{122}• per β2 with protein recoveries ranging from 80 to 95 %. The UV–vis (Figure 8–7A) and EPR spectrum (Figure 8–7B) of Y–β2, treated in this fashion, are shown. These spectra are identical to those of recombinant wt β2 indicating that the Y_{122}• and diferric center are intact.

A similar procedure was carried out with 2,3,5–F_3Y–β2 and 2,3,5–F_3Y–ββ'. UV–vis and EPR spectral analysis of the former is shown in Figure 8–7C/D. These spectra, as with Y–β2, indicate that the Y_{122}• and diferric center are intact. A similar result was obtained for 2,3,5–F_3Y–ββ' (data not shown). Accordingly, the 2,3,5–F_3Y probe does not interfere with the reconstitution reaction presumably due to the similarity of its reduction potential (0.84 V) with that of Y (0.79 V) at pH 7.6.

To ensure that the chelation/reconstitution procedure did not result in loss of nucleotide reduction activity, spectrophotometric assays were performed with semisynthetic β2s before and after application of this procedure. The results revealed that the specific activity correlates with Y_{122}• content before and after chelation/reconstitution (data not shown). In addition, SDS PAGE analysis, before and after this procedure, yields a similar result (Figure 8–8). Thus, this method increases the Y_{122}• content without affecting the nucleotide reduction ability of semisynthetic β2s.

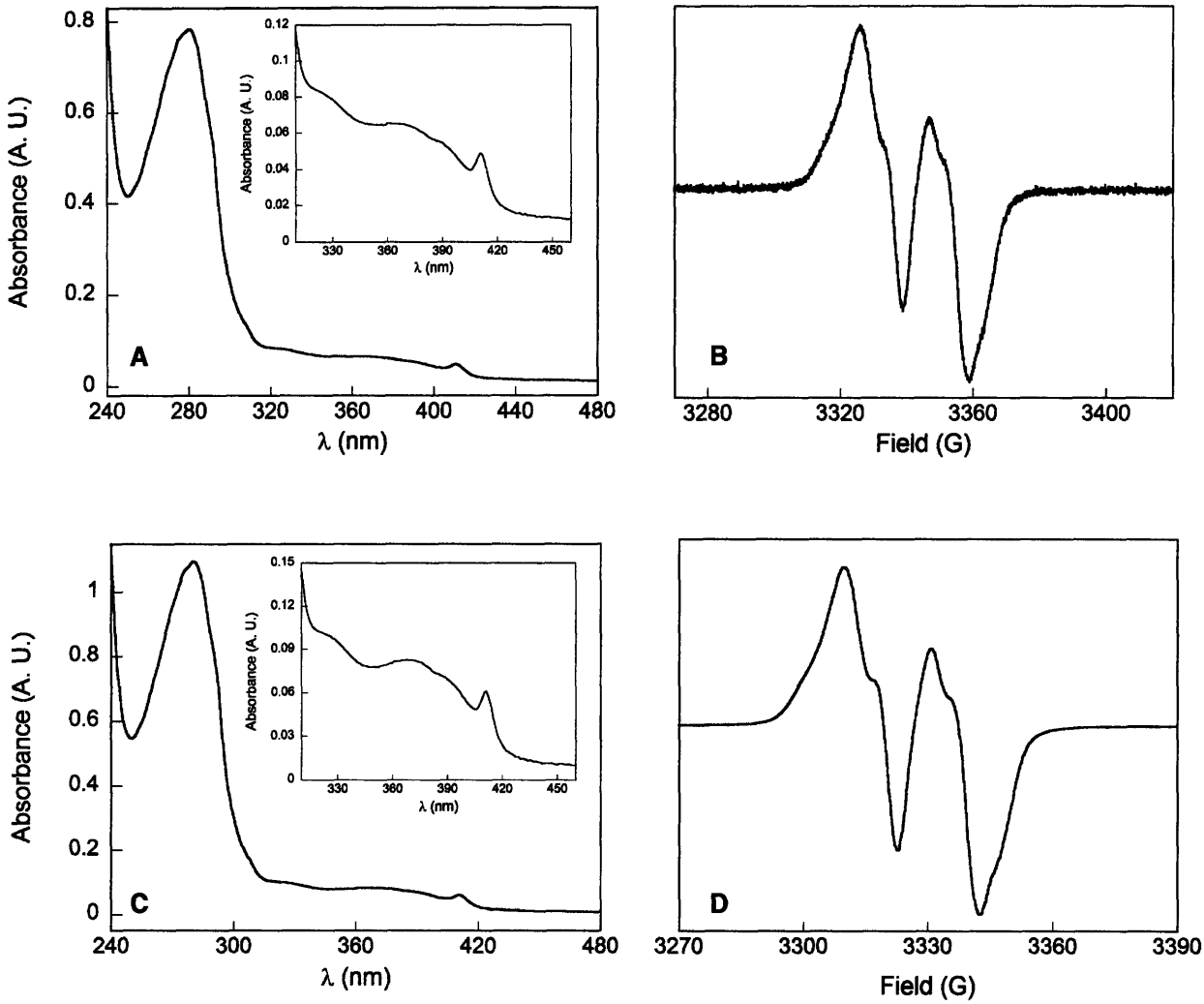

Figure 8–7. Increasing the radical content of Y–β2 and 2,3,5–F_3Y–β2. UV–vis (A) and EPR (B) spectra of Y–β2 (1.1 Y_{122}•/dimer) after the chelation/reconstitution procedure. The inset (A) is a magnified view of the features associated with the diiron Y_{122}• cluster. UV–vis (C) and EPR (D) spectra of 2,3,5–F_3Y–β2 (1.2 Y_{122}•/dimer) after the chelation/reconstitution procedure. The inset (C) shows a magnified view of the features associated with the diiron Y_{122}• cluster.

Figure 8–8. SDS PAGE analysis of 2,3,5–F_3Y–β2 and 2,3,5–F_3Y–ββ' after chelation/reconstitution. Lane 1, 4 μg of 2,3,5–F_3Y–β2; lane 2, 4 μg of 2,3,5–F_3Y–ββ'.

Diode array SF UV–vis spectroscopy with 2,3,5–F_3Y–ββ'/α2. The results in Chapter 3 revealed that semisynthetic heterodimeric DOPA–ββ' generates a DOPA• only in the presence of substrate and effector, similar to DOPA–β2. In addition, by the criteria of EPR spectroscopy, the DOPA• in DOPA–ββ' is in an environment that is very similar to that of the DOPA• in DOPA–β2. The ability to initiate radical transfer does not require the C–terminal tail in the second β–monomer. Therefore, we reasoned that heterodimeric 2,3,5–F_3Y–ββ', which is a major side product of the ligation procedure, may serve as a model for 2,3,5–F_3Y–β2, even though our sensitivity in detecting intermediates would be 2–fold lower with heterodimeric β2 based on yields of DOPA• in DOPA–ββ' vs. DOPA–β2. To optimize conditions for SF UV–vis experiments with 2,3,5–F_3Y–β2, experiments were first carried out with 2,3,5–F_3Y–ββ'. The most likely species that may build up in the pH range where radical transfer is rate–determining is $W_{48}H^{\bullet+}$ (or W_{48}•). However, the absorption profile of this species may be subject to spectral shift due to the protein environment. Therefore, diode array SF UV–vis studies were performed first.

Pre–reduced α2 and ATP were rapidly mixed with 2,3,5–F_3Y–ββ' (1.2 Y_{122}•/dimer) and CDP and a diode array spectrum was recorded at defined time intervals in the spectral range of 400–850 nm. The result is shown in Figure 8–9. Throughout the spectral range, only a minor absorbance increase is observed at 410 (Figure 8–8B) nm and ~630 nm (Figure 8–9C). No changes are observed at the wavelengths corresponding to W• or $WH^{\bullet+}$. Thus, with

2,3,5–F_3Y–ββ', at pH 8.4, where radical transfer is proposed to be rate–determining, no W• or $WH•^+$ is detectable under these experimental conditions.

Experiments were also carried out with substrate GDP and effector TTP, and with Y_{730}F–α2. However, using diode array detection, no changes were observed throughout the spectrum (data not shown).

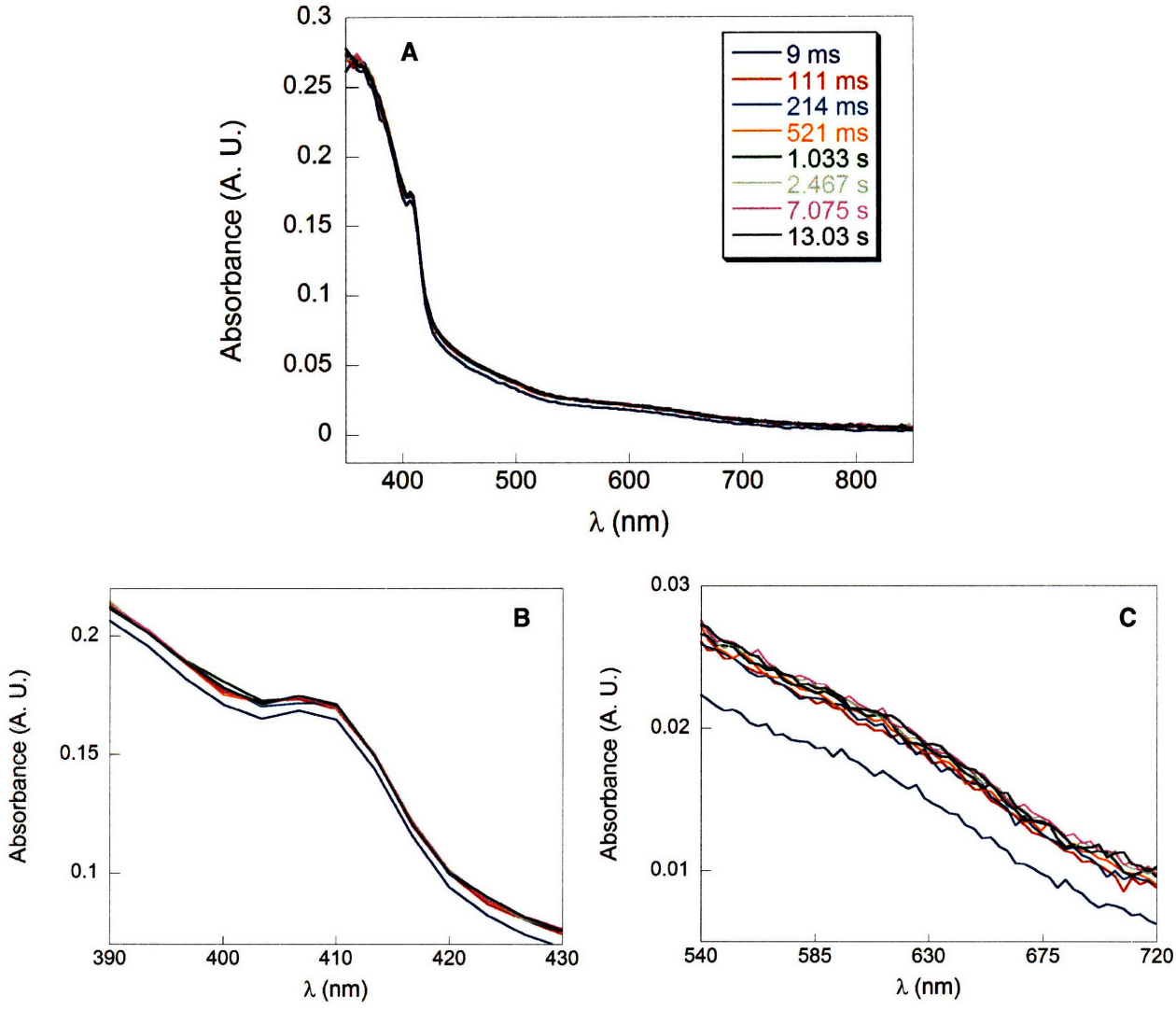

Figure 8–9. Diode Array SF UV–vis spectroscopy of 2,3,5–F_3Y–ββ'/α2 (1.2 Y_{122}•/dimer) in the presence of CDP/ATP at pH 8.4. (A) Reaction conditions were described in the Methods Section. The reaction time, at which each diode array spectrum was acquired, is indicated. (B) Magnified view of the spectral region associated with the Y_{122}•. (C) Magnified view of the changes occurring at ~630 nm.

SF UV–vis spectroscopy with 2,3,5–F_3Y–β2/α2. To test whether spectral changes would occur with 2,3,5–F_3Y–β2, similar experiments as above were carried out. In this case, 2,3,5–F_3Y–β2 containing 1.2 Y_{122}• per dimer was used. The results are presented in Figure 8–10. They show that no changes occur at 410 nm, 510 nm and 560 nm. Therefore, under these experimental conditions, no absorption features that might be associated with a W• or $WH•^+$ are apparent.

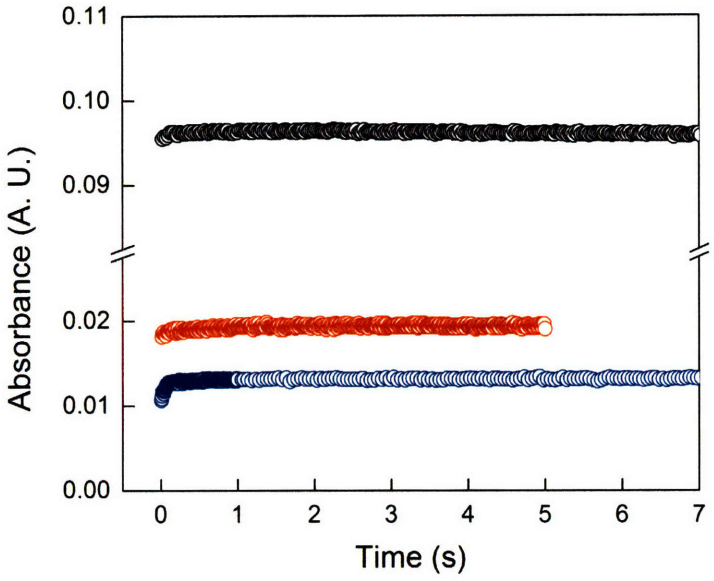

Figure 8–10. Single wavelength SF UV–vis spectroscopy of 2,3,5–F_3Y–β2/α2 (1.2 Y_{122}•/dimer) in the presence of CDP/ATP at pH 8.4. Single λ kinetics were monitored at 410 nm (black), 510 nm (red) and 560 nm (blue).

RFQ EPR spectroscopy with 2,3,5–F_3Y–β2 and 2,3,5–F_3Y–ββ'. The results above show that a W• is not detectable in the first turnover with 2,3,5–F_3Y–β2. Other than W_{48}, only the diferric center may be postulated to be involved in oxidation of residue 356. In addition, EPR is more sensitive to small changes in [W•] or [$WH•^+$], as both of these species have low extinction coefficients. Thus, to validate the results from SF UV–vis experiments and to examine whether radicals other than W_{48} build up, RFQ–EPR experiments were carried.

RFQ–EPR was carried out under conditions similar to those in the SF UV–vis experiments. In these experiments a packing factor of 0.60 ± 0.05 was routinely obtained, as measured with wt β2. Further, the dead time of the instrument was measured at 16 ± 2 ms using the NaN_3/sperm whale myoglobin test reaction (data not shown). The results with 2,3,5–F_3Y–ββ' are shown in Figure 8–11. EPR spectroscopy and spin quantitation at 77 K shows that the [Y_{122}•] does not change relative to the t=0 time point. To examine if perhaps the diiron center was involved in radical transfer via its $(Fe^{III})_2$–Fe^{II}/Fe^{III} redox couple, EPR spectra were also recorded at low temperatures. The Fe^{II}/Fe^{III} state has been generated in *E. coli* β2 before by photolysis at 77 K.[21,22] Because of its relaxation properties, the diiron center is only observed at temperatures <30 K. However, spectra collected at 20 K revealed no features other than those related to the Y_{122}•.

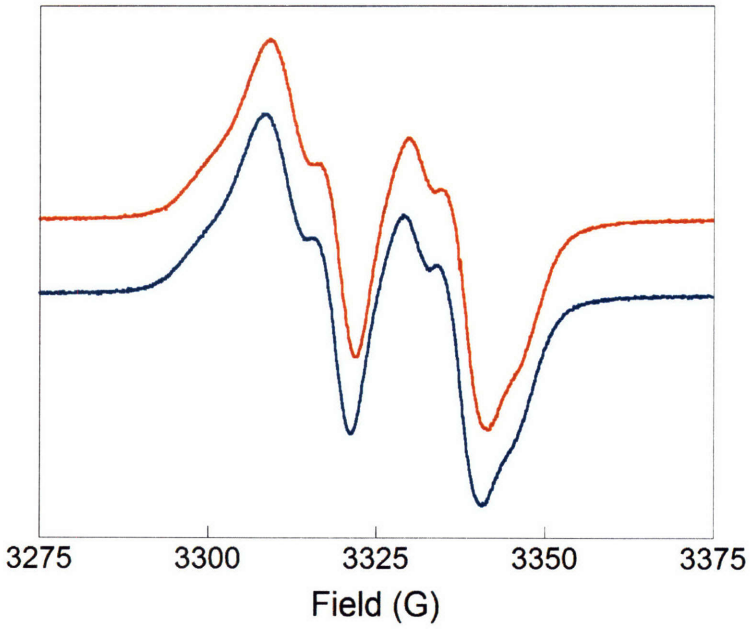

Figure 8–11. RFQ EPR spectroscopy of the reaction of 2,3,5–F_3Y–ββ' (1.2 Y_{122}•/dimer) and CDP with α2 and ATP. Contents of the syringes were mixed to yield final concentrations of 70 μM 2,3,5–F_3Y–ββ'/α2, 1 mM CDP and 3 mM ATP at pH 8.4. The reaction was quenched at 55 ms (blue) and 155 ms (red) and the EPR spectrum recorded at 77 K. Spectra at 20 K did not reveal any additional featuers (data not shown). The [spin] at these quench times remained constant relative to the zero time point.

Similar studies were performed with 2,3,5–F_3Y–β2. The results are shown in Figure 8–12. EPR spectroscopy at 77 K failed to reveal decay of Y_{122}•. No new features were observed at this temperature. EPR spectra were also acquired at 20 K and 15 K. As with 2,3,5–F_3Y–ββ', these spectra did not reveal features other than those associated with Y_{122}•.

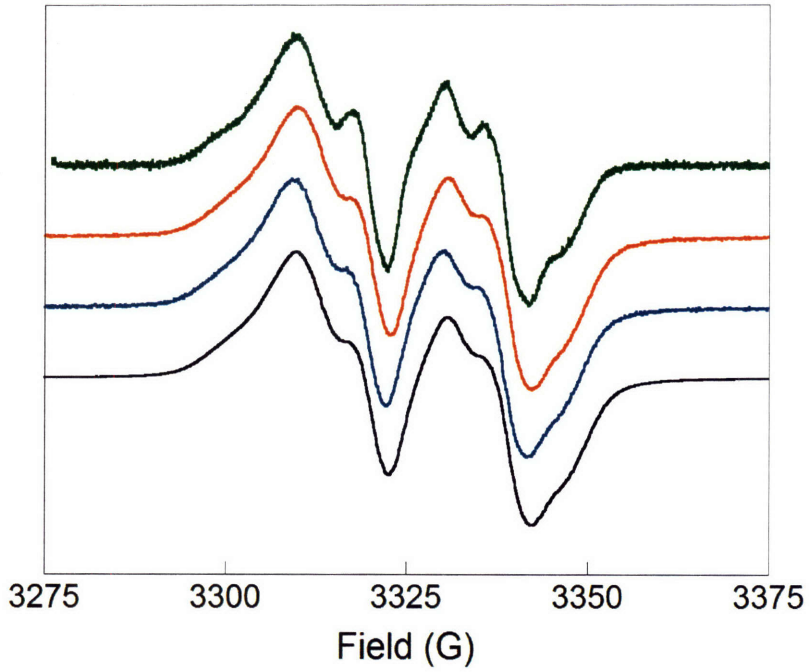

Figure 8–12. RFQ EPR spectroscopy of the reaction of 2,3,5–F_3Y–β2 (1.2 Y_{122}•/dimer) and CDP with α2 and ATP. Contents of the syringes were mixed to yield final concentrations of 60 μM 2,3,5–F_3Y–β2/α2, 1 mM CDP, and 3 mM ATP at pH 8.4. The reaction was quenched at 72 ms (black), 138 ms (blue) and 1.9 s (red) and the EPR spectrum recorded at 77 K. An EPR spectrum of the 1.9 s quench time point was also collected at 15 K (green). EPR spectra of the reactions quenched at 72 ms (black) and 138 ms (blue) were also recorded at 15 K, however, only the Y_{122}• signal was observed (not shown). Additional reactions were quenched at 28 ms and 612 ms and EPR spectra recorded at 77 K, 20 K and 15 K; however, in no case were features other than those associated with the Y_{122}• observed (data not shown). In all cases, the [spin] remained constant relative to the zero time point.

Figure 8–13 presents a comparison of the EPR spectrum 2,3,5–F_3Y–β2 and the spectrum obtained after reaction of 2,3,5–F_3Y–β2/α2 with CDP/ATP quenched after 612 ms. Comparison of these spectra indicates that a low intensity signal may be masked by the Y_{122}• profile.

Subtraction and quantitation reveals the red trace in Figure 8–13. This spectrum consists of 5 % of the total spin and may in fact represent a new species that forms in the first turnover. A similar subtracted spectrum was observed with the 1.9 s time point. However, in both cases, the difference between the observed quenched spectrum and that of 2,3,5–F_3Y–β2 may also be due to a small changes in the spectrum of Y_{122}• upon complex formation.

The RFQ–EPR experiments in this section have failed to reveal build up of any intermediates during radical propagation. Additional studies are necessary to examine whether the signal observed in Figure 8–13C is associated with a new intermediate in the pathway. A kinetic model to account for the lack of observable intermediates is necessary.

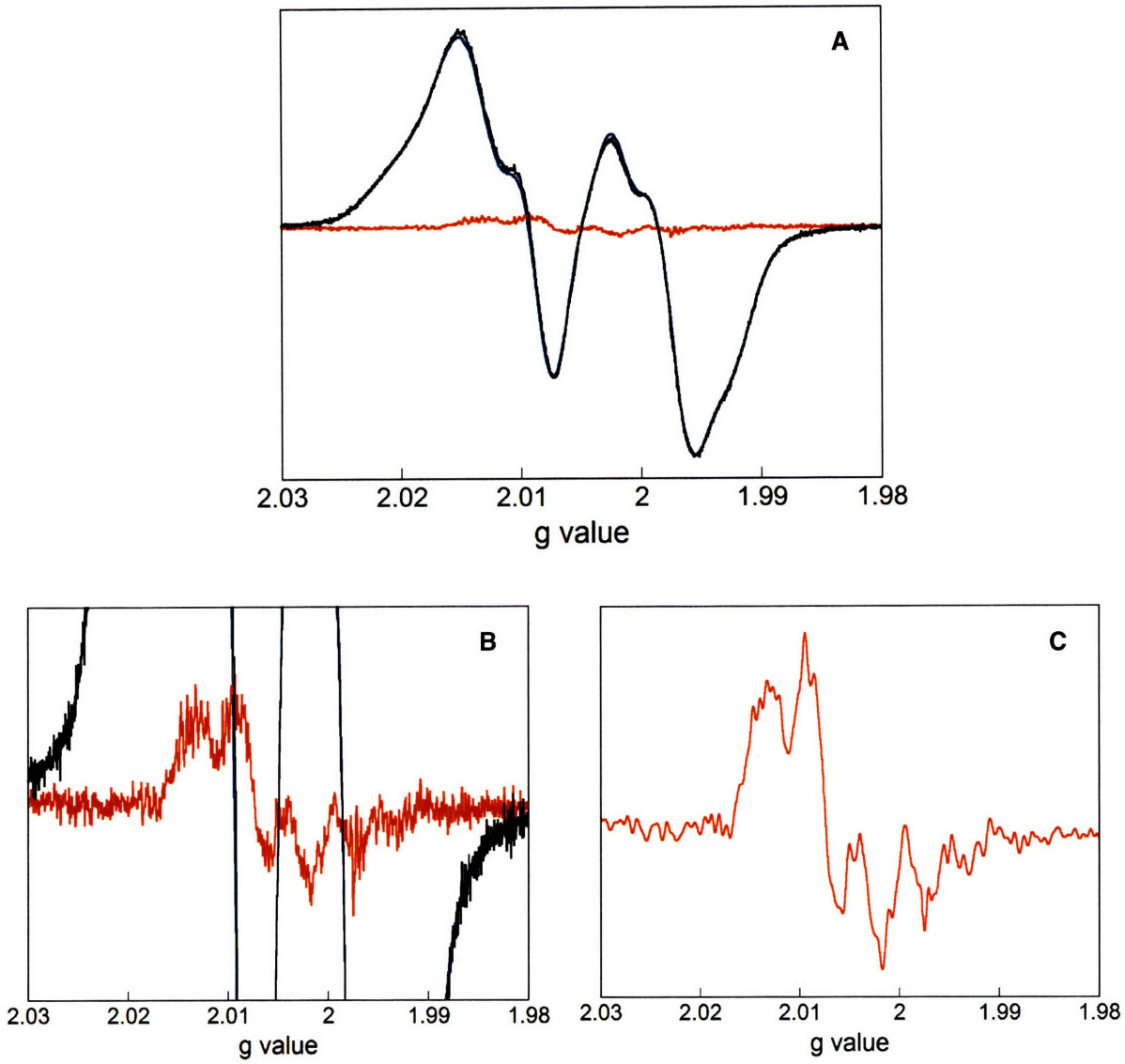

Figure 8–13. RFQ EPR spectroscopy of the reaction of 2,3,5–F_3Y–β2 (1.2 Y_{122}•/dimer) and CDP with α2 and ATP. Contents of the syringes were mixed to yield final concentrations of 60 μM 2,3,5–F_3Y–β2/α2, 1 mM CDP and 3 mM ATP at pH 8.4. The reaction was quenched at 612 ms and the EPR spectrum recorded at 77 K (black trace). (A) The spectrum was analyzed by subtracting the Y_{122}• (blue trace) yielding a signal (red trace) which accounts for 5 % of the total spin. (B) Magnified view of the resulting spectrum after subtraction of Y_{122}• spectrum. (C) Magnified view of the resulting subtraction spectrum after application of a 12–point smoothing procedure.

Rationale for kinetic simulations of the α2/F_nY–β2 catalytic cycle. The results above show that no intermediates are detected even though the rate constant for radical transfer appears to have been diminished, as we suggested in Chapter 7. To try to understand why no intermediates appear to build up in the experiments above, kinetic simulations were performed. Our aim was to see whether radical transfer could be rate–limiting during turnover without resulting in intermediate buildup, and if so, which step, forward or reverse radical transfer, would be affected. We also wanted to find a kinetic model that would reproduce the pH dependence of activity presented in Chapter 7. A suitable kinetic model should recapitulate three main experimental observations, which were delineated above: (1) As reported by DOPA–β2, in the presence of CDP/ATP, a conformational change with a k_{obs} of ~1 s^{-1} occurs prior to radical transport, (2) no intermediates build–up is observed in the pre–steady state and (3) there is no burst of dCDP formation in the pre–steady state. The models that were assessed are based on our previous kinetic models of the wt RNR reaction, which we were able to reproduce in the current study.[13]

First, we wanted to generate a model for the Y–β2 reaction. Using our previous kinetic scheme, we tested the minimal model for Y–β2 shown in Figure 8–14. This model is based on that shown in Figure 8–2, except that the K_d for CDP has been replaced with 0.1 mM (Figure 8–14A) and the rate constant for active–site chemistry has been replaced with 100 s^{-1} (Figure 8–14D). The K_d for CDP has been changed because a K_d of 0.25 mM and 0.1 mM have been measured in the presence of TTP and dATP, respectively.[14] In our reactions, we are using ATP as the allosteric regulator of CDP, however, the K_d for CDP in the presence of ATP has not been determined. In the current simulations, we prefer the K_d measured for CDP under low [dATP] because the effects of low [dATP] and high [ATP] are similar on the activity of RNR and because ATP/dATP represent the natural effectors for CDP. The rate constant for the nucleotide reduction chemistry has only been determined in the class II RNR from *L. leichmannii*. There, a k_{obs} 55 s^{-1} was determined for substrate ATP in the presence of its allosteric regulator dGTP.[23,24] We chose a nucleotide reduction rate constant of 100 s^{-1} because it is closer to the actual

measured rate constants in the class II case. The result of this kinetic scheme is shown in Figure 8–14. As observed in RCQ experiments for Y–β2, a linear production of dCDP is recapitulated by this model. Changes in concentration of other intermediates are minimal, as exemplified by the time course of C_{439}• in Figure 8–14. The k_{cat} of 0.75 s^{-1}, which results from this simulation, is similar to the measured k_{cat} for Y–β2 (~0.6 s^{-1}). This model thus reproduces the main observations with Y–β2 and allows us to examine the reaction of 2,3,5–F_3Y–β2.

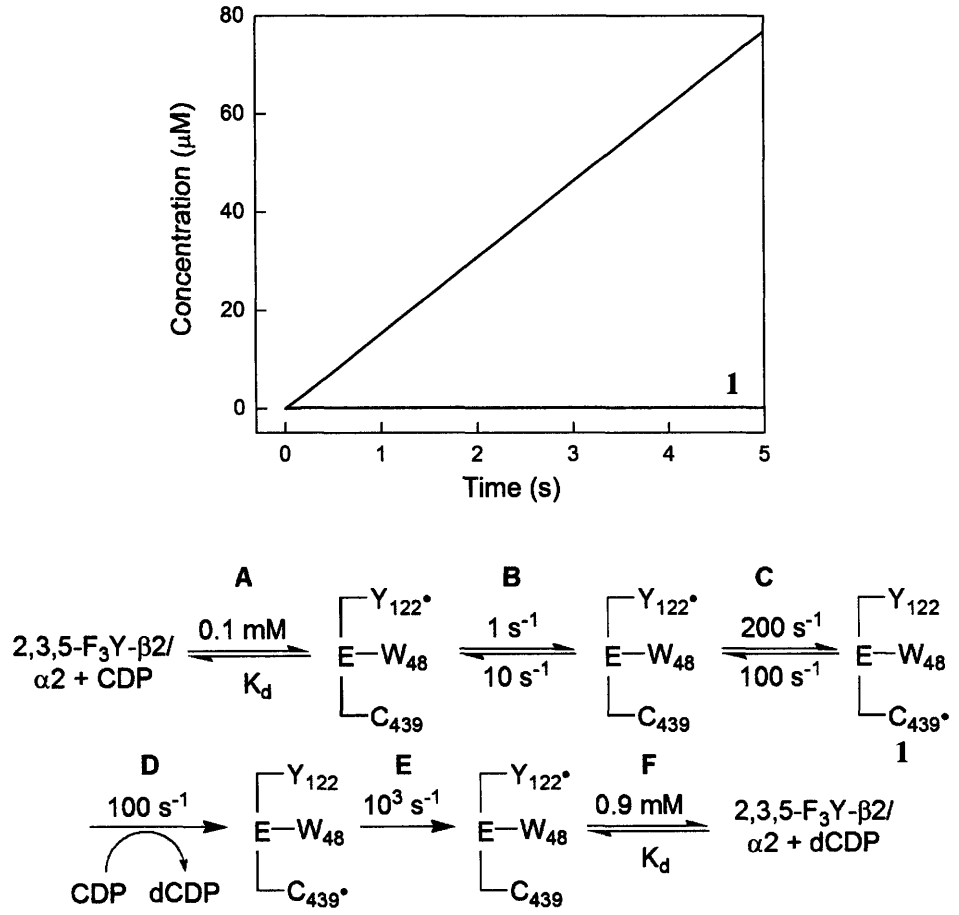

Figure 8–14. Kinetic model and result of simulation for the reaction of Y–β2. (A) Binding to CDP, see text for a K_d choice of 0.1 mM. (B) Conformational change preceding radical transfer. The forward rate constant of 1 s^{-1} is observed with DOPA–β2, the reverse rate constant has been chosen based on studies of Ge et al where a 10–fold larger reverse k was used. (C) Forward radical transfer, rate constants based on Ge et al.[13] (D) Nucleteotide reduction, see text for choice of rate constant. (E) Reverse radical transfer, rate constant based on Ge et al. (F) Dissociation of dCDP. The simulation shows a time course of dCDP formation (black) and thiyl radical formation, species **1**.

Kinetic simulations: forward or reverse radical propagation? We first wanted to test whether radical transfer can be rate–determining without leading to observable intermediates. Several models were tested. In the first model, it was assumed that reverse radical transfer is solely rate–determining. In the second model, we assumed that forward radical transfer is solely rate–determining. In the third model, we make the assumption that forward and reverse radical transfer are both partially rate–determining.

The model, in which reverse radical transfer is assumed to be solely rate–limiting is shown in Figure 8–15. In this model, all steps are identical to the parameters in Figure 8–14, except step F. We have assumed that this step, hopping between Y_{731}• and 2,3,5–F_3Y is slow in reverse radical transfer. This assumption is based on the measured reduction potentials of 2,3,5–F_3Y and Y in solution, which are 0.85 V and 0.74 V at pH 8.4, respectively (Chapter 6). In the forward direction, this step is highly favorable, in the reverse direction however, oxidation of 2,3,5–F_3Y by Y• is thermodynamically uphill. Therefore, the measured steady state rate constant of ~0.2 s^{-1} (Chapter 7) at pH 8.4, where we have proposed slow radical transfer, has been assigned to step F. The simulation shows that this kinetic model yields a build–up of Y_{731}• to 15 μM. In addition, production of dCDP occurs with an initial lag followed by a linear phase. In our experiments, SF UV–vis may fail in detecting build–up of Y_{731}•, as depletion of Y_{122}• and build–up of another Y•, are spectroscopically indistinguishable. However, the RFQ–EPR studies would have detected this large build–up of another Y•. Changes in concentration of other intermediates were below our lower level of detection as demonstrated for C_{439}• in Figure 8–15. Thus, the current model and the chosen parameters suggest reverse radical migration cannot be solely rate–limiting.

We reconsidered the parameters in the model of Figure 8–15 to see if changes in these parameters could reflect our experimental observations. However, changing the parameters for step B (0.5–1 s^{-1} for forward k), step C (100–200 s^{-1} and 100–300 s^{-1} for forward and reverse k, respectively), step D (50–100 s^{-1}) and step E (300–1000 s^{-1}) all yielded >14 μM of Y_{731}•. Thus,

we conclude that in the current kinetic frame work, reverse radical transfer is likely not the solely rate–determining step.

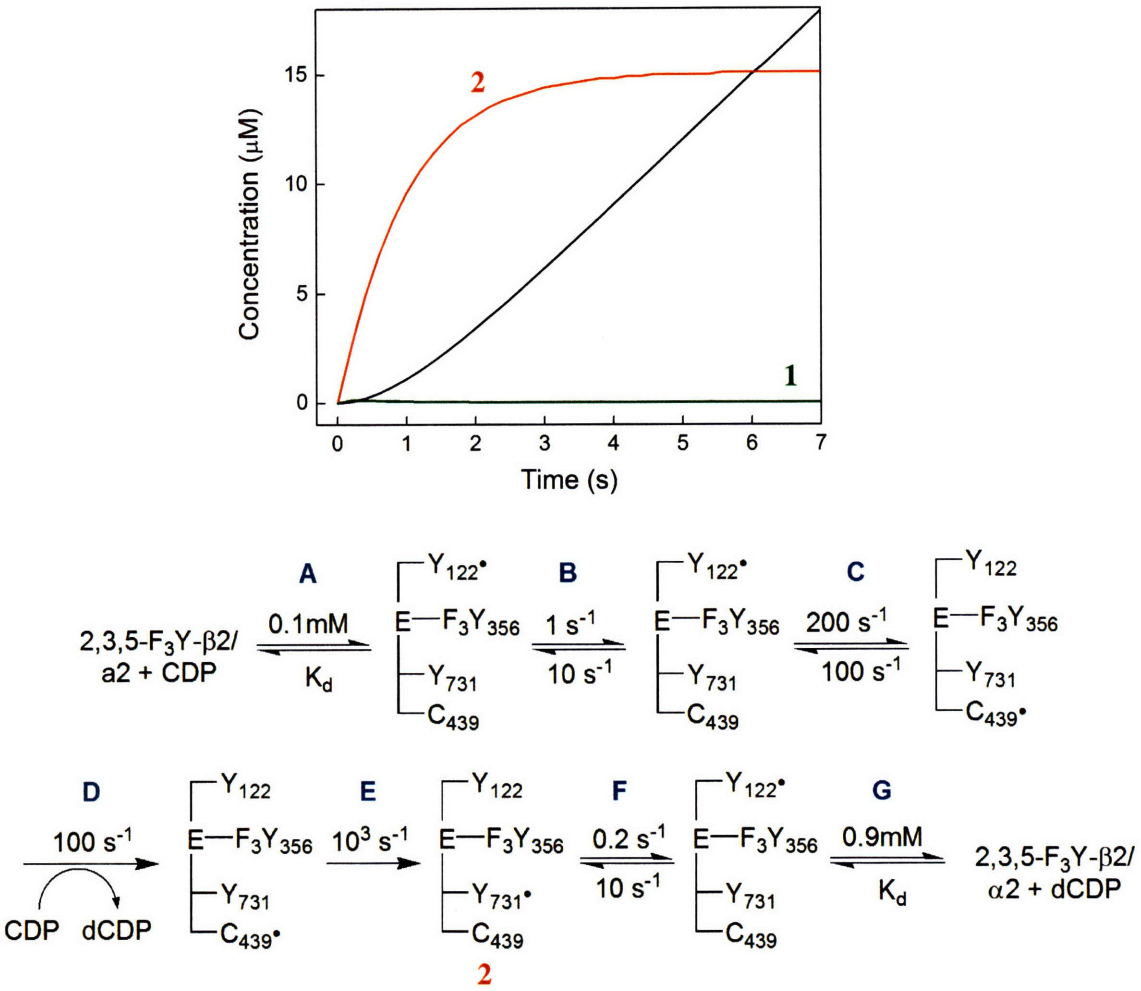

Figure 8–15. Kinetic model and result of simulation for the reaction of 2,3,5–F_3Y–β2 in which reverse radical transfer is rate–limiting. (A) Binding to CDP, see text for a K_d choice of 0.1 mM. (B) Conformational change preceding radical transfer. The forward rate constant of 1 s^{-1} is observed with DOPA–β2, the reverse rate constant has been chosen based on studies of Ge et al where a 10–fold larger reverse k was used. (C) Forward radical transfer, rate constants based on Ge et al. (D) Nucleteotide reduction, see text for choice of rate constant. (E) Reverse radical transfer, rate constant based on Ge et al. (F) The slow step in the model, oxidation of 2,3,5–F_3Y by Y_{731}•, see text for details. (G) Dissociation of dCDP. The simulation shows a time course of dCDP formation (black line), thiyl radical formation, species **1** (green line), and Y_{731}• formation, species **2**, (red line).

We next examined the effect of a rate–determining forward radical transfer step in our simulations. The model used is shown in Figure 8–16. In this case we have assumed that oxidation of 2,3,5–F_3Y by W_{48}• is the slow hop in the forward direction. This is consistent with the solution reduction potentials of 2,3,5–F_3Y and W•, which are 0.85 V and 0.8 V at pH 8.4, where we have proposed that radical transfer is slow. Therefore, the measured steady state rate constant of ~0.2 s^{-1} at pH 8.4 (Chapter 7) has been assigned to this step. The parameters for the remaining steps are unchanged. The results of this simulation are shown in Figure 8–16. They show a build–up of W• (or $WH•^+$) to 2.5 μM. W• and $WH•^+$ have ε of 2200 and 3000 $M^{-1}\,cm^{-1}$ at 510 and 560 nm, respectively.[20] Therefore, a build–up of W• or $WH•^+$ would have resulted in an observable ΔA of 0.0055 and 0.0075 AU, respectively. We conclude that with the chosen parameters in this kinetic model, forward radical transfer is not solely rate–determining.

We undertook changes in the parameters of our kinetic scheme to examine whether our experimental results could be replicated. We varied the rate constant of step E (nucleotide reduction chemistry) in Figure 8–16 between 100 and 250 s^{-1} and the rate constant for step B (forward k for conformational change) between 0.7 to 1 s^{-1}. However, these changes still resulted in an experimentally detectable build–up of W• (≥1.5 μM). We also varied the reverse rate constants of step D and F between 2–100 s^{-1} and 500–1000 s^{-1}, respectively. These changes also resulted in build up of W• to ≥2 μM. Combining changes in the rate constants in steps B and E to 0.7 and 250 s^{-1}, respectively, also gave a build–up of W• to ~2.0 μM. Therefore, changes in the rate constant for steps B, D, E and F do not appear to diminish the build–up of W•. However, variation in the formation rate constants of W• (step C) resulted in a decrease in the concentration of W• to levels that would not be observable in our experiments. Specifically, when the reverse rate constant for step C was equal to or greater than the forward rate constant, W• build–up to only <1 μM was observed. This kinetic model is shown in Figure 8–17 and is identical to the model in Figure 8–16 except that the parameters in step C have been reassigned. A simulation with this model shows that W• builds up to ~0.9 or 1.4 μM, when the reverse rate constant for step C is 300 or 200 s^{-1}, respectively. This concentration of W• is not detectable by

our methods. Thus, the simulations under conditions in which we assume forward radical propagation to be slow, show that the experimental observations can be replicated with the model and rate constants in Figure 8–17.

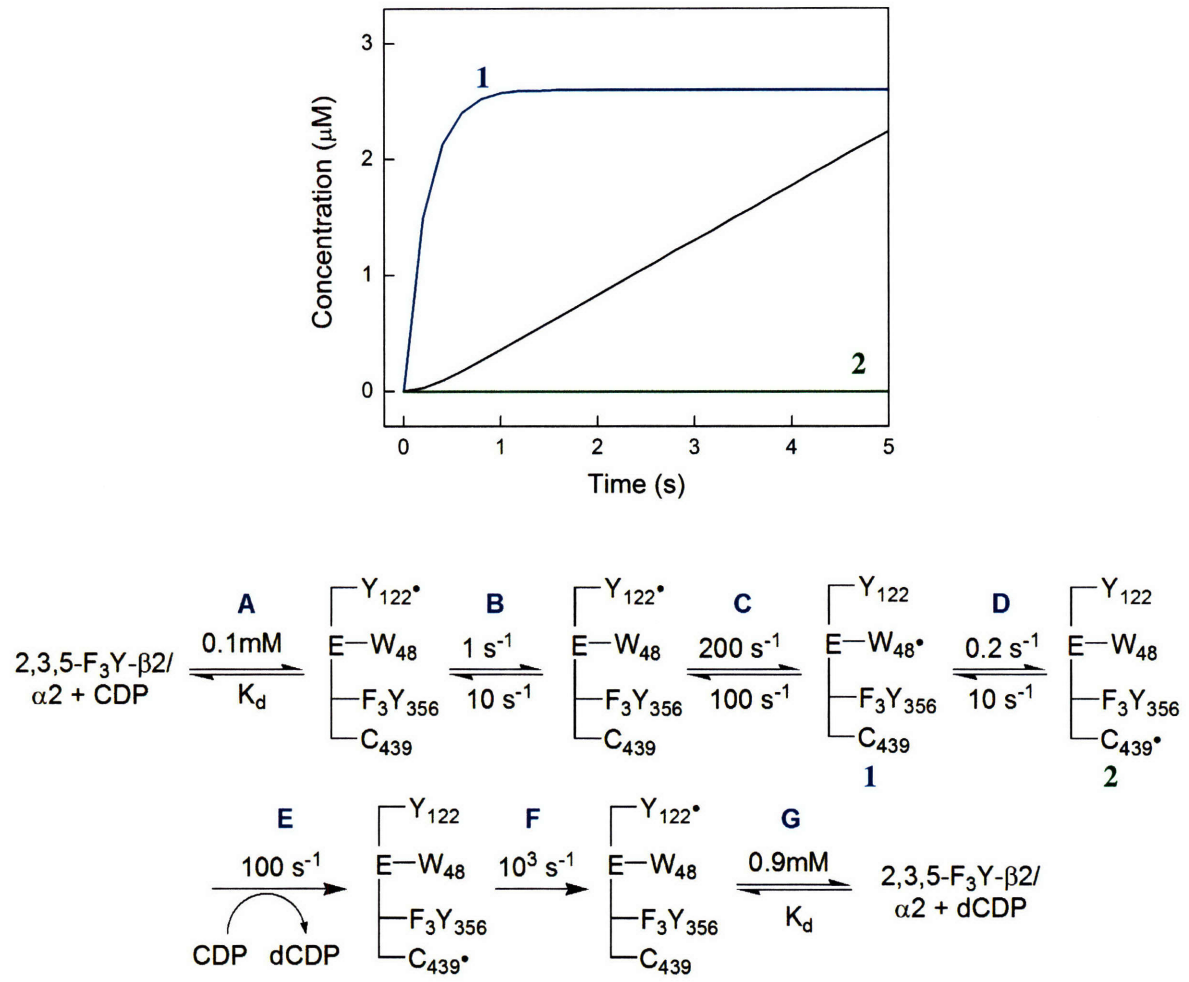

Figure 8–16. Kinetic model and result of simulation for the reaction of 2,3,5–F_3Y–β2 in which forward radical transfer is rate–limiting. (A) Binding to CDP, see text for a K_d choice of 0.1 mM. (B) Conformational change preceding radical transfer. The forward rate constant of 1 s^{-1} is observed with DOPA–β2, the reverse rate constant has been chosen based on studies of Ge et al where a 10–fold larger reverse k was used. (C) Forward radical transfer, rate constants based on Ge et al. (D) The slow step in the model, oxidation of 2,3,5–F_3Y by W_{48}•, see text for details. (E) Nucleteotide reduction, see text for choice of rate constant. (F) Reverse radical transfer, rate constant based on Ge et al. (G) Dissociation of dCDP. The simulation shows a time course of dCDP formation (black line), W_{48}• formation, species **1** (blue line), and thiyl radical formation, species **2**, (green line).

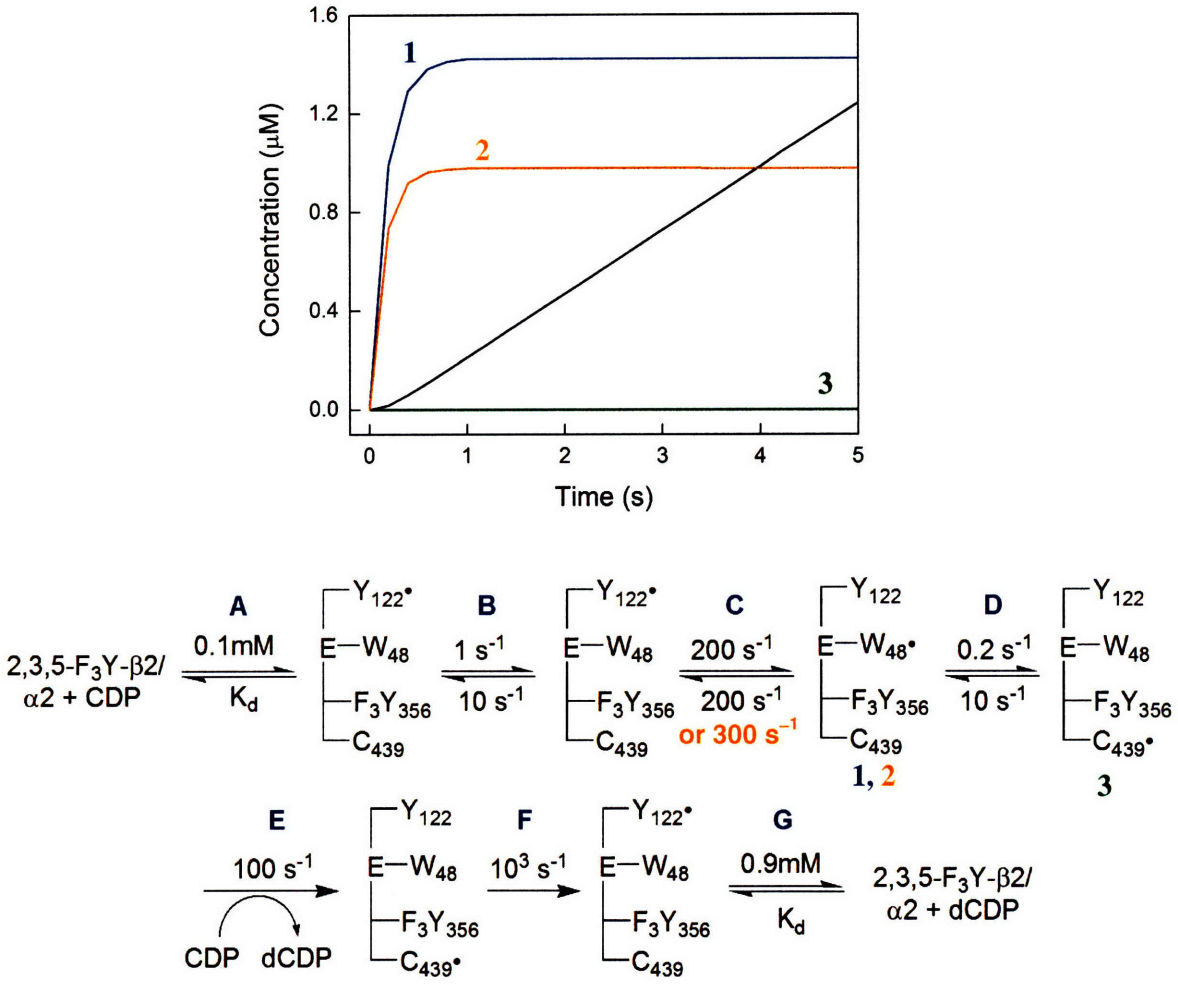

Figure 8–17. Kinetic model and result of simulation for the reaction of 2,3,5–F_3Y–β2 in which forward radical transfer is rate–limiting with an altered Y_{122}• reformation rate constant. This Figure is identical to Fig. 8–16, except that the Y_{122}• reformation rate constant in step C has been changed to 200 or 300 s^{-1}. (A) Binding to CDP, see text for K_d choice of 0.1 mM. (B) Conformational change preceding radical transfer. The forward rate constant of 1 s^{-1} is observed with DOPA–β2, the reverse rate constant has been chosen based on studies of Ge et al where a 10–fold larger reverse k was used. (C) Forward radical transfer, rate constants based on Ge et al. The reverse k in this step has been changed to 200 or 300 s^{-1} to reproduce lack of observable intermediates. (D) The slow step in the model, oxidation of 2,3,5–F_3Y by W_{48}•, see text for details. (E) Nucleteotide reduction, see text for choice of rate constant. (F) Reverse radical transfer, rate constant based on Ge et al. (G) Dissociation of dCDP. The simulation shows a time course of dCDP formation (black line), W_{48}• formation, species **1** with 200 s^{-1} (blue line) or species **2** with 300 s^{-1} (orange line), and thiyl radical formation, species **3** (green line).

Finally, we examined a kinetic model in which both forward and reverse radical transfer are both partially rate–determining. The model is shown in Figure 8–18 and is a combination of the models in Figures 8–15 and 8–16. In the forward direction, oxidation of 2,3,5–F_3Y by W_{48}• has been assigned as the partially rate–limiting step. In the reverse direction, oxidation of 2,3,5–F_3Y by Y_{731}• has been attributed with the slow rate constant of ~0.2 s^{-1}, which was measured in Chapter 7 at pH 8.4. All other parameters are identical to those in Figure 8–15 (or 8–16). The result shows that a build–up of W• to 2.6 μM would occur under these conditions, similar to the simulations in which only forward radical propagation was slow. As discussed above, this build–up of W• would be observable by SF UV–vis and EPR methods. We varied the parameters to see which set of rate constants would recapitulate our experimental observations. As above, a change in the reverse rate constant for step C, results in diminished build–up of W•, to levels that are not observable by our methods. Therefore, these parameters also reproduce the main features of our experimental observations.

The simulations in Figure 8–18 show a prolonged lag phase in dCDP formation when forward and reverse radical transfer are partially rate–determining. While we have observed lag phases in our RCQ experiments, they are not as pronounced as those in Figure 8–18. Thus, the model reproduces our lack of observation of intermediates, however, a long lag phase is inconsistent with our data. This issue will be explored further below, when we attempt to simulate the kinetics of dCDP formation as a function of pH.

We have also examined the effect of the conformational change that precedes radical transfer by omitting it from the model. In this case, the simulations indicate a major rapid build–up of W_{48}• to 60 % or 12 μM out of the initial 20 μM (data not shown) and a concomitant loss in Y_{122}•. Thus, the slow conformational change maintains a low concentration of W_{48}• even with F_nY–β2s, where we propose that radical transfer has become rate–limiting during turnover.

We conclude from the simulations above that within our kinetic frame work, based on previous results (Chapter 7) and experimental observations presented in this Chapter, that reverse hole propagation cannot be solely rate–determining. The simulations are consistent with a

rate–determining step in forward radical propagation and perhaps with partially limiting forward and reverse radical transfers. However, the reverse rate constant for formation of W• (step C, Figure 8–17) must be equal to or greater than the forward rate constant, the implications of which will be discussed below.

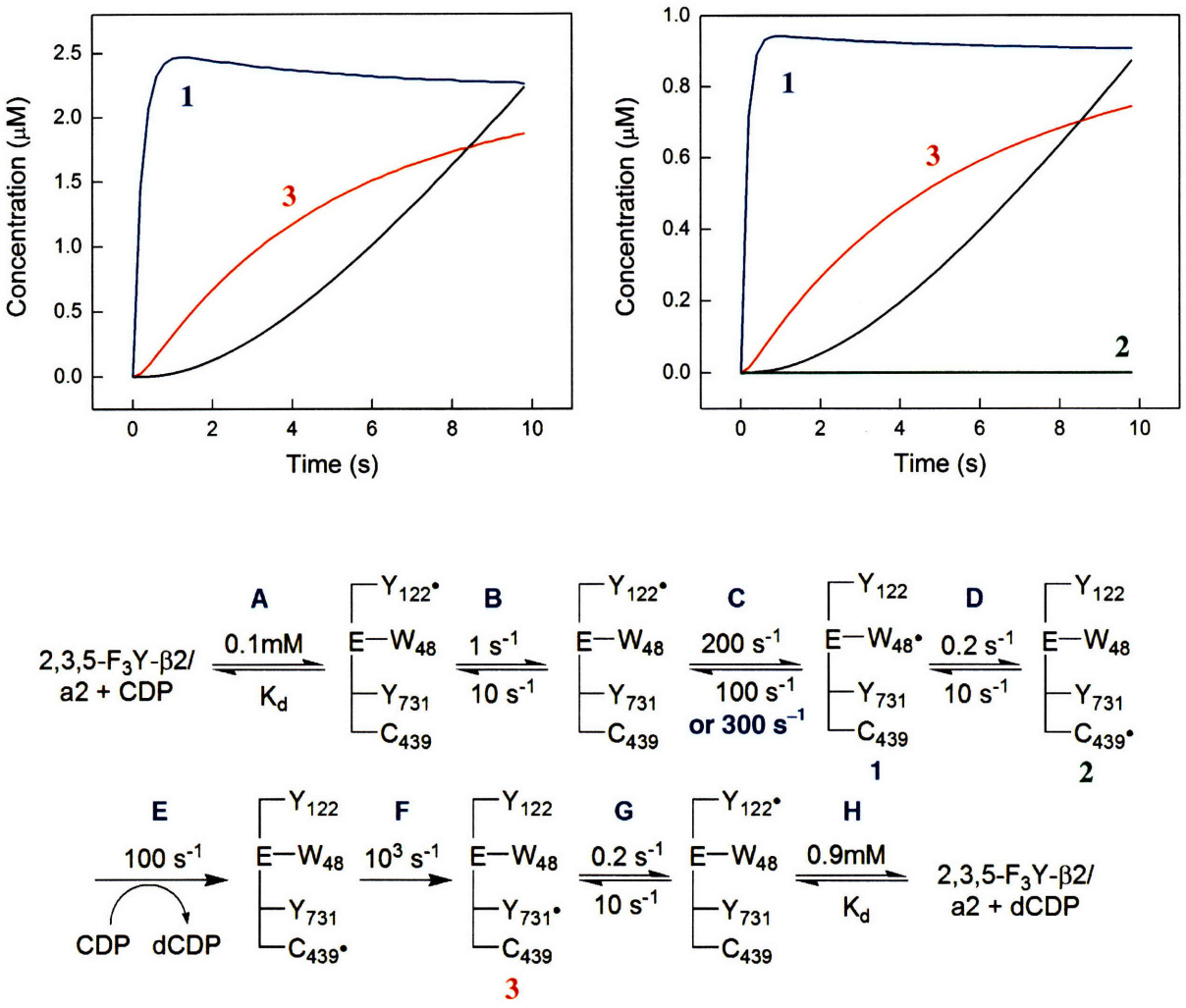

Figure 8–18. Kinetic model and result of simulations for the reaction of 2,3,5–F_3Y–β2 in which forward and reverse radical transfer are partially rate–limiting. (A) Binding to CDP, see text for a K_d choice of 0.1 mM. (B) Conformational change preceding radical transfer. The forward rate constant of 1 s^{-1} is observed with DOPA–β2, the reverse rate constant has been chosen based on studies of Ge et al where a 10–fold larger reverse k was used. (C) Forward radical transfer, rate constants based on Ge et al. The reverse k in this step is either to 100 s^{-1} (left panel) or 300 s^{-1} (right panel) to reproduce lack of observable intermediates. With 100 s^{-1}, an observable build–up of W_{48}• occurs (left), with 300 s^{-1}, however, the amount of W_{48}• is below our level of detection (right). (D) The partially rate–limiting step in the model, oxidation of 2,3,5–F_3Y by W_{48}•, see text for details. (E) Nucleteotide reduction, see text for choice of rate constant. (F) Reverse radical transfer, rate constant based on Ge et al. (G) The partially rate–limiting step in the model, oxidation of 2,3,5–F_3Y by Y_{731}•, see text for details. The simulation on the left shows a time course of dCDP formation (black line), W_{48}• formation (species **1**) with 100 s^{-1} in step C (blue line), and Y_{731}• formation, species **3** (red line). The simulation on the right shows a time course of dCDP formation (black line), W_{48}• formation (species **1**) with 300 s^{-1} in step C (blue line), thiyl radical formation, species **2** (green line) and Y_{731}• formation, species **3** (red line).

Kinetic simulations: reproducing the effect of pH on k_{cat} with 2,3,5–F_3Y–β2. The simulations above show that radical transfer may be rate–determining without resulting in a build–up of observable intermediates. Further, they suggest that only forward hole propagation or forward and reverse propagation are rate–determining in turnover. To examine our kinetic model further, we explored whether the effect of pH on steady state activity, which was presented in Chapter 7, could be reproduced.

We used the models in Figure 8–14 and Figure 8–17 to reproduce the pH rate profile of 2,3,5–F_3Y–β2 (Chapter 7). Within the pH range, where the conformational change was rate–determining (pH 6.5–7.6), we used the model in Figure 8–14 and replaced the forward rate constant of step B with the measured k_{cat} in Chapter 7. Within the pH range, where we have proposed a switch in the rate–determining steps (pH 8–9), we used the model in Figure 8–17 (with 200 s^{-1} for reverse k of step C) and replaced the forward rate constant for step C with the rate constants that were measured as a function of pH in Chapter 7. The rates of dCDP formation were then simulated. These were compared to the actual measured values as shown in Table 8–2. The results reveal that the kinetic model can only reproduce the observed pH effect on activity in the low pH range. In the range, where we have postulated a change in the rate–limiting step, the kinetic model is not sufficient.

We examined the basis for the inconsistency between the observed and simulated rates of dCDP formation. Variation in the parameters of steps B, C, E, and F in Figure 8–17 did not pose a solution. However, changing the parameters in steps D in Figure 8–17 provided solutions, which both kept the [W•] low and yielded dCDP formation rates consistent with those measured in Chapter 7. The observed results can be simulated by directly varying the decay rate constant of W• (step D) in the model of Figure 8–17. Comparison of the decay rate constant for W• (step D), the simulated and measured rates of dCDP formation are shown in Table 8–3. All other parameters in Figure 8–17 (with 200 s^{-1} for reverse k of step C) were kept constant. This Table shows that the rate of dCDP formation can be fit to the data in Chapter 7 by only altering the

decay rate constant of W• in our current model. Thus, the dCDP formation rate correlates with the decay rate constant of W• (step C, Figure 8–17).

Table 8–2. Measured and simulated k_{cat} for 2,3,5–F_3Y–β2 as a function of pH using the kinetic model in Figure 8–17.

pH	Measured k_{cat} (s^{-1})[a]	Simulated k_{cat} (s^{-1})
6.5	0.2	0.16[b]
7.0	0.32	0.25[b]
7.5	0.5	0.39[b]
8.45	0.1	0.017[c]
8.5	0.07	0.031[c]
8.65	0.03	0.0013[c]
8.85	0.02	0.001[c]

[a] Rate constants determined in Chapter 7 with 2,3,5–F_3Y–β2. [b] Rate constants simulated by inserting the measured k_{cat} at the same pH into step C of the model in Fig. 8–14. [c] Rate constants simulated by inserting the measured k_{cat} at the same pH into step D of the model in Fig. 8–17.

Similar simulations were carried out with the model in Figure 8–18 (with 200 s^{-1} for reverse k of step C). These results are also summarized in Table 8–3 and show that the experimental k_{cat} is approximated by this model reasonably well. In this case, the dCDP formation rate directly correlates with the W_{48}• and Y_{731}• decay rate constants. However, the pronounced lag phase, as shown in Figure 8–18, remained under all conditions shown in Table 8–3 above pH 8.45. Therefore, we prefer the model in which only forward radical transfer is rate–determining. The validity of the model in Figure 8–18 requires further theoretical and experimental assessment.

In conclusion, the kinetic simulations in this chapter have provided one possible solution for the catalytic cylcle of 2,3,5–F_3Y–β2 and for explaining the lack of observable intermediates, a linear rate of dCDP formation and, as presented in Chapter 7, dependence of k_{cat} on the reduction potential difference between 2,3,5–F_3Y and Y in the pH range of 8–9. Two models have been found that are consistent with a slow radical transfer model in the forward or forward and reverse directions. To obtain direct evidence for a switch in the rate–limiting step as a result of 2,3,5–F_3Y incorporation, we considered the use of NH_2Y–α2 as a readout of the rate constant for forward radical transfer using SF UV–vis spectroscopy.

Table 8–3. Measured and simulated k_{cat} for 2,3,5–F_3Y–β2 as a function of pH using the kinetic models in Figures 8–17 and 8–18.

pH	Measured k_{cat} (s^{-1}) [a]	W• Decay k (s^{-1}) (forward, reverse) [b]	Simulated k_{cat} (s^{-1}) [c]	[W•] (μM) [d]	Simulated k_{cat} (s^{-1}) [e]	[W•] (μM) [f]
6.5	0.2	–	–	–	–	–
7.0	0.32	–	–	–	–	–
7.5	0.5	–	–	–	–	–
8.45	0.1	1.0, 1.0	0.065	1.3	0.059	1.2
8.5	0.05	0.8, 1.0	0.054	1.3	0.048	1.2
8.65	0.03	0.5, 1.0	0.034	1.4	0.030	1.3
8.85	0.02	0.2, 1.0	0.014	1.4	0.009	1.3

[a] Rate constants determined in Chapter 7 with 2,3,5–F_3Y–β2. [b] Forward and reverse rate constants inserted into step D of the model in Figure 8–17 or steps D and G of the model in Figure 8–18. [c] Simulated k_{cat} determined using the model in Figure. 8–17. Note that the rate constants for step D have been changed as listed in this Table. [d] The concentration of W• from the simulation in Figure 8–17. [e] Simulated k_{cat} determined using the model in Figure. 8–18. Note that the rate constants for steps D and G have been changed as listed in this Table. [f] The concentration of W• from the simulation in Figure 8–18.

SF UV–vis spectroscopy with 2,3,5–F_3Y–β2, NH_2Y–α2 and CDP/ATP as a readout for forward radical transfer. The simulations above are consistent with rate–limiting radical propagation despite the lack of observable intermediates during this process. As pointed out, the simulations are also consistent with a rate–determining forward or forward and reverse radical transfer. To directly interrogate whether forward radical transfer has in fact become slow during turnover, we took advantage of NH_2Y–α2s, which were prepared in Chapter 4. Because reaction of NH_2Y–α2s with β2, substrate and effector results in NH_2Y• formation, NH_2Y–α2 offers a readout of forward radical transfer. This includes the step that was modeled as the rate–determining step in the simulations above, oxidation of 2,3,5–F_3Y by W_{48}•. One caveat with these experiments is that NH_2Y–α2s are competent in turnover, as we proposed in Chapter 4. However, we also pointed out that formation of NH_2Y• (biphasic, 12 s^{-1} and 2.5 s^{-1} for NH_2Y_{730}•) is much more rapid than decay of NH_2Y• (monophasic, 0.26 min^{-1} for NH_2Y_{730}•). Thus, within the time scale of our experiment, we may treat NH_2Y as an irreversible trap reporting on the rate constant of forward radical propagation.

If forward radical transfer is slow, then the pre–steady state pH rate profile for NH_2Y• formation with 2,3,5–F_3Y–β2 and CDP/ATP should be similar to the steady state pH rate profile of dCDP formation with 2,3,5–F_3Y–β2 and wt α2, which was determined in Chapter 7; that is, the rate constant for NH_2Y• formation as a function of pH should reveal a similar profile as the pH rate profile of 2,3,5–F_3Y–β2. If, however, forward radical transfer is not slow, then the pre–steady state pH rate profile of NH_2Y• formation should approximate that of Y–β2, which was also determined in Chapter 7.

To distinguish between these mechanistic possibilities, SF UV–vis experiments were carried out. In these experiments pre–reduced $Y_{730}NH_2$Y–α2 or $Y_{731}NH_2$Y–α2 and ATP were mixed with 2,3,5–F_3Y–β2 (1.2 Y_{122}•/dimer) and CDP to yield final protein concentrations of 4 μM. It was necessary to choose a final protein concentration similar to those used in the steady state pH rate profiles (3 μM), as higher concentrations may result in a change in the rate–limiting step, which has been observed with wt RNR. The high extinction coefficients of the NH_2Y_{730}•

and NH_2Y_{731}•, which were determined in Chapter 4, and our ability to reconstitute the Y_{122}• of 2,3,5–F_3Y–β2 to wt levels, allowed these experiments to be carried out at protein concentrations similar to those used in the steady state pH rate profiles.

The results of pH–dependent SF UV–vis experiments with $Y_{730}NH_2Y$–α2 and 2,3,5–F_3Y–β2 are shown in Figure 8–19. Representative data and fits for the reaction of $Y_{730}NH_2Y$–α2 with 2,3,5–FY–β2 at pH 8.3 are shown in Figure 8–19A/B. Representative data and fits for the reaction of $Y_{730}NH_2Y$–α2 at pH 6.6 are shown in Figure 8–19C/D. The kinetic traces for all pHs examined for $Y_{730}NH_2Y$–α2 and $Y_{731}NH_2Y$–α2 are shown in Figures 8–20A and 8–20B, respectively. Qualitatively, it can be seen that the pH has a discernible effect on the rate constant for NH_2Y• formation. To analyze these quantitatively, iterative rounds of fitting and calculation of the R^2 correlation value and residual plot were carried out until the R^2 value was maximized (≥0.99) and the residual plot was randomly scattered around zero with a maximal scatter of 0.001 AU. The kinetic parameters thus obtained are shown in Table 8–4 for $Y_{730}NH_2Y$–α2 and $Y_{731}NH_2Y$– α2.

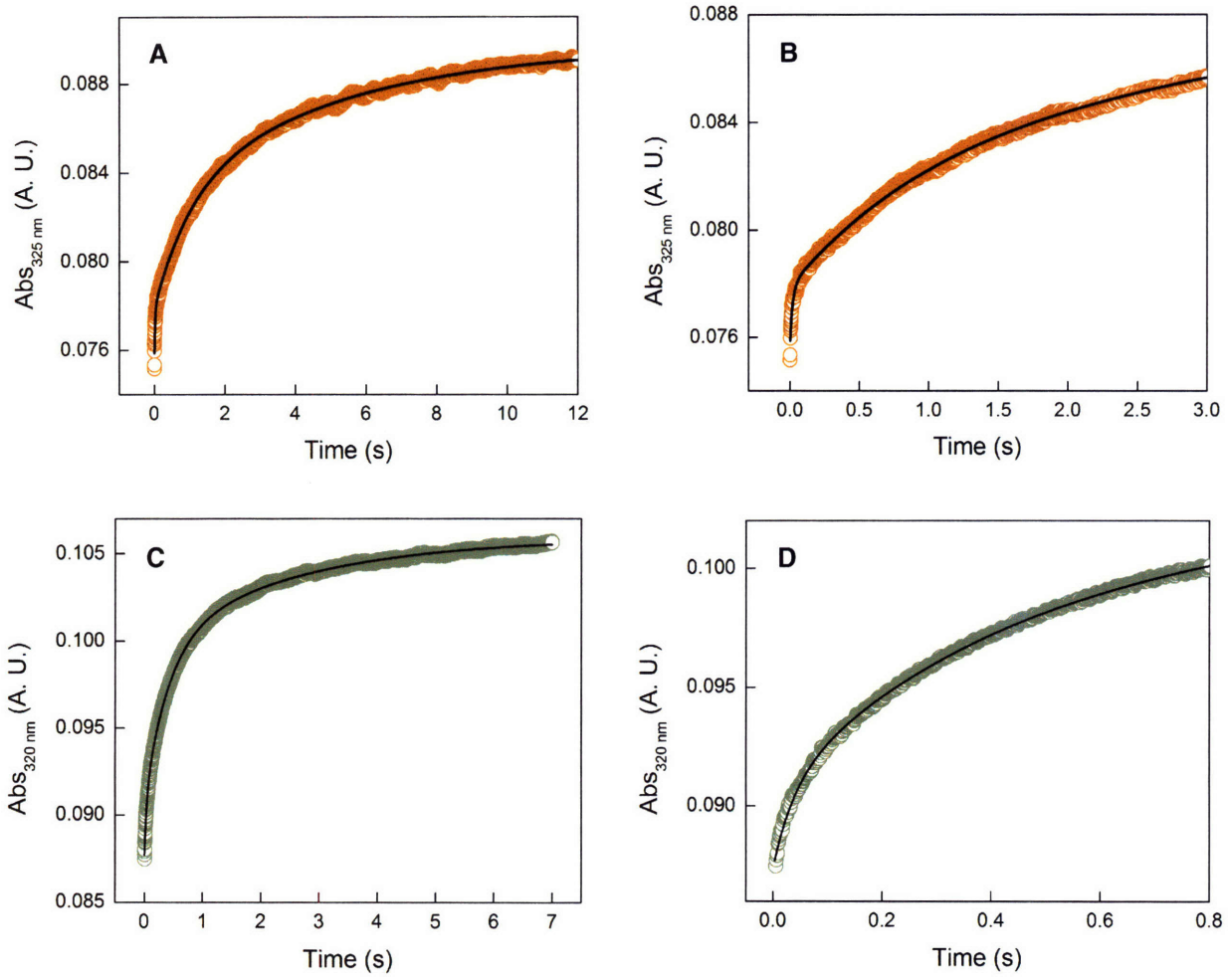

Figure 8–19. Representative time courses for the reaction of NH_2Y–α2s with 2,3,5–F_3Y–β2 and CDP/ATP monitored by SF UV spectroscopy. (A) Reaction of 2,3,5–F_3Y–β2 (1.2 Y_{122}•/dimer) with $Y_{730}NH_2Y$–α2 and CDP/ATP at pH 8.35 and 4 μM final protein concentration. (B) Magnified view of the initial 3 s of the trace in (A). (C) Reaction of 2,3,5–F_3Y–β2 (1.2 Y_{122}•/dimer) with $Y_{731}NH_2Y$–α2 and CDP/ATP at pH 7.0 and 4 μM final subunit concentration. (D) Magnified view of the initial 0.8 s of the trace in (C).

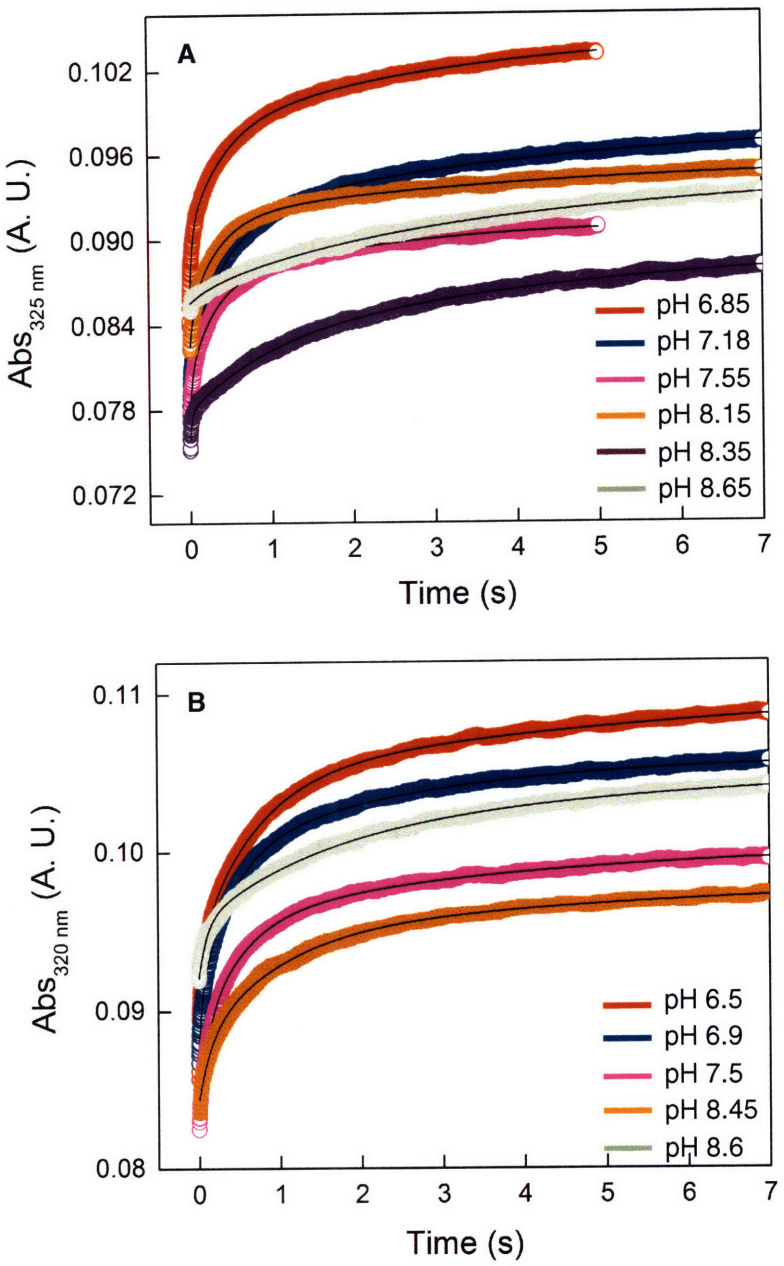

Figure 8–20. SF UV spectroscopy of NH_2Y–α2s with 2,3,5–F_3Y–β2 and CDP/ATP as a function of pH. (A) Reaction of 2,3,5–F_3Y–β2 (1.2 Y_{122}•/dimer) with $Y_{730}NH_2Y$–α2 (A) or $Y_{731}NH_2Y$–α2 (B) as a function of pH with CDP/ATP. Each trace is an average of 5–7 traces. Black lines describe tri–exponential fits to the data. See Table 8–4 for kinetic parameters.

Table 8–4. Summary of the kinetic parameters for $NH_2Y\bullet$ formation in the reaction of $Y_{730}NH_2Y$–α2 or $Y_{731}NH_2Y$–α2 with 2,3,5–F_3Y_{356}–β2 in the presence of CDP/ATP.

pH	1st Phase k_{obs} (s^{-1}) [a]	1st Phase Amp [b] (% $Y_{122}\bullet$)	2nd Phase k_{obs} (s^{-1}) [a]	2nd Phase Amp [b] (% $Y_{122}\bullet$)	3rd Phase k_{obs} (s^{-1}) [a]	3rd Phase Amp [b] (% $Y_{122}\bullet$)
			$Y_{730}NH_2Y$–α2			
6.85	31.6 ± 2.2	10 ± 1	2.4 ± 0.2	14 ± 1	0.30 ± 0.02	14 ± 1
7.18	37.0 ± 2.6	7 ± 1	2.4 ± 0.2	17 ± 2	0.33 ± 0.02	14 ± 1
7.55	48.5 ± 3.4	6 ± 1	3.8 ± 0.3	12 ± 1	0.52 ± 0.04	10 ± 1
8.15	21.7 ± 1.5	5 ± 1	2.8 ± 0.2	13 ± 1	0.23 ± 0.02	8 ± 1
8.35	50.5 ± 3.5	4 ± 1	1.0 ± 0.1	10 ± 1	0.20 ± 0.02	13 ± 1
8.65	4.0 ± 0.3	2 ± 1	0.45 ± 0.03	8 ± 1	0.10 ± 0.01	10 ± 1
			$Y_{731}NH_2Y$–α2			
6.5	17.9 ± 1.3	11 ± 1	1.4 ± 0.1	21 ± 2	0.14 ± 0.01	12 ± 1
6.9	26.2 ± 1.8	6 ± 1	2.5 ± 0.2	18 ± 2	0.40 ± 0.03	12 ± 1
7.5	13.5 ± 1.0	7 ± 1	2.6 ± 0.2	15 ± 2	0.42 ± 0.03	10 ± 1
8.45	6.7 ± 0.5	7 ± 1	1.0 ± 0.1	14 ± 1	0.12 ± 0.01	8 ± 1
8.6	9.0 ± 0.6	7 ± 1	0.63 ± 0.04	13 ± 1	0.09 ± 0.01	9 ± 1
9.2	–	–	–	–	–	–

[a] Estimated error not based on fits but on reproducibility of rate constant from multiple separate experiments. [b] The amount of $NH_2Y\bullet$ trapped has been reported as a % of total initial $Y_{122}\bullet$, which in these experiments was 4.8 μM. Estimated error based on systematic factors.

Analysis of all kinetic traces required three exponentials to fit the data. This is similar to results with DOPA–β2, which contains the $V_{353}G/C_{354}S$ mutations that are also present in 2,3,5–F_3Y–β2 and revealed three kinetic phases in the presence of CDP/ATP. As with DOPA–β2, the physical nature of the two fast rate constant is not understood. Our interpretation has been that the slow rate constant is indicative of the conformational change that gates radical transfer and limits turnover in the steady state.

Inspection of the data in Table 8–4 reveals that the three kinetic phases have different pH dependencies. For $Y_{730}NH_2Y$–α2, the k_{obs} of the 1st kinetic phase varies from 21.7 to 50.5 s^{-1} in the pH range of 6.85–8.35. The trace at pH 8.65 is unusual with a k_{obs} of 4.0 s^{-1}. The amplitudes in this phase account for ~10–25 % of the total change. This kinetic phase reveals no discernible pH dependence. The second kinetic phase occurs with k_{obs} of 0.45–3.8 s^{-1} with amplitudes of 37–50 % of the total absorbance change. Interestingly, the pH profile of this phase has a very similar shape to that of the activity of 2,3,5–F_3Y–β2 determined in Chapter 7 (Figure 8–21A); however, the rate constants are ~4–fold higher. The k_{obs} for the slow kinetic phase, varies from 0.1–0.52 s^{-1} with amplitudes of 30–50 % of the overall change. The pH profile of this phase is also very similar to the activity profile of 2,3,5–F_3Y–β2 in that it peaks at pH 7.55 and drops sharply between pH 7.55 and 8.65 (Figure 8–21B). The implications of this will be elaborated below.

For $Y_{731}NH_2Y$–α2, the k_{obs} of the 1st kinetic phase varies from 6.7 to 26.2 s^{-1}. The amplitudes in this phase account for ~17–25 % of the total change, similar to the results with $Y_{730}NH_2Y$–α2. No trend in the pH dependence of this phase is apparent. The k_{obs} for the second phase varies from 0.63 s^{-1} at pH 8.6 to 2.6 s^{-1} at pH 7.5. This phase contains 45–50 % of the overall change and the shape of its pH dependence is marked by a peak at pH 7.5 and a sharp drop between pH 7.5 and 8.6 (Figure 8–21A). This is reminiscent of the pH rate profile of 2,3,5–F_3Y–β2, although it is ~4–fold faster than the k_{cat} measured in activity assays (Chapter 7). The rate constants for NH_2Y• formation in the slow kinetic phase vary from 0.09 s^{-1} at pH 8.6 to 0.42 s^{-1} at pH 7.5 accounting for 27–31 % of the total absorbance change. Similar to the 2nd phase, the pH dependence of this is phase reminiscent of the pH rate profile of 2,3,5–F_3Y–β2 (Figure 8–21B).

As noted above, we have interpreted the slow phase as the physical gating step that initiates radical propagation. To examine the pH dependence of this step further, the k_{obs} obtained in this phase with $Y_{730}NH_2Y$–α2 and $Y_{731}NH_2Y$–α2 have been overlaid with the pH rate profile of 2,3,5–F_3Y–β2 activity (Figure 8–21C). This analysis shows that the three profiles

overlap in all three activity regimes, which we described in Chapter 7. Thus, the pre–steady state pH rate profile for $NH_2Y\bullet$ formation is very similar to that measured by the radioactive assay for [^{14}C]–dCDP formation in the steady state. Consistent with the kinetic simulations, these results strongly suggest that at high pH, the rate–determining step has shifted from a physical step to radical transfer in the 2,3,5–F_3Y–β2 analogue.

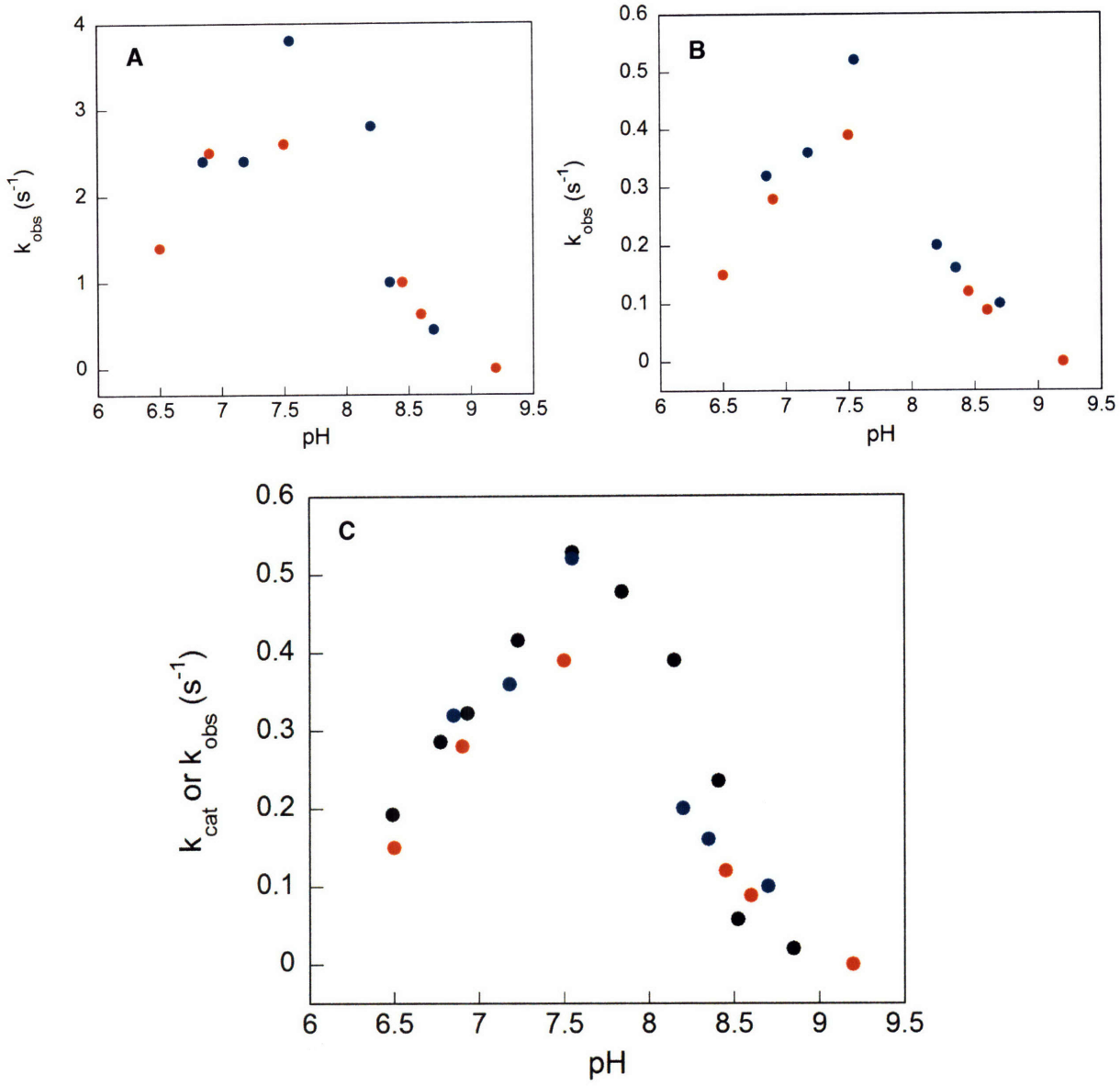

Figure 8–21. pH rate profile for NH_2Y• formation in the reaction of NH_2Y–α2 with 2,3,5–F_3Y–β2. (A) pH dependence of the rate constant from the second kinetic phase determined from the tri–exponential fits in Fig. 8–20 and Table 8–4. The rate constant from the reaction with $Y_{730}NH_2Y$–α2 (blue dots) and $Y_{731}NH_2Y$–α2 (red dots) have been plotted against pH. (B) pH dependence of the rate constant from the third (slowest) kinetic phase determined from Figure 8–20 and Table 8–4 with $Y_{730}NH_2Y$–α2 (blue dots) or $Y_{731}NH_2Y$–α2 (red dots). (C) The data in (B) has been overlaid with the pH rate profile for [^{14}C]–dCDP formation with 2,3,5,–F_3Y–β2 and wt α2, determined in Chapter 7 (black dots).

DISCUSSION

Amino acid radicals are a hallmark of class I RNRs. The β2 subunit contains the stable Y_{122}•, the in vitro generation of which requires formation of a transient $W_{48}H^{\bullet+}$.[25-29] The active site chemistry in α2 involves formation of a transient C_{439}• and a C_{225}–C_{462} disulfide radical anion,[4,30,31] and the radical transfer event contains three Tyr residues, in addition to Y_{122}•, W_{48} and C_{439}, that are redox active (Chapters 2–5). However, despite extensive efforts, a transient amino acid radical has never been observed in active wt RNR turnover.[32] It appears the system is poised to avoid build–up of any oxidized amino acid intermediates during catalysis. This is accomplished by rapid electron hopping between the residues in the radical transfer pathway and by a slow physical change that precedes rapid chemistry.

To study this pathway the rate–limiting step must be changed from a conformational to the radical transfer step. In chapter 6, we synthesized a series of F_nY analogues and showed that they span ranges of 320 mV in reduction potential and almost 4.5 units in pK_a. Our hypothesis was that insertion of these analogues into residue 356 would provide an energetic barrier by changing the driving force to slow hole migration. The results in Chapter 7 showed that replacing Y_{356} with F_nYs had a profound effect on nucleotide reduction activity, presumably by altering radical transfer. We proposed that the correlation between reduction potential difference and nucleotide reduction activity indicated that the rate–determining step had shifted from the conformational change to radical transfer. In this Chapter, we conducted a series of steady state and pre–steady state experiments and theoretical studies to test this hypothesis.

At least three models may be envisioned to explain the results in Chapter 7: the rate–determining step has changed to forward radical transfer, or reverse, or both. If forward radical transfer is solely rate–limiting, then the elementary step most likely affected is oxidation of F_nY by W_{48}•. Presumably, the rate constant for oxidation of W_{48} by Y_{122}• is not affected by insertion of F_nY at residue 356. Further, oxidation of Y_{731} by F_nY_{356}• is thermodynamically more favorable than oxidation by Y_{356}•. Consequently, W_{48}• would be expected to form rapidly,

and decay slowly, leading to a build–up of W_{48}•. Thus, if forward radical transfer is slow with F_nY–β2s at high pH, one may expect to see formation of W_{48}•, which may be detected by SF UV–vis and EPR spectroscopies.

If reverse radical transfer has become solely rate–determing, then the elementary step most likely affected is oxidation of F_nY_{356} by Y_{731}•. Presumably, other reactions in reverse radical transfer (i.e. oxidation of Y_{731} by Y_{730}•) are unaffected by insertion of F_nY at residue 356. In addition, oxidation of W_{48} by F_nY• is now more favorable than oxidation by Y_{356}•. In this case, Y_{731}• would be formed rapidly, but would decay slowly leading to a build–up of Y_{731}• which could be detected by RFQ EPR studies. Also if reverse radical transfer is slow, a burst in dCDP production would be expected, followed by a linear dCDP formation phase.

If both forward and reverse electron transfers are partially rate–limiting, then build–up of intermediates will depend on the relative rate constants for formation and decay in the forward and reverse directions.

To test whether any intermediates occur in the reaction of 2,3,5–F_3Y–β2 at high pH, where radical transfer was proposed to be rate–limiting, SF UV–vis and RFQ EPR experiments were carried out. These studies failed to reveal build–up of any oxidized amino acid intermediates in pre–steady state or steady state turnover with 2,3,5–F_3Y–β2 or 2,3,5–F_3Y–ββ'. In these experiments, an intermediate build–up of ≥10 % would have been detected based on the extinction coefficients Y•s and W•s, and EPR quantitation methods. Thus, any intermediates formed are below the lower limit of detection.

Compelling evidence, however, for a shift in the rate–limiting steps as a result of 2,3,5–F_nY insertion was obtained in SF UV–vis experiments with NH_2Y–α2s. Reaction of 2,3,5–F_3Y–β2 with NH_2Y–α2s monitors all the steps up to and including NH_2Y• formation. Therefore, NH_2Y–α2s offer a readout of forward radical transfer. Experiments with NH_2Y–α2s are complicated by two factors: First, all kinetic traces for NH_2Y• formation with 2,3,5–F_3Y–β2 were tri–phasic. The slow phase observed likely corresponds to the conformation that is catalytically active in multiple turnover. This is because RCQ studies monitoring dCDP

formation with intein–generated wt β2 (see below), no longer show a burst of dCDP formation (as with wt β2) but exhibit a single rate constant of ~0.7 s^{-1}. Second, the NH_2Y• has been proposed to partition between decay and C_{439}• formation as discussed in Chapter 4. However, these reactions are slow relative to NH_2Y• formation. Therefore, for the purposes of the current experiment, NH_2Y–α2s report solely on forward radical transfer.

The results show that the pH rate profile for pre–steady state NH_2Y• formation with 2,3,5–F_3Y–β2 is similar to that of steady state dCDP formation, and not like that of intein wt β2. The latter would have been expected if (1) reverse radical transfer was slow in turnover, or (2) the activity profiles observed in Chapter 7 were not the result of a shift in the rate–limiting step. Therefore, these results establish that with 2,3,5–F_3Y–β2, a step in forward radical transfer has the same pH–dependent rate constant as that measured by multiple turnover assays with 2,3,5–F_3Y–β2,. This strongly suggests that insertion of 2,3,5–F_3Y results in a decrease in the rate constant for forward radical transfer as the reaction pH is increased.

RCQ experiments reveal two important findings. First, the mutations necessary for intein chemistry result in β2 variants that no longer display burst kinetics in pre–steady state dCDP production. Therefore, the mutations have slowed down a step prior to formation of dCDP. Second, with F_nY–β2s, where radical transfer is thought to be rate–limiting in turnover, linear (F_4Y–β2, pH 6.8) or lag phase (F_4Y–β2, pH 7.6 and 2,3,5–F_3Y–β2, pH 8.4) kinetics in pre–steady state dCDP formation is observed. Thus, the results may be consistent with forward radical transfer, reverse or both being rate–determining in catalysis.

To distinguish between these options, and to test whether lack of intermediate build–up is consistent with rate–limiting hole migration, kinetic simulations were carried out. The kinetic paramters for these simulations were based on previously measured rate constants and binding constants, as well as on simulations of the wt RNR catalytic cycle. An important insight from these simulation, which is corroborated by the experimental results discussed above, is that reverse radical propagation is not solely rate–determining in the current kinetic frame work. The simulations show a build up of Y_{731}• to >14 μM, which would detectable.

Perhaps the most important conclusion from the simulations is that radical transfer can be slow during turnover without resulting in a build–up of oxidized amino acid intermediates. Thus, lack of observation of transient amino acid radicals and rate–limiting hole transfer are kinetically not inconsistent. We were able to generate two kinetic models which reproduced the pre–steady state kinetics results presented in this Chapter. In one of these models, forward radical transfer is the rate–determining step. The results show that one explanation for the lack of W• build up is that while oxidation of 2,3,5–F_3Y by W_{48}• is slowed, the rate constant for reformation of Y_{122}• (reverse k, step C, Fig. 8–17) is increased. This is required to obtain agreement between our model and experimental results. Therefore, formation of W_{48}• is followed by its rapid decay and reverse hole migration to Y_{122}•, where the radical is stable. Consequently, though we have managed to diminish the rate constant of radical transfer to the extent that it is rate–limiting in turnover, this model indicates that intermediate build–up does not occur because of rapid reverse hole transfer to Y_{122}•. A second model consistent with the results of the current Chapter is one in which forward and reverse radical transfer are both partially rate–determining. In this case build–up of intermediates appears to be avoided by the same reasoning as described above, i.e. rapid reverse hole migration to Y_{122}•.

These two models were also able to reproduce the trend of our pH rate profiles in Chapter 7. Both models show, even though the slowest step in turnover is assigned to an elementary step within radical transfer, no detectable build–up of intermediates occurs. In addition, we were able to recapitulate the trends in k_{cat} as function of pH by only changing the rate constant for a step in forward radical migration (decay of W•). Therefore, both models are consistent with the lack of observable intermediates and dCDP formation as a function of changes in radical transfer rate constants. However, the second model, where forward and reverse radical transfer are partially rate–determining predicts a prolonged lag phase which was not observed in our experiments. Therefore, we prefer the first model, in which only forward hole propagation is rate–determining in turnover.

Our studies have suggested a model that describes the pH rate profiles of Chapter 7 where the reduction potential difference between F_nY and Y was found to be inversely proportional to the forward radical transfer rate. Another model that is worth considering is that the reduction potential difference is inversely proportional to the fraction of active enzyme: the larger the reduction potential difference between F_nY and Y, the smaller the fraction of RNR competent in turnover. In this model, the kinetics of forward radical transfer are similar to those in Y–β2, however, the larger activation barrier for radical transfer renders the enzyme inactive, rather than slowing down hole migration. The major drawback of this model is that it is inconsistent with the NH_2Y–α2 experiments, which clearly show a decrease in the rate constant for NH_2Y• formation as a function of reduction potential increase at residue 356.

In conclusion, the experiments and simulations performed in this Chapter validate the hypothesis that insertion of F_nYs at residue 356 results in a change in the rate–limiting step when the reduction potential difference between F_nY and Y is between 80 and 200 mV. Kinetic simulations and SF UV–vis experiments with NH_2Y–α2s suggest that forward radical transfer, presumably oxidation of F_nY by W_{48}•, has become rate–limiting. This model further indicates that the changes in the pH rate profile are due to changes in the decay rate constant of W_{48}• during forward radical transfer. However, detection of intermediates is hampered by a slow conformational change that precedes radical transfer and by the increase in the rate constant for Y_{122}• reformation in forward hole migration. Perhaps tweaking of the reduction potential of W_{48} by incorporation of unnatural W analogues in conjunction with 2,3,5–F_3Y will result in observable build–up of an intermediate during radical transport.

REFERENCES

(1) Stubbe, J.; van der Donk, W. A. *Chem. Rev.* **1998**, *98*, 705.

(2) Jordan, A.; Reichard, P. *Annu. Rev. Biochem.* **1998**, *67*, 71.

(3) Nordlund, P.; Reichard, P. *Annu. Rev. Biochem.* **2006**, *75*, 681.

(4) Stubbe, J. *Proc. Natl. Acad. Sci. U. S. A.* **1998**, *95*, 2723.

(5) Brown, N. C.; Canellakis, Z. N.; Lundin, B.; Reichard, P.; Thelander, L. *Eur J Biochem* **1969**, *9*, 561.

(6) Ehrenberg, A.; Reichard, P. *J Biol Chem* **1972**, *247*, 3485.

(7) Uhlin, U.; Eklund, H. *Nature* **1994**, *370*, 533.

(8) Uhlin, U.; Eklund, H. *J. Mol. Biol.* **1996**, *262*, 358.

(9) Nordlund, P.; Sjöberg, B.-M.; Eklund, H. *Nature* **1990**, *345*, 593.

(10) Ekberg, M.; Birgander, P.; Sjoberg, B.-M. *J. Bacteriol.* **2003**, *185*, 1167.

(11) Ekberg, M.; Sahlin, M.; Eriksson, M.; Sjöberg, B.-M. *J. Biol. Chem.* **1996**, *271*, 20655.

(12) Climent, I.; Sjoberg, B. M.; Huang, C. Y. *Biochemistry* **1992**, *26*, 4801.

(13) Ge, J.; Yu, G.; Ator, M. A.; Stubbe, J. *Biochemistry* **2003**, *42*, 10071.

(14) von Dobeln, U., Reichard, P. *J. Biol. Chem.* **1976**, *253*, 3616.

(15) Allard, P.; Kuprin, S.; Shen, B.; Ehrenberg, A. *Eur. J. Biochem.* **1992**, *280*, 635.

(16) Yee, C. S.; Seyedsayamdost, M. R.; Chang, M. C. Y.; Nocera, D. G.; Stubbe, J. *Biochemistry* **2003**, *42*, 14541.

(17) Yee, C. S.; Chang, M. C. Y.; Ge, J.; Nocera, D. G.; Stubbe, J. *J. Am. Chem. Soc.* **2003**, *125*, 10506.

(18) Frieden, C. *J. Biol. Chem.* **1970**, *245*, 5788.

(19) Atkin, C. L.; Thelander, L.; Reichard, P. *J. Biol. Chem.* **1973**, *248*, 7464.

(20) Aubert, C., Vos, M. H.; Mathis, P.; Eker, A. P.; Brettel, K. *Nature* **2000**, *405*, 586.

(21) Gerez, C.; Gaillard, J.; Latour, J. M.; Fontecave, M. *Angew. Chem. Int. Ed. Engl.* **1991**, *30*, 1135.

(22) Gerez, C.; Fontecave, M. *Biochemistry* **1992**, *31*, 780.

(23) Licht, S. S.; Lawrence, C. C.; Stubbe, J. *J. Am. Chem. Soc.* **1999**, *121*, 7463.

(24) Licht, S.; Stubbe, J. In *Comprehensive Natural Products Chemistry*; Barton, S. D., Nakanishi, K., Meth-Cohn, O., Poulter, C. D., Eds.; Elsevier Science: New York, 1999; p. 163.

(25) Bollinger, J. M., Jr.; Tong, W.-H.; Ravi, N.; Huynh, B.-H.; Edmonson, D. E.; Stubbe, J. *J. Am. Chem. Soc.* **1994**, *116*, 8015.

(26) Ravi, N.; Bollinger Jr., J. M.; Huynh, B. H.; Edmondson, D. E.; Stubbe, J. *J. Am. Chem. Soc.* **1994**, *116*, 8007.

(27) Bollinger Jr., J. M.; Tong, W. H.; Ravi, N.; Huynh, B. H.; Edmondson, D. E.; Stubbe, J. *J. Am. Chem. Soc.* **1994**, *116*, 8024.

(28) Bollinger Jr., J. M.; Edmondson, D. E.; Huyuh, B. H.; Filley, J.; Norton, J. R.; Stubbe, J. *Science* **1991**, *253*, 292.

(29) Stubbe, J. *Chem. Commun.* **2003**, 2511.

(30) Licht, S.; Gerfen, G. G.; Stubbe, J. *Science* **1996**, *271*, 477.

(31) Lawrence, C. C.; Bennati, M.; Obias, H. V.; Bar, G.; Griffin, R. G.; Stubbe, J. *Proc Natl Acad Sci U S A* **1999**, *96*, 8979.

(32) Stubbe, J.; Nocera, D. G.; Yee, C. S.; Chang, M. C. Y. *Chem. Rev.* **2003**, *103*, 2167.

MOHAMMAD R. SEYEDSAYAMDOST

EDUCATION

2007 -	**Harvard Medical School**	Boston, MA
	Postdoctoral Student with Profs. Jon Clardy and Roberto Kolter	
2001 - 2007	**Massachusetts Institute of Technology**	Cambridge, MA
	Ph.D. Biological Chemistry with Prof. JoAnne Stubbe	
1997 - 2001	**Brandeis University**	Waltham, MA
	B.A./M.S. Biochemistry with Prof. Lizbeth Hedstrom, B.S. Biology	

PUBLICATIONS

Seyedsayamdost, M. R., Chan, C. T. Y., Mugnaini, V., Stubbe, J., Bennati, M. *J. Am. Chem. Soc.*, in press (2007).

Seyedsayamdost, M. R., Xie, J., Chan, C. T. Y., Schultz, P. G., Stubbe, J. *J. Am. Chem. Soc.*, in press (2007).

Reece, S. Y., **Seyedsayamdost, M. R.**, Stubbe, J., Nocera, D. G. *J. Am. Chem. Soc.* 129, 8500 (2007).

Seyedsayamdost, M. R., Yee, C. S., and Stubbe J. *Nat. Protoc.* 2, 1225-35 (2007).

Seyedsayamdost, M. R., and Stubbe, J. *J. Am. Chem. Soc.* 129, 2226-7 (2007).

Reece, S. Y., **Seyedsayamdost, M. R.**, Stubbe, J., and Nocera, D. G. *J. Am. Chem. Soc.* 128, 13654-5 (2006).

Seyedsayamdost, M. R., and Stubbe, J. *J. Am. Chem. Soc.* 128, 2522-3 (2006).

Seyedsayamdost, M. R., Reece, S. Y., Nocera, D. G., and Stubbe, J. *J. Am. Chem. Soc.* 128, 1569-79 (2006).

Seyedsayamdost, M. R., Yee, C. S., Reece, S. Y., Nocera, D. G., and Stubbe, J. *J. Am. Chem. Soc.* 128, 1562-68 (2006).

Guillen Schlippe, Y. V., Riera, T. V., **Seyedsayamdost, M. R.**, and Hedstrom, L. *Biochemistry* 43, 4511 (2004).

Yee, C. S., **Seyedsayamdost, M. R.**, Chang, M. C. Y., Nocera, D. G., and Stubbe, J. *Biochemistry* 42, 14541 (2003).

Gan, L., **Seyedsayamdost, M. R.**, Shuto, S., Matsuda, A., Petsko, G. A., and Hedstrom, L. *Biochemistry* 42, 857 (2003).

Hedstrom, L., Gan, L., Guillen Schlippe, Y. V., Riera, T. V., and **Seyedsayamdost, M. R.** *Nucleic Acids Res. Suppl.* 3, 97 (2003).

Seyedsayamdost, M. R. and Stubbe, J. *M.I.T. Chemistry Department Seminar*, Cambridge, MA (2007).

Seyedsayamdost, M. R., Yee, C. S., Reece, S. Y., Nocera, D. G., and Stubbe, J. *Frontiers in Metallobiochemistry*, Pennsylvania State University, State College, PA (2006).

Seyedsayamdost, M. R., Yee, C. S., Reece, S. Y., Nocera, D. G., and Stubbe, J. *Gordon Research Conference "Protein Cofactors, Radicals and Quinones,* Ventura, CA (2006).